

2023

Investigation of expanding diffuser based wind generation system for use in scaled hydrodynamic testing of floating offshore wind turbines

Guichard, Jessica

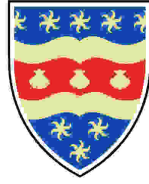
<https://pearl.plymouth.ac.uk/handle/10026.1/20621>

<http://dx.doi.org/10.24382/2670>

University of Plymouth

All content in PEARL is protected by copyright law. Author manuscripts are made available in accordance with publisher policies. Please cite only the published version using the details provided on the item record or document. In the absence of an open licence (e.g. Creative Commons), permissions for further reuse of content should be sought from the publisher or author.

This copy of the thesis has been supplied on condition that anyone who consults it is understood to recognize that its copyright rests with its author and that no quotation from the thesis and no information derived from it may be published without the author's prior consent.



**UNIVERSITY OF
PLYMOUTH**

**Investigation of expanding diffuser based wind
generation system for use in scaled hydrodynamic
testing of floating offshore wind turbines**

by

Jessica Guichard

A thesis submitted to the University of Plymouth
in partial fulfilment for the degree of

DOCTOR OF PHILOSOPHY

School of Engineering, Computing and Mathematics

March 2023

Acknowledgements

I want to thank my director of studies, Dr. Martyn Hann and my other supervisors, Prof. Deborah Greaves, Dr. Dave Simmonds, and Prof. Gregorio Iglesias for allowing me to work on this fascinating project and supporting me throughout.

I want to thank the various technicians at the university who made the experimental component of this project possible. I want to thank in particular Peter Arber, Alastair Reynolds and Dr. Kieran Monk for their important contribution to the experimental set-up and assistance during the measurements I did in the COAST Laboratory.

I also want to thank Dr. Carlos Pérez-Collazo for his contribution to the model wind turbine.

I would like to thank Dr. Martin Coath for help with the use of Latex, the software in which this thesis was written.

I want to thank my close and extended family for support with child minding, financial, and emotional support throughout my studies, which made it possible to get to the end of it.

Abstract

Investigation of expanding diffuser based wind generation system for use in scaled hydrodynamic testing of floating offshore wind turbine platforms

Jessica Guichard

Floating offshore wind turbines present a great potential for harnessing the power of offshore wind and meeting future energy demands. Though some floating offshore wind farms have already been commissioned, research on floating offshore wind turbine platforms needs to be pursued, in particular for the purpose of cost reduction. In this context, the ability to conduct scaled hydrodynamic testing of floating offshore wind turbine platforms is an important advantage for a wave tank. The COAST Laboratory of the University of Plymouth aims to provide this possibility. The wave tank being built before the decision to add a wind generation system had been made, the space available for the installation of a wind generation system is only limited, in particular without the use of a costly gantry to install axial fans at the location of where the wind is needed. This created the need for the investigation presented in this thesis on producing wind in the laboratory using centrifugal fans and a ducting system as well as an expanding diffuser. Flow distribution at the outlet of the wind generation system was determined both thanks to CFD in OpenFOAM and experimentally for various prototypes. The comparison of the results of 7 turbulence models to the experimental data provided by measurements done with the first prototype allowed the determination of 4 appropriate turbulence models in the context of indoor air flow, namely the standard $k - \epsilon$, the $k - \omega$ SST, the realizable $k - \epsilon$, and the RNG $k - \epsilon$ model. CFD simulations for larger prototypes using the 2 best turbulence model, that is, the $k - \omega$ SST and the realizable $k - \epsilon$ model, were done to predict the flow distribution of air coming out of a 33° angle conic diffuser with various structures inside and choose the best one to be built and studied experimentally. Structures inside the diffuser cone as well as honeycombs and meshed screens were able to help even flow distribution to a certain degree. However, the asymmetry of the flow caused by the 35° angle with which the air flow arrived at the beginning of the conic diffuser was too significant to be evened out. The laboratory wind generation system was used with a model version of the NREL 5 MW wind turbine at scale 1:50, using blades with low Reynolds number aerodynamic profiles. In spite of the asymmetry of the flow distribution, it showed that the model could be used in Froude scaled environment with a wind speed only slightly higher than Froude scaled wind to produce correct thrust. The wind generation system in combination with the low Reynolds number wind turbine allowed to study in laboratory conditions wind speeds corresponding to 13 m/s at full size on a model wind turbine.

Authors declaration

AT no time during the registration for the degree of Doctor of Philosophy has the author been registered for any other University award. Work submitted for this research degree at the University of Plymouth has not formed part of any other degree either at the University of Plymouth or at another establishment.

Word count for the main body of this thesis: **60589**

Signed:  _____

Date: 21/03/2023

Conference presentation:

2nd International Conference on Offshore Renewable Energy Glasgow *Design of a small wind generator for the experimental study of floating offshore wind turbines* 2016

Contents

Acknowledgements	iii
Abstract	iv
Author's declaration	v
1 Introduction	1
2 Literature review	6
2.1 Different types of floating platforms	6
2.1.1 Examples of SPAR Buoy platforms	8
2.1.2 Examples of semi-submersible platforms	10
2.1.3 Tension-Leg platform - Blue H Technologies	13
2.1.4 Barge/pontoon platform - IDEOL	14
2.1.5 Hybrid concept	15
2.2 Experimental testing of model wind turbines	15
2.2.1 Forces to be modelled when designing a floating wind turbine model	15
2.2.2 Choice of a wind turbine model - Properties of the NREL 5 MW wind turbine	17
2.2.3 Non-dimensional numbers to be considered when designing a floating wind turbine model	18
2.2.4 Reynolds number and Froude number conflict	21

2.3	Various methods for laboratory testing to overcome Froude and Reynolds scale conflict	22
2.3.1	Mechanical pulley system	22
2.3.2	Actuator system	25
2.3.3	Simulating varying aerodynamic thrust by means of a fan on the tower top	28
2.3.4	Wind generation on drag disc	30
2.3.5	Wind generation on model turbine	36
2.4	Literature review on wind generators	45
2.4.1	Requirements for wind speed	45
2.4.2	Requirements for outlet size	46
2.4.3	Requirements for turbulence levels	46
2.4.4	Literature review on honeycombs and meshed screens	48
2.4.5	Existing wind tunnels	50
2.4.6	Literature review on conical diffusers	56
2.5	CFD simulations of turbulent steady state indoor air flow	68
2.5.1	Description of one and two equation turbulence models	69
2.5.2	Finite Volume Method	72
2.5.3	Law of the wall	73
2.5.4	Description of discretization schemes	74
2.5.5	SIMPLE algorithm	75
2.5.6	Review of indoor air simulation using steady state airflow	75
3	Design and testing of a small wind generation system	78
3.1	Set up of the small wind generation system	78
3.2	Evolution of wind speed with the electric frequency of the fans and its dependence on the flow straighteners used	81
3.3	Impact of flow straighteners on turbulence intensity	83

3.4	Variation of wind speed and turbulence intensity with distance from the outlet on the central axis	87
3.5	Comparison of theoretical and experimental turbulence reduction factor	87
3.6	Variation of wind speed and turbulence intensity as a function of location in space	91
3.7	Conclusion for the measurements done on the small wind generation system	97
4	CFD simulation of wind generation in the laboratory	99
4.1	General set-up of all the CFD simulations	99
4.2	Wind field produced by the small wind generator determined through CFD simulation	99
4.2.1	Set up of the CFD simulations	100
4.2.2	Mesh convergence study	102
4.2.3	Comparison between calculated data and experimental values .	107
4.2.4	Difference between CFD results and experimental data	107
4.3	CFD simulation of the wind field produced by the large wind generator using a diffuser cone	115
4.3.1	Wind generator with 3 m diameter circular outlet and 1 m diameter inlet	116
4.3.2	Wind generator with 3 m diameter circular outlet and long inner cone	130
4.4	Conclusion for the CFD study of 3 different types of wind generation systems	139
5	Wind generation system using two 35.2 kW centrifugal fans	141
5.1	Wind generator with 1.6 m square outlet	144
5.1.1	Experimental Set-up	145
5.1.2	Results	149

5.2	Wind generator with 3 m diameter circular outlet and 1 m diameter inlet	
	- Outlet 2a and 2b	154
5.2.1	Experimental set up of the large wind generator	154
5.2.2	Wind field measured for the large wind generator	156
5.3	Wind generator with 3 m diameter circular outlet and long inner cone -	
	Outlet 3a	160
5.3.1	Improvements on previous set-up	160
5.3.2	Wind field measured for Outlet 3a	167
5.4	3 m diameter outlet in the centre of the basin - Outlet 3b	169
5.4.1	Description of measurements	169
5.4.2	Results	172
5.5	Conclusion for the experimental study of the wind generation systems	
	using two 35.2 kW centrifugal fans	176
6	Model wind turbine design and test using the laboratory wind genera-	
	tion system	178
6.1	Choice of a wind turbine model	180
6.2	Blade Element Momentum theory applied to the Drela AG04 blade . . .	180
6.2.1	Prandtl tip loss factor and Glauert correction	181
6.2.2	Results obtained using the Matlab code for the BEM theory ap-	
	plied to the Drela AG04 blade	182
6.3	Blade manufacture	184
6.4	Experimental testing of the wind turbine	184
6.4.1	Description of the wind turbine model	184
6.4.2	Experimental conditions	185
6.4.3	Results	186
6.4.4	Comparison to target thrust and thrust calculated through BEM	
	calculations	189
6.5	Discussion on the use of this method with a floating platform	190

6.6	Conclusion for the experimental study of the model wind turbine	190
7	Conclusion	192
	Appendices	196
	Appendix A NREL 5 MW reference wind turbine data	197
A.1	Properties of the NREL 5 MW reference wind turbine at full scale and at reduced scale	197
A.2	NREL 5 MW reference wind turbine blade geometry	201
	Appendix B Additional information on experiments with the small fans	202
B.1	Overview of measurements done for the set up with the small fans . . .	202
B.2	Properties of the small centrifugal fans	204
B.2.1	Flow rate	204
	Appendix C Snapshots of CFD simulations for the large wind generation system	205
C.1	Snapshots of CFD simulations for 1 m to 3 m diameter diffuser with and without various inner concentric cones	205
C.1.1	Empty cone	205
C.1.2	Set of 3 concentric cones	206
C.1.3	2 external cones only	207
C.1.4	2 inner cones	208
C.1.5	Most outer cone	209
C.1.6	Most inner cone	210
C.1.7	Most inner and most outer cone	211
C.1.8	Central cone	212
C.2	Snapshots of CFD simulations with long inner cone	213
C.2.1	Cone length 3.4 m, 1 m diameter inlet, no subdivisions, narrow .	213
C.2.2	Cone length 2.72 m, 1.4 m diameter inlet, no subdivisions, narrow	214

CONTENTS

C.2.3	Cone length 2.04 m, 1.8 m diameter inlet, no subdivisions, narrow	215
C.2.4	Cone length 1.36 m, 2.2 m diameter inlet, no subdivisions, narrow	216
C.2.5	Cone length 3.4 m, 1 m diameter inlet, no subdivisions, wide . . .	217
C.2.6	Cone length 2.04 m, 1.8 m diameter inlet, 4 subdivisions, wide . .	218
C.2.7	Cone length 2.04 m, 1.8 m diameter inlet, 6 subdivisions, wide . .	219
C.2.8	Cone length 2.04 m, 1.8 m diameter inlet, 8 subdivisions, wide . .	220
Appendix D Additional information for the experiments with the large fans		222
D.1	Properties of the large centrifugal fans	222
D.2	Measurement results presented for the whole area for the 1 m to 3 m diameter outlet	223
D.3	Overview of the measuring points for the 1.8 m to 3 m diameter outlet placed in the centre of the basin	229
Appendix E Technical drawing of a wind turbine blade		230
Appendix F Blade geometry of the low Reynolds wind turbine based on the Drela AG04 profile		236
F.1	Original Drela AG04 profile coordinates	236
F.2	Centreline of Drela AG04 airfoil	240
F.3	Blade offsets for the MARIN stock wind turbine taken from Kimball et al. (2014)	244
F.4	Aerodynamic profile coordinates	245
F.4.1	Section 1	245
F.4.2	Section 2	246
F.4.3	Section 3	247
F.4.4	Section 4	248
F.4.5	Section 5	248
F.4.6	Section 6	249
F.4.7	Section 7	250

CONTENTS

F.4.8	Section 8	254
F.4.9	Section 9	258
F.4.10	Section 10	262
F.4.11	Section 11	266
F.4.12	Section 12	270
F.4.13	Section 13	274
F.4.14	Section 14	278
F.4.15	Section 15	282
F.4.16	Section 16	286
F.4.17	Section 17	290
F.4.18	Section 18	294
F.4.19	Section 19	298
F.4.20	Section 20	301
F.4.21	Section 21	305
F.4.22	Section 22	309
F.4.23	Section 23	313
F.4.24	Section 24	317
F.4.25	Section 25	321
Appendix G Additional information for the experiments with the model		
wind turbine		
		326
G.1	Iterative procedure for applying the BEM Method	326
G.2	Various suggestions for Glauert correction found in literature	328
G.3	Lift and Drag coefficients used in the BEM method	330
G.4	Design and manufacture of the blades	333
G.4.1	CFD calculation of aerodynamic loads	333
G.4.2	Finite Element (FE) Analysis of the wind turbine blade	335
G.4.3	Properties of material used in FEA calculation	337
G.5	List of measurements done with the model wind turbine	338

List of Figures

1.1	Flow chart illustrating the link between topics treated in different chapters	5
2.1	Different types of support structures for floating offshore wind turbines (Inspired by image found in Courbois (2013), originally from Philippe (2012), wind turbine line drawing from SeekPNG (n.d.))	6
2.2	Centre of gravity, centre of buoyancy and metacentre, wind turbine line drawing from SeekPNG (n.d.)	7
2.3	Hywind SPAR buoy platform (taken from EWEA-WindEurope (2013) with the permission of WindEurope (formerly EWEA))	9
2.4	Advanced SPAR concept used for Fukushima Hamakaze (5 MW), taken from Ishihara et al. (2014) with the permission of T. Ishihara	9
2.5	Fukushima Hamakaze (5 MW), taken from Fukushima Offshore Wind Consortium (n.d.b) with the permission of T. Ishihara. Original image taken from Sawaji (2016) had to be taken out, as the copyright owner could not be contacted.	10
2.6	Platform for Fukushima Hamakaze wind turbine keeled to 45 degrees during installation phase (taken from Foster (2016))	10
2.7	2 MW floating demonstration wind turbine Fukushima Mirai, installed in 2013, (taken from Fukushima Offshore Wind Consortium (n.d.a) with the permission of T. Ishihara)	12

2.8	Fukushima Shinpu 7 MW wind turbine using V-shaped semi-submersible platform (taken from Ishihara et al. (2014) with the permission of T. Ishihara). Original image from PowerTechnology (n.d.) was taken out as copyright owner could not be contacted	12
2.9	Fukushima Shinpu 7 MW wind turbine using V-shaped semi-submersible platform (taken from Sawaji (2016), also found in Fukushima Offshore Wind Consortium (n.d.b), with the permission of T. Ishihara)	13
2.10	Towed Fukushima Mirai wind turbine. Photo taken from Ishihara et al. (2014) with permission of T. Ishihara. Original photo: Photo of the Wind-Float 2 MW prototype installed in 2011 near Portugal. Ballasting and connection to the offshore tug vessel Bourbon Liberty 228 (Principle Power, 2011). Had to be taken out, as copyright owner could not be contacted	13
2.11	Blue H Technologies concept for tension leg platform (Jakubowski, 2009), with the permission of M. Jakubowski	14
2.12	Blue H Technologies prototype during installation (Jakubowski, 2009), with the permission of M. Jakubowski	14
2.13	Blue H Technologies 80 kW prototype (Permission granted by M. Jakubowski, founder of Blue H Technologies)	14
2.14	Moonpool platform by IDEOL (Molga, 2021), permission granted by Ideol	14
2.15	TetraSpar concept by Henrik Stiesdal tested at DHI (OffshoreWIND.biz, 2017), permission granted by Stiesdal	15
2.16	Degrees of freedom of a floating wind turbine platform (Tran and Kim, 2015)	16
2.17	Yaw moment experienced by the platform in the case of rotation about the pitch axis, wind turbine line drawing from SeekPNG (n.d.)	17
2.18	Pitch moment experienced by the platform in the case of rotation about the yaw axis, wind turbine line drawing from SeekPNG (n.d.)	17

2.19 Variables used to calculate the tip speed ratio of a wind turbine, wind turbine line drawing from SeekPNG (n.d.)	20
2.20 Schematic of laboratory set-up for the mechanical pulley system (side view), adapted from Matha et al. (2015), with the permission of The Royal Society Publishing obtained via the Copyright Clearance Center .	23
2.21 Schematic of Laboratory set-up for mechanical pulley system (Top view), adapted from Matha et al. (2015), with the permission of The Royal Society Publishing obtained via the Copyright Clearance Center	23
2.22 Schematic illustrating concept of actuator system. Reproduced from Hall et al. (2014), permission given by ASME Publishing.	25
2.23 Schematic of six-wire pulley system that applies aerodynamic forces calculated by Aerodyn on the tower top, reproduced from Bachynski et al. (2016) with the permission of M. Thys from SINTEF Ocean	28
2.24 Actuator system set up by MARINTEK, reproduced from Sauder et al. (2016b) with the permission of ASME Publishing	28
2.25 Measurement of thrust produced through ducted fan by means of a bending load cell (Wright et al., 2015)	29
2.26 Measurement of thrust produced through ducted fan by means of a sheet metal and strain gauges, reproduced from Wright et al. (2015a) with the permission of MARINET	29
2.27 Use of a multi-propeller device to simulate various aerodynamic forces (Otter et al., 2020)	30
2.28 Evolution of the drag coefficient of a solid disc with the Reynolds number, reproduced from White (2016), with the permission of McGraw Hill . . .	31
2.29 Experimental testing of floating wind turbine using drag disc model for operational and extreme conditions. Reproduced (Wan et al., 2014a) with the permission of ASME Publishing	32

LIST OF FIGURES

2.30 Drag disc experiments at CNR-INSEAN, Rome, Italy. Found in Wright et al. (2015a), originally from (Wan et al., 2014b). Permission obtained by MARINET	33
2.31 Trifloater scaled experiment with gauzed discs representing the wind turbines reproduced from Ishihara et al. (2007), permission given by T. Ishihara	33
2.32 Porous disc used by Aubrun et al. (2011), permission granted by S. Aubrun	34
2.33 Dimensionless velocity deficit 0.5 rotor diameters behind the rotor or the porous disc (Aubrun et al., 2011), permission granted by S. Aubrun . . .	34
2.34 Drag disc used by University of California Berkeley. Reproduced from Roddier et al. (2010), with the permission of AIP Publishing obtained via the Copyright Clearance Center	35
2.35 Drag disc and driven rotor at Worcester Polytechnic Institute. Found in Wright et al. (2015a). Originally from Naqvi (2012). Permission given by MARINET	36
2.36 Definition of camber and chord	37
2.37 Comparison of C_P and C_T vs TSR between the prototype and a geometrically scaled model wind turbine (taken from Martin et al. (2012) with the permission of ASME Publishing obtained through the Copyright Clearance Center)	38
2.38 Comparison of lift and drag coefficients for the NACA 64-618 profile for high and low Reynolds numbers (taken from Martin et al. (2012) with the permission of ASME Publishing obtained through the Copyright Clearance Center)	38
2.39 Lift and drag coefficient of Mark Drela AG04 profile and comparison to NACA profile at low and high Reynolds numbers (taken from Martin et al. (2012) with the permission of ASME Publishing obtained through the Copyright Clearance Center)	40

2.40 Comparison of the NACA 64-618 profile with the Drela AG04 and the modified Drela AG04 profile (coordinates taken from Kimball et al. (2014) for the modified Drela profile, Jackman (2005) for the original Drela AG04 profile, and UIUC Applied Aerodynamics Group - Department of Aerospace Engineering (n.d.) for the NACA 64-618 profile)	41
2.41 Pressure distribution on Drela AG04 profile calculated by XFOIL (taken from De Ridder et al. (2014) with the permission of ASME Publishing) .	41
2.42 Pressure distribution on modified Drela AG04 profile calculated by XFOIL (taken from De Ridder et al. (2014) with the permission of ASME Publishing)	42
2.43 Comparison of the C_T and C_P of the Marine Stock Wind turbine using the modified Drela AG04 profile determined through BEM (Propid), CFD (ReFRESCO) and experimentally with the target values of the NREL 5 MW wind turbine (De Ridder et al., 2014) with the permission of ASME Publishing	42
2.44 Comparison of RG14 profile and NACA 64-618 profile	43
2.45 Blade chord as function of blade span of low Reynolds rotor compared to NREL 5 MW (Sandner et al., 2014), with the permission of F. (Sandner) Lemmer	44
2.46 Low Reynolds rotor used by Sandner et al. (2014), with the permission of F. (Sandner) Lemmer	44
2.47 Thrust coefficient C_T as a function of laboratory wind speed for the low Reynolds number model wind turbine used by Pegalajar-Jurado et al. (2016)	45

2.49 Classic closed circuit wind tunnel adapted from Barlow et al. (1999). re-produced with the permission of John Wiley & Sons obtained via the Copyright Clearance Center. Legend: (a) test section (b) diffuser (c) "first corner" with turning vanes (d) second leg: continues diffuser or constant area (e) safety screen to prevent parts of failed models or other unintended flying objects from reaching the fan (f) "second corner" (g) transition from rectangular to circular cross section to take flow into the fan (h) Fan and straightener section (i) return or second diffuser: transition back to rectangular from the circular cross section at the fan (j) "third corner" (k) third leg that may be constant area (l) heat exchanger (m) "fourth corner" (n) wide-angle diffuser with separation control screens (o) settlement area (p) flow conditioners typically including flow straighteners and turbulence control screens (q) contraction or nozzle	51
2.50 Open circuit wind blower with closed test section adapted from Imperial College London (n.d.), originally from Mehta and Bradshaw (1979)	51
2.51 Wind generator at INSEAN (Wan et al., 2014b)	52
2.52 Wind blower system at the Ecole Centrale de Nantes (taken from Courbois (2013) with the permission of A. Courbois)	53
2.53 Diagram showing the set up of the Wind blower system in the Ecole Centrale de Nantes (taken from Courbois (2013) with the permission of A. Courbois), with translated annotations	53
2.54 Wind blower at Ifremer Brest (taken from Ohana et al. (2014a) with the permission of J. Ohana)	54
2.55 Wind blower at Ifremer Brest (taken from Ohana et al. (2014) with the permission of J. Ohana). (1) Flow generated by axial fans passes through square section cells. Each fan's flow is divided in 4 parts. (2) Independent settling chambers for each row of fans (3) Mesh screen (4) Honeycomb with rectangular cells. This section diminishes the swirl and lateral/vertical mean velocities.	54

2.56 Sheared wind profiles produced by the wind blower at Ifremer Brest (Ohana et al., 2014). With the permission of J. Ohana	55
2.57 Wind blower at MARIN (found in Wright et al. (2015a), originally taken from Gao (2013)). From left to right is shown: the bank of fans, screens and the nozzle	55
2.58 Wind blower at University of California, Berkeley. Reproduced from Roddier et al. (2010) with the permission of AIP Publishing obtained via the Copyright Clearance Center	56
2.59 Wind blower University of Malta. Reproduced from Farrugia et al. (2014) with permission from Elsevier	56
2.60 Cross section of the conical diffuser described in this section. The figure shows the ideal homogeneous flow distribution.	57
2.61 Boundary layer profiles for various pressure gradients, reproduced from White (2016) with permission from McGraw Hill	58
2.62 Diffuser with boundary layer separation. Reproduced from White (2016) with permission from McGraw Hill	59
2.63 (a) geometry of flat-walled diffuser (b) geometry of conical diffuser (c) Stability map of diffuser flow patterns. 2θ is the opening angle of the diffuser. $\frac{L}{W_1}$ is the ratio between the length and the inlet width of the diffuser (See also Subfigures (a) and (b)). C_p is the pressure recovery coefficient. Published originally by Fox and Kline (1962), taken from White (2016), who took it from Runstadler and Dolan (1975). Permission granted by McGraw Hill	59
2.64 Inner conical diffusers used by Prync-Skotniczny (2006) to improve performance of conical diffuser with very large opening angle. Image can be found in Prync-Skotniczny (2006). Figure 3 on page 73	60
2.65 Solution to push boundary layer separation further downstream: Blow through walls of diffuser (drawing inspired by diagram found in Idelchik (1966))	62

2.66 Suction of boundary layer to push occurrence of boundary layer further downstream (drawing inspired by diagram found in Idelchik (1966)) . . .	62
2.67 Illustration of guide vanes for even flow distribution inside a diffuser (drawing inspired by diagram found in Idelchik (1966))	63
2.68 Illustration of dividing walls inside a diffuser (drawing inspired by diagram found in Idelchik (1966))	64
2.69 Curved diffuser (drawing inspired by diagram found in Idelchik (1966)) .	65
2.70 Multistage diffuser (drawing inspired by diagram found in Idelchik (1966))	65
2.71 Installation of a honeycomb or meshed screen for even flow distribution (drawing inspired by diagram found in Idelchik (1966))	66
2.72 Ring shaped Karman Vortex Generator (not to scale)	67
2.73 Karman Vortex Generator on airplane wing, in front of flap, for flow separation and stall prevention and increase of lift. Figure 6 b on page 5 of Veldhuis et al. (2012), with permission from L. Veldhuis	67
2.74 Screw tape insert for conical diffuser (Shukri, 2018)	68
2.75 Typical velocity profile for a turbulent boundary layer. Graph inspired by graph found in Wilcox (2006). Original graph can be found in Wilcox (2006). Figure 1.7 on page 17	74
3.1 Sketch of the wind generator	78
3.2 Dimensions of the duct	79
3.3 Set-up of the small scale wind generator prototype	79
3.4 Set-up of the outlet and the anemometer	81
3.5 Wind speed as a function of the electric frequency of the fans, for different flow straightening screens	82
3.6 Wind speed as a function of the electric frequency of the fans for different flow straightening honeycombs	83
3.7 Lateral turbulence intensity for various honeycombs combined with the 73 μ m screen at 25 cm from the outlet on the central axis	84

LIST OF FIGURES

3.8	Longitudinal turbulence intensity for various honeycombs combined with the 73 μm screen at 25 cm from the outlet on the central axis	84
3.9	Lateral turbulence intensity without any flow straightener and with a 12 mm honeycomb only at 25 cm from the outlet on the central axis	85
3.10	Longitudinal turbulence intensity without any flow straightener and with a 12 mm honeycomb only at 25 cm from the outlet on the central axis	85
3.11	Lateral turbulence intensity u at 25 cm from the outlet along the central axis	86
3.12	Longitudinal turbulence intensity v at 25 cm from the outlet along the central axis	86
3.13	Increase of longitudinal and lateral turbulence intensity with distance from the outlet (12 mm honeycomb/320 μm screen, 45 Hz) along the central axis	87
3.14	Longitudinal TRF of the 12 mm honeycomb when combined with the 1000 μm screen, the 500 μm screen or used alone ('no screen')	88
3.15	Longitudinal TRF of the 1000 μm screen when combined with the 12 mm screen or used alone ('no honeycomb')	89
3.16	Lateral TRF for the 12 mm honeycomb	90
3.17	Lateral TRF of the 1000 μm screen when combined with the 12 mm honeycomb and when used by itself	90
3.18	Situation in space of the wind speed shown in Figure 3.19	92
3.19	V/V_{max} at 50 cm from the outlet and 20 cm above the central axis	92
3.20	Longitudinal turbulence intensity at 20 cm above the central axis and at 50 cm from the outlet	93
3.21	Situation in space of turbulence intensity shown in Figure 3.22	93
3.22	Longitudinal turbulence intensity at 50 cm from the outlet and 25 cm above the central axis	94
3.23	V/V_{max} at 50 cm from the outlet and 25 cm above the central axis	95

3.24	Wind speed distribution in plane perpendicular to main direction of air flow at 1 m from the outlet with 4 mm honeycomb and 320 μm screen . . .	96
3.25	Distribution of wind speed in plane perpendicular to main direction of flow at 1 m from the outlet with no honeycomb and a 73 μm screen . . .	97
4.1	Size of simulation domain	100
4.2	Boundary conditions	101
4.3	Evolution of wind speed with number of cells 0.3 m from the central axis of the flow and at mid height of the outlet	103
4.4	Evolution of turbulence kinetic energy with number of cells 0.3 m from the central axis of the flow and at mid height of the outlet	104
4.5	Rate of change of the wind speed with the number of cells for various turbulence models	105
4.6	Rate of change of the turbulence kinetic energy with the number of cells for various turbulence models	106
4.7	Comparison between the average wind speed calculated by various turbulence models and the experimental data at four different distances from the outlet and at mid-height of the outlet	108
4.8	Comparison between the turbulence kinetic energy calculated by various turbulence models and the experimental data at four different distances from the outlet and at mid-height of the outlet	109
4.9	Comparison of relative differences between wind speed calculated by various turbulence models and measured data at various distances from the central axis of the flow	110
4.10	Comparison of relative differences between wind speed calculated by various turbulence models and measured data at various distances from the central axis of the flow - zoom of Figure 4.9	111
4.11	Comparison of relative differences between the turbulence kinetic energy of various turbulence models and measured data at various distances from the central axis of the flow	112

4.12 Average relative difference for each turbulence model for the wind speed	113
4.13 Average relative difference for each turbulence model for the turbulence kinetic energy	113
4.14 Schematic of the general set up of the large wind generation system . .	115
4.15 Stability map (see Figure 2.63 from Section 2.4.6 adapted from White (2016)) with position of diffuser cone studied. 2θ is the opening angle of the diffuser. $\frac{L}{w_1}$ is the ratio between the length and the inlet width of the diffuser.	116
4.16 Slice across basic domain parallel to the main direction of the air flow. Inner cones are not represented	117
4.17 Wind speed calculated at 130 mm from the end of the outlet using the $k - \omega$ -SST model for various mesh sizes	118
4.18 Wind speed calculated at 130 mm from the end of the outlet using the $k - \omega$ -SST model for the most relevant mesh sizes	119
4.19 Standard deviation of wind speed calculated at 130 mm from the end of the outlet using the $k - \omega$ -SST model for the most relevant mesh sizes .	120
4.20 Wind speed calculated at 130 mm from the end of the outlet using the realizable $k - \varepsilon$ model for various mesh sizes	121
4.21 Wind speed calculated at 130 mm from the end of the outlet using the realizable $k - \varepsilon$ model for most relevant mesh sizes	122
4.22 Standard deviation of wind speed calculated at 130 mm from the end of the outlet using the realizable $k - \varepsilon$ model for the most relevant mesh sizes	122
4.23 Comparison of the wind speed calculated for the realizable $k - \varepsilon$ model and the wind speed calculated for the $k - \omega$ SST model when no concentric inner cones are used inside the diffuser	123
4.24 Dimensions of concentric cones	124
4.25 Wind speed calculated at 130 mm from the end of the outlet using the $k - \omega$ -SST model for various mesh sizes when diffuser cones are inside the outlet cone	124

4.26 Wind speed calculated at 130 mm from the end of the outlet using the $k - \omega$ -SST model for most relevant mesh sizes when diffuser cones are inside the outlet cone	125
4.27 Standard deviation of wind speed varying with mesh size for the $k - \omega$ SST model	125
4.28 Wind speed calculated at 130 mm from the end of the outlet using the realizable $k - \epsilon$ model for various mesh sizes when diffuser cones are inside the outlet cone	126
4.29 Wind speed calculated at 130 mm from the end of the outlet using the realizable $k - \epsilon$ model for various mesh sizes when diffuser cones are inside the outlet cone	127
4.30 Standard deviation of wind speed varying with mesh size for the $k - \epsilon$ model	127
4.31 Comparison of the wind speed calculated for the realizable $k - \epsilon$ model and the wind speed calculated for the $k - \omega$ SST model when 3 concentric inner cones are used inside the diffuser	128
4.32 Wind speed in slice parallel to the main direction of the airflow	129
4.33 Wind speed	129
4.34 Wind speed in slice parallel to the main direction of air flow	130
4.35 Wind speed in slice parallel to the main direction of the air flow	130
4.36 Slice across basic domain parallel to the main direction of the air flow. The inner cones and subdivisions are not represented	132
4.37 Cross section parallel to the main direction of the flow for the diffuser with a 1 m inlet diameter and a long inner cone with a diameter measuring a 1/3 of the outer diffuser. No subdivisions were used	133
4.38 Cross section perpendicular to the main direction of the flow for the diffuser with a 1 m inlet diameter and a long inner cone with a diameter measuring a 1/3 of the outer diffuser. No subdivisions were used	133

LIST OF FIGURES

4.39	Cross section parallel to the main direction of the flow for the diffuser with a 1.8 m inlet diameter and a long inner cone with a diameter measuring a 1/3 of the outer diffuser. No subdivisions were used	134
4.40	Cross section perpendicular to the main direction of the flow for the diffuser with a 1.8 m inlet diameter and a long inner cone with a diameter measuring a 1/3 of the outer diffuser. No subdivisions were used	134
4.41	Cross section parallel to the main direction of air flow for a diffuser with a 1 m inlet diameter and a long inner cone with a diameter measuring a 1/2 of the outer diffuser. No subdivisions were used	136
4.42	Cross section perpendicular to the main direction of air flow for a diffuser with a 1 m inlet diameter and a long inner cone with a diameter measuring a 1/2 of the outer diffuser. No subdivisions were used	136
4.43	Cross section parallel to the main direction of the flow for a 1.8 m diameter inlet using 6 subdivisions and an inner cones measuring 1/2 of the outer diameter	137
4.44	Cross section perpendicular to the main direction of the flow for a 1.8 m diameter inlet using 6 subdivisions and an inner cones measuring 1/2 of the outer diameter	138
4.45	Cross section parallel to the main direction of the flow for a 1.8 m diameter inlet using 8 subdivisions and an inner cones measuring 1/2 of the outer diameter	138
4.46	Cross section perpendicular to the main direction of the flow for a 1.8 m diameter inlet using 8 subdivisions and an inner cones measuring 1/2 of the outer diameter	139
5.1	Schematic of general set up of the wind generation system version 1	142
5.2	Schematic of general set up of the wind generation system version 2	142
5.3	Technical drawing of fan set up	143
5.4	Overview of experimental set ups using the two large centrifugal fans	144
5.5	View from above of the set up for the 1.6 m square outlet	145

LIST OF FIGURES

5.6	Dimensions of square to round outlet	146
5.7	Outlet on wooden frame during installation phase	146
5.8	Metal structure that combines air flow coming from the 2 centrifugal fans	147
5.9	Technical drawing of structure combining the flow of the 2 fans	147
5.10	Polythene duct that guides air from fans to outlet situated at the centre of the basin	148
5.11	Traverse and anemometer used to measure the wind at various positions near the outlet	148
5.12	Honeycombs inside outlet, held in place through aluminium T's	149
5.13	Fan power 30 %, without additional honeycomb, 0 m from outlet	150
5.14	Fan power 50 %, without additional honeycomb, 0 m from outlet	150
5.15	Fan power 30 % with honeycomb, 1 m from outlet	151
5.16	Fan power 50 % with additional honeycomb, 0 m from outlet	151
5.17	Fan power 50 %, with additional honeycomb, 1 m from outlet	152
5.18	Fan power 80 %, with additional honeycomb, 1 m from outlet	152
5.19	Total flow rate of the two large centrifugal fans as a function of the per- centage of the maximum rotational speed	153
5.20	Average wind speed across the 1.6 by 1.6 m square outlet produced by the 2 large centrifugal fans	153
5.21	Truncated cone diffuser	154
5.22	Set of nested concentric cones situated inside the diffuser cone	155
5.23	Diffuser cone with concentric cones on the inside	155
5.24	Dimensions of inner cones (same as Figure 4.24)	156
5.25	Coordinate system used for graphs	156
5.26	Average longitudinal wind speed measured at various horizontal posi- tions at heights -800, 0 and 800 mm for a fan rotational speed of 50 % of the maximum rotational speed, scaled CFD results at height 0 mm . .	157
5.27	Instantaneous longitudinal wind speed over 30 min. without concentric cones	158

LIST OF FIGURES

5.28 Average longitudinal wind speed measured over 1 minute at various heights for a fan rotational speed of 50 % of the maximum rotational speed, scaled CFD results at height 0 mm	159
5.29 View from above of the whole wind generation system, including fans, structure to combine fan air flow, polythene duct and diffuser	160
5.30 Wooden structure to combine the airflow of the two fans	161
5.31 Wooden structure to combine the air flow of the two fans	161
5.32 Polythene duct guiding air from wooden structure which combines air flow of the two fans to the diffuser	161
5.33 Technical drawing of Outlet 3	162
5.34 Diffuser	162
5.35 Long inner cone and dividing walls inside the conical diffuser and structure to hold anemometer for measurements	163
5.36 Honeycomb upstream of diffuser cone	165
5.37 Short straight cylindrical section holding the meshed screen (visible) and the honeycomb in place (hidden)	166
5.38 Diffuser cone with flow straighteners installed and structure to hold anemometer for measurements	166
5.39 Average longitudinal wind speed measured with and without flow straighteners 400 mm below the centre of the outlet	167
5.40 Average longitudinal wind speed measured with and without flow straighteners at the centreline of the outlet, CFD results	167
5.41 Average longitudinal speed measured across the whole area when the flow straighteners are not present	168
5.42 Average longitudinal speed measured across the whole area when the flow straighteners are present	168
5.43 Longitudinal turbulence intensity calculated from measurements done with and without flow straighteners 400 mm below the centre of the outlet	168

LIST OF FIGURES

5.44 Longitudinal turbulence intensity calculated from measurements done with and without flow straighteners at the centreline of the outlet	168
5.45 Longitudinal turbulence intensity (%) calculated from measurements across the whole area when flow straighteners are not present	169
5.46 Longitudinal turbulence intensity (%) calculated from measurements across the whole area when flow straighteners are present	169
5.47 Guide vanes	170
5.48 Structure near fans including wooden structure to combine air flow of the two fans and first set of guide vanes	170
5.49 Diffuser cone in centre of basin with second set of guide vanes	171
5.50 Ducting system from fans to outlet	171
5.51 Ducting system from fans to outlet	171
5.52 Comparison of average longitudinal wind speed at 130 mm from the outlet at 100% fan power and at Height=-1100mm for straight and angled duct	173
5.53 Comparison of average longitudinal wind speed at 130 mm from the outlet at 100% fan power and at Height=-840mm for straight and angled duct	173
5.54 Comparison of average longitudinal wind speed at 130 mm from the outlet at 100% fan power and at Height=0mm for straight and angled duct	174
5.55 Comparison of average longitudinal wind speed at 130 mm from the outlet at 100% fan power and at Height=800mm for straight and angled duct	174
5.56 Evolution of the average longitudinal wind speed with distance from the outlet for different fan powers	175
5.57 Evolution of longitudinal turbulence intensity with distance from outlet for various fan powers	176
6.1 Model wind turbine	179
6.2 Model wind turbine	179

LIST OF FIGURES

6.3	C_T before and after Glauert correction, graph inspired by graph from Hansen (2000). Original image is Figure 6.5 on page 54.	181
6.4	Wind field behind an ideal wind turbine, drawing inspired by image found in Hansen (2000). Original image is Figure 4.6 on page 34.	182
6.5	Turbulent-wake state induced by the unstable shear flow at the edge of the wake, drawing inspired by image found in Hansen (2000). Original image if Figure 4.7 on page 35.	182
6.6	Thrust calculated compared to the target thrust	183
6.7	Torque calculated for varying blade pitch through BEM code for scaled down combinations of wind speed and rotor speed used for the NREL 5 MW wind turbine	183
6.8	Wind turbine blades	184
6.9	Model wind turbine with wind generation system	185
6.10	Model wind turbine	185
6.11	Thrust as a function of rotor speed	186
6.12	Evolution of C_T with TSR for wind speeds 7 and 13 m/s (full scale wind speeds)	187
6.13	Measurements obtained at MARIN using the MSWT (MARIN stock wind turbine) with the modified Drela AG04 profile for three different wind speeds speeds (Kimball et al., 2014). Permission granted by ASME Publishing.	188
6.14	Thrust as a function of rotor speed for the case of no wind speed and a blade pitch angle of -30°	189
6.15	Comparison of thrust to be achieved, thrust calculated through BEM method and thrust measured	190
A.1	Rotor speed of model wind turbine	199
A.2	Rotor speed of full size wind turbine	199
A.3	Tip Speed ratio	199
A.4	Blade pitch	200

LIST OF FIGURES

A.5 Rotor thrust of model wind turbine	200
A.6 Rotor thrust full size wind turbine	200
B.1 Properties of the 1.8 kW centrifugal fans (Fans & Blowers Ltd. (2016))	204
C.1 Wind speed in slice parallel to the main direction of the airflow	205
C.2 Wind speed in slice perpendicular to the main direction of the air flow	206
C.3 Wind speed in slice parallel to the main direction of the airflow	206
C.4 Wind speed in slice perpendicular to the main direction of the flow	207
C.5 Wind speed in slice parallel to the main direction of the flow	207
C.6 Wind speed in slice perpendicular to the main direction of the flow	208
C.7 Wind speed in slice parallel to the main direction of the air flow	208
C.8 Wind speed in slice perpendicular to the main direction of the air flow	209
C.9 Wind speed in slice parallel to the main direction of air flow	209
C.10 Wind speed in slice perpendicular to the main direction of air flow	210
C.11 Wind speed in slice parallel to the main direction of air flow	210
C.12 Wind speed in slice perpendicular to the main direction of air flow	211
C.13 Wind speed in slice parallel to the main direction of air flow	211
C.14 Wind speed in slice perpendicular to the main direction of air flow	212
C.15 Wind speed in slice parallel to the main direction of the air flow	212
C.16 Wind speed in slice perpendicular to the main direction of the air flow	213
C.17 Slice parallel to main direction of flow	213
C.18 Slice perpendicular to main direction of airflow	214
C.19 Slice parallel to main direction of flow	214
C.20 Slice perpendicular to main direction of flow	215
C.21 Slice parallel to main flow direction	215
C.22 Slice perpendicular to main flow direction	216
C.23 Cross section parallel to main direction of flow	216
C.24 Cross section perpendicular to main direction of flow	217
C.25 Cross section parallel to main direction of air flow	217

LIST OF FIGURES

C.26	Cross section perpendicular to main direction of flow	218
C.27	Cross section parallel to main direction of flow	218
C.28	Cross section perpendicular to main direction of flow	219
C.29	Cross section parallel to main direction of flow	219
C.30	Cross section perpendicular to main direction of airflow	220
C.31	Cross section parallel to main direction of flow	220
C.32	Cross section perpendicular to main direction of airflow	221
D.1	Characteristics of large centrifugal fans	222
D.2	Average longitudinal wind speed over the whole area for 50 % fan rotational speed and before smoothing near fans, with cones	223
D.3	Longitudinal turbulence intensity for 50 % fan rotational speed and before smoothing near fans, with cones	224
D.4	Average longitudinal wind speed over the whole area for 70 % fan rotational speed and before smoothing near fans, with cones	224
D.5	Longitudinal turbulence intensity for 70 % fan rotational speed and before smoothing near fans, with cones	225
D.6	Average longitudinal wind speed over the whole area for 50 % fan rotational speed and after smoothing near fans, with cones	225
D.7	Longitudinal turbulence intensity for 50 % fan rotational speed and after smoothing near fans, with cones	226
D.8	Average longitudinal wind speed over the whole area for 70 % fan rotational speed and after smoothing near fans, with cones	226
D.9	Longitudinal turbulence intensity for 70 % fan rotational speed and after smoothing near fans, with cones	227
D.10	Average longitudinal wind speed at 50 % rotational fan speed without cones	227
D.11	Longitudinal turbulence intensity at 50 % fan rotational speed without cones	228

E.1	Blade Sections	230
E.2	Blade sections - zoom on the blade tip	231
E.3	Blade tip without additional sections	231
E.4	Blade tip with additional sections	231
E.5	Curve that the chord should follow for creating new values for the chord	232
E.6	Blade profile obtained when all points are connected automatically by the CAD software	234
E.7	Open-ended curve obtained before manual addition of trailing edge . . .	234
E.8	Blade profile with manually added trailing edge	234
E.9	Blade profile with manually added profile-zoom	235
G.1	CFD domain for aerodynamic loads on the model wind turbine blade . .	333
G.2	Mesh around blade	334
G.3	Pressure distribution on pressure side of the blade	334
G.4	Pressure distribution on suction side of the blade	334
G.5	Blade deflection when applying a tip load (4.42 N) which gives an ex- treme flapwise bending moment (5.44 Nm) obtained in extreme sea con- ditions	335
G.6	Stress distribution on blade when applying load at tip of the blade (4.42 N) giving a bending moment near the root of 5.44 Nm, which correspond to extreme load obtained in simulation of extreme sea conditions.	336
G.7	Deflection of blade at rated wind speed conditions (determined through CFD calculation in Ansys)	336
G.8	Maximum stress under rated wind speed conditions determined through CFD in Ansys	337
G.9	Properties of Epoxy Carbon Woven (230 GPa) PrePreg	337
G.10	Properties of XPRregXC110	338

List of Tables

2.1	Comparison of different types of platforms	8
2.2	Mass and geometrical characteristics of the NREL 5 MW wind turbine at full scale (taken from Jonkman et al. (2009)) and at reduced scale (1:50) when using Froude scaling (see Section 2.2.4)	18
2.3	Non-dimensional numbers to be potentially considered during model floating wind turbine experiments	21
2.4	Scale factors to be applied to different types of dimensions when Froude scaling is used	22
2.5	Advantages and drawbacks of the simple version of the mechanical pulley system	24
2.6	Advantages and drawbacks of motor-driven rotor combined with mechanical pulley system	24
2.7	Impact of the omission of each force component on the rotor according to Bachynski et al. (2015)	27
2.8	Advantages and drawbacks of the Actuator system	28
2.9	Advantages and drawbacks of the thruster system according to Wright et al. (2015a)	29
2.10	Advantages and drawbacks of drag disc	33
2.11	Advantages and drawbacks of drag disc with driven rotor	36
2.12	Advantages and drawbacks of using a model wind turbine rotor	39
2.13	Number of recommended dividing walls as a function of the opening angle	64
3.1	Overview of the honeycombs tested	80
3.2	Overview of the screens tested	80

LIST OF TABLES

4.1	Initial boundary condition values	102
4.2	Cell sizes and amount of cells used for mesh convergence study	102
4.3	Cell sizes for which the various turbulence models were considered converged	106
4.4	Comparison of number of cells and execution time necessary for a converged mesh for the best turbulence models	114
4.5	First layer thickness determined through calculation for obtaining y^+ values compatible with the law of the wall	117
4.6	Number of cells generated for average cell size	118
4.7	List of combinations of concentric cones tested	128
4.8	Combinations of cone lengths and inlet diameters	131
4.9	Overview of the CFD simulations carried out for a diffuser cone using a long inner cone	131
4.10	Comparison of standard deviation of wind speed across the outlet for various inlet diameters of the diffuser with a long inner cone that has a diameter 1/3 of the diameter of the diffuser and no subdivisions	135
4.11	Comparison of standard deviation for various diameters of the inner cone for an inlet diameter of 1 m and no subdivisions	135
4.12	Comparison of standard deviation of wind speed across the outlet cross section for various numbers of subdivisions between the inner and the outer cone, for an inlet diameter of 1.8 m and an inner cone measuring 1/2 of the diffuser	137
5.1	Pressure drop coefficient calculated for honeycomb with 1/2 inch cell diameter for various cell lengths and wind speeds	164
5.2	Pressure drop coefficient calculated using Wieghardt's formula for various wire diameters and porosities of meshed screen at a wind speed of 2 m/s	164
5.3	Comparison of average wind speed measured at 100 % power of the fans at 130 mm from the outlet when using straight and angled duct	172

5.4	Comparison of standard deviation of average wind speed over measurements done on one height at 100% fan power and at 130 mm from the outlet for straight and angled duct	172
A.1	Properties of the NREL 5 MW reference wind turbine (source: NREL (2019))	197
A.1	Properties of the NREL 5 MW reference wind turbine (source: NREL (2019))	198
A.2	NREL 5 MW reference wind turbine blade geometry	201
B.1	Overview of experiments done	203
B.2	Flow rate calculated for one small centrifugal fan as a function of electric frequency	204
D.1	Overview of measurement positions	229
F.1	Drela AG04 coordinates taken from Jackman (2005)	237
G.1	Lift coefficient of modified Drela AG04 profile (taken from Kimball et al. (2014))	330
G.2	Drag coefficient of modified Drela AG04 profile (taken from Kimball et al. (2014))	332
G.3	Overview of measurements done with the model wind turbine set at blade pitch=0°	338

Chapter 1

Introduction

According to Josset (2018), the global offshore wind resources alone have the potential to provide an annual production of electricity of 20,000 TWh, which would be higher than the global electricity consumption in 2018, which was 16,000 TWh, according to Ministère de la transition écologique (2018). This would mean in theory that the dream expressed by the captain Nemo from *Twenty Thousand Leagues Under the Sea* (Verne, 1870) : "... I wanted to make demands only on the sea itself for the sources of my electricity." could become reality, if only the technology needed to exploit those resources is developed. Other sources, such as International Energy Agency (2019), give estimations for annual electricity production from shallow water (<60 m) wind alone as high as 87,000 TWh, and 330,000 TWh for annual electricity production coming from wind located in deeper water, thus requiring the use of floating wind turbines.

The energy production coming from floating wind turbines is higher for several reasons: wind further off the coast is not only stronger, but also more constant (Wang et al., 2010). And of course a larger area of the ocean has water depth higher than those economically feasible for bottom-fixed wind turbines (typically ~ 50 m depth). Floating wind turbines are a quite recent concept in the domain of energy production. The first floating wind turbine was installed end of 2007 off the coast of Italy by Blue H Technologies (OLDSAILOR, 2007). The world's first floating wind farm was installed in 2017 by Equinor (formerly Statoil) off the coast of Scotland (Harvey, 2017), but this domain still requires research and development to make this an economically competitive energy resource. Though floating wind turbines present some technological challenges, installation of large amounts of floating wind turbines could allow significantly increasing the percentage of renewable energies in the energy mix. In particular, floating wind turbines can be installed in deeper water, further off the coast or in areas where the seabed is quickly at a depth too deep to install bottom fixed wind turbines. This would allow on one hand accessing areas of higher and more constant wind speeds and areas where coastal activity is not as important as near the coast. Another advantage they present is the fact that if well designed, they can be assembled completely in the harbour, then towed to their location, which requires the use of less expensive towing vessels instead of a jack-up vessel required for the installation of bottom-fixed wind turbines. They are also more acceptable by the general public for various reasons: Their installation seems less permanent and the fact that they do not have to be close to the coast will make them less of an obstacle visually. Various concepts for floating platforms as well as turbines are in various stages of development.

According to International Energy Agency (2019), offshore wind offers several advantages over other sources of energy. Recent projects have capacity factors (that is, the ratio of an actual electrical energy output over a given period of time to the maximum

possible electrical energy output over that period) of 40-50 %, thanks to larger wind turbines and other technology improvements. This means that in some regions of the world, the capacity factor of offshore wind matches that of gas- and coal-fired plants. The capacity factor of offshore wind exceeds the capacity factor of onshore wind and is double of the capacity factors of solar photovoltaic panels. Though wind is variable, offshore wind's hourly variability is lower than that of solar photovoltaic panels. It varies up to 20 % from hour to hour, whereas for solar photovoltaic panels, it changes up to 40% from hour to hour. Concerning seasonal variability, the capacity factors are higher in the winter months for northern regions of the globe (United States, United Kingdom, China) and during the monsoon for a tropical climate such as the one found in India. This makes it complementary to solar power. The high capacity factors of offshore wind make its system value comparable to base load technologies and higher than that of onshore wind.

International Energy Agency (2019) details the costs of offshore wind turbines in 2018. It indicates that nearly half of the levelized cost of electricity (LCOE) came from the capital costs of a project. The average LCOE in 2018 fell below \$140 per MWh. The capital costs were divided up as follows: 15-20 % went to the cost of installation, 30-40 % to the cost of the turbine, 20-25 % towards the cost of the foundation and 20-30 % to the cost of transmission and inter-array cabling. The report further states that in 2018, the weighted average cost of capital (WACC) was at 8 %. Half of the LCOE was attributable to financing of the project. They state that if the WACC was at 4 %, the LCOE would be reduced by 30 %, dropping to \$100/MWh. This means that facilitating the financing of offshore wind projects is powerful in reducing the overall cost of a project.

In International Energy Agency (2019), two scenarios are used to predict the growth of offshore wind until 2040. One of them is the Stated Policies Scenario, which takes into account the current and planned policies in various countries concerning goals for energy production and reduction in carbon emissions. This scenario also takes into account how realistic these policies are (International Energy Agency, 2020a). The second scenario is the Sustainable Development Scenario in which the ideal measures which need to be taken to achieve the energy-related Sustainable Development Goals (SDG's) set by the UN are determined. The three energy-related SDG's are universal access to energy, reduction of severe health impacts of air pollution, and to address climate change. This shows that current government policies are insufficient. Concerning climate change, the Sustainable Development Scenario complies with the Paris Agreement. In the Paris Agreement, the goal is to "hold the increase in the global average temperature to well below 2°C above pre-industrial levels and pursue efforts to limit the temperature increase to 1.5°C above pre-industrial levels" (International Energy Agency, 2020b). To achieve the target set by the Paris Agreement, in the Sustainable Development Scenario, the aim is to keep the temperature rise to below 1.8°C with a 66% probability.

According to International Energy Agency (2019), the Stated Policies Scenario predicts that by 2040, 340 GW will have been installed in the world and that offshore wind will provide 3 % of global electricity supply. Although this represents already an important increase when compared to the level in 2020, which is 29.1 GW, the Sustainable De-

velopment Scenario states that what is needed is to have installed 560 GW by 2040, which would contribute to 5% of global energy production.

In the UK specifically, the UK Offshore Sector Deal aims to have installed 30 GW of offshore wind capacity by 2030. In 2020, 10 GW are installed (renewableUK, 2020).

In Wiser et al. (2016), the results of the answers of 163 experts on the future of wind energy are presented. It names the 5 domains which will impact reduction of LCOE most importantly by 2030 for each type of wind energy (onshore, offshore bottom-fixed and offshore floating). For floating wind energy, advancements in the following areas are named to have the most impact: foundation/support structure design, installation process efficiencies, foundation/support structure manufacturing, economies of scale via project size, and installation/transport equipment.

To be able to make advances in those domains, after a first stage of design, which in some cases may involve laboratory tests, a prototype needs to be developed and built. For a prototype to be certified by DNV-GL, model tests are required (DNV-GL, 2018). Bureau Veritas (Bureau Veritas, 2019) requires for the certification of a floating wind turbine platform that air gaps are determined by appropriate model tests, though detailed hydrodynamic analysis can be accepted. Calculations that determine loads on a floating wind turbine platform need to be presented. Those calculations can be calibrated using model tests. Concerning the determination of wave loads, appropriate hydrodynamic analysis and model tests are mandatory. Model tests are also useful to prove the stability of the structure and are necessary to estimate damping effects.

Concerning the platforms, though some concepts have already been developed, improvements need to be made, to reduce production or transportation costs or improve stability. Future platforms will also need to support more powerful wind turbines. Existing concepts are largely based on existing concepts in the oil and gas industry. Though the first floating offshore wind turbine prototype installed was a tension leg platform, the first commercial scale farm used the SPAR (Single Point Anchor Reservoir) buoy concept. Many other installed platforms are of the type semi-submersible. One interesting concept is also the articulated water column (DiSchino et al., 2016). Concerning the turbine part, some innovative ideas are the use of vertical axis wind turbines, which could have some advantages over their horizontal axis counterparts, largely developed, in particular when used offshore (Borg et al., 2014). Another one is the use of several turbines on a single platform, which could present some advantages over single turbine platforms (MacMahon et al., 2015). Another idea still is to combine marine renewable energies, such as wave energy devices with a floating wind turbine (Sarmiento et al., 2019).

Model testing involves the need to follow certain scaling laws. In general, not all scaling laws can be followed, so a compromise needs to be made allowing at least the conformity of the most important dimensions in a scaled test. Froude scaling is necessary for testing scaled devices exposed to inertial and gravity loads, which is the case for devices exposed to waves. In this case, the Reynolds number cannot be respected and is several orders of magnitude smaller than for the prototype. This means that aerodynamic loads on the wind turbine rotor are not conserved when using geometrical scaling for the blades. Several methods have been developed to simulate correctly

the aerodynamic loads or at least the most important ones, in particular the thrust. Constant thrust can be simulated most easily. Some of the methods require a wind generation system, some others do not. Some use real-time numerical simulation for the calculation of aerodynamic loads applied by various means on a physical model in a wave tank.

The COAST laboratory of the University of Plymouth has an ocean basin which can have variable depth, up to 3 m deep. It is 15.5 m wide and 35 m long and can produce waves up to 1 m high. It was not designed originally to accommodate a wind generation system. A wind generation system would allow using a wind turbine model rotor using Froude-scaled wind speed and modified blade shape for overcoming Froude and Reynolds number conflict. It was decided to use centrifugal fans placed at one edge of the basin and then guide the wind to the centre of the basin via a duct. Due to space constraints, the cross section of the duct had to be smaller than the cross section of the final outlet, which required the use of a diffuser.

The aim of the thesis was to examine the use of a diffuser to create a homogeneous wind field for testing scaled floating wind turbines. To achieve this aim, the following objectives were pursued:

- Determine the applicability of flow straightener design guidelines, normally used in wind tunnels with a settlement chamber, followed by a closed test section, to an open jet blower type wind generation system.
- Establish suitable turbulence models for CFD simulation of flow through conical diffusers.
- Investigate numerically the use of flow control methods in a conical diffuser.
- Investigate experimentally the use of flow control methods in a conical diffuser.
- Demonstrate the use of a conical diffuser-based wind generation system with a model wind turbine.

The literature review first presents the state of development of various types of floating wind turbine platforms. It then introduces the difficulty and the basic notions necessary to model correctly aerodynamic forces in a scaled experiment of a floating wind turbine platform. Requirements for wind generation in the laboratory as well as various examples of existing wind generation systems are presented next. The difficulty of producing even flow distribution in an expanding diffuser as well as various methods to overcome this are presented next. The last part presents CFD simulations of turbulent steady state indoor airflow.

The literature review is followed by the description of a first series of experiments during which wind was produced over a small area, where the impact of flow straighteners was investigated, presented in Chapter 3. In Chapter 4, this first series of experiments was used for comparison to the results of CFD simulations using various turbulence models. The best two turbulence models were then used to study numerically flow distribution inside a conical diffuser containing various shapes and numbers of inner cones. Some of the conical diffusers studied numerically were built and studied experimentally in

Chapter 5. One of the wind generation systems studied experimentally was used to measure thrust on the wind turbine model rotor, and the results are presented in the Chapter 6. Chapter 7 is the conclusion of the thesis.

Figure 1.1 is a flow chart illustrating the link between same topics treated in different chapters.

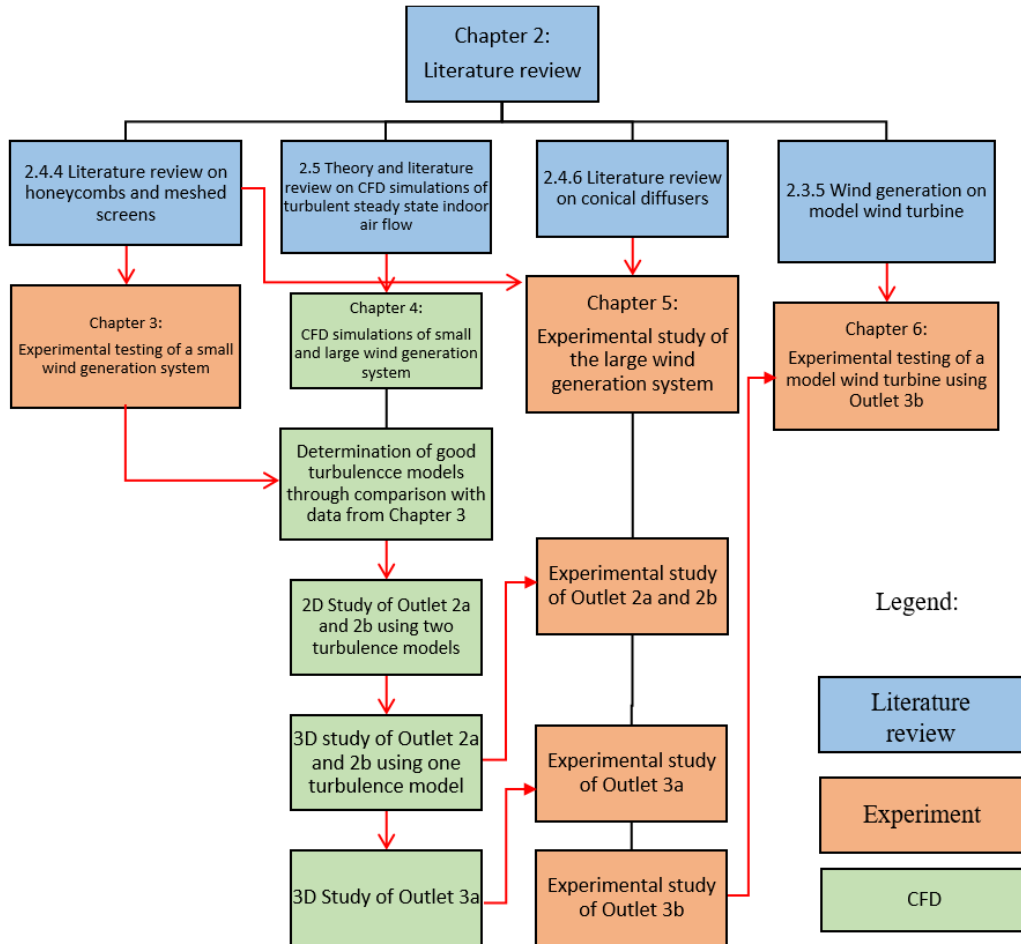


Figure 1.1: Flow chart illustrating the link between topics treated in different chapters

Chapter 2

Literature review

2.1 Different types of floating platforms

One important aspect of a floating offshore wind turbine is the choice of the support structure. Wang et al. (2010) provide a thorough review of the study of wind turbines done by 2010. They mention four main types of support structures: spar-type, semi-submersible, pontoon type and tension leg platform (See Figure 2.1). Many of these support structures are inspired by structures in use in the oil and gas industry.

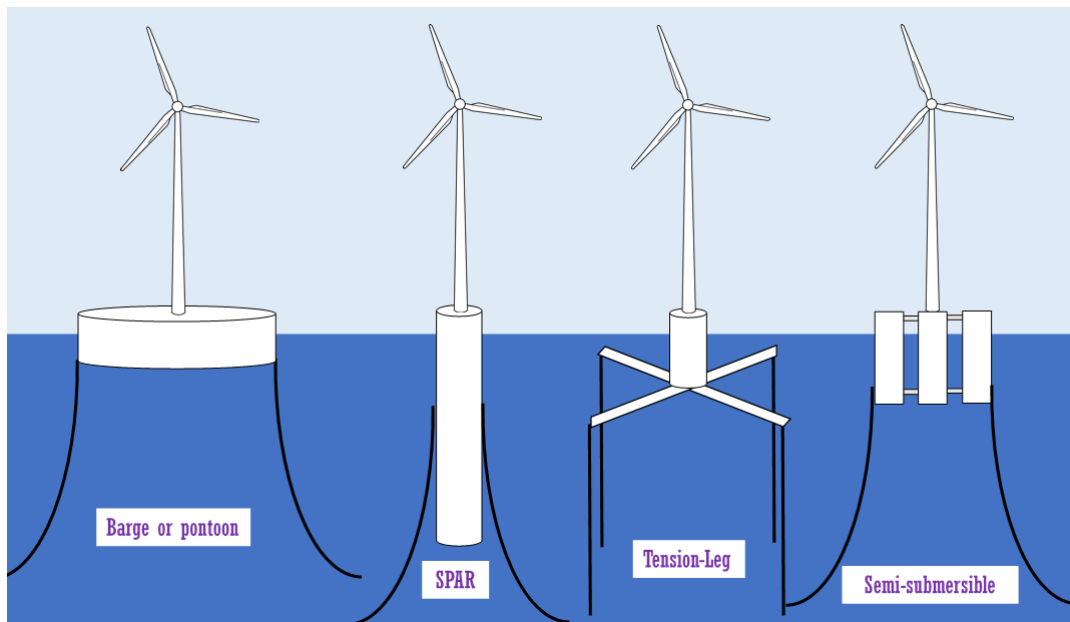


Figure 2.1: Different types of support structures for floating offshore wind turbines (Inspired by image found in Courbois (2013), originally from Philippe (2012), wind turbine line drawing from SeekPNG (n.d.))

To explain how the turbine platforms are stabilized, as a first approach, the criterion for transverse stability in calm waters and small inclinations (without mooring) can be looked at (Equation 2.1 and Figure 2.2).

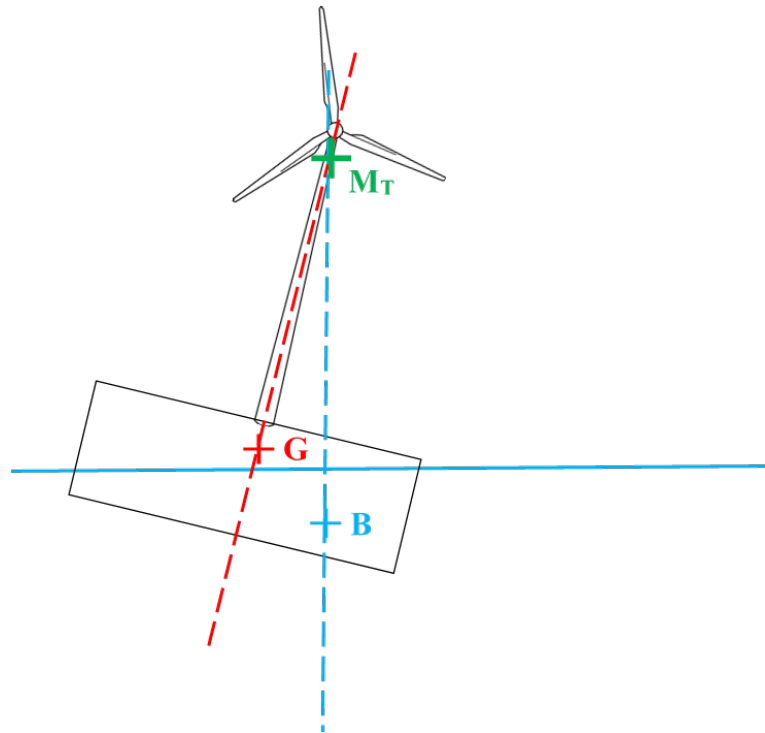


Figure 2.2: Centre of gravity, centre of buoyancy and metacentre, wind turbine line drawing from SeekPNG (n.d.)

$$GM_T = \frac{J}{Vol} + GB > 0 \quad (2.1)$$

with G the global centre of gravity of the platform and the wind turbine, M_T the metacentre of the floating platform, GM_T the distance between G and M_T , J the second moment of area of the intersecting surface of the floating platform with the mean water surface, Vol the volume of buoyancy, B the centre of buoyancy, and GB the distance between G and B .

GM_T needs to be positive when projected on a vertical axis pointing upwards, that is, M_T needs to be situated above G , or else the platform is unstable and bound to tilt. For GM_T to be positive, GB needs to be positive or else this needs to be compensated through a large ratio between the second moment of area and the submerged volume. The Spar buoy concept accomplishes stability by having a heavy weight at the bottom of a long cylinder, almost as deep as the hub is high. The second moment of area is close to negligible. The pontoon platform, on the contrary, has a very shallow draft. The centre of gravity is above the sea level. Therefore, the width of the platform needs to ensure stability by providing a large second moment of area. The semi-submersible platform has a moderate draft, and stability is achieved partly through ballast, which lowers the centre of gravity, and partly through large second moment of area. For a tension leg platform, Equation 2.1 is not verified. Stability for this type of platform is achieved by using a platform which would float higher without mooring, therefore generating tension in the mooring lines which keeps it from tilting. Table 2.1 summarizes

2.1. DIFFERENT TYPES OF FLOATING PLATFORMS

the definitions of these platforms as well as their advantages and drawbacks.

Table 2.1: Comparison of different types of platforms

Type	Definition	Advantages	Drawbacks
SPAR buoy	Long cylindrical platform with vertical axis (name is acronym for Single Point Anchor Reservoir)	High stability even in agitated waters due to low centre of gravity and small wave loads	Water depth needs to be over 200 m (draft of platform around 100 m)
Barge or pontoon	Wide and shallow platform	Stability in calm and shallow waters	High wave loads
Semi-submersible	Structure that goes wide and deep (compromise between SPAR buoy and pontoon)	Usable in a large variety of environments	Less stable compared to SPAR buoy type platform
Tension Leg	Instead of catenary mooring, tight mooring, achieved through excessive buoyancy of the platform (can be applied to various designs of the platform types mentioned above)	Very small displacements in all 6 DOF (Degrees of Freedom)	Cannot be used in shallow waters with high tidal range: mooring should never go slack to avoid breaking, though the possibility exists to adapt the length of the cables

The following sub-sections present some examples for the different types of platforms.

2.1.1 Examples of SPAR Buoy platforms

In 2009, a 2.3 MW Hywind wind turbine prototype was installed by Statoil off the coast of Norway. The water depth at the installation site is 200 m and therefore suitable for this type of platform. After 8 years of demonstration, this wind turbine platform concept was ready to be used for the first commercial-scale floating wind turbine farm, which was installed off the coast of Scotland and connected to the grid in October 2017 (Harvey (2017), see Figure 2.3). It is composed of 5 wind turbines, each delivering 6 MW of electricity, a total of 30 MW for the whole wind farm. One other current project of this company, now called Equinor, is an 88 MW wind farm which would provide power for oil and gas offshore stations off the coast of Norway (Equinor, 2020). Construction

2.1. DIFFERENT TYPES OF FLOATING PLATFORMS

has started in October 2020 (offshorewind.biz, 2020a). It will be constituted of 11 8 MW wind turbines and is planned to be ready in 2022.

In 2016, a floating wind turbine using an advanced SPAR concept for the platform was installed off the coast of Japan (Figure 2.4 and Figure 2.5, see also Section 2.1.2). According to Foster (2016), during the installation phase, there was an incident where the platform keeled, which caused a delay of nearly 5 days.



Figure 2.3: Hywind SPAR buoy platform (taken from EWEA-WindEurope (2013) with the permission of WindEurope (formerly EWEA))



Figure 2.4: Advanced SPAR concept used for Fukushima Hamakaze (5 MW), taken from Ishihara et al. (2014) with the permission of T. Ishihara

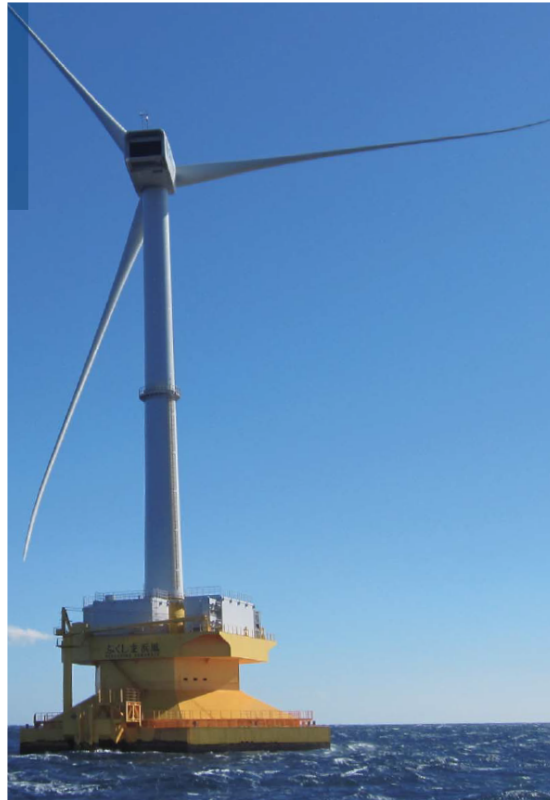


Figure 2.5: Fukushima Hamakaze (5 MW), taken from Fukushima Offshore Wind Consortium (n.d.b) with the permission of T. Ishihara. Original image taken from Sawaji (2016) had to be taken out, as the copyright owner could not be contacted.

Image absent as copyright owner
could not be contacted

Figure 2.6: Platform for Fukushima Hamakaze wind turbine keeled to 45 degrees during installation phase (taken from Foster (2016))

2.1.2 Examples of semi-submersible platforms

Various semi-submersible platforms have been developed and built, using slightly different geometries. They all base their stability on the same principle: Stability is achieved thanks to round or square vertical columns situated at a certain distance from one another. This creates a high second moment of area of the structure's intersection with the water surface, without having a large area of intersection with the water surface, therefore limiting wave loads on the structure. The columns are connected above or below the water surface, with minimal intersection with the water surface. In addition, ballasting can be used to lower the global centre of gravity.

After the nuclear disaster caused by an earthquake near Fukushima in 2011, Japan

launched the project Fukushima FORWARD by installing the 2 MW floating demonstration wind turbine Fukushima Mirai in 2013 (Figure 2.7). This platform has a triangular shape when seen from above. The turbine is situated at the centre of the platform. The wind turbine is of the downwind type. This was followed in 2015 by the installation of a 7 MW wind turbine, at the time the world's largest floating wind turbine (Fukushima Offshore Wind Consortium (2015), see Figure 2.8 and Figure 2.9). These two demonstrators alongside a third one at 5 MW (see Section 2.1.1), formed the largest floating wind farm demonstration project in 2016 (Sawaji, 2016). Although the smallest demonstrator (2MW) had a good capacity factor (34 %), the two larger ones (5 MW and 7 MW) only had capacity factors of 12 % and 2 % respectively (Radtke, 2018). The 7 MW demonstrator started to be dismantled in June 2020 (Skopljak, 2020). According to Ishii (2018), the gearbox (world's first hydraulic gearbox) and other parts regularly had defects, making maintenance too expensive to continue using it. The other two turbines are kept and more wind turbines are planned to be installed in the future.

Figure 2.10 shows the semi-submersible platform developed by WindFloat. The support structure has a triangular shape. Three cylinders on the corners of the triangle provide buoyancy. The wind turbine from Vestas is installed on one of the three corners. Stability is achieved through patented water entrapment (heave) plates. Another patented technique, called active ballast, is used to distribute water ballast between the three columns to compensate for changes in the turbine thrust. The whole structure, platform and wind turbine can be assembled onshore, which is due in part to its relatively shallow draft (10-20 m). It is then towed fully assembled to its final location.

According to EWEA-WindEurope (2013), a 2 MW prototype was installed off the coast of Portugal in 2011. At the beginning of 2020, according to the company's website (Principle Power News, 2020), the first of three 8.4 MW floating wind turbines (which was at the time the largest floating wind turbine installed in the world) was installed and connected to the grid. The two other turbines were installed by July 2020 (offshoreWIND.biz, 2020b), making this the world's first semi-submersible floating wind turbine farm. The rated power is 25 MW. In September 2020, the first three floating foundations of a 50 MW floating wind farm were ready for load-out. The wind farm using this platform will be commissioned off the coast of Scotland, becoming the world's largest floating wind farm and featuring 5 9.5 MW wind turbines and one 2 MW wind turbine (Cobra, n.d.; NS Energy, n.d.).

2.1. DIFFERENT TYPES OF FLOATING PLATFORMS

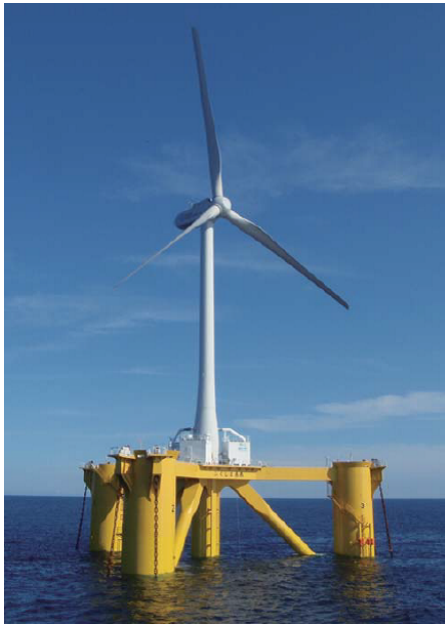


Figure 2.7: 2 MW floating demonstration wind turbine Fukushima Mirai, installed in 2013, (taken from Fukushima Offshore Wind Consortium (n.d.a) with the permission of T. Ishihara)



Figure 2.8: Fukushima Shinpu 7 MW wind turbine using V-shaped semi-submersible platform (taken from Ishihara et al. (2014) with the permission of T. Ishihara). Original image from PowerTechnology (n.d.) was taken out as copyright owner could not be contacted



Figure 2.9: Fukushima Shinpu 7 MW wind turbine using V-shaped semi-submersible platform (taken from Sawaji (2016), also found in Fukushima Off-shore Wind Consortium (n.d.b), with the permission of T. Ishihara)



Figure 2.10: Towed Fukushima Mirai wind turbine. Photo taken from Ishihara et al. (2014) with permission of T. Ishihara. Original photo: Photo of the WindFloat 2 MW prototype installed in 2011 near Portugal. Ballasting and connection to the offshore tug vessel Bourbon Liberty 228 (Principle Power, 2011). Had to be taken out, as copyright owner could not be contacted

2.1.3 Tension-Leg platform - Blue H Technologies

The first prototype floating wind turbine was installed in 2007 by Blue H technologies (Netherlands) and had a tension leg platform. It was installed off the Italian coast. The rated capacity of this turbine was 80 kW. It worked for one year and was then decommissioned (Figures 2.11,2.12 and 2.13).

2.1. DIFFERENT TYPES OF FLOATING PLATFORMS

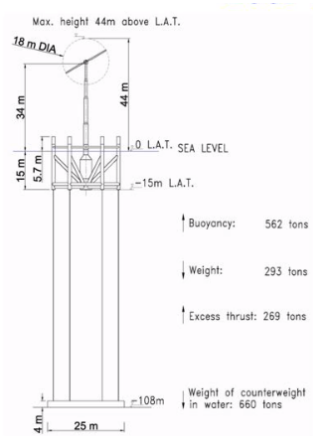


Figure 2.11: Blue H Technologies concept for tension leg platform (Jakubowski, 2009), with the permission of M. Jakubowski

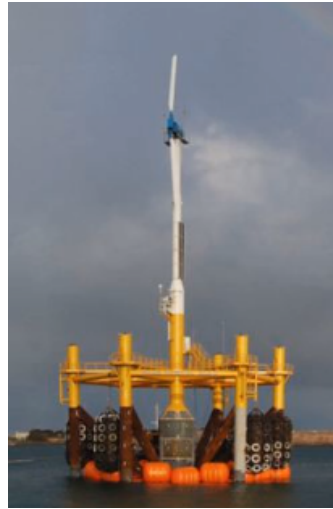


Figure 2.12: Blue H Technologies prototype during installation (Jakubowski, 2009), with the permission of M. Jakubowski



Figure 2.13: Blue H Technologies 80 kW prototype (Permission granted by M. Jakubowski, founder of Blue H Technologies)

2.1.4 Barge/pontoon platform - IDEOL

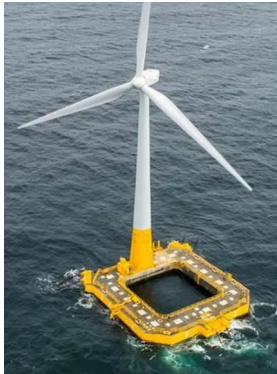
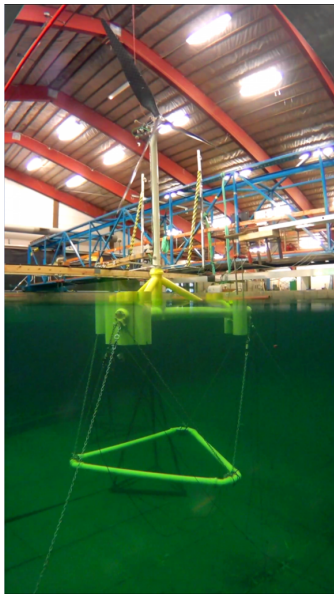


Figure 2.14: Moon-pool platform by IDEOL (Molga, 2021), permission granted by Ideol

In 2011-2012, IDEOL, a French company patented its platform concept (Figure 2.14). This damping pool system uses hydrodynamic properties of water entrapped into a central well. In 2013-2014, it joined the European Consortium called Floatgen. The aim of this consortium is to operate a floating demonstrator and the platform is the one from IDEOL. Furthermore, in 2015, Japan chose to use this platform concept for a floating demonstrator. 2016 marked the launch of the construction of both the Floatgen project with an installation site in France (2 MW) and the Japanese project (3 MW). The two demonstrators have successfully been operational since 2018 (King, 2020). The first offshore wind turbine in France was therefore a floating one, using the IDEOL damping pool concept (IDEOL, 2017).

2.1.5 Hybrid concept



The former CEO of Siemens Power, Henrik Stiesdal, proposes a hybrid platform concept with an adaptable centre of gravity (Stiesdal, 2016) thanks to a counterweight attached to a semi-submersible platform through chains (see Figure 2.15). The depth of this counterweight can be adapted to adjust to different situations. While being towed, the platform works as a semi-submersible one with the counterweight at a relatively shallow draft. This allows towing out of harbours that do not allow deep drafts. Once at the installation site, the counterweight can be lowered to lower the global centre of gravity, thus attaining stability in the same way as a SPAR buoy platform would.

Figure 2.15: TetraSpar concept by Henrik Stiesdal tested at DHI (OffshoreWIND.biz, 2017), permission granted by Stiesdal

2.2 Experimental testing of model wind turbines

When designing a new wind turbine, before building and testing a prototype in full-scale sea-environment, the design concept needs to be verified. This can partly be done through numerical simulations. Performing physical tests at laboratory scale completes the validation and provides data to verify the numerical model results. This section is a summary on the various methods for physical testing of wind turbine models at laboratory scale. The first part presents the non-dimensional numbers that should be considered when scaling the model and which of them are most relevant and crucial to be conserved. The second part presents various methods to overcome scaling issues mentioned in the first part or to simplify the testing when it is focused on the validation of a new platform concept.

2.2.1 Forces to be modelled when designing a floating wind turbine model

2.2.1.1 Degrees of freedom of a floating wind turbine platform

Figure 2.16 shows the names for the degrees of freedom used when describing the movements of a floating wind turbine platform.

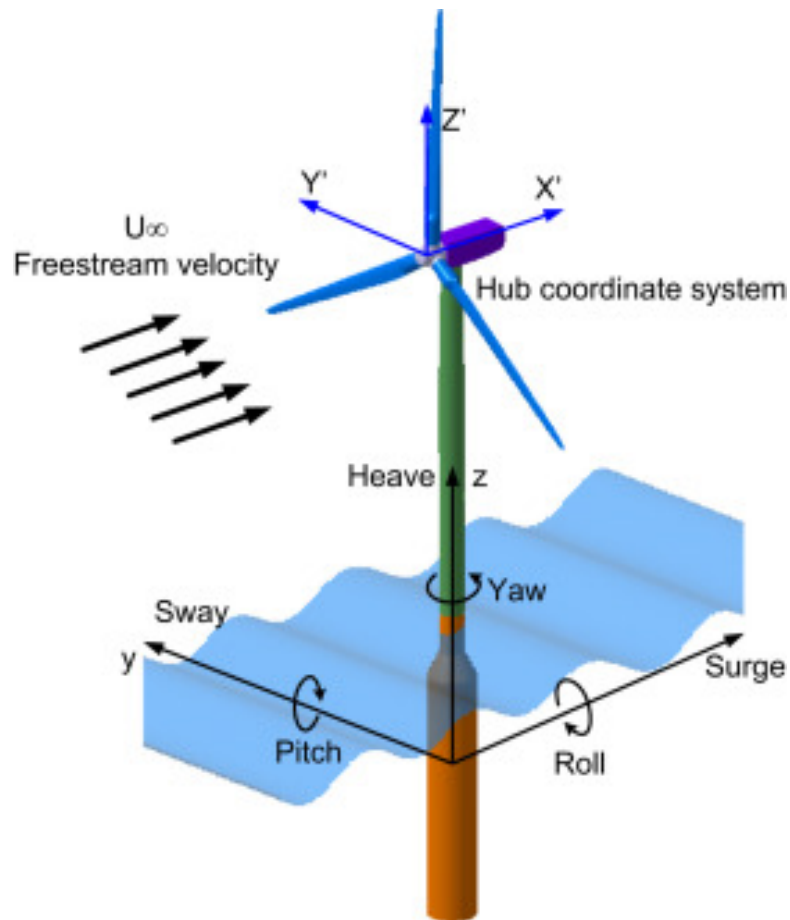


Figure 2.16: Degrees of freedom of a floating wind turbine platform (Tran and Kim, 2015)

2.2.1.2 Thrust

The aerodynamic loads on the rotating wind turbine blades create a global aerodynamic load. This global load is transmitted to the rotor hub in the form of two main components: a force perpendicular to the rotor plane, called the thrust and a torque that has a direction perpendicular to the rotor plane, which causes the blades to spin. The movement caused by the torque allows power generation and does not directly affect the platform. However, when the platform rotates about the pitch or yaw axis, this is at the origin of gyroscopic loads described in the next subsection.

2.2.1.3 Gyroscopic forces

As the wind turbine rotor is rotating, this can be the origin of gyroscopic forces. If the wind turbine experiences pitch movement because of wave loads on the platform, this can induce a yaw moment. Inversely, if the wind turbine experiences yaw movement because of wave loads on the platform, this will induce a pitch moment. This is illustrated in Figures 2.17 and 2.18.

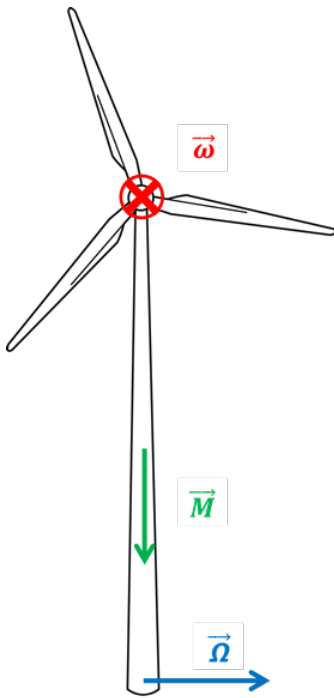


Figure 2.17: Yaw moment experienced by the platform in the case of rotation about the pitch axis, wind turbine line drawing from SeekPNG (n.d.)

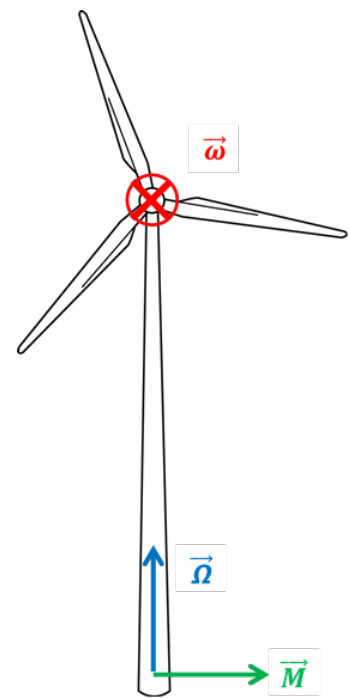


Figure 2.18: Pitch moment experienced by the platform in the case of rotation about the yaw axis, wind turbine line drawing from SeekPNG (n.d.)

The gyroscopic moment can be calculated according to equation 2.2.

$$\vec{M}_{gyro} = I \vec{\omega} \times \vec{\Omega} \quad (2.2)$$

with I the moment of inertia of the spinning rotor, $\vec{\omega}$ the rotational velocity vector of the rotor around its axis and $\vec{\Omega}$ the rotational velocity vector of platform around pitch or yaw axes. The majority of the time the resulting gyroscopic load will not be purely composed of either yaw or pitch, but rather a combination of both, as the movement of the platform is very unlikely to be a rotation purely about a single axis.

2.2.2 Choice of a wind turbine model - Properties of the NREL 5 MW wind turbine

The NREL 5 MW wind turbine was developed to provide offshore wind energy researchers with detailed information on a prototype that was not kept secret due to intellectual property. It is widely studied in literature, theoretically, through CFD, in experiments. It is therefore not only easy to get detailed information on the geometry, mass properties and expected performance, but also results obtained in other laboratories/research institutions for scaled models of the turbine. For this reason, this turbine was frequently chosen to be modelled in laboratory tests, whether a model wind turbine having its characteristics was actually built, or whether its characteristics were

simulated in a different way.

The majority of the information on the geometry and mass properties of the turbine can be found in Jonkman et al. (2009). This document also presents results of simulations done with the FAST software developed by NREL. The turbine is designed to produce 5 MW of electricity for a rated wind speed of 11.4 m/s. Some of the results relevant for designing and running a model wind turbine can be found in Appendix A, that is rotor speed, Tip Speed Ratio, blade pitch and rotor thrust as a function of wind speed for the full size wind speed, and rotor speed and rotor thrust that should be achieved with a model wind turbine at scale 1:50. Graphs in Appendix A also show the evolution of these values with wind speed. Table 2.2 shows some geometrical and mass characteristics of the NREL 5 MW wind turbine which should be taken into account when designing the model.

Table 2.2: Mass and geometrical characteristics of the NREL 5 MW wind turbine at full scale (taken from Jonkman et al. (2009)) and at reduced scale (1:50) when using Froude scaling (see Section 2.2.4)

Property	Prototype	Model
Blade mass (kg)	17,740	0.14
rotor diameter (m)	126	2.52
Hub height (m)	90	1.8
Rated Power	5 MW	5.7 W
rated rotor speed (rpm)	12.1	85.6
rated wind speed (m/s)	11.4	1.6
cut-in wind speed (m/s)	3	0.42
cut-out wind speed (m/s)	25	3.54
cut-in rotor speed (rpm)	6.9	49.3
TSR at rated wind speed	7	7
Rated tip speed (m/s)	80	11.29

Data on the NREL 5 MW wind turbine blade geometry can be found in Appendix A.2.

2.2.3 Non-dimensional numbers to be considered when designing a floating wind turbine model

When conducting scaled testing, the physical quantities vary between the prototype and the model. Once a scale (that is, the ratio between the prototype and the model properties) is chosen, physical quantities such as weight, lengths, loads, velocities, etc. have to be changed based on this scale following certain rules. Ideally various non-dimensional numbers that are ratios of diverse physical properties are all equal at model and prototype scale. However, as will be seen below, this is impossible when using strict geometric scaling for all features. Therefore, a choice has to be made in which the most relevant ratios are determined to be conserved between model and prototype and chosen to be the ones determining the properties of the prototype. If non-dimensional numbers that are not respected are relevant during testing, methods

should be found to get good results with the model in spite of it.

By default, geometric scaling is used. Equation 2.3 gives the definition of the scale of a model used in this document:

$$\lambda = \frac{L_p}{L_m} \quad (2.3)$$

with L_p a length of the prototype and L_m the same length of the model. The scale λ defined this way was varying between 2 and 150 for physical testing of floating wind turbines found in literature. The ratios for areas and volumes between the prototype and the model are by default as in Equations 2.4 and 2.5. The angles are kept constant.

$$R_A = \frac{A_p}{A_m} = \lambda^2 \quad (2.4)$$

with R_A the ratio between areas of the prototype and areas of the model, A_p an area of the prototype, A_m the same area of the model.

$$R_{Vol} = \frac{Vol_p}{Vol_m} = \lambda^3 \quad (2.5)$$

with R_{Vol} the ratio between volumes of the prototype and volumes of the model, Vol_p a volume of the prototype, Vol_m the corresponding volume of the model.

The Reynolds number is the ratio of inertial forces over viscous forces. It can be calculated according to equation 2.6.

$$Re = \frac{\text{inertial forces}}{\text{viscous forces}} = \frac{l_c V_c}{\nu} \quad (2.6)$$

with Re the Reynolds number, l_c the characteristic length, V_c the characteristic speed and ν the kinematic viscosity.

In experiments where aerodynamic loads play a role, as the impact of viscosity is non-negligible, the Reynolds number is a non-dimensional number which should not be neglected.

The Froude number is the ratio of inertial forces over gravitational forces. The Froude number can be calculated according to equation 2.7.

$$Fr = \frac{\text{inertial forces}}{\text{gravitational forces}} = \frac{C_w}{gl_c} \quad (2.7)$$

with Fr the Froude number, C_w the wave celerity, g the acceleration of gravity, l_c the characteristic length.

It is necessary to maintain this ratio for any scaled testing where inertial and gravitational forces have significant impact, such as ship hydrodynamics.

The tip speed ratio (TSR) is the ratio of the rotor velocity over the free stream velocity of the wind. It can be calculated according to equation 2.8.

$$TSR = \frac{\text{rotor tip velocity}}{\text{wind free stream velocity}} = \frac{\omega_r R}{V_\infty} \quad (2.8)$$

with ω , the rotor rotational speed, R the radius of the wind turbine and V_∞ the free stream velocity. Figure 2.19 illustrates the variables involved in this equation.

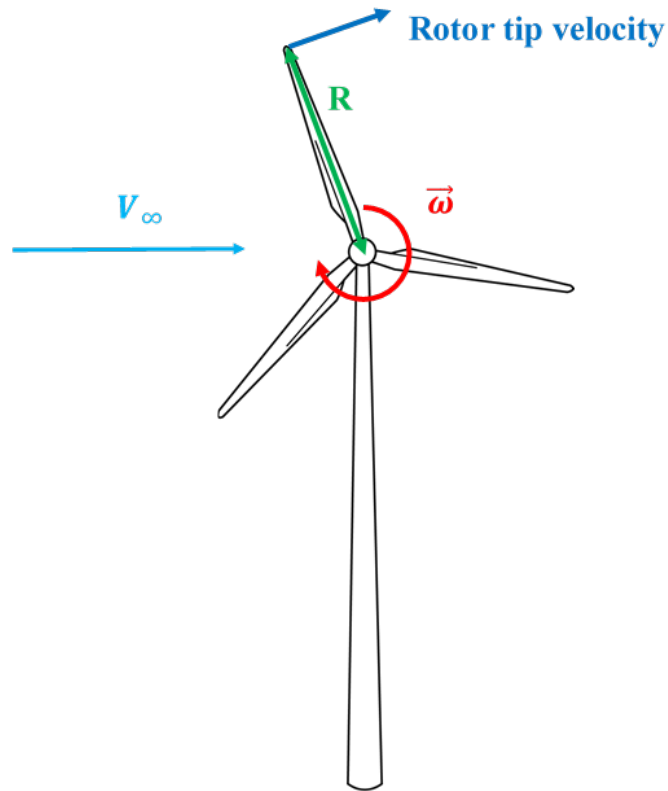


Figure 2.19: Variables used to calculate the tip speed ratio of a wind turbine, wind turbine line drawing from SeekPNG (n.d.)

The TSR will be conserved automatically for strict Froude scaling.

Larsen et al. (2012) and Azcona et al. (2017) mention several other non-dimensional numbers one could consider in the experimental study of a scaled wind turbine (Table 2.3). Some of those are automatically preserved by using Froude scaling, others not, but can either be neglected or worked around.

2.2. EXPERIMENTAL TESTING OF MODEL WIND TURBINES

Table 2.3: Non-dimensional numbers to be potentially considered during model floating wind turbine experiments

Name	Definition and domain of application	Justification for neglecting or automatic conservation
Mach	$\frac{\text{flow velocity}}{\text{speed of sound}}$	Lower than 0.25 both at full scale and at scale 1/45
Strouhal	Dimensionless vortex shedding frequency, significant in cases with vortex induced vibration (VIV) driven effects	Though dependant on Reynolds number, stays constant to 0.2 for Reynolds numbers lower than $2 \cdot 10^5$, thus effects have been neglected in past experiments
Keulegan Carpenter	Characteristic number for planar oscillatory flows	Conserved with Froude scaling
Weber (Azcona et al., 2017)	Measures balance of surface tension to inertial loads	Unimportant except at very small scales
Cauchy (Azcona et al., 2017)	Necessary to represent correct hydro-elastic effects, requires same ratio for torsional and longitudinal bending	Necessary but difficult to find material that allows both correct torsional and longitudinal bending at reduced scale. Can be worked around by making the structure of the platform out of several pieces and regulating the stiffness of the hinges
Lock	$\frac{\text{aerodynamic forces}}{\text{inertia forces}}$	Conserved with Froude scaling

2.2.4 Reynolds number and Froude number conflict

When Froude scaling is applied, the Reynolds number for the model can be expressed as a function of the Reynolds number of the prototype according to equation 2.9.

$$Re_m = \frac{V_m l_m}{\nu} = \frac{1}{\lambda} \frac{V_p}{\lambda^{0.5}} \frac{l_p}{\lambda} = \frac{Re_p}{\lambda^{1.5}} \quad (2.9)$$

with Re_m the Reynolds number characterizing the model, V_m the wind speed characteristic of the model, l_m the length characteristic of the model, V_p the wind speed characteristic of the prototype, λ the scale, ν the kinematic viscosity, l_p the length characteristic

2.3. VARIOUS METHODS FOR LABORATORY TESTING TO OVERCOME FROUDE AND REYNOLDS SCALE CONFLICT

of the prototype, and Re_p , the Reynolds number characterizing the prototype.

If Froude scaling is respected, Reynolds scaling cannot be respected. The Reynolds number of the model is smaller than the Reynolds number of the prototype. Therefore, where the flow is turbulent at full scale, the flow at reduced scale can be laminar. For a blade profile, this can push the boundary layer separation closer to the leading edge and thus increase the drag and decrease the lift (Martin et al., 2012). It is however possible to find strategies to have Froude scaled aerodynamic loads in spite of this conflict. This approach of using Froude scaling for the majority of the dimensions and finding a method to compensate for the non-respect of the Reynolds number was chosen by all references that presented floating wind turbine laboratory experiments consulted. Table 2.4 gives the factors to be applied to different types of dimensions in order to respect Froude scaling.

Table 2.4: Scale factors to be applied to different types of dimensions when Froude scaling is used

	Dimension	Scale
Length	L	λ
Weight	M	$1.025 \times \lambda^3$
Force (other than buoyancy)	MLT^{-2}	λ^3
Frequency	T^{-1}	$\lambda^{-0.5}$
Speed	LT^{-1}	$\lambda^{0.5}$
Acceleration	LT^{-2}	1
Moment of inertia	ML^2	λ^5

with L a length dimension, M a mass dimension and T a time dimension. λ is the ratio between lengths in the prototype and lengths in the model, or the scale.

2.3 Various methods for laboratory testing to overcome Froude and Reynolds scale conflict

This section presents a list of methods simulating loads of the wind turbine on the platform when testing under Froude scaling, on what scientific principle the methods are based, how many loads can be tested, the laboratories that have done this type of testing and the theoretical advantages and drawbacks. Whether the results obtained using one method or another were satisfactory in answering the question of loads on the platform was not always possible to determine. The classification of the methods is based on (Wright et al., 2015a). The majority of the literature references come from this document, as well.

2.3.1 Mechanical pulley system

The main load applied on the foundation from the turbine that needs to be simulated is the thrust. With varying wind and wave conditions, the thrust varies, however to get a general idea of the behaviour of the platform, one can simulate a constant thrust on

2.3. VARIOUS METHODS FOR LABORATORY TESTING TO OVERCOME FROUDE AND REYNOLDS SCALE CONFLICT

the platform using a mechanical pulley system. A non-extendable line is attached to the location on the nacelle where the hub would be. This non-extendable line is guided horizontally to a location where there is a pulley system. The pulley system changes the direction of the wire from a horizontal to a vertical, and a mass attached to the end of the line provides the restoring force. Figure 2.20 shows the basic set-up for an experiment using this type of method from the side. Figure 2.21 shows the same set-up as the one from Figure 2.20 but shown from above.

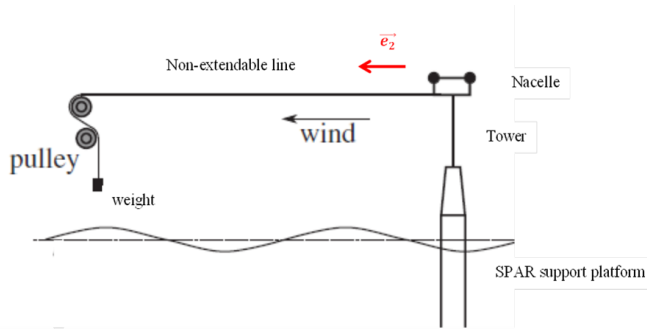


Figure 2.20: Schematic of laboratory set-up for the mechanical pulley system (side view), adapted from Matha et al. (2015), with the permission of The Royal Society Publishing obtained via the Copyright Clearance Center

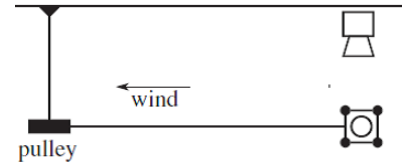


Figure 2.21: Schematic of Laboratory set-up for mechanical pulley system (Top view), adapted from Matha et al. (2015), with the permission of The Royal Society Publishing obtained via the Copyright Clearance Center

One can consider that the force exerted by the weight on the wire is transmitted as it is to the tower top and therefore the thrust exerted on the tower top equates the weight of the suspended item, with a change of direction. A more complex formula is given by Matha et al. (2015) which does not neglect inertia and mass of the pulley wheel. Friction between the pulley wheel and its rotational shaft is considered to be zero. The wire is considered moving on the pulley without slipping. The problem is supposed to be contained in a plane, vertical to the mean water surface and containing the wire and the central plane of the pulley wheel. By applying the second law of motion to a single pulley wheel one obtains equation 2.10.

$$\vec{F}_p = (m(g - \vec{a}_t \cdot \vec{e}_2) - \frac{I_p \vec{a}_t \cdot \vec{e}_2}{R_p^2}) \vec{e}_2 \quad (2.10)$$

with \vec{F}_p : Force applied at the scaled model tower top

m : mass of suspended weight

g : acceleration of gravity

\vec{a}_t : acceleration vector at connection to the platform tower top

I_p : rotational inertia of pulley wheel around axis going through the centre of the pulley wheel

R_p : radius of pulley wheel

\vec{e}_2 : normalized vector in pulling wire's direction

2.3. VARIOUS METHODS FOR LABORATORY TESTING TO OVERCOME FROUDE AND REYNOLDS SCALE CONFLICT

If the pulley wheel can be considered a solid disc with uniform mass distribution, equation 2.10 can be simplified to equation 2.11.

$$\vec{F}_p = (mg - (m + m_p)\vec{a}_t \cdot \vec{e}_2)\vec{e}_2 \quad (2.11)$$

with m_p the mass of the pulley wheel.

Table 2.5 summarizes the advantages and drawbacks of this method and is taken from Wright et al. (2015a).

Table 2.5: Advantages and drawbacks of the simple version of the mechanical pulley system

Advantages	Drawbacks
Low cost	Very simplistic representation
Reliable	Not time variable
Simple to build and use	No turbine control strategy
No wind generation required	no gyroscopic forces
Flexibility to model different turbines	

This method was used by the Hydraulics and Maritime Research Centre of the University College Cork, connected to the Marine Renewable Energy Ireland (MaREI) Centre, the COAST Laboratory of the University of Plymouth and ICTS-CIEM, Barcelona (Matha et al., 2015).

The Danish Hydraulic Institute did a more sophisticated version of the mechanical pulley system at scale 1:40. A geometrically scaled model rotor of the NREL 5 MW wind turbine was built and was driven by a motor. According to Tomasicchio et al. (2014), when the rotor is turning at the rated rotor speed (Froude scaled), a thrust of 4 N (256 kN at full scale) is created. To add the missing thrust, a weight corresponding to 7 N is suspended at the end of the pulley system. Table 2.6 summarizes the advantages and drawbacks of this method and is taken from Wright et al. (2015a).

Table 2.6: Advantages and drawbacks of motor-driven rotor combined with mechanical pulley system

Advantages	Drawbacks
Reliable	Not time variable
Gyroscopic forces	No turbine characteristics, power gen, etc.
Effective for low TRL (Technology Readiness Level) testing	
No wind generation required	

2.3.2 Actuator system

Instead of a model wind turbine and wind, an actuator is used, as illustrated in Figure 2.22. The actuator simulates the loads that the turbine would apply to the support structure. For this purpose, a motion tracking system measures live the displacement of the support structure. Using this data and the chosen wind spectrum to be tested, a software code, such as FAST, calculates the loads in real time to be applied by the actuator.

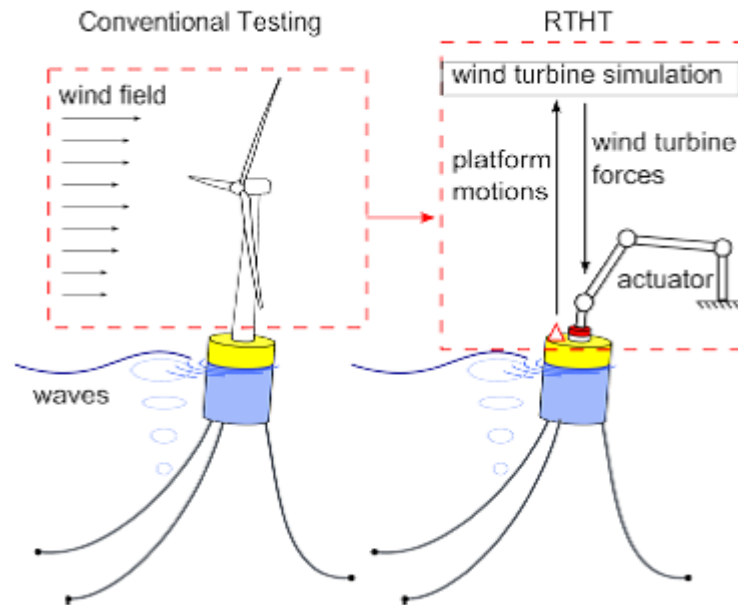


Figure 2.22: Schematic illustrating concept of actuator system. Reproduced from Hall et al. (2014), permission given by ASME Publishing.

A feasibility study of the actuator system method has been conducted by the University of Maine (Hall et al., 2014), but appears to not have been followed by actual experiments. MARINTEK (Bachynski et al., 2015) conducted a study preceding experiments allowing the determination of most crucial loads to be applied on the structure. Marintek calls their wind turbine testing method Real-Time Hybrid Model (ReaTHM) testing. This method coupling experimental testing and numerical simulations in real-time was first used by the Japanese to do testing for resistance to earthquakes. It is also used in the automobile industry. It is very useful when resistance to destructive events needs to be tested. Other names for it are “real-time hybrid testing”, “real-time hybrid simulations”, “real-time dynamic substructuring”, “hardware-in-the-loop”, “software-in-the-loop” and “model-in-the-loop”. This type of testing is now increasingly feasible thanks to higher capacity of computers and better numerical models. Using this type of method means using knowledge in four different types of scientific domains, that is numerical simulation, experiments on models, signal processing and control engineering. ReaTHM testing is useful when part of the model is too big to be put in the testing facility or the environmental conditions necessary for testing cannot be reproduced, in the case of scaling conflict, or when only one part of the system needs to be tested. One could ar-

2.3. VARIOUS METHODS FOR LABORATORY TESTING TO OVERCOME FROUDE AND REYNOLDS SCALE CONFLICT

gue that if one relies partially on numerical simulation, there is not much reason not to do all of the calculations numerically. However, Sauder et al. (2016a) mentions several situations for floating wind turbines where numerical simulation is not possible yet and where it is needed to have a physical model of the platform at least. Amongst these are extreme wave loads (slamming, ringing, green-water on deck), viscous loads (roll and yaw damping of ship-shaped floaters, or viscous effects limiting gap resonance in side-by-side configurations) and wave-current interaction effects on floating moored structures.

Amongst its advantages one can cite the absence of a need to design and build a new model wind turbine for each type of turbine to be tested. The conflict that exists between Reynolds and Froude scaling is absent. All types of forces can be simulated, including gyroscopic forces and wind turbine control can be tested. There is no need for the complicated production of good quality wind. Amongst the drawbacks it is the fact that the accuracy of the experimental results depend partially on the accuracy of the numerical model. Also, the model, the control system and the actuator need to respond quickly enough to avoid issues with latency, which further increases uncertainty of the results. Furthermore, the software used for the calculations needs to be adapted to run in real time. So far, there has not been extended testing using this concept.

In order to examine its accuracy and the requirements for an actuator that would apply the forces needed, the University of Maine (Hall et al., 2014) conducted a feasibility study at scale 1:50 . A fully numerical simulation using FAST to calculate maximum displacements and loads for three different types of support structures was conducted. It was determined that the maximum displacements that the actuator system would have to accomplish were 27 m at full scale in the surge direction and for the SPAR platform (For a sea state with $H_s = 10.5\text{ m}$ (significant wave height) and $T_p = 14.3\text{ s}$ (peak period) and a wind speed of 16.98 m/s). In the same met-ocean conditions, the largest displacement in the sway direction was determined to be 22.8 m for the semi-submersible platform. Maximum loads were obtained for the tension leg platform. The maximum force was in the heave direction and had a value of 6975 kN. The maximum moment (at the base of the tower) was in the direction of the pitch and its value was 400 MNm. In the conclusion it is stated that the distances that will need to be covered by an actuator are reasonable distances, that is, actuators from existing commercial robots are able to execute the maximum translational and rotational movements. The required forces and moments are achievable as well. The accelerations needed are smaller than those that can be achieved by actuators of commercial robots. Concerning the precision of the actuators, the force actuation error should not exceed 0.1 %, which is achievable. What is much more challenging is that the motion tracking system should achieve an error of less than 0.001 %. Concerning the latency, it should not exceed 1.77 ms, which is another great challenge.

The approach of Marintek, Norway consists in applying forces not at the position of the tower base, but on a frame situated at the tower top. The aerodynamic forces exerted by the wind on the rotor are calculated by Aerodyn and then applied to the tower top through a system of six wires pulling from different directions, as can be seen in Figure 2.23.

Before setting up the experiments, Bachynski et al. (2015) studied the importance of in-

2.3. VARIOUS METHODS FOR LABORATORY TESTING TO OVERCOME FROUDE AND REYNOLDS SCALE CONFLICT

cluding each component of the forces applied on the rotor. The conclusion summarizes the impact of the omission of each component on the platform motions and the forces applied on it (Table 2.7). It also recommends consulting the outcome of the simulations to determine the usefulness of applying each component depending on the purpose of the experiment.

Table 2.7: Impact of the omission of each force component on the rotor according to Bachynski et al. (2015)

Force	affects
Aerodynamic pitch moment (\neq pitch moment of thrust on tower base)	Pitch motions and mooring line tension (10 - 15 % changes in standard deviation)
Aerodynamic yaw moment	Yaw motions (80 % change in standard deviation)
Aerodynamic sway force + horizontal thrust directionality	Sway and roll motions (which are of small value)
Vertical directionality of thrust	Only during storm/parked conditions
Gyroscopic moments	Limited effects on low-frequency yaw response, near the yaw and pitch natural frequencies of the platform, in operational conditions

When doing the experiment, MARINTEK neglected two types of forces, the vertical aerodynamic force (heave) and the gyroscopic forces. The forces and moments which were considered and reproduced were: forces in the sway (coming from the thrust) and surge direction, moment in the roll direction (coming from the generator torque), and pitch and yaw moment. There are strings pulling in the following directions (Figure 2.24):

2.3. VARIOUS METHODS FOR LABORATORY TESTING TO OVERCOME FROUDE AND REYNOLDS SCALE CONFLICT

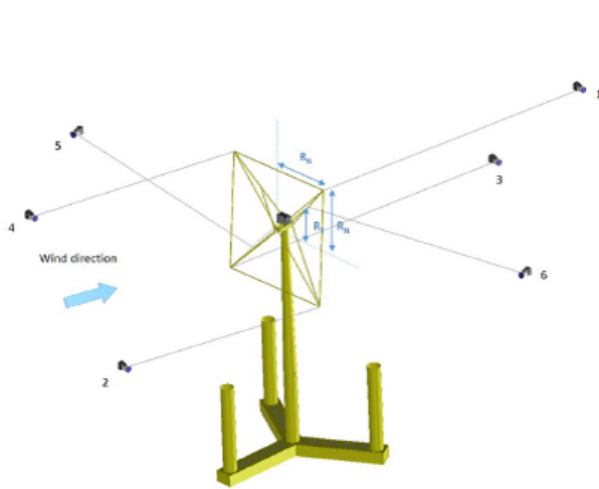


Figure 2.23: Schematic of six-wire pulley system that applies aerodynamic forces calculated by Aerodyn on the tower top, reproduced from Bachynski et al. (2016) with the permission of M. Thys from SINTEF Ocean

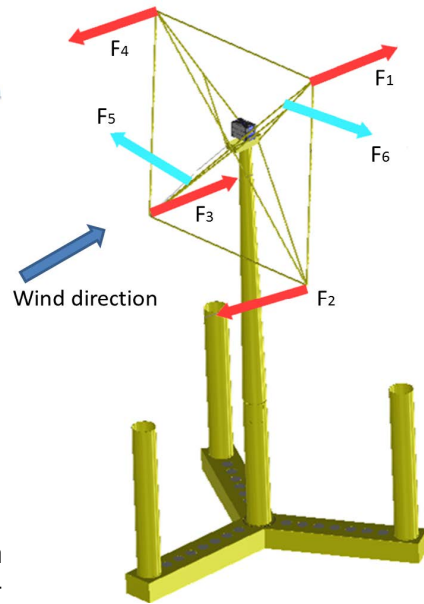


Figure 2.24: Actuator system set up by MARINTEK, reproduced from Sauder et al. (2016b) with the permission of ASME Publishing

One important point to note is that the mass of the wind turbine is not produced by the actuator system but by placing weights at the tower top. The cables that provide forces F_1 to F_4 are pre-tensioned to avoid slack. The wires are controlled through servomotors. The forces are measured through load cells. The motions of the platform are measured twice: once through a visual motion tracking system, then through gyro meters and accelerometers. The former provides accuracy, whereas the latter provides fast information. More information can be found in Sauder et al. (2016a,b). Table 2.8 summarizes the advantages and drawbacks of this system according to Wright et al. (2015a).

Table 2.8: Advantages and drawbacks of the Actuator system

Advantages	Drawbacks
All forces modelled	Latency issues
No wind generation required	Force error issues
Full WT model numerically, including power gen, etc.	
Variable wind conditions	
Flexibility to model different turbines	

2.3.3 Simulating varying aerodynamic thrust by means of a fan on the tower top

Instead of making a wind turbine turn through wind, one can instead use a fan powered by an electric motor placed on the tower top to produce the correct thrust. In Wright

2.3. VARIOUS METHODS FOR LABORATORY TESTING TO OVERCOME FROUDE AND REYNOLDS SCALE CONFLICT

et al. (2015), a tension leg platform is tested experimentally. The wind turbine is replaced by a ducted fan. By adapting the rotational speed of the fan, thrust variations are simulated at the top of the tower. Weights were added to the tower top, as the ducted fan's weight was smaller than the scaled weight of the rotor. In order to obtain the relationship between the rotational speed of the fan and the thrust produced, one can use a bending load cell, as in Figure 2.25, or measure the strain in a metallic sheet as in Figure 2.26. Wright et al. (2015) recommends obtaining the curve before deciding on the scale of the experiments, as the maximum thrust that can be produced needs to be known for this purpose.

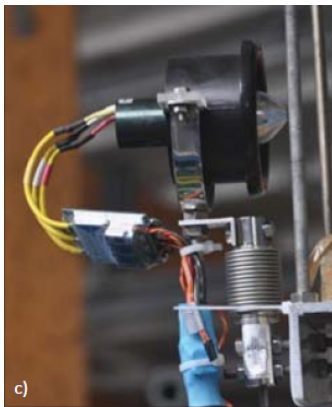


Figure 2.25: Measurement of thrust produced through ducted fan by means of a bending load cell (Wright et al., 2015)



Figure 2.26: Measurement of thrust produced through ducted fan by means of a sheet metal and strain gauges, reproduced from Wright et al. (2015a) with the permission of MARINET

Sandner et al. (2014) also used a ducted fan to simulate thrust on wind turbine. The difference to Wright et al. (2015) is that the rotational speed of the fan was controlled not manually but through real time simulations (comparable to those used by the actuator system described in Section 2.3.2). Here again, the platform motion needs to be monitored in real-time. The ducted fan used by Sandner et al. (2014) is said to provide thrusts of up to 18 N. Only free decay tests in pitch with varying wind speeds were performed with this set-up, but were judged satisfactory, as they reflected correctly the expected impact of wind speed on the platform motion. The simulation software used was FAST with Aerodyn. Table 2.9 summarises the advantages and drawbacks of this method.

Table 2.9: Advantages and drawbacks of the thruster system according to Wright et al. (2015a)

Advantages	Drawbacks
Variable wind conditions	Latency issues
No wind generation required	No gyroscopic forces
Full WT model numerically, including power gen, etc.	
Flexibility to model different turbines	

2.3.3.1 Multi-Propeller Device (MPD)

In Otter et al. (2020), a more sophisticated version of the ducted fan is presented. In this version, a total of six propellers are used to produce not only thrust but also rotor torque and gyroscopic moments, as well as the effect of wind shear. The MPD was used to simulate aerodynamic loads of the NREL 5 MW reference wind turbine at scale 1:37. The electronic speed controllers, electric motor and blades were the same parts as those used in a recreational aerial drone. FAST was used to calculate the aerodynamic loads to be applied. The set-up of the device had to take into account that the propellers could only produce thrust in one direction. The arms of the device are extendable to adjust for the need of larger moments. To cancel gyroscopic moments due to each individual propeller, each propeller is set up as a pair with another propeller rotating in the opposite direction.

The accuracy of the device was assessed through comparison between the loads calculated by FAST and those actually produced by the MPD. The Fraction of Measurements within a user-defined Tolerance (FMT) was close to 1 (perfect case) for thrust and torque. This value was much lower for the yaw moment induced by gyroscopic effect. Unintended vibrations and a time lag are given as reasons for the difficulty of reproducing gyroscopic loads adequately.

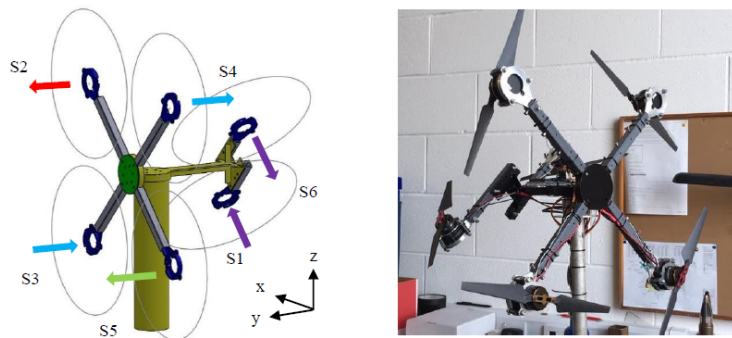


Figure 2.27: Use of a multi-propeller device to simulate various aerodynamic forces (Otter et al., 2020)

2.3.4 Wind generation on drag disc

For a laboratory that has a wind generation system, various methods can be used to model the aerodynamic loads from the wind turbine. The simplest consists of replacing the wind turbine rotor by a drag disc. This disc can be solid or a gauze. The idea is to use this disc to simulate the aerodynamic thrust of the wind on the rotor. The thrust that can be produced on the disc depends on the wind speed, the drag coefficient and the disc diameter.

2.3.4.1 Solid drag disc

According to Twele and Gasch (2007), a perfect wind turbine that achieves a power coefficient of 0.59, corresponding to the Betz limit (the maximum value of the power coefficient determined theoretically thanks to the 1D Momentum theory for an ideal wind turbine (Hansen, 2000)), would have a thrust coefficient of 0.89. Various papers

2.3. VARIOUS METHODS FOR LABORATORY TESTING TO OVERCOME FROUDE AND REYNOLDS SCALE CONFLICT

in which experiments using a drag disc were described, considered that the value for the thrust coefficient of a solid disc was 1.2 (Naqvi, 2012; Wan et al., 2014a; Roddier et al., 2010; Frye et al., 2011). Twele and Gasch (2007) considers this value to be 1.1. Looking at Figure 2.28, one can see that drag coefficient varies with the Reynolds number.

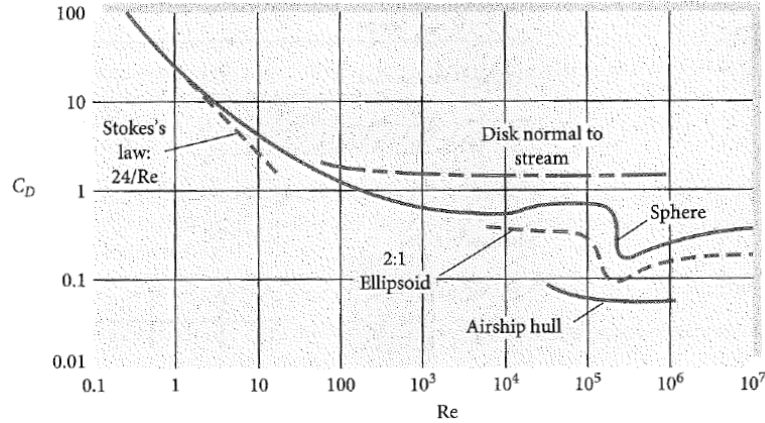


Figure 2.28: Evolution of the drag coefficient of a solid disc with the Reynolds number, reproduced from White (2016), with the permission of McGraw Hill

A quick calculation of the Reynolds number for wind blowing at a drag disc in laboratory conditions, allows to determine the value for the drag disc and confirms the values found in literature used for the drag coefficient. Supposing that the disk diameter is of the order of a meter and the wind speed is of the order of a meter at laboratory scale, the Reynolds number can be calculated as in Equation 2.12:

$$Re = \frac{1 \times 1}{1.51 \times 10^{-5}} \approx 6.62 \times 10^4 \quad (2.12)$$

It can be seen on Figure 2.28, that the drag coefficient is constant at about 1.2 for Reynolds numbers varying between 10^3 and 10^6 , so this value is not expected to change even with different conditions of drag disc diameter and laboratory wind speed.

If one wanted to use the same wind speed as for a wind turbine, the disc diameter would be smaller than the one of the model wind turbine. When one wants to use a disc with the same diameter as the model wind turbine, a porous disc needs to be used. In order to determine the size of the disc, equation 2.13 can be used:

$$D_{disc} = \sqrt{\frac{8 \times T_M}{\pi \rho_{air} v_{airM}^2 C_D}} \quad (2.13)$$

with T_M the scaled wind turbine thrust, ρ_{air} the density of air, v_{airM} the model air velocity and C_D the drag coefficient of the disc.

Alternatively, the disc size can be fixed, and the corresponding laboratory wind speed

2.3. VARIOUS METHODS FOR LABORATORY TESTING TO OVERCOME FROUDE AND REYNOLDS SCALE CONFLICT

that needs to be used can be calculated using Equation 2.14.

$$v_{airM} = \sqrt{\frac{8 \times T_M}{\pi \rho_{air} D_{disc}^2 C_D}} \quad (2.14)$$

The thrust being significantly smaller in extreme conditions, when the blades are pitched out, Wan et al. (2014a) describes using one disc for operational conditions and a smaller one for extreme wind conditions. The experimental set-up can be seen in Figure 2.29.

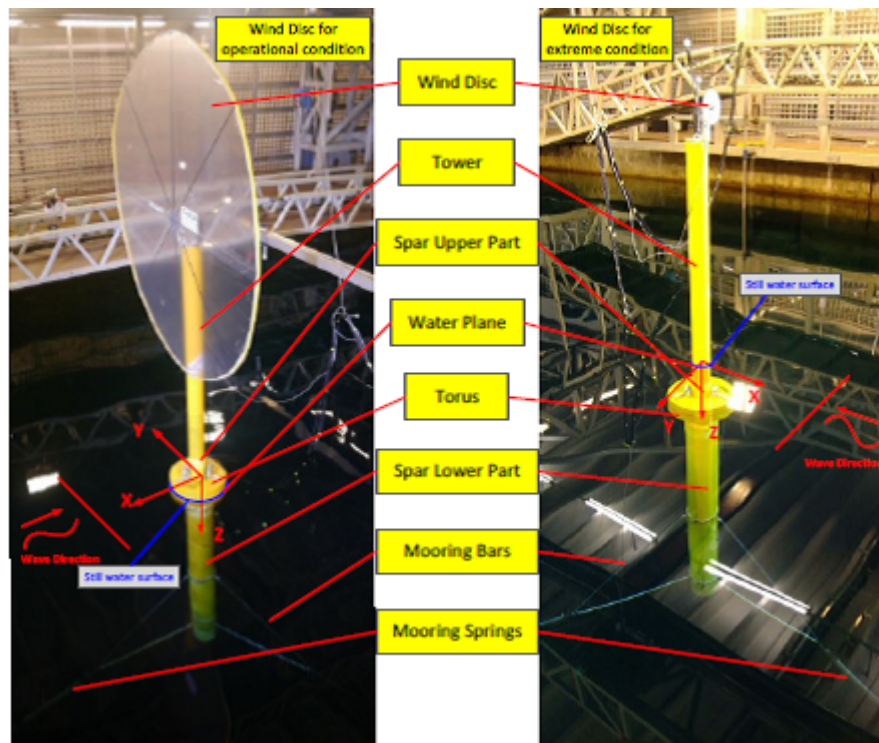


Figure 2.29: Experimental testing of floating wind turbine using drag disc model for operational and extreme conditions. Reproduced (Wan et al., 2014a) with the permission of ASME Publishing

Similar experiments were also done at the CNR-INSEAN in Rome, Italy and are reported in Wan et al. (2014b). Figure 2.30 shows the wind generator and the drag disc.

2.3. VARIOUS METHODS FOR LABORATORY TESTING TO OVERCOME FROUDE AND REYNOLDS SCALE CONFLICT



Figure 2.30: Drag disc experiments at CNR-INSEAN, Rome, Italy. Found in Wright et al. (2015a), originally from (Wan et al., 2014b). Permission obtained by MARINET

Table 2.10 summarizes the advantages and drawbacks of the method using a drag disc.

Table 2.10: Advantages and drawbacks of drag disc

Advantages	Drawbacks
Variable wind conditions	Wind generation complexity
Thrust load modelled	Wind generation uncertainties
	No gyroscopic forces
	No testing of turbine control strategy, power gen

2.3.4.2 Gauze, grid, porous disc

Not mentioned by Wright et al. (2015a) is the use of a porous disc to simulate a wind turbine. Only one paper was found where a porous disc was actually used on a floating platform. Ishihara et al. (2007) conducted a scaled experiment of a trifloater at scale 1:150, by replacing actual rotors with gauzed discs as can be seen in Figure 2.31. The thrust coefficient of these grids was determined to be 0.33 at a wind speed of 14 m/s. This was designed to simulate operating conditions. The full scale turbine diameter is 92 m. Neither the reduced scale diameter, nor the full scale thrust, or the porosity of the discs are indicated.

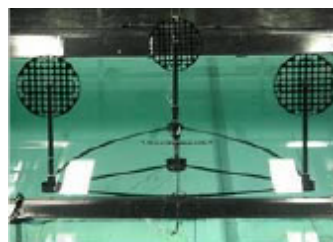


Figure 2.31: Trifloater scaled experiment with gauzed discs representing the wind turbines reproduced from Ishihara et al. (2007), permission given by T. Ishihara

2.3. VARIOUS METHODS FOR LABORATORY TESTING TO OVERCOME FROUDE AND REYNOLDS SCALE CONFLICT

Nevertheless, several papers (Lignarolo et al., 2016; Aubrun et al., 2011, 2013; Sheerin et al., 1981) are available describing the use of porous discs to simulate wind turbine rotors not necessarily in a marine environment. The purpose of these experiments is most of the time to see whether the use of a porous disc can simulate the wake behind a wind turbine. And the verification of this serves numerical models where in the study of array layout of wind turbines, the wind field behind each turbine needs to be close to reality. Replacing a rotor by a disc reduces complexity and calculation time. Though not specifically mentioned, it seems reasonable to think that using the results of these experiments, experimental study of array layout of wind turbines can be performed.

Lignarolo et al. (2016) compares the wake produced behind a gauze and a wind turbine rotor, in order to see if the former could replace the latter when studying the behaviour of wind turbines in array set-up. The purpose of the study is to prove the effectiveness of the actuator disc theory in numerical modelling. It was concluded that though the turbulence intensity behind the real rotor and the simulated rotor through a disc were not the same, thrust, energy, wind speed, pressure and enthalpy were similar, which looks promising for a use of gauze in array study.

Aubrun et al. (2011) used a porous disc with the same diameter as the rotor (Figure 2.32). The mesh had a solidity of 45 %. In addition a circle of a diameter of 0.1 of the rotor diameter was placed at the centre. Its solidity was 35 %. At a distance measuring half of the rotor diameter downstream of the disc as well as the rotor, the dimensionless velocity deficit on a horizontal line crossing the main axis of flow was determined to be very similar (Figure 2.33).

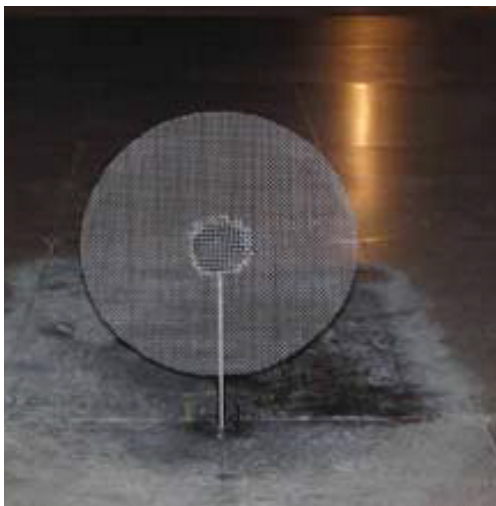


Figure 2.32: Porous disc used by Aubrun et al. (2011), permission granted by S. Aubrun

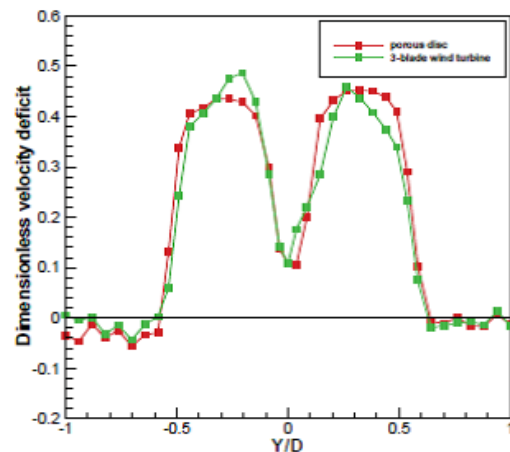


Figure 2.33: Dimensionless velocity deficit 0.5 rotor diameters behind the rotor or the porous disc (Aubrun et al., 2011), permission granted by S. Aubrun

In Aubrun et al. (2013) another porous disc is mentioned. This disc had a diameter of 0.1 times the wind turbine rotor diameter. The wind turbine that was tested had a rotor diameter of 40 m at full scale. The disc solidity was 45 %. It corresponds to a wind turbine with a thrust coefficient of 0.61 and a power coefficient of 0.5.

2.3. VARIOUS METHODS FOR LABORATORY TESTING TO OVERCOME FROUDE AND REYNOLDS SCALE CONFLICT

In Sheerin et al. (1981), two different porous discs are used to simulate the wake behind wind turbines. Both of them had a disc diameter of 152 mm and were used to simulate a wind turbine of a rotor diameter of 100 m at full scale. The first disc was used to simulate conditions where the thrust would be high, using a porosity of 0.43, giving a thrust coefficient of 0.92. For lower thrust, a second disc with a porosity of 0.83 was used, giving a thrust coefficient of 0.26.

2.3.4.3 Adding gyroscopic forces to a drag disc

The University of California Berkeley added the simulation of gyroscopic forces to a solid drag disc (Roddier et al., 2010). They used a disc that corresponded to a disc at prototype scale of 72.7 m, which corresponds to an area that is 1/3 of the total area covered by the wind turbine rotor. Figure 2.34 shows the system used by the University of California Berkeley. Item number 5 is the drag disc made of foam board. Item number 6 is a motor which turns rod number 8. On this rod, two masses are suspended (Items number 7). This rotating rod simulates the rotational inertia of the blades, therefore reproducing the turbine's gyroscopic forces.

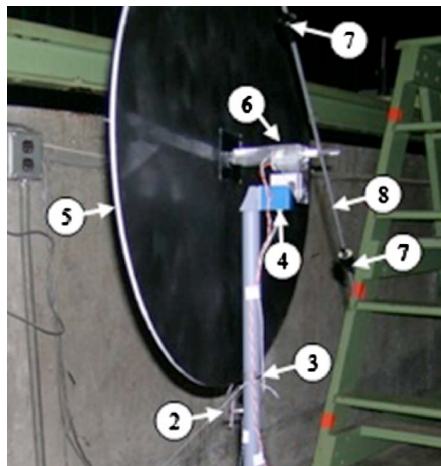


Figure 2.34: Drag disc used by University of California Berkeley. Reproduced from Roddier et al. (2010), with the permission of AIP Publishing obtained via the Copyright Clearance Center

A similar set-up is described by Frye et al. (2011). In this set-up, a set of blades is placed behind a drag disc. The blades are correctly scaled in terms of mass, but are not required to provide the correct thrust according to Froude scaling, as this is compensated for through the thrust on the drag disc. The disc was placed between the wind blower and the blades as can be seen in Figure 2.35.

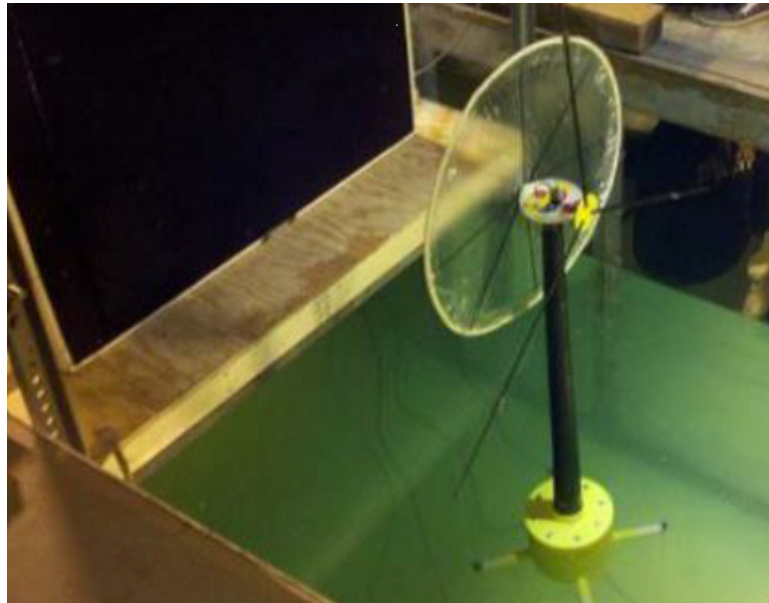


Figure 2.35: Drag disc and driven rotor at Worcester Polytechnic Institute. Found in Wright et al. (2015a). Originally from Naqvi (2012). Permission given by MARINET

Table 2.11 summarizes the advantages and drawbacks of this method according to Wright et al. (2015a).

Table 2.11: Advantages and drawbacks of drag disc with driven rotor

Advantages	Drawbacks
Variable wind conditions	Wind generation complexity
Thrust load modelled	Wind generation uncertainties
Gyroscopic forces modelled	No turbine characteristics, power gen

2.3.5 Wind generation on model turbine

In spite of the Froude-Reynolds number conflict presented in Section 2.2.4, it is possible to test a floating wind turbine platform by blowing wind on a model turbine. 2 methods to resolve them are presented here: One can chose to modify the blade properties, not keeping a purely geometrically scaled version of the blade, and try to obtain correct thrust force and rated rotor speed at the correct wind speed. Another method consists in getting a correct thrust force and rated rotor speed (including tip speed ratio) with an incorrect wind speed, by using redesigned blades or not. Both methods will require that the model wind turbine is driven by a motor, to ensure correct rotational speed. In both methods, a manual or servo-driven adjustable blade pitch system can be implemented.

The following subsections will present in this order: the definition of some terms specific to aerodynamic profiles, blades, and rotors used here; a detailed analysis of the issues with a geometrically scaled blade and possible solutions; how to obtain correct thrust

at incorrect wind speed; and how to obtain correct thrust at correct wind speed.

2.3.5.1 Definition of terms used to describe aerodynamic profiles, blades and rotors

This subsection will give the definition of several terms specific to aerodynamic profiles, blades and wind turbine rotors, which will be used in the following subsections. The blade chord is the length of an aerodynamic profile, or the distance between the leading edge and the trailing edge. The blade camber defines the convexity of an airfoil (see Figure 2.36). A symmetric airfoil is an airfoil that has no camber.

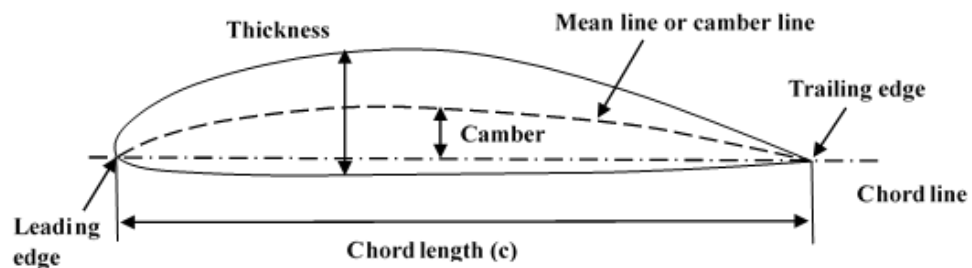


Figure 2.36: Definition of camber and chord

The rotor solidity is the ratio of total blade area to the disk area. Blade span can be defined in several ways. It can be the length of the blade, that is the distance between the rotor hub and the blade tip. In some cases it indicates the rotor diameter. In Figure 2.45 of the subsection "Correct wind speed", it indicates the location on the blade relative to the hub centre.

2.3.5.2 Problems with a geometrically scaled blade and solutions

In this subsection, it is first explained what happens when the blades are simply scaled down geometrically. It then presents the reasons behind the drop in performance of the model wind turbine when compared to the prototype in the situation of geometrical scaling of the blades. It then goes on to present why it is important to conserve certain forces, that conserving them all is hard to achieve and that a choice/compromise needs to be made. It explains which forces should be prioritized and why. It then goes on to present 3 methods that can be used to overcome the drop in performance. They are presented and compared. The best one is presented and explained in detail.

The most straightforward way to make a blade for a model wind turbine is to simply conserve the shape of the prototype and draw the same geometry 50 times smaller. Martin et al. (2012) tried testing a geometrically scaled blade of the NREL 5 MW wind turbine. C_p (power coefficient) and C_T (thrust coefficient) as a function of TSR were determined and compared to those of the prototype. They were significantly less than those of the prototype (see Figure 2.37). A detailed explanation for this is given in this document. When looking at the contribution of lift and drag to torque and thrust – which in turn influence C_T and C_p – it is explained that a decrease in lift contributes greatly to a decrease in thrust, while an increase in drag is mainly responsible for a decrease in torque.

2.3. VARIOUS METHODS FOR LABORATORY TESTING TO OVERCOME FROUDE AND REYNOLDS SCALE CONFLICT

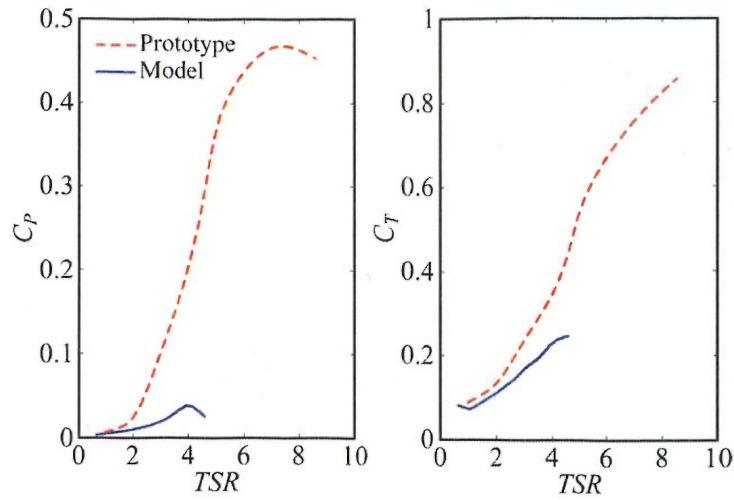


Figure 2.37: Comparison of C_P and C_T vs TSR between the prototype and a geometrically scaled model wind turbine (taken from Martin et al. (2012) with the permission of ASME Publishing obtained through the Copyright Clearance Center)

When comparing C_L (lift coefficient) and C_D (drag coefficient) for the prototype and the model, it can be observed that there is a drop in the lift coefficient and an increase in the drag coefficient for the model for one of the aerodynamic profiles of the wind turbine (see Figure 2.38). The reason for this is a change in the Reynolds number, which causes the flow regime, turbulent at full scale, to be laminar at reduced scale. Laminar flow is more sensitive to adverse pressure gradients, causing flow separation to occur closer to the leading edge. This creates a thick boundary layer around the airfoil, increasing the drag and causing a drop in lift.

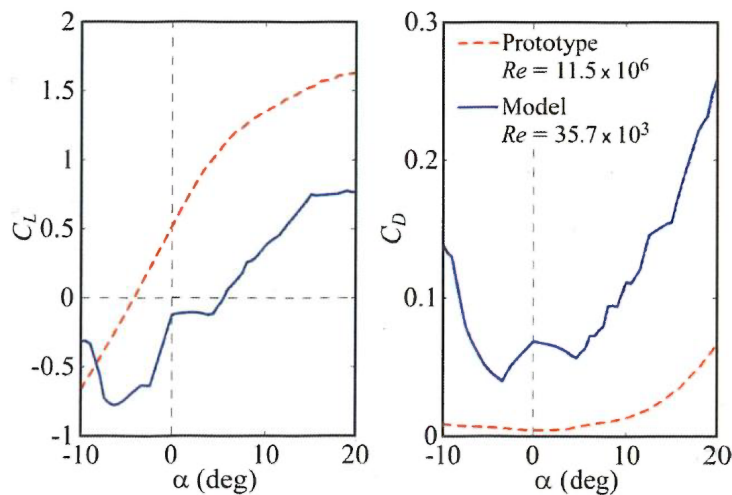


Figure 2.38: Comparison of lift and drag coefficients for the NACA 64-618 profile for high and low Reynolds numbers (taken from Martin et al. (2012) with the permission of ASME Publishing obtained through the Copyright Clearance Center)

2.3. VARIOUS METHODS FOR LABORATORY TESTING TO OVERCOME FROUDE AND REYNOLDS SCALE CONFLICT

Martin et al. (2012) describes 3 methods to solve this problem. The first one is to increase the wind speed, with the aim to have at least a correct thrust on the model wind turbine. The second one is to roughen the leading edge to trigger transition from laminar to turbulent. The third one is to change the design of the airfoils, replacing the geometrically scaled airfoils by airfoils that are high performing at low Reynolds numbers. One could even combine several methods.

They have tested the first two methods and reported the results. The results of roughening the blade were not very encouraging. First of all, improvement was only seen beyond a TSR of 4, and even those were insufficient. And below TSR=4, the performance was actually worse. This was because at lower speeds, flow regime transition does not occur, and drag is increased due to friction. Also, the transition of flow regime was described to result in sudden changes of thrust.

The results of the method of increased wind speed are presented in the following paragraph, alongside those of another research facility.

2.3.5.3 Increased wind speed

Correct constant thrust can be achieved by increasing the wind speed blown on the model wind turbine. In the tests described in Martin et al. (2012) a wind turbine model of the NREL 5 MW wind turbine at scale 1:50 was used with blades that were scaled geometrically. They aimed to get the correct thrust at rated wind speed. The rated wind speed for the NREL 5 MW wind turbine is 11.4 m/s for the prototype, which corresponds to 1.6 m/s for the model. It was found that a wind speed of 2.94 m/s needed to be blown at the model wind turbine to achieve the correctly scaled thrust according to Froude scaling. However, variations in thrust force are not expected to be represented accurately. This means that it is not possible to study active pitch damping through an increase in wind speed. It also means that the effect of high wind speeds cannot be studied, unless the laboratory has the capability to produce very high wind speeds. They checked however whether aerodynamic damping at least was correctly represented and found that it was the case.

Courbois (2013) also tested an NREL 5 MW model wind turbine at scale 1:50. He decided to use a higher wind speed than Froude scaled wind speed in order to obtain Froude scaled lift on the geometrically scaled airfoils. Changing the wind speed implies though not only changing the relative velocity value, but also the angle of attack and therefore the lift and drag coefficient, which in turn changes the rotational speed, and therefore again the value of the relative velocity. Using an iterative method, he determined a combination of the wind speed and the twist of the blade that would yield the correct thrust coefficient. Table 2.12 summarizes the advantages and drawbacks of this method.

Table 2.12: Advantages and drawbacks of using a model wind turbine rotor

Advantages	Drawbacks
Variable wind conditions	Wind generation complexity
Thrust load modelled	Wind generation uncertainties
Gyroscopic forces modelled	Unique to turbine

2.3.5.4 Correct wind speed

To avoid increasing the wind speed, low Reynolds number profiles need to be used. Martin et al. (2012) presents the Drela AG04 profile (normalized xy coordinates can be found in Appendix F.1) which performs well at low Reynolds numbers. The lift coefficient is higher than the one of the NACA 64-618 profile at Reynolds numbers for the model wind turbine, and the drag coefficient is lower than the one of the NACA 64-618 profile at the same Reynolds numbers, as can be seen in Figure 2.39.

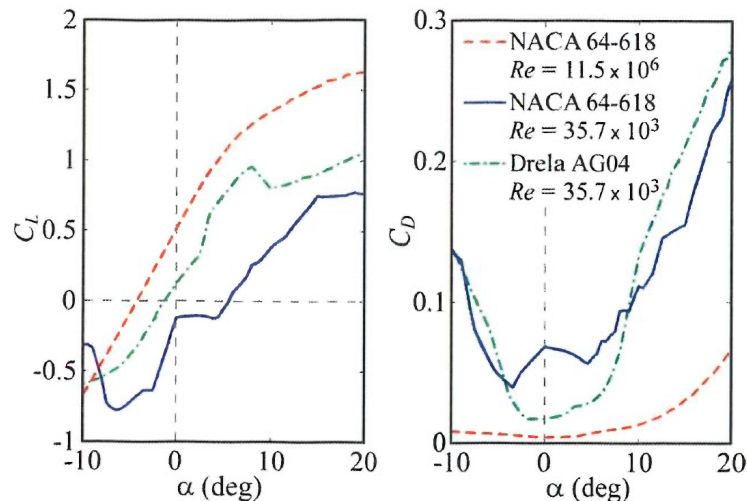


Figure 2.39: Lift and drag coefficient of Mark Drela AG04 profile and comparison to NACA profile at low and high Reynolds numbers (taken from Martin et al. (2012) with the permission of ASME Publishing obtained through the Copyright Clearance Center)

Martin (2011) proposes a first geometry for the modified blade using the Drela AG04 profile (coordinates can be found in Appendix F.1), that would allow to match the scaled-down thrust of the full size wind turbine. This geometry is too slender, however.

Kimball et al. (2014) describes tests performed on a low Reynolds rotor using a slightly different geometry with the same profile. The thickness profile is however doubled and increased towards the trailing edge, to increase structural rigidity and facilitate manufacture. Near the root, instead of the slender Drela AG04 profile, a series of profiles were used that allowed a smooth transition from a cylindrical shape to the Drela AG04 profile. This made a slightly thicker root than the first design and allowed the blade to be stronger. See Figure 2.40 for a comparison of the profiles.

2.3. VARIOUS METHODS FOR LABORATORY TESTING TO OVERCOME FROUDE AND REYNOLDS SCALE CONFLICT

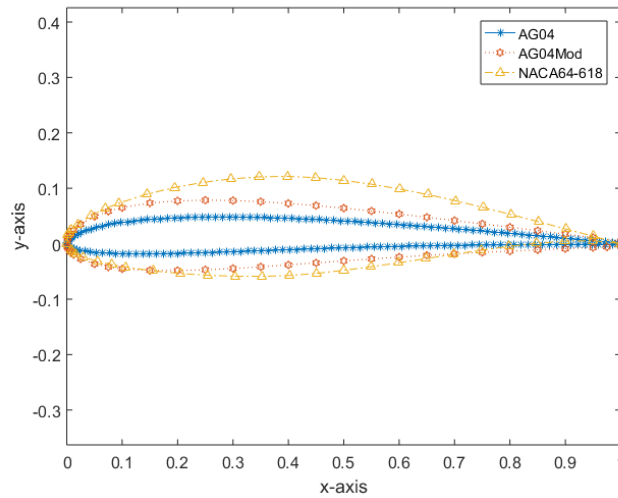


Figure 2.40: Comparison of the NACA 64-618 profile with the Drela AG04 and the modified Drela AG04 profile (coordinates taken from Kimball et al. (2014) for the modified Drela profile, Jackman (2005) for the original Drela AG04 profile, and UIUC Applied Aerodynamics Group - Department of Aerospace Engineering (n.d.) for the NACA 64-618 profile)

De Ridder et al. (2014) describes in detail design and experimental testing of the wind turbine using the Drela AG04 profile. The modified blade geometry is justified by the insignificant change in the pressure distribution on the modified profile when compared to the original Drela AG04 profile, as well as the only slightly changed value of the maximum value of $\frac{C_L}{C_D}$ which can be seen in Figure 2.41 and Figure 2.42.

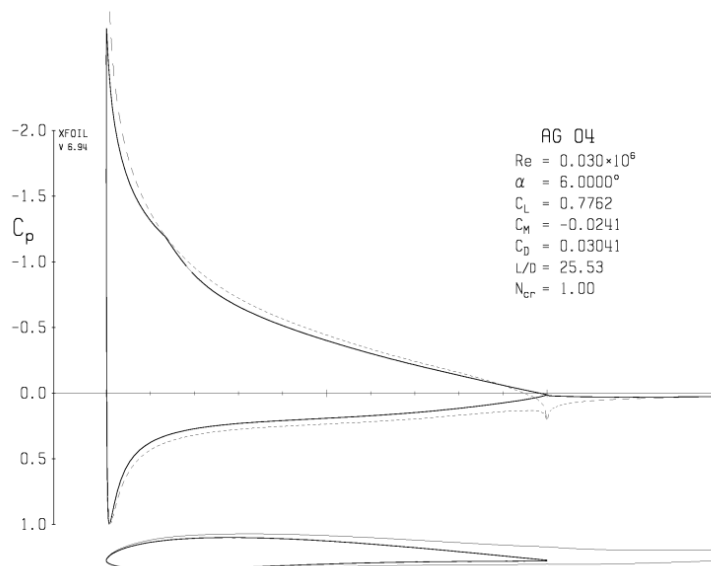


Figure 2.41: Pressure distribution on Drela AG04 profile calculated by XFOIL (taken from De Ridder et al. (2014) with the permission of ASME Publishing)

2.3. VARIOUS METHODS FOR LABORATORY TESTING TO OVERCOME FROUDE AND REYNOLDS SCALE CONFLICT

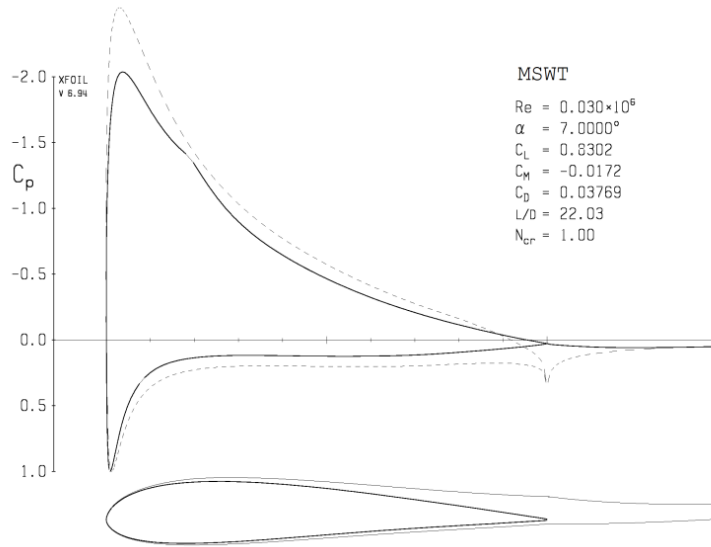


Figure 2.42: Pressure distribution on modified Drela AG04 profile calculated by XFOIL (taken from De Ridder et al. (2014) with the permission of ASME Publishing)

They also analysed the whole blade using the modified Drela AG04 profile, both through the software PROPID, which uses the Blade Element Momentum (BEM) Theory and through the CFD software ReFRESH. Model tests were also performed. The model wind turbine had active pitch control and the rotor speed was controlled by an electric engine. The results were compared to the target values, that is C_T and C_P as a function of TSR of the NREL 5 MW wind turbine. Figure 2.43 shows all the results and the target value.

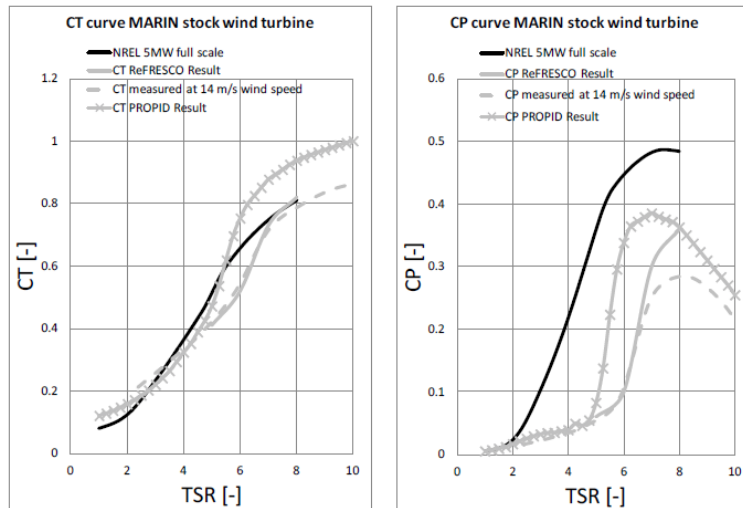


Figure 2.43: Comparison of the C_T and C_P of the Marine Stock Wind turbine using the modified Drela AG04 profile determined through BEM (Propid), CFD (ReFRESHCO) and experimentally with the target values of the NREL 5 MW wind turbine (De Ridder et al., 2014) with the permission of ASME Publishing

2.3. VARIOUS METHODS FOR LABORATORY TESTING TO OVERCOME FROUDE AND REYNOLDS SCALE CONFLICT

It can be seen that the C_T is matched fairly well in the experimental results, and the CFD results are very close to the experimental results. The results for C_T of the BEM Method are slightly higher than reality. The C_p is lower than the target value. Again, the BEM Method predicts higher results than in reality. This time, the CFD also predicts better results than those found through experiment, at least for higher TSR. The wind turbine is nevertheless considered of sufficient quality, as matching the thrust is the most crucial element. The slight difference between the target value and the measured results can be adjusted through slight modification of the blade pitch. The fact that C_p of the model does not match C_p of the prototype is less important, as it does not affect floater movement significantly.

Sandner et al. (2014) performed tests using a low Reynolds rotor, which allowed to model the NREL 5 MW wind turbine at scale 1:60. They increased the rotor solidity by increasing the blade chord and used low Reynolds number airfoils. This rotor used the airfoil blade RG 14 (RG stands for Rolf Girsberger). The profile is shown in Figure 2.44 alongside the NACA 64-618 profile, used in the most outer sections of the NREL 5 MW blade.

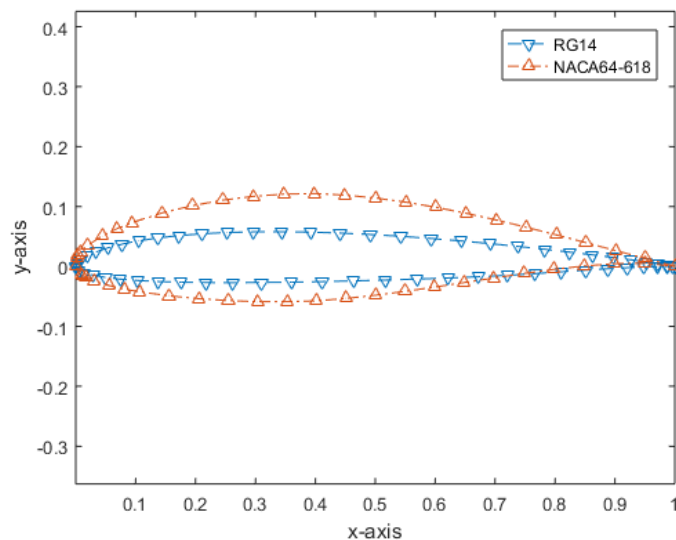


Figure 2.44: Comparison of RG14 profile and NACA 64-618 profile

Figure 2.45 shows the evolution of the blade chord of the low Reynolds rotor along the blade span next to the one of the NREL 5 MW wind turbine.

2.3. VARIOUS METHODS FOR LABORATORY TESTING TO OVERCOME FROUDE AND REYNOLDS SCALE CONFLICT

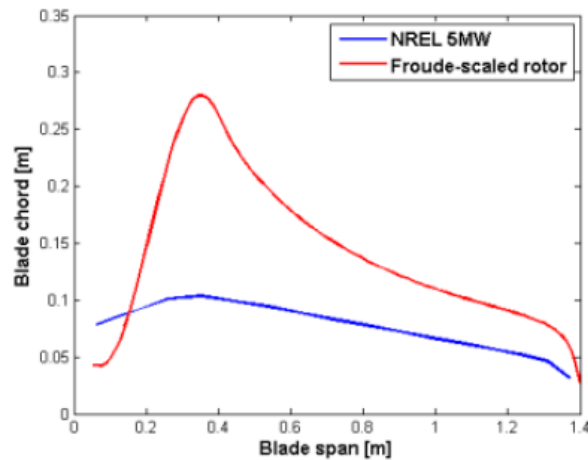


Figure 2.45: Blade chord as function of blade span of low Reynolds rotor compared to NREL 5 MW (Sandner et al., 2014), with the permission of F. (Sandner) Lemmer

The rotor can be seen in Figure 2.46.



Figure 2.46: Low Reynolds rotor used by Sandner et al. (2014), with the permission of F. (Sandner) Lemmer

Pitch control is needed to obtain the right C_T as a function of the tip speed ratio, that is, the same as the one obtained for the prototype. When doing experiments at very small scales, the Froude scaled wind speeds will be very low. This is not always easy to do, as it is difficult to get low enough turbulence intensity with slow wind speeds. When the correct wind speed according to Froude scaling is used and through modified blade design the lift and drag coefficients are identical to the prototype, the Tip Speed Ratio is preserved. Therefore, the rotational speed of the rotor is Froude scaled.

Pegalajar-Jurado et al. (2016) managed to make a model rotor that reproduces the

key aerodynamic characteristics of the DTU 10 MW turbine. They used Selig/Donovan 70xx airfoils. The majority of the profiles are Sd7003, and Sd 7032 and Sd 7062 are used for transition from cylinder to Sd7003. The scale of the experiment was 1:60. As for the model wind turbine described in Sandner et al. (2014), the chord was increased when compared to the original geometrically scaled blade profile. A motor is used to achieve the correct rotational speed of the turbine. To get the correct thrust, the pitch angle was slightly adjusted for certain wind speeds in order to match the downscaled thrust of the DTU 10 MW wind turbine. Pegalajar-Jurado et al. (2016) reports that aerodynamic damping was correctly modelled.

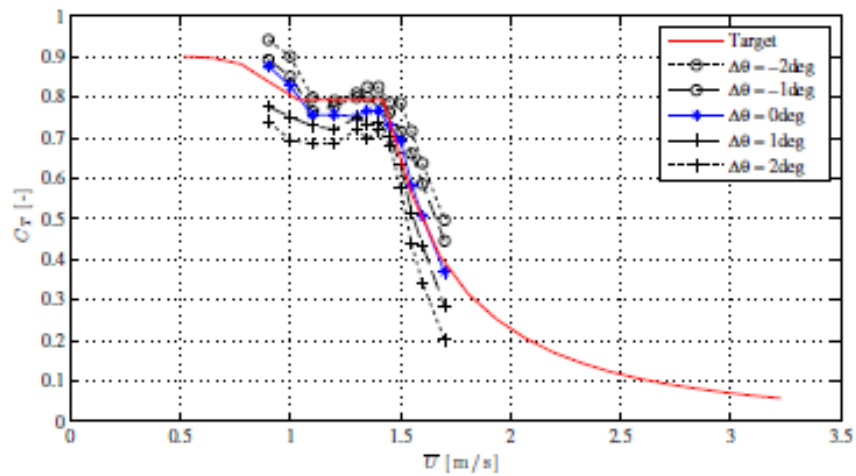


Figure 2.47: Thrust coefficient C_T as a function of laboratory wind speed for the low Reynolds number model wind turbine used by Pegalajar-Jurado et al. (2016)

2.4 Literature review on wind generators

When using the method of wind blowing on a drag disc or on a model turbine, wind needs to be produced in the laboratory. The wind speed that needs to be produced depends on the environmental conditions that are aimed to be reproduced, and the scale of the experiment.

2.4.1 Requirements for wind speed

The cut-off wind speed of the NREL 5 MW wind turbine is 25 m/s. So to test this wind turbine in operational conditions, one would need to be able to produce the equivalent of 25 m/s at reduced scale. For testing extreme conditions, it is good to have an idea of the 50 year return of maximum winds of the site at which the turbine would be installed. In Gomez et al. (2015), the 50 year wind at hub height for three different sites in the Atlantic ocean can be found. This study was done for a 10 MW wind turbine for three different types of met-ocean conditions. The moderate met-ocean conditions came from the Golfe de Fos in France and gave a 50 year wind at hub height of 37 m/s. The medium met-ocean conditions were taken from the Gulf of Maine in the USA and gave a 50 year wind at hub height of 44 m/s. The severe met-ocean conditions were taken from West of the Isle of Barra in Scotland and the 50 year wind was 50 m/s. The hub height was at 120 m above sea level.

If the model wind turbine used with the wind generator needs increased wind speed to produce sufficient thrust (see Section 2.3.5.3), the maximum available wind speed needs to be higher correspondingly.

To correspond more precisely to real wind conditions, the wind generator would ideally produce sheared wind. Hansen (2000) and DNV (2014) give two suggestions for formulas for the vertical profile of the wind can be found. Equation 2.15 assumes a logarithmic profile.

$$\frac{V_{10min}(z)}{V_{10min}(h)} = \frac{\ln(z/z_0)}{\ln(h/z_0)} \quad (2.15)$$

with $V_{10min}(z)$ the time averaged value for a period of 10 minutes at a height z above the ground, $V_{10min}(h)$ the time averaged value at a fixed height h and z_0 the roughness length. The roughness length can be estimated to have a value of 10^{-4} over water without waves. With waves it can be as high as 0.01 (DNV, 2010). DNV (2014) and DNV (2010) mention Equation 2.16, which allows to solve for z_0 .

$$z_0 = \frac{A_C}{g} \left(\frac{\kappa V_{10}}{\ln(z/z_0)} \right)^2 \quad (2.16)$$

with g acceleration of gravity, $\kappa = 0.4$ the von Karman's constant, A_C Charnock's constant. $A_C=0.011$ to 0.014 is recommended for open sea with fully developed waves and $A_C \geq 0.018$ for near coastal locations.

Equation 2.17 assumes a power law profile.

$$V_{10min}(z) = V_{10min}(h) \left(\frac{z}{h} \right)^{\alpha_c} \quad (2.17)$$

with α_c a parameter giving the amount of shear. α_c is in the range between 0.1 and 0.25, according to Hansen (2000). DNV (2014) recommends using $\alpha_c = 0.14$ for off-shore locations. DNV (2010) recommends using $\alpha_c = 0.12$ for open sea with waves.

2.4.2 Requirements for outlet size

In 2020 the largest wind turbine installed has a rotor diameter of 220 m (Haliade-X 12 MW (Steffen, 2019)). To determine the wind blower outlet, one needs to add to the maximum size of the model that would be used, the zone where the wind is strongly influenced by the surrounding air that is not in motion and where the gradient is important. Furthermore, the wind turbine can have sway motion, which could reach 22.8 m at full scale for a semi-submersible platform (Hall et al., 2014). Concerning the height of the blower outlet, it is good to provide the laboratory with the possibility to test wind turbines with varying hub heights.

2.4.3 Requirements for turbulence levels

Another parameter that should be aimed to be reproduced is turbulence intensity. The relationship between the measured instantaneous wind speed, the calculated average wind speed and the instantaneous turbulent component can be expressed according

2.4. LITERATURE REVIEW ON WIND GENERATORS

to Equations 2.18, 2.19 and 2.20:

$$U = \bar{U} + u' \quad (2.18)$$

$$V = \bar{V} + v' \quad (2.19)$$

$$W = \bar{W} + w' \quad (2.20)$$

with W the instantaneous wind speed in the vertical direction, V the instantaneous wind speed in the main horizontal direction, U the instantaneous wind speed perpendicular to the main flow direction, \bar{U} , \bar{V} , \bar{W} the average wind speeds in the above 3 directions and u' , v' , w' the turbulent components in the above 3 directions.

In this configuration, v' is called the longitudinal turbulence component. u' and w' are called the lateral turbulence components. Turbulence intensity is defined for each of the three components by Equations 2.21, 2.22 and 2.23.

$$I_{uu} = \frac{\sqrt{\overline{u'^2}}}{\overline{Vel}} \quad (2.21)$$

$$I_{vv} = \frac{\sqrt{\overline{v'^2}}}{\overline{Vel}} \quad (2.22)$$

$$I_{ww} = \frac{\sqrt{\overline{w'^2}}}{\overline{Vel}} \quad (2.23)$$

with $\overline{Vel} = \frac{\sum Vel}{N_m}$ and $Vel = \sqrt{U^2 + V^2 + W^2}$, using the same definition as in Ohana et al. (2014), where N_m is the number of measuring points. As the turbulence intensity is dimensionless, the turbulence intensity will be identical at reduced scale.

To decide what kind of turbulence level is good to have in the laboratory, real wind conditions measured at an offshore wind turbine site (bottom mounted wind turbines) were consulted. The data was found in Hansen and Sommers (2002).

Figure 2.48 shows the evolution of the longitudinal turbulence intensity with average longitudinal wind speed at 62 m above sea level. The longitudinal turbulence intensity at 15 m/s is 7.9 %.

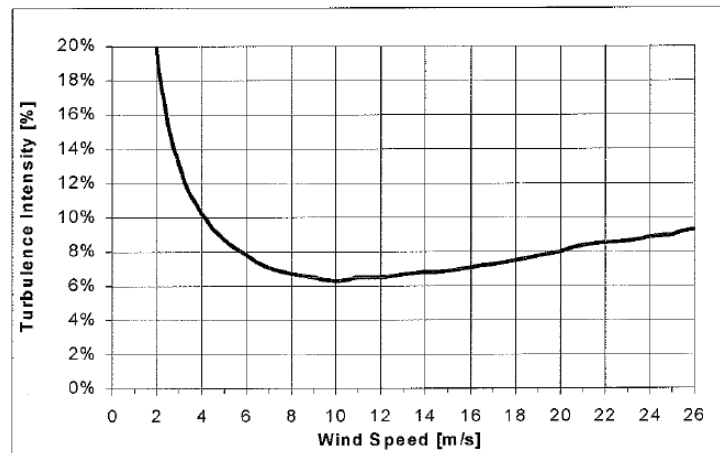


Figure 2.48: Evolution of longitudinal turbulence intensity with wind speed (Hansen and Sommers, 2002), with the permission of K. S. Hansen and A. Sommers

2.4.4 Literature review on honeycombs and meshed screens

Though the wind generation systems used over wave tanks differ from classic wind tunnels, recommendations for the choice of the fans as well as the choice of the flow straighteners are taken from literature for classic wind tunnels, as these systems have been developed over several decades. According to Wright et al. (2015a), centrifugal fans are recommended for achieving lower turbulence levels whereas axial fans are recommended for obtaining a greater operational range. Mehta and Bradshaw (1979) recommend the use of centrifugal fans for low speed wind tunnels. It is from this paper that the majority of the recommendations for honeycombs and meshed screens were taken. The two types of turbulence mentioned in Section 2.4.3, that is longitudinal and lateral turbulence, need to be reduced by two types of flow straighteners. Lateral turbulence, is mainly reduced using honeycomb flow straighteners. Longitudinal turbulence is mainly reduced through screens, "made of thin wires interwoven to form square or rectangular meshes" (Kulkarni et al., 2011).

Mehta and Bradshaw (1979) recommend having 150 honeycomb cells across the settlement chamber diameter, or 25000 honeycomb cells in the whole area. The pressure drop coefficient is recommended to have a value of 0.5. The ratio of the cell length over the cell diameter is recommended to have values between 6 and 8 according to Mehta and Bradshaw (1979). According to Kulkarni et al. (2011), the various studies performed on honeycombs have found ratios between 8 and 12 to be most effective. Their own numerical simulations have given the information that ratios between 8 and 10 were most effective. For the screens, the porosity, or open area ratio is recommended to have a value above 58%. The pressure drop coefficient is recommended to have a value of 1.5.

Eckert et al. (1976) present a formula (Equation 2.24) to calculate the pressure drop coefficient of honeycombs. The pressure drop coefficient is defined by Scheimann (1981) as the "static pressure drop across the manipulator Δp divided by the dynamic pressure q of the main flow through the manipulator". Its value helps determine the

turbulence reduction provided by the flow straightener.

$$K = \lambda_h \left(\frac{L_h}{D_h} + 3 \right) \left(\frac{1}{\beta} \right)^2 + \left(\frac{1}{\beta} - 1 \right)^2 \quad (2.24)$$

$$\lambda_h = \begin{cases} 0.375 \left(\frac{\Delta_h}{D_h} \right)^{0.4} Re_{\Delta_h}^{-0.1} & , for Re_{\Delta_h} \leq 275 \\ 0.214 \left(\frac{\Delta_h}{D_h} \right)^{0.4} & , for Re_{\Delta_h} > 275 \end{cases} \quad (2.25)$$

with Δ_h the surface roughness in honeycomb cells assumed to be 1×10^{-5} m, taking the value for roughness of PVC given in a table on p. 536 of Fanchon (2008). β is the porosity of the honeycomb ($\beta \simeq 0.8$ according to Barlow et al. (1999)). Re_{Δ_h} is the Reynolds number inside the honeycomb, using the roughness as length scale, defined by Equation 2.26.

$$Re_{\Delta_h} = \frac{V_c \times \Delta_h}{\nu} \quad (2.26)$$

D_h is the hydraulic diameter, defined by Equation 2.27.

$$D_h = \frac{4 \times \text{cross-sectional area}}{\text{perimeter}} \quad (2.27)$$

For the screens, Mehta and Bradshaw (1979) recommend Wieghardt's formula (Equation 2.28) for the calculation of the pressure drop coefficient.

$$K = 6.5 \left(\frac{1-\beta}{\beta^2} \right) \left(\frac{V_s d}{\beta \nu} \right)^{-\frac{1}{3}} \quad (2.28)$$

with K the pressure drop coefficient, V_s the wind speed across the screen, ν the kinematic viscosity and d the wire diameter.

The definition of the Turbulence Reduction Factor (TRF) is as follows (Equation 2.29):

$$TRF = \frac{\text{turbulence with flow straightener}}{\text{turbulence without flow straightener}} \quad (2.29)$$

The higher the factor, the less the turbulence is reduced. Dryden and Schubauer (1947) give the following formula (Equation 2.30) for the lateral turbulence reduction of screens:

$$TRF = \frac{1}{\sqrt{1+K}} \quad (2.30)$$

Prandtl (1933) gives the following formula (Equation 2.31) for the longitudinal TRF of screens:

$$TRF = \frac{1}{1+K} \quad (2.31)$$

According to equations 2.30 and 2.31, screens will have more impact on the reduction of longitudinal turbulence than on the reduction of lateral turbulence. The higher

the wind speed, the less the turbulence is reduced. According to Scheimann (1981), equation 2.31 can also be used for the determination of the longitudinal *TRF* of honeycombs. The smaller the cell diameter, the more the honeycomb is expected to reduce turbulence. For the lateral *TRF* of honeycombs, Lumley and McMahon (1967) gives equation 2.32 for the square of the *TRF*.

$$TRF^2 = 8 \left(\frac{K l_i}{3\pi L_h} \right)^2 \times \int_0^1 \frac{dy}{\left(\frac{4Kl_i(K+1)}{3\pi L_h} \right)^2 + y^2 \left(1 + \frac{8K l_i}{3\pi L_h} \frac{1}{\sqrt{1-y^2}} \right)^2} \quad (2.32)$$

with *TRF* the turbulence reduction factor, *K* the pressure drop coefficient, *l_i* the Integral scale of initial turbulence, and *L_h* the length of the honeycomb cell.

2.4.5 Existing wind tunnels

Classic wind tunnels usually have a closed circuit, necessary in particular when one wants to attain high pressure or wind speeds (Figure 2.49). The duct necessarily requires bends. Also, the tunnel needs to be much bigger than the actual test area. This is difficult to realize and in particular to add onto an existing wave tank. The wind speeds required for testing wind turbines are not as high as those required for the study of aeronautics and only atmospheric pressure is needed. Figure 2.50 shows an alternative to this for low speeds. However, even in this configuration, the size of the test section is very small when compared to the whole assembly.

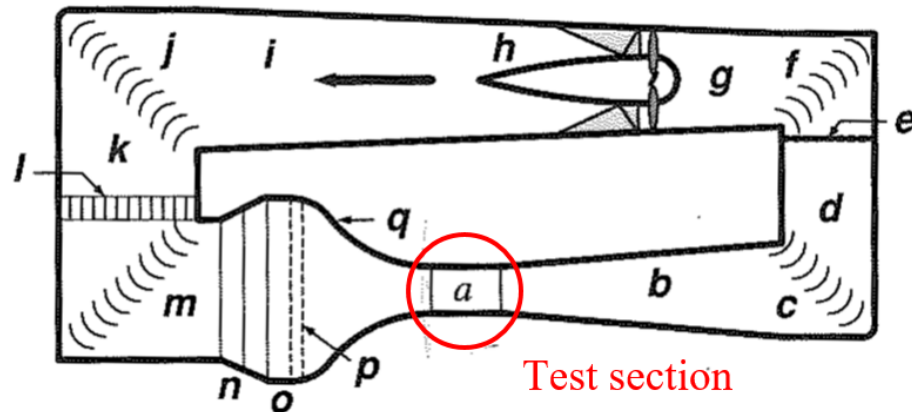


Figure 2.49: Classic closed circuit wind tunnel adapted from Barlow et al. (1999). reproduced with the permission of John Wiley & Sons obtained via the Copyright Clearance Center. Legend: (a) test section (b) diffuser (c) "first corner" with turning vanes (d) second leg: continues diffuser or constant area (e) safety screen to prevent parts of failed models or other unintended flying objects from reaching the fan (f) "second corner" (g) transition from rectangular to circular cross section to take flow into the fan (h) Fan and straightener section (i) return or second diffuser: transition back to rectangular from the circular cross section at the fan (j) "third corner" (k) third leg that may be constant area (l) heat exchanger (m) "fourth corner" (n) wide-angle diffuser with separation control screens (o) settlement area (p) flow conditioners typically including flow straighteners and turbulence control screens (q) contraction or nozzle

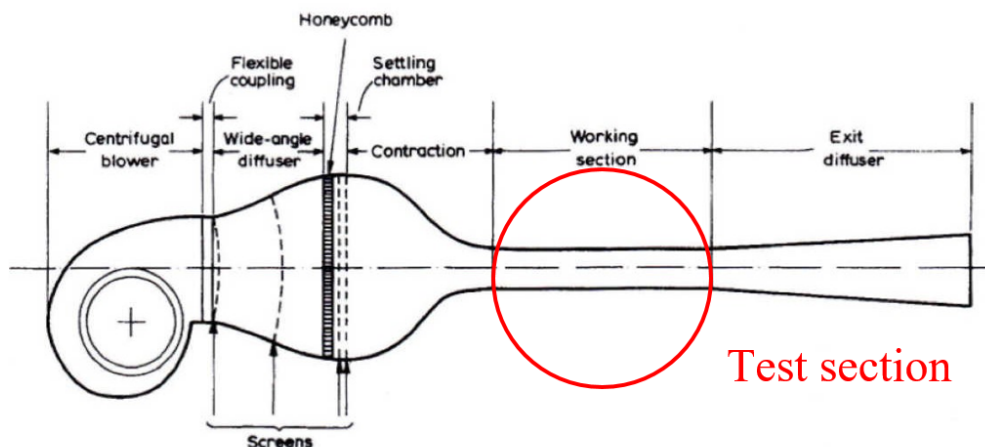


Figure 2.50: Open circuit wind blower with closed test section adapted from Imperial College London (n.d.), originally from Mehta and Bradshaw (1979)

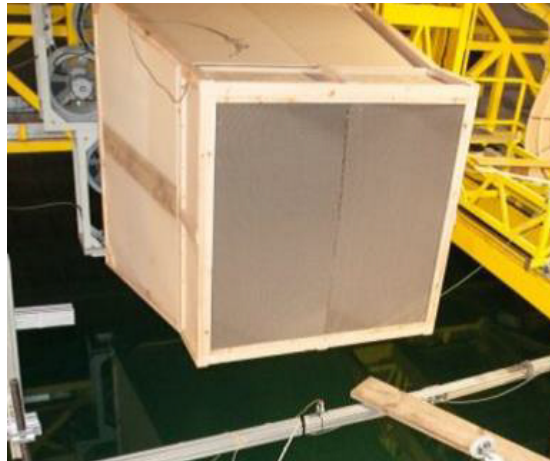


Figure 2.51: Wind generator at INSEAN (Wan et al., 2014b)

The majority of laboratories which have added a wind blower to a wave tank use an assembly of several fans blowing wind over an area several meters wide and high. Some use honeycombs or meshed screens as flow straighteners. The INSEAN Wave tank in Rome, Italy has a wind generator with two rows of 6 axial fans. A converging piece directs the wind to the testing location. A honeycomb mesh is used as a flow straightener, that is, to reduce the average lateral wind speed and turbulence intensity (Figure 2.51).

The Ecole Centrale de Nantes has a wind generator made up of 8 centrifugal fans (Figure 2.52). The fans are situated on the edge of the wave tank. The wind produced by these fans is guided from the fans to the test location in the wave tank through a system of ducts. The 8 centrifugal fans are grouped by 4 pairs of two. Each pair of fans is situated on a support structure, one on top of the other. The outlet of the lower fan is situated on top, whereas the outlet of the upper fan is situated at the bottom, in order for the outlets to be situated as close as possible to one another. A reducing Y guides the flow coming out of each fan into a single duct. 4 long ducts then guide the airflow coming from each pair of fans to a diffuser. The air flow quality is then improved through a honeycomb and a meshed screen. Furthermore, Courbois (2013) noticed that because the air was assembled from 4 different ducts, the average wind speed was not very evenly distributed over the whole area. Therefore an additional, slightly converging piece was added between the end of the diffuser and the flow straighteners which improved the quality effectively (See Figure 2.53). The turbulence intensity achieved was 5 %. The maximum average wind speed that could be produced was 15 m/s. Below 5 m/s it was noticed that the quality was not sufficient. The diffuser had an outlet that measured 2.8 by 2.8 m. This system allows having a relatively small support structure, as it is only needed to support the weight of the outlet instead of the weight of all the fans.

Furthermore, the wind generator is not in the way of tests that necessitate more space, as the outlet and the ducting system can be taken away. To define a usable zone, the wind speeds measured were divided by the average longitudinal wind speed at the centre of the air flow. With U^* being the ratio of the measured wind speed over the

2.4. LITERATURE REVIEW ON WIND GENERATORS

central wind speed, a usable zone was defined, using the criterion: $0.9 < U^* < 1.1$. The height and width determined using this criterion were both 2.6 m.

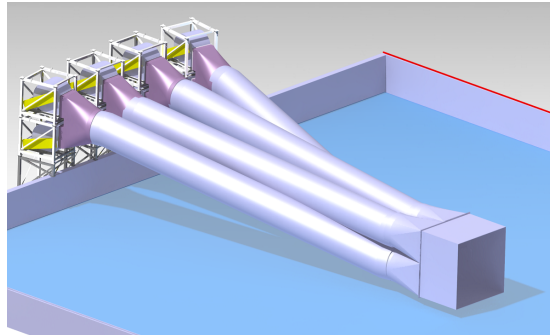


Figure 2.52: Wind blower system at the Ecole Centrale de Nantes (taken from Courbois (2013) with the permission of A. Courbois)

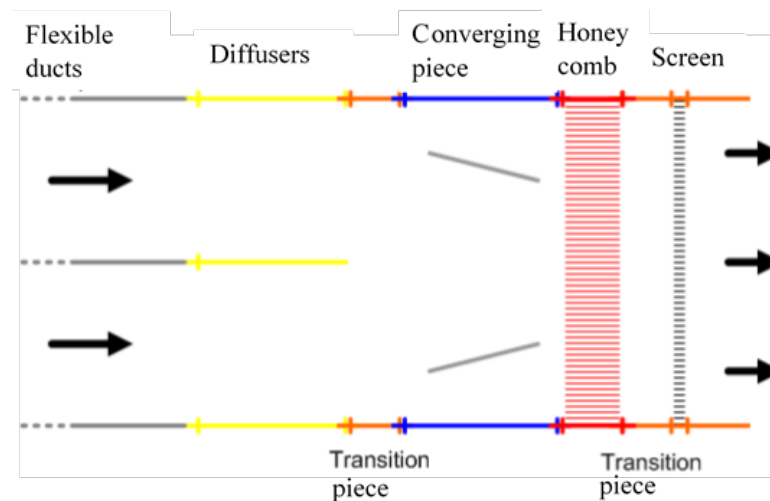


Figure 2.53: Diagram showing the set up of the Wind blower system in the Ecole Centrale de Nantes (taken from Courbois (2013) with the permission of A. Courbois), with translated annotations

2.4. LITERATURE REVIEW ON WIND GENERATORS

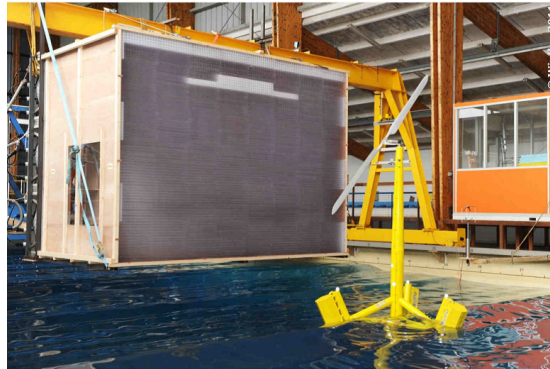


Figure 2.54: Wind blower at Ifremer Brest (taken from Ohana et al. (2014a) with the permission of J. Ohana)

The Ifremer test tank situated in Brest (see Figure 2.54) used a series of 12 axial fans assembled in 3 rows of 4 fans. The rectangular cross section is 4.3 m wide and 3.2 m high. Each fan is driven by a 9 kW asynchronous motor. Each row of fans is controlled by a 37 kW inverter. Again, a meshed screen and a honeycomb were used as flow straighteners to achieve a turbulence intensity of 5 % over an area which is 3.8 m wide and 2.8 m high. Detailed set up can be seen in Figure 2.55. The maximum wind speed of 9 m/s can be achieved over almost all of an area measuring 11 m^2 , 3.9 m wide and 2.8 m high and at up to a distance of 3 m from the outlet. As the fans were situated on a gantry installed across the wave tank, no ducting system is needed. However, the gantry needs to be very strong. This wind generation system is capable of producing sheared wind profiles, allowing to reproduce the atmospheric boundary layer (Figure 2.56). This wind blower is also capable of reproducing slow wind variations with an upper frequency limit between 1 and 2 Hz.

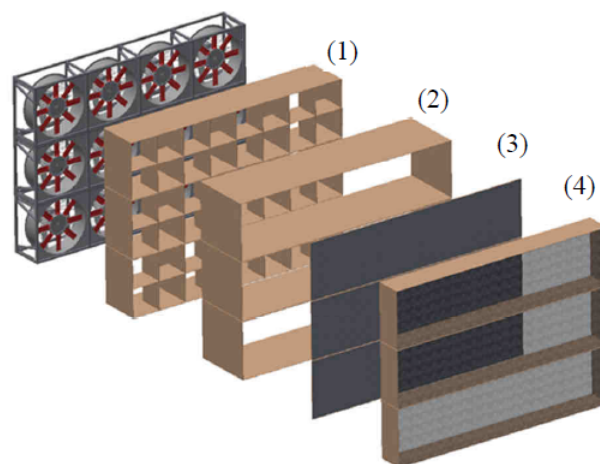


Figure 2.55: Wind blower at Ifremer Brest (taken from Ohana et al. (2014) with the permission of J. Ohana). (1) Flow generated by axial fans passes through square section cells. Each fan's flow is divided in 4 parts. (2) Independent settling chambers for each row of fans (3) Mesh screen (4) Honeycomb with rectangular cells. This section diminishes the swirl and lateral/vertical mean velocities.

2.4. LITERATURE REVIEW ON WIND GENERATORS

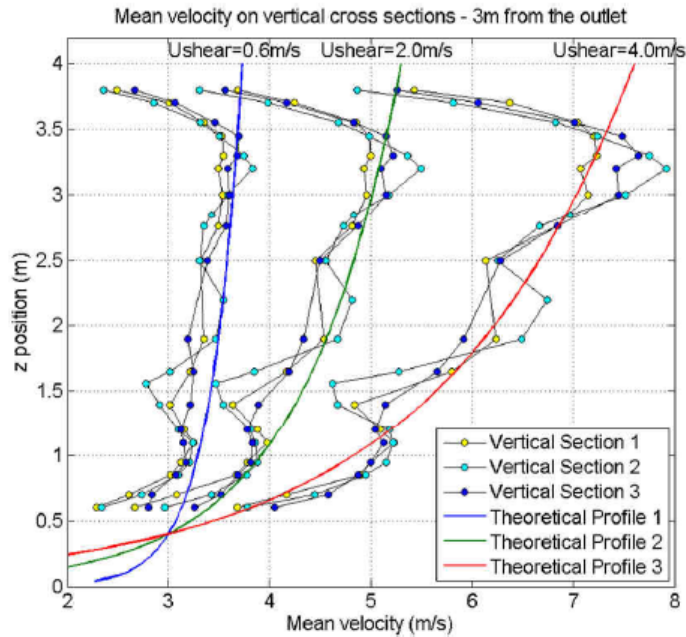


Figure 2.56: Sheared wind profiles produced by the wind blower at Ifremer Brest (Ohana et al., 2014). With the permission of J. Ohana

In MARIN, Netherlands, an assembly of 5 rows of 7 axial fans was used (see Figure 2.57) (De Ridder et al., 2014). The surface is 4 m wide and 3 m high. A contracting nozzle is used to guide the airflow produced into an oval shaped area. Clockwise rotating fans are alternated with counter-clockwise fans in a chequerboard pattern. The maximum wind speed produced is 6 m/s. Just as at the Ifremer facility, sheared wind can be produced and wind speed varying over time. The wind blower was positioned sufficiently high for the wind not to interact with the waves. To compensate for the lack of wind in the lower region, the nozzle was slightly tilted downward by an angle of 2.6 degrees. The turbulence intensity is below 5 %.

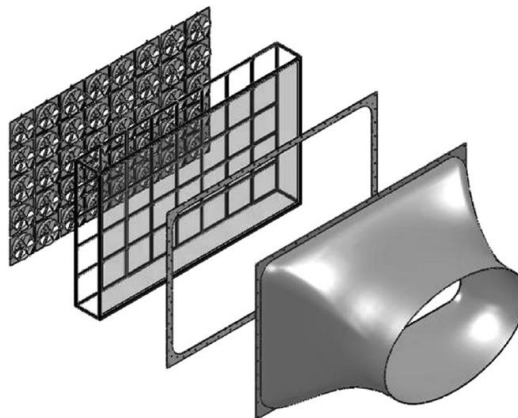


Figure 2.57: Wind blower at MARIN (found in Wright et al. (2015a), originally taken from Gao (2013)). From left to right is shown: the bank of fans, screens and the nozzle

2.4. LITERATURE REVIEW ON WIND GENERATORS

At the University of California, Berkeley (Roddier et al., 2010), a system of 5 axial fans was used. Each fan was covered by a screen for flow straightening (see Figure 2.58).

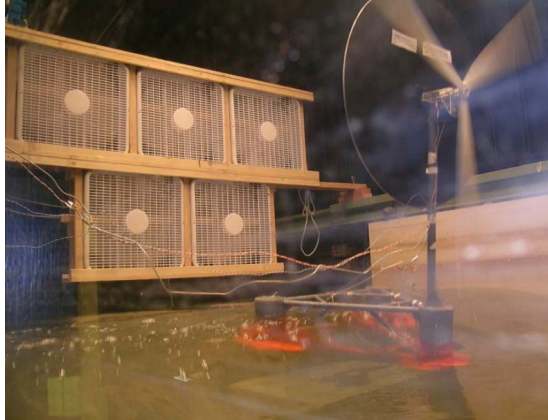


Figure 2.58: Wind blower at University of California, Berkeley. Reproduced from Roddier et al. (2010) with the permission of AIP Publishing obtained via the Copyright Clearance Center

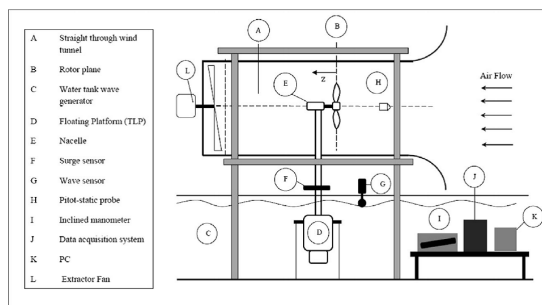


Figure 2.59: Wind blower University of Malta. Reproduced from Farrugia et al. (2014) with permission from Elsevier

At the University of Malta (Farrugia et al., 2014), the wind was guided through a tunnel to ensure higher wind quality. What was also particular about this wind system is that the wind was not blown but sucked by a fan situated behind the wind turbine (Figure 2.59). One could also use a combination of blowing and sucking. One needs to be careful though not to make the tunnel too small, as this would affect the thrust on the rotor. If the air is blocked around the wind turbine, it is as if the rotor was ducted. The Betz limit, which indicates the maximum power that can be extracted from the wind blowing on a wind turbine, could be exceeded because of this and falsify the test results. When using this type of method, one needs to make sure to make the tunnel is sufficiently large for the average wind speed not to be affected by the presence of the wind turbine rotor.

2.4.6 Literature review on conical diffusers

For this thesis, to be able to produce wind in the laboratory, a conical diffuser was needed. Centrifugal fans produced wind, the wind was then guided through a single

duct to an outlet which needed to be larger than the duct diameter. This required looking at the air flow inside a conical diffuser, such as the one shown in Figure 2.60.

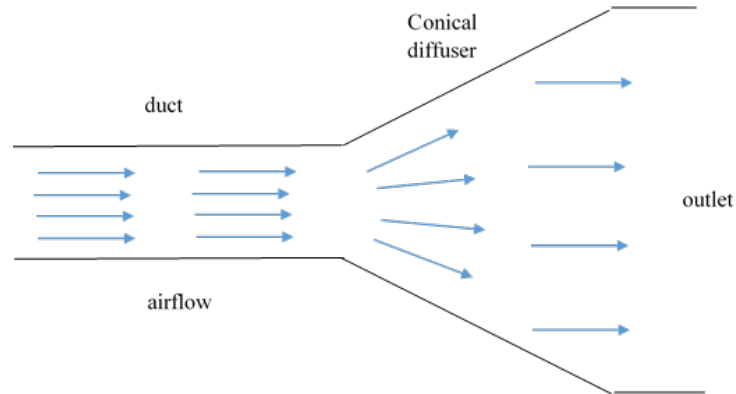


Figure 2.60: Cross section of the conical diffuser described in this section. The figure shows the ideal homogeneous flow distribution.

Conical diffusers were studied both experimentally and numerically during the project described in this thesis. Several documents describing experimental and numerical studies of conical diffusers were consulted.

The problem with conical diffusers is that flow separation can occur in them. Flow separation can be triggered in boundary layers with an adverse pressure gradient. When fluid flow slows down, due to an expansion for example, the pressure increases. When $\frac{dp}{dx} > 0$, $\frac{\partial^2 u}{\partial y^2} > 0$ at the wall. However, $\frac{\partial^2 u}{\partial y^2}$ "must be negative at the outer layer of the boundary layer to merge smoothly with the mainstream flow" (White, 2016). This causes the appearance of a point of inflection and causes boundary layers with an adverse pressure gradient to have an "S" shape.

Figure 2.61 shows the shape of various boundary layer profiles as a function of the pressure gradient. For a weak pressure gradient, such as in Figure 2.61c, there is no flow separation. Figure 2.61d illustrates the case where the wall shear is equal to zero, and $\frac{\partial u}{\partial y} = 0$. Beyond this point, flow separation occurs because of the appearance of backflow (Figure 2.61e). This is why flow separation can occur in diffusers with large opening angles.

2.4. LITERATURE REVIEW ON WIND GENERATORS

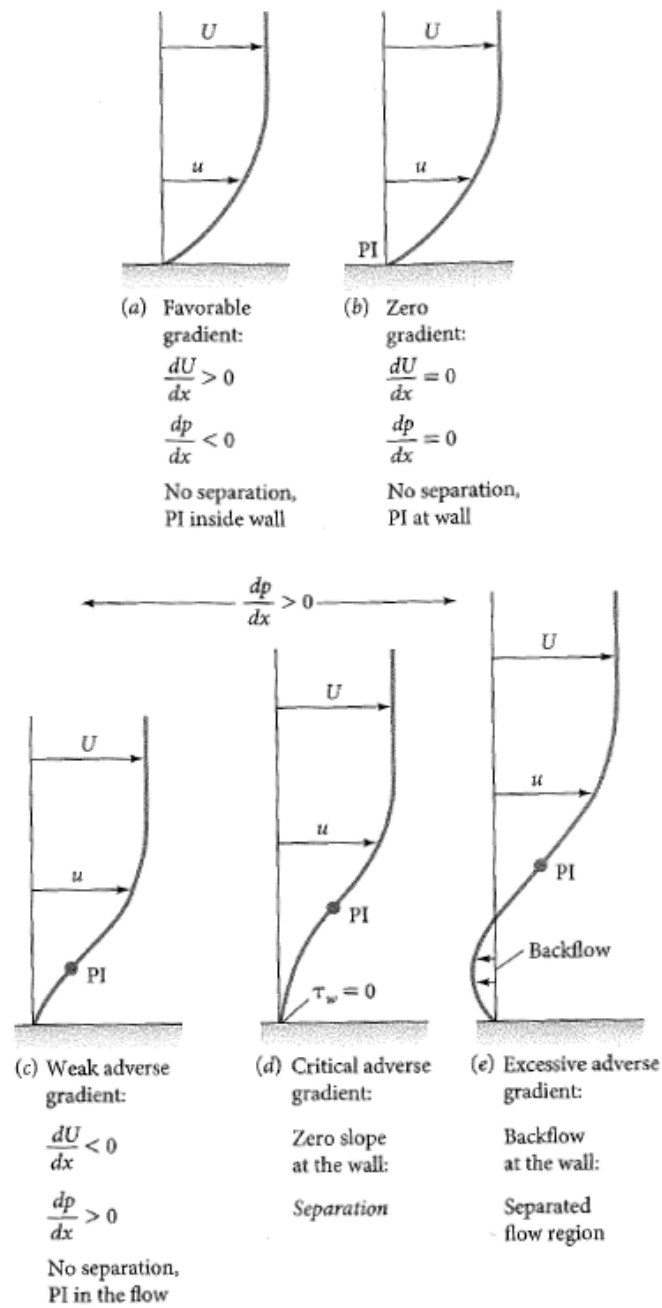


Figure 2.61: Boundary layer profiles for various pressure gradients, reproduced from White (2016) with permission from McGraw Hill

Figure 2.62 shows a diffuser with boundary layer separation.

2.4. LITERATURE REVIEW ON WIND GENERATORS

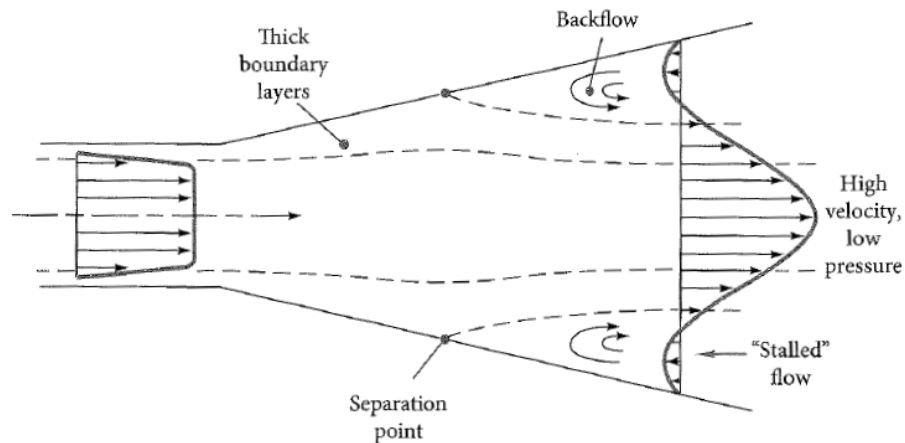


Figure 2.62: Diffuser with boundary layer separation. Reproduced from White (2016) with permission from McGraw Hill

A stability map of diffuser patterns was published in Fox and Kline (1962) and is shown in Figure 2.63.

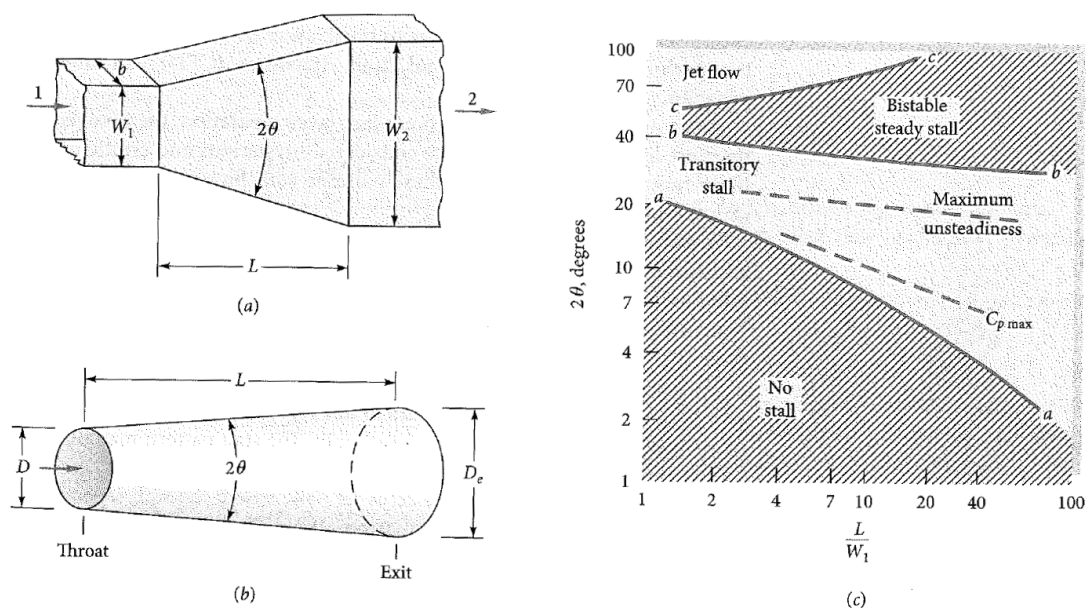


Figure 2.63: (a) geometry of flat-walled diffuser (b) geometry of conical diffuser (c) Stability map of diffuser flow patterns. 2θ is the opening angle of the diffuser. $\frac{L}{W_1}$ is the ratio between the length and the inlet width of the diffuser (See also Subfigures (a) and (b)). C_p is the pressure recovery coefficient. Published originally by Fox and Kline (1962), taken from White (2016), who took it from Runstadler and Dolan (1975). Permission granted by McGraw Hill

According to White (2016), below line aa in Figure 2.63(c), "there is a steady viscous flow ... Between lines aa and bb, there is a transitory stall pattern with strongly unsteady flow. Best performance (highest C_p) occurs in this region". C_p is the pressure recovery

coefficient defined by Equation 2.33.

$$C_p = \frac{p_e - p_t}{p_{0t} - p_t} \quad (2.33)$$

p is the pressure, subscripts e and t mean exit and throat (or inlet), respectively.

Between lines bb and cc, there occurs a "steady bistable stall from one wall only ... stall pattern may flip-flop from one wall to the other, and performance is poor."

"Above line cc, there is jet flow. The wall separation is so gross and pervasive that the main stream ignores the walls and simply passes on through at nearly constant area. Performance is extremely poor in this region."

Nevertheless, certain applications require conical diffusers with a large opening angle and a small ratio between the length and the width of the diffuser. Prynck-Skotniczny (2006) present the study of a catalytic afterburner inlet diffuser with an opening angle of $2\theta = 70^\circ$ (albeit with the ratio $\frac{L}{W_1} = 0.82$, so outside of the diagram of Figure 2.63(c)). They studied the use of inner truncated cones (shown on Figure 2.64) to improve the performance of the diffuser numerically and experimentally (for some of the configurations only). According to them, two inner cones gave the most even flow distribution when compared to no inner cones or three inner cones.

Image absent as copyright owner
could not be contacted

Figure 2.64: Inner conical diffusers used by Prynck-Skotniczny (2006) to improve performance of conical diffuser with very large opening angle. Image can be found in Prynck-Skotniczny (2006). Figure 3 on page 73

According to Lai et al. (1989), conical diffusers are widely used in wind tunnels and turbomachinery. At that time, according to Lai et al. (1989), the calculation of flow inside vaneless diffusers requires a level of sophistication not available in the turbulence models present at that time. It is therefore very likely that any turbulence model dating from before 1989 is bound to give inaccurate results, whereas models created after 1989 have a chance of being sophisticated enough to model the flow phenomena inside vaneless conical diffusers.

In Meyer et al. (2004), the experimental study of the flow in two different conical diffusers is described. The opening angles of those diffusers are 18° and 30° . The flow was measured using Particle Image Velocimetry. The Reynolds number in this study was 100,000 (calculated with upstream diameter and velocity). Before the diffuser section, there was a straight cylindrical pipe. The diffuser that had an opening angle of 18° was also tested with an incoming duct that had an angle of 30° slightly upstream of the diffuser. The measurements for both opening angles and a straight incoming duct showed that the flow was highly asymmetrical, had a reverse flow region indicating flow separation, was highly turbulent and unstable. The average velocity over a certain time period was not identical for two consecutive measurement series (in between which the

flow was stopped), that is, the flow distribution had changed. Calculating the average speed over a certain area, but looking at the instantaneous speed also showed high instability. The asymmetry was a little less severe for the smaller opening angle, as was the instability. For the case of an incoming duct which was bent and created an asymmetrical flow field at the beginning of the diffuser, the flow "sticks" to one side. It is symmetric about the symmetry axis which would cut the geometry that includes the bent duct in half. Turbulence levels are lower than in the cases with a straight incoming pipe. Average calculations over a certain area also showed less extreme fluctuations in the flow.

Sparrow et al. (2009) cites White (2008) stating that flow separation occurs for opening angles beyond 15° . They also cite Idelchik (1966) who states that flow separation can occur beyond 7° . To reconcile these two differing affirmations, Sparrow et al. (2009) studied numerically the impact of the Reynolds number on the opening angle at which flow separation occurs and concluded that the exact angle is impacted by the Reynolds number of the flow.

According to Idelchik (1966), for opening angles of up to 8° , the boundary layer does not separate from the wall and the velocity is distributed symmetrically. Beyond these angles, the flow will start to separate from one of the walls, and as a result this flow separation does not occur on the other side. The flow distribution is therefore asymmetric. If there is not even a small asymmetry in the geometry of the duct or the diffuser, the separation occurs alternately at one or the other side of the diffuser, which causes strong fluctuations in the flow. For angles $\alpha < 40 - 50^\circ$, pressure losses are still smaller than for a sudden expansion (opening angle of 180°). Beyond 50° , and up to 90° , losses in this diffuser will be higher than for a sudden expansion. Above 90° , the losses are similar to a sudden expansion. In cases where the flow does not need to be evenly distributed at the exit, when the angle is between 50° and 90° , it is preferable to replace the diffuser by a sudden expansion. However, if the flow distribution needs to be even, and if therefore baffles, dividing walls or grids are used to help achieve this purpose, even a large divergence angle is preferable to a sudden expansion. Idelchik (1966) proposes 7 different solutions to reduce pressure losses and achieve uniform flow distribution. Each of them is presented in a short subsection (Subsection 2.4.6.1-2.4.6.7), alongside the instructions given by Idelchik (1966) for their design in certain cases. Subsection 2.4.6.8 presents more recent research on the suppression of boundary layer separation in conical diffusers.

2.4.6.1 Blowing onto boundary layer

When air is blown into the expanding walls of the diffuser, as illustrated in Figure 2.65, the stream velocity increases near the walls. Boundary layer separation therefore occurs further downstream.

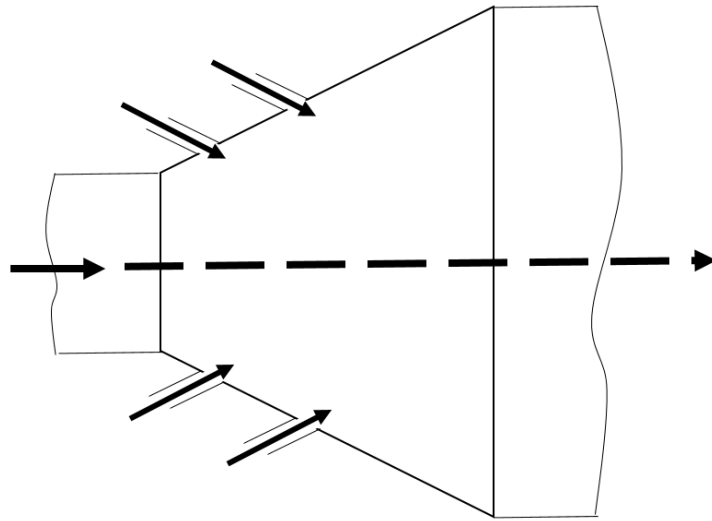


Figure 2.65: Solution to push boundary layer separation further downstream: Blow through walls of diffuser (drawing inspired by diagram found in Idelchik (1966))

2.4.6.2 Suction of boundary layer

When sucking the boundary layer, as shown on Figure 2.66, flow separation also occurs further downstream.

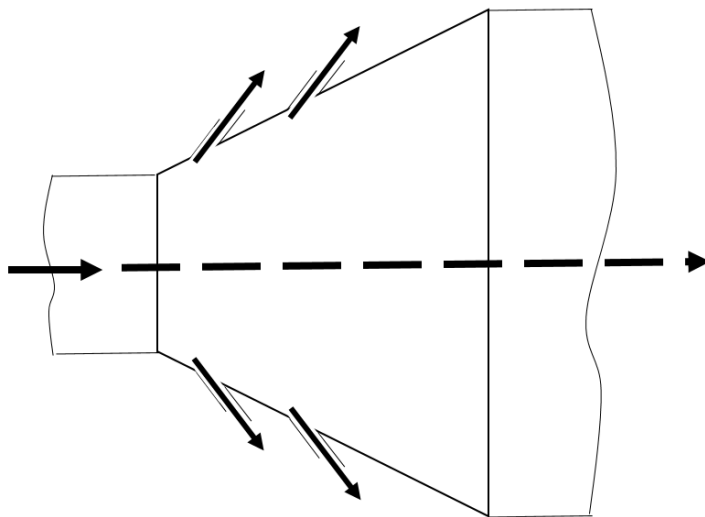


Figure 2.66: Suction of boundary layer to push occurrence of boundary layer further downstream (drawing inspired by diagram found in Idelchik (1966))

2.4.6.3 Guide vanes

A succession of small guide vanes or baffles can be placed inside the diffuser, as seen in Figure 2.67. Their presence causes the liquid to be displaced from the centre of the flow towards the wall. The effect of these guide vanes is particularly good for wide angles. If $50^\circ < \alpha < 180^\circ$, the resistance coefficient is reduced by a factor of almost 2. Some of the guide vanes should be situated before the entrance angle to the diffuser, and some behind. As the opening angle increases, the number of guide vanes should be increased.

When progressing downstream, the guide vanes should be situated closer and closer to the wall. Equation 2.34 and Equation 2.35 are indications for the ratio $\frac{h_1}{h_2}$ for two different angles, where h_1 is the distance between the first guide vanes and the outer wall and h_2 is the distance between the central axis of the diffuser and the first guide vane.

$$\frac{h_1}{h_2} = .95 \text{ for } \alpha = 90^\circ \quad (2.34)$$

$$\frac{h_1}{h_2} = 1.4 \text{ for } \alpha = 180^\circ \quad (2.35)$$

where α is the opening angle of the conic diffuser.

Guide vanes must have a small curvature and can be made of sheet metal. The chord of the vanes can represent 20 to 25 % of the diameter or height of the diffuser section. The ideal angle of inclination can be determined trough trial and error, by trying out various angles of inclination until the resistance is the lowest.

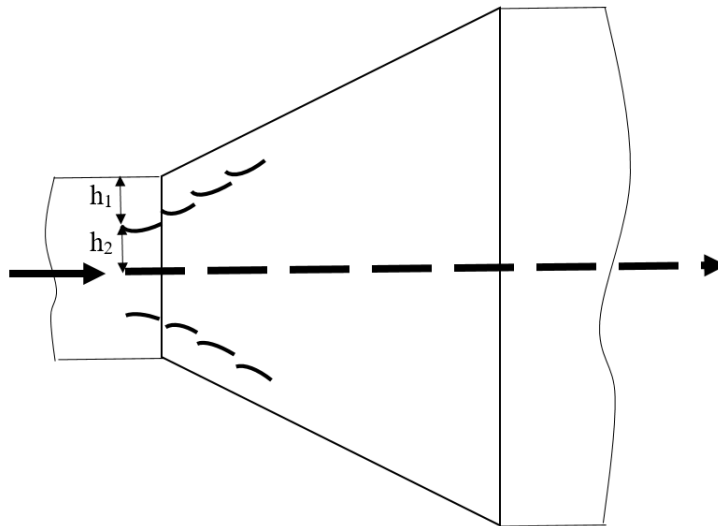


Figure 2.67: Illustration of guide vanes for even flow distribution inside a diffuser (drawing inspired by diagram found in Idelchik (1966))

2.4.6.4 Dividing walls

Dividing walls are walls that split up the diffuser into several more narrow diffusers as can be seen on Figure 2.68. They should only be used with not too narrow diffusers, as, if the diffuser is too narrow, friction is increased and the diffuser resistance is increased. The distances between the dividing walls at the diffuser inlet should be exactly equal, the distances between them at the exit should be approximately equal. The dividing walls should extend in both directions beyond the diffuser. The protruding parts should be parallel to the diffuser axis. The length of the protruding parts should be at least 0.1 of the distances between the dividing walls at the inlet, and at least 0.1 of the distances between the dividing walls at the exit. Table 2.13 shows how many dividing walls should be used depending on the value of the opening angle.

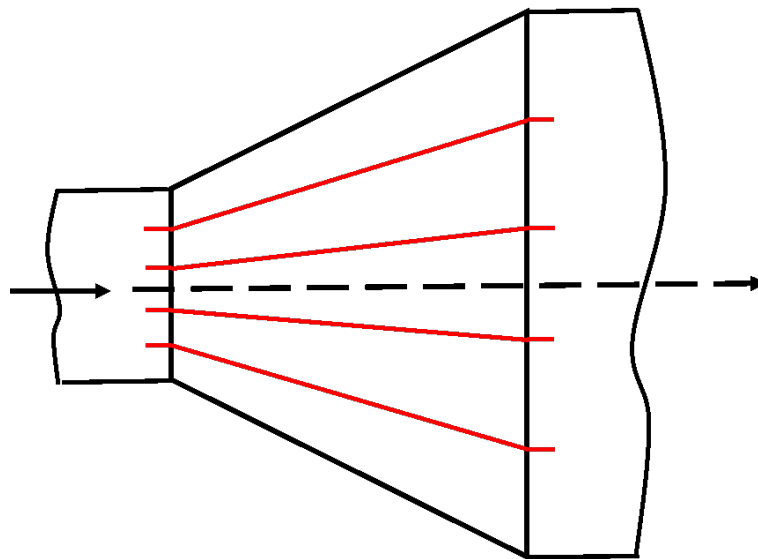


Figure 2.68: Illustration of dividing walls inside a diffuser (drawing inspired by diagram found in Idelchik (1966))

Table 2.13: Number of recommended dividing walls as a function of the opening angle

$\alpha(^{\circ})$	30	45	60	90	120
number of dividing walls	2	4	6	6	6-8

2.4.6.5 Curved diffuser

In a diffuser with curved walls, the rate of increase of the cross-section area is lower in the initial section than in the end section. Therefore, the variation of the pressure gradient is smoother. Building a diffuser in which the pressure gradient is constant ($\frac{dp}{dx} = const$) is the best choice.

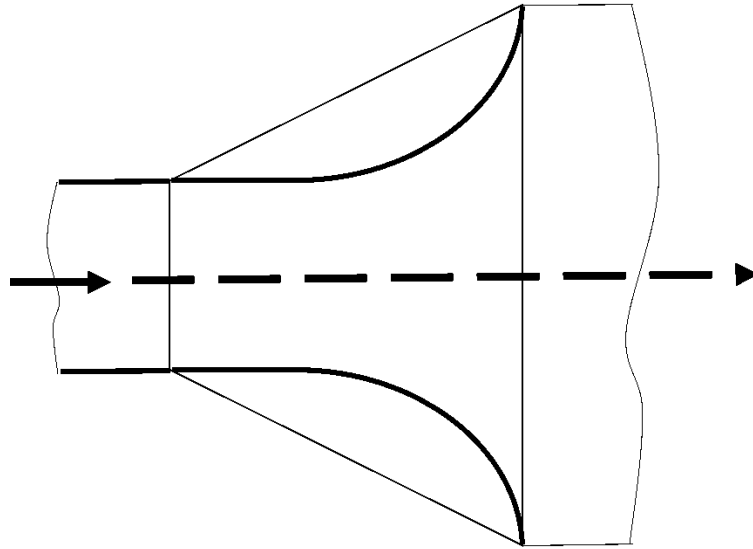


Figure 2.69: Curved diffuser (drawing inspired by diagram found in Idelchik (1966))

Losses can be reduced by up to 40 %. This is the case for diffusers with angles $25^\circ \leq \alpha \leq 90^\circ$. For lower angles, curving the walls could increase the losses.

2.4.6.6 Multistage diffuser

The idea of using a succession of a very narrow diffuser followed by a sudden expansion (Figure 2.70), takes advantage of the fact that narrow angles can have smaller losses than a straight section, and that the velocity has been slightly lowered before arriving at the sudden expansion, reducing the losses again, than if a straight duct had gone directly into a sudden expansion.

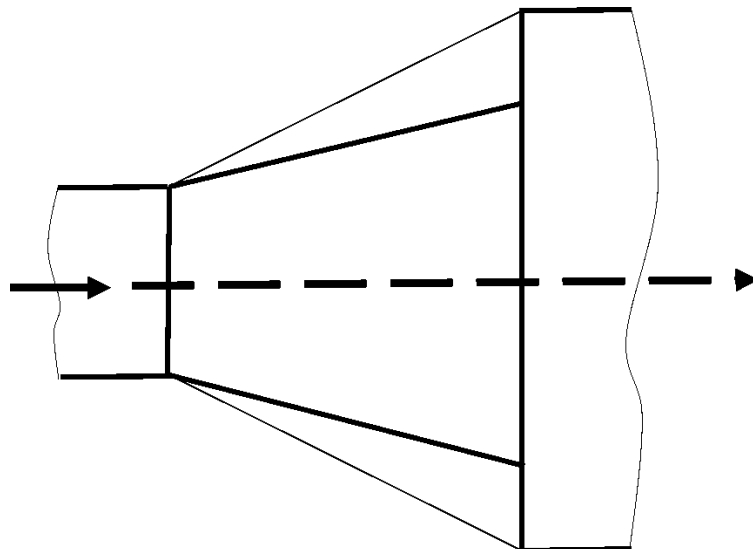


Figure 2.70: Multistage diffuser (drawing inspired by diagram found in Idelchik (1966))

2.4.6.7 Honeycomb or meshed screen

The idea of using a honeycomb or meshed screen to distribute flow evenly inside a diffuser is not cited directly by Idelchik (1966). However, the method for calculating the losses through this type of device is indicated in the same chapter. Installing flow straighteners at the end of the outlet will not only improve turbulence levels, it can also help distribute the flow more evenly. On its own, however, if it is not very thick, it will be insufficient, as will be seen in the measurements done with the square outlet that measured 1.6 by 1.6 m (Section 5.1). If it is thick enough to allow even distribution of the air on its own, without other improvement to the diffuser, it is very likely to cause high pressure drops. The fans providing the air flow need to be sufficiently powerful to compensate for the loss in wind speed.

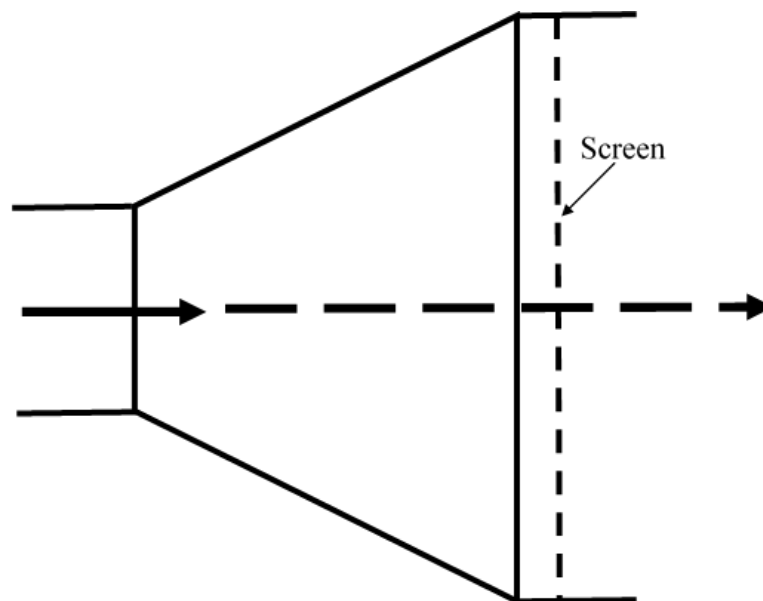


Figure 2.71: Installation of a honeycomb or meshed screen for even flow distribution (drawing inspired by diagram found in Idelchik (1966))

2.4.6.8 Karman-Vortex Generator and Screw Tape Inserts

Sajben et al. (1977) and Yang et al. (2020) present the effect of a ring-shaped Karman Vortex Generator (Figure 2.72) on the flow distribution inside a conical diffuser.

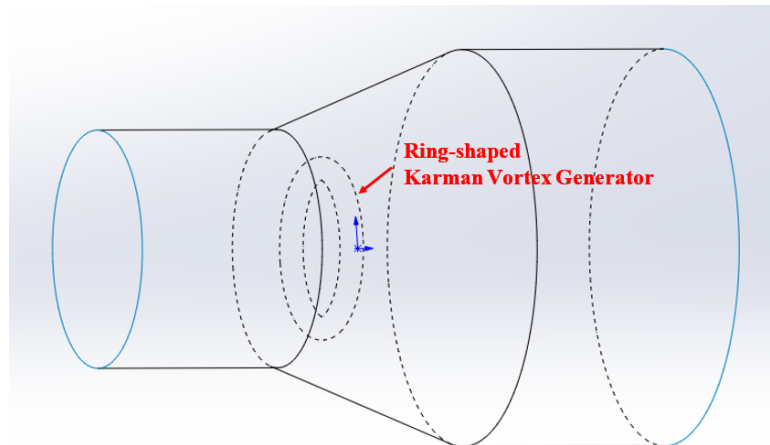


Figure 2.72: Ring shaped Karman Vortex Generator (not to scale)

The presence of an obstacle several boundary layers away from the diffuser wall, shortly after the throat (or inlet), triggers von Karman vortices which prevent boundary layer separation.

This type of solution had actually previously been studied to prevent boundary layer separation and stall on airplane wings and increase lift, according to Sajben et al. (1977). Veldhuis et al. (2012) presents the experimental study of the presence of a cylinder in front of a wing flap. This passive method of flow control is effective and more easy to implement than active flow control methods, such as blowing, suction or plasma actuators (Veldhuis et al., 2012).

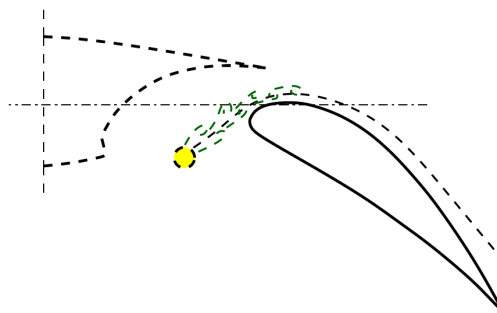


Figure 2.73: Karman Vortex Generator on airplane wing, in front of flap, for flow separation and stall prevention and increase of lift. Figure 6 b on page 5 of Veldhuis et al. (2012), with permission from L. Veldhuis

Such an approach is considered to be unsuitable for wind tunnel or wind generator applications due to the additional turbulence generated. This is also likely to be an issue in the approach proposed by Shukri (2018) who presents a study about conical diffusers with screw tape inserts. Figure 2.74 shows such a screw tape insert.

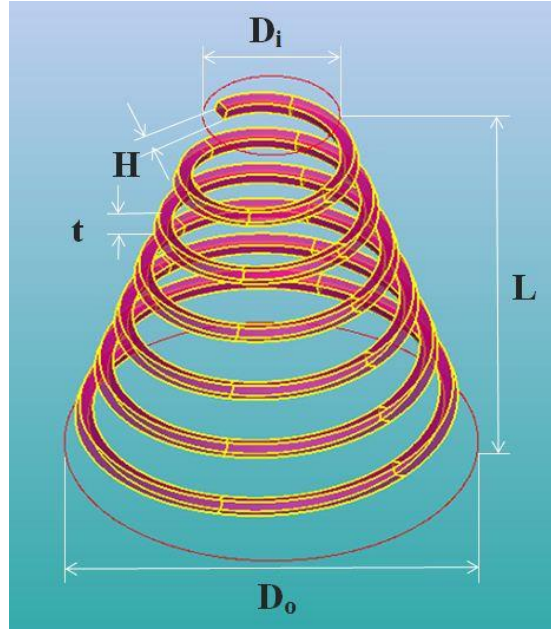


Figure 2.74: Screw tape insert for conical diffuser (Shukri, 2018)

This method prevents the flow separation, and ensures mixing, necessary for certain aerospace applications. However, this is done at the cost of producing intensive swirl, not desirable in a wind tunnel or wind generation system.

2.5 CFD simulations of turbulent steady state indoor air flow

CFD simulations were used for this thesis to give predictions of the flow field for various geometries of the diffuser of the wind generator. All simulations were done in OpenFOAM, a code that solves the Navier-Stokes equations by using the Finite Volume Method.

Air being a Newtonian fluid, the viscous stresses arising from its flow are linearly proportional to the local strain rate. The fluid is considered incompressible, as the wind speeds involved give a Mach number lower than 0.3. The dynamic viscosity μ is considered constant throughout the fluid, as the variations of temperature are considered small. With these assumptions, the Navier-Stokes equations in tensor notation are as in Equation 2.36.

$$\rho \frac{DU_i}{Dt} = -\frac{\partial P}{\partial x_i} + \mu \frac{\partial^2 U_i}{\partial x_k \partial x_k} \quad (2.36)$$

with ρ the density of the fluid, U_i the instantaneous velocity in tensor notation, t time, P the instantaneous pressure, x_i the position vector in tensor notation, and $\frac{D}{Dt}$ the material derivative. In addition to this, the continuity equation is solved, which for an incompressible fluid is expressed as in Equation 2.37 in tensor notation.

$$\frac{\partial U_i}{\partial x_i} = 0 \quad (2.37)$$

By averaging Equation 2.36, using the decomposition of the variables into an aver-

age component and a fluctuating as in Equation 2.38 and 2.39, one can establish the Reynolds-averaged Navier-Stokes (RANS) equations (Equation 2.40).

$$U_i = \bar{U}_i + u'_i \quad (2.38)$$

$$P = \bar{P} + p' \quad (2.39)$$

with U_i the instantaneous velocity, \bar{U}_i the mean velocity, and u'_i the fluctuating velocity, all in tensor notation. P is the instantaneous pressure, \bar{P} is the average pressure and p' is the fluctuating pressure.

$$\rho \frac{\partial \bar{U}_i}{\partial t} + \rho \bar{U}_j \frac{\partial \bar{U}_i}{\partial x_j} = -\frac{\partial \bar{P}}{\partial x_i} + \frac{\partial}{\partial x_j} (\mu \frac{\partial \bar{U}_i}{\partial x_j} - \rho \overline{u'_j u'_i}) \quad (2.40)$$

This makes a term appear, $-\overline{u'_j u'_i}$, called the Reynolds stress tensor, typically written τ_{ij} .

2.5.1 Description of one and two equation turbulence models

The Boussinesq approximation is used to express τ_{ij} as in Equation 2.41.

$$\tau_{ij} = 2\nu_T S_{ij} - \frac{2}{3}k\delta_{ij} \quad (2.41)$$

with ν_T the kinematic eddy viscosity, S_{ij} the mean strain-rate tensor, k the turbulence kinetic energy and δ_{ij} the Kronecker delta.

Wilcox (2006) describes the Spalart Allmaras one equation model, developed in 1992. This model solves a transport equation for the kinematic eddy viscosity (Equation 2.43). More precisely, it solves for a value called $\tilde{\nu}$, which is linked to ν_T through a function (Equation 2.42).

$$\nu_T = \tilde{\nu} f_{v1} \quad (2.42)$$

$$\frac{\partial \tilde{\nu}}{\partial t} + U_j \frac{\partial \tilde{\nu}}{\partial x_j} = c_{b1} \tilde{S} \tilde{\nu} - c_{w1} f_w \left(\frac{\tilde{\nu}}{d} \right)^2 + \frac{1}{\sigma} \frac{\partial}{\partial x_k} \left[(\nu + \tilde{\nu}) \frac{\partial \tilde{\nu}}{\partial x_k} \right] + \frac{c_{b2}}{\sigma} \frac{\partial \tilde{\nu}}{\partial x_k} \frac{\partial \tilde{\nu}}{\partial x_k} \quad (2.43)$$

with the closure coefficients and auxiliary relationships defined in Equations 2.44-2.48. Closure coefficients are generally empirically determined values in the equations of one or two equation models that allow the elimination of unknowns which appear when averaging the Navier-Stokes equations.

$$c_{b1} = 0.1355, \quad c_{b2} = 0.622, \quad c_{v1} = 7.1, \quad \sigma = 2/3 \quad (2.44)$$

$$c_{w1} = \frac{c_{b1}}{\kappa^2} + \frac{(1 + c_{b2})}{\sigma}, \quad c_{w2} = 0.3, \quad c_{w3} = 2, \quad \kappa = 0.41 \quad (2.45)$$

$$f_{v1} = \frac{\chi^3}{\chi^3 + c_{v1}^3}, \quad f_{v2} = 1 - \frac{\chi}{1 + \chi f_{v1}}, \quad f_w = g \left[\frac{1 + c_{w3}^6}{g^6 + c_{w3}^6} \right]^{1/6} \quad (2.46)$$

$$\chi = \frac{\tilde{\nu}}{\nu}, \quad g = r + c_{w2}(r^6 - r), \quad r = \frac{\tilde{\nu}}{\tilde{S} \kappa^2 d^2} \quad (2.47)$$

$$\tilde{S} = S + \frac{\tilde{v}}{\kappa^2 d^2} f_{v2}, \quad S = \sqrt{2\Omega_{ij}\Omega_{ij}} \quad (2.48)$$

with $\Omega_{ij} = \frac{1}{2}(\partial U_i/\partial x_j - \partial U_j/\partial x_i)$ the rotation tensor and d the distance from the closest surface. The model also includes a transition correction (not listed here) that introduces 4 additional closure coefficients and two more empirical functions, which can be found in Spalart and Allmaras (1994).

Like the Baldwin-Barth one equation model (from 1992), this model is complete. It predicts skin friction for attached boundary layer as good as algebraic models. It is better than algebraic models for separated flows. Its differential equation presents no serious numerical difficulties. It has trouble predicting asymptotic spreading rates for plane, round and radial jets. In the case of flow involving a mixing layer, the free shear flow spreading rate is comparable to numbers obtained through measurements.

In two-equations models, to determine τ_{ij} , a transport equation is solved for the turbulence kinetic energy k (Equation 2.51 for $k - \varepsilon$ models and Equation 2.55 for $k - \omega$ models). The turbulence kinetic energy is defined by Equation 2.49.

$$k = \frac{1}{2}(u_x'^2 + u_y'^2 + u_z'^2) \quad (2.49)$$

with u_x', u_y' and u_z' the fluctuating components of velocity in the x, y and z directions.

In addition to this, a second transport equation for either ε or ω is solved.

$k - \varepsilon$ models solve a transport equation for k and a transport equation for ε . ε is the turbulent dissipation or rate of dissipation of the turbulence kinetic energy per unit mass. v_T is linked to ε using Equation 2.50.

$$v_T = C_\mu k^2 / \varepsilon \quad (2.50)$$

with C_μ a constant specific to the $k - \varepsilon$ model equal to 0.09.

The transport equations for the standard $k - \varepsilon$ model are:

$$\frac{\partial k}{\partial t} + U_j \frac{\partial k}{\partial x_j} = \tau_{ij} \frac{\partial U_i}{\partial x_j} - \varepsilon + \frac{\partial}{\partial x_j} \left[\left(v + \frac{v_T}{\sigma_k} \right) \frac{\partial k}{\partial x_j} \right] \quad (2.51)$$

with ε the dissipation per unit mass and σ_k a closure coefficient.

$$\frac{\partial \varepsilon}{\partial t} + U_j \frac{\partial \varepsilon}{\partial x_j} = C_{\varepsilon 1} \frac{\varepsilon}{k} \tau_{ij} \frac{\partial U_i}{\partial x_j} - C_{\varepsilon 2} \frac{\varepsilon^2}{k} + \frac{\partial}{\partial x_j} \left[\left(v + \frac{v_T}{\sigma_\varepsilon} \right) \frac{\partial \varepsilon}{\partial x_j} \right] \quad (2.52)$$

with the following closure coefficients (Equation 2.53):

$$C_{\varepsilon 1} = 1.44, \quad C_{\varepsilon 2} = 1.92, \quad \sigma_k = 1.0, \quad \sigma_\varepsilon = 1.3 \quad (2.53)$$

$k - \omega$ models solve a transport equation for k and a transport equation for ω . ω is the specific dissipation rate and is the rate of dissipation of energy per unit volume and

time. v_T is linked to ω using Equation 2.54.

$$v_T = k/\omega \quad (2.54)$$

The transport equations for the Wilcox (1988) $k - \omega$ model used in OpenFOAM are (according to OpenFOAM (2012, 2016) which cite Wilcox (1998)):

$$\frac{\partial k}{\partial t} + U_j \frac{\partial k}{\partial x_j} = \tau_{ij} \frac{\partial U_i}{\partial x_j} - \beta^* k \omega + \frac{\partial}{\partial x_j} \left[\left(\nu + \sigma^* \frac{k}{\omega} \right) \frac{\partial k}{\partial x_j} \right] \quad (2.55)$$

$$\frac{\partial \omega}{\partial t} + U_j \frac{\partial \omega}{\partial x_j} = \alpha \frac{\omega}{k} \tau_{ij} \frac{\partial U_i}{\partial x_j} - \beta \omega^2 + \frac{\partial}{\partial x_j} \left[\left(\nu + \sigma \frac{k}{\omega} \right) \frac{\partial \omega}{\partial x_j} \right] \quad (2.56)$$

with the following closure coefficients (Equation 2.57):

$$\alpha = \frac{13}{25}, \quad \beta = 0.072, \quad \beta^* = \frac{9}{100}, \quad \sigma = \frac{1}{2}, \quad \sigma^* = \frac{1}{2} \quad (2.57)$$

The two equation models used here were the standard $k - \varepsilon$, the realisable $k - \varepsilon$, the RNG $k - \varepsilon$, the $k - \omega$, the $k - \omega$ SST model and the non linear $k - \varepsilon$ Shih model.

According to Wilcox (2006), the standard $k - \varepsilon$ model was the most widely used 2 equation model until the 1990s. It was not always applied with success. It is more inaccurate than the Baldwin-Barth one equation model for flows with adverse pressure gradient. It is inaccurate for separated flows. Its predictions for free shear flows is also a bit erratic. Since then, the $k - \omega$ model replaced the $k - \varepsilon$ model as most widely used two equation model. It is more accurate for 2D boundary layers, in cases of both adverse and favourable pressure gradient. This model reproduces accurately measured spreading rates for all five types of free shear flows. It reproduces accurately subtle features of turbulence kinetic energy behaviour close to the boundary surface. It also describes well boundary layer transition. The main drawback of the $k - \omega$ model is its dependency on free-stream turbulence.

To solve this problem, the $k - \omega$ SST model was proposed. SST stands for "Shear Stress Transport". Near the wall, the $k - \omega$ model is used, whereas in the free stream, $k - \varepsilon$ is used (Menter (1993)), thanks to a blending function. When transforming the $k - \varepsilon$ model into a $k - \omega$ formulation, an additional term appears, proportional to $\frac{1}{\omega} \frac{\partial k}{\partial x_j} \frac{\partial \omega}{\partial x_j}$. This term is referred to as cross diffusion. The blending function is tailored such that near walls, this term is not present, to resemble the $k - \omega$ turbulence model, and when going further away from the wall, the importance of this term is gradually increased, to resemble the $k - \varepsilon$ turbulence model.

The RNG $k - \varepsilon$ model is derived from the standard $k - \varepsilon$ model. The difference to the standard $k - \varepsilon$ model is that instead of having a single turbulence length scale, the contribution of all scales of motion to the turbulent diffusion are taken into account. This is done by renormalizing the Navier-Stokes equations using Re-Normalization Group methods. The method developed by Yakhot et al. (1992) was revolutionary at the time, but the improvement of accuracy when compared to the standard $k - \varepsilon$ model was shown only for rotating flows. It is used preferably for indoor air simulations (CFD-

Online (2010)).

According to Bulat and Bulat (2013), the realizable $k - \varepsilon$ model provides improved predictions for the distribution of the dissipation rate of flat and round jets when compared to the standard $k - \varepsilon$ model. It also "provides a better prediction of the boundary layer characteristics in large pressure gradients, separated and recirculating flows". Equations can be found in Shaheed and Mohammadian (2019). In summary, the reasons the realizable $k - \varepsilon$ model gives improved results are as follows: "The model satisfies certain mathematical constraints on the normal stresses, consistent with the physics of turbulent flows", that is, negative values of eddy viscosity are excluded in the calculation of high-gradient streams (Bulat and Bulat, 2013). The turbulent viscosity is calculated differently and "the transport of mean-squared vorticity fluctuation equation was used to derive the dissipation rate transport equation" (Shaheed and Mohammadian, 2019).

The non linear $k - \varepsilon$ Shih model accounts for anisotropic effects. It introduces a non linear Reynolds stress term into the standard $k - \varepsilon$ model (Brown, 2017).

2.5.2 Finite Volume Method

To apply the Finite Volume Method, the Navier Stokes equations need to be converted from the form of Partial Differential Equations to the form of Control Volume Integration.

For this conversion, Gauss's divergence theorem is used (Equation 2.58).

$$\int_{CV} \text{div}(\vec{a})dV = \int_A \vec{n} \cdot \vec{a} dA \quad (2.58)$$

where \vec{a} is a vector, CV is the control volume, dV is a volume element, A is the bounding surface of the control volume, dA is a surface element and \vec{n} is a vector normal to the surface element dA .

Applying Gauss's theorem to the steady state transport equation for property ϕ (Equation 2.59) yields Equation 2.60.

$$\text{div}(\rho\phi\vec{u}) = \text{div}(\Gamma\text{grad}\phi) + S_\phi \quad (2.59)$$

where \vec{u} is the velocity, Γ is the diffusion coefficient and S_ϕ is a source term.

$$\int_A \vec{n} \cdot (\rho\phi\vec{u})dA = \int_A \vec{n} \cdot (\Gamma\vec{\text{grad}}\phi)dA + \int_{CV} S_\phi dV \quad (2.60)$$

The computational domain is split up into polyhedrons. Each face of a polyhedron is shared with one other polyhedron only or is part of the boundary of the computational domain. Properties are calculated at the centre of the control volume. To be able to calculate the integrals over the faces, the values need to be calculated at the faces using some kind of interpolation scheme.

Several options for interpolation are available. Basic examples are central differencing and upwind differencing. There are advantages and drawbacks to the scheme chosen.

Equation 2.60 can be further transformed into Equation 2.61.

$$\sum_f F_f \phi_f = \sum_f A_f \vec{n}_f \cdot (\Gamma \vec{grad} \phi)_f + \bar{S}_\phi \Delta V \quad (2.61)$$

where f is the index of the face, F_f is the mass flux across a face, A_f is the area of a face, \vec{n}_f is the normal to a face, \bar{S}_ϕ is the average value of source S_ϕ over the control volume and ΔV is the volume. The source term S_ϕ can be dependent on ϕ . In this case, the Finite Volume Method approximates the source term by means of a linear form (Equation 2.62):

$$S_\phi = S_u + S_p \phi \quad (2.62)$$

Examples of the Finite Volume Method for steady state diffusion for one-, two- and three-dimensional problems and for steady-state convection and diffusion for a one-dimensional problem can be found in Versteeg and Malalasekera (2007). Jasak (1996) presents a detailed description of the discretization of a general transport equation.

2.5.3 Law of the wall

In a turbulent flow, it can be shown empirically, that at a given distance from a wall, stream-wise velocity near the wall varies logarithmically with distance from the surface. This is called the law of the wall. Figure 2.75 shows for which distances from the wall the logarithmic function can be applied. Equation 2.63 defines the law of the wall.

$$u^+ = \frac{1}{\kappa} \ln y^+ + C \quad (2.63)$$

where u^+ is the dimensionless, sublayer-scaled, velocity, y^+ the dimensionless, sublayer-scaled, distance, and C is an additive constant. They are defined by Equation 2.64 and Equation 2.65.

$$u^+ = \frac{u}{u_\tau} \quad (2.64)$$

$$y^+ = \frac{u_\tau y}{\nu} \quad (2.65)$$

where u_τ is the friction velocity, defined by Equation 2.66, ν is the kinematic viscosity, and y is the distance to the wall.

$$u_\tau = \sqrt{\frac{\tau_w}{\rho}} \quad (2.66)$$

where τ_w is the surface shear stress and ρ is the density. It is typically considered that for values of y^+ between 30 and 300, the law of the wall is valid.

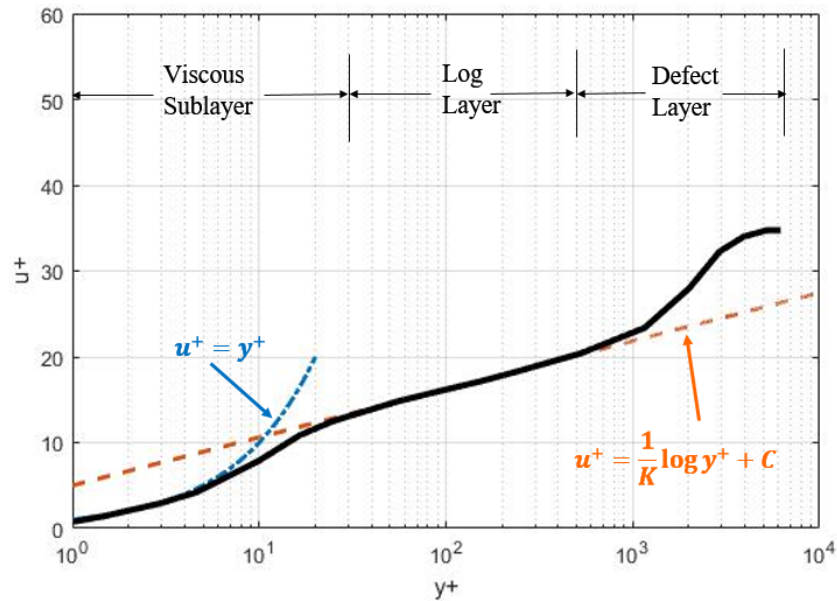


Figure 2.75: Typical velocity profile for a turbulent boundary layer. Graph inspired by graph found in Wilcox (2006). Original graph can be found in Wilcox (2006). Figure 1.7 on page 17

To calculate the first layer thickness necessary to obtain a given value of y^+ , one can use Equation 2.67.

$$\Delta_s = \frac{y^+ \nu Re^{1/4}}{U_\infty \sqrt{0.013}} \quad (2.67)$$

where Δ_s is the first layer thickness, Re is the Reynolds number and U_∞ is the free-stream velocity.

2.5.4 Description of discretization schemes

The discretization schemes available in OpenFOAM can be found in the online OpenFOAM User Guide (see OpenFOAM (2015b)). As all simulations done for this project were done in steady state, talking about time schemes is not relevant here. The default discretization scheme for gradients is called "Gauss linear" in OpenFOAM. The term "Gauss" indicates the method used to approximate the integral over the finite volume used in the calculations. The term "linear" indicates that the interpolation method to determine the values of the variables on the cell faces from the values of the cell centres is a linear one, also called central differencing. The discretization scheme for divergence of non-advective terms is usually "Gauss linear". For the advective terms, they are also based on the Gauss integration. What differs between the wide range of choices for the discretization of the divergence for advective terms is the interpolation method to get the values on the cell faces using the values at the cell centres. It can be "linear" (= central difference) or upwind or a combination of both. In the case of incompressible steady state flow, the "bounded" version is useful, as it helps maintain the boundedness of the solution variable.

2.5.5 SIMPLE algorithm

To solve the Navier Stokes equations, where pressure and velocity are linked, an algorithm for solving them needs to be chosen. According to Jasak (1996), simultaneous algorithms, that solve the complete system of equations simultaneously over the whole domain, exist, but should only be used for a small number of computational points and simultaneous equations. For other cases, the equations need to be solved in sequence and a way of coupling them needs to be chosen. The PISO (Pressure-Implicit with Splitting of Operators) and the SIMPLE (Semi-Implicit Method for Pressure-Linked Equations) algorithm are the most popular methods. The SIMPLE algorithm can only be used for a steady state solution. The PISO algorithm was developed for unsteady flows, but can be adapted to steady state flows.

At the start of SIMPLE algorithm, initial pressure and velocity are guessed. Then, the steps below are done iteratively until the difference between the values guessed initially and those obtained through calculation is sufficiently low.

- Solve for velocity using the discretised momentum equation
- Use the velocity obtained at the previous step to solve for pressure correction using the pressure correction equation, which is derived from the discretized continuity equation
- Using the pressure correction obtained, new values for pressure and velocity are obtained
- Additional transport equations are solved using the corrected pressure and velocity

Repeating the above steps until convergence is reached, is possible for steady state flow, but too costly for transient flow to be done at every time step. The PISO algorithm has been developed to be used for transient flow.

The PISO algorithm starts with the first three steps of the SIMPLE algorithm. Then a second pressure correction equation is solved, followed by a second set of values for pressure and velocity, which are then used in the additional transport equations. No iteration of the steps is done for a given time step. Rather, the procedure is repeated for the next time step, taking as initial values the values of velocity and pressure obtained previously. This works for small time steps.

The PISO algorithm can also be used for steady state flow, by using iteration steps instead of time steps.

Detailed equations for a 2D steady state laminar flow are given in Versteeg and Malalasekera (2007) for the SIMPLE and the PISO algorithm.

2.5.6 Review of indoor air simulation using steady state airflow

Courbois (2013) describes the CFD simulation of the wind distribution produced by the wind generation system described in Section 2.4.5. The CFD simulation described in Courbois (2013) used a simplified configuration of the wind blowing system of the Ecole Centrale de Nantes to calibrate the numerical tool Fluent. Fluent is a CFD code

that solves the Navier-Stokes equations by using the Finite Volume Method. This same numerical tool was then used for designing a bigger wind blowing system. The problem was considered to be steady state. The momentum equations and the turbulence equations were treated using a first order upwind discretization scheme. Several turbulence models were tested. The standard $k - \epsilon$ model was chosen, as it was considered that it was the most appropriate model to predict free flowing jets that used two equations. The author considered that when using models that use second moment closure such as the Reynolds Stress model, accuracy is not increased greatly. However, calculation time is longer. On the water surface, as well as the lateral walls of the laboratory wall, boundary conditions were applied. The side of the domain opposite of the wind blower was considered to be of the type "pressure outlet". To include effects of the pressure gradient, a non-equilibrium wall function was used. The mesh was chosen to be adapted to high Reynolds numbers and therefore unstructured. The duct and diffuser were modelled as rigid structures. It is not completely clear from the descriptions whether the inlet was situated at the end of the diffuser or whether the flow was simulated inside the duct, but it is very likely that the inlet was situated at the end of the diffuser, just when the air inside the duct exits into the large open space, as the author presents in the paragraph following the description of the numerical simulation the properties of a free stream jet. The end of the diffuser was situated well inside the domain, slightly above the water surface. The results of this simulation coincided rather well with measured results.

A few other cases of simulation of movement of air in a closed room were looked at. One of them is the case of the study of an indoor environment with a ceiling fan (Zhu et al. (2014)). The purpose of this study was to develop a CFD model that could correctly reproduce indoor air movement produced by a ceiling fan as well as the impact of this ventilation system on the efficiency of an ultraviolet germicidal irradiation system. Experimental data was available for the validation of the model. The simulation was done in steady state, a rotating reference frame was used to simulate the rotation of the fan blades. The turbulence model used is the realizable $k - \epsilon$ model. A two-layer approach was used, which allowed the $k - \epsilon$ model to be applied in the viscous sublayer. This is possible by specifying the turbulent dissipation rate and turbulent viscosity as functions of the wall distance.

The inlet of the domain was situated at the ceiling. The outlet was situated on one of the walls, near one of the bottom corners of the cuboid-shaped domain. The domain was composed of a total of 1.5 million cells. Surrounding the fan blades, there was a cylindrical subdomain which contained 86 % of the cells. A few objects present in the room were represented with simple 3D geometries, such as cuboids and prisms.

A finite volume method was applied (Star-CCM+). The differencing scheme used was second-order upwind for velocity and pressure, and first-order upwind for temperature and passive scalars. Near the walls, a treatment was available in this particular software which allowed to automatically adapt the right wall treatment depending on the $y+$ value.

Kurnia et al. (2014) presents the study of a ventilation system used to disperse methane near mining faces. A CFD simulation was set up with the mine represented by a tunnel with constant cross section. One end of the tunnel was the mining face, near which

sources of methane were simulated. The other end was the outlet. The inlet was the beginning of the ventilation duct which started at the same side as where the outlet was situated. The duct then lets air into the tunnel at a certain distance before the mining wall. 4 different turbulence models were tested and the data produced compared to experimental data in various points. The turbulence models were Spalart Allmaras, $k - \varepsilon$, $k - \omega$ and Reynolds Stress. The $k - \varepsilon$ was deemed sufficiently accurate and fast enough. The results were off by 30 % from the experimental data. The experimental data itself was estimated to be off by up to 10 %.

Zhu et al. (2014) studied the use of a ceiling fan in a closed room with a high ceiling for even air temperature distribution. The study was done in Fluent. Two turbulence models were tested: $k - \varepsilon$ and Reynolds Stress. The ceiling fan was not modelled directly. Instead, speed and turbulence were prescribed at two different heights above and below the position of the ceiling fan, to simulate the air flow produced by the fan. This air flow data was obtained through measurements done near an existing fan. It was found that the Reynolds Stress model gave results closed to measured data, whereas the results obtained using the $k - \varepsilon$ model were unsatisfactory. The domain was composed of a total of 534,204 cells.

Vadlamani (2010) looked at the use of the $k - \varepsilon$ model to simulate the airflow in the mixing box of an air conditioning unit and study the impact of leakage. The CFD simulation results were compared to experimental data and the comparison was reasonable. The mesh was made up of tetrahedral cells. 5 layers were applied at the walls of the domain. A mesh convergence study was done for the simulation and the results were presented in the thesis. 5 different mesh sizes were studied. The coarsest mesh had 167,000 elements, the finest mesh had 552,000 elements. The final mesh chosen showed a difference of less than 1% for temperature readings in a chosen location of the domain when compared to the previous mesh (consisting of 454,000 cells), and was thus deemed sufficiently refined. For the speed, the difference between the final mesh and the one before that was under 2%.

Chapter 3

Design and testing of a small wind generation system

This chapter presents the set up and testing of a small wind generation system, which served as a prototype for the final version. The purpose of this set up was to test the concept of combining the air flow of two centrifugal fans through a system of ducts into a single airflow. At the time of the experiment, it had not been determined yet that the wind generation system would need an expanding diffuser. The scale of the experiments with the model wind turbine had not been decided at that point and the size of the large fans had also not been determined. The wind speed was measured at various distances from the outlet of the system on the central axis of the flow, and also in various locations in planes perpendicular to the main direction of the flow. A large number of combinations of various flow straighteners was used and their impact on turbulence intensity and average wind speed tested. This allowed to verify theories found in literature on flow straighteners and see whether those could be followed to design a larger wind generation system. The area over which wind speed was consistent and over which turbulence intensity levels were acceptable was also determined.

3.1 Set up of the small wind generation system

Before testing a wind generation system that blows wind over an area that is 3 m wide, it was decided to test the concept for a smaller version of the system. The concept was inspired by the one from Centrale Nantes (Courbois (2013)), where wind would be produced by centrifugal fans and then guided to the centre of the basin through a ducting system to a diffuser outlet. At Centrale Nantes, 8 fans were used. Here, only two were used. The fans were 1.8 kW backward bladed straight centrifugal fans. Figure 3.1 shows the set up used in this first experiment.

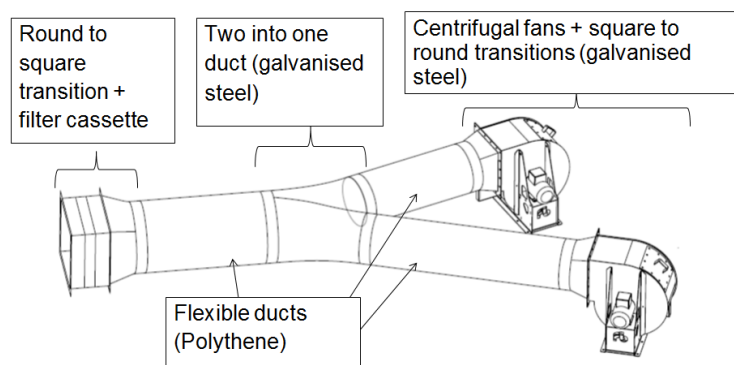


Figure 3.1: Sketch of the wind generator

3.1. SET UP OF THE SMALL WIND GENERATION SYSTEM

The angle of the two into one duct was 30° . See Figure 3.2 for lengths of the different parts of the duct.

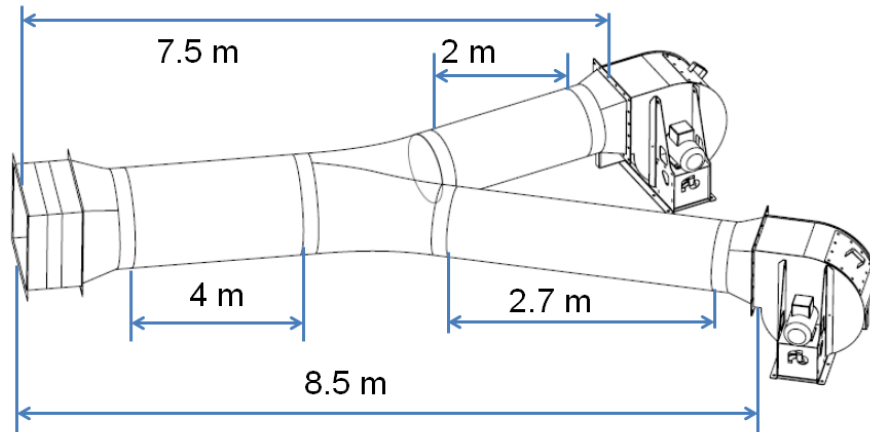


Figure 3.2: Dimensions of the duct

Figure 3.3 shows the set up in reality.

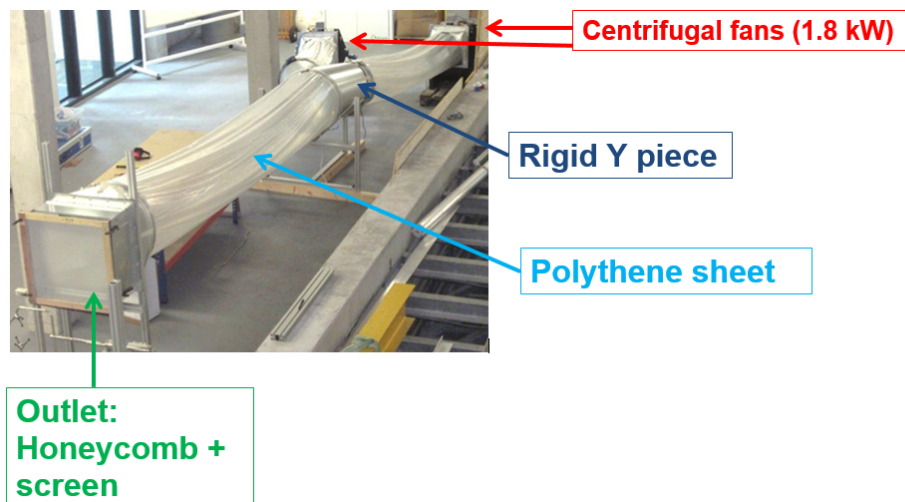


Figure 3.3: Set-up of the small scale wind generator prototype

The final outlet was 560 mm higher than the outlets of the two fans. It was decided to keep a constant cross section all along the system. The final outlet was a square measuring 590 by 590 mm. A filter cassette held a honeycomb and a meshed screen was positioned using a wooden frame at the very end of the outlet.

Four different honeycombs were tested as well as four different meshed screens. Table 3.1 shows the dimensions of the four honeycombs. The choice for these dimensions are based on recommendations found in literature. Mehta and Bradshaw (1979) recommend having 150 cells per settlement chamber diameter or 25,000 cells per settlement

3.1. SET UP OF THE SMALL WIND GENERATION SYSTEM

chamber cross section. This gave in the present case a cell diameter of 4 mm. The other diameters in the list were chosen above and below this dimension amongst those available by the manufacturer. The cell length (or honeycomb thickness) was chosen to be 8 times the cell diameter for every honeycomb, which gives a ratio recommended in various sources of literature, that is, Mehta and Bradshaw (1979) recommend that the cell length be 6 to 8 times the cell diameter. Later papers recommend a ratio of 8 to 10 (Kulkarni et al. (2011), Courbois (2013)). All the honeycombs are made from polycarbonate. When talking about one of the honeycombs used, it will be referred to by its cell diameter.

Table 3.1: Overview of the honeycombs tested

Cell diameter (mm)	Cell length (mm)
3	24
4	32
6	48
12	96

Table 3.2 shows the dimensions of the meshed screens. All meshed screens have a minimum open area of 58 %, as is recommended. Mehta and Bradshaw (1979) recommend Wieghardt's formula (Equation 2.28) for the calculation of the pressure drop coefficient, recommended to be equal to 1.5. Using this formula, it can be determined that to have a pressure drop coefficient of 1.5, one needs a wire diameter of 300 μm . The closest available by manufacturers had a wire diameter of 320 μm . The other dimensions were again chosen amongst those available from the manufacturer above and below the recommended wire diameter. When talking about a meshed screen, it will be referred to by its wire diameter.

Table 3.2: Overview of the screens tested

Wire diameter (μm)	Open area (%)	Side of open area (μm)	Material
73	59	240	polyester
320	58	1000	polyester
500	61	1800	nylon
1000	59	3300	nylon

Using these two types of flow straighteners, a total of 25 combinations was studied, which included combinations with one (or both) types of flow straighteners absent.

The wind speed was measured with a 3D ultrasonic anemometer. The measurements were done at a frequency of 32 Hz. Figure 3.4 shows the set up of the anemometer as well as the 3 directions in which wind was measured.

3.2. EVOLUTION OF WIND SPEED WITH THE ELECTRIC FREQUENCY OF THE FANS AND ITS DEPENDENCE ON THE FLOW STRAIGHTENERS USED

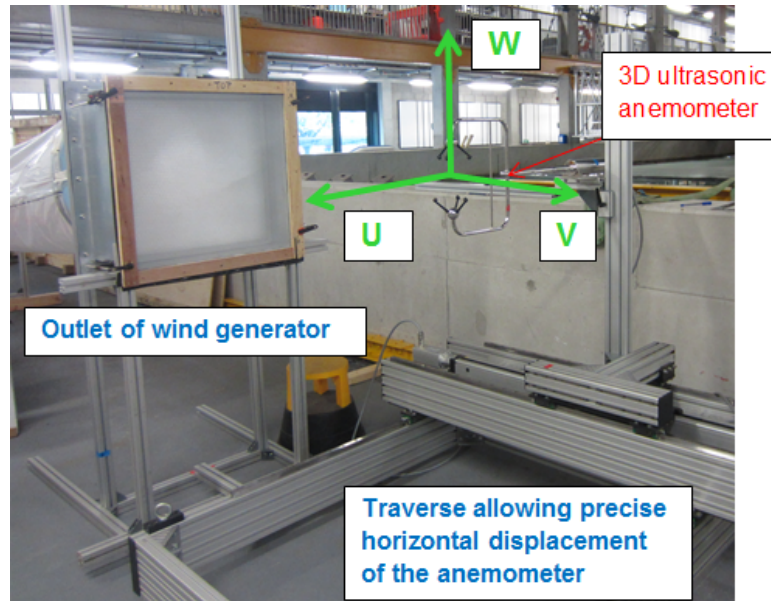


Figure 3.4: Set-up of the outlet and the anemometer

Appendix B.1 shows all the combinations and fan electric frequencies for which measurements were done, as well as at what distances from the outlet they were done. For eight combinations, measurements were done not only on the central axis of the flow, but at various distances to the side or above the central axis.

The following paragraphs will present

- evolution of wind speed with the electric frequency of the fans and its dependence on the kind of flow straightener used
- the impact of the flow straighteners on the turbulence intensity
- variation of wind speed and turbulence intensity with distance from outlet
- comparison between theoretical and experimental turbulence
- evolution of wind speed and turbulence intensity in area perpendicular to main direction of airflow
- determination of flow rate of the fans

3.2 Evolution of wind speed with the electric frequency of the fans and its dependence on the flow straighteners used

The wind speed was measured for various electric frequencies of the fan. The electric frequency is proportional to the rotational speed of the fan. The maximum electric frequency is 50 Hz and corresponds to a rotational speed of 3000 rpm. Figure 3.5 shows the evolution of the average longitudinal wind speed with the fan electric frequency for the 12 mm honeycomb and various meshed screens.

3.2. EVOLUTION OF WIND SPEED WITH THE ELECTRIC FREQUENCY OF THE FANS AND ITS DEPENDENCE ON THE FLOW STRAIGHTENERS USED

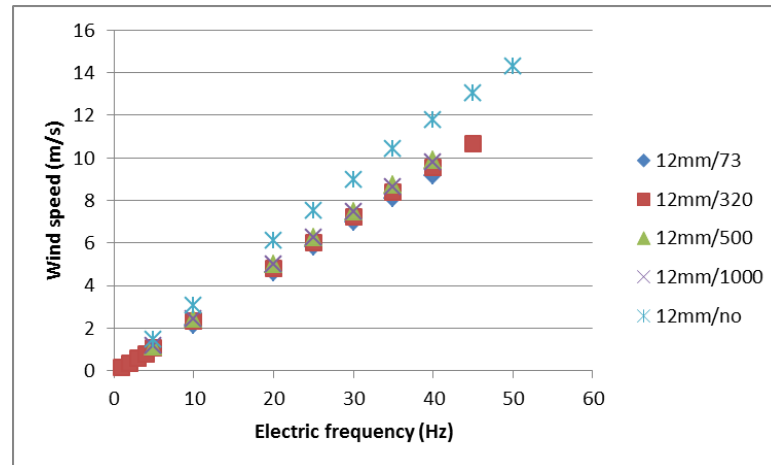


Figure 3.5: Wind speed as a function of the electric frequency of the fans, for different flow straightening screens

It can be seen that the evolution of the average longitudinal wind speed on the central axis at 250 mm from the outlet is roughly linear. It can also be observed that when adding any meshed screen, there is a drop in this average longitudinal wind speed. This drop is the largest when the meshed screen of 73 μm is used. At an electric fan frequency of 40 Hz, the wind speed is 7 % lower than when the meshed screen of 500 μm is used, which lowers the wind speed the least. The fact that the 500 μm screen reduces wind speed less than the 1000 μm screen is due to the fact that the open area ratio of the 500 μm screen is larger than the open area ratio of the 1000 μm screen (see Table 3.2). The 73 μm meshed screen lowers the average longitudinal wind speed by 22 % when compared to using a honeycomb only. The drop in wind speed increases with wind speed.

Figure 3.6 gives an overview of average wind speeds measured for different honeycombs combined with the 1000 μm screen at 25 cm from the outlet, on the central axis.

3.3. IMPACT OF FLOW STRAIGHTENERS ON TURBULENCE INTENSITY

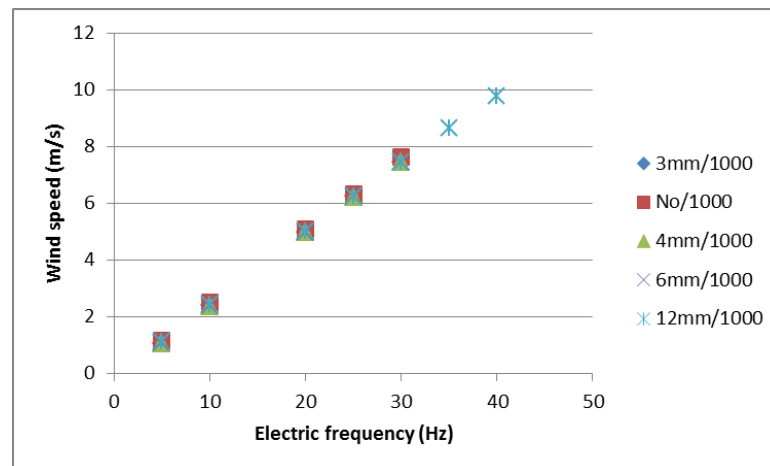


Figure 3.6: Wind speed as a function of the electric frequency of the fans for different flow straightening honeycombs

As can be seen, adding a honeycomb has little impact on the average longitudinal wind speed. Also, the type of honeycomb has very little influence on the amount by which the wind speed drops. At an electric frequency of 30 Hz, the wind speed obtained when using the honeycomb that lowers the wind speed the most is only 0.16 % lower than for the honeycomb that lowers the wind speed the least. And the drop of speed between no honeycomb and the honeycomb that lowers it the most is only 2.4 %.

3.3 Impact of flow straighteners on turbulence intensity

This section will focus on the impact of flow straighteners on the turbulence intensity. All of the observations are done on the central axis of the flow. The following observations will be made:

- Difference of impact between meshed screens and honeycombs
- Impact of size of meshed screen or honeycomb
- Difference of impact on longitudinal and lateral turbulence intensity
- Impact depending on the wind speed

The variation of turbulence intensity as a function of wind speed for different combinations of honeycomb/screen was measured. The main observation is that any given combination involving the presence of both a honeycomb and a screen gave very low levels of turbulence intensity (~ 1 -2 % for lateral turbulence, 1-3 % for longitudinal turbulence at 25 cm from the outlet). The impact of honeycombs was found to be more important than the one of screens. The average longitudinal and lateral turbulence intensities at 20 Hz and 50 cm from the outlet when only a honeycomb was used are 4.3 % and 1.5 % respectively. When using only a screen, at the same frequency and the same distance, the average longitudinal and lateral turbulence intensities are 4.6 % and 6.1 % respectively. The difference between the various honeycombs is negligible. It should be remembered that though the cell size varies, the cell length/cell size ratio

3.3. IMPACT OF FLOW STRAIGHTENERS ON TURBULENCE INTENSITY

remains constant, which is believed to explain the small variation. Figure 3.7 shows the effect of several honeycombs, each combined with the same screen.

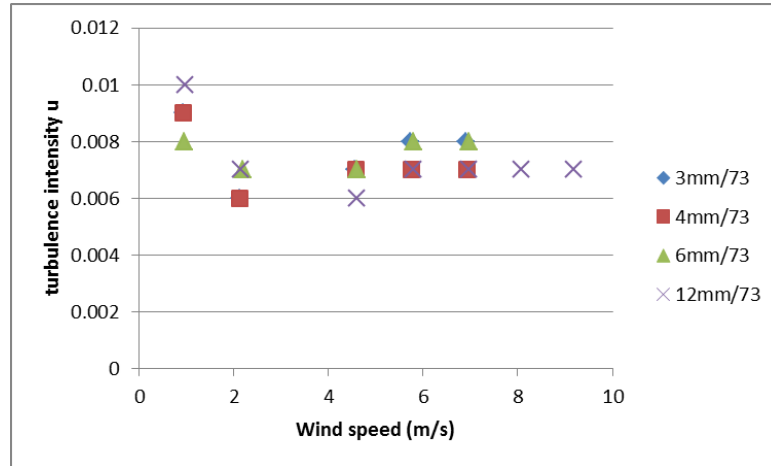


Figure 3.7: Lateral turbulence intensity for various honeycombs combined with the 73 μm screen at 25 cm from the outlet on the central axis

Figure 3.8 shows the same for longitudinal turbulence intensity.

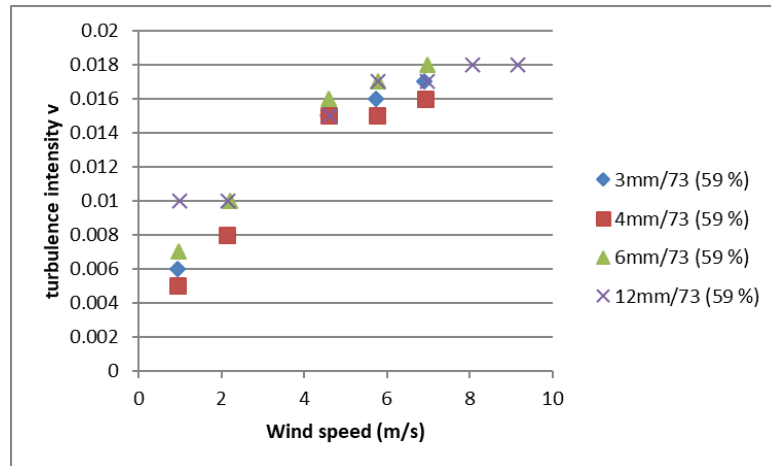


Figure 3.8: Longitudinal turbulence intensity for various honeycombs combined with the 73 μm screen at 25 cm from the outlet on the central axis

For comparison, Figure 3.9 shows lateral turbulence intensity without flow straighteners or with a 12 mm honeycomb only.

3.3. IMPACT OF FLOW STRAIGHTENERS ON TURBULENCE INTENSITY

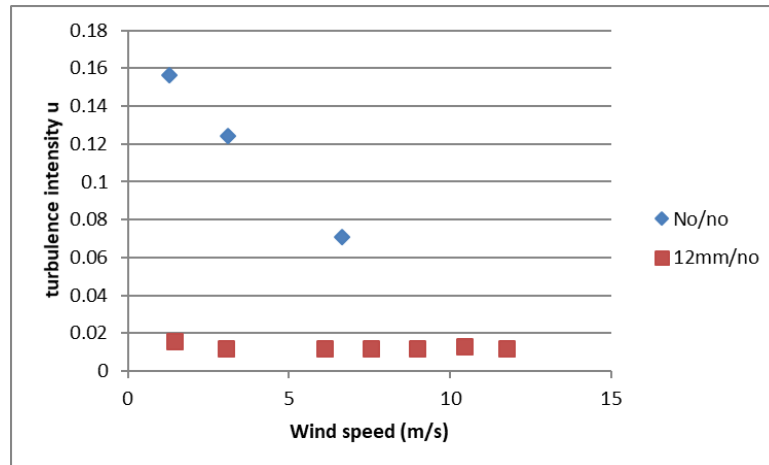


Figure 3.9: Lateral turbulence intensity without any flow straightener and with a 12 mm honeycomb only at 25 cm from the outlet on the central axis

Figure 3.10 shows longitudinal turbulence intensity without flow straighteners or with a 12 mm honeycomb only.

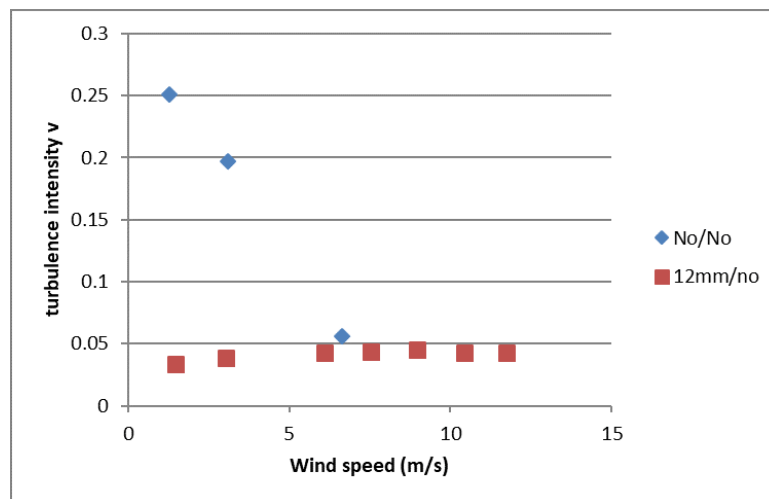


Figure 3.10: Longitudinal turbulence intensity without any flow straightener and with a 12 mm honeycomb only at 25 cm from the outlet on the central axis

For the screens, the screen with the smallest wire diameter ($73 \mu\text{m}$) results in the biggest reduction of both types of turbulence across all wind speeds tested (Figure 3.11 and Figure 3.12). Next is the second smallest diameter ($320 \mu\text{m}$). For the $500 \mu\text{m}$ wire diameter and the $1000 \mu\text{m}$ wire diameter, however, the turbulence reduction is sometimes more important for the $1000 \mu\text{m}$ screen than for the $500 \mu\text{m}$ screen. This is most probably due to the difference in the open area (61 % for the $500 \mu\text{m}$, 59 % for the $1000 \mu\text{m}$).

3.3. IMPACT OF FLOW STRAIGHTENERS ON TURBULENCE INTENSITY

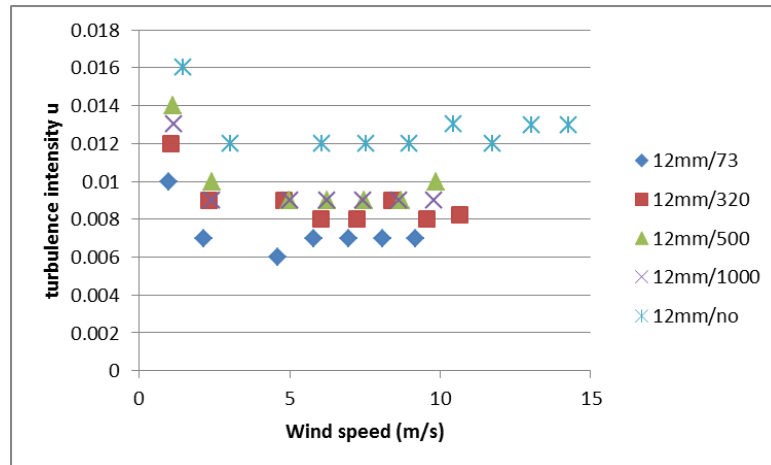


Figure 3.11: Lateral turbulence intensity u at 25 cm from the outlet along the central axis

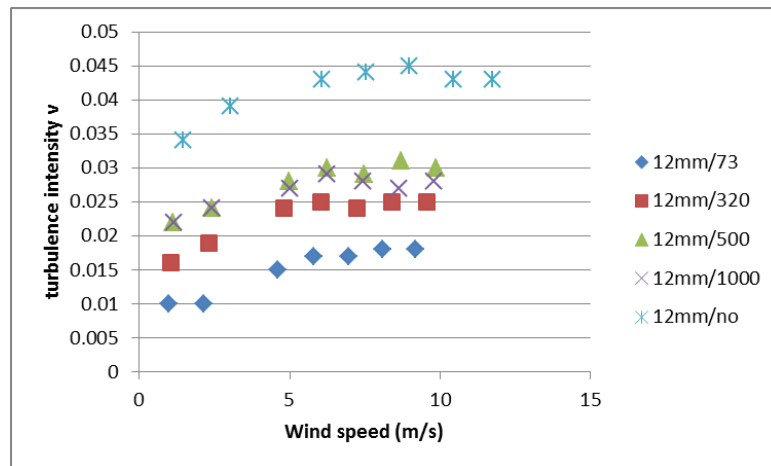


Figure 3.12: Longitudinal turbulence intensity v at 25 cm from the outlet along the central axis

As expected, the variation of turbulence intensity of u and w is very comparable, both of these components being lateral turbulence and having equivalent values. Though the main function of honeycombs is the reduction of lateral turbulence, reduction in longitudinal turbulence was also observed. The opposite is true for screens. Their influence on longitudinal turbulence is more significant, but they also have an influence on lateral turbulence.

Both longitudinal and lateral turbulence were observed to vary with wind speed. For lateral turbulence, for any honeycomb/screen combination involving a honeycomb, the intensity measured at the lowest wind speed was at least a third higher than that measured at the higher wind speeds.

3.4 Variation of wind speed and turbulence intensity with distance from the outlet on the central axis

Figure 3.13 shows the typical evolution of wind speed and turbulence intensity with distance from the outlet on the central axis. For the wind speed, a 5 % drop is observed over a distance of 1 m. Over the same distance, the longitudinal turbulence intensity increases by 62 %. For the lateral turbulence intensity, the increase is 197 % for the horizontal component and 146 % for the vertical component. As the turbulence intensity at 0.25 m from the outlet is very low, the turbulence intensity at 1.25 m from the outlet is still below the maximum acceptable level (7.9 %) on the central axis.

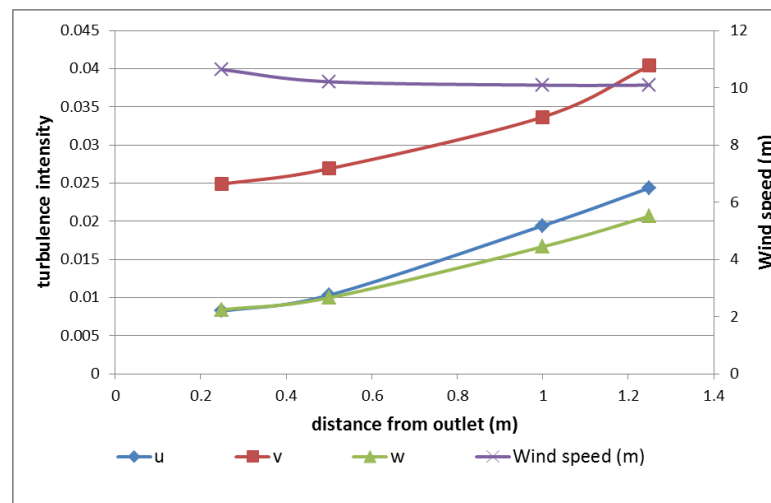


Figure 3.13: Increase of longitudinal and lateral turbulence intensity with distance from the outlet (12 mm honeycomb/320 μ m screen, 45 Hz) along the central axis

3.5 Comparison of theoretical and experimental turbulence reduction factor

If the turbulence intensity at the outlet had been known prior to preparing the experimental set up, in the absence of any flow straightening system, theoretical turbulence reduction factors could have been used to decide exactly which honeycombs and meshed screens to use to bring the turbulence intensity to acceptable levels. Instead, general guidelines were used to decide on the dimensions of the flow straightening tools, independent of initial turbulence levels. The goal of this paragraph is to determine how accurately the turbulence reduction could have been predicted using theoretical formulas introduced in Section 2.4.4. It is to be noted that given the definition of the turbulence reduction factor (TRF) in Equation 2.29, the lower the TRF, the better the turbulence reduction, whereas a high TRF indicates that turbulence has not been reduced a lot.

To compare the measured efficiency of the flow straighteners to theoretical predictions both longitudinal and lateral turbulence reduction factors for both honeycombs and screens were considered. All examples shown here are determined from data measured on the central axis of the flow and at 25 cm from the outlet. The TRF of a single flow straightener was calculated using two approaches. In the first, turbulence intensity with the flow straightener alone is compared to turbulence intensity without

3.5. COMPARISON OF THEORETICAL AND EXPERIMENTAL TURBULENCE REDUCTION FACTOR

any flow straightener, using the ratio of equation 2.29, where I_A in this case is the turbulence intensity with the flow straightener and I_B is the turbulence intensity without flow straightener.

$$TRF = \frac{I_A}{I_B} \quad (3.1)$$

In the second approach, turbulence intensity of one flow straightener combined with a second flow straightener is compared to turbulence intensity with the second flow straightener alone to determine the TRF of the first flow straightener. In Equation 2.29, I_A is now the turbulence intensity with flow straightener 1 and flow straightener 2 and I_B is the turbulence intensity with flow straightener 2.

3.5.0.1 Longitudinal turbulence reduction factor

Figure 3.14 compares theory to experimental data for the longitudinal TRF of the 12 mm honeycomb.

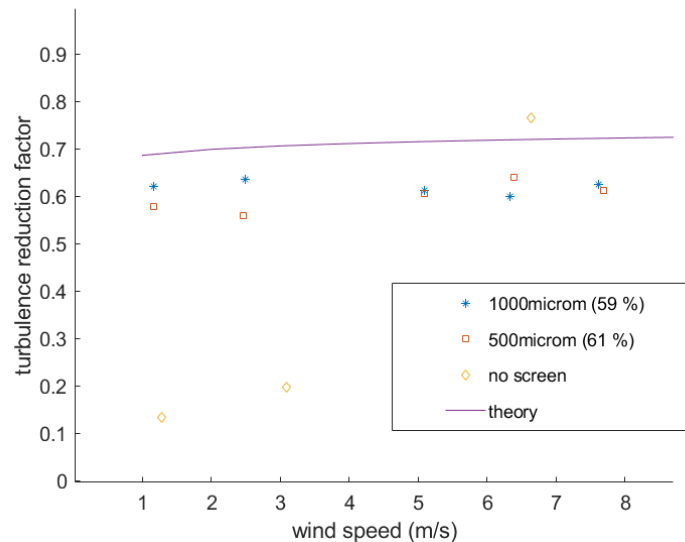


Figure 3.14: Longitudinal TRF of the 12 mm honeycomb when combined with the 1000 μm screen, the 500 μm screen or used alone ('no screen')

Theoretical values were calculated using equations 2.24 and 2.31 (Section 2.4.4) for this honeycomb. Theory and measurement both show only small variation with wind speed, and are of similar magnitude, although experiments consistently outperformed the theoretical prediction in regards to turbulence reduction factor, by an average of 17 %, when the honeycomb is combined with a screen. Figure 3.14 also shows the TRF determined experimentally when the honeycomb is used alone. In this case, theory and experimental data are very different.

The measured longitudinal TRF for a screen (1000 μm) is compared to predicted values in Figure 3.15.

3.5. COMPARISON OF THEORETICAL AND EXPERIMENTAL TURBULENCE REDUCTION FACTOR

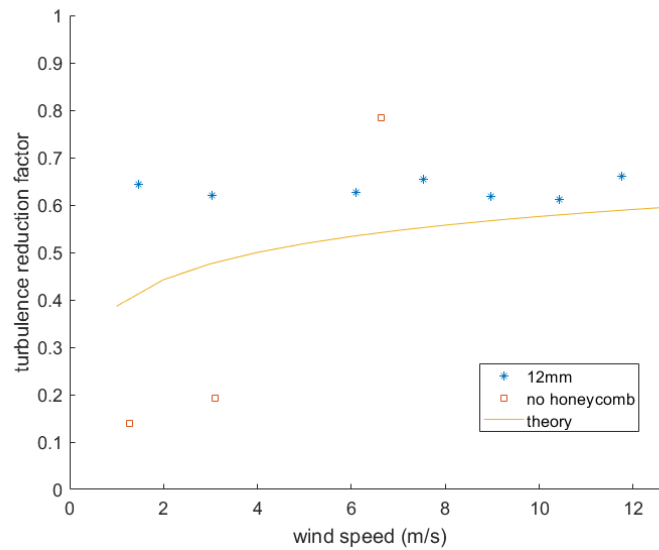


Figure 3.15: Longitudinal TRF of the 1000 μm screen when combined with the 12 mm screen or used alone ('no honeycomb')

The experimental data is within 18 % of the theory for wind speeds above 6 m/s. For lower wind speeds, theory predicts an increase of the turbulence reduction factor with wind speed, whereas the trend for the experimental values is to stay constant. The turbulence reduction is consistently less than predicted. The experimental TRFs calculated when the screen was used alone were again significantly different from the theoretical values, both in terms of magnitude and the changes with respect to wind speed.

3.5.0.2 Lateral turbulence reduction factor

For the case of the lateral TRF for honeycombs (Figure 3.16), measured and predicted values were of a similar magnitude, especially at higher wind speeds. However at lower speeds the measured and predicted values increasingly diverged.

3.5. COMPARISON OF THEORETICAL AND EXPERIMENTAL TURBULENCE REDUCTION FACTOR

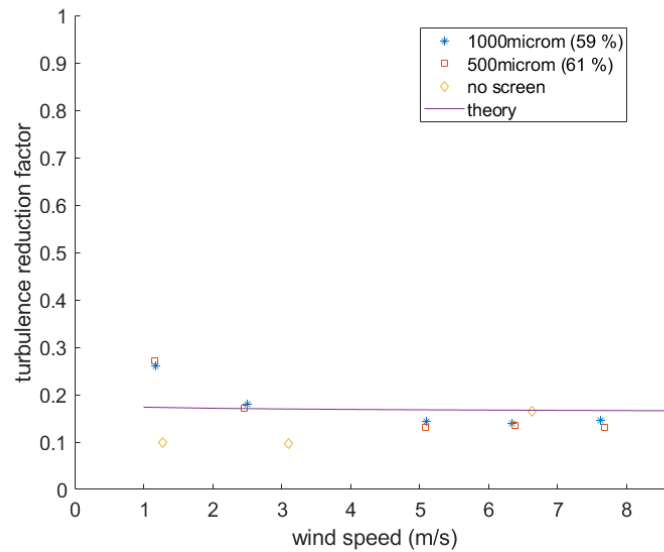


Figure 3.16: Lateral TRF for the 12 mm honeycomb

For the case of the lateral TRF for screens, the example of the 1000 μm screen can be seen in Figure 3.17. The experimental data was determined when it was used alone or combined with the 12 mm honeycomb.

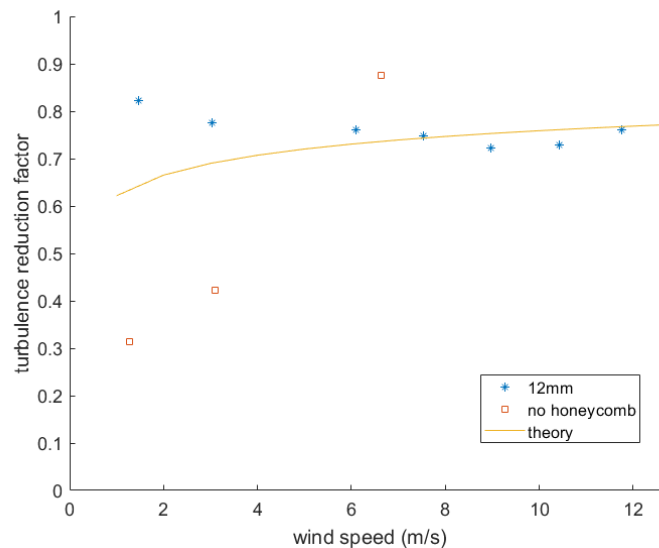


Figure 3.17: Lateral TRF of the 1000 μm screen when combined with the 12 mm honeycomb and when used by itself

As for the longitudinal TRF for screens, the agreement with theory is good when it is used with a honeycomb and for wind speeds above 6 m/s. However at lower wind speeds, the theoretical value decreases whereas the experimental value increases. Again, when the screen is used alone, the turbulence reduction factor determined is

different from theory, both in terms of magnitude and changes with respect to wind speed.

One possible explanation for this divergence between theory and experimental values for the TRF when a flow straightener is used alone to reduce turbulence from a state where no flow straightening was applied is that in that situation the initial turbulence levels are rather high ($\sim 10-20\%$), in particular for low wind speeds. It is possible that the equations used for the calculation of the pressure drop and the TRF of screens and honeycombs found in Eckert et al. (1976); Mehta and Bradshaw (1979); Dryden and Schubauer (1947); Prandtl (1933); Scheimann (1981); Lumley and McMahon (1967), which are basically mathematical models determined through experiments, are only valid for a given range of initial turbulence level. For a different range of turbulence level, another mathematical model might be needed to accurately predict turbulence reduction. This is confirmed by Scheimann (1981), who states that "Some common assumptions in the theories are that the flow upstream of the manipulator is isotropic and homogeneous, that the turbulence level is small compared with the main free-stream level, and that the fluid is incompressible."

The results for the lateral turbulence reduction measured/calculated in the vertical direction (component w) were almost identical to the ones calculated for the horizontal lateral component (u). It can thus be concluded that concerning this aspect, the two lateral components work in the same way. Calculations were also done for measurements on the central axis of the flow at 50 cm, 1 m and 1.25 m from the outlet. As a general rule, with increasing distance from the outlet, the difference between measured and predicted values increased. This is not a surprising fact, as the equations for the turbulence reduction factors are valid for closed tunnels. The further the distance from the outlet, the less likely the experimental values correspond to theory, as the influence of the surrounding air increases.

3.6 Variation of wind speed and turbulence intensity as a function of location in space

The wind speed was measured in planes perpendicular to the main flow direction situated at various distances from the outlet for several combinations of screens and honeycombs. To determine a usable area, it was chosen to accept a 5 % drop in the longitudinal average wind speed, as compared to the maximum wind speed in a given plane. For an acceptable level of longitudinal turbulence intensity, a maximum level of 7.9 % was chosen, corresponding to the average longitudinal turbulence intensity given in Hansen and Sommers (2002). Figure 3.19 shows how longitudinal velocity varies across the horizontal plane 50 cm from the outlet at a height 20 cm above the central axis (see Figure 3.18). Velocities are normalised with respect to the maximum velocity measured in this plane for each honeycomb/screen combination presented. The usable area is observed to be at least 50 cm wide based on the wind speed criteria (assuming symmetry in the plane). Figure 3.20 confirms that the criterion for the turbulence level is also respected in this area.

3.6. VARIATION OF WIND SPEED AND TURBULENCE INTENSITY AS A FUNCTION OF LOCATION IN SPACE

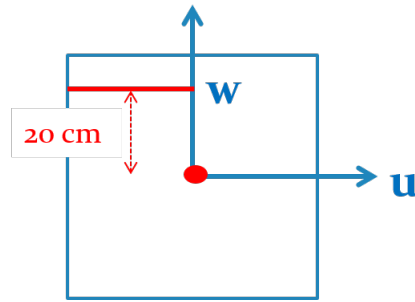


Figure 3.18: Situation in space of the wind speed shown in Figure 3.19

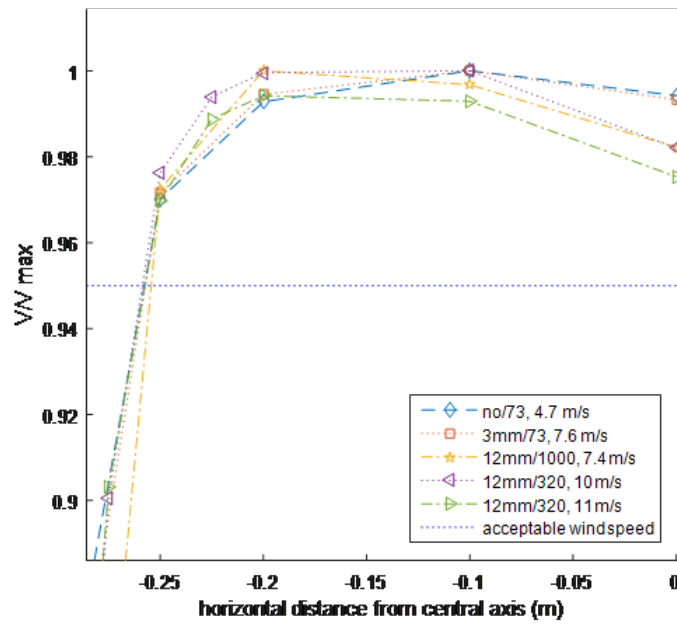


Figure 3.19: V/V_{max} at 50 cm from the outlet and 20 cm above the central axis

3.6. VARIATION OF WIND SPEED AND TURBULENCE INTENSITY AS A FUNCTION OF LOCATION IN SPACE

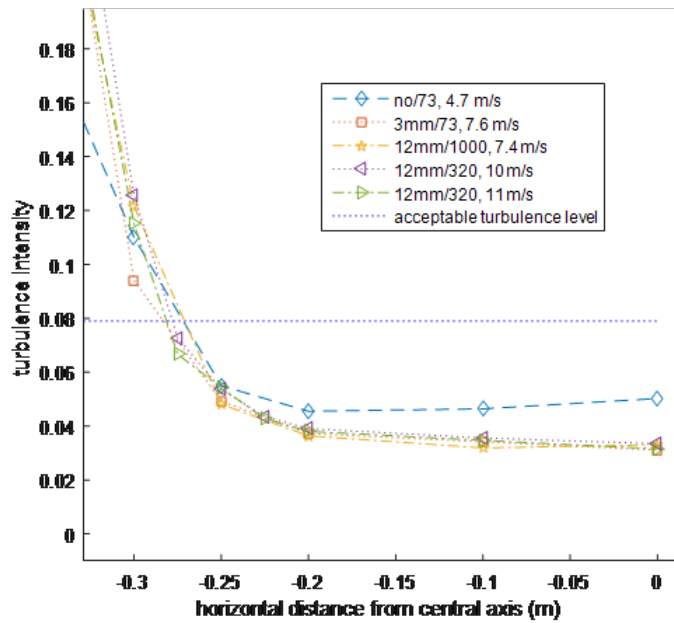


Figure 3.20: Longitudinal turbulence intensity at 20 cm above the central axis and at 50 cm from the outlet

Figure 3.22 reproduces Figure 3.20 but at 25 cm above the central axis (see Figure 3.21). Turbulence intensity is still sufficiently low for all represented combinations, except for the case without a honeycomb ('no/73').

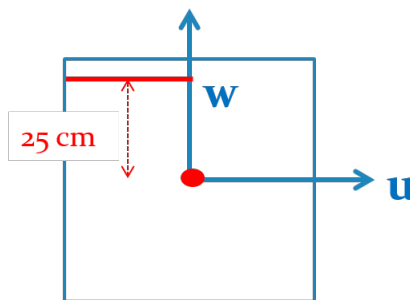


Figure 3.21: Situation in space of turbulence intensity shown in Figure 3.22

3.6. VARIATION OF WIND SPEED AND TURBULENCE INTENSITY AS A FUNCTION OF LOCATION IN SPACE

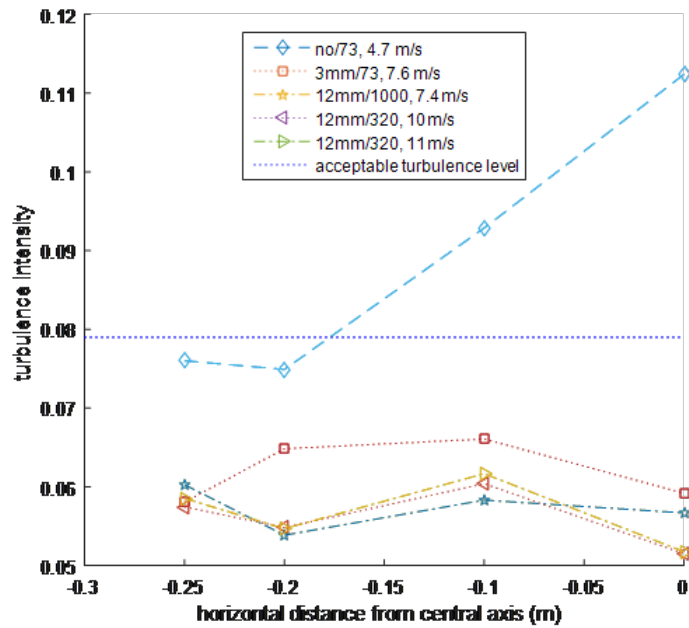


Figure 3.22: Longitudinal turbulence intensity at 50 cm from the outlet and 25 cm above the central axis

However, at 25 cm above the central axis and 50 cm from the outlet, the criterion for wind speed is not respected for any of the represented cases (Figure 3.23). Thus, though the outlet is symmetric, the distribution of the wind speed is not identical in the vertical and in the horizontal direction. The usable area at 50 cm from the outlet is thus rectangular-shaped, about 50 cm wide and 40 cm high, when using the chosen criteria for wind speed and turbulence intensity. When looking at measurements done for the whole area instead of just a quarter of the area, it was seen that the flow was not symmetric, that on the quarter of the area measured there was stronger air flow.

3.6. VARIATION OF WIND SPEED AND TURBULENCE INTENSITY AS A FUNCTION OF LOCATION IN SPACE

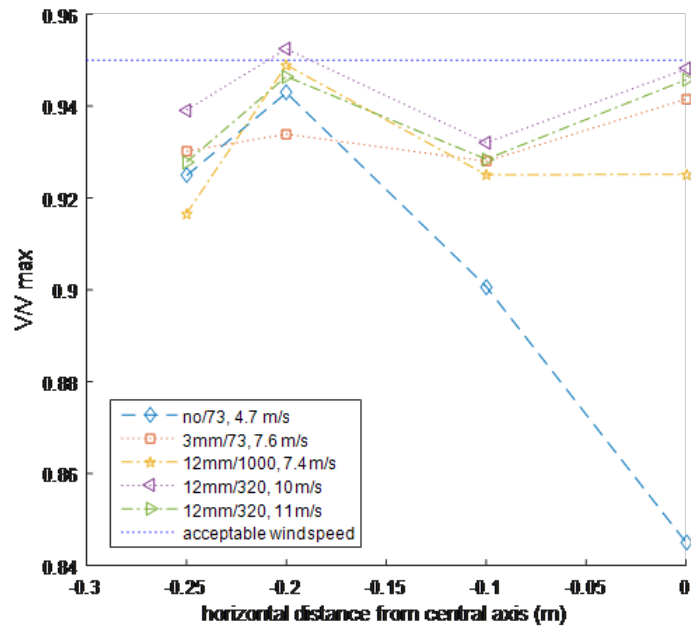


Figure 3.23: V/V_{max} at 50 cm from the outlet and 25 cm above the central axis

Figure 3.24 shows the average lateral wind speeds in a plane perpendicular to the main flow direction at 1 m from the outlet where both a screen and a honeycomb were used. The maximum lateral wind speed in this case is 0.4 m/s with a maximum longitudinal wind speed of 4.8 m/s. The fact that the flow goes in a single direction could be explained through lack of symmetry in the geometry of the laboratory space surrounding the area.

3.6. VARIATION OF WIND SPEED AND TURBULENCE INTENSITY AS A FUNCTION OF LOCATION IN SPACE

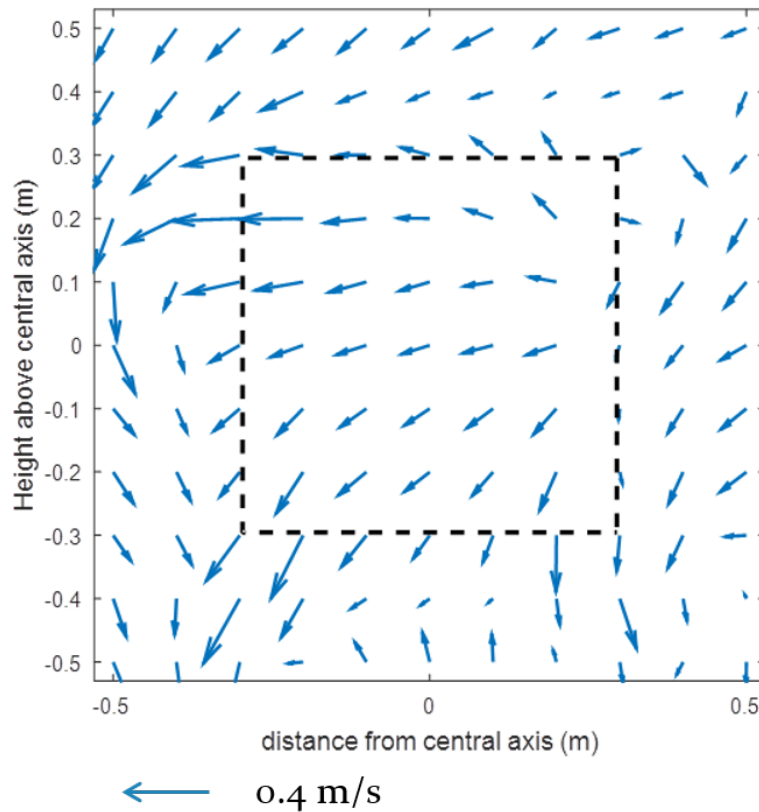


Figure 3.24: Wind speed distribution in plane perpendicular to main direction of air flow at 1 m from the outlet with 4 mm honeycomb and 320 μm screen

The study of the average lateral wind speed in a plane perpendicular to the main flow direction, confirmed the effect of honeycombs on lateral wind speeds. Figure 3.25 shows the flow field measured at 1 m from the outlet when only a screen is used. A rotational movement ('swirl') is clearly visible. It should be noted that the maximum lateral wind speed is 1.2 m/s and the maximum longitudinal wind speed measured in this plane is 4.5 m/s. Whereas in Figure 3.24, the lateral wind speed is probably more impacted by the environment, the flow structure seen in Figure 3.25, is clearly influenced by the wind produced by the fans.

3.7. CONCLUSION FOR THE MEASUREMENTS DONE ON THE SMALL WIND GENERATION SYSTEM

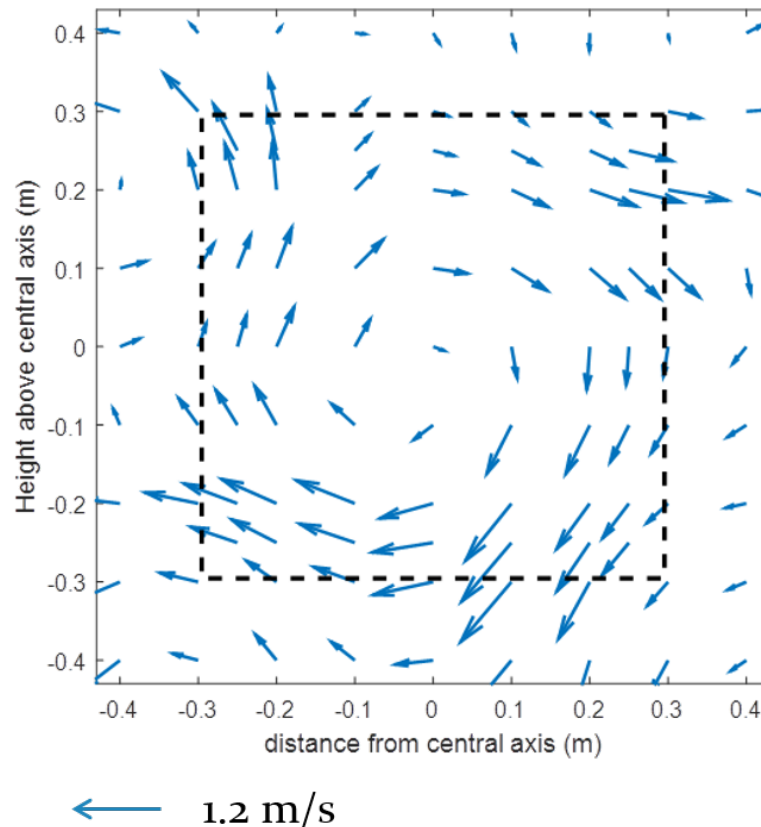


Figure 3.25: Distribution of wind speed in plane perpendicular to main direction of flow at 1 m from the outlet with no honeycomb and a $73 \mu\text{m}$ screen

3.7 Conclusion for the measurements done on the small wind generation system

Results of initial measurements of the output of a wind generation system designed for testing scaled models of floating offshore wind turbines have been presented. These have shown a linear relationship between fan speed and eventual wind speed, indicating good control over the generated conditions. The impact of various combinations of flow straighteners on generated turbulence levels has been reported. Comparisons between measured turbulence levels and predictions based on closed wind tunnel theory demonstrate relatively good agreement when examining the impact of adding a straightener to a system which already has a different straightener present (i.e. adding a honeycomb to a system with a screen or vice versa). The theory used here slightly under predicts the longitudinal turbulence reduction of honeycombs and over predicts the one of screens. According to the experiments, honeycombs reduce the longitudinal turbulence to a similar level as screens, though theory predicts the impact of screens to be more significant for this component.

Theory predicted that the $73 \mu\text{m}$ screen would reduce turbulence the most and the $500 \mu\text{m}$ screen would reduce turbulence the least, which was confirmed through experiments. For the honeycombs however, though theory predicted differences in turbu-

3.7. CONCLUSION FOR THE MEASUREMENTS DONE ON THE SMALL WIND GENERATION SYSTEM

lence reduction, this was not confirmed through the experimental values.

The theory failed to predict the effect of a flow straightener used on its own, indicating that the theories are valid only when the initial level of turbulence is not too high.

It should also be noted that the theoretical values are calculated using values found in literature, which could be different using other sources. Both longitudinal and lateral turbulence were reduced to levels lower than required to model realistic conditions on the central axis of the flow. Concerning the spatial analysis, it is very important to note that in order to ensure a minimum area with constant wind speed, up to a third of the outlet width or height will not be usable. Only criteria for longitudinal wind speed and turbulence intensity were considered for evaluating the usable area. The experiments described in this chapter demonstrate the feasibility of good quality airflow produced in the laboratory when the cross section is kept constant.

The next chapter compares these experimental results to CFD simulations.

Chapter 4

CFD simulation of wind generation in the laboratory

CFD simulations were carried out in OpenFOAM to develop a better understanding of how different design parameters would influence the quality of wind generated in the laboratory. The simulations can be grouped into 3 series:

- Simulations of the small scale experimental set-up presented in Chapter 3. This enabled comparison between simulation and experimental results and an investigation into the influence of the chosen turbulence model.
- Simulations investigating the influence of the geometry of concentric cones inside a large angle diffuser designed to expand air flow from a 1m to 3m diameter outlet.
- Simulations investigating the influence of the geometry of a long inner cone inside a diffuser cone.

The results from the 2nd and 3rd series of simulations were used to inform the geometry of flow diffusers examined experimentally (reported in Chapter 5).

4.1 General set-up of all the CFD simulations

All the simulations were done in OpenFOAM with the steady state solver for incompressible fluids `simpleFoam`. This solver uses the semi-implicit method for pressure-linked equations (SIMPLE) algorithm, used also by Zhu et al. (2014); Vadlamani (2010); Kurnia et al. (2014), developed for steady-state air flow (see also Section 2.5.5). For the outlet boundary conditions, the `inletOutlet` boundary condition of OpenFOAM was used. This boundary condition can be used when it is not certain whether the outlet lets fluid out or in. The discretization scheme for the divergence of non-advective terms was bounded Gauss upwind, which is a first order upwind discretization scheme.

4.2 Wind field produced by the small wind generator determined through CFD simulation

The simulation aimed to reproduce the flow conditions measured for one of the cases studied in Chapter 3. The case chosen was one where the average longitudinal wind speed at 250 mm behind the outlet on the central axis of the flow was 8.31 m/s and the flow straighteners were the 1000 μm meshed screen and the 12 mm honeycomb (for further details refer to Section 3.1). It was chosen to be used for comparison to CFD simulations, because it was one of the cases where the wind speed had been measured on and at various positions outside of the central axis for 4 different distances behind the outlet.

4.2. WIND FIELD PRODUCED BY THE SMALL WIND GENERATOR DETERMINED THROUGH CFD SIMULATION

4.2.1 Set up of the CFD simulations

The simulation reproduced the air flow coming out of the ducting system and blowing into the room.

The inlet for the CFD simulation corresponded to the outlet of the duct used in the experiments described in Chapter 3, the inlet wind speed used was 8.4 m/s and uniform all across the outlet. An attempt had been made to apply a non-uniform wind speed across the inlet, with lower wind speeds towards the edges of the outlet, but this approach was not chosen, as it gave results further away from the measured results.

Figure 4.1 shows the size of the domain used for the simulation. Figure 4.2 shows a slice of the domain and the boundary conditions applied at its limits.

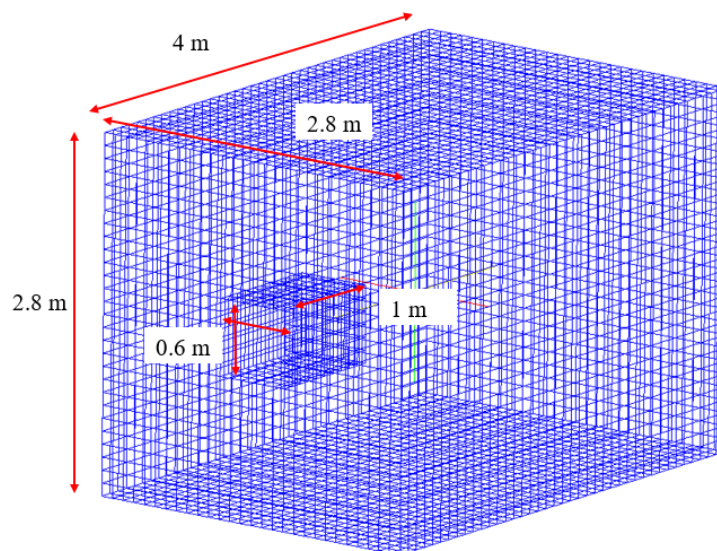


Figure 4.1: Size of simulation domain

4.2. WIND FIELD PRODUCED BY THE SMALL WIND GENERATOR DETERMINED THROUGH CFD SIMULATION

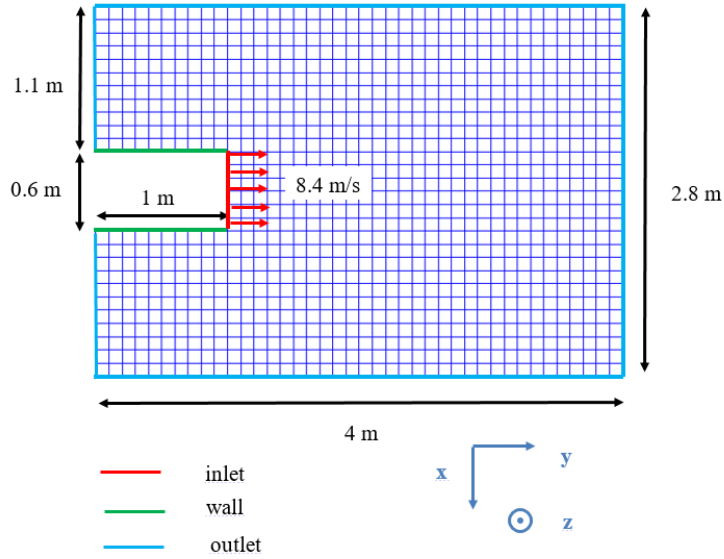


Figure 4.2: Boundary conditions

The following turbulence models were tested: Spalart Allmaras, $k - \varepsilon$, $k - \omega$, $k - \omega$ SST, RNG $k - \varepsilon$, realizable $k - \varepsilon$ and non linear $k - \varepsilon$ Shih. For information on the drawbacks and the advantages of the various turbulence models, see Section 2.5.1.

All $k - \varepsilon$ turbulence models solve one transport equation for k , the turbulence kinetic energy and one for ε , the turbulent dissipation or rate of dissipation of the turbulence kinetic energy per unit mass from which the kinematic eddy viscosity ν_T is determined to obtain the Reynolds stress tensor τ_{ij} of the RANS equation. At the beginning of the CFD simulation initial k and ε , and k and ε at the boundaries need to be given.

Both $k - \omega$ turbulence models solve one transport equation for k , the turbulence kinetic energy and one for ω , the specific dissipation rate from which the kinematic eddy viscosity ν_T is determined to obtain the Reynolds stress tensor τ_{ij} of the RANS equation. At the beginning of the CFD simulation initial k and ω , and k and ω at the boundaries need to be given.

To calculate the initial boundary conditions, u'_x , u'_y and u'_z were assumed to be all equal to 5 % of the speed (following a recommendation in Maric et al. (2014)). Initial k was therefore calculated using Equation 4.1.

$$k = \frac{3}{2} \left(\frac{5}{100} U \right)^2 \quad (4.1)$$

with U the average initial velocity.

To calculate the initial and boundary conditions of ε , Equation 4.2 was used.

$$\varepsilon = \frac{C_\mu^{0.75} k^{1.5}}{l} \quad (4.2)$$

4.2. WIND FIELD PRODUCED BY THE SMALL WIND GENERATOR DETERMINED THROUGH CFD SIMULATION

with C_μ the constant of the $k - \varepsilon$ model equal to 0.09 and l the turbulence length scale, assumed to be 5 % of study domain length. To calculate initial ω , Equation 4.3 was used (taken from Maric et al. (2014))

$$\omega = \frac{\sqrt{k}}{C_\mu^{1/4} L} \quad (4.3)$$

with L the domain length. This gave the following values for k , ε and ω (Table 4.1).

Table 4.1: Initial boundary condition values

k	0.2646
ε	0.745
ω	31.31

For the Spalart-Allmaras model, one equation solves one transport equation for the kinematic viscosity. The initial value taken for $\tilde{\nu}$ was 0.14 (OpenFOAM, 2015a). At the walls, $\tilde{\nu}$ was taken to be 0.

4.2.2 Mesh convergence study

It was found that a separate mesh converge study was required for each turbulence model.

The mesh consisted of cube-shaped cells only. All cubes had the same size. The lengths of the sides of the cubes can be seen in Table 4.2, which also shows the corresponding amount of cells for each cell size.

Table 4.2: Cell sizes and amount of cells used for mesh convergence study

cell size (cm)	10	5	3.33	2.5	2	1.67	1.4	1.25	1.11
amount of cells	31,000	248,000	837,000	1,984,000	3,875,000	6,696,000	10,633,000	15,872,000	22,599,000

The mesh convergence study was conducted for the average longitudinal wind speed and the turbulence kinetic energy at a distance of 25 cm from the outlet and $x=-30$ cm, the point at which the largest changes in wind speed were found.

For each turbulence model, the mesh for which convergence occurred was determined. Figure 4.3 shows how average wind speed changed with grid size for the different turbulence models used. It can be seen, that whereas the $k - \varepsilon$, the $k - \omega$, the $k - \omega$ SST model and the Spalart Allmaras model came close to a final value for a small number of cells, the RNG $k - \varepsilon$, realizable $k - \varepsilon$ and non linear $k - \varepsilon$ Shih turbulence models needed a smaller mesh to get close to a final value. All models reached a final value for the average longitudinal wind speed relatively close to each other, except for the Spalart Allmaras model.

4.2. WIND FIELD PRODUCED BY THE SMALL WIND GENERATOR DETERMINED THROUGH CFD SIMULATION

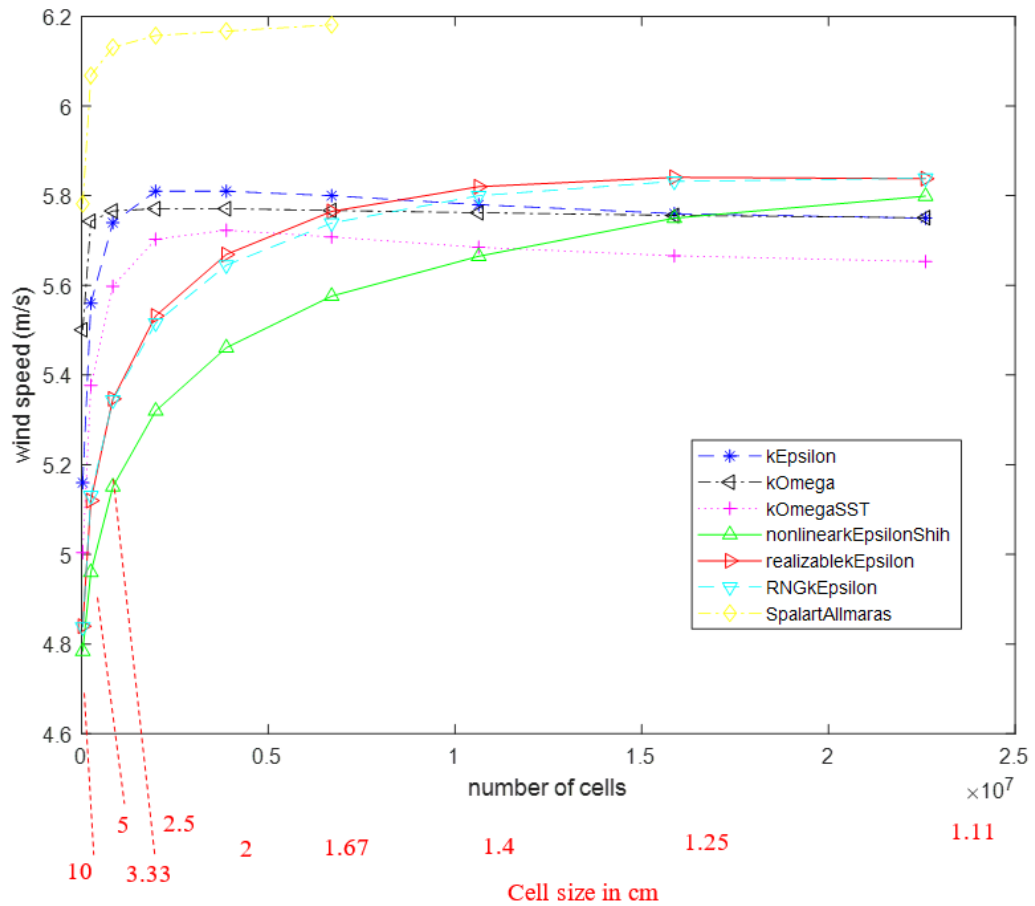


Figure 4.3: Evolution of wind speed with number of cells 0.3 m from the central axis of the flow and at mid height of the outlet

Figure 4.4 shows how turbulence kinetic energy changed with grid size for the different turbulence models used. Again, the $k-\epsilon$, the $k-\omega$ and the $k-\omega$ SST model came close to a final for a relatively coarse grid, whereas the RNG $k-\epsilon$, realizable $k-\epsilon$ and non linear $k-\epsilon$ Shih turbulence models needed a finer grid. It can be noted that the final values for all turbulence models were relatively close to each other when compared to the final value of the $k-\omega$ model.

4.2. WIND FIELD PRODUCED BY THE SMALL WIND GENERATOR DETERMINED THROUGH CFD SIMULATION

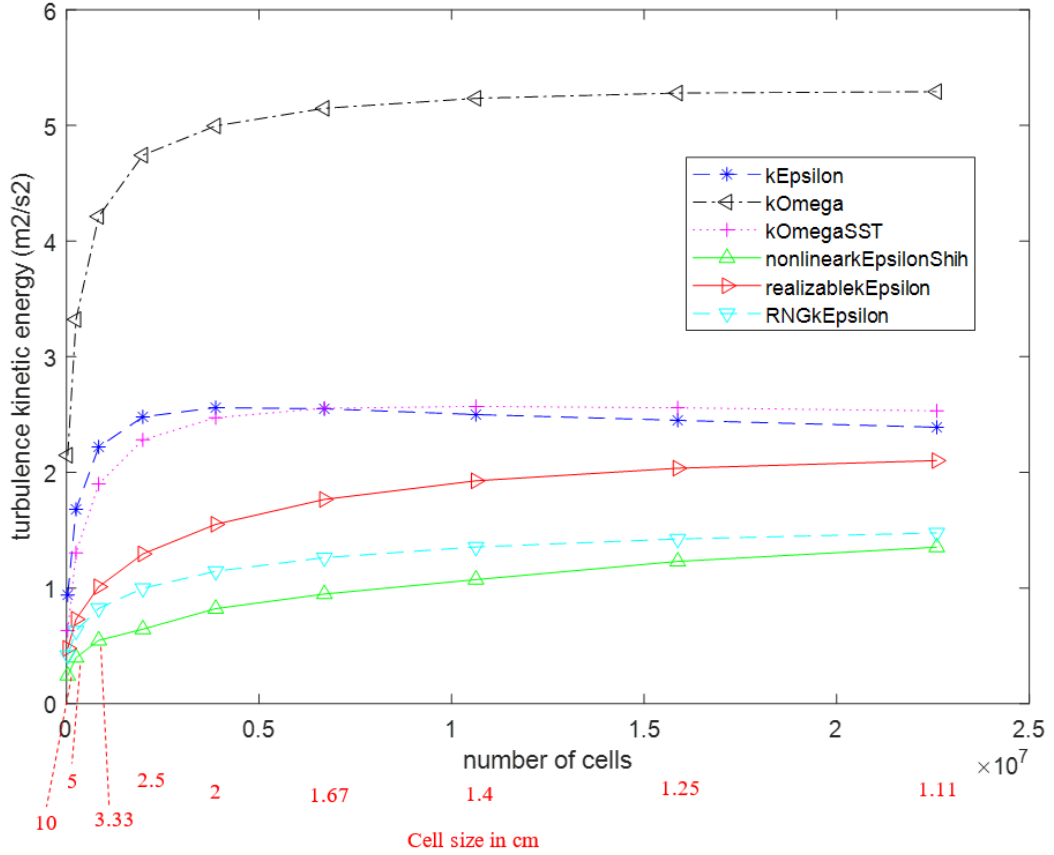


Figure 4.4: Evolution of turbulence kinetic energy with number of cells 0.3 m from the central axis of the flow and at mid height of the outlet

As the final values for the turbulence models were different from one another, it was decided not to apply a criterion for convergence that would involve reaching 95 or 99 % of the final value, or similar, as for turbulence models where the final value is higher, this would create an 'easier' convergence criterion than for those where the final value was relatively low. Instead, it was decided to look at the rate of change of wind speed and turbulence kinetic energy with the number of cells, which basically is the slope of the graphs in Figure 4.3 and Figure 4.4. The rate of change was calculated according to Equation 4.4.

$$\text{rate of change}_v = \left| \frac{V_{\text{current mesh}} - V_{\text{previous mesh}}}{\text{number of cells}_{\text{current mesh}} - \text{number of cells}_{\text{previous mesh}}} \right| \quad (4.4)$$

Equation 4.5 is the same for the turbulence kinetic energy.

$$\text{rate of change}_k = \left| \frac{V_{\text{current mesh}} - V_{\text{previous mesh}}}{\text{number of cells}_{\text{current mesh}} - \text{number of cells}_{\text{previous mesh}}} \right| \quad (4.5)$$

Visually, it was decided that the value for both the average longitudinal wind speed and the turbulence kinetic energy was still evolving for finest mesh for the non linear

4.2. WIND FIELD PRODUCED BY THE SMALL WIND GENERATOR DETERMINED THROUGH CFD SIMULATION

$k - \varepsilon$ Shih model, whereas all other turbulence models seemed to stabilize. Figure 4.5 shows the evolution of the rate of change of the wind speed with the number of cells. It can be seen that the rate of change is highest for the non linear $k - \varepsilon$ Shih model. For the $k - \varepsilon$, the $k - \omega$, the $k - \omega$ SST and Spalart Allmaras turbulence models, when the rate of change drops below $6e^{-9}m/s/number\ of\ cells$, it remains fairly constant with the increase of the number of cells. This value excludes the non linear $k - \varepsilon$ Shih model from convergence. This value was therefore chosen for all remaining turbulence models as a cut-off rate of change which determined the cell size at which the model had converged. Figure 4.6 shows the evolution of the rate of change of the turbulence kinetic energy with the number of cells. A cut-off value for the rate of change of $1e^{-8}m^2/s^2/number\ of\ cells$, corresponds for all turbulence models to grid size, where the final value seems to stabilize visually. It was therefore decided the apply this value as a cut-off rate of change for all turbulence models to determine the mesh size for which they had converged.

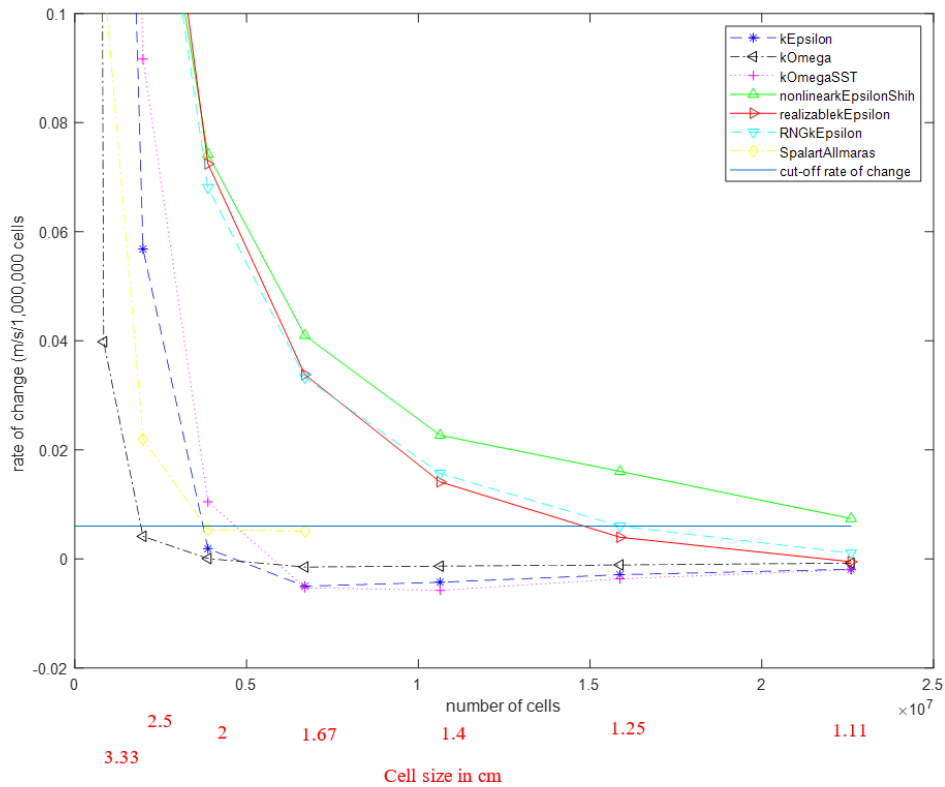


Figure 4.5: Rate of change of the wind speed with the number of cells for various turbulence models

4.2. WIND FIELD PRODUCED BY THE SMALL WIND GENERATOR DETERMINED THROUGH CFD SIMULATION

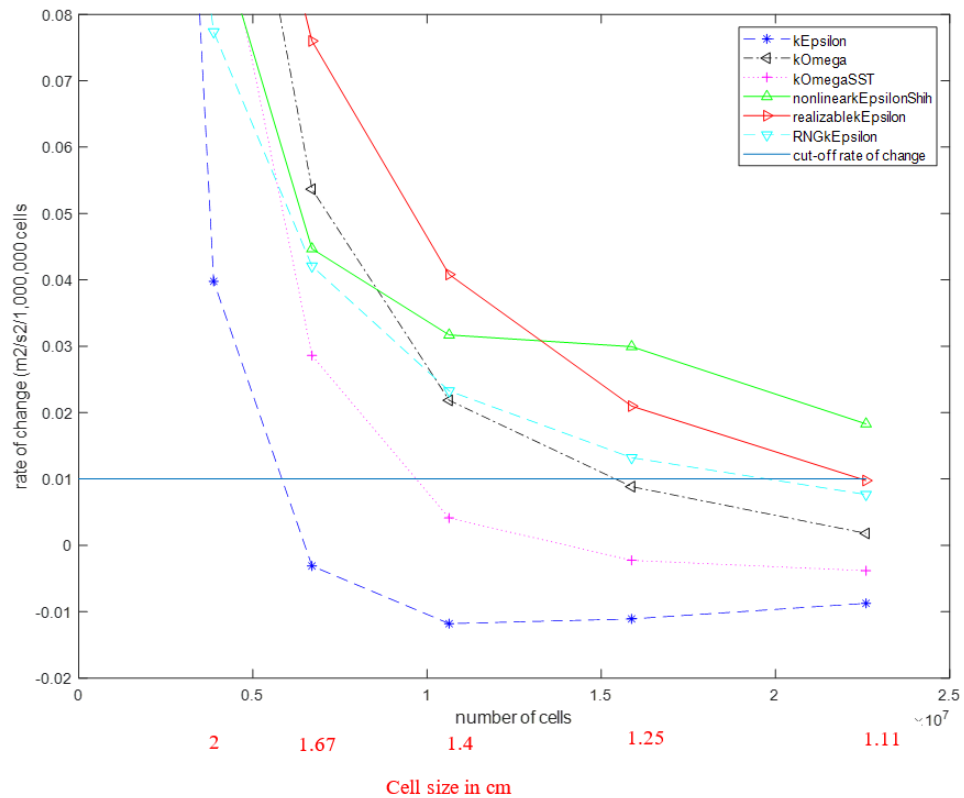


Figure 4.6: Rate of change of the turbulence kinetic energy with the number of cells for various turbulence models

It was noted that for certain turbulence models, the wind speed converged rather quickly, when the turbulence kinetic energy has not converged yet. Generating a finer mesh than the finest mentioned in Table 4.2 was not possible, due to the limitations of the memory of the computer used. Table 4.3 shows the mesh size for which each turbulence models was deemed converged, either by looking at the average longitudinal wind speed or the turbulence kinetic energy. When the turbulence kinetic energy was converged, the wind speed had always converged, so the grid size for the turbulence kinetic energy was chosen as the one for which convergence occurred.

Table 4.3: Cell sizes for which the various turbulence models were considered converged

	Mesh convergence wind speed	Mesh convergence turbulence kinetic energy
$k - \varepsilon$	2 cm	1.67 cm
$k - \omega$	2.5 cm	1.25 cm
$k - \omega_{SST}$	1.67 cm	1.4 cm
non linear $k - \varepsilon$ Shih	not converged	not converged
realizable $k - \varepsilon$	1.25 cm	1.11 cm
RNG $k - \varepsilon$	1.11 cm	1.11 cm
Spalart Allmaras	2 cm	

4.2.3 Comparison between calculated data and experimental values

In this section the simulation results using the different turbulence models are compared with the experimental data of the experiments described in Chapter 3.

Figure 4.7 shows the average longitudinal wind speed calculated by the various turbulence models and the experimental data at four different distances from the outlet away from the outlet. Measurements are compared along a horizontal profile at the mid-height of the outlet. Figure 4.8 shows the turbulence kinetic energy calculated by the various turbulence models and the experimental data at four different distances from the outlet and at mid-height of the outlet.

4.2.4 Difference between CFD results and experimental data

To compare the various models to the experimental data, relative difference between the calculated wind speed and the measured wind speed was calculated according to equation 4.6:

$$D = 100 \frac{A}{V_{meas}} = 100 \frac{|V_{cal} - V_{meas}|}{V_{meas}} \quad (4.6)$$

with D the relative difference in %, A the unsigned absolute difference, V_{meas} the measured wind speed and V_{cal} the calculated wind speed.

Figure 4.9 shows the relative differences for each model. Those differences were averaged over 4 different distances from the outlet for various distances from the central axis of the flow. It can be seen that close to the central axis of the flow, all of the models calculate the correct wind speed. The difference between the models can be seen when moving away from the centre of the flow to the area where the moving air meets the still air (near the edge of the outlet), where turbulence is the highest.

4.2. WIND FIELD PRODUCED BY THE SMALL WIND GENERATOR DETERMINED THROUGH CFD SIMULATION

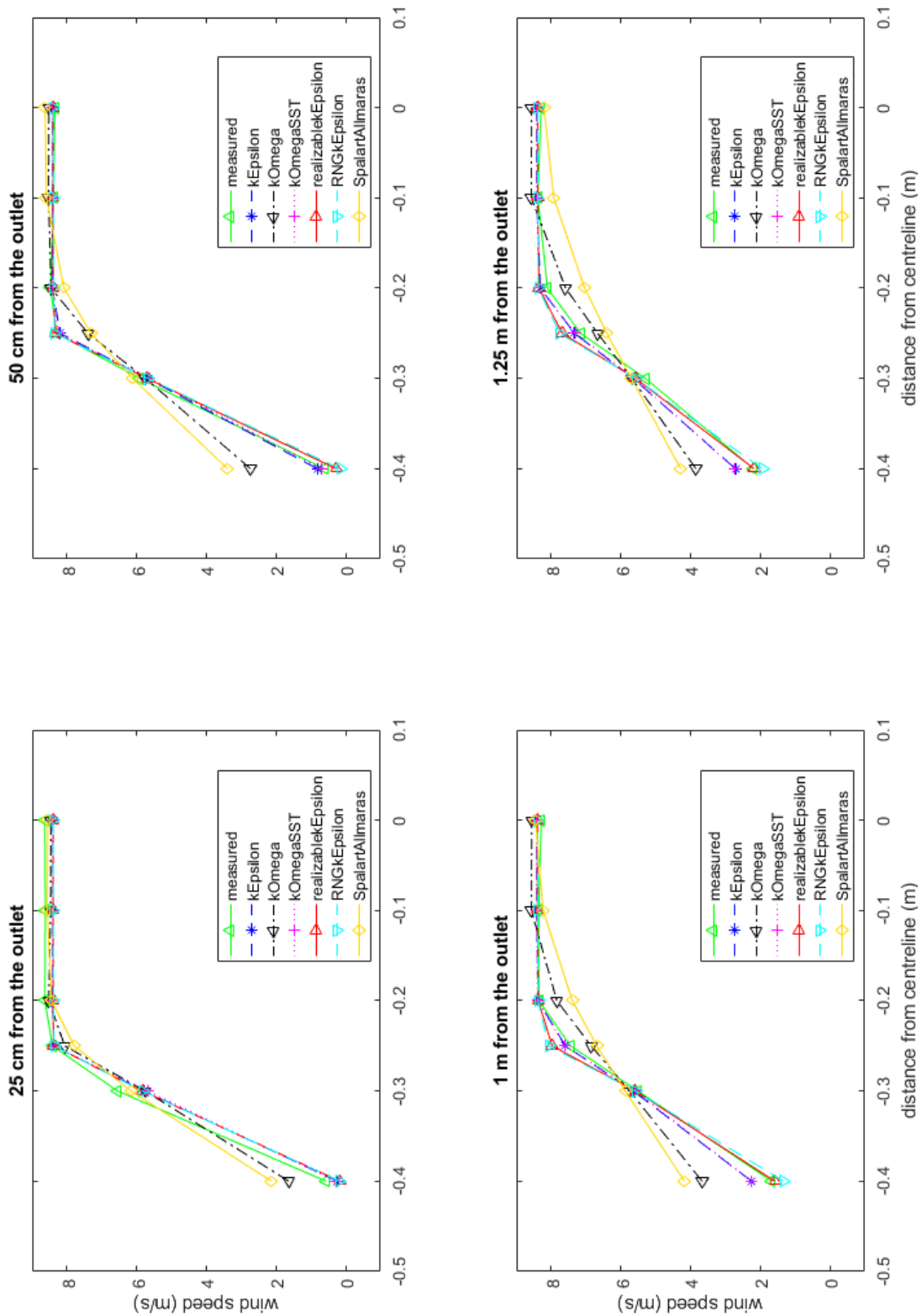


Figure 4.7: Comparison between the average wind speed calculated by various turbulence models and the experimental data at four different distances from the outlet and at mid-height of the outlet

4.2. WIND FIELD PRODUCED BY THE SMALL WIND GENERATOR DETERMINED THROUGH CFD SIMULATION

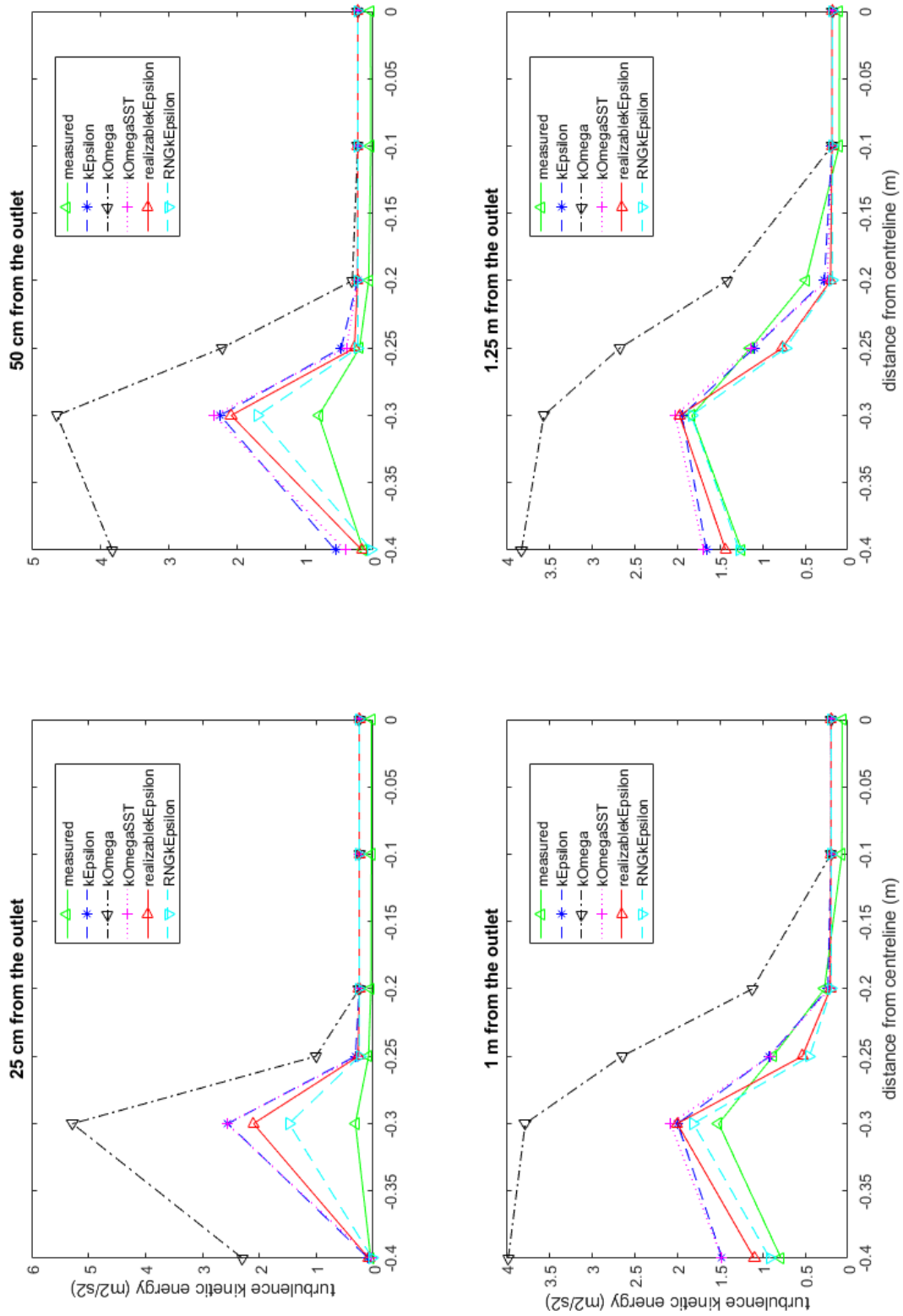


Figure 4.8: Comparison between the turbulence kinetic energy calculated by various turbulence models and the experimental data at four different distances from the outlet and at mid-height of the outlet

4.2. WIND FIELD PRODUCED BY THE SMALL WIND GENERATOR DETERMINED THROUGH CFD SIMULATION

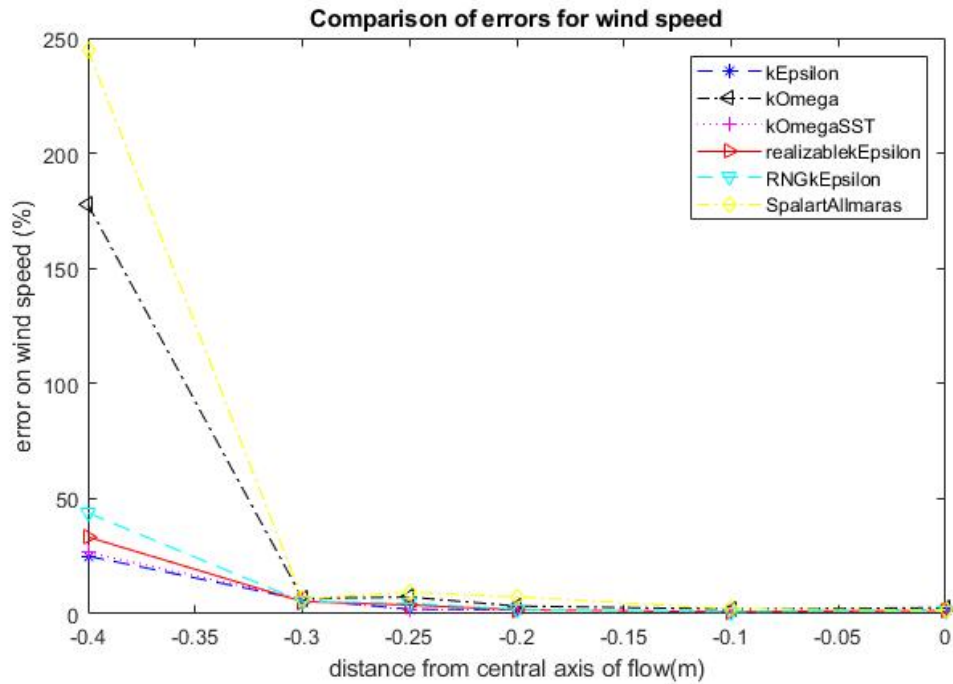


Figure 4.9: Comparison of relative differences between wind speed calculated by various turbulence models and measured data at various distances from the central axis of the flow

The errors at position $x=-0.4$ were inflated due to the fact that the wind speeds at this location were rather small and therefore even small relative differences showed up as a high percentage. Figure 4.10 is a zoom of Figure 4.9.

4.2. WIND FIELD PRODUCED BY THE SMALL WIND GENERATOR DETERMINED THROUGH CFD SIMULATION

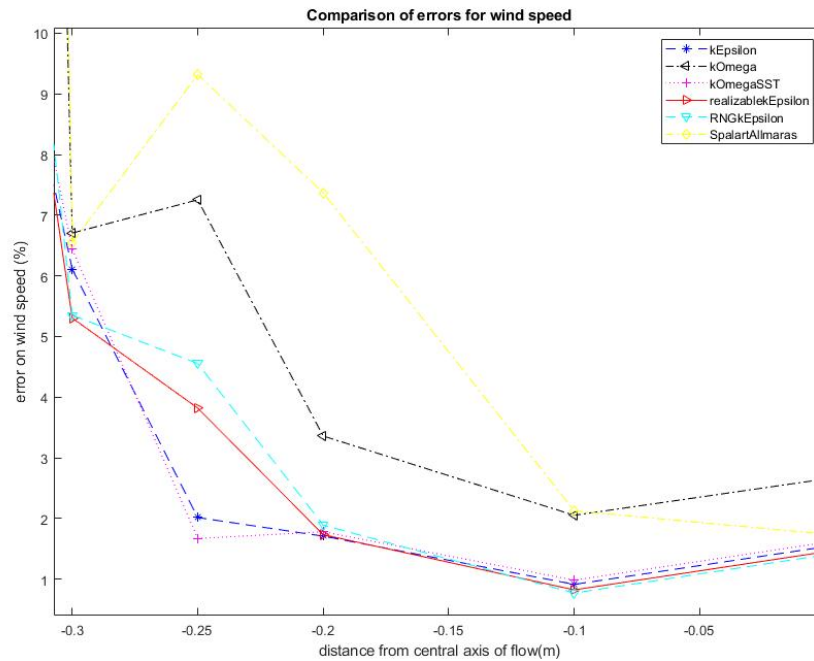


Figure 4.10: Comparison of relative differences between wind speed calculated by various turbulence models and measured data at various distances from the central axis of the flow - zoom of Figure 4.9

Figure 4.11 shows the relative difference of the turbulence kinetic energy calculated with a given turbulence model when compared to the turbulence kinetic energy calculated directly from the measured data. The difference for the $k - \omega$ model is not shown here as it reached values higher than 2000 %, which would have made the visual examination of the differences of the other turbulence models difficult.

4.2. WIND FIELD PRODUCED BY THE SMALL WIND GENERATOR DETERMINED THROUGH CFD SIMULATION

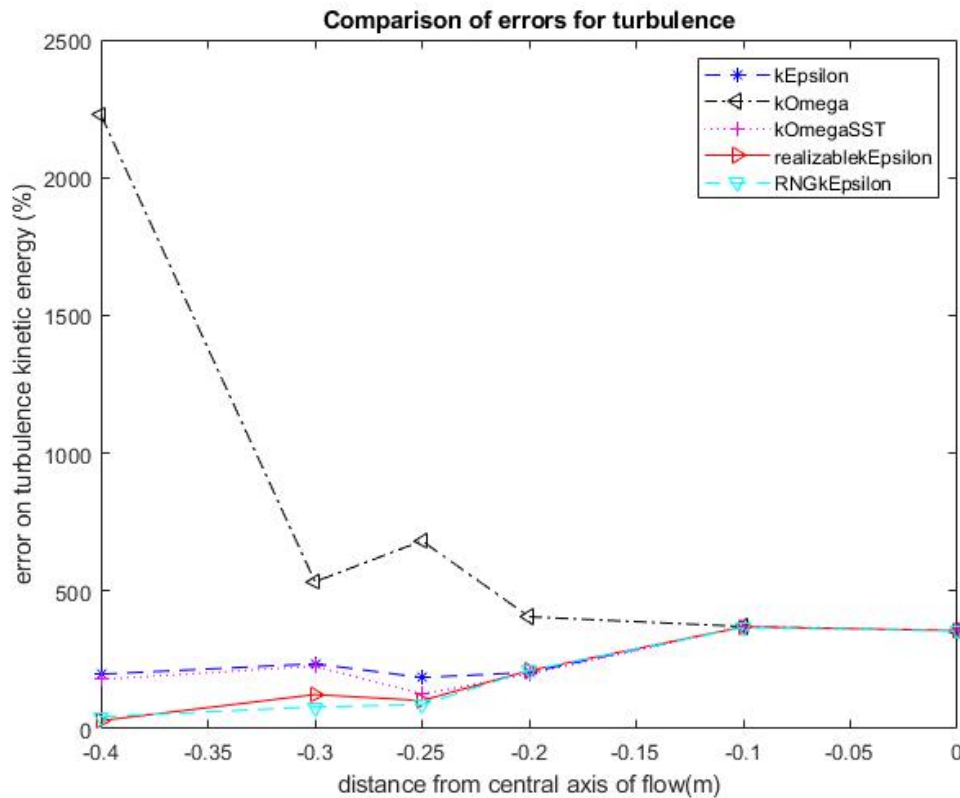


Figure 4.11: Comparison of relative differences between the turbulence kinetic energy of various turbulence models and measured data at various distances from the central axis of the flow

Concerning the overall average relative difference for all the measuring points, Figure 4.12 shows it for the wind speed and Figure 4.13 shows this for the turbulence kinetic energy. For comparison, the anemometer used for the measurements has a route mean square error lower than 1.5 % at a wind speed of 12 m/s.

4.2. WIND FIELD PRODUCED BY THE SMALL WIND GENERATOR DETERMINED THROUGH CFD SIMULATION

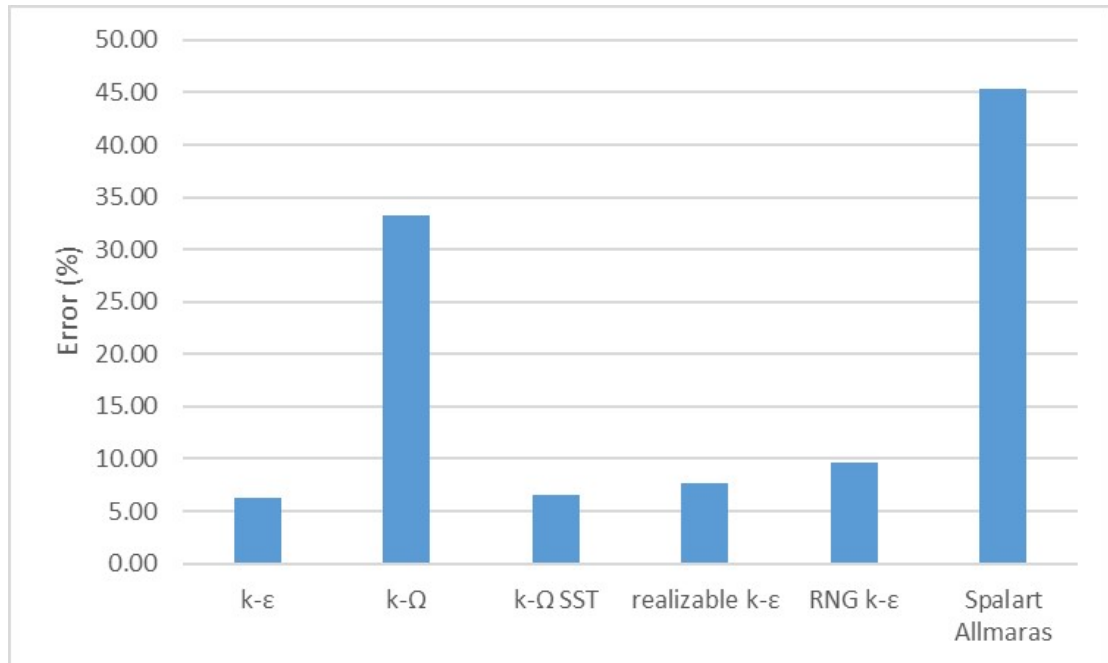


Figure 4.12: Average relative difference for each turbulence model for the wind speed

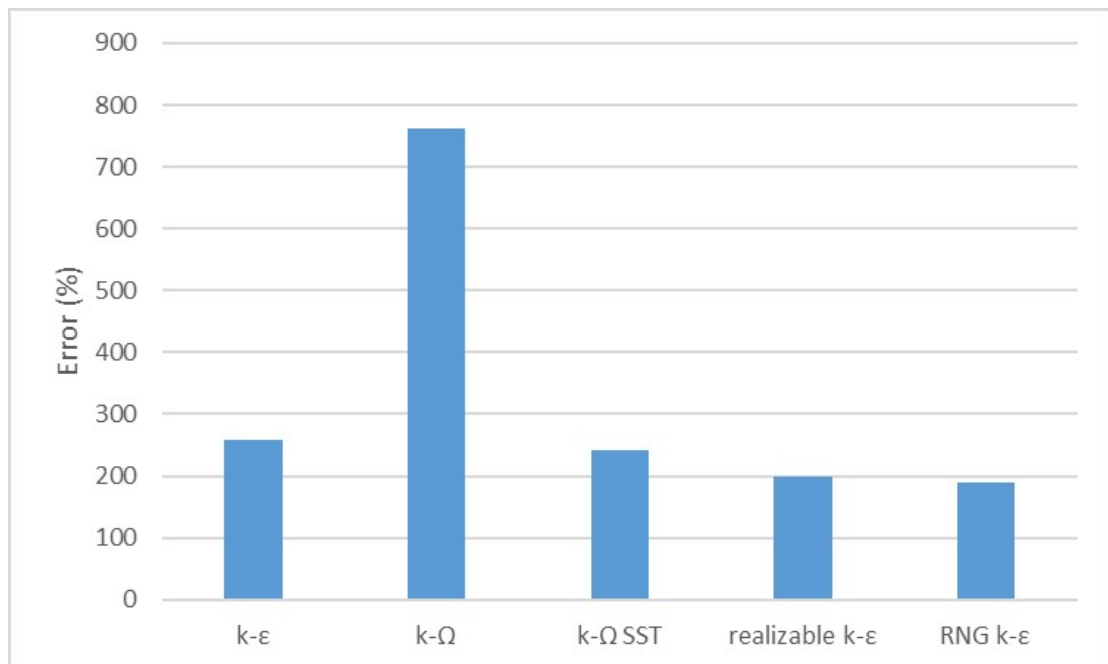


Figure 4.13: Average relative difference for each turbulence model for the turbulence kinetic energy

The standard $k - \epsilon$ model and the $k - \omega$ SST model compare best with the experimental measurements. The realizable $k - \epsilon$ model and the RNG $k - \epsilon$ model follow closely behind. The worst results are obtained for the Spalart Allmaras model, the only 1

4.2. WIND FIELD PRODUCED BY THE SMALL WIND GENERATOR DETERMINED THROUGH CFD SIMULATION

equation model tested. According to Wilcox (2006), it is good at predicting the free shear flow spreading rate of a mixing layer, which could have been promising for this particular calculation. It is calibrated for airfoil and wing applications, for which results are satisfactory. However it cannot predict jet spreading rates accurately, which shows its limitations. The standard $k - \omega$ model is also clearly not good for calculating correct wind speed in this kind of set-up, that is, air coming out of a duct and blowing into an open area.

Concerning the calculation of the turbulence kinetic energy, none of the models is very close to the measured levels of turbulence. The Realizable $k - \epsilon$ and RNG $k - \epsilon$ are the best. Again, the standard $k - \omega$ model gives results very different from reality.

Choice of the best turbulence model could be done depending on whether one wants to make sure the calculated wind speed is correct, or whether one wants to have accurate information on the turbulence levels as well. For this particular situation, the realizable $k - \epsilon$ model is the best compromise, but the standard $k - \epsilon$, $k - \omega$ SST and RNG $k - \epsilon$ also give good results.

In terms of efficiency, the standard $k - \epsilon$ and the $k - \omega$ SST model are better than the realizable $k - \epsilon$ and the RNG $k - \epsilon$ model. Table 4.4 show the number of cells and the execution time necessary to get the result of a converged mesh for those 4 turbulence models. The $k - \epsilon$ model converges the fastest, the $k - \omega$ SST model is a little slower, and the realizable $k - \epsilon$ and the RNG $k - \epsilon$ model require a high amount of cells and therefore execution time to deliver calculations for a converged mesh.

Table 4.4: Comparison of number of cells and execution time necessary for a converged mesh for the best turbulence models

turbulence model	number of cells	execution time (s)
$k - \epsilon$	6,696,000	17,360.6
$k - \omega$ SST	10,633,000	24,482
Realizable $k - \epsilon$	22,599,000	110,769
RNG $k - \epsilon$	22,599,000	65,376.5

This study shows that choosing the wrong turbulence model for a given situation can give results that are far off from data that is obtained from experiments. For free-shear flows such as the one studied here, for fast results, the standard $k - \epsilon$ and the $k - \omega$ SST model are recommended, if a high level of accuracy for the prediction of the level of turbulence is not required. For accurate results on turbulence level predictions, and in the case of the possibility to have a high number of cells, the realizable $k - \epsilon$ and the RNG $k - \epsilon$ model are recommended. For a flow involving walls and free shear flow, these recommendations do not necessarily apply anymore. For wall-bounded flow which also involves free-shear flow, the $k - \omega$ SST model is promising. For a flow with strong adverse pressure gradients the realizable $k - \epsilon$ is recommended. As the cases studied in the subsequent paragraphs both involve walls and strong adverse pressure gradients, those 2 models were selected to be used.

4.3 CFD simulation of the wind field produced by the large wind generator using a diffuser cone

In the development of the full scale wind generator tested in Chapter 5, the use of a diffuser to expand the generated wind field from a 1 m diameter to a 3 m diameter outlet was investigated. This diffuser cone was needed to go from a duct, which transported the wind from the fans close to the location where the wind is needed, to the needed outlet size to blow wind on a wind turbine which was 2.5 m wide. The diffuser can be seen in Figure 4.14 (same as Figure 5.2). Further details can be found in Chapter 5.

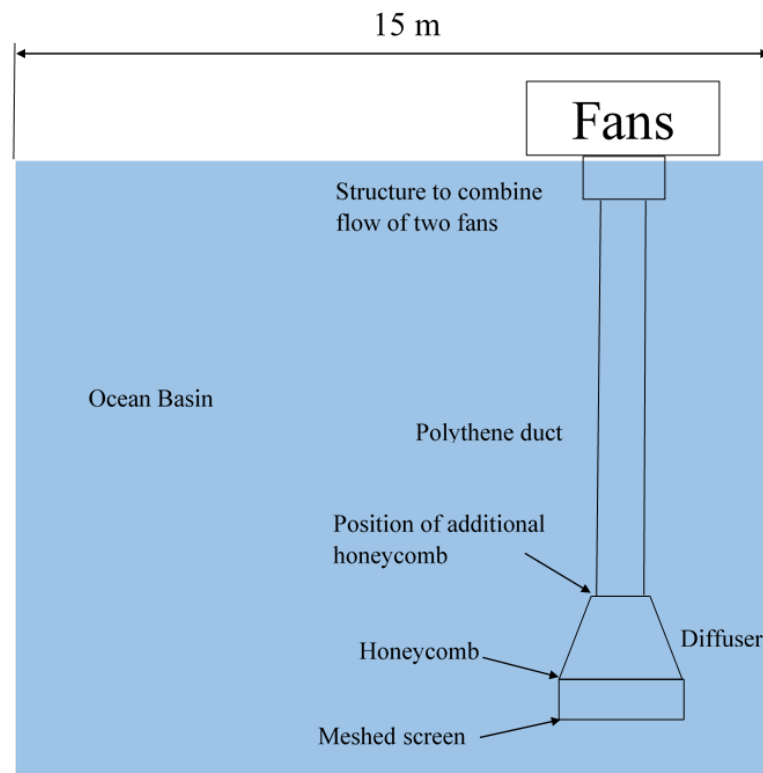


Figure 4.14: Schematic of the general set up of the large wind generation system

As was seen in Section 2.4.6, flow separation occurs for diffusers with opening angles greater than 15° , creating asymmetric flow. In Figure 4.15, the position of the diffuser cone used here was plotted on a stability map, which confirms that it is in a region of high instability.

4.3. CFD SIMULATION OF THE WIND FIELD PRODUCED BY THE LARGE WIND GENERATOR USING A DIFFUSER CONE

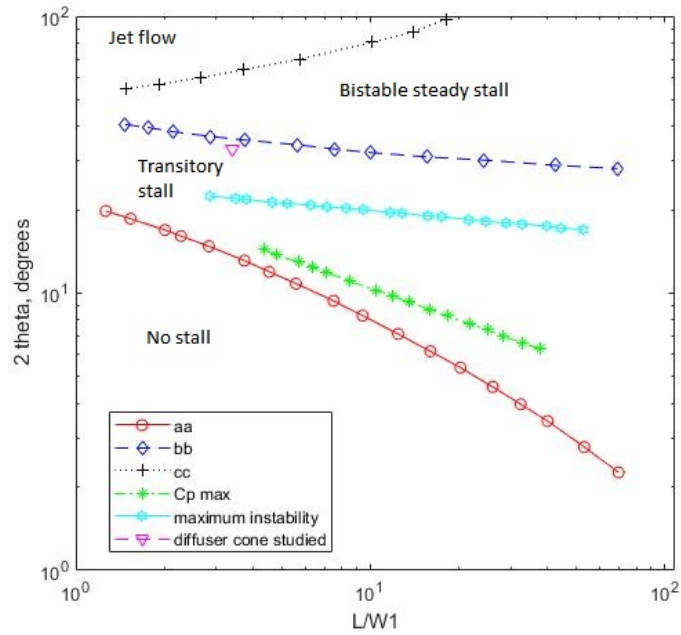


Figure 4.15: Stability map (see Figure 2.63 from Section 2.4.6 adapted from White (2016)) with position of diffuser cone studied. 2θ is the opening angle of the diffuser. $\frac{L}{W_1}$ is the ratio between the length and the inlet width of the diffuser.

It was chosen to adapt the solution proposed in Section 2.4.6.4, which would correspond to inner cones for the diffuser used here. CFD simulations were carried out to investigate the use of internal cones within the diffuser on the generated wind field. These simulations are presented here. Both the impact of the number of cones and their size are considered.

4.3.1 Wind generator with 3 m diameter circular outlet and 1 m diameter inlet

Figure 4.16 shows a slice of the basic domain used for the CFD simulation. The domain was axisymmetric, that is, made up of cylinders and one cone shape. It starts with a 2 m long duct that has a 1 m diameter. It is then followed by a truncated cone, with a total length of 3.4 m, that has a diameter of 1 m at the beginning and a diameter of 3 m at the end. The opening angle of this cone is 33° . This cone is followed by a cylindrical domain representing the space behind the end of the outlet. This domain is a 10 m long cylinder, with a 10 m diameter. This was the basic domain.

4.3. CFD SIMULATION OF THE WIND FIELD PRODUCED BY THE LARGE WIND GENERATOR USING A DIFFUSER CONE

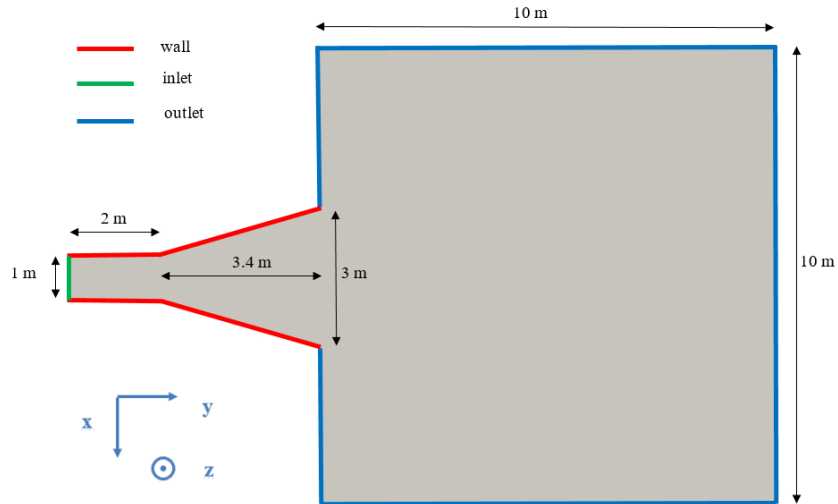


Figure 4.16: Slice across basic domain parallel to the main direction of the air flow. Inner cones are not represented

The initial boundary condition for the wind speed at the inlet was a uniform speed of 18 m/s, value determined thanks to the flow rate calculated by using the wind speed measured during the experiments described in Section 5.1. The initial value used for k was 1.2 and for ω was 3.6 for the $k - \omega$ SST model. The initial value used for k was 1.2 and for ε was 4.4 for the realisable $k - \varepsilon$ model. Those values were used both for the 2D and the 3D Study.

It was determined that the first layer thickness near the walls needed to be 7 mm to obtain y^+ values between 30 and 300, necessary to apply a wall function for the calculations near the walls of the domain (see Section 2.5.3 of Chapter 2). To get acceptable values for y^+ from the inlet to the outlet, a value that fitted both was determined. Table 4.5 shows the values calculated for the first layer thickness using Equation 2.67 at the inlet and the outlet. According to this table, the common value for the whole wall, should be higher than 5 mm and lower than 6 mm. In the CFD calculations, however, the first layer thickness value that gave y^+ values between 30 and 300 on all of the walls was 7 mm.

Table 4.5: First layer thickness determined through calculation for obtaining y^+ values compatible with the law of the wall

	Wind speed (m/s)	typical size (m)	first layer thickness (in m) determined to get	
			$y^+=30$	$y^+=300$
Values at inlet	18	1	0.0006	0.0059
Values at outlet	2	3	0.0049	0.0494

3 layers were used to transition from the first layer thickness to the cell size of the domain, using a growth rate of 1.2. The average cell size went from 10 cm to 1 cm for the 2D mesh convergence study. For structures on the inside of the diffuser, such as

4.3. CFD SIMULATION OF THE WIND FIELD PRODUCED BY THE LARGE WIND GENERATOR USING A DIFFUSER CONE

inner cones and dividing walls, the size of the elements was reduced to 1 cm.

4.3.1.1 2D Mesh convergence study

An initial 2D Mesh convergence study was done. In this 2D mesh convergence study, the cross section of this domain was used, using only one cell in the third direction, with a thickness corresponding to the average cell size.

The 2D Mesh was studied using 2 different turbulence models, found to be promising for indoor air flow in Section 4.2: $k - \omega$ -SST and realizable $k - \epsilon$. Table 4.6 shows the average cell sizes used and the corresponding number of cells.

Table 4.6: Number of cells generated for average cell size

average cell size (cm)	10	9	8	7	6	5	4	3	2	1
number of cells	23,028	28,116	35,550	46,827	63,828	92,078	144,779	253,868	566,528	2,248,136

To be able to compare wind fields generated for the various mesh sizes, the wind speed at 130 mm from the end of the outlet was looked at (which is also the location at which the wind speed was measured at in various test campaigns).

Figure 4.17 and Figure 4.18 show this wind speed for various mesh sizes calculated using the $k - \omega$ -SST model. It can be seen in Figure 4.17 that for mesh sizes 4 cm to 10 cm, the profile shape is fairly similar, with an asymmetric distribution. For mesh size 3 cm, the flow is fairly symmetric, with wind speeds similar to the ones for the previous meshes. For mesh size 2 cm, the structure changes completely, which becomes worse for 1 cm.

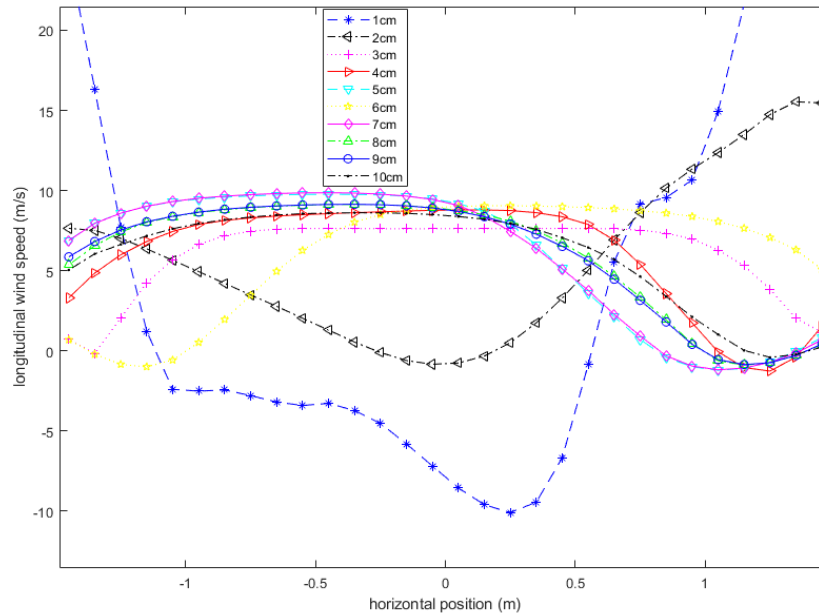


Figure 4.17: Wind speed calculated at 130 mm from the end of the outlet using the $k - \omega$ -SST model for various mesh sizes

4.3. CFD SIMULATION OF THE WIND FIELD PRODUCED BY THE LARGE WIND GENERATOR USING A DIFFUSER CONE

It was therefore decided that the mesh sizes smaller or equal to 3 cm should not be considered in the mesh convergence study, as they seem due to dispersive error (Anderson, 1995) (and are also not confirmed by the experimental data). When looking at the remaining mesh sizes (Figure 4.18), for some sizes, the results hardly differ. The mesh sizes 5 cm and 7 cm nearly overlap. The mesh sizes 9 cm, 8 cm and 6 cm are also very close. For mesh size 6 cm, the high wind speed is on the opposite side as the one for all other the other wind speeds, but by making a symmetry across the y axis of the graph, its similarity to the mesh sizes 9 cm and 8 cm can be seen. As the set up for the CFD simulation is perfectly symmetric, it is expected that the side on which the high wind speeds are is chosen randomly, so taking a symmetry across the vertical axis to see resemblance with other mesh sizes is acceptable. The wind profile for the mesh size 4 cm is quite different from all other mesh sizes between 5 and 9 cm. 5 cm is therefore the smallest mesh size which does not display erratic behaviour.

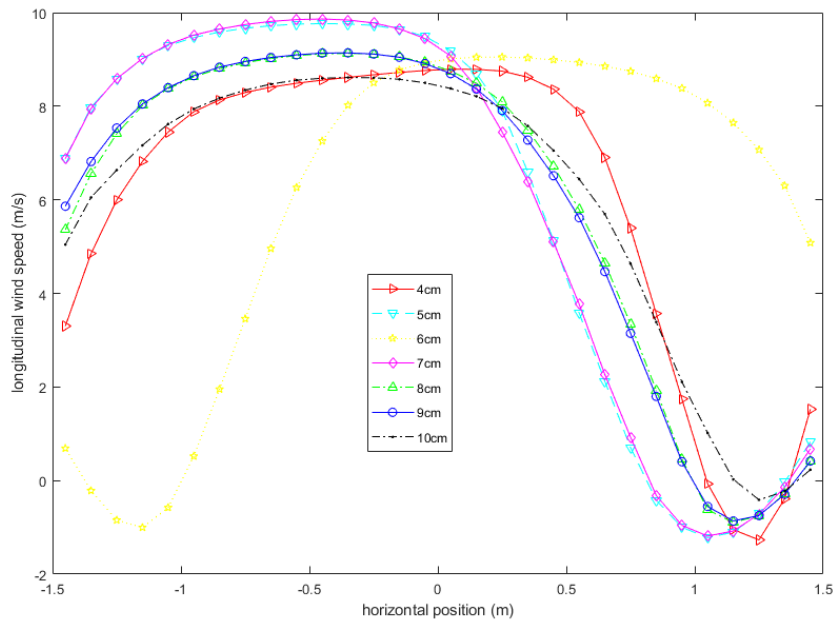


Figure 4.18: Wind speed calculated at 130 mm from the end of the outlet using the $k - \omega$ -SST model for the most relevant mesh sizes

The standard deviation of the wind field at this location was also calculated. Figure 4.19 shows the standard deviation for mesh sizes 10 cm to 4 cm (number of cells going from 23,028 to 144,779). Though the stabilization is not perfect, the value does not seem to evolve much beyond 5 cm.

4.3. CFD SIMULATION OF THE WIND FIELD PRODUCED BY THE LARGE WIND GENERATOR USING A DIFFUSER CONE

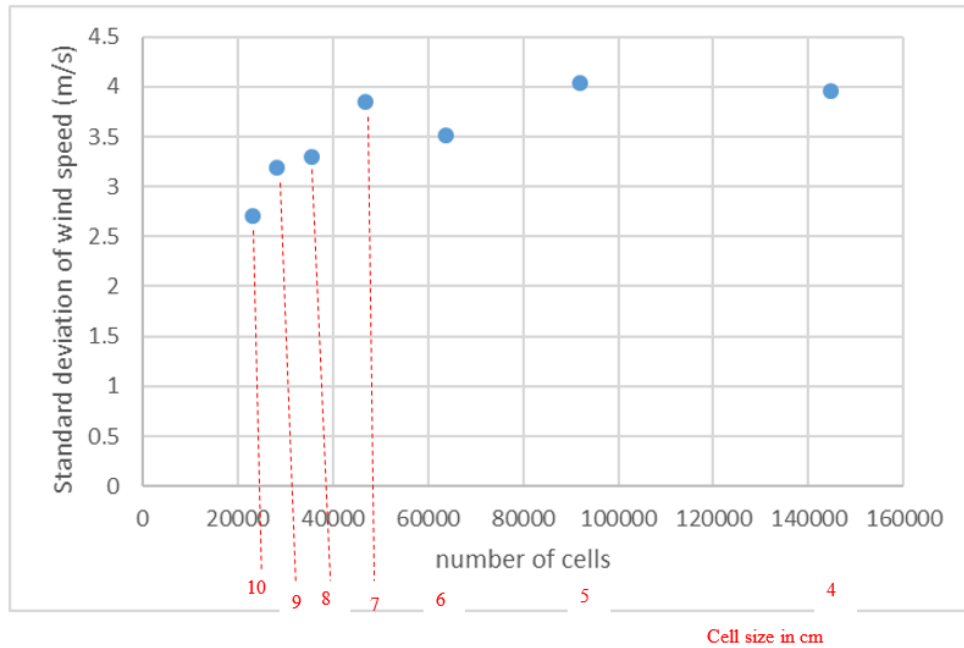


Figure 4.19: Standard deviation of wind speed calculated at 130 mm from the end of the outlet using the $k-\omega$ -SST model for the most relevant mesh sizes

Figure 4.20 shows the wind speed calculated using the realizable $k-\varepsilon$ model at 130 mm from the end of the outlet for various mesh sizes. As was the case for the $k-\omega$ -SST model, mesh sizes 1 cm and 2 cm show a completely different wind profile from the rest of the mesh sizes. Those results are therefore attributed to the mesh becoming too small, as the results are neither confirmed through experimental nor through literature review.

4.3. CFD SIMULATION OF THE WIND FIELD PRODUCED BY THE LARGE WIND GENERATOR USING A DIFFUSER CONE

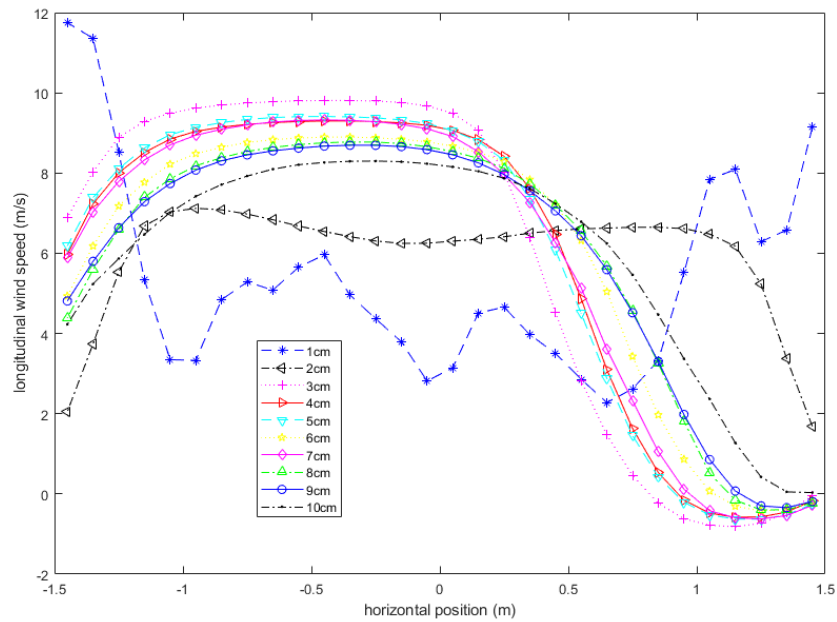


Figure 4.20: Wind speed calculated at 130 mm from the end of the outlet using the realizable $k - \epsilon$ model for various mesh sizes

Figure 4.21 shows only the mesh sizes giving similar shapes. It can be seen that for mesh sizes 4 cm, 5 cm and 7 cm the shape is nearly the same. The mesh size 6 cm is a little different. When going to mesh size 3 cm, there is a sudden jump.

4.3. CFD SIMULATION OF THE WIND FIELD PRODUCED BY THE LARGE WIND GENERATOR USING A DIFFUSER CONE

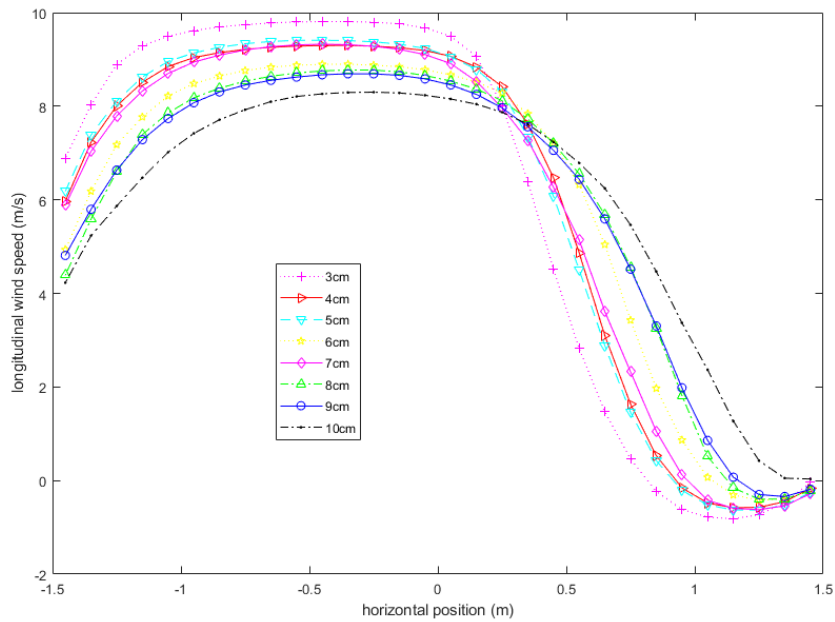


Figure 4.21: Wind speed calculated at 130 mm from the end of the outlet using the realizable $k - \epsilon$ model for most relevant mesh sizes

This jump can also be seen when looking at the standard deviation of the wind speed shown in Figure 4.22 for mesh sizes 3 cm to 10 cm (number of cells 23,028 to 253,868).

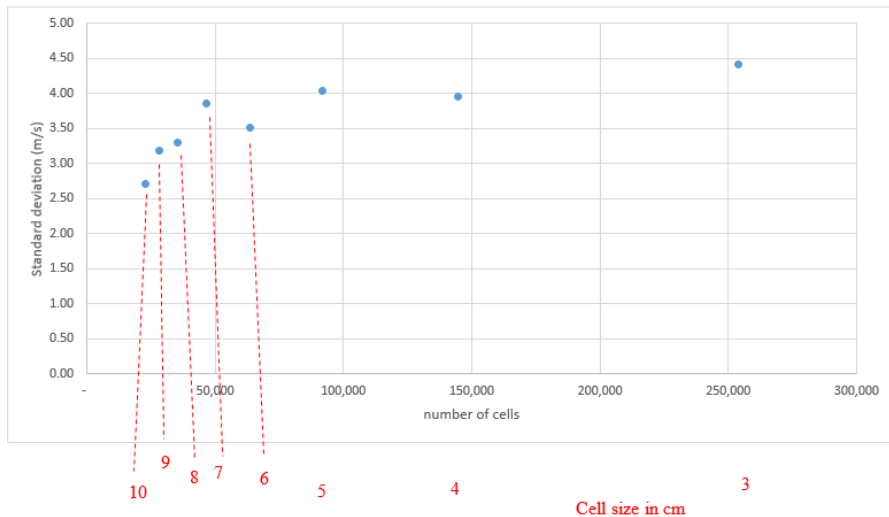


Figure 4.22: Standard deviation of wind speed calculated at 130 mm from the end of the outlet using the realizable $k - \epsilon$ model for the most relevant mesh sizes

The realizable $k - \epsilon$ model seems to work better when approaching smaller mesh sizes and shows more similarity between profiles calculated using the different mesh sizes

4.3. CFD SIMULATION OF THE WIND FIELD PRODUCED BY THE LARGE WIND GENERATOR USING A DIFFUSER CONE

for the smallest ones. For this model, it looks like 7 cm could be small enough, but to be certain, one would take 5 cm (due to the unexplained non-alignment of the results for 6 cm with the rest of the values).

What is reassuring is the similarity of the profiles between the two different models used, as can be seen in Figure 4.23.

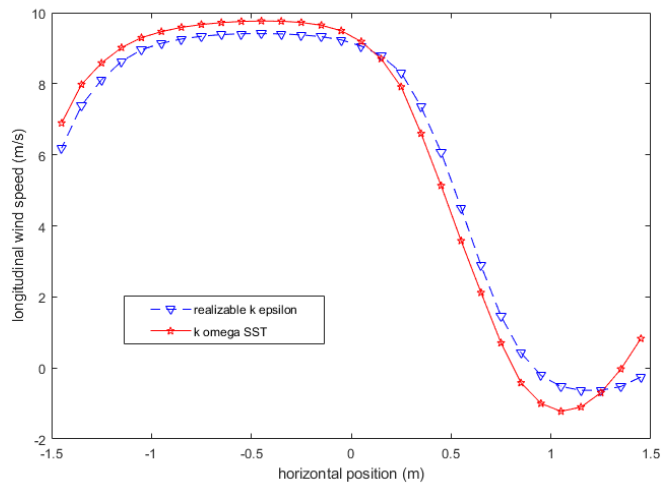


Figure 4.23: Comparison of the wind speed calculated for the realizable $k - \epsilon$ model and the wind speed calculated for the $k - \omega$ SST model when no concentric inner cones are used inside the diffuser

To check which model and mesh size are good for the case where diffuser cones are inside the structure, cases were set up for a diffuser containing three concentric cones inside, as shown in Figure 4.24.

4.3. CFD SIMULATION OF THE WIND FIELD PRODUCED BY THE LARGE WIND GENERATOR USING A DIFFUSER CONE

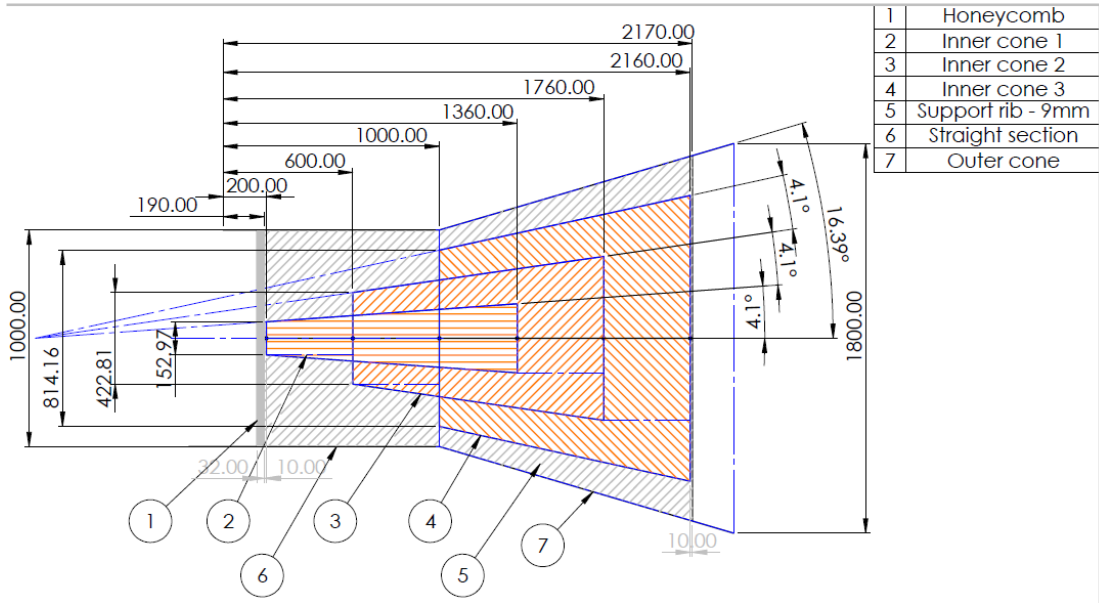


Figure 4.24: Dimensions of concentric cones

The mesh was refined at the inner structure to 1 cm regardless of the general mesh size. As can be seen on Figure 4.25, showing results for the $k - \omega$ -SST model, the behaviour was erratic again for the smallest mesh sizes (1, 2 and 3 cm).

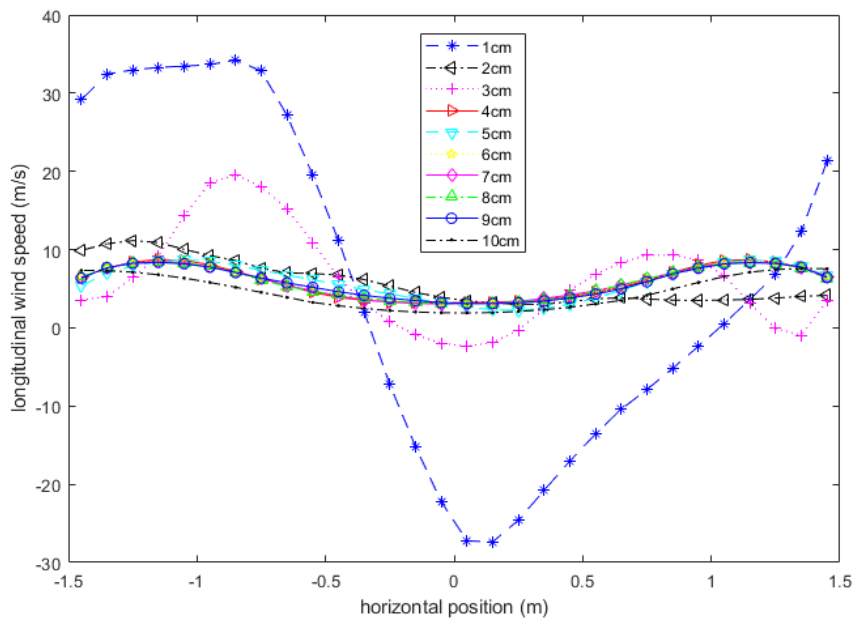


Figure 4.25: Wind speed calculated at 130 mm from the end of the outlet using the $k - \omega$ -SST model for various mesh sizes when diffuser cones are inside the outlet cone

When looking at mesh sizes 4 to 10 cm only (Figure 4.26), one can see that the profile

4.3. CFD SIMULATION OF THE WIND FIELD PRODUCED BY THE LARGE WIND GENERATOR USING A DIFFUSER CONE

shapes are almost the same for all sizes, except for 5 cm and 10 cm.

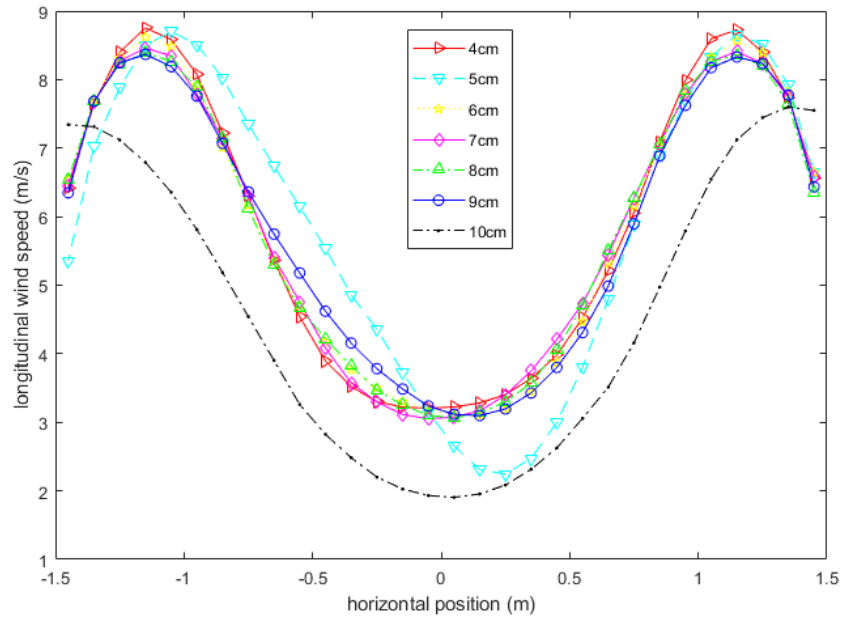


Figure 4.26: Wind speed calculated at 130 mm from the end of the outlet using the $k - \omega$ -SST model for most relevant mesh sizes when diffuser cones are inside the outlet cone

The fact that the general wind speed profile does not vary too much when going from one mesh size to another can also be seen through the calculation of the standard deviation of wind speed (Figure 4.27).

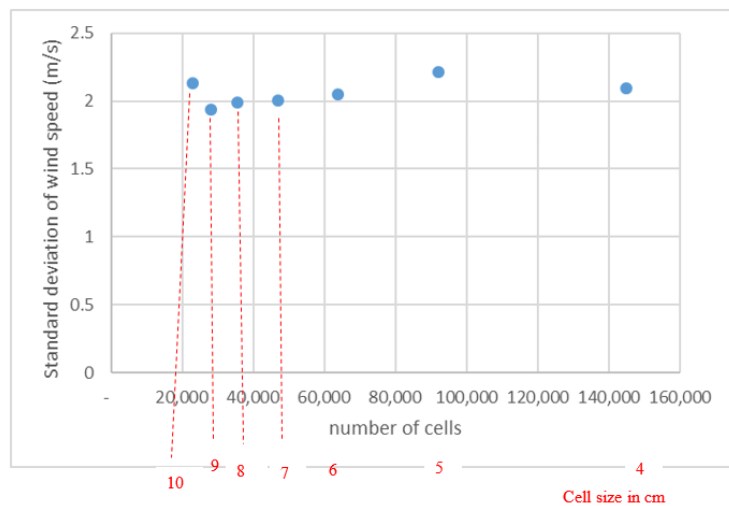


Figure 4.27: Standard deviation of wind speed varying with mesh size for the $k - \omega$ SST model

In Figure 4.28, it can be seen that for the realizable k-epsilon model, the behaviour is

4.3. CFD SIMULATION OF THE WIND FIELD PRODUCED BY THE LARGE WIND GENERATOR USING A DIFFUSER CONE

again erratic for the 3 smallest mesh sizes used.

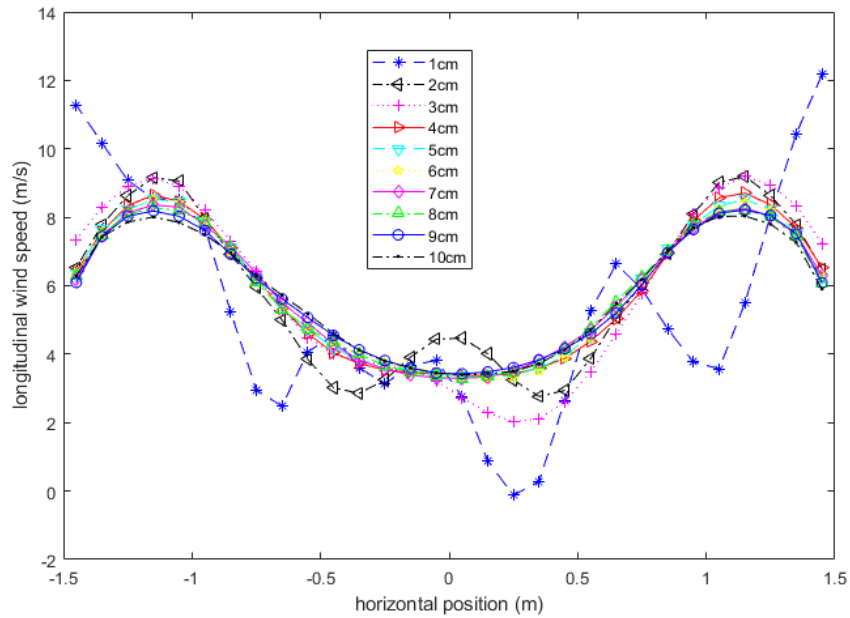


Figure 4.28: Wind speed calculated at 130 mm from the end of the outlet using the realizable $k - \epsilon$ model for various mesh sizes when diffuser cones are inside the outlet cone

When looking at Figure 4.29, one can see that all remaining profiles are fairly similar. This shows that the realizable $k - \epsilon$ model shows more stable solutions and is most likely the better choice again.

4.3. CFD SIMULATION OF THE WIND FIELD PRODUCED BY THE LARGE WIND GENERATOR USING A DIFFUSER CONE

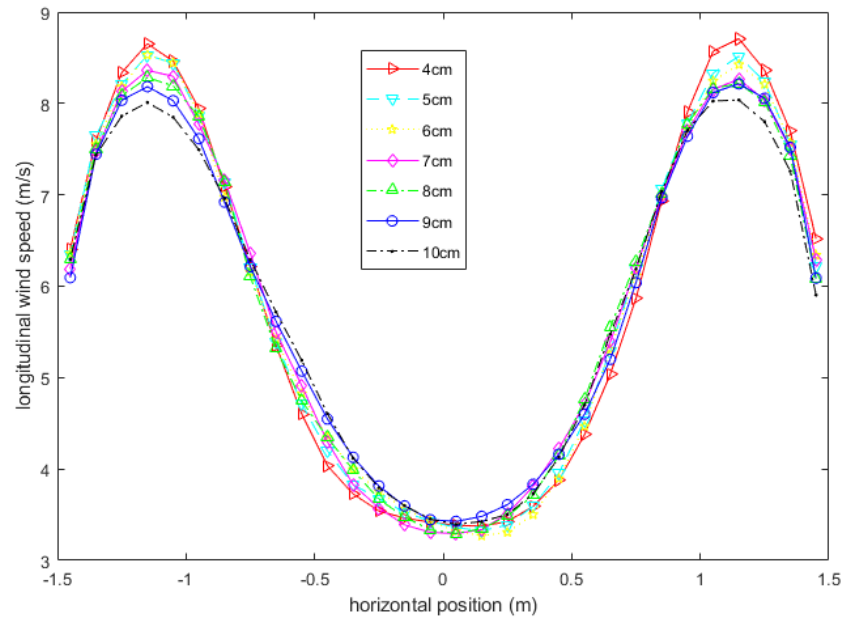


Figure 4.29: Wind speed calculated at 130 mm from the end of the outlet using the realizable $k - \epsilon$ model for various mesh sizes when diffuser cones are inside the outlet cone

Figure 4.30 presents the standard deviation of wind speed for various mesh sizes. It does not evolve significantly with mesh size. In particular between mesh size 6 cm and mesh size 5 cm, it is very stable.

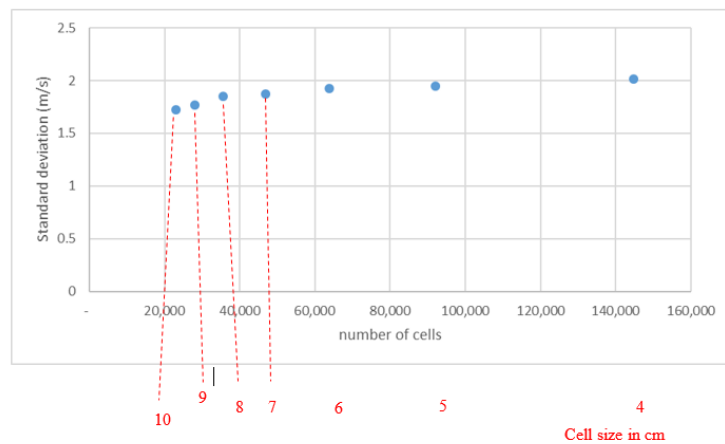


Figure 4.30: Standard deviation of wind speed varying with mesh size for the $k - \epsilon$ model

Reassuring is again the similarity between the two different turbulence models, as can be seen in Figure 4.31.

4.3. CFD SIMULATION OF THE WIND FIELD PRODUCED BY THE LARGE WIND GENERATOR USING A DIFFUSER CONE

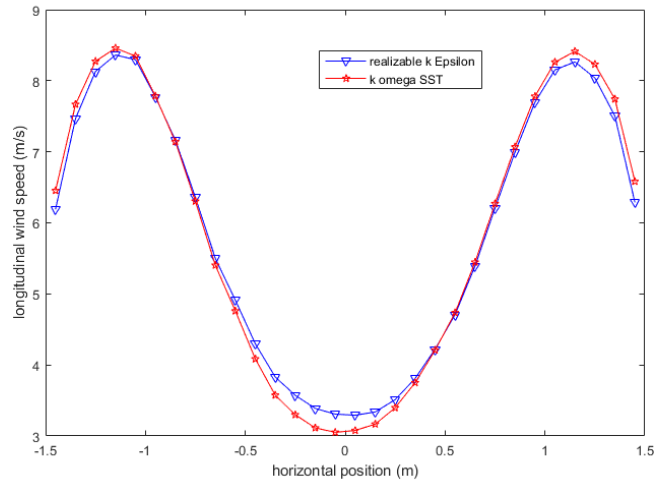


Figure 4.31: Comparison of the wind speed calculated for the realizable $k - \varepsilon$ model and the wind speed calculated for the $k - \omega$ SST model when 3 concentric inner cones are used inside the diffuser

4.3.1.2 3D Study

Based on the findings from the grid convergence study presented in Section 4.3.1.1, several variations of internal cones within the diffuser were studied using 3D simulations using the realisable $k - \varepsilon$ model. The number of elements for each case was about 8 million, with the exact number varying slightly with the exact geometry. Figure 4.24 shows the dimensions of a set of three inner cones.

Various combinations of these three inner cones were simulated (see Table 4.7).

Table 4.7: List of combinations of concentric cones tested

Combination of cones	Description of flow observed
all three cones	symmetric, high speed near wall of diffuser cone
2 outer cones	slight asymmetry, high speed near wall of diffuser cone
2 inner cones	symmetric, high speed near wall of diffuser cone
most outer cone only	slightly asymmetric, high flow towards the centre, backflow on the outer edge
most inner cone only	symmetric, high speed near wall of diffuser cone
central cone only	asymmetric flow separation
most inner and most outer cone	ring of high speed at a little distance from the outer wall

Figure 4.32 shows the flow distribution, when no concentric cones are present inside. The flow is severely asymmetric, with high speeds on one side of the diffuser and backflow on the opposite side. This set-up was studied experimentally and the results are presented in Chapter 5, Section 5.2.2.1.

4.3. CFD SIMULATION OF THE WIND FIELD PRODUCED BY THE LARGE WIND GENERATOR USING A DIFFUSER CONE



Figure 4.32: Wind speed in slice parallel to the main direction of the airflow

Figure 4.33 shows the flow distribution when all 3 concentric cones are present. The flow distribution is symmetric. There is high wind speed near the outer edge of the diffuser and backflow at the centre. This set up was studied experimentally and the results are presented in Section 5.2.2.2 of Chapter 5.



Figure 4.33: Wind speed

At the time when the structure of the inner cones had to be decided, not all simulations had conclusive results. It was therefore decided to build the 3 inner cones shown in Figure 4.24, though later some simulations had shown that the same or slightly better air flow distribution could have been obtained using only a set of two of these inner cones.

According to the CFD simulations, using the most inner and the most outer cone only could have been a better solution, as can be seen in Figure 4.34. Indeed, though the flow is slightly asymmetric, the large velocities are more central to the diffuser, instead of being situated on the outer edge.

4.3. CFD SIMULATION OF THE WIND FIELD PRODUCED BY THE LARGE WIND GENERATOR USING A DIFFUSER CONE



Figure 4.34: Wind speed in slice parallel to the main direction of air flow

When using the central cone only, the resulting flow was nearly as bad as when using no inner cones (Figure 4.35), as the flow was highly asymmetric.



Figure 4.35: Wind speed in slice parallel to the main direction of the air flow

What can be observed in general, is that the flow tends to be strongest in the zones where the passage is not narrow, that is, the flow tends to avoid the zones where there is a high number of cones. If there are more cones in the centre, the flow will tend to stick to the outer wall of the diffuser, whereas, if there are more cones near the outer wall, the flow will tend to pass mostly through the centre of the diffuser.

All flow distributions obtained for these simulations can be seen in Appendix C.1.

4.3.2 Wind generator with 3 m diameter circular outlet and long inner cone

In the third CFD study the impact of increasing the inlet diameter of the diffuser simulated in Section 4.3.1 was studied. This was motivated by both the results presented in Section 4.3.1, and the physical measurements presented in Section 5.2.2.2 giving an insufficiently consistent wind field across the outlet. In this study, all simulations are conducted with a single inner cone present which, unlike in Section 4.3.1, extended over the entire length of the diffuser. This change reflected lessons learnt from the

4.3. CFD SIMULATION OF THE WIND FIELD PRODUCED BY THE LARGE WIND GENERATOR USING A DIFFUSER CONE

experimental study presented in Section 5.2.2.2. The influence of the ratio of diffuser to inner cone diameter was also studied.

The following inlet diameters, and corresponding cone lengths, were studied (see Table 4.8). These lengths were chosen to reflect what could be physically obtained using the experimental diffuser.

Table 4.8: Combinations of cone lengths and inlet diameters

Inlet diameter (m)	Length (m)
1	3.4
1.4	2.72
1.8	2.04
2.2	1.36

The influence of subdivisions between the inner and the outer cone was also investigated in this numerical study. The following CFD simulations were therefore carried out (Table 4.9):

Table 4.9: Overview of the CFD simulations carried out for a diffuser cone using a long inner cone

Case number	Inlet diameter (m)	Cone length (m)	Inner cone diameter/outer cone diameter	special features of inner cone
1	1	3.4	$\frac{1}{3}$	/
2	1	3.4	$\frac{1}{2}$	/
3	1.4	2.72	$\frac{1}{3}$	/
4	1.8	2.04	$\frac{1}{3}$	/
5	2.2	1.36	$\frac{1}{3}$	/
6	1.8	2.04	$\frac{1}{2}$	4 subdivisions
7	1.8	2.04	$\frac{1}{2}$	6 subdivisions
8	1.8	3	$\frac{1}{2}$	8 subdivisions

The wind speed at the inlet was considered uniform (18 m/s for a 1 m diameter inlet, less for larger inlet diameters to conserve volume flow). The basic domain was as follows:

4.3. CFD SIMULATION OF THE WIND FIELD PRODUCED BY THE LARGE WIND GENERATOR USING A DIFFUSER CONE



Figure 4.37: Cross section parallel to the main direction of the flow for the diffuser with a 1 m inlet diameter and a long inner cone with a diameter measuring a 1/3 of the outer diffuser. No subdivisions were used

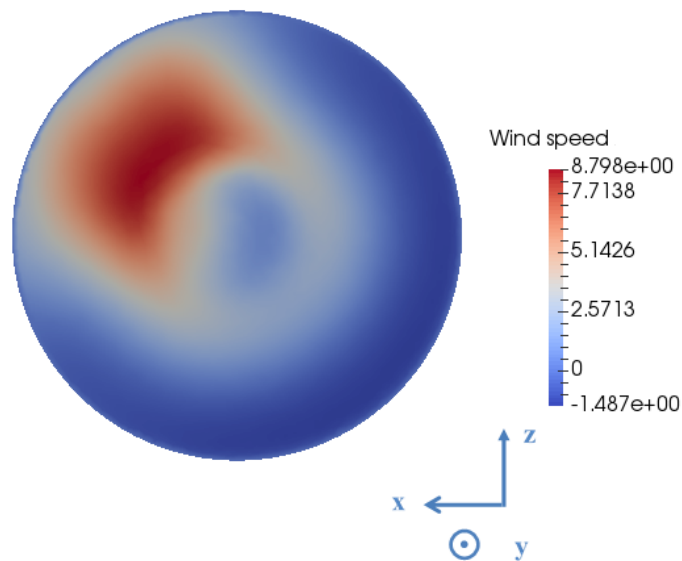


Figure 4.38: Cross section perpendicular to the main direction of the flow for the diffuser with a 1 m inlet diameter and a long inner cone with a diameter measuring a 1/3 of the outer diffuser. No subdivisions were used

Figure 4.39 shows the flow distribution for the diffuser with a 1.8 m inlet diameter and a long inner cone with a diameter measuring a 1/3 of the outer diffuser, using no subdivisions, in a plane parallel to the main direction of the flow. Figure 4.40 shows the flow distribution for the diffuser with a 1.8 m inlet diameter and a long inner cone with a diameter measuring a 1/3 of the outer diffuser, using no subdivisions, in a plane perpendicular to the main direction of the flow. This is clearly an improvement over the diffuser using 3 inner cones, as the highest wind speed is only 2.5 m/s and there is no more backflow.

4.3. CFD SIMULATION OF THE WIND FIELD PRODUCED BY THE LARGE WIND GENERATOR USING A DIFFUSER CONE



Figure 4.39: Cross section parallel to the main direction of the flow for the diffuser with a 1.8 m inlet diameter and a long inner cone with a diameter measuring a 1/3 of the outer diffuser. No subdivisions were used

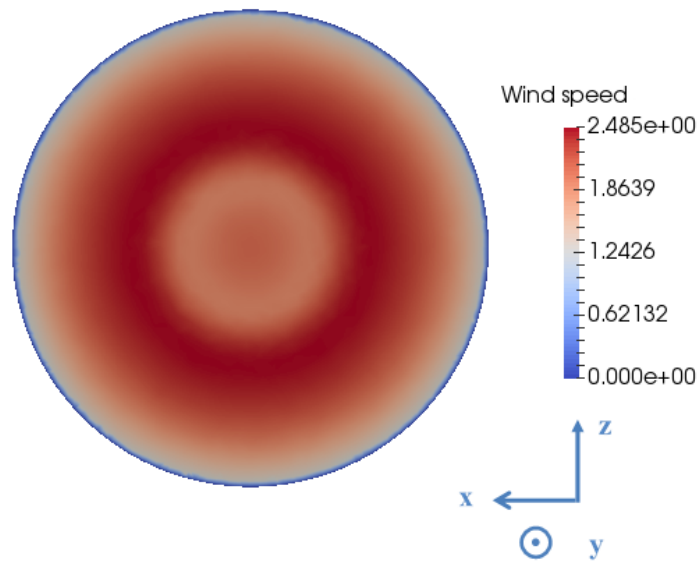


Figure 4.40: Cross section perpendicular to the main direction of the flow for the diffuser with a 1.8 m inlet diameter and a long inner cone with a diameter measuring a 1/3 of the outer diffuser. No subdivisions were used

Flow rate across the outlet was calculated, as well as standard deviation of the wind speed across the outlet were calculated to determine numerically the case which gave the most evenly distributed flow across the cross section of the diffuser outlet.

Table 4.10 compares the standard deviation for various diffuser inlet diameters. Without surprise, a larger inlet diameter results in a more even distribution of the wind speed across the diffuser outlet.

4.3. CFD SIMULATION OF THE WIND FIELD PRODUCED BY THE LARGE WIND GENERATOR USING A DIFFUSER CONE

Table 4.10: Comparison of standard deviation of wind speed across the outlet for various inlet diameters of the diffuser with a long inner cone that has a diameter 1/3 of the diameter of the diffuser and no subdivisions

Case number	Inlet diameter (m)	Inner cone diameter/outer cone diameter	Standard deviation (m/s)
1	1	$\frac{1}{3}$	2.81
3	1.4	$\frac{1}{3}$	1.09
4	1.8	$\frac{1}{3}$	0.39
5	2.2	$\frac{1}{3}$	0.20

The largest inlet diameter (2.2 m) would of course be the best. However, it would imply having a duct measuring 2.2 m, which would have technically been difficult to set up between the fans and the beginning of the diffuser. The next largest inlet diameter is therefore chosen to be used in the experiment.

Table 4.11 shows what happens to the standard deviation of the wind speed across the outlet when the shape of the inner cone is changed. 2 different cases were studied: In the first case, the diameter of the inner cone made up 1/3 of the diameter of the outer cone. This is what was recommended by Idelchik (1966) (see also Section 2.4.6.4). In the second case, the inner cone had a diameter half as big as the diameter of the outer cone.

Table 4.11: Comparison of standard deviation for various diameters of the inner cone for an inlet diameter of 1 m and no subdivisions

Case number	Inner cone geometry	Standard deviation (m/s)
1	narrow (diameter 1/3 of outer cone on both ends)	2.81
2	large (diameter 1/2 of outer cone on both ends)	2.05

As can be seen, the standard deviation is lower for the case where the inner cone is wider.

Figure 4.41 shows the flow distribution for the diffuser with a 1 m inlet diameter and a long inner cone with a diameter measuring a 1/2 of the outer diffuser, using no subdivisions, in a plane parallel to the main direction of the flow. Figure 4.42 shows the flow distribution for the diffuser with a 1 m inlet diameter and a long inner cone with a diameter measuring a 1/2 of the outer diffuser, using no subdivisions, in a plane perpendicular to the main direction of the flow.

4.3. CFD SIMULATION OF THE WIND FIELD PRODUCED BY THE LARGE WIND GENERATOR USING A DIFFUSER CONE



Figure 4.41: Cross section parallel to the main direction of air flow for a diffuser with a 1 m inlet diameter and a long inner cone with a diameter measuring a 1/2 of the outer diffuser. No subdivisions were used

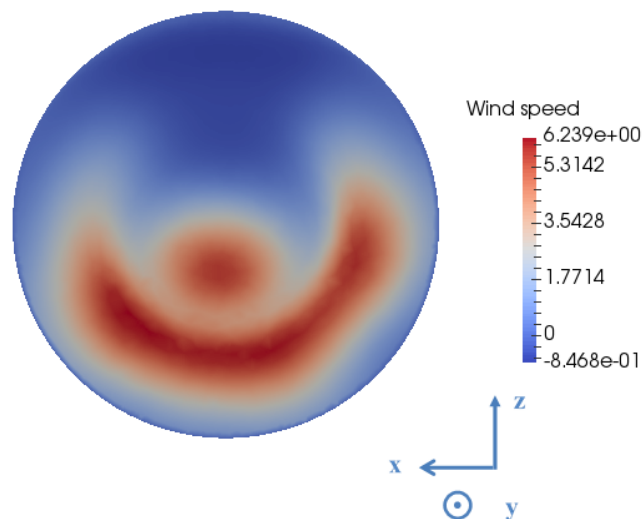


Figure 4.42: Cross section perpendicular to the main direction of air flow for a diffuser with a 1 m inlet diameter and a long inner cone with a diameter measuring a 1/2 of the outer diffuser. No subdivisions were used

It can be seen that contrary to the flow distribution observed on Figure 4.38, where very little flow goes through the inner cone, for the case where the inner cone is wider, more air comes through the inner cone, creating a more even distribution of the flow. A possible explanation for this could be that the inner cone being too narrow, the air flow can get more easily into the outer zone rather than the inner zone.

Table 4.12 compares the standard deviation of the wind speed across the diffuser outlet calculated for different numbers of subdivisions of the space between the inner and the outer cone. These cases were studied with the best length of cone which could be built (1.8 m diameter inlet, 2.04 m cone length) and an inner cone measuring half the

4.3. CFD SIMULATION OF THE WIND FIELD PRODUCED BY THE LARGE WIND GENERATOR USING A DIFFUSER CONE

diameter of the outer cone.

Table 4.12: Comparison of standard deviation of wind speed across the outlet cross section for various numbers of subdivisions between the inner and the outer cone, for an inlet diameter of 1.8 m and an inner cone measuring 1/2 of the diffuser

Case number	Number of divisions	Standard deviation (m/s)
6	4	0.64
7	6	0.47
8	8	0.54

As can be seen, the standard deviation is the lowest for the case of 6 divisions between the inner and the outer cone.

Figure 4.43 shows the flow distribution for the diffuser with a 1.8 m inlet diameter and a long inner cone with a diameter measuring a 1/2 of the outer diffuser, using 6 subdivisions, in a plane parallel to the main direction of the flow. Figure 4.40 shows the flow distribution for the diffuser with a 1.8 m inlet diameter and a long inner cone with a diameter measuring a 1/2 of the outer diffuser, using 6 subdivisions, in a plane perpendicular to the main direction of the flow.



Figure 4.43: Cross section parallel to the main direction of the flow for a 1.8 m diameter inlet using 6 subdivisions and an inner cones measuring 1/2 of the outer diameter

4.3. CFD SIMULATION OF THE WIND FIELD PRODUCED BY THE LARGE WIND GENERATOR USING A DIFFUSER CONE

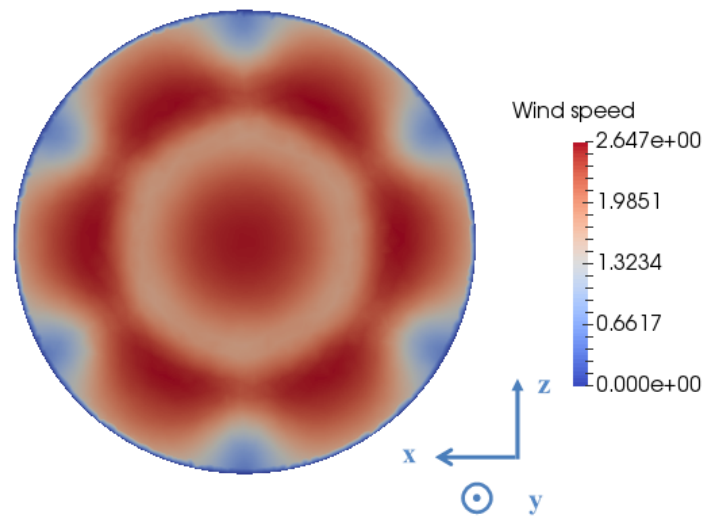


Figure 4.44: Cross section perpendicular to the main direction of the flow for a 1.8 m diameter inlet using 6 subdivisions and an inner cones measuring 1/2 of the outer diameter

Figure 4.45 shows the flow distribution for the diffuser with a 1.8 m inlet diameter and a long inner cone with a diameter measuring a 1/2 of the outer diffuser, using 8 subdivisions, in a plane parallel to the main direction of the flow. Figure 4.46 shows the flow distribution for the diffuser with a 1.8 m inlet diameter and a long inner cone with a diameter measuring a 1/2 of the outer diffuser, using 8 subdivisions, in a plane perpendicular to the main direction of the flow.

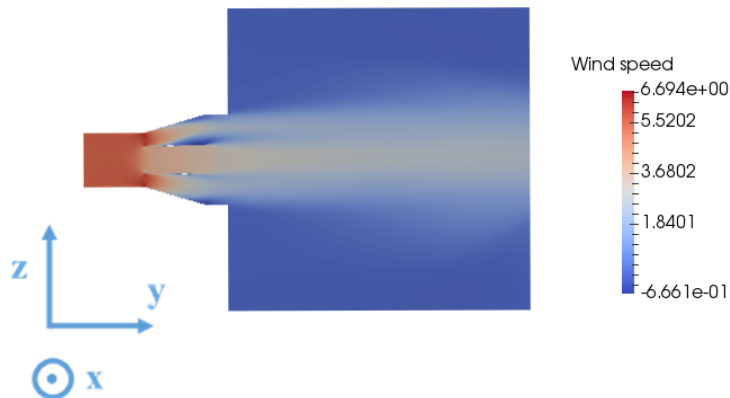


Figure 4.45: Cross section parallel to the main direction of the flow for a 1.8 m diameter inlet using 8 subdivisions and an inner cones measuring 1/2 of the outer diameter

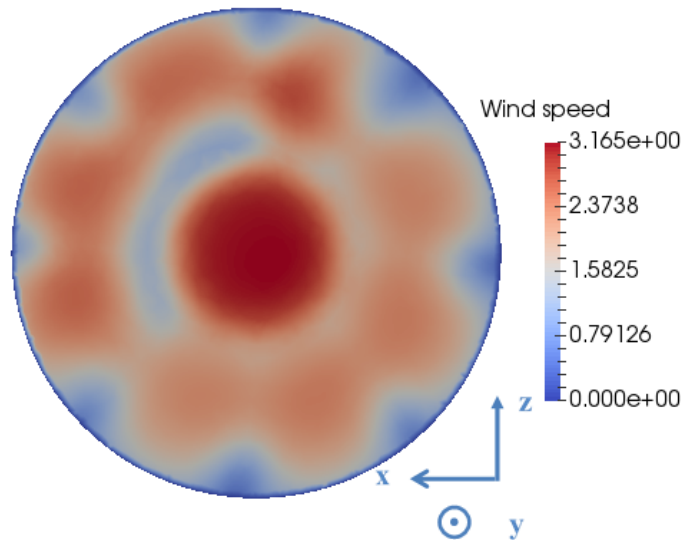


Figure 4.46: Cross section perpendicular to the main direction of the flow for a 1.8 m diameter inlet using 8 subdivisions and an inner cones measuring 1/2 of the outer diameter

It can be seen that using 8 subdivisions creates wind speed higher in the centre of the outlet than in the surrounding 8 subdivisions. A possible explanation for this is that the air goes preferentially into a zone that is larger. Whereas when going from 4 subdivisions to 6 subdivisions, increasing the number of subdivisions is an improvement, this is not the case when going from 6 subdivisions to 8, where the individual compartments are more narrow, possibly causing frictions at the wall to slow down the flow. Figures of the flow distribution of each of the simulations can be found in Appendix C.2.

4.4 Conclusion for the CFD study of 3 different types of wind generation systems

This chapter presented a comparison of the use of various turbulence models in the case of steady state turbulent indoor air flow. A first section presented the comparison of the results for 7 different turbulence models with experimental data on the flow distribution of air coming out of a wind blowing system. Measured wind speed and experimental turbulence kinetic energy were compared to the results obtained from the various turbulence models studied. The Spalart Allmaras and the standard $k - \omega$ turbulence models were excluded for not giving satisfying results for this type of air flow. The standard $k - \epsilon$ and the $k - \omega$ SST models gave results close to the experimental data in terms of average longitudinal wind speed. The relative difference averaged over several distances and locations in space was at 6 %. All turbulence models gave results for turbulence kinetic energy which were far off from the experimental data, at least close to the outlet. The realisable $k - \epsilon$ and the RNG $k - \epsilon$ were closest to the experimental data, though still with an average relative difference coming close to 200 %.

For the subsequent simulations, two turbulence models were chosen. The $k - \omega$ SST model was chosen for its ability to predict well free stream and wall-bounded air flows, as the two types of simulations on the flow distribution inside conical diffusers involved

4.4. CONCLUSION FOR THE CFD STUDY OF 3 DIFFERENT TYPES OF WIND GENERATION SYSTEMS

wall-bounded flows. The realisable $k-\varepsilon$ turbulence model was also investigated due its performance in the case of strong adverse pressure gradients and flow separation, as it was expected that this type of flow would occur in the conical diffusers used here. A 2D mesh convergence study allowed the determination of a mesh size giving convergence of the results and also showed that the results obtained by the realizable $k-\varepsilon$ model gave more stable results than the $k-\omega$ SST model. The mesh size obtained and the realizable $k-\varepsilon$ model were therefore used for 3D simulations for various shapes and numbers of inner cones inside a diffuser. It was determined that using a inlet diameter of 1 m to go to a 3 m diameter outlet gave an uneven flow distribution, when an opening angle of 33° was used. Satisfying results were obtained for an inlet diameter of 1.8 m and an inner cone covering the whole length of the diffuser and measuring half the diameter of the diffuser. To hold the inner cone in place, panels going from the inner cone to the outer diffuser were needed. It was determined that the flow distribution was better when 6 panels were used rather than 4 or 8. Several combinations study numerically were studied experimentally and the set up and the results are presented in Chapter 5.

Chapter 5

Wind generation system using two 35.2 kW centrifugal fans

This chapter reports on the performance of various versions of wind generation systems, all using two 35.2 kW centrifugal fans, the properties of which can be consulted in Appendix D.1. Those wind generation systems were all set up over the Ocean Basin and aimed at providing the possibility to blow wind on a model Floating Offshore Wind Turbine. The general set-up of all wind generation systems resembled the one shown in Figure 5.1 or Figure 5.2. The fans being very heavy, they had to be set up on a structure situated at one corner of the ocean basin. The fans are situated one on top of the other (see Figure 5.3). The fans were placed in the corner of the basin rather than the middle, because otherwise the structure would be in the way of models being transported in and out of the ocean basin. The location where the wind was needed was at the centre of the basin 13 m away from the edge of the ocean basin. After a structure combining the wind from the two fans, a polythene duct guides the air near the centre of the basin where a round to square or round to round diffuser further guides the wind to a final outlet equipped with flow straighteners.

The centres of the outlets of the fans are situated 2.5 m from the side of the ocean basin and are 1.03 metres apart. The centre of the structure which combines the flow of the two fans (circular outlet) is situated 2.9 m above the laboratory floor and 2.5 m above the mean water level.

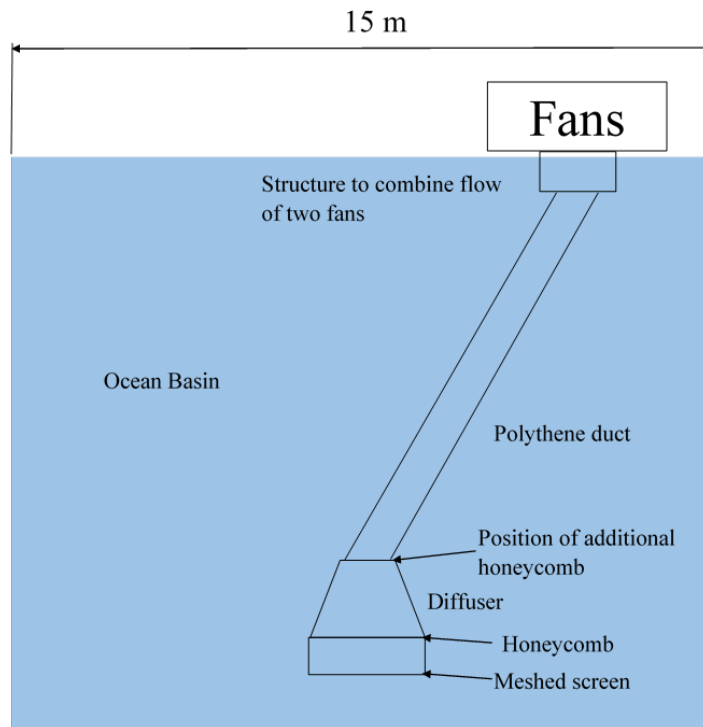


Figure 5.1: Schematic of general set up of the wind generation system version 1

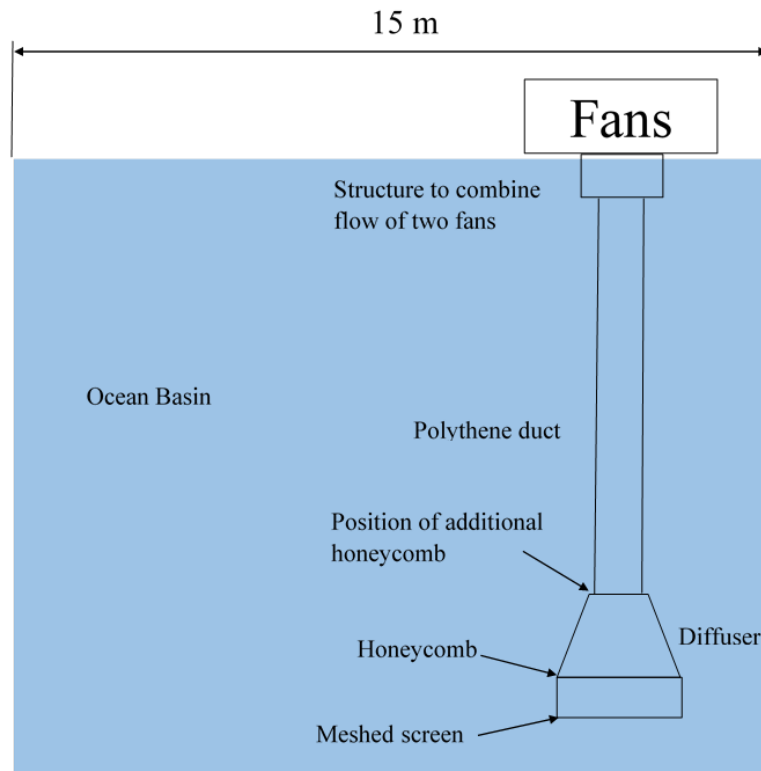


Figure 5.2: Schematic of general set up of the wind generation system version 2

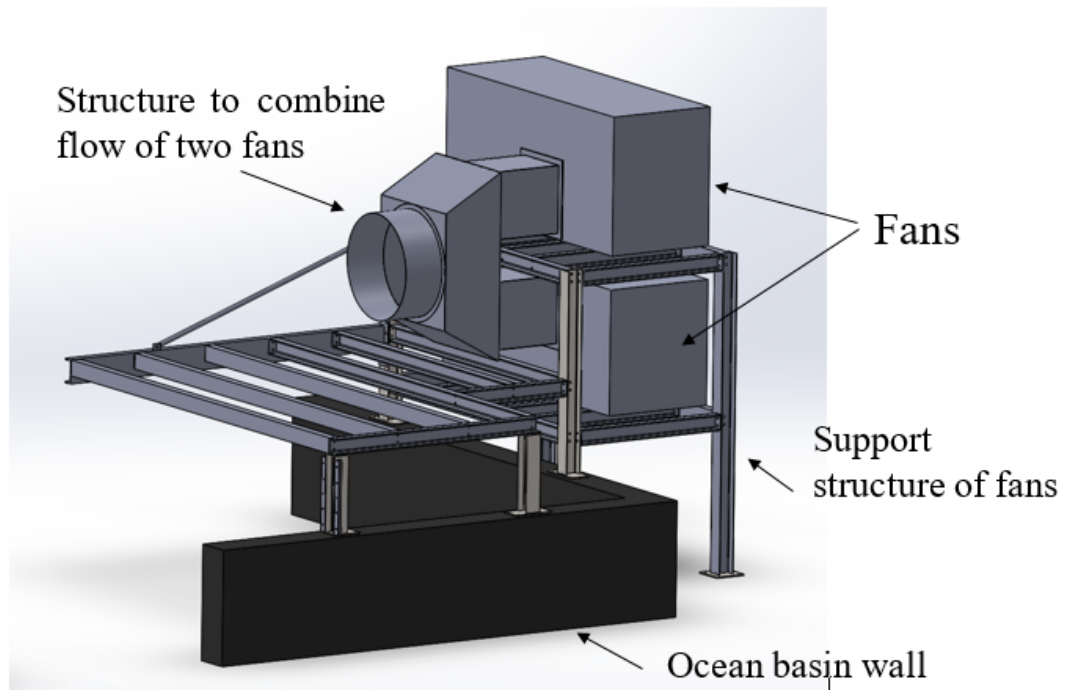


Figure 5.3: Technical drawing of fan set up

Figure 5.4 shows a flow chart presenting all experimental set ups. As they are numerous, it was considered useful for the reader to have a good overview.

Two different sizes were used for the outlet section, a 1.6 m square outlet and a 3 m diameter circular outlet. For the 1.6 m square outlet, a honeycomb and a meshed screen were used as flow straighteners at the end of a round to square diffuser.

For the 3 m diameter outlet, the diffuser cone had two different sizes for the inlet: a 1 m diameter inlet and a 1.8 m diameter inlet. For the 1 m diameter inlet, the diffuser cone was tested with and without a set of 3 concentric inner cones inside. There was a honeycomb after the end of the polythene duct and before the inlet of the diffuser, but no honeycomb or meshed screen at the outlet.

The diffuser cone with a 1.8 m diameter inlet was tested with a straight duct (Diffuser cone placed on one side of the ocean basin) and a duct arriving with an angle (diffuser cone placed in the centre of the ocean basin). In both cases, the structure inside the cone was the same, that is, an inner cone going from one end of the diffuser to the other with 6 dividing walls around it (geometry determined in Section 4.3.2). The case of the straight duct was tested with and without flow straighteners (honeycomb and meshed screen) at the outlet. With no flow straighteners at the outlet, there was a honeycomb between the polythene duct and the inlet. In the case of flow straighteners at the outlet, it was tested whether this honeycomb was still necessary. In the case of the angled duct, the wind field was only measured with flow straighteners at the outlet. There was one additional honeycomb between the polythene duct and the inlet of the

diffuser. This case was also tested with 2 additional honeycombs, where one more honeycomb was placed before the beginning of the polythene duct, right after a first bend in the duct.

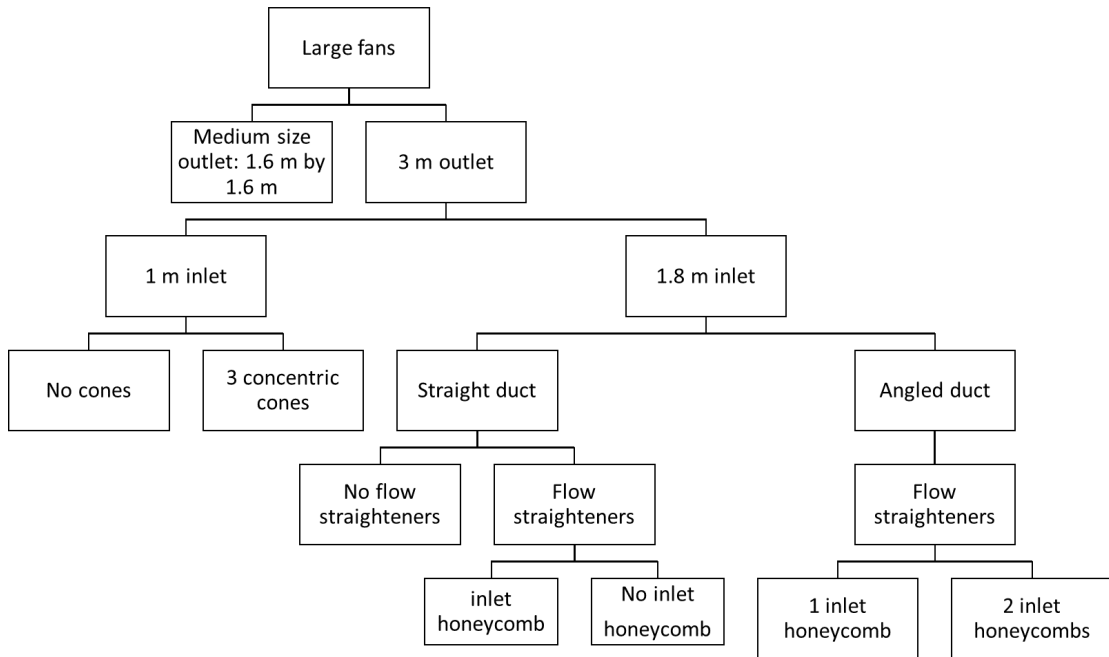


Figure 5.4: Overview of experimental set ups using the two large centrifugal fans

This chapter will present the experimental set up and the wind field measured for the following configurations in the following order:

- 1.6 m x 1.6 m square outlet named Outlet 1 in the rest of the Chapter
- 1 m inlet, 3 m outlet without cones on the inside named Outlet 2a in the rest of the Chapter
- 1 m inlet, 3 m outlet with 3 cones inside named Outlet 2b in the rest of the Chapter
- 1.8 m inlet 3 m outlet, long inner cone, straight duct, named Outlet 3a
- 1.8 m inlet, 3 m outlet, long inner cone, angled duct, named Outlet 3b

5.1 Wind generator with 1.6 m square outlet

In order to blow wind over the whole rotor area of a model wind turbine of the NREL 5 MW reference wind turbine at scale 1:50 (see Section 2.2.2), the outlet should measure at least 2.8 m. Before building such an outlet and finding a way of installing it over the ocean basin, a smaller version was built and tested. Measurements were done in 2 configurations, the first one only had flow straighteners at the very end of the outlet,

5.1. WIND GENERATOR WITH 1.6 M SQUARE OUTLET

the second one had a honeycomb at the end of the polythene duct before the round to square section. Measurements were done for several fan rotational speeds and are presented here. Conclusions are drawn for this first use of the larger fans and result in recommendations for the 3 m diameter outlet.

5.1.1 Experimental Set-up

The 2 centrifugal fans are positioned near the paddles of the ocean basin. They are situated one on top of the other thanks to a structure specifically designed for this purpose. They are not situated at the centre of the basin wall, but near one corner, as otherwise this would obstruct loading and unloading of devices to be tested inside the ocean basin. The outlet was positioned 13.5 m downstream of the fans and 5 m to the side of the fans. The duct that guided the air to the outlet was therefore arriving at the outlet with an angle of 20° (see Figure 5.5). The outlet was positioned on top of a wooden frame which was suspended through 8 wires attached at various points in the laboratory (see Figure 5.7).

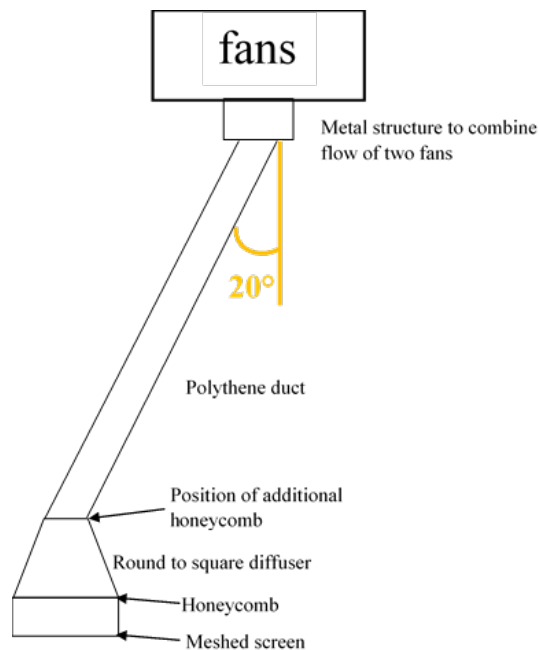


Figure 5.5: View from above of the set up for the 1.6 m square outlet

Figure 5.6 shows the dimensions of the round to square diffuser (lengths in mm).

5.1. WIND GENERATOR WITH 1.6 M SQUARE OUTLET

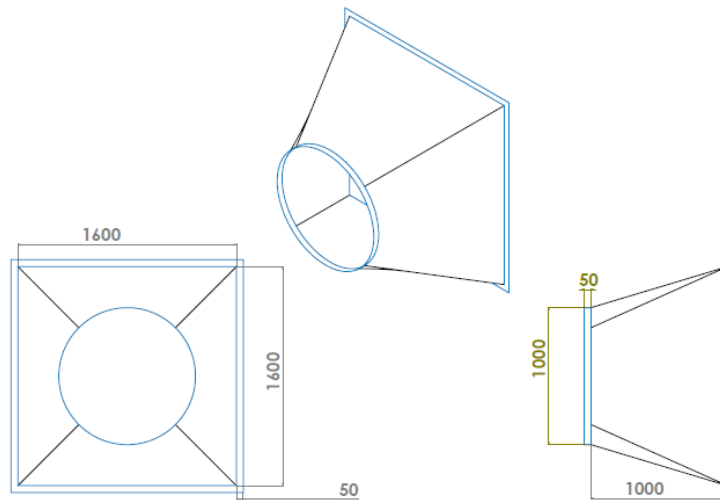


Figure 5.6: Dimensions of square to round outlet

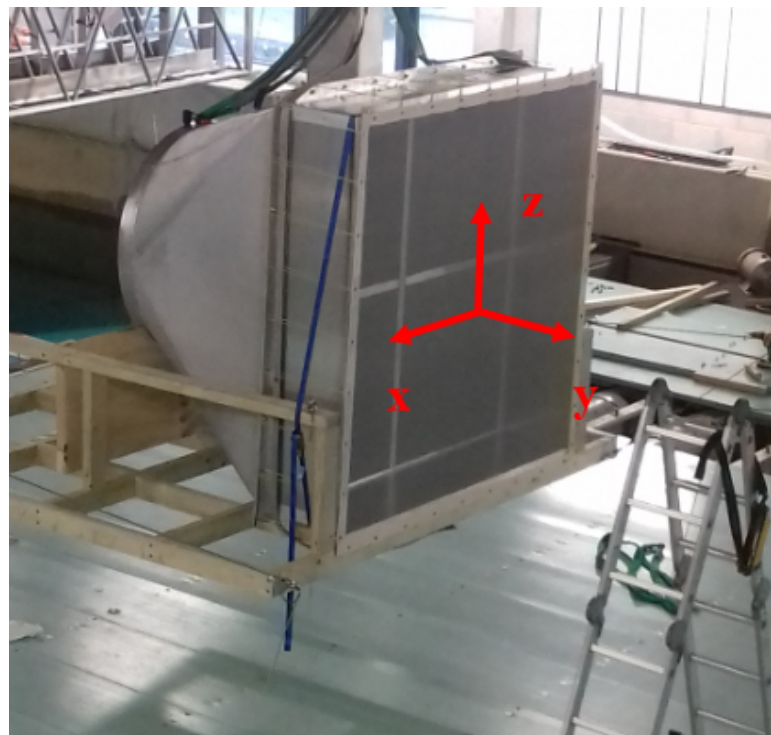


Figure 5.7: Outlet on wooden frame during installation phase

Near the fans, a metal structure combines the air flow coming out of the fans into a single stream (see Figure 5.8). From there, a duct made from polythene guides the airflow to the round section of the round to square diffuser (see Figure 5.8 and Figure 5.10). Its diameter is 1 m. Figure 5.9 shows a technical drawing of this structure.

5.1. WIND GENERATOR WITH 1.6 M SQUARE OUTLET

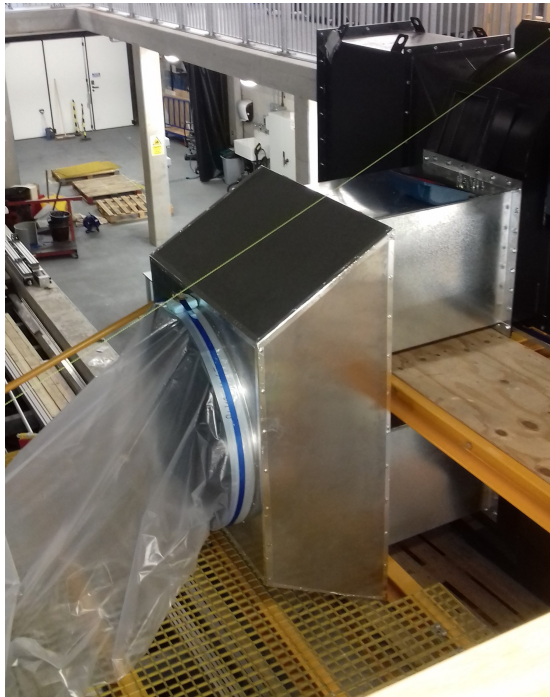


Figure 5.8: Metal structure that combines air flow coming from the 2 centrifugal fans

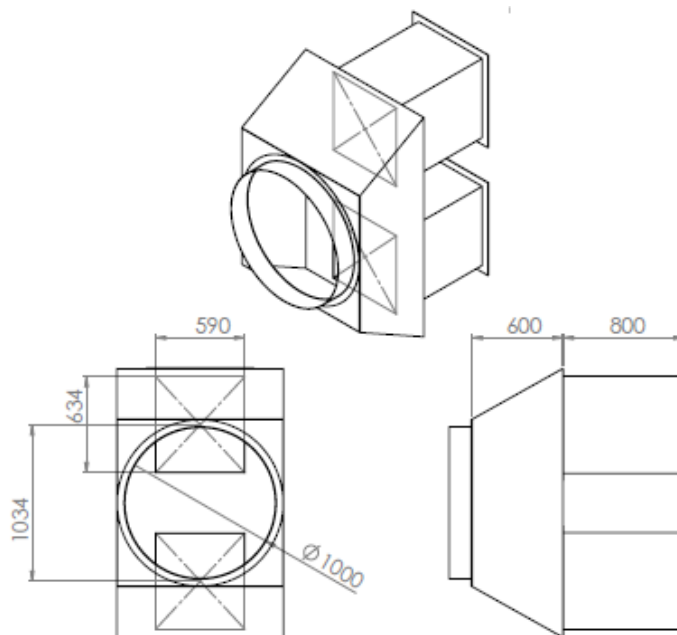


Figure 5.9: Technical drawing of structure combining the flow of the 2 fans

5.1. WIND GENERATOR WITH 1.6 M SQUARE OUTLET



Figure 5.10: Polythene duct that guides air from fans to outlet situated at the centre of the basin

Honeycombs and a meshed screen were used for flow straightening purposes. The experiments in Chapter 3 showed that all honeycomb cell sizes used gave good results. Which is why for this set-up, the cell size most easily obtained was used and the ratio $\frac{\text{cell length}}{\text{cell diameter}}$ was maintained at 8. The honeycomb had a cell diameter of 4 mm, cell length (= thickness) of 32 mm. The material was polycarbonate. For the meshed screen, the fabric which was closest to the required criteria presented in Section 2.4.4 amongst those which were available in one piece (width = 1700 mm) was chosen. The meshed screen was made from nylon. The wire diameter was 1100 μm . The open area was 59 %. And the mesh opening was 3300 x 3300 μm .

The wind speed was measured with a 3D ultrasonic anemometer at a frequency of 32 Hz. A traverse was used which displaced the anemometer along the 3D coordinates. The range of the traverse was limited to 1 m. Therefore, the traverse had to be placed at two different positions to measure wind inside the whole area behind the outlet. To cover the full height of the outlet, the anemometer had to be placed on a long arm at two different heights, as seen on Figure 5.11.



Figure 5.11: Traverse and anemometer used to measure the wind at various positions near the outlet

5.1. WIND GENERATOR WITH 1.6 M SQUARE OUTLET

The measurements were done for 1 minute. The first series of measurements was done with flow straighteners only at the very end of the outlet. The meshed screen is visible on figure 5.7. The honeycomb is invisible in that figure, hidden behind the meshed screen. Figure 5.12 shows the 4 pieces of honeycomb held in place by aluminium T's, before the meshed screen was installed.

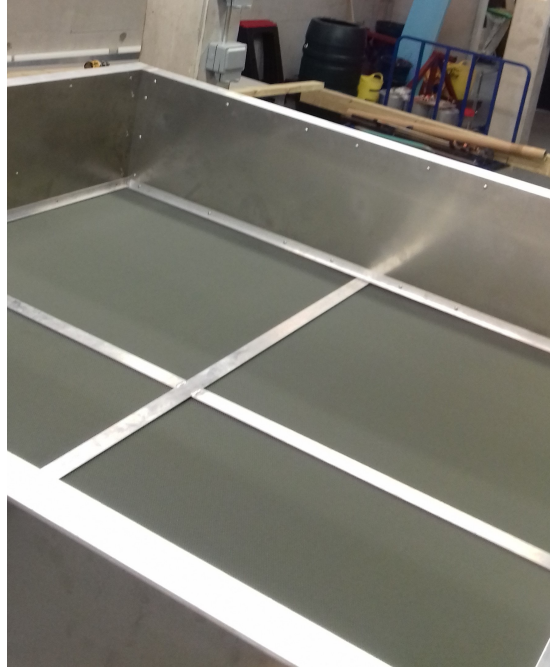


Figure 5.12: Honeycombs inside outlet, held in place through aluminium T's

The distance between the honeycomb and the meshed screen is 360 mm. This distance was chosen following recommendations in Mehta and Bradshaw (1979) which were confirmed to be good through the measurements done previously and presented in Chapter 3. The distance between flow straighteners is recommended to be $0.2 \times \text{diameter}$ of area over which wind is blown. A circular area that would have the same area as the square outlet would have a diameter of 1805 mm. It was therefore decided to set the distance between the honeycomb and the meshed screen to $1800 \times 0.2 = 360$ mm.

It was easily noticed, even before measuring, that there was a severe asymmetry in the flow due to the angle at which the duct arrived, which is why it was decided to introduce an additional honeycomb before the beginning of the round to square outlet (see Figure 5.5) to see if the flow could be improved. Due to material availability, the width of the honeycomb was 200 mm shorter than that of the inlet, so the duct had to go through a narrow section.

5.1.2 Results

Figure 5.13 and Figure 5.14 show the average longitudinal wind speeds measured for two different fan rotational speeds without the additional honeycomb. It can be seen that all of the flow is on one side of the outlet only, very likely due to the angle with

5.1. WIND GENERATOR WITH 1.6 M SQUARE OUTLET

which the duct arrives at the outlet.

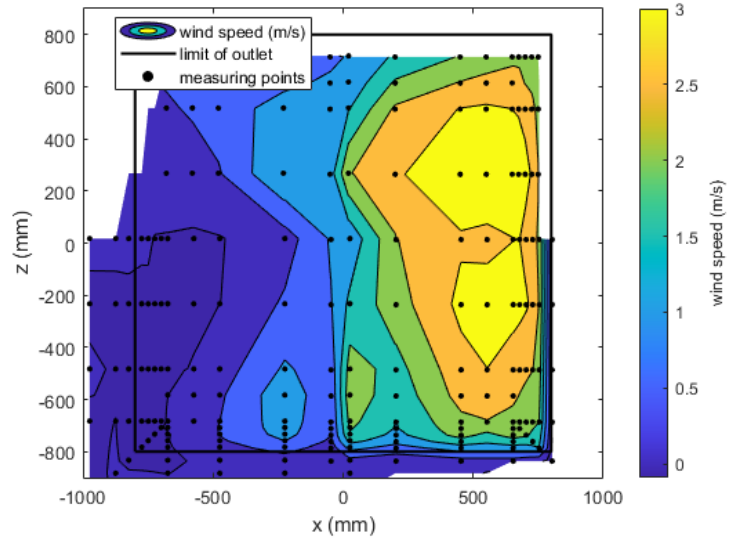


Figure 5.13: Fan power 30 %, without additional honeycomb, 0 m from outlet

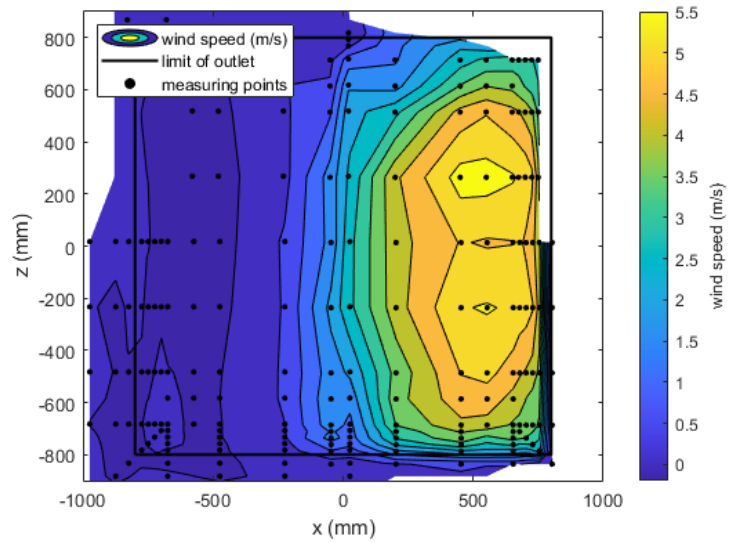


Figure 5.14: Fan power 50 %, without additional honeycomb, 0 m from outlet

5.1. WIND GENERATOR WITH 1.6 M SQUARE OUTLET

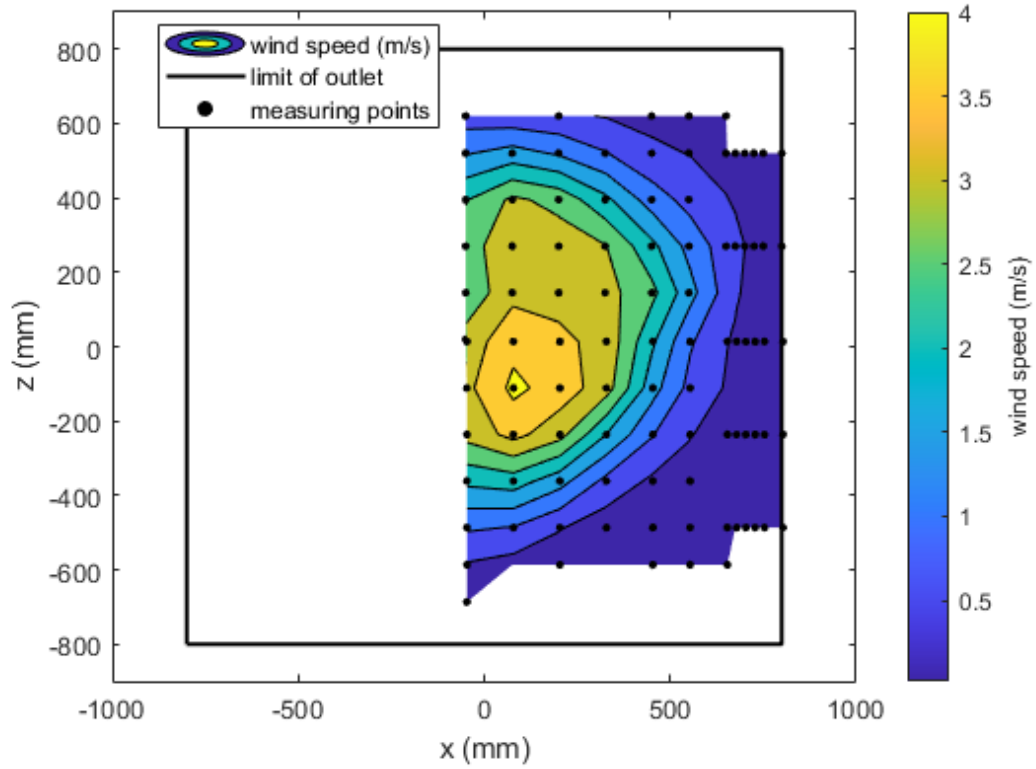


Figure 5.15: Fan power 30 % with honeycomb, 1 m from outlet

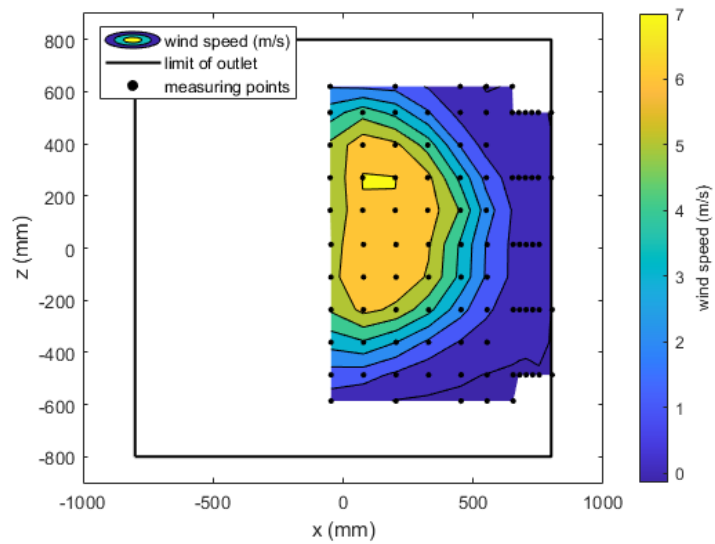


Figure 5.16: Fan power 50 % with additional honeycomb, 0 m from outlet

5.1. WIND GENERATOR WITH 1.6 M SQUARE OUTLET

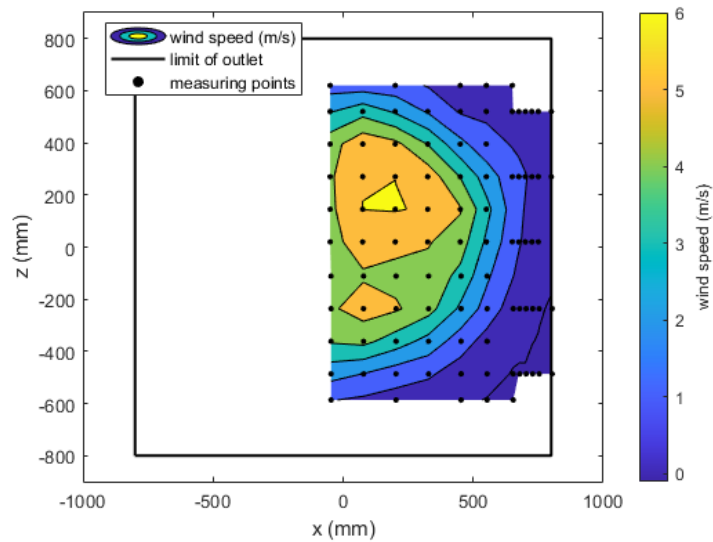


Figure 5.17: Fan power 50 %, with additional honeycomb, 1 m from outlet

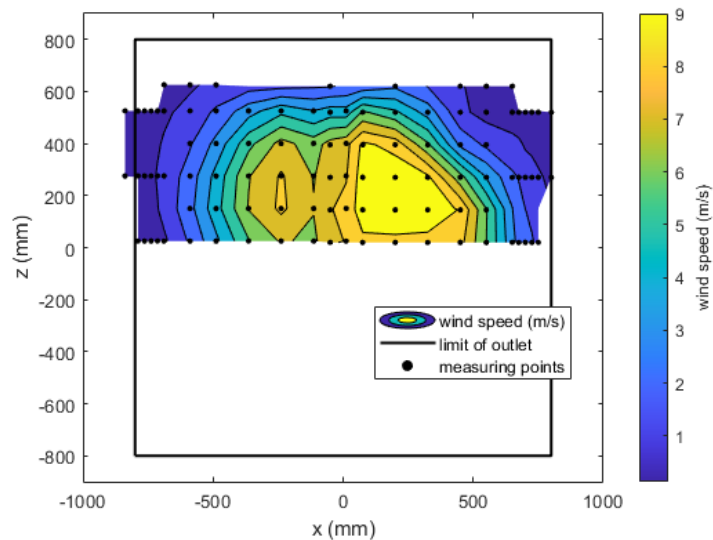


Figure 5.18: Fan power 80 %, with additional honeycomb, 1 m from outlet

The outlet was clearly not well designed, as the flow stayed at the centre of the outlet, not at all expanding into the full square shape at the very end of it. It can clearly be seen that the flow was concentrated over a circular area, which roughly corresponds to the shape of the duct.

The flow quality could potentially be improved through vanes on the inside of the outlet. This was not studied, as this outlet was just a trial version for the outlet that would be 3 m wide, but it raised awareness that a structure inside the outlet was crucial to a successful distribution of the flow.

5.1. WIND GENERATOR WITH 1.6 M SQUARE OUTLET

The fans were not turned on 100 % of the rotational speed. As the metal structure near the fans that made the flow of the 2 fans come together was not designed for smooth flow conditions, the turbulence levels were very high. The polythene duct was shaking a lot, and turning the speed up higher seemed risky. The wind speeds measured were used to determine the flow rate provided by the two fans (see Figure 5.19).

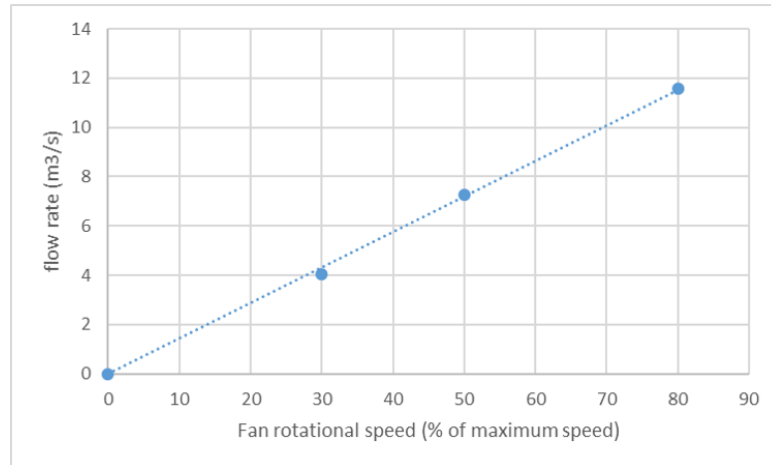


Figure 5.19: Total flow rate of the two large centrifugal fans as a function of the percentage of the maximum rotational speed

The curve was extrapolated to determine the expected flow rate when going up to 100 %. Figure 5.20 shows the evolution of the average wind speed across the area with the fan rotational speed.

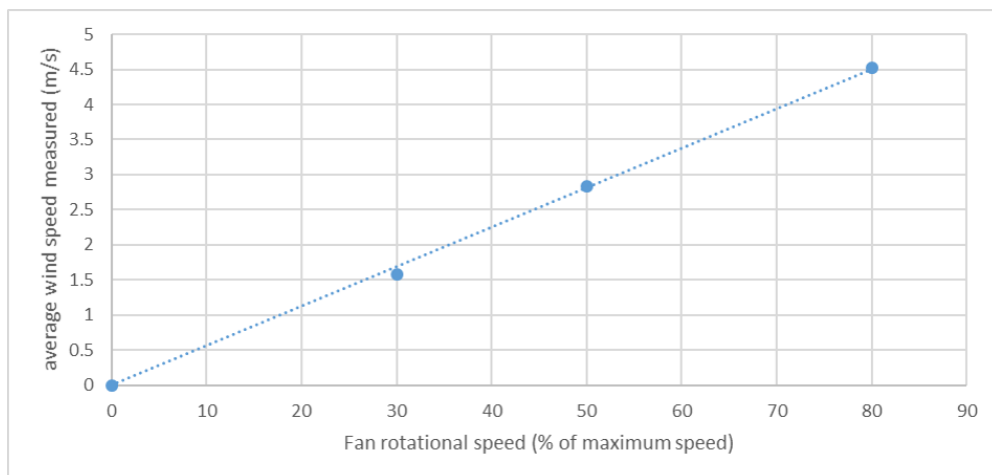


Figure 5.20: Average wind speed across the 1.6 by 1.6 m square outlet produced by the 2 large centrifugal fans

Supposing that the evolution of wind speed with fan rotational speed had a linear evolution, it was estimated that the flow rate for the case of 100 % would be $14.5 \text{ m}^3/\text{s}$ and the expected average wind speed would be 5.7 m/s.

5.2 Wind generator with 3 m diameter circular outlet and 1 m diameter inlet - Outlet 2a and 2b

To be able to blow wind over a model wind turbine that would have a width of 2.52 m, it was decided to build an outlet that would be 3 m wide. This would account for lateral and vertical displacement of the floating wind turbine, as well as for the fact that the area over which wind would be blown would necessarily be more narrow than the actual outlet.

From the previous set of experiments, it was also seen that the flow distribution inside the outlet would largely influence the quality of the wind. For practical reasons, the duct guiding the wind from the fans to the outlet could not have a larger diameter.

In the first set of experiments, it was therefore decided that the duct would only be 1 m wide. The outlet is a hollow truncated cone (see Figure 5.21), with a circular inlet of 1 m and a circular outlet of 3 m. The total length of this truncated cone is 3.4 m. The opening angle of this cone is therefore $\sim 33^\circ$.



Figure 5.21: Truncated cone diffuser

No angle was given to the duct this time, the cone was situated on a straight line with the fans, when moving away from the paddles. The main purpose of this series of measurements was to determine whether it was actually possible to distribute the air evenly when diffusing it over such a large expansion.

As was mentioned in Section 4.3.1, several versions of inner cones were studied numerically. One of them was built and tested.

5.2.1 Experimental set up of the large wind generator

Figure 5.22 shows the set of three nested inner cones before installation inside the diffuser cone. 4 walls were holding them together and helping to position them inside the diffuser cone.

5.2. WIND GENERATOR WITH 3 M DIAMETER CIRCULAR OUTLET AND 1 M DIAMETER INLET - OUTLET 2A AND 2B



Figure 5.22: Set of nested concentric cones situated inside the diffuser cone

Figure 5.23 shows this set of inner cones set up inside the diffuser cone.

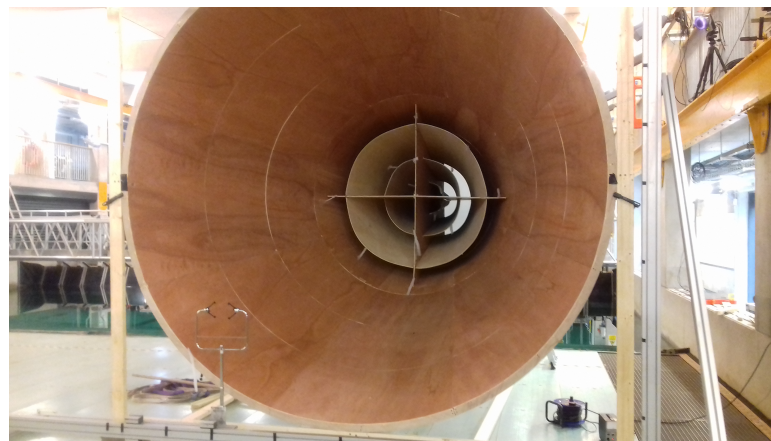


Figure 5.23: Diffuser cone with concentric cones on the inside

Figure 5.24 shows the dimensions of these inner cones.

5.2. WIND GENERATOR WITH 3 M DIAMETER CIRCULAR OUTLET AND 1 M DIAMETER INLET - OUTLET 2A AND 2B

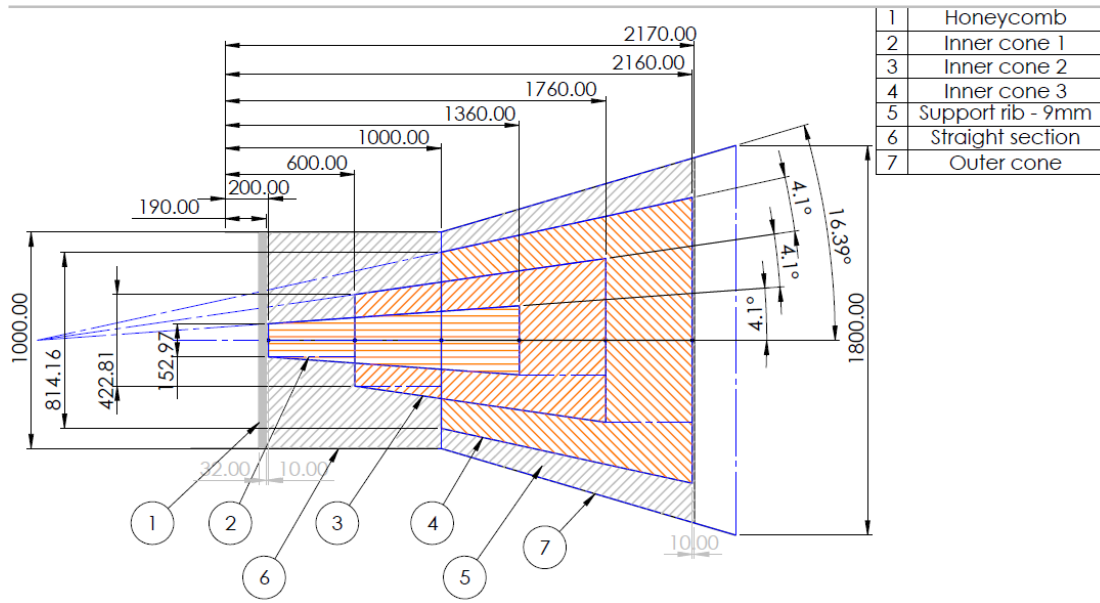


Figure 5.24: Dimensions of inner cones (same as Figure 4.24)

No flow straighteners such as honeycomb or meshed screen were installed at the outlet, to provide for comparison with CFD simulations.

One honeycomb was installed at the entrance of the diffuser. It had a cell diameter of 4 mm, cell length (= thickness) of 32 mm.

5.2.2 Wind field measured for the large wind generator

The wind field was measured with and without the concentric cones inside the diffuser cone. All measurements were done in a plane perpendicular to the main flow direction situated at 130 mm from the end of the outlet. The measuring frequency was 32 Hz. Figure 5.25 shows the coordinate system used for the graphs showing the results.

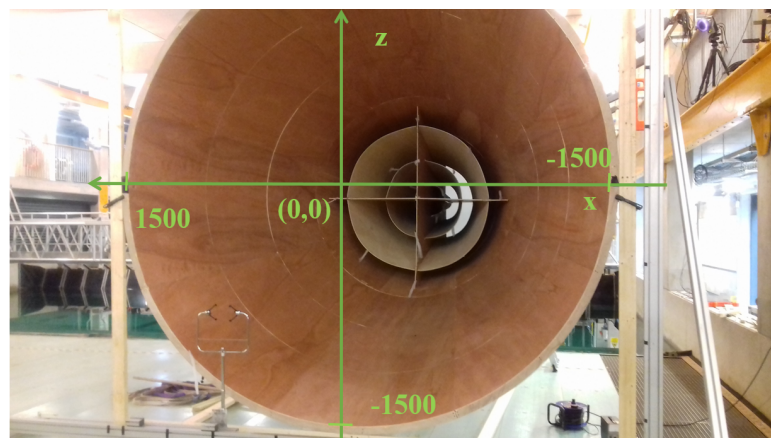


Figure 5.25: Coordinate system used for graphs

5.2.2.1 Measurements without concentric cones

When there were no concentric cones inside the diffuser cone, the airflow was clearly asymmetrical and unstable. The majority of the time, the highest speed was situated on the side of positive x . This can be seen in Figure 5.26, which shows average values of time periods at least 7 minutes long. For comparison, the CFD results obtained for a diffuser cone without concentric cones are shown. The CFD results were scaled down to match the maximum value obtained in the experimental results, as the flow rate obtained in the experiments was not as high as the flow rate used for the CFD simulations, which were carried out before the experiments. Also the measurements were not done with the fans running at full power. CFD results and experimental results are a good match for the height $z=0$ mm.

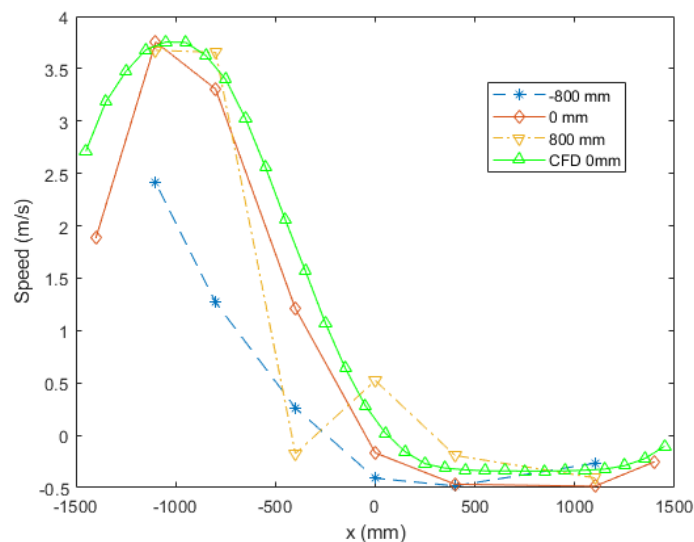


Figure 5.26: Average longitudinal wind speed measured at various horizontal positions at heights -800, 0 and 800 mm for a fan rotational speed of 50 % of the maximum rotational speed, scaled CFD results at height 0 mm

A 30 minutes measurement of wind speed at a single point was carried out to assess the stability of the wind field (Figure 5.27). What can be observed when looking at the instantaneous wind speed measured, is that though for over 15 min (~ 900 s) the wind speed was oscillating around a constant mean, there are two time intervals during which the average wind speed around which the wind speed oscillates is clearly lower than before. This shows that not only is the flow highly asymmetric, but it is in addition unstable, that is not stable in a given location. Some measurements lasting 30 minutes did not show such changes in average wind speed. In some measurements lasting 7 minutes, such changes in average wind speed were observed. For each long measurement, the data was divided up into 1 minute intervals over which the average was calculated individually. The maximum average was compared to the minimum average. For the measurements lasting 7 minutes, the largest difference between the maximum average and the minimum average of any of the measurements lasting 7 minutes was 2.9 m/s. For the measurement shown in Figure 5.27, lasting 30 minutes, the difference

5.2. WIND GENERATOR WITH 3 M DIAMETER CIRCULAR OUTLET AND 1 M DIAMETER INLET - OUTLET 2A AND 2B

between the maximum average and the minimum average (over 1 min) was 3.5 m/s. This was the most unstable of the 30 minute measurements.

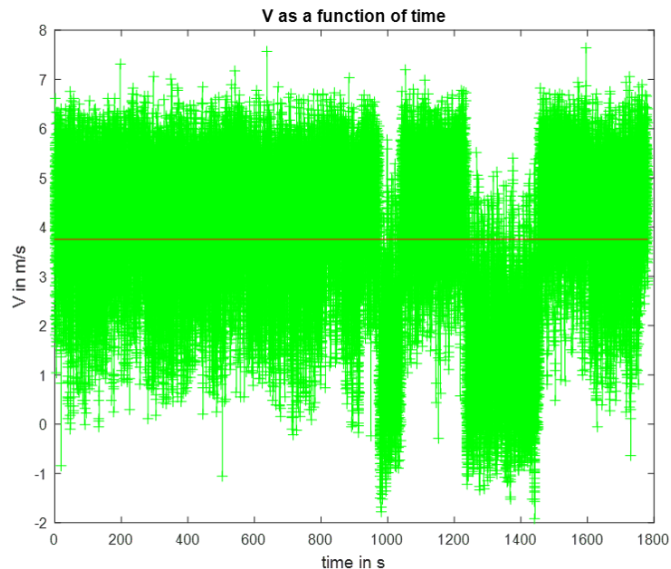


Figure 5.27: Instantaneous longitudinal wind speed over 30 min. without concentric cones

Literature showed that diffusers should not have angles above 15° for the quality of the flow to stay correct. This would have meant that the diffuser would need to be 7.6 m long, which was not possible in the given laboratory geometry.

5.2.2.2 Measurements with concentric cones

The wind speed was measured at 9 different heights: -1400, -1100, -800, -400, 0, 400, 800, 1100, 1400 mm, with 0 at the centre of the circular outlet (see Figure 5.25). The horizontal positions were at the same positions, again with the centre of the circular outlet as 0 reference point.

Figure 5.28 shows the average longitudinal wind speed measured at heights -1100, -400 and 0 mm for a fan rotational speed 50 % of the maximum rotational speed. For the heights -1100 mm, -400 mm and '0 mm March 12', it can be seen that at the central horizontal position, not only is the speed very low, but it is even slightly negative. In short, there is a small region with backflow. The highest speeds are situated in an area close to the outer edge of the outlet. The yellow line with hexagram shaped markers (named '0 mm March 11'), shows a series of measurements done 24 hours before the ones named '0 mm March 12' (purple line, diamond markers) at the same locations (after various other positions have been measured and when the fans have been turned off and turned on again). If the flow was stable, these two lines should be showing the same results, which is not the case. While for the measurements done on March 11, the highest speed is situated on the positive side of x and the lowest wind speed is situated on the negative side of x, for the measurements done on March 12, the lowest speed is situated at the centre of the outlet. It should be noted that the individual measurements were not done at the same time, but rather one after another.

5.2. WIND GENERATOR WITH 3 M DIAMETER CIRCULAR OUTLET AND 1 M DIAMETER INLET - OUTLET 2A AND 2B

All measurements shown here were done for 1 min. For comparison, CFD results obtained for a diffuser cone with 3 inner concentric cones are shown in Figure 5.28 for a height of $z=0$ mm. The CFD results were scaled to match the maximum of the speed measured experimentally at this height and on that day for ease of comparison. The flow rate used for the CFD simulations was higher than the actual flow rate obtained experimentally, in particular since experimental results were not done at the maximum power of the fans but only at 50%. The correspondence between CFD and experiments is not as good as for the diffuser cone with no inner cones. The general shape of the flow distribution obtained thanks to CFD is similar to the one obtained thanks to measurements, with a trough at the centre and a maximum speed near the edge of the diffuser cone. The correspondence is better on the side of positive x than on the side of negative x and only valid for one of the days on which these measurements were obtained.

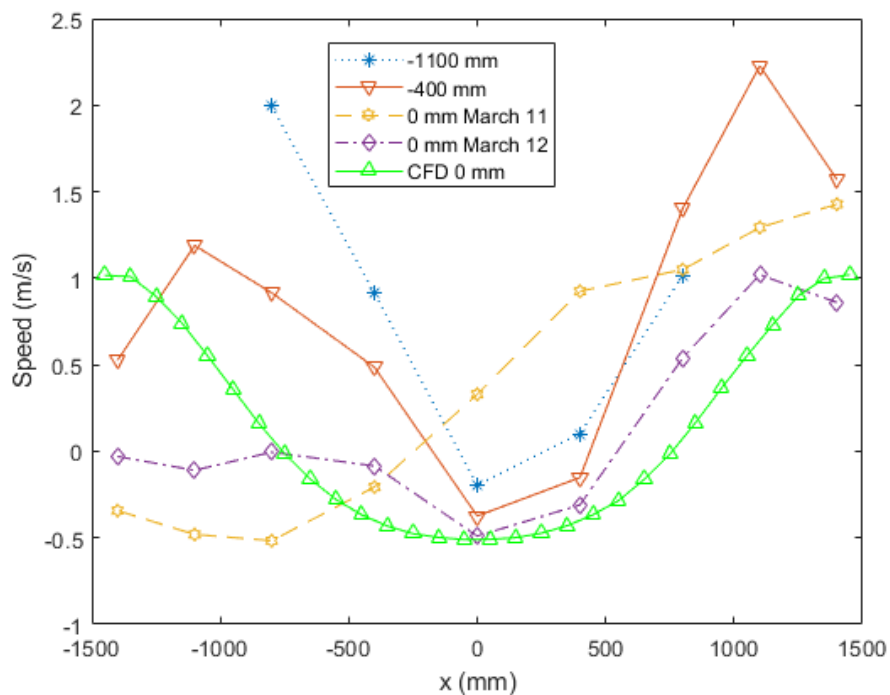


Figure 5.28: Average longitudinal wind speed measured over 1 minute at various heights for a fan rotational speed of 50 % of the maximum rotational speed, scaled CFD results at height 0 mm

Several measurements lasting 20 minutes were done for this configuration. Two of them showed a clear change in average wind speed. Average wind speeds over each of the 20 intervals lasting 1 minutes were calculated and compared. For one of the 20 minute measurements the difference between the highest and the lowest average of each of the 20 intervals was 1.1 m/s, which was the highest difference observed for all long measurements. This could indicate that this configuration was more stable than the one without cones, though without guarantee, since the changes in average wind speed happen randomly.

5.3. WIND GENERATOR WITH 3 M DIAMETER CIRCULAR OUTLET AND LONG INNER CONE - OUTLET 3A

Measurement results presented over the whole area can be found in Appendix D.2.

5.3 Wind generator with 3 m diameter circular outlet and long inner cone - Outlet 3a

In response to the system presented in Section 5.2 not generating the required wind field a series of changes were made to both the outlet and the ducting system. This section presents these changes and the measured wind field.

5.3.1 Improvements on previous set-up

5.3.1.1 Improvement made on ducting

The metal structure which combined the flow of the two centrifugal fans very close to the fans was source of a lot of turbulence. It was decided that it should be replaced by a structure that would combine the air flow much more progressively. Two expanding ducts with a rectangular cross section led the air to a large rectangular box. This set up can be seen in Figures 5.29, 5.30 and 5.31.

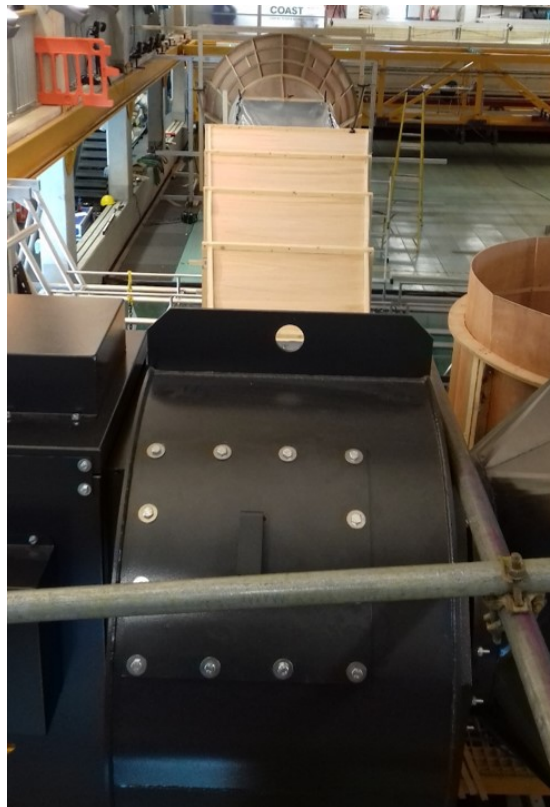


Figure 5.29: View from above of the whole wind generation system, including fans, structure to combine fan air flow, polythene duct and diffuser

5.3. WIND GENERATOR WITH 3 M DIAMETER CIRCULAR OUTLET AND LONG INNER CONE - OUTLET 3A



Figure 5.30: Wooden structure to combine the airflow of the two fans



Figure 5.31: Wooden structure to combine the air flow of the two fans

A short section ($\sim 5m$) of the duct is still made from polythene (Figure 5.32).



Figure 5.32: Polythene duct guiding air from wooden structure which combines air flow of the two fans to the diffuser

5.3. WIND GENERATOR WITH 3 M DIAMETER CIRCULAR OUTLET AND LONG INNER CONE - OUTLET 3A

The duct is square shaped, measuring 1.4 m on each side.

5.3.1.2 Improvement made on outlet

The outlet starts with a square shaped section measuring 1.4 by 1.4 m. It then transitions to a circular cross section with a 1.8 m diameter. The diffuser therefore goes from 1.8 m to 3 m over a length of 2.04 m. The geometry for dividing walls which was determined to be the most efficient in the chapter on CFD (Section 4.3.2) was built inside the cone. It consists of a truncated cone on the inside of the outer cone. The diameter of the cross section of this cone was half the diameter of the outer cone. There are also 6 dividing walls connecting the inner to the outer cone, and holding the inner cone in place. See Figure 5.33, Figure 5.34 and Figure 5.35.

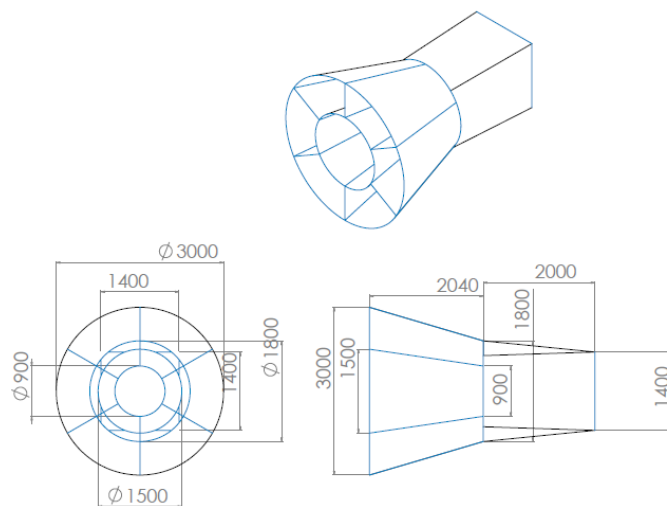


Figure 5.33: Technical drawing of Outlet 3



Figure 5.34: Diffuser

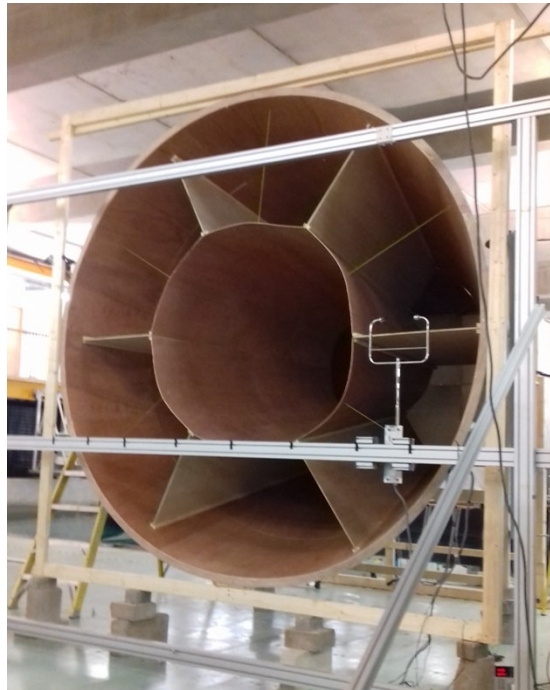


Figure 5.35: Long inner cone and dividing walls inside the conical diffuser and structure to hold anemometer for measurements

5.3.1.3 Improvement on the flow-conditioning

As for the 2 previous set ups, a honeycomb was installed at the beginning of the outlet (It can be seen on Figure 5.36). Measurements were done with and without flow straighteners at the very end of the outlet (visible in Figures 5.37 and 5.38). There was no doubt that these flow straighteners are necessary.

As was seen in Section 2.4.4, the following recommendations are given for flow straighteners in wind tunnels.

- Use one honeycomb followed by at least one screen.
- There should be 150 honeycomb cells across the settlement chamber diameter.
- The ratio of the cell length over the cell diameter should have values between 6 and 12.
- The pressure drop coefficient of the honeycomb should be about 0.5.
- The open area ratio of the meshed screen should be at least 58 %.
- The pressure drop coefficient of the meshed screen should be about 1.5
- The distance between various flow straighteners should be $0.2 \times$ the settlement chamber diameter.

5.3. WIND GENERATOR WITH 3 M DIAMETER CIRCULAR OUTLET AND LONG INNER CONE - OUTLET 3A

As was seen in Chapter 3, applying those recommendations to the type of wind generation system used here worked well to reduce turbulence levels. Furthermore theoretical calculations of the TRF, which required the calculation of the pressure drop coefficients, were close to experimental results (provided that initial turbulence levels are not too high), which is why those equations were used again to determine the ideal honeycomb and meshed screen dimensions.

Given the fact that the outlet diameter is 3 m, the ideal cell diameter would have been 2 cm. The closest cell diameter available was $\frac{1}{2}$ in ($\approx 12.7mm$). Table 5.1 shows calculations done using Equation 2.24 for this cell diameter and various cell lengths and wind speeds.

Table 5.1: Pressure drop coefficient calculated for honeycomb with 1/2 inch cell diameter for various cell lengths and wind speeds

Honeycomb pressure drop coefficient K (-)	Wind speed (m/s)				
	Length (m)	2	3	4	5
0.12		0.47	0.45	0.44	0.43
0.13		0.49	0.48	0.47	0.46
0.14		0.52	0.50	0.49	0.48
0.15		0.55	0.53	0.51	0.50

It can be seen that to get a pressure drop coefficient of 0.5 for a wind speed of 2 m/s, the ideal cell length should be 130 mm. The actual cell length was 120 mm. The cell length over cell diameter ratio is therefore 10.5, higher than 8, which was the case in the experiments presented in Chapter 3. The honeycomb was made from aluminium. The honeycomb was built out of 4 pieces held in place through wooden beams.

Table 5.2 shows the pressure drop coefficient calculated using Equation 2.28 for various combinations of open area ratio and wire diameters of meshed screens at a wind speed of 2 m/s. The combinations for which the correct pressure drop coefficient is achieved, that is 1.5, are highlighted in yellow.

Table 5.2: Pressure drop coefficient calculated using Wieghardt's formula for various wire diameters and porosities of meshed screen at a wind speed of 2 m/s

Meshed screen pressure drop coefficient K (-)	wire diameter (μm)									
	porosity (%)	300	350	400	450	500	550	600	650	700
58	1.98	1.88	1.80	1.73	1.67	1.62	1.57	1.53	1.50	
59	1.88	1.79	1.71	1.64	1.59	1.54	1.49	1.45	1.42	
60	1.79	1.70	1.62	1.56	1.51	1.46	1.42	1.38	1.35	
61	1.69	1.61	1.54	1.48	1.43	1.38	1.34	1.31	1.28	
62	1.61	1.53	1.46	1.40	1.35	1.31	1.27	1.24	1.21	
63	1.52	1.45	1.38	1.33	1.28	1.24	1.21	1.18	1.15	
64	1.44	1.37	1.31	1.26	1.22	1.18	1.15	1.11	1.09	
65	1.37	1.30	1.24	1.19	1.15	1.12	1.08	1.06	1.03	
66	1.29	1.23	1.18	1.13	1.09	1.06	1.03	1.00	0.98	

5.3. WIND GENERATOR WITH 3 M DIAMETER CIRCULAR OUTLET AND LONG INNER CONE - OUTLET 3A

Using this information the best screen available from a meshed screen manufacturer was chosen. The meshed screen was a Nylon screen. The mesh opening of this screen is $1550 \mu\text{m}$, the open area ratio is 60 % and the wire diameter is $450 \mu\text{m}$.

Given the fact that the outlet measured 3000 mm, the ideal distance between the honeycomb and the meshed screen would have been $0.2 \times 3000 = 600 \text{ mm}$. For technical reasons, however, this distance was shorter. The meshed screen was positioned at a distance of 490 mm from the end of the honeycomb.



Figure 5.36: Honeycomb upstream of diffuser cone

5.3. WIND GENERATOR WITH 3 M DIAMETER CIRCULAR OUTLET AND LONG INNER CONE - OUTLET 3A



Figure 5.37: Short straight cylindrical section holding the meshed screen (visible) and the honeycomb in place (hidden)



Figure 5.38: Diffuser cone with flow straighteners installed and structure to hold anemometer for measurements

5.3.2 Wind field measured for Outlet 3a

Measurements were done with and without flow straighteners for the following fan rotational speeds: 50, 70, 100 % of the maximum fan rotational speed. Wind speed was measured at various heights and horizontal positions. All measuring points are situated 130 mm behind the end of the outlet, as was the case for Outlet 2a and 2b. The wind was not measured at other distances from the outlet.

For the measurements without flow straighteners, measurements lasting 7 minutes were done at three different heights to check for stability of the flow. None of those measurements showed a clear change in the average wind speed, as can be observed on Figure 5.27, which were observed for measurements lasting only 7 minutes for Outlet 2a. Though this is not a guarantee that there are no such fluctuations anywhere in the whole area, it indicates higher stability of Outlet 3a even before adding flow straighteners. In particular, one minute averages were calculated over each of the 7 minutes and compared for Outlet 3a, and the largest variations found between two of those averages was about 0.56 m/s.

The addition of the flow straightening system clearly improved the air flow, both in terms of turbulence and spatial distribution of average wind speed. As an example, the average longitudinal wind speed, for a fan rotational speed of 100 %, is shown in Figure 5.39 and 5.40 for two different heights. For comparison, Figure 5.40 also shows the CFD results obtained. It can be seen that though in the CFD, the troughs correspond to the position of the dividing panels, in the experimental results, the troughs and peaks are situated in more random positions.

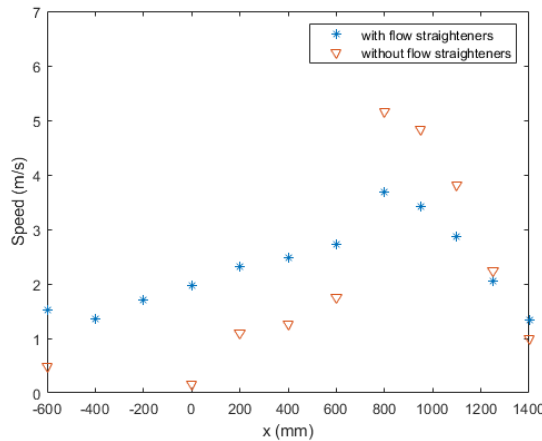


Figure 5.39: Average longitudinal wind speed measured with and without flow straighteners 400 mm below the centre of the outlet

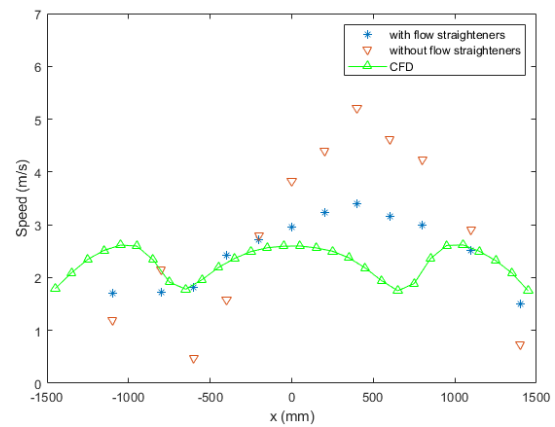


Figure 5.40: Average longitudinal wind speed measured with and without flow straighteners at the centreline of the outlet, CFD results

The same effect can be seen when looking at the whole area (Figures 5.41 and 5.42).

5.3. WIND GENERATOR WITH 3 M DIAMETER CIRCULAR OUTLET AND LONG INNER CONE - OUTLET 3A

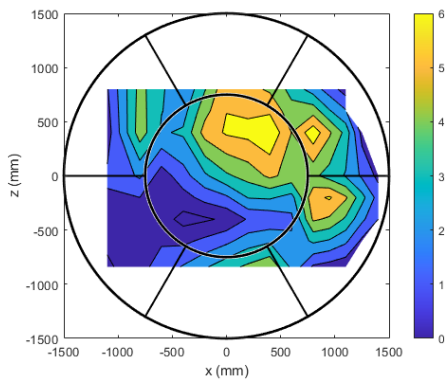


Figure 5.41: Average longitudinal speed measured across the whole area when the flow straighteners are not present

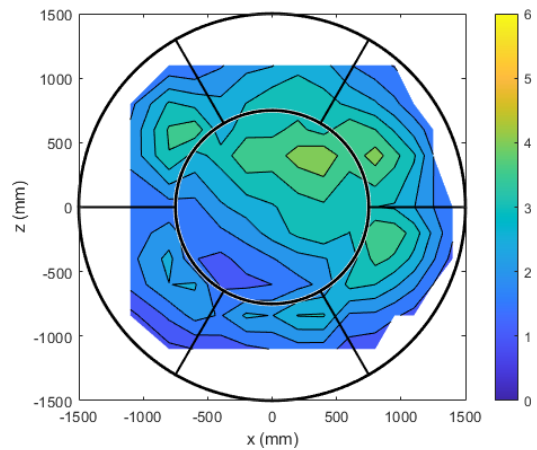


Figure 5.42: Average longitudinal speed measured across the whole area when the flow straighteners are present

The turbulence intensity is also greatly reduced when adding the flow straighteners. Figures 5.43 and 5.44 show the longitudinal turbulence intensity calculated from the wind measurements at the same locations as in Figures 5.39 and 5.40.

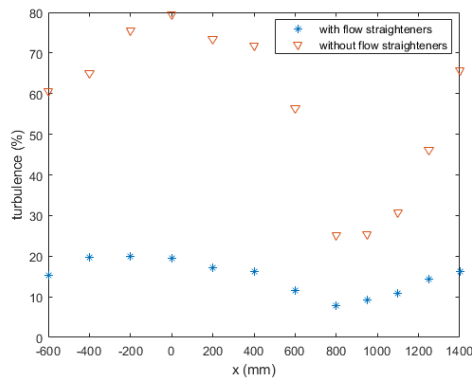


Figure 5.43: Longitudinal turbulence intensity calculated from measurements done with and without flow straighteners 400 mm below the centre of the outlet

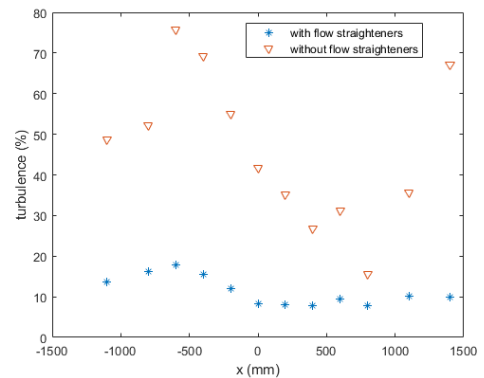


Figure 5.44: Longitudinal turbulence intensity calculated from measurements done with and without flow straighteners at the centreline of the outlet

5.4. 3 M DIAMETER OUTLET IN THE CENTRE OF THE BASIN - OUTLET 3B

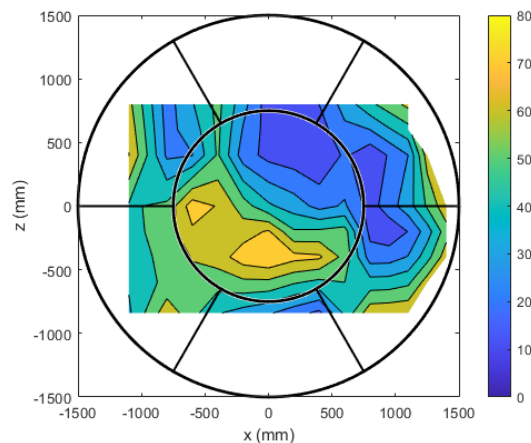


Figure 5.45: Longitudinal turbulence intensity (%) calculated from measurements across the whole area when flow straighteners are not present

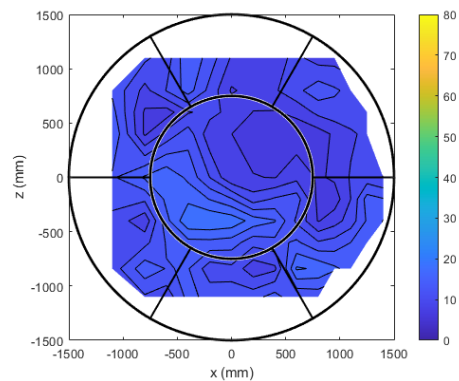


Figure 5.46: Longitudinal turbulence intensity (%) calculated from measurements across the whole area when flow straighteners are present

A comparison was done between the wind generated with and without the inlet honeycomb at the entrance of the diffuser. This first honeycomb significantly improved the longitudinal turbulence at the measured location, causing the turbulence intensity to drop from 25 % to 14 %. One might think that the presence of the honeycomb would cause a slight decrease in the average longitudinal wind speed, as it causes a pressure drop. However, not only is the speed maintained, it is even raised from 1.59 m/s to 1.85 m/s at this location (800 mm above centre, $x=-1100$ mm, fan rotational speed=100 %). The average lateral wind speeds do not change too much. The lateral turbulence intensity is also slightly lowered.

5.4 3 m diameter outlet in the centre of the basin - Outlet 3b

5.4.1 Description of measurements

A last set of experiments consisted in measuring the wind speed produced with Outlet 3a installed at the centre of the basin. For this purpose, the duct arrived with an angle. To correct for the flow instability seen in the measurements for Outlet 1, two set of guide vanes were installed. A schematic drawing can be seen in Figure 5.47 and the set-up is shown in Figure 5.50 and Figure 5.51.

5.4. 3 M DIAMETER OUTLET IN THE CENTRE OF THE BASIN - OUTLET 3B

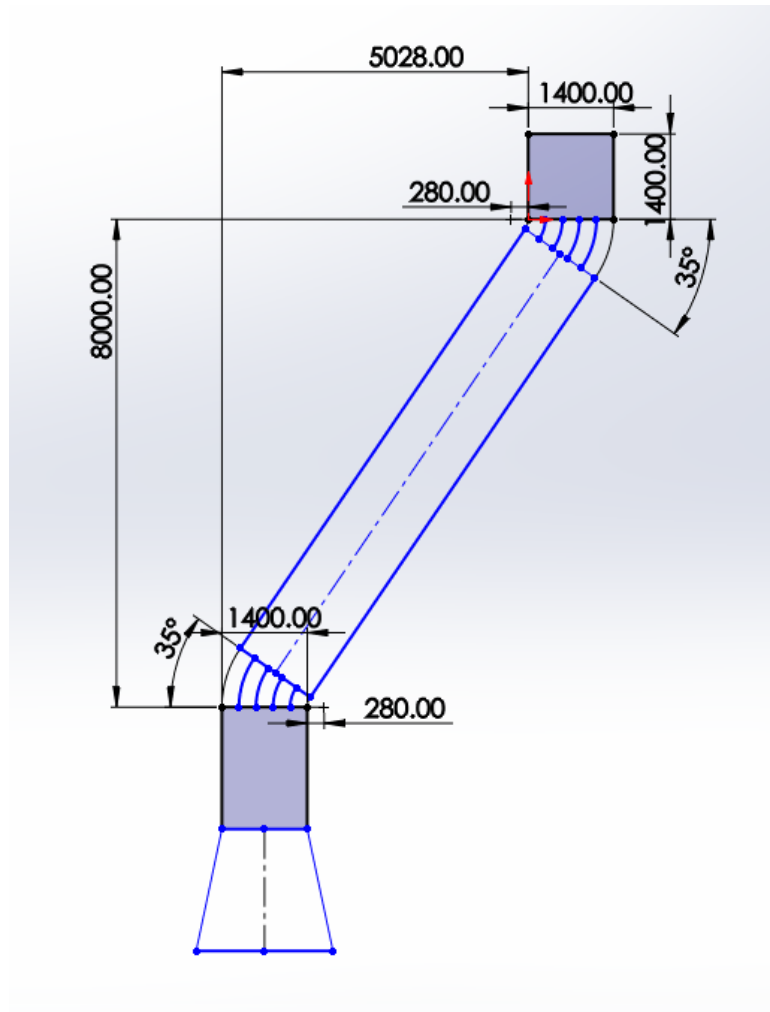


Figure 5.47: Guide vanes



Figure 5.48: Structure near fans including wooden structure to combine air flow of the two fans and first set of guide vanes

5.4. 3 M DIAMETER OUTLET IN THE CENTRE OF THE BASIN - OUTLET 3B



Figure 5.49: Diffuser cone in centre of basin with second set of guide vanes

Figure 5.50 and Figure 5.51 show a general view of the whole system from two different angles.



Figure 5.50: Ducting system from fans to outlet



Figure 5.51: Ducting system from fans to outlet

5.4. 3 M DIAMETER OUTLET IN THE CENTRE OF THE BASIN - OUTLET 3B

Table D.1 in Appendix D.3 shows all the measuring points done at each of the 3 different distances the wind speed was measured at.

The distances at which the wind speed was measured were 130, 630 and 1130 mm from the outlet. The duration of the measurements were again 1 min at a frequency of 32 Hz.

5.4.2 Results

5.4.2.1 Comparison to previous set up

The wind speeds in each of the 3 directions were averaged. Turbulence intensity in each of the 3 directions was calculated. The results were compared to the previous set of measurements, where the duct was arriving straight at the outlet. Table 5.3 shows how the average longitudinal wind speed calculated over one row for the set up where the duct arrives straight and the set up where the duct arrives with an angle.

Table 5.3: Comparison of average wind speed measured at 100 % power of the fans at 130 mm from the outlet when using straight and angled duct

Wind speed (m/s)	Vertical position in mm			
	-1100	-840	0	800
Duct arriving straight	1.32	2.04	2.51	2.63
Duct arriving with an angle	1.43	2.01	2.34	2.55

Table 5.4 shows the standard deviation of the average wind speed on each row (measuring points situated at the same height) for the straight and the angled duct.

Table 5.4: Comparison of standard deviation of average wind speed over measurements done on one height at 100% fan power and at 130 mm from the outlet for straight and angled duct

Standard deviation of wind speed (m/s)	Vertical position in mm			
	-1100	-840	0	800
Duct arriving straight	0.31	0.67	0.66	0.67
Duct arriving with an angle	0.26	0.61	0.9	0.52

Figures 5.52 through 5.55 show the average longitudinal wind speed on each row for the two set ups.

5.4. 3 M DIAMETER OUTLET IN THE CENTRE OF THE BASIN - OUTLET 3B

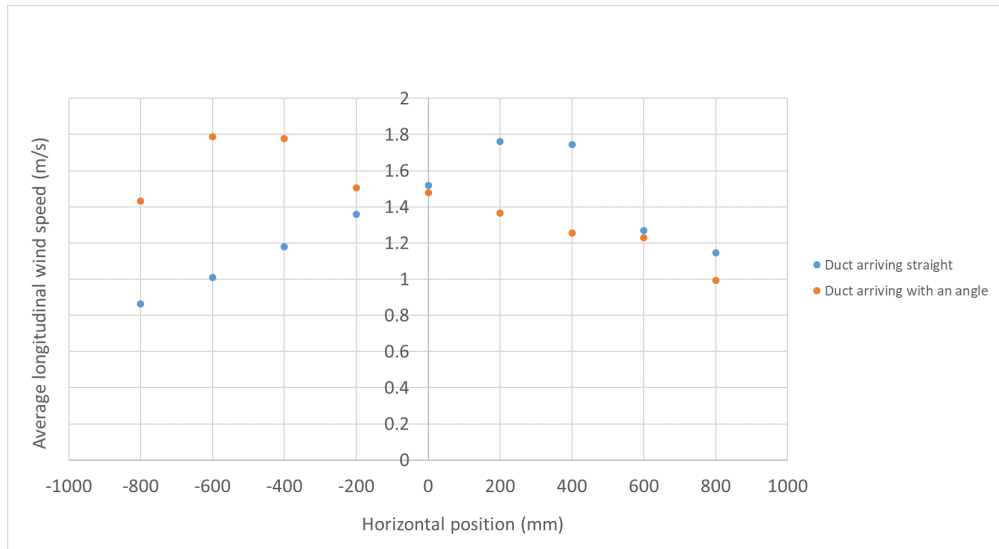


Figure 5.52: Comparison of average longitudinal wind speed at 130 mm from the outlet at 100% fan power and at Height=-1100mm for straight and angled duct

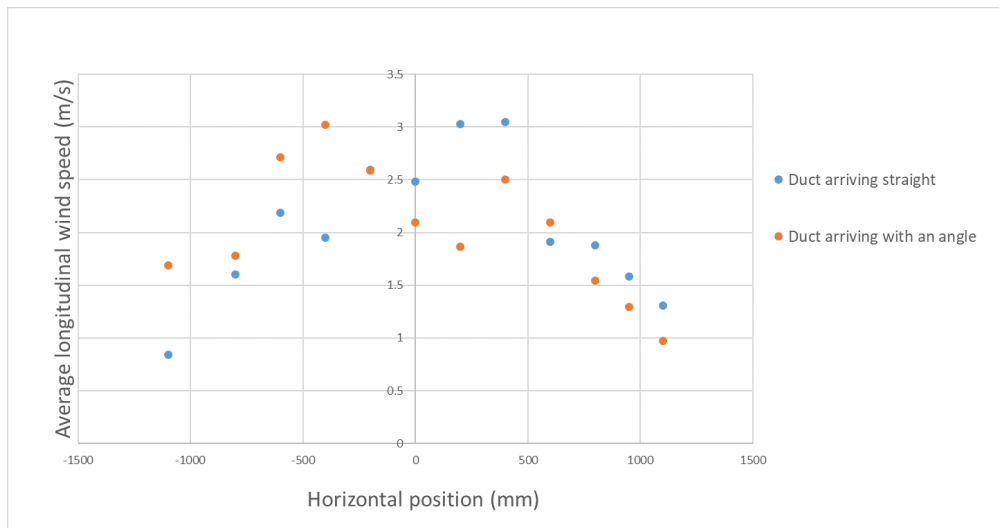


Figure 5.53: Comparison of average longitudinal wind speed at 130 mm from the outlet at 100% fan power and at Height=-840mm for straight and angled duct

5.4. 3 M DIAMETER OUTLET IN THE CENTRE OF THE BASIN - OUTLET 3B

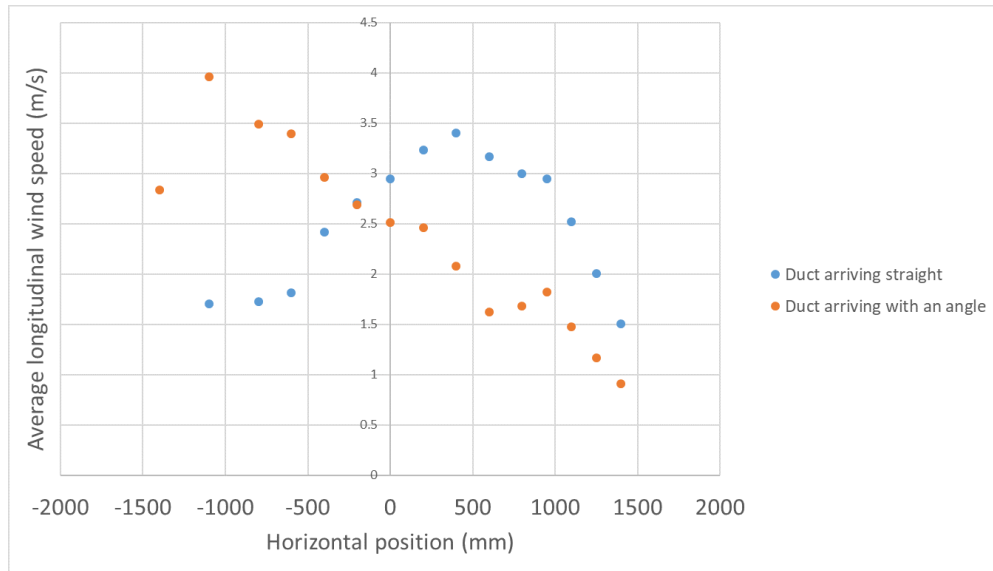


Figure 5.54: Comparison of average longitudinal wind speed at 130 mm from the outlet at 100% fan power and at Height=0mm for straight and angled duct

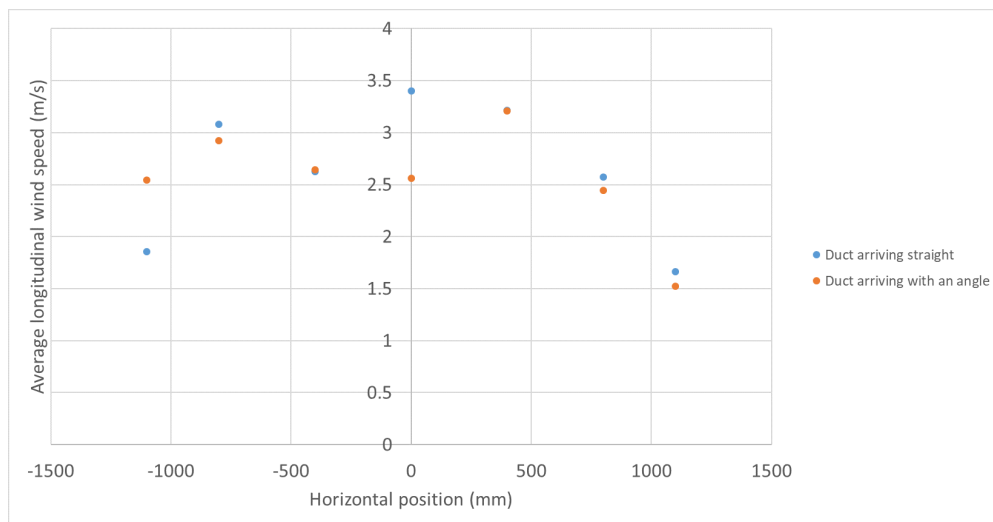


Figure 5.55: Comparison of average longitudinal wind speed at 130 mm from the outlet at 100% fan power and at Height=800mm for straight and angled duct

From the above graphs and tables it can be seen that the angled duct did not affect too much the distribution of the flow on the majority of the rows except the central one. It can be seen that where previously there was a slightly higher wind on the side of positive x values, it is now situated on the side of the negative x values. For heights -1100 mm, -840 mm and 800 mm, the severity of the asymmetry did not get worse. However for the centre line (Height = 0 mm), there is an abnormally high peak on the side of negative x, which should not be there for this flow to be sufficiently evenly distributed to be acceptable.

5.4.2.2 Evolution of wind speed with distance from the outlet

In the first few sets of measurements, the wind speed was measured at the closest position to the outlet where the anemometer could be placed. The wind speed was measured at 2 other distances this time. When the wind is used for a wind turbine, the position of the wind turbine could be at various positions. It was therefore important to get an idea of the evolution of the wind speed and the turbulence intensity when moving away from the outlet.

There is a drop of 0.02 m/s over 1 m (-1%). The evolution seems roughly linear. For the fans working at 70 and 100 % of the full power, the slope is similar. It is steeper for the fans working at 50 % of the full power.

Concerning the longitudinal turbulence intensity, for the fans working at 50 % of the full power, the turbulence intensity increases while moving away from the outlet. For the fans working at 70 and 100 % of the full power, the turbulence intensity is lower at 630 mm than at 130 mm from the outlet. It then is higher at 1130 mm than at 130 mm at 70%. At 100 %, it is still lower at 1130 mm than at 130 mm.

This can be seen in Figure 5.56 and Figure 5.57.

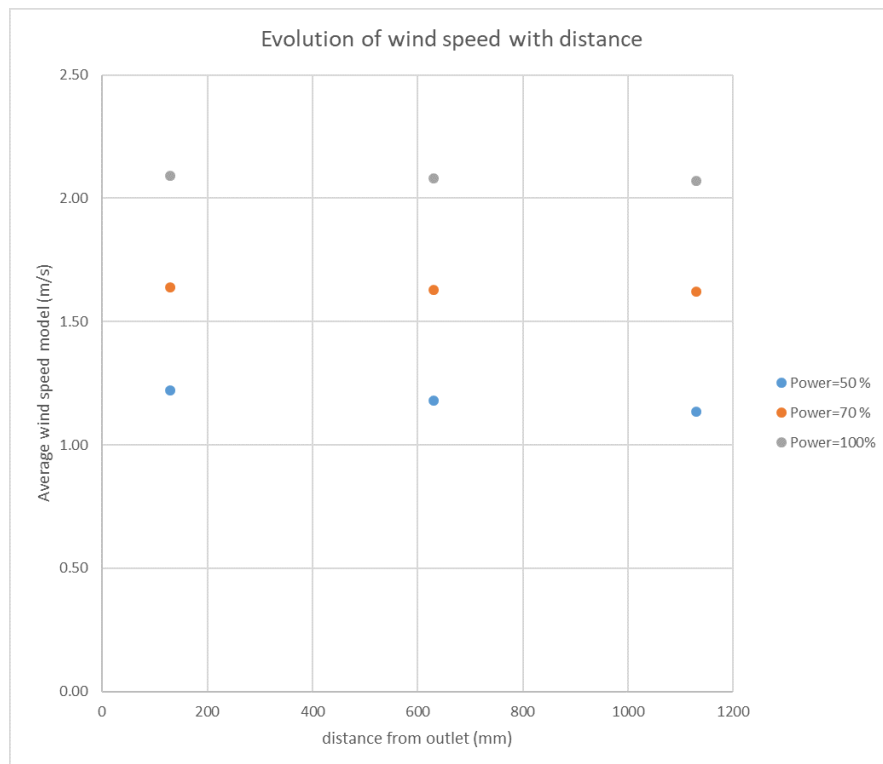


Figure 5.56: Evolution of the average longitudinal wind speed with distance from the outlet for different fan powers

5.5. CONCLUSION FOR THE EXPERIMENTAL STUDY OF THE WIND GENERATION SYSTEMS USING TWO 35.2 KW CENTRIFUGAL FANS

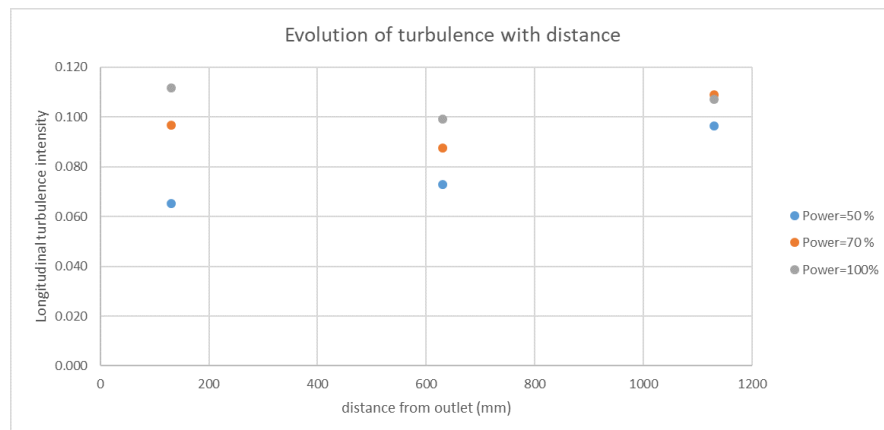


Figure 5.57: Evolution of longitudinal turbulence intensity with distance from outlet for various fan powers

5.5 Conclusion for the experimental study of the wind generation systems using two 35.2 kW centrifugal fans

In Sections 5.1 and 5.2.2.1, it can be seen that blowing air into an expanding diffuser with opening angles of 30° or greater will give an uneven distribution of wind at the outlet, even in the presence of flow straighteners. This fact had also been seen in literature (Section 2.4.6). Furthermore, as had been seen in literature, when the air arrived with an angle in the diffuser (Section 5.1), this asymmetry predetermines the location of the highest wind speed, whereas a symmetric configuration (Section 5.2.2.1) will show high instability.

When looking at the stability map from White (2016) (See Figure 2.63 of Section 2.4.6) and the position of the diffuser cone studied here on this stability map (See Figure 4.15 of Section 4.3), it can be seen that it is indeed in the region of high instability, but also close to the region where the flow tends to stick to one side and flip-flopping back and forth, which actually corresponds more to the behaviour observed for the diffuser cone studied. It is concluded that the boundaries between those regions or zones are not necessarily very strict, and that in particular, as had been mentioned in Sparrow et al. (2009), the Reynolds number also impacts the flow separation, which may have influenced the behaviour observed here, even though the diffuser cone is outside the zone of bistable steady stall.

To mitigate these issues, two configurations with inner cones were studied experimentally. The first one used 3 concentric cones, but only at the beginning of the outlet. The second one used an expansion going over a shorter length, though with the same opening angle, with an inner cone throughout the whole length of the outer cone. The second configuration generated a more even distribution and eliminated areas of back-flow.

A crucial element to not only turbulence intensity, but also even distribution of air flow are flow straighteners (meshed screens and honeycombs). Their presence at the outlet allows great reduction in turbulence intensity but also more even spatial distribution of the wind. The use of a second honeycomb was found useful in some situations. The

5.5. CONCLUSION FOR THE EXPERIMENTAL STUDY OF THE WIND GENERATION SYSTEMS USING TWO 35.2 KW CENTRIFUGAL FANS

asymmetry created by the arrival of the duct with an angle of 35° could however not be improved in spite of their presence.

One could conclude that setting up fans away from the location of where the wind is needed and guiding it to the needed location by means of a system of ducts is not a very efficient method. However, it is believed that the flow could have been better if three conditions had been met. The first one is the use of more powerful fans, which in turn would allow using flow straighteners that would reduce the average wind speed but allow a more even distribution of the wind speed. The second one is the absence of a bend in the duct. In a laboratory where the fans can be installed at the middle of the edge of the basin, instead of near a corner, as was done here, this is a problem which does not need to be overcome. As can be seen in Courbois (2013), the ducting system provided an adequate wind field. The third condition which was met at Ecole Centrale de Nantes was the fact that the wind was not guided from a small diameter to a large one, but instead the 4 ducts used already had the cross section area of the final outlet when added up.

It can be concluded that to achieve even wind distribution using centrifugal fans placed at a location different from where the wind is needed, the combined use of a structure on the inside of the diffuser cone and of flow straighteners is needed. Starting with a larger cross section of the duct can help even if the opening angle is not changed. A duct arriving with an angle should be avoided.

Chapter 6

Model wind turbine design and test using the laboratory wind generation system

The last part of the thesis was dedicated to the design, construction and experimental testing of a model wind turbine rotor, hub and blades. Contrary to a full size wind turbine, where the aerodynamic forces would not only produce sufficient strength to make the turbine spin, but even to produce electricity, the torque produced by the aerodynamic forces at low Reynolds number would comparatively be much lower than the scaled down torque. Indeed, as can be seen in Figure 2.43 of Section 2.3.5.4, though the thrust coefficient of the model wind turbine using a modified blade profile matches closely the thrust coefficient of the full size wind turbine, the power coefficient of the model wind turbine is below the power coefficient of the full size wind turbine. Therefore, rather than have a power take off, the model wind turbine needs a motor to trigger spinning and then allow control of the rotational speed to match the rotor speed of the model wind turbine to the Froude scaled rotor speed of the full size wind turbine.

The motor used was the Maxon DCX26L GB KL 24V motor and it was combined with the planetary gearhead GPX26 LZ 35:1 and the Sensor ENX10 EASY 1024IMP (to measure rotational speed).

Figure 6.1 and Figure 6.2 show images of the wind turbine model built and used for experiments.



Figure 6.1: Model wind turbine



Figure 6.2: Model wind turbine

This chapter will present Blade Element Momentum Method calculations for the model wind turbine, experimental testing of the model wind turbine and comparison of the experimental results to the target thrust and the thrust calculated through the Blade Element Momentum Method.

6.1 Choice of a wind turbine model

It was decided to make a model of the NREL 5 MW reference wind turbine presented in Section 2.2.2. The method to model the wind turbine was to use wind on a model wind turbine using correct wind speed (See Section 2.3.5.4), which requires using a different blade geometry when compared to the prototype. The scale chosen was 1:50. The technical drawing of the wind turbine blade is explained in Appendix E.

6.2 Blade Element Momentum theory applied to the Drela AG04 blade

To be able to predict the performance of the model wind turbine at various combinations of wind speeds, rotor speeds and blade pitch angles, it is useful to be able to do some quick calculations of the aerodynamic loads on the wind turbine. This can also be useful for structural analysis of the turbine blades. One method to do this, when the lift and drag coefficients of the aerodynamic profiles are known, is the Blade Element Momentum (BEM) theory. In the Blade Element Momentum theory, the total aerodynamic force on the blade is determined by summing up the aerodynamic loads on short sections of the blade. On each of those sections, the properties that determine the aerodynamic load are considered to be constant. It is assumed that what happens on one section does not influence what happens on the surrounding sections. The following properties are constant all over the rotor: global pitch of the blade, rotational speed and incoming wind.

The following properties are specific to each section of the blade and are assumed to be constant on one section: the angle of attack (which depends on the global pitch of the blade, the local twist and the local speed triangle), the relative wind speed (which depends on the incoming wind, rotor speed, distance from rotor centre, the global pitch and the local twist), the lift coefficient, the drag coefficient, the chord length and the distance from the hub centre.

The aerodynamic coefficients (lift and drag) depend on the aerodynamic profile, the Reynolds number and the angle of attack. Those coefficients can be obtained from experimental data for a specific aerodynamic profile (Look-up tables), or calculated using XFOIL.

In Hansen (2000), all the calculation steps needed to apply the BEM Method to a given blade are given. In particular, an iterative procedure to calculate axial and tangential induction factors (a and a') is needed, as to calculate those, C_t (tangential load coefficient), C_n (normal load coefficient) and the flow angle are needed, which in turn are impacted by the induction factors. All the formulas needed to apply this method are given in Appendix G.1 in the required order.

In order to apply this theory on the model wind turbine, a code was written in Matlab that followed the iterative procedure described in Hansen (2000) (can be found in Appendix G.1) to determine the axial and tangential induction factors. The lift and drag coefficients were taken from Kimball et al. (2014) and can be found in Appendix G.3. The values of the lift and drag coefficients for the aerodynamic profiles near the hub ("Blends", transition between circular section and Drela AG04 profiles) were not available. Lift and drag coefficients were assumed to be equal to those given by Kimball et al. (2014) for the Drela AG04 profile. The discrepancies between this and the blade

designed here occur near hub, where there is relative low velocity, and are therefore not expected to make a significant difference.

The Matlab code was applied to the wind turbine data at reduced scale, that is, various combinations of wind speed, rotor speed, pitch angle were used as inputs for the code, in addition to the blade geometry data (information on the various sections and the parameters considered constant on each section, that is distance from hub centre, chord length and local twist). The calculations for each section are independent.

6.2.1 Prandtl tip loss factor and Glauert correction

To correct the assumption that the rotor is made up of an infinite number of blades, Prandtl tip loss factor needs to be applied. The fact that the number of blades is finite creates a different vortex system in the wake than if the number of blades was infinite. Some sources also apply Prandtl hub loss correction.

When the axial induction factor a exceeds 0.4, Glauert correction needs to be applied. Figure 6.3 shows the thrust coefficient calculated through the simple momentum theory and compares it with two models determined empirically.

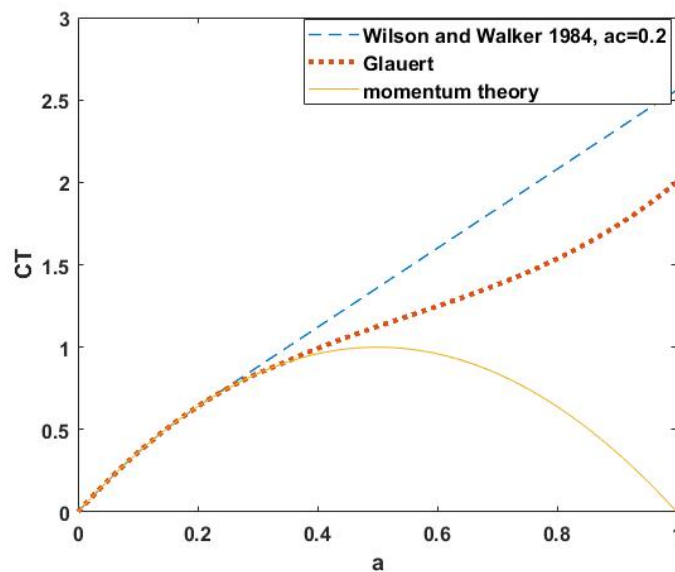


Figure 6.3: C_T before and after Glauert correction, graph inspired by graph from Hansen (2000). Original image is Figure 6.5 on page 54.

Figure 6.4 shows how the wind field is assumed to be when considering the wind turbine to be ideal for the calculation of the thrust coefficient according to the simple momentum theory. The assumption is made that the wind field in the wake of the wind turbine at reduced speed (u_1) when compared to the upstream wind speed (V_0) does not interact with the surrounding wind field. Experience shows that this assumption works when the difference between u_1 and V_0 is not too important. However when $V_0 - u_1$ becomes too important, the free-shear layer at the edge of the wake creates eddies, as seen in Figure 6.5. When the axial induction factor a exceeds 0.4, C_T does

not correspond to the theoretical curve any more, and so various empirical relations for C_T have been established.

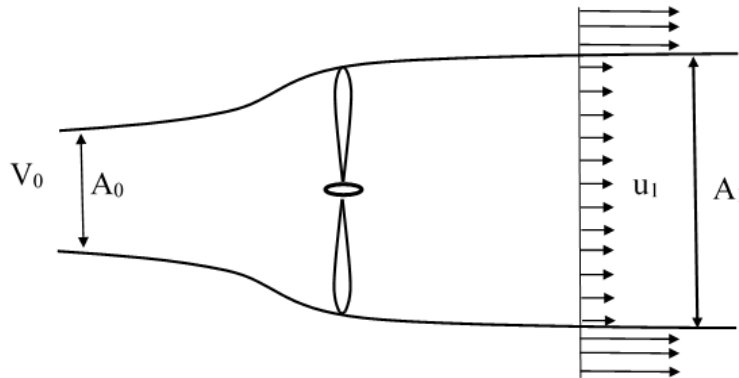


Figure 6.4: Wind field behind an ideal wind turbine, drawing inspired by image found in Hansen (2000). Original image is Figure 4.6 on page 34.

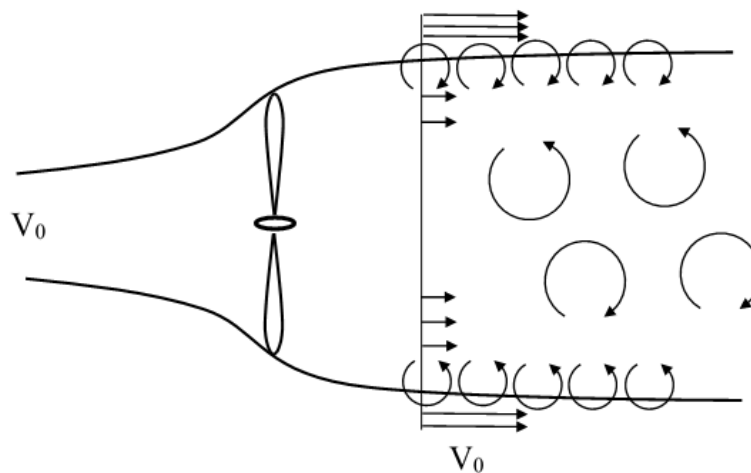


Figure 6.5: Turbulent-wake state induced by the unstable shear flow at the edge of the wake, drawing inspired by image found in Hansen (2000). Original image if Figure 4.7 on page 35.

Formulas for the model used here and alternative models found in literature can be found in Appendix G.2.

6.2.2 Results obtained using the Matlab code for the BEM theory applied to the Drela AG04 blade

The maximum number of iterations was limited to 40. Figure 6.6 shows the thrust calculated when the blade pitch is set at the same angle as the full size wind turbine compared to the thrust aimed to be obtained at scale 1:50.

6.2. BLADE ELEMENT MOMENTUM THEORY APPLIED TO THE DRELA AG04 BLADE

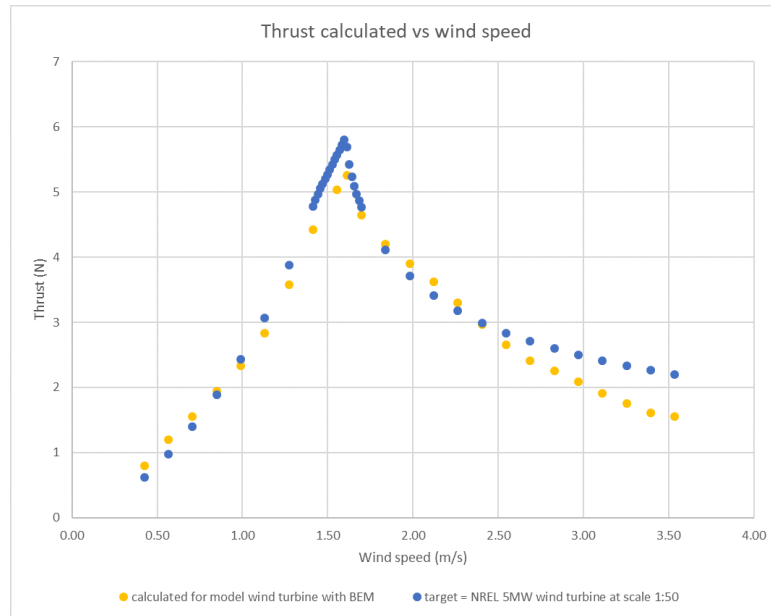


Figure 6.6: Thrust calculated compared to the target thrust

Figure 6.7 shows the torque calculated when the blade pitch is set at the same angle as the full size wind turbine.

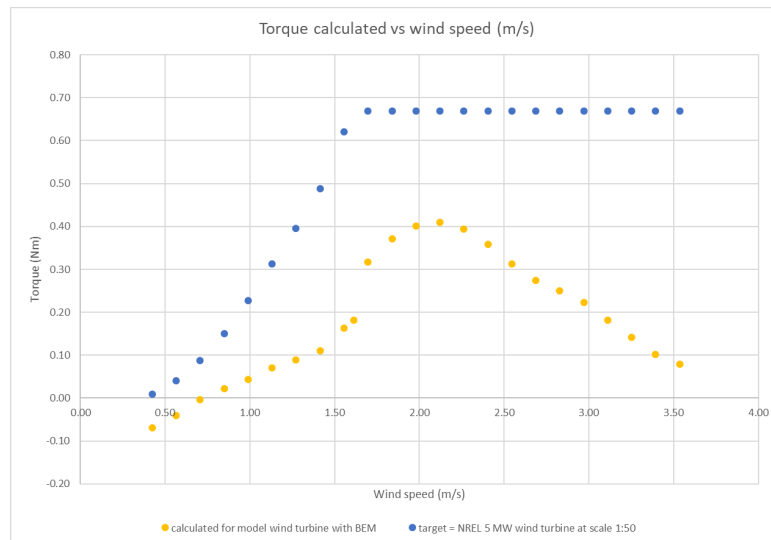


Figure 6.7: Torque calculated for varying blade pitch through BEM code for scaled down combinations of wind speed and rotor speed used for the NREL 5 MW wind turbine

The discrepancy between the target torque and the torque calculated is expected. The blade is designed to yield a correct thrust and the lack of torque is compensated for through the motor. These first calculations seem to show that the model wind turbine was rather well designed to match the scaled down thrust of the full size wind turbine. Small adjustments in the exact pitch angle could be helpful, as well as going slightly

over the scaled down rated wind speed to achieve the maximum thrust. If the experiments confirm the close match between the target thrust and model wind turbine thrust, this shows that the BEM algorithm created for predicting the behaviour of the model wind turbine worked well.

6.3 Blade manufacture

Figure 6.8 shows the three blades manufactured for the experiment. The material used was a carbon fibre prepreg. Calculations for the solidity of the blade are presented in Appendix G.4, and include a CFD calculation followed by an FEA analysis. The thickness of the blades was 0.6 mm, slightly above the total thickness used in the FE Analysis. This thickness was reached using only one layer of a thicker material than what was used for the FE Analysis.



Figure 6.8: Wind turbine blades

The target weight of 140 g per blade could not be met. The blades weighed 285, 286 and 289 g (including an aluminium ring weighing 17 g). This is not expected to create issues in the case of a fixed wind turbine, except that the torque needed to make it spin at a given rotational speed will be more important. And this is only an issue if the capacity of the motor assisting the spinning motion of the rotor is exceeded. However, when combined with a platform, several types of load are expected to be affected, in particular the gyroscopic loads. The difference between the weights of the blades was compensated thanks to balancing, by adding weight on the hub opposite of the heaviest blade.

6.4 Experimental testing of the wind turbine

6.4.1 Description of the wind turbine model

The model wind turbine was equipped with a motor to be able to control the rotational speed. Though at reduced scale one can achieve correctly scaled thrust, the torque is expected to be much lower, possibly insufficient to make the turbine spin through wind alone, even in the absence of a power take off. Furthermore, as there was no power take off, the spinning could get out of hand when the torque would become sufficient, so the motor was also there to work as a break.

6.4. EXPERIMENTAL TESTING OF THE WIND TURBINE

Figure 6.9 shows the model wind turbine set up with the wind generation system. This system was the one described in Section 5.4, with the duct arriving with an angle, and a 3 m diameter outlet. Figure 6.10 shows a close-up look of the model wind turbine.



Figure 6.9: Model wind turbine with wind generation system



Figure 6.10: Model wind turbine

6.4.2 Experimental conditions

The wind turbine was tested with the following conditions: 2 different blade angles were tested, 0° and -30° . For the blade pitch set at -30° , no wind was used. This was to see how much thrust the turbine would produce without a wind generation system, working as a propeller. Additional thrust would need to be provided thanks to a mechanical pulley system, which would correspond to the set-up described in Section 2.3.1 carried out by the Danish Hydraulic Institute (Tomasicchio et al., 2014). For the blade pitch set at 0° , the following wind speeds were tested (described in full size wind speed): 0, 3,

6.4. EXPERIMENTAL TESTING OF THE WIND TURBINE

7, 9, 10, 11.4, 12, 12.5, 13, 13.5 and 14 m/s. A large number of rotational speeds were tested, going from 38 rpm to 104 rpm. A complete list of all measurements done is given in Appendix G.5.

6.4.3 Results

This section will go through the results in the following order: It will first describe the results of the measurements done with the blade pitch angle set at an angle of 0° (to the rotor plane). Only average values of thrust will be looked at. The second subsection will describe the use of the wind turbine without wind, when thrust is solely produced through the motor which makes the turbine spin.

6.4.3.1 Blade pitch angle at 0° with and without wind

The thrust was measured when no wind was blown at the wind turbine and the turbine was made to spin through the motor. In this case, the thrust is negative and the absolute value of the thrust increases as the rotor speed increases. This can be seen in Figure 6.11.

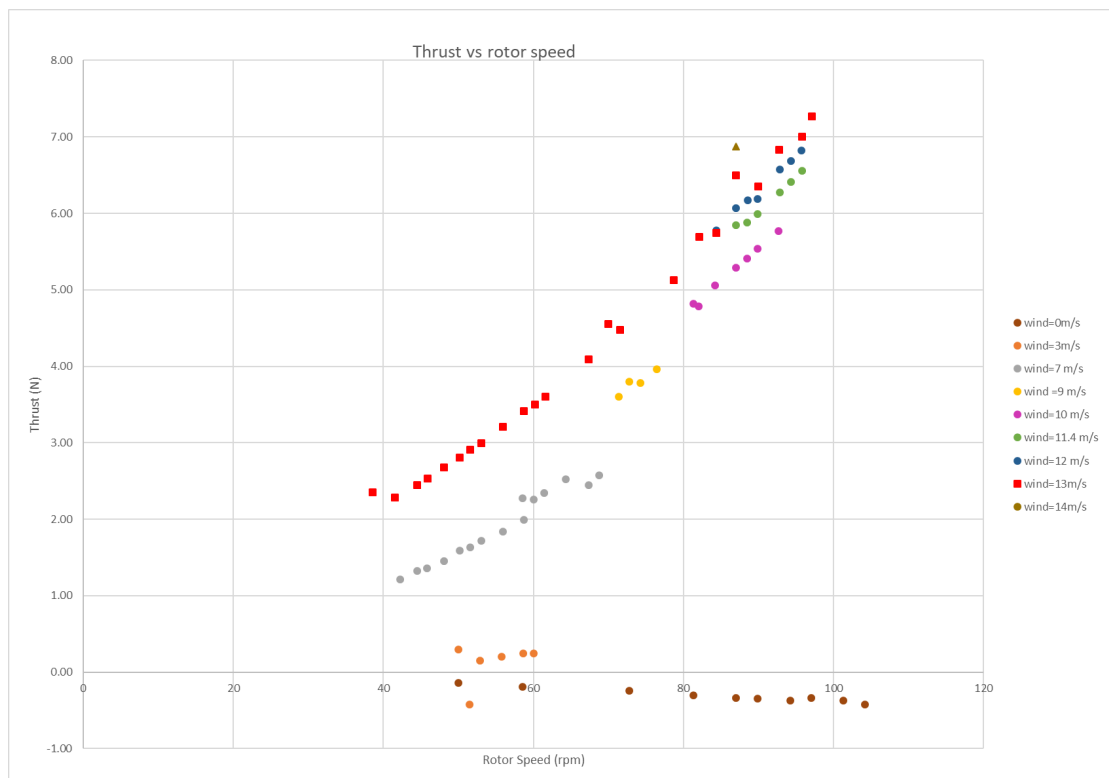


Figure 6.11: Thrust as a function of rotor speed

The thrust produced when the wind speed is at 3 m/s (full size), is just above 0, except for one odd measurement. No real correlation between the evolution of rotor speed and the evolution of the thrust could be established for this case. The increase of thrust with rotor speed can be observed as well as the increase of thrust with wind speed for wind speeds above 7 m/s. This can also be observed when looking at the calculation of

6.4. EXPERIMENTAL TESTING OF THE WIND TURBINE

thrust in the BEM theory (Equation 6.1).

$$Tr = \frac{3}{2}\rho \sum_{\text{Blade section}=1}^{N-1} V_{rel}^2 C_n c \Delta r \quad (6.1)$$

with Tr the thrust, ρ the density of air, N the number of blade sections, V_{rel} the relative wind speed, C_n the normal load coefficient, c the chord and Δr the width of the blade section. The relative wind speed can be calculated according to Equation 6.2.

$$V_{rel} = \sqrt{(V_0(1-a))^2 + (\omega_r r(1+a'))^2} \quad (6.2)$$

with V_0 the upstream wind speed, a the axial induction factor, ω_r the rotor speed, and a' the tangential induction factor. This shows that thrust will increase both with incoming wind speed and with rotor speed. Of course, C_N , a and a' will also depend on incoming wind speed and rotor speed.

A large number of rotor speeds were tested for the wind speed corresponding to 13 m/s at full size. The reason for this was that in Kimball et al. (2014), it was indicated that at this wind speed rated thrust was achieved for rated rotor speed. Also this gives the possibility to compare to the data given in this article, as the blade data from this article was used when manufacturing the blade. Figure 6.12 shows the evolution of C_T with TSR for wind speeds corresponding to 7 and 13 m/s at full scale. Figure 6.13 shows results obtained at MARIN using the MSWT (MARIN stock wind turbine) using the modified Drela AG04 profile. The blade pitch angle was set at 1° , and not 0° as was done here, but it is believed that the results are still comparable. What can be noted is that the curves for "wind speed=13" are very similar, that is starting at $C_T \sim 0.2$ for $TSR=3$ and reaching $C_T \sim 0.7$ for $TSR=7$. Concerning the results of the experiments performed here, the difference between the two wind speeds 7 and 13 m/s is not as important as for the results obtained at MARIN.

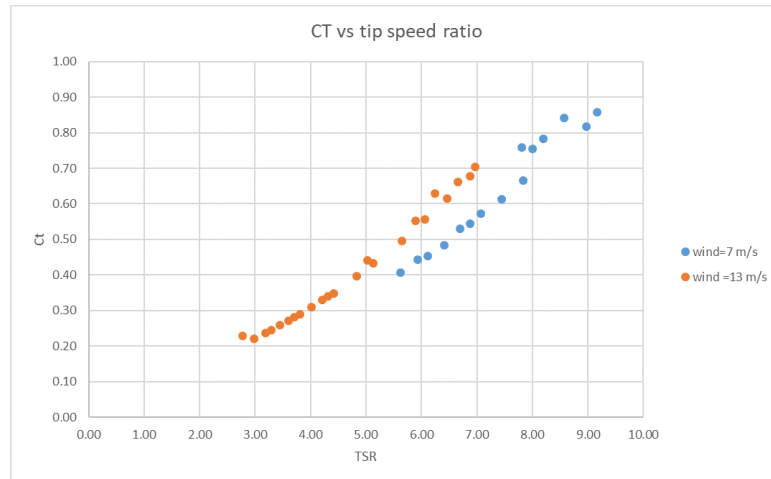


Figure 6.12: Evolution of C_T with TSR for wind speeds 7 and 13 m/s (full scale wind speeds)

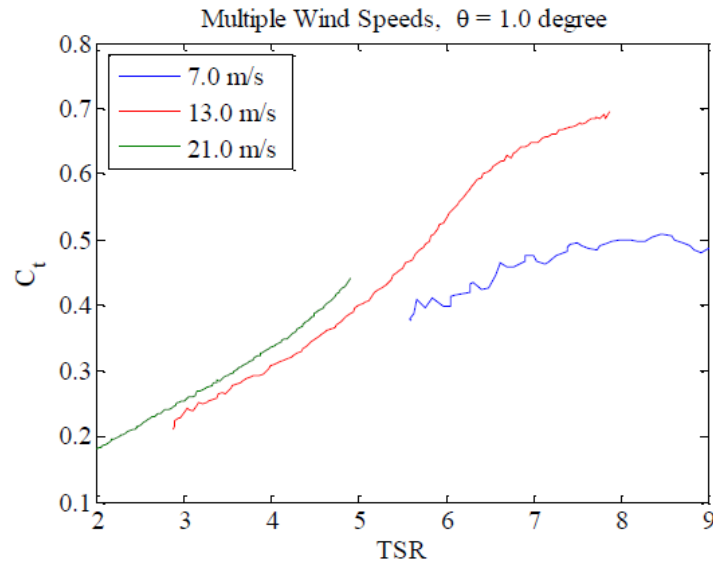


Figure 6.13: Measurements obtained at MARIN using the MSWT (MARIN stock wind turbine) with the modified Drela AG04 profile for three different wind speeds speeds (Kimball et al., 2014). Permission granted by ASME Publishing.

6.4.3.2 Wind turbine used as propeller

The performance of the model turbine was investigated with blade pitch set to -30° , similar to Tomasicchio et al. (2014), so that positive thrust was generated when the blades were rotated without wind.

When doing the measurements, the motor reached a limit at about 70 rpm. When the blades are set to an angle of -30° , this puts the turbine in a position to work as a propeller, which produces thrust without the input of wind. The maximum power of the motor was therefore reached. The turbine could not be spun faster. Rated rotor speed can therefore not be obtained through the method. Figure 6.14 shows the results measured. The maximum thrust obtained was 4 N. If the blades had been closer to the target weight, this value could have been higher. A more powerful motor would probably be needed.

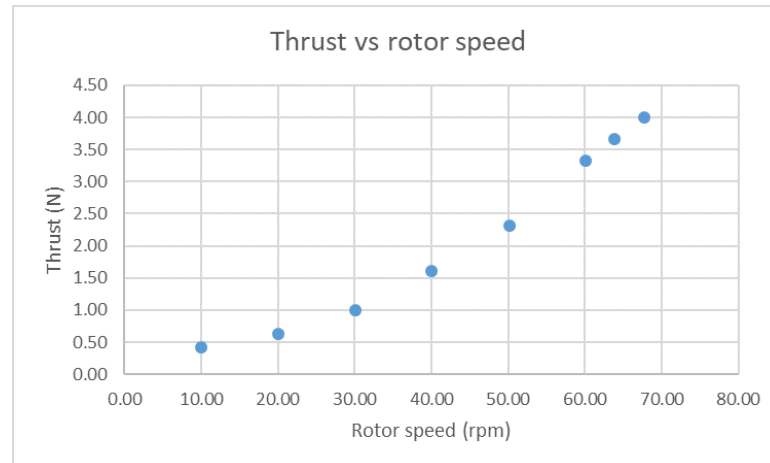


Figure 6.14: Thrust as a function of rotor speed for the case of no wind speed and a blade pitch angle of -30°

6.4.4 Comparison to target thrust and thrust calculated through BEM calculations

The graph of Figure 6.15 allows the comparison of the thrust measured in the experiments to the thrust that needs to be produced to match the scaled-down thrust of the NREL 5 MW reference wind turbine, as well as the thrust calculated for the model wind turbine using the BEM method code. The reason for which the measured thrust keeps on increasing when the thrust should be going down, is that, since modifying the blade pitch was not straightforward for the model wind turbine, all measurements were done with a blade pitch set at 0° , even when the rated wind speed was exceeded. The measured thrust fits rather well for all wind speeds before the rated wind speed, except for 3 m/s. Beyond the rated wind speed, the target thrust should easily be reached by adjusting the exact blade pitch. This means that the model wind turbine is correctly adapted to reproduce the average thrust that one needs to have for a given wind speed. The thrust calculated by the BEM model shows greater deviation from the target thrust. This is believed to be due to the algorithm not converging for every blade section at every wind speed.

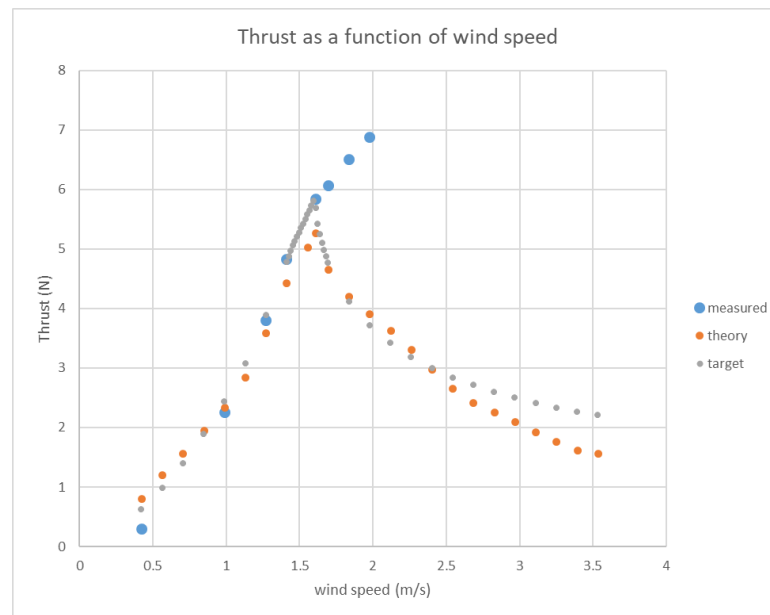


Figure 6.15: Comparison of thrust to be achieved, thrust calculated through BEM method and thrust measured

6.5 Discussion on the use of this method with a floating platform

Though the main load, that is, the average thrust measured, corresponded to what was required, using the model wind turbine in combination with the wind generation system as they are on a floating platform is expected to create a number of problems. One of them is that the wind field being asymmetric, this would create a moment along the vertical axis, due to the wind load on the side of higher wind speeds being more important than on the side of lower wind speeds. This moment would impact the movements of the platform. Another problem is the one related to the blades being over the target weight. Not only is the total weight of the rotor exceeded, but also the inertia of the blades, which will affect gyroscopic loads.

6.6 Conclusion for the experimental study of the model wind turbine

Though the wind field produced by the wind generation system in the laboratory had an asymmetric profile, a first series of experiments done on the model wind turbine showed that it was still possible to obtain an average target thrust on the model wind turbine which corresponded well to the thrust which needed to be produced in order to respect the scaling. This confirms the findings by Kimball et al. (2014) and is an indication that their low Reynolds number design for the blades had been applied properly. Provided that the blade weight issue and can be solved as well as a uniform wind field provided, the turbine could be used for testing floating wind turbine platforms. The wind turbine also demonstrated its potential to be used as a driven rotor in combination with a mechanical pulley system. The total weight of the blades will need to be reduced. The total weight of the nacelle-hub-rotor system, including the instrumentation needs to be determined and compared to the target weight.

Further experiments will need to be done with the current system or an improved ver-

6.6. CONCLUSION FOR THE EXPERIMENTAL STUDY OF THE MODEL WIND TURBINE

sion, on one hand to study the impact of changing the blade pitch angle on the thrust. Also, higher wind speeds need to be tested. Furthermore, dynamic behaviour needs to be looked at. The University of Plymouth intends to adapt the model wind turbine to conduct experiments using the IEA 15 MW reference wind turbine (IEA Wind, 2020).

The BEM code developed to make calculations to predict the performance of the model wind turbine, showed promising results. This confirms that the BEM method is useful for predicting aerodynamic loads on a wind turbine, and could be used to make predictions for various designs of model wind turbine blades, provided the lift and drag coefficients are available beforehand in a look-up table for a given Reynolds number. This could potentially be used as a tool to design variations of wind turbine models using other combinations of aerodynamic profiles and blade offsets.

Chapter 7

Conclusion

Floating offshore wind turbines present several advantages over onshore and offshore bottom-founded wind turbines, amongst which, higher wind and larger areas available for installation, which make the development of floating offshore wind turbine farms key to meeting sustainability goals. Four main types of platform concepts exist, inspired by concepts for oil platforms. For all of them, demonstrators have been installed. The SPAR buoy platform and the semi-submersible platform have been used in commercial scale wind turbine farms. To reduce the cost, improvements in the design and manufacture of the platform as well as the installation process are expected to make a significant impact. Certification of new floating wind turbine platform concepts requires model testing in laboratory.

Froude scaling is crucial for the model study of the platform, as it is exposed to waves, which involves inertial and gravity loads. The Reynolds number being lower in a Froude scaled model test than for a prototype, aerodynamic loads on a geometrically scaled model turbine are expected to not satisfy the loads required in a Froude scaled test. If the purpose of the experimental study of a floating wind turbine is not the study of the wind turbine itself, but the platform, a large number of methods are available to overcome the scaling issues. The choice of these methods can be done depending on the funds or already existing facilities available and the level of accuracy and type of study required.

This project has researched the use of ducted wind generation for applying the aerodynamic loads during scaled model testing. Several conclusions can be drawn from the work presented.

Initial testing used a small wind generation system with a square outlet measuring 0.59 m by 0.59 m. This system was used to study an approach where the cross-sectional area of the ducting between two fans and the outlet was constant and equal to the outlet cross-sectional area. These results demonstrated that such a system could generate an approximately homogenous wind field across 85 % of the outlet width at a distance of 0.5 m from the outlet.

Results using the small wind generation system with 24 different combinations of flow straightening systems, consisting of either a meshed screen, honeycomb or combination of both have been presented. Predictions from previously published equations for pressure drop coefficients and turbulence reduction factors, based on wind tunnels with a settlement chamber and a closed test section, were compared with these measurements. These methods were concluded to work relatively well for open jet blower systems. The formulas slightly under-predicted the effect of honeycombs (experimental TRF is 17 % lower than theoretical TRF on average) and over-predicted the effect of screens on the reduction of longitudinal turbulence (Experimental TRF up to 18 %

higher than theoretical TRF for wind speeds above 6 m/s, and up to 54 % higher than theoretical TRF for wind speeds below 6 m/s).

It can also be concluded from the measurements that the design guidelines for flow straighteners in wind tunnels with a settlement chamber and a closed test section generally worked for the open jet blower system. These predicted well the difference in performance of various meshed screens. However, though differences between the turbulence reduction performance of various honeycombs was predicted, this was not confirmed in the experiments. Honeycomb flow straighteners have also been shown to be effective at suppressing swirl in the generated flow.

Simulations of the measured wind field generated by the small wind generation system have been presented using seven different turbulence models. From these it was found that four models, namely the $k - \omega$ SST, the standard $k - \epsilon$, the RNG $k - \epsilon$ and the realizable $k - \epsilon$ model gave results for the average longitudinal wind speed with a less than 10 % difference compared to the experimental data. However the predictions for turbulence intensity were off by 190-258 % for those four turbulence models.

Due to laboratory size constraints, the constant cross-sectional ducting system was not able to be expanded to the larger system with a 3 m diameter that was required for the COAST laboratory Ocean Basin. As such the use of a conical diffuser outlet to create an evenly distributed wind field over a larger cross-sectional area than the ducting between the fans and outlet has been studied.

Initial experimental and CFD studies using a conical diffuser with an opening angle of 33° with no internal structure generated a wind field that was highly asymmetric and unstable. This supports previously published studies that indicate similar behaviour at these opening angles.

Several methods for distributing wind evenly inside a diffuser cone were investigated. This included the use of a combination of 1 to 3 inner cones at the beginning of the diffuser cone. A second method consisted of a single inner cone covering the whole length of the diffuser cone. These methods were investigated both experimentally and numerically. From the numerical RANS CFD simulations, it can be concluded that:

- Simulations using both the $k - \omega$ SST and the realizable $k - \epsilon$ turbulence models are able to successfully predict the presence of asymmetry in flow due to the presence of an adverse pressure gradient and flow separation that occurs in the diffuser cone without a flow control method.
- The realizable $k - \epsilon$ turbulence model is more stable than the $k - \omega$ SST model when considering the behaviour of grid convergence studies.
- CFD simulations over predict the effectiveness of the flow control methods in generating a perfectly symmetric flow field. This is believed to be due to the assumptions in the simulations that the initial flow field is uniform and that the inner cones had a perfect shape. In reality, this was not the case.
- CFD simulations are able to successfully predict the correct ranking of the experimentally tested flow control methods by order of effectiveness.

The use of inner cones clearly impacted the flow distribution and in many cases suppressed flow separation. Concerning the quality of the improvement of the flow, the following observations were made:

- Certain combinations of inner cones that were present at the beginning of the diffuser cone create symmetric flow but without creating uniform flow (Stronger flow towards the outer edge or on the contrary strong flow only at the centre).
- All combinations of three or less inner cones covering the beginning of the diffuser were investigated at least numerically. However, even the combination which showed the best results amongst all (most inner and most outer cone) did not show a satisfying flow. As the flow measured experimentally tended to be less even than what was shown in the CFD simulations, it was important to find a flow control method which showed satisfying results at least numerically.
- The replacement of the three cones by a long inner cone covering the whole length of the diffuser, according to 3D CFD simulations, was insufficient to create an even flow field.
- Shortening the length of the diffuser without changing the opening angle (therefore using a larger inlet diameter), had an impact on the flow distribution, and this impact was more significant the greater the inlet diameter.
- Two different widths of the long inner cone were studied. The flow distribution was better for the inner cone measuring half the width of the diffuser cone, than when the width was divided in three equal parts by the inner cone (width of inner=1/3 of outer cone).
- The impact of the number of panels holding the long inner cone in place was also investigated and found to have an impact. Between 4, 6 and 8 panels, 6 was found to be give the most even flow distribution.
- A general observation which was made, was that even flow distribution tended to be created thanks to the flow control structures which divided the space up more evenly (same area sizes in each subdivision), whether this was for the effect of the width of the inner long cone, or how the panels surrounding the inner cone divided up the space. This information could potentially be applied when investigating a different type of subdivision.

From these observations, the following conclusions can be drawn regarding the use of a conical diffuser:

- If the cross section of the final outlet needs to be larger than the fan outlet cross section, making this increase early on and also progressively can contribute to a better flow distribution.
- The best combination of short inner cones at the beginning of the diffuser cone was to have two cones, the most outer, and the most inner cone.

-
- When using a cone covering the whole length, the best combination was one with a diameter half the diameter of the diffuser cone, with 6 panels holding it in place.
 - The long inner cone held in place by 6 panels is more efficient for flow control than the two inner cones at the beginning of the diffuser cone.
 - In all cases, the larger the inlet diameter, the better.

Future research could include the following points:

- Refine the CFD simulations by running time-varying simulations or more sophisticated turbulence models to capture fluctuations and turbulent structures in the flow.
- Investigate flow control method efficiencies for opening angles above and below the one studied here.
- Investigate the impact of a small contraction at the end of the outlet.

Flow control methods inside a diffuser cone can alter and improve the flow distribution. However, its application in the context of a wind generation system remains difficult. Such flow control methods can be used in alternative applications, such as in ventilation systems. For a wind generation system, a bank of axial fans is an alternative solution, which presents the added benefit of the potential to produce sheared wind profiles.

Appendices

Appendix A

NREL 5 MW reference wind turbine data

A.1 Properties of the NREL 5 MW reference wind turbine at full scale and at reduced scale

Table A.1: Properties of the NREL 5 MW reference wind turbine (source: NREL (2019))

Wind speed full size (m/s)	Wind speed model (m/s)	TSR (-)	Rotor speed full size (rpm)	Rotor speed model (rpm)	Blade pitch (°)	Rotor thrust (kN)	Rotor thrust model (N)
3	0.42	15.32	6.97	49.30	0	77.65	0.62
4	0.57	11.84	7.18	50.79	0	121.85	0.97
5	0.71	9.90	7.51	53.08	0	174.85	1.40
6	0.85	8.72	7.94	56.16	0	236.25	1.89
7	0.99	7.97	8.47	59.88	0	304.55	2.44
8	1.13	7.54	9.16	64.74	0	383.95	3.07
9	1.27	7.54	10.30	72.80	0	485.15	3.88
10	1.41	7.54	11.43	80.83	0	597.45	4.78
10.1	1.43	7.53	11.55	81.65	0	609.27	4.87
10.2	1.44	7.53	11.66	82.45	0	621.20	4.97
10.3	1.46	7.50	11.73	82.94	0	631.72	5.05
10.4	1.47	7.45	11.75	83.09	0	640.83	5.13
10.5	1.48	7.39	11.77	83.23	0	649.99	5.20
10.6	1.50	7.33	11.80	83.43	0	659.20	5.27
10.7	1.51	7.28	11.82	83.58	0	668.48	5.35
10.8	1.53	7.23	11.84	83.72	0	677.78	5.42
10.9	1.54	7.18	11.87	83.93	0	687.14	5.50
11	1.56	7.13	11.89	84.07	0	696.55	5.57
11.1	1.57	7.08	11.92	84.26	0	706.05	5.65
11.2	1.58	7.03	11.94	84.43	0	715.62	5.72
11.3	1.60	6.98	11.97	84.61	0	725.22	5.80
11.4	1.61	7.00	12.11	85.61	0.60	711.06	5.69

A.1. PROPERTIES OF THE NREL 5 MW REFERENCE WIND TURBINE AT FULL SCALE AND AT REDUCED SCALE

Table A.1: Properties of the NREL 5 MW reference wind turbine (source: NREL (2019))

Wind speed full size (m/s)	Wind speed model (m/s)	TSR (-)	Rotor speed full size (rpm)	Rotor speed model (rpm)	Blade pitch (°)	Rotor thrust (kN)	Rotor thrust model (N)
11.5	1.63	6.93	12.10	85.55	1.45	677.62	5.42
11.6	1.64	6.88	12.10	85.56	2.08	654.69	5.24
11.7	1.65	6.82	12.10	85.56	2.59	636.67	5.09
11.8	1.67	6.76	12.10	85.56	3.04	621.36	4.97
11.9	1.68	6.70	12.10	85.56	3.45	607.94	4.86
12	1.70	6.65	12.10	85.56	3.82	595.95	4.77
13	1.84	6.14	12.10	85.56	6.60	514.35	4.11
14	1.98	5.70	12.10	85.56	8.67	463.85	3.71
15	2.12	5.32	12.10	85.56	10.45	426.45	3.41
16	2.26	4.98	12.10	85.56	12.06	397.15	3.18
17	2.40	4.69	12.10	85.56	13.54	373.65	2.99
18	2.55	4.43	12.10	85.56	14.92	354.35	2.83
19	2.69	4.20	12.10	85.56	16.23	338.25	2.71
20	2.83	3.99	12.10	85.56	17.47	324.75	2.60
21	2.97	3.80	12.10	85.56	18.70	312.65	2.50
22	3.11	3.63	12.10	85.56	19.94	301.25	2.41
23	3.25	3.47	12.10	85.56	21.18	291.05	2.33
24	3.39	3.32	12.10	85.56	22.35	282.65	2.26
25	3.54	3.19	12.10	85.56	23.47	275.25	2.20

The values given in NREL (2019) for the rotor thrust included a portion of the weight of the wind turbine. This is because because the values given by NREL are values that would be measured on a tilted shaft. They thus included a value corresponding to $m_{rotor}g \sin(5^\circ)$ which needed to be taken off to get the pure aerodynamic thrust, which is the value indicated in Table A.1.

A.1. PROPERTIES OF THE NREL 5 MW REFERENCE WIND TURBINE AT FULL SCALE AND AT REDUCED SCALE

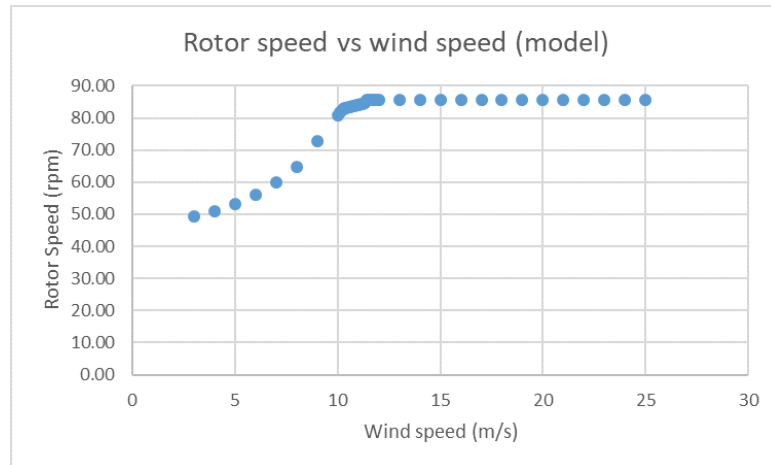


Figure A.1: Rotor speed of model wind turbine

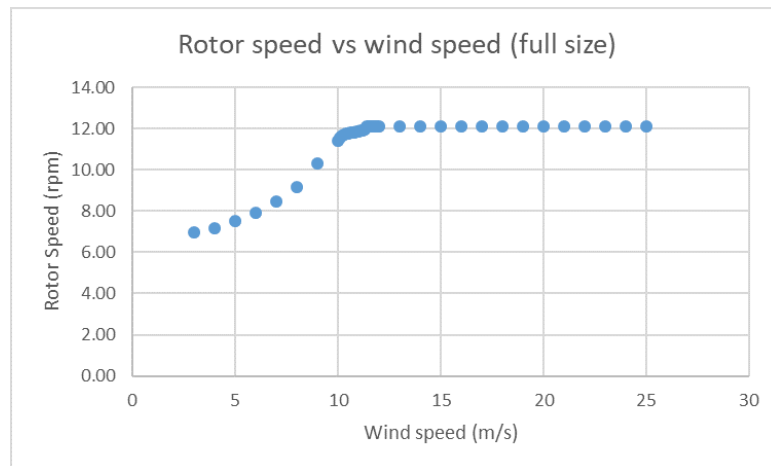


Figure A.2: Rotor speed of full size wind turbine

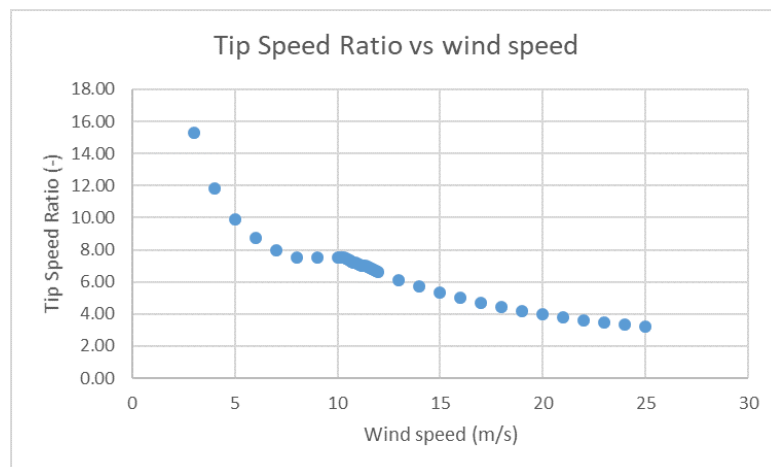


Figure A.3: Tip Speed ratio

A.1. PROPERTIES OF THE NREL 5 MW REFERENCE WIND TURBINE AT FULL SCALE AND AT REDUCED SCALE

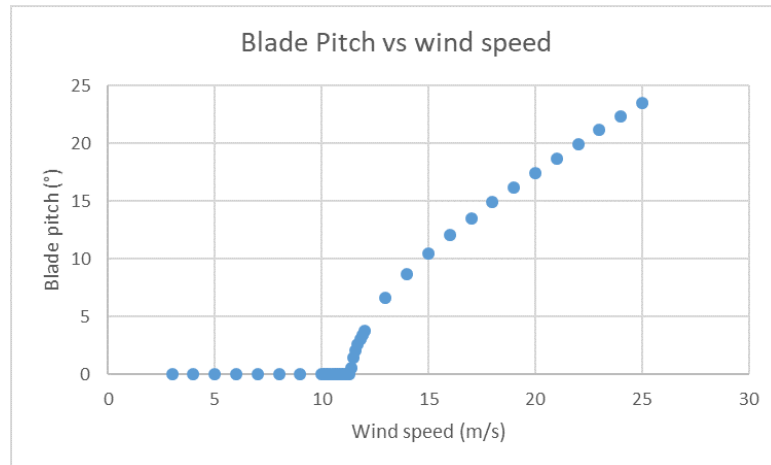


Figure A.4: Blade pitch

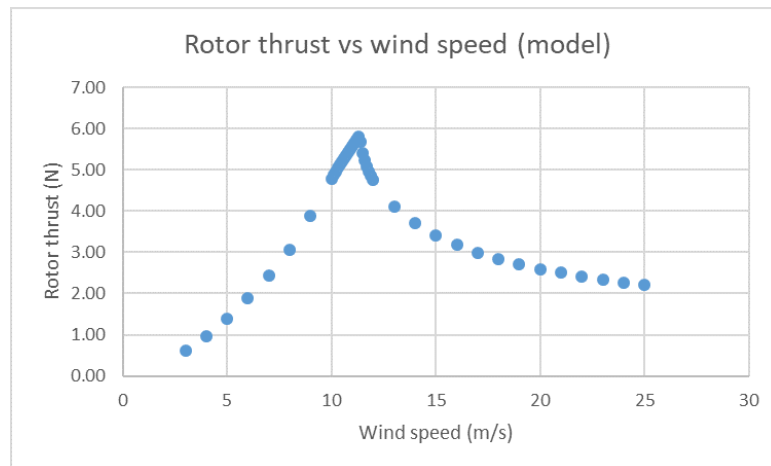


Figure A.5: Rotor thrust of model wind turbine

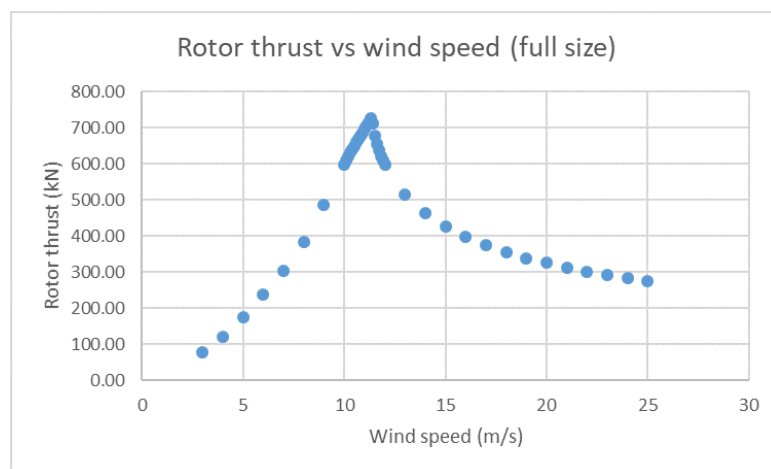


Figure A.6: Rotor thrust full size wind turbine

A.2 NREL 5 MW reference wind turbine blade geometry

Table A.2: NREL 5 MW reference wind turbine blade geometry

Blade section number	distance from rotor centre (m)	chord (m)	twist (°)	Airfoil
1	2.8667	3.542	13.308	Cylinder 1
2	5.6	3.854	13.308	Cylinder 1
3	8.3333	4.167	13.308	Cylinder 2
4	11.75	4.557	13.308	DU40_A17
5	15.85	4.652	11.48	DU35_A17
6	19.95	4.458	10.162	DU35_A17
7	24.05	4.249	9.011	DU30_A17
8	28.15	4.007	7.795	DU25_A17
9	32.25	3.748	6.544	DU25_A17
10	36.35	3.502	5.361	DU21_A17
11	40.45	3.256	4.188	DU21_A17
12	44.55	3.010	3.125	NACA64_A17
13	48.65	2.764	2.319	NACA64_A17
14	52.75	2.518	1.526	NACA64_A17
15	56.1667	2.313	0.863	NACA64_A17
16	58.9	2.086	0.37	NACA64_A17
17	61.6333	1.419	0.106	NACA64_A17

Appendix B

Additional information on experiments with the small fans

B.1 Overview of measurements done for the set up with the small fans

Table B.1 shows all combinations and fan electric frequencies for which measurements were done and at what distances from the outlet. The ones highlighted in yellow are those for which measurements were done not only on the central axis, but at various distances to the side or above the central axis, staying in a plane perpendicular to the central axis.

B.1. OVERVIEW OF MEASUREMENTS DONE FOR THE SET UP WITH THE SMALL FANS

Table B.1: Overview of experiments done

	Honeycomb cell diameter (mm)				
Screen wire diameter (μm)	3	4	6	12	No honeycomb
73	5 Hz, 10 Hz, 20 Hz, 20.9 Hz, 25 Hz, 30 Hz, 35 Hz	5 Hz, 10 Hz, 20 Hz, 20.9 Hz, 25 Hz, 30 Hz	5 Hz, 10 Hz, 20 Hz, 20.9 Hz, 25 Hz, 30 Hz	5 Hz, 10 Hz, 20 Hz, 20.9 Hz, 25 Hz, 30 Hz, 35 Hz, 40 Hz	20.9 Hz
320	20.9 Hz	5 Hz, 10 Hz, 20 Hz, 20.9 Hz, 25 Hz, 30 Hz, acceleration and deceleration to and from 30 Hz	20.9 Hz	1 Hz, 2 Hz, 3 Hz, 4 Hz, 5 Hz, 10 Hz, 20 Hz, 20.9 Hz, 25 Hz, 30 Hz, 35 Hz, 40 Hz, 45 Hz, 50 Hz	20.9 Hz
500	5 Hz, 10 Hz, 20 Hz, 25 Hz, 30 Hz	5 Hz, 10 Hz, 20 Hz, 25 Hz, 30 Hz	5 Hz, 10 Hz, 20 Hz, 25 Hz, 30 Hz	5 Hz, 10 Hz, 20 Hz, 25 Hz, 30 Hz, 35 Hz, 40 Hz	5 Hz, 10 Hz, 20 Hz, 25 Hz, 30 Hz
1000	5 Hz, 10 Hz, 20 Hz, 25 Hz, 30 Hz	5 Hz, 10 Hz, 20 Hz, 25 Hz, 30 Hz	5 Hz, 10 Hz, 20 Hz, 25 Hz, 30 Hz	5 Hz, 10 Hz, 20 Hz, 25 Hz, 30 Hz, 35 Hz, 40 Hz	5 Hz, 10 Hz, 20 Hz, 25 Hz, 30 Hz
No screen	20.9 Hz	20.9 Hz	20.9 Hz	5 Hz, 10 Hz, 20 Hz, 20.9 Hz, 25 Hz, 30 Hz, 35 Hz, 40 Hz, 45 Hz, 50 Hz	5 Hz, 10 Hz, 20 Hz

The colour code for this table is as follows:

- 0.25 m, 0.5 m, 1 m
- 0.5 m, 1 m
- 0.25 m, 0.5 m, 1 m, 1.25 m
- 0.25 m

B.2 Properties of the small centrifugal fans

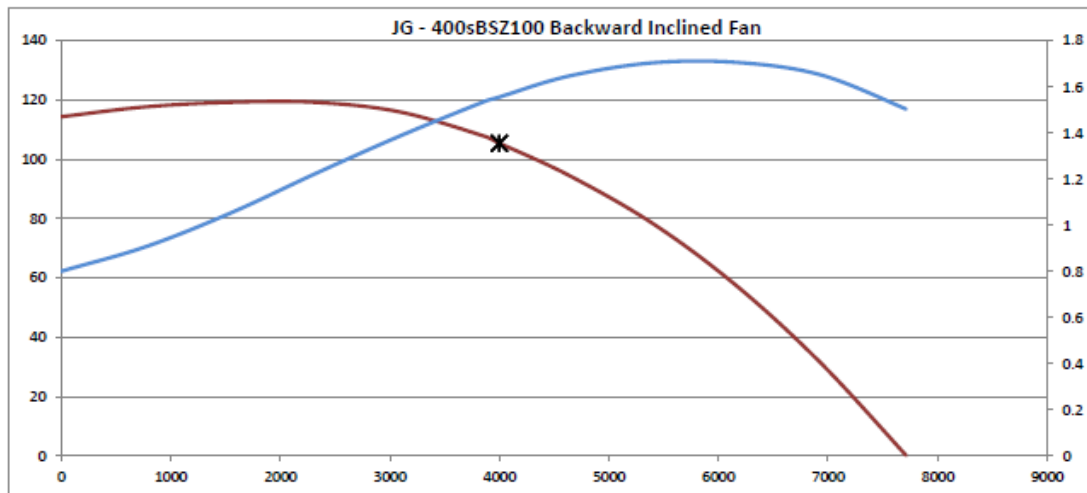


Figure B.1: Properties of the 1.8 kW centrifugal fans (Fans & Blowers Ltd. (2016))

B.2.1 Flow rate

To make estimations for the power needed to produce sufficient wind for a larger outlet, the measurements done with this set up were used to calculate the flow rate produced by one of the two 1.8 kW fans. The result is given in Table B.2 as a function of the electric frequency.

Table B.2: Flow rate calculated for one small centrifugal fan as a function of electric frequency

Frequency (Hz)	Flow rate (1 fan, m^3/s)	Flow rate (1 fan, m^3/h)
50	1.92	6900
45	1.76	6300
40	1.64	5900
35	1.39	4950
30	1.25	4500
20.9	0.76	2750

When compared to the data given by the company who sold the fan (Appendix B.2), it can be seen that the set up studied here led to a relatively small pressure drop only.

Appendix C

Snapshots of CFD simulations for the large wind generation system

C.1 Snapshots of CFD simulations for 1 m to 3 m diameter diffuser with and without various inner concentric cones

C.1.1 Empty cone



Figure C.1: Wind speed in slice parallel to the main direction of the airflow

C.1. SNAPSHOTS OF CFD SIMULATIONS FOR 1 M TO 3 M DIAMETER DIFFUSER WITH AND WITHOUT VARIOUS INNER CONCENTRIC CONES

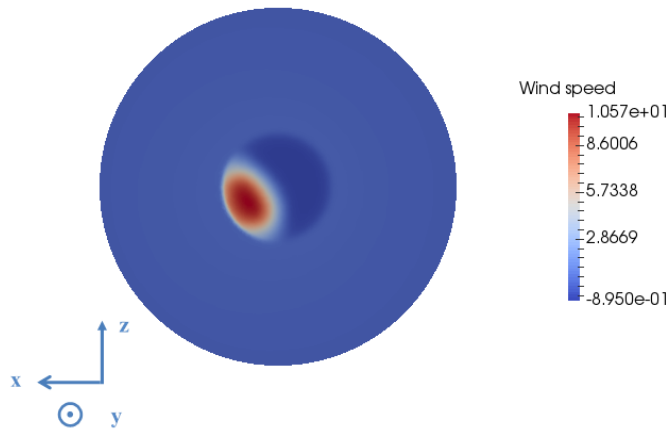


Figure C.2: Wind speed in slice perpendicular to the main direction of the air flow

C.1.2 Set of 3 concentric cones



Figure C.3: Wind speed in slice parallel to the main direction of the airflow

C.1. SNAPSHOTS OF CFD SIMULATIONS FOR 1 M TO 3 M DIAMETER DIFFUSER WITH AND WITHOUT VARIOUS INNER CONCENTRIC CONES

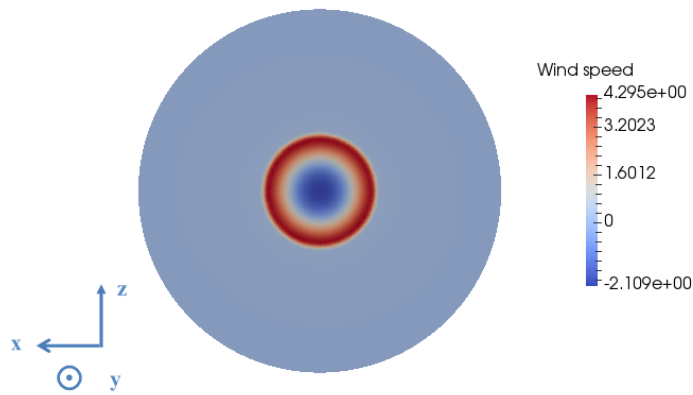


Figure C.4: Wind speed in slice perpendicular to the main direction of the flow

C.1.3 2 external cones only



Figure C.5: Wind speed in slice parallel to the main direction of the flow

C.1. SNAPSHOTS OF CFD SIMULATIONS FOR 1 M TO 3 M DIAMETER DIFFUSER WITH AND WITHOUT VARIOUS INNER CONCENTRIC CONES

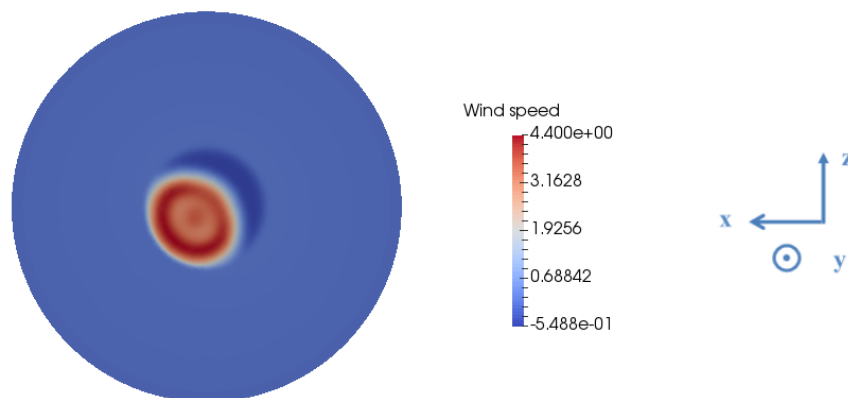


Figure C.6: Wind speed in slice perpendicular to the main direction of the flow

C.1.4 2 inner cones



Figure C.7: Wind speed in slice parallel to the main direction of the air flow

C.1. SNAPSHOTS OF CFD SIMULATIONS FOR 1 M TO 3 M DIAMETER DIFFUSER WITH AND WITHOUT VARIOUS INNER CONCENTRIC CONES

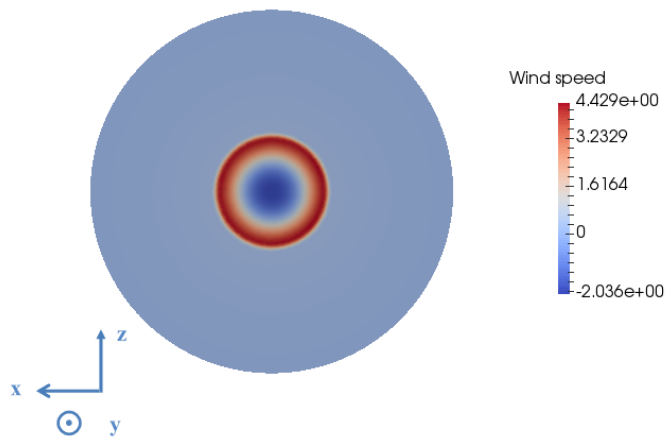


Figure C.8: Wind speed in slice perpendicular to the main direction of the air flow

C.1.5 Most outer cone



Figure C.9: Wind speed in slice parallel to the main direction of air flow

C.1. SNAPSHOTS OF CFD SIMULATIONS FOR 1 M TO 3 M DIAMETER DIFFUSER WITH AND WITHOUT VARIOUS INNER CONCENTRIC CONES

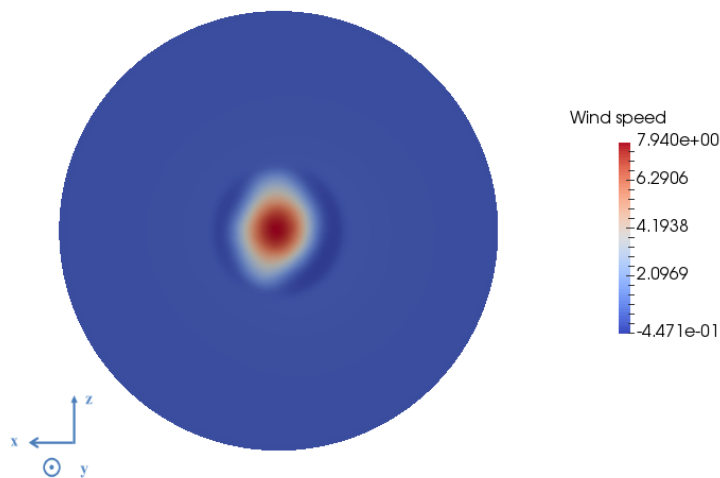


Figure C.10: Wind speed in slice perpendicular to the main direction of air flow

C.1.6 Most inner cone



Figure C.11: Wind speed in slice parallel to the main direction of air flow

C.1. SNAPSHOTS OF CFD SIMULATIONS FOR 1 M TO 3 M DIAMETER DIFFUSER WITH AND WITHOUT VARIOUS INNER CONCENTRIC CONES

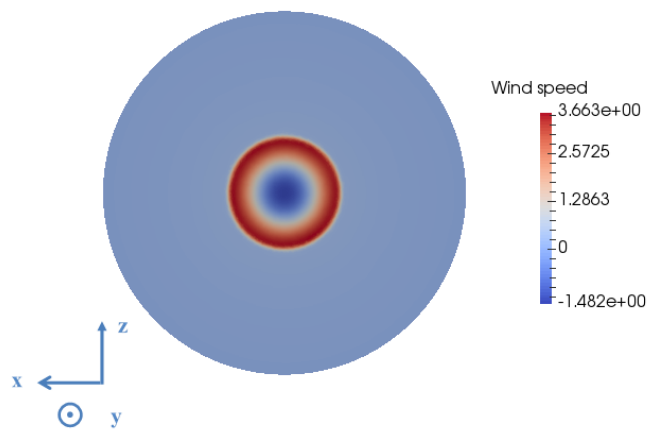


Figure C.12: Wind speed in slice perpendicular to the main direction of air flow

C.1.7 Most inner and most outer cone



Figure C.13: Wind speed in slice parallel to the main direction of air flow

C.1. SNAPSHOTS OF CFD SIMULATIONS FOR 1 M TO 3 M DIAMETER DIFFUSER WITH AND WITHOUT VARIOUS INNER CONCENTRIC CONES

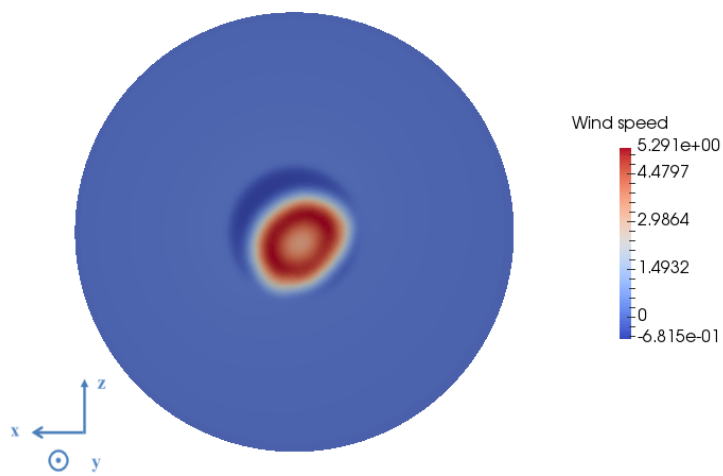


Figure C.14: Wind speed in slice perpendicular to the main direction of air flow

C.1.8 Central cone



Figure C.15: Wind speed in slice parallel to the main direction of the air flow

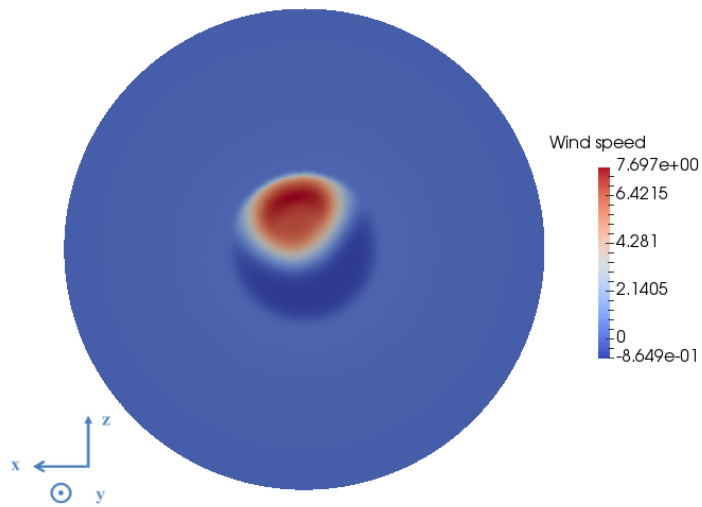


Figure C.16: Wind speed in slice perpendicular to the main direction of the air flow

C.2 Snapshots of CFD simulations with long inner cone

C.2.1 Cone length 3.4 m, 1 m diameter inlet, no subdivisions, narrow



Figure C.17: Slice parallel to main direction of flow

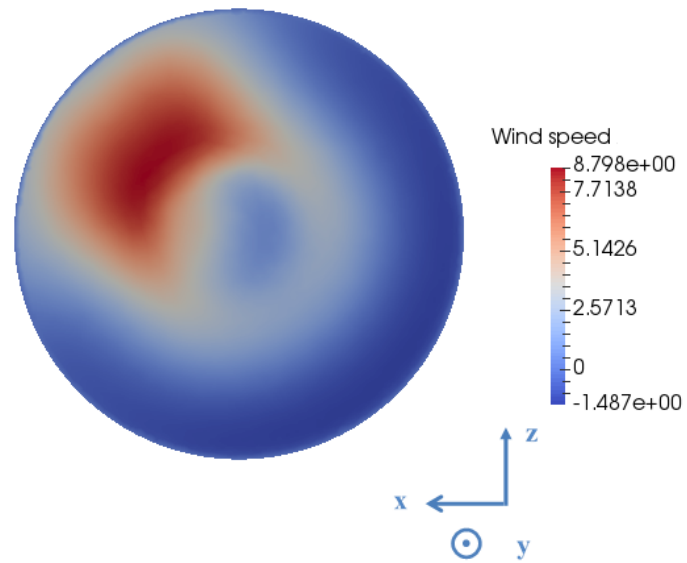


Figure C.18: Slice perpendicular to main direction of airflow

C.2.2 Cone length 2.72 m, 1.4 m diameter inlet, no subdivisions, narrow

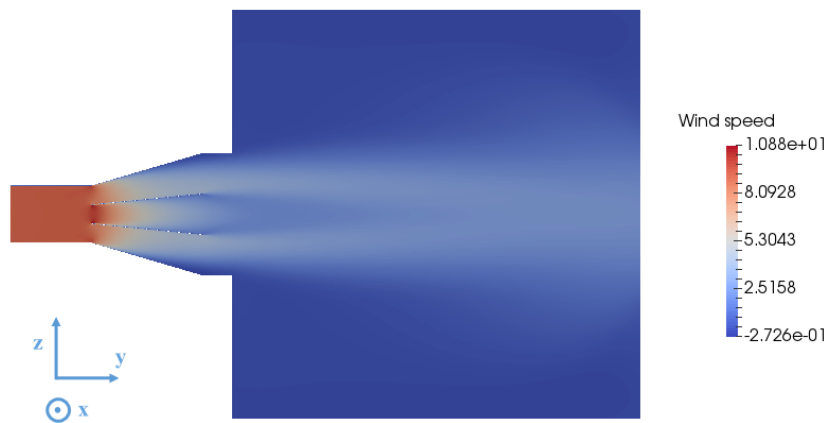


Figure C.19: Slice parallel to main direction of flow

C.2. SNAPSHOTS OF CFD SIMULATIONS WITH LONG INNER CONE

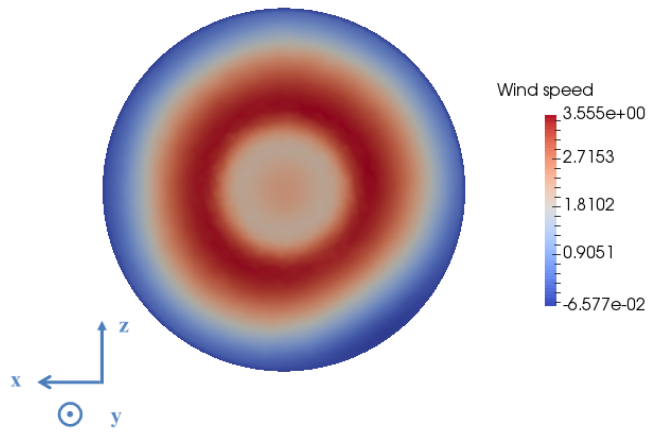


Figure C.20: Slice perpendicular to main direction of flow

C.2.3 Cone length 2.04 m, 1.8 m diameter inlet, no subdivisions, narrow

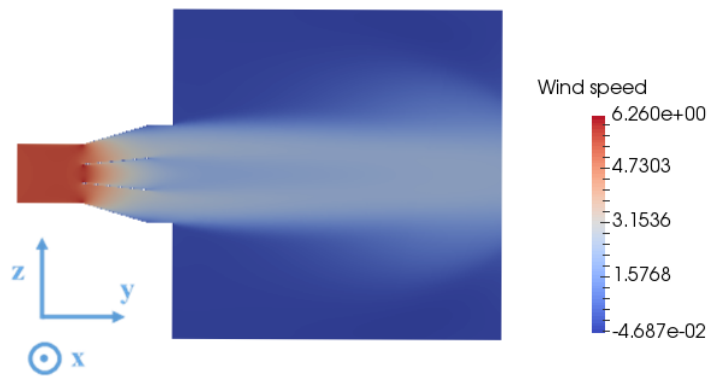


Figure C.21: Slice parallel to main flow direction

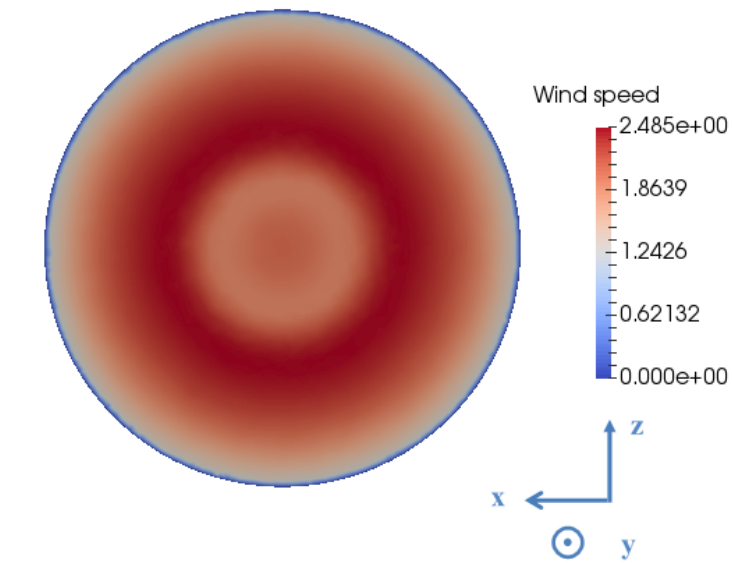


Figure C.22: Slice perpendicular to main flow direction

C.2.4 Cone length 1.36 m, 2.2 m diameter inlet, no subdivisions, narrow



Figure C.23: Cross section parallel to main direction of flow

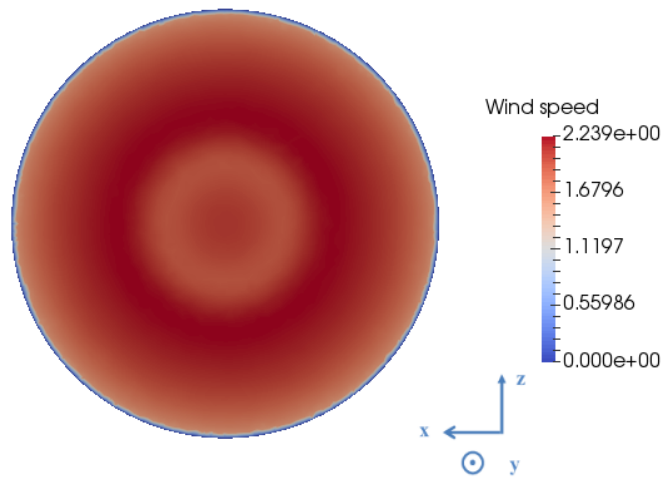


Figure C.24: Cross section perpendicular to main direction of flow

C.2.5 Cone length 3.4 m, 1 m diameter inlet, no subdivisions, wide



Figure C.25: Cross section parallel to main direction of air flow

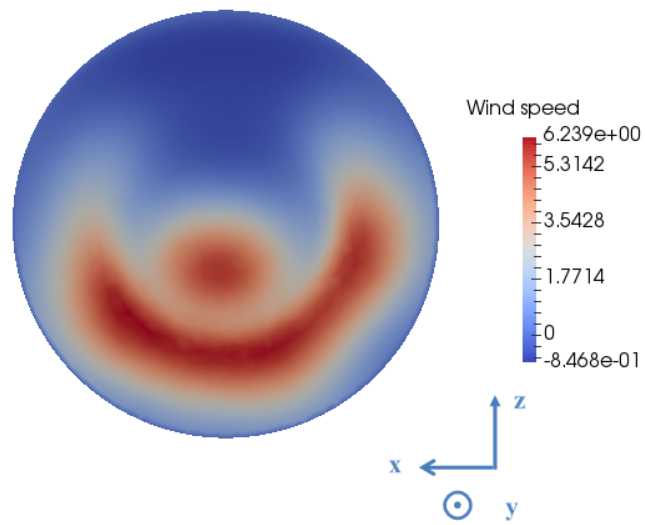


Figure C.26: Cross section perpendicular to main direction of flow

C.2.6 Cone length 2.04 m, 1.8 m diameter inlet, 4 subdivisions, wide

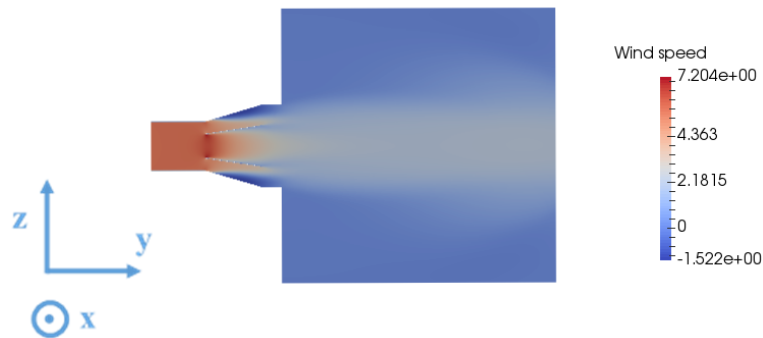


Figure C.27: Cross section parallel to main direction of flow

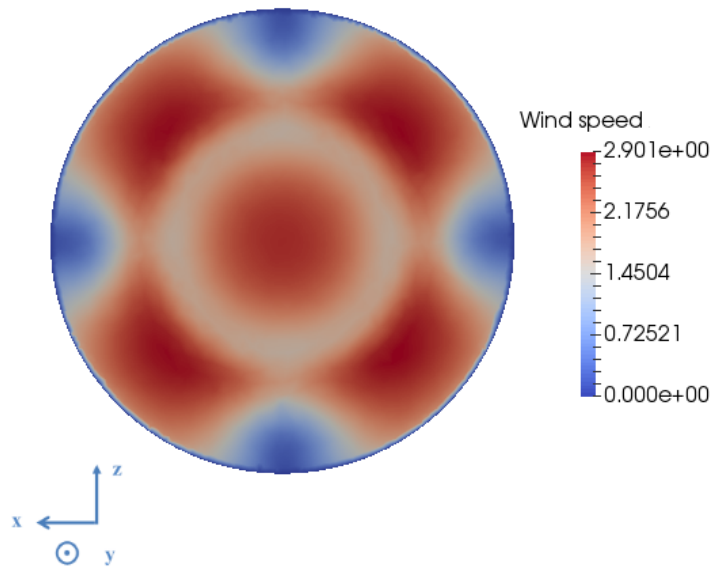


Figure C.28: Cross section perpendicular to main direction of flow

C.2.7 Cone length 2.04 m, 1.8 m diameter inlet, 6 subdivisions, wide



Figure C.29: Cross section parallel to main direction of flow

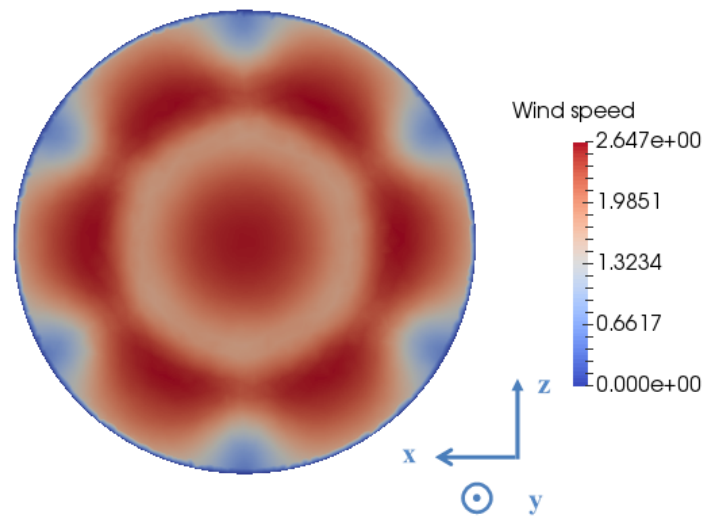


Figure C.30: Cross section perpendicular to main direction of airflow

C.2.8 Cone length 2.04 m, 1.8 m diameter inlet, 8 subdivisions, wide

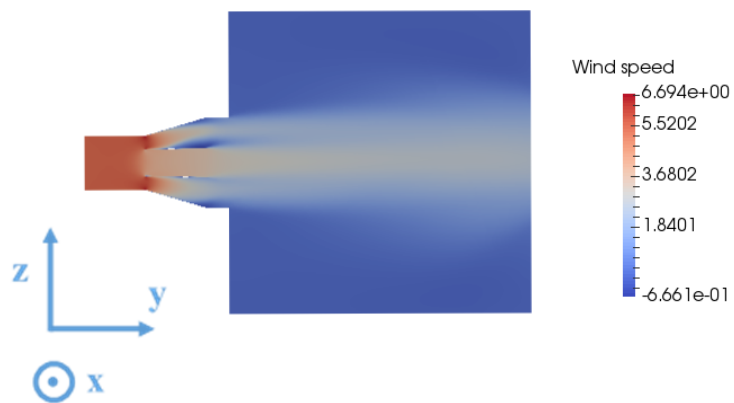


Figure C.31: Cross section parallel to main direction of flow

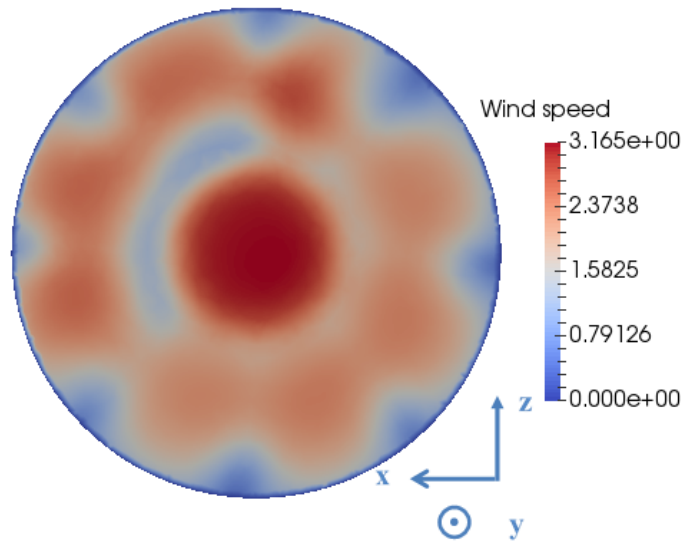


Figure C.32: Cross section perpendicular to main direction of airflow

Appendix D

Additional information for the experiments with the large fans

D.1 Properties of the large centrifugal fans

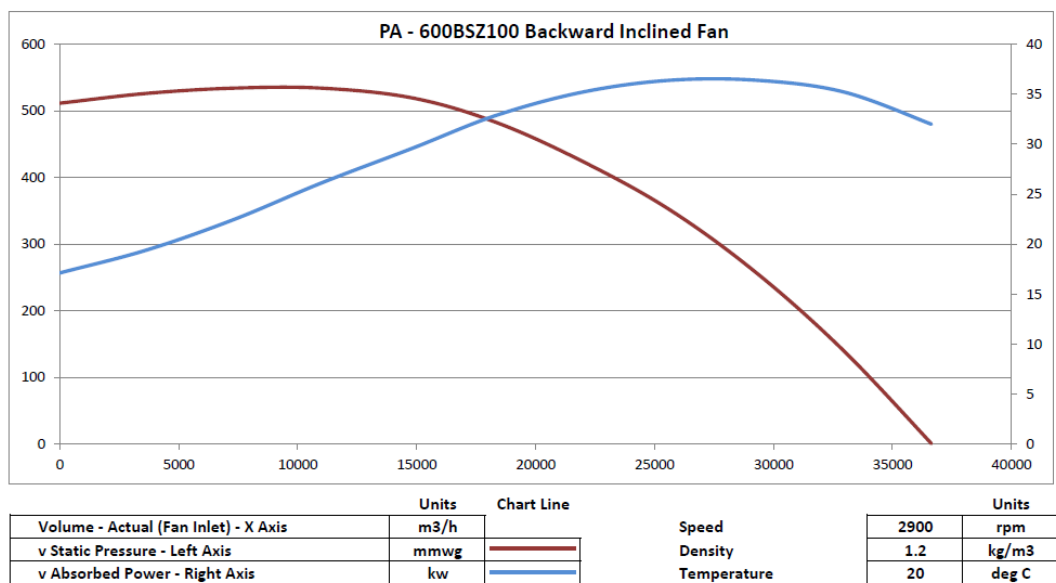


Figure D.1: Characteristics of large centrifugal fans

D.2 Measurement results presented for the whole area for the 1 m to 3 m diameter outlet

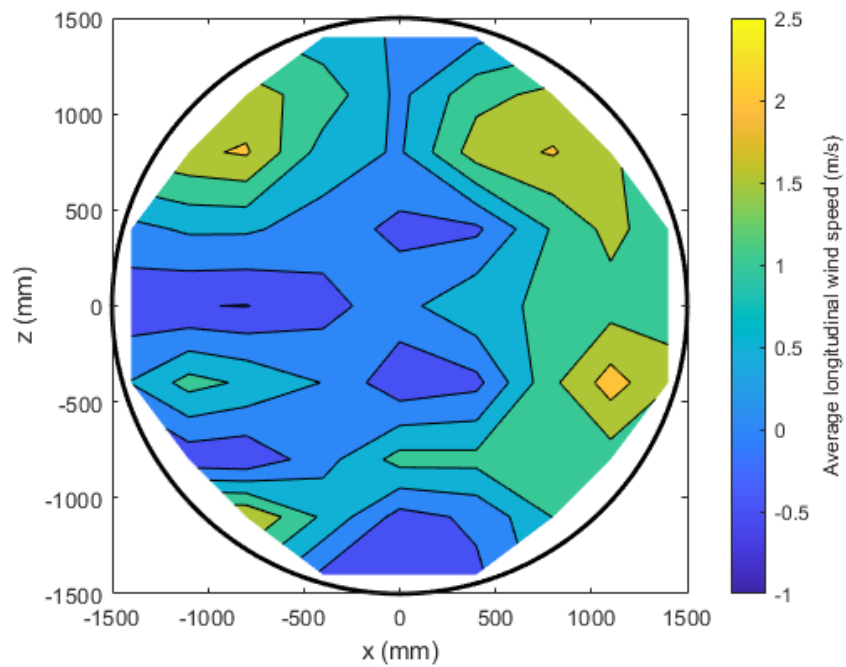


Figure D.2: Average longitudinal wind speed over the whole area for 50 % fan rotational speed and before smoothing near fans, with cones

D.2. MEASUREMENT RESULTS PRESENTED FOR THE WHOLE AREA FOR THE 1 M TO 3 M DIAMETER OUTLET

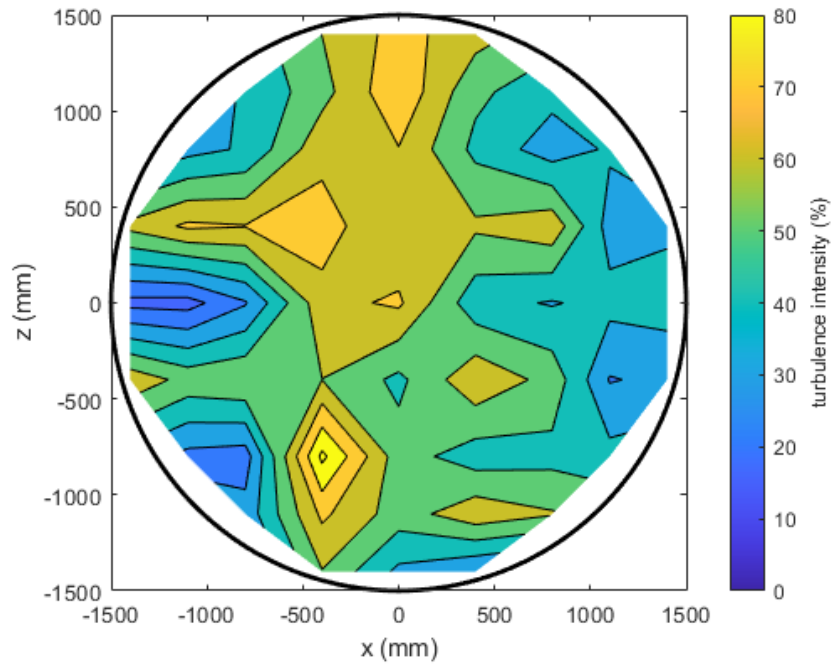


Figure D.3: Longitudinal turbulence intensity for 50 % fan rotational speed and before smoothing near fans, with cones

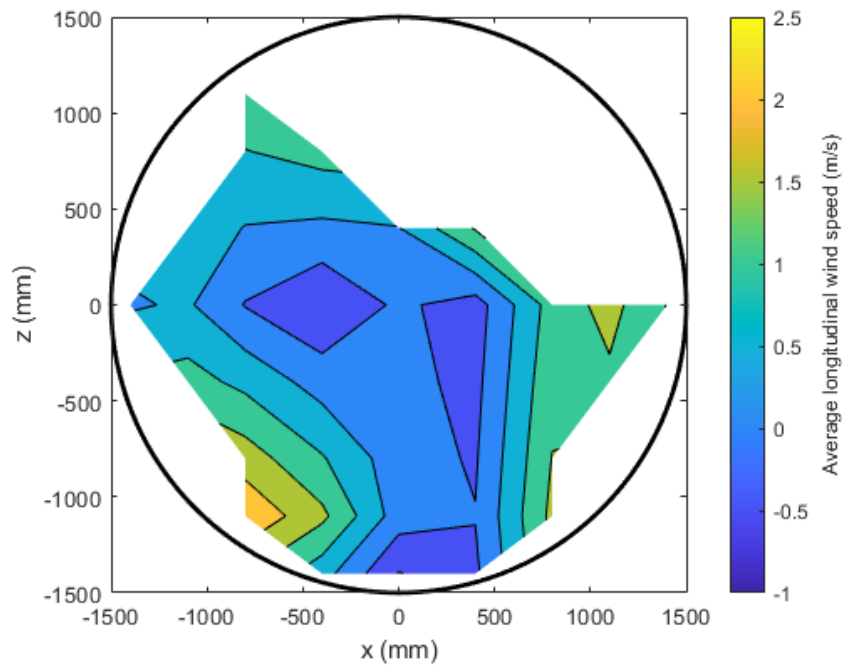


Figure D.4: Average longitudinal wind speed over the whole area for 70 % fan rotational speed and before smoothing near fans, with cones

D.2. MEASUREMENT RESULTS PRESENTED FOR THE WHOLE AREA FOR THE 1 M TO 3 M DIAMETER OUTLET

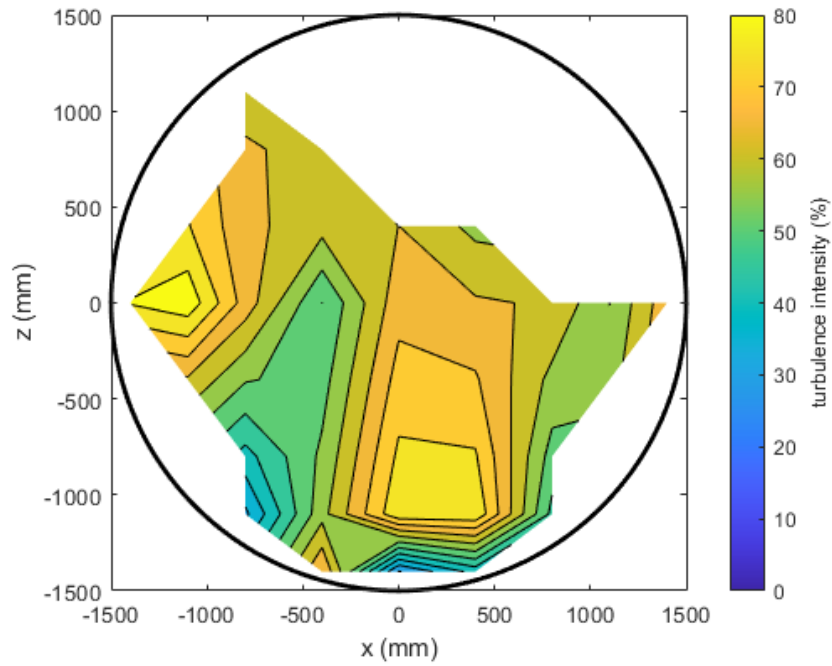


Figure D.5: Longitudinal turbulence intensity for 70 % fan rotational speed and before smoothing near fans, with cones

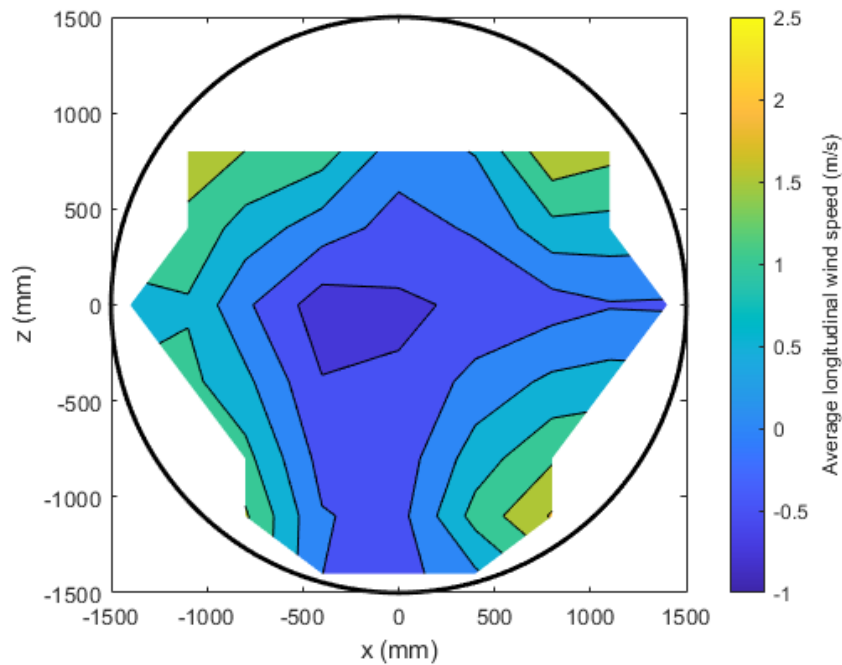


Figure D.6: Average longitudinal wind speed over the whole area for 50 % fan rotational speed and after smoothing near fans, with cones

D.2. MEASUREMENT RESULTS PRESENTED FOR THE WHOLE AREA FOR THE 1 M TO 3 M DIAMETER OUTLET

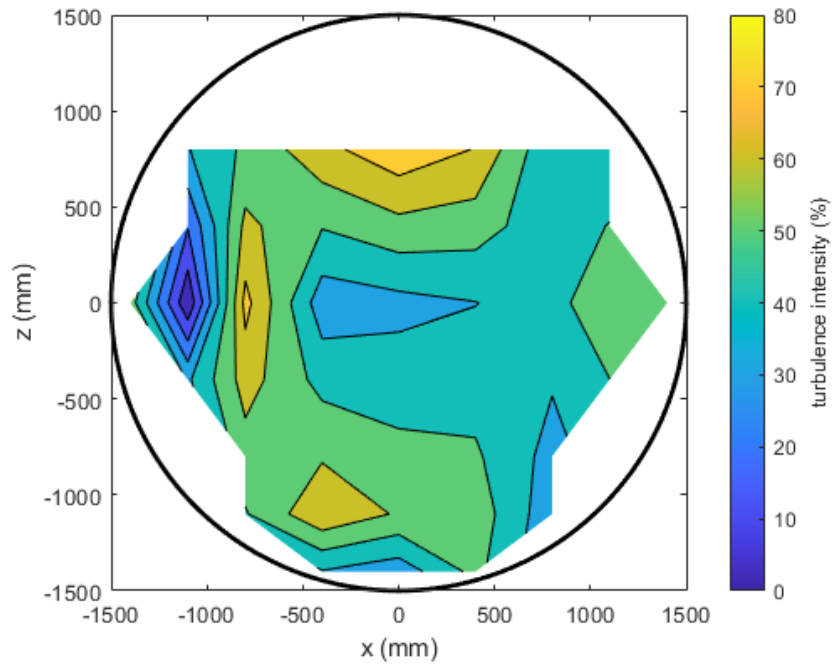


Figure D.7: Longitudinal turbulence intensity for 50 % fan rotational speed and after smoothing near fans, with cones

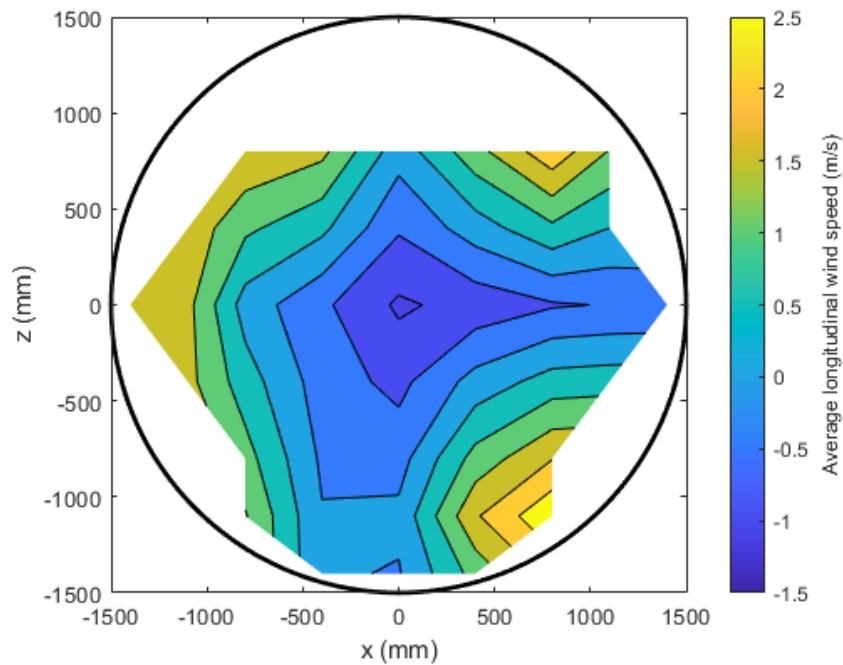


Figure D.8: Average longitudinal wind speed over the whole area for 70 % fan rotational speed and after smoothing near fans, with cones

D.2. MEASUREMENT RESULTS PRESENTED FOR THE WHOLE AREA FOR THE 1 M TO 3 M DIAMETER OUTLET

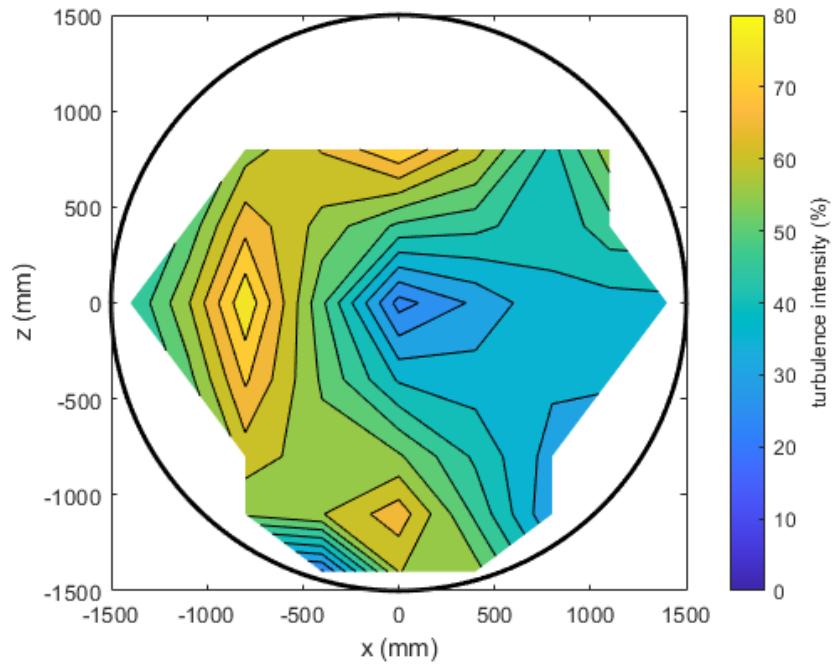


Figure D.9: Longitudinal turbulence intensity for 70 % fan rotational speed and after smoothing near fans, with cones

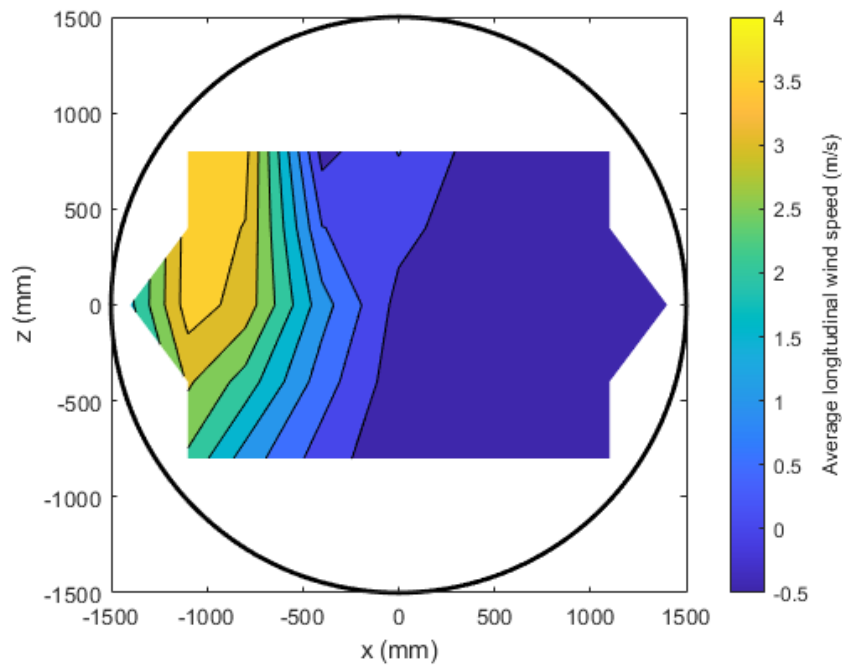


Figure D.10: Average longitudinal wind speed at 50 % rotational fan speed without cones

D.2. MEASUREMENT RESULTS PRESENTED FOR THE WHOLE AREA FOR THE 1 M TO 3 M DIAMETER OUTLET

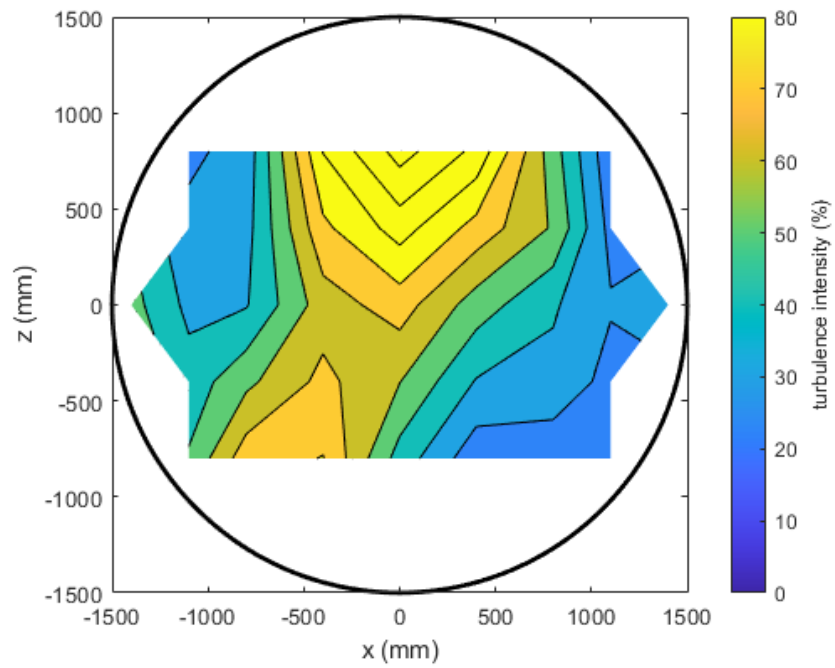


Figure D.11: Longitudinal turbulence intensity at 50 % fan rotational speed without cones

*D.3. OVERVIEW OF THE MEASURING POINTS FOR THE 1.8 M TO 3 M DIAMETER
OUTLET PLACED IN THE CENTRE OF THE BASIN*

D.3 Overview of the measuring points for the 1.8 m to 3 m diameter outlet placed in the centre of the basin

Table D.1: Overview of measurement positions

	Height (mm)			
% of fan rotational speed	-1100	-840	0	800
50			-1400, -1100, -800, -400, 0, 400, 800, 1100, 1400	-1100, -800, -400, 0, 400, 800, 1100
70		-1100, -800, -400, 0, 400, 800, 1100	-1400, -1100, -800, -400, 0, 400, 800, 1100, 1400	-1100, -800, -400, 0, 400, 800, 1100
100	-800, -600, -400, -200, 0, 200, 400, 600, 800	-1100, -950, -800, -600, -400, -200, 0, 200, 400, 600, 800, 1100	-1400, -1250, -1100, -950, -800, -600, -400, -200, 0, 200, 400, 600, 800, 1100, 1400	-1100, -800, -400, 0, 400, 800, 1100

Appendix E

Technical drawing of a wind turbine blade

Using the Mark Drela AG04 profile (coordinates in Appendix F.1) recommended in Martin (2011), Martin et al. (2012) and Kimball et al. (2014), a blade was drawn. A good part of the information used to draw the blade was taken from Kimball et al. (2014), that is, the blade offsets for sections 1 through 17 and number 25 (Appendix F.3) were the same, and the profiles for section 1 through 6 were also the same (The blade sections are numbered in increasing order when going from the root to the tip of the blade - see Figure E.1). The profile for the modified AG04 profile was obtained the same way as described in Kimball et al. (2014), that is, by getting double thickness of the original profile and thickening the trailing edge slightly. As can be seen when comparing Figure 2.41 and Figure 2.42 of Section 2.3.5.4, doubling the thickness of the Drela AG04 profile does not significantly affect the pressure distribution on the blade. However, as the trailing edge thickness chosen was most likely not the same, the exact coordinates are very likely to be slightly different. In addition to this, 7 additional sections (section 18-24) were added between the last and the second to last section given in Kimball et al. (2014) (see Figure E.2).

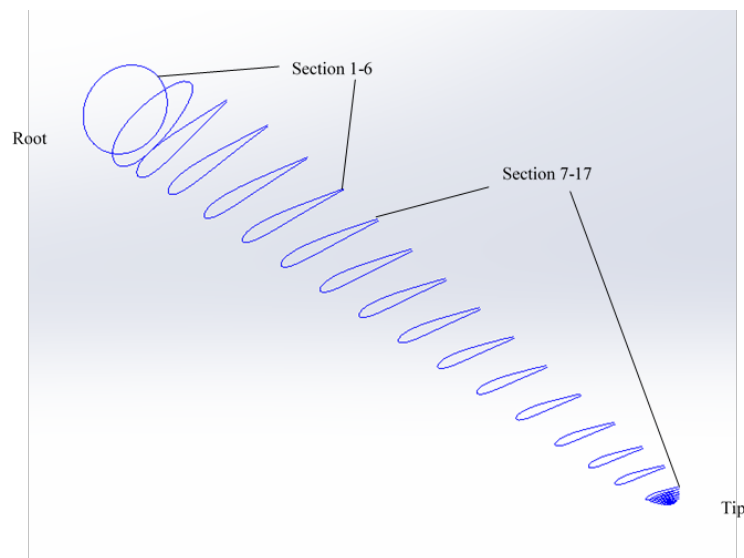


Figure E.1: Blade Sections

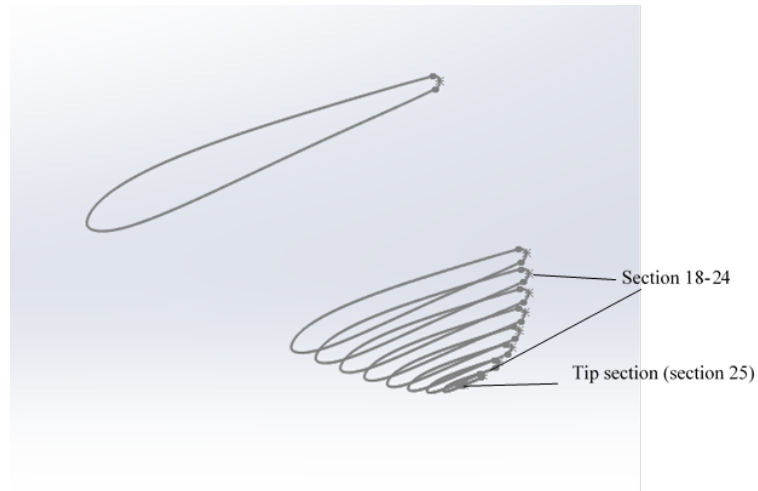


Figure E.2: Blade sections - zoom on the blade tip

Limiting the drawing to the curves that define the aerodynamic profile alone and not the exact shape of the tip, leads to a very pointy tip. Figure E.3 shows how the blade tip would look without additional sections. Figure E.4 shows the blade tip with additional sections.

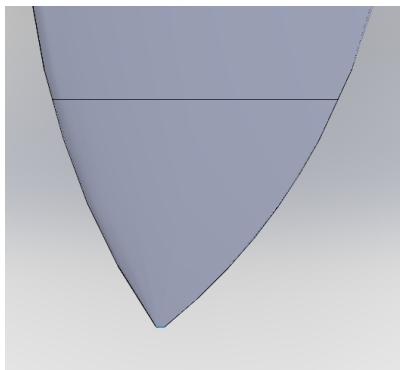


Figure E.3: Blade tip without additional sections

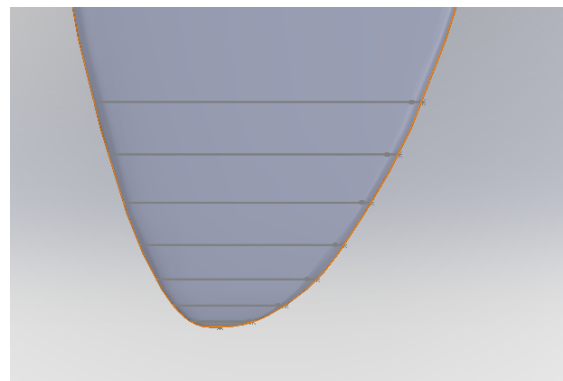


Figure E.4: Blade tip with additional sections

As was done at the University of Maine for the geometrically scaled blade (see Martin (2011)), small additional profile curves near the blade tip were drawn that would lead the end of the blade to a well rounded tip. They were drawn between the second to last and the last aerodynamic profile, using the modified AG04 profile. When going from the second to last to the last profile, the distance between the various aerodynamic section profiles was progressively decreased. To determine the chord of each of these sections, the chord length was calculated in a way that it formed a square root function when drawn as a function of distance from the rotor centre. To get profiles that are closer to one another when getting closer to the tip, a cosine distribution was applied, that is, it was decided to have 7 additional profiles in between the second to last and last profile, therefore going from 18 to 25 sections in total. Equation E.1 indicates how

the additional blade section distances were calculated.

$$r_n = \cos\left(\frac{\pi}{2}\left(\frac{25-n}{8}\right)\right)\left(1 - \frac{r_{17}}{R}\right) + r_{17} \quad (\text{E.1})$$

with r_n the radius for blade section number n , and n the number of the blade section.

Equation E.2 indicates a general formula to calculate the same positions with section numbers not specific to this case. This method is adapted from Martin (2011).

$$r_n = \cos\left(\frac{\pi}{2}\left(\frac{N_{new} - n}{N_{new} - N_{old} + 1}\right)\right)\left(1 - \frac{r_{N_{old}-1}}{R}\right) + r_{N_{old}-1} \quad (\text{E.2})$$

with N_{new} the new number of sections and N_{old} the previous number of sections.

Using these distances from the rotor centre, the chord is made to be shaped like a square root function between the second to last and the last section from the previous set. The desired shape can be seen in Figure E.5. Point A corresponds to the values of the second to last profile and Point B corresponds to the values of the last profile.

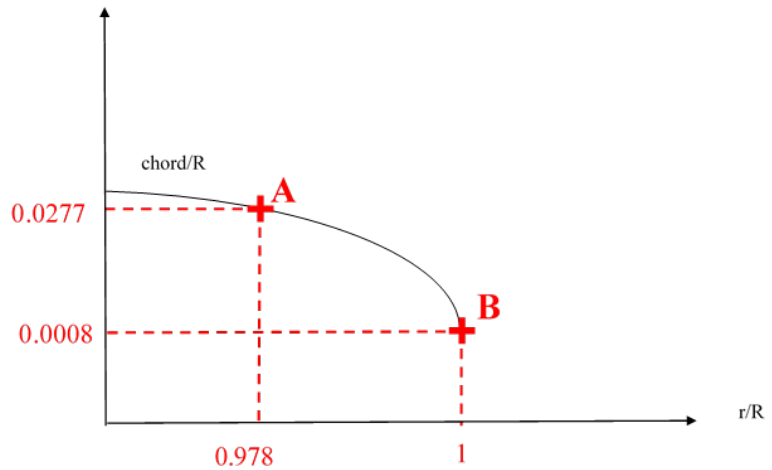


Figure E.5: Curve that the chord should follow for creating new values for the chord

The equation that the points on it need to follow is Equation E.3.

$$y = \sqrt{a(x-1)} + 0.0008 \quad (\text{E.3})$$

with $a = -\frac{(0.0277 - 0.0008)^2}{0.022}$.

For the general case, this equation would be like Equation E.4:

$$y = \sqrt{a(x-x_B)} + y_B \quad (\text{E.4})$$

with $a = \frac{(y_A - y_B)^2}{x_A - x_B}$.

The mathematical formula and reasoning are presented here, for anyone who would like to apply this formula for drawing their own blade.

As was mentioned in Section 2.3.5.2, taking the Drela AG04 profile as it is to make a model wind turbine blade would result in a rather fragile blade. The profile thickness was therefore doubled, as was described in Kimball et al. (2014). Furthermore, it was thickened progressively towards the trailing edge, to reach a thickness of 2 mm at the trailing edge. To do this, the centreline of the profiles needed to be found, which was done using an iterative procedure analog to the one described in Martin (2011). The coordinates of the centreline of the Mark Drela AG04 profile determined can be found in Appendix F.2. The formula found in Kimball et al. (2014) was then applied (Equation E.5).

$$\frac{t_{new}}{c} = \frac{t_{old}}{c} + \frac{TE}{c} \frac{x_{LE}}{c} \quad (E.5)$$

with t_{new} the newly calculated thickness, c the chord, t_{old} the original thickness, TE the new target thickness of the trailing edge, x_{LE} the distance from the leading edge.

For blade sections 7 through 18, the trailing edge thickness was made to be 2 mm. For blade sections 19 to 25, this thickness was progressively diminished. The thickness of section number 25 was simply double thickness, when compared to the original Drela AG04 profile. No extra thickness was added to the trailing edge. The exact shape of each profile is therefore slightly different from one blade section to another.

Once the correct thickness is applied, the following formulas can be applied to get from the normalized airfoil coordinates and blade offsets to a 3 dimensional blade (Equation E.6):

$$\begin{cases} X = c [(x_n - x_p) \cos\theta + y_n \sin\theta] \\ Y = c [(x_n - x_p) \sin\theta - y_n \cos\theta] \\ Z = r \end{cases} \quad (E.6)$$

with X, Y, Z the 3D blade section coordinates, x_n, y_n the normalised airfoil coordinates, x_p the airfoil pitch axis location, most likely close to or coinciding with the centre of pressure/lift, c the chord, θ the local twist, r the radius/distance of blade section from the rotor centre.

One could also apply all these changes manually in the chosen CAD software, once a third dimension has been added to the normalised airfoil coordinates, as translations, scaling and rotations can usually be done directly in CAD software. But making the changes to the coordinates in a code beforehand facilitates the drawing, and corrections can also easily be made.

In Solidworks, xyz curves can be imported. When a complete curve was imported, that is, with the beginning point corresponding to the end point, the trailing edge drawn automatically by the CAD software had some bumps in it (see Figure E.6). This is why the curve was imported as an open-ended curve (Figure E.7), after which a spline that was tangent to the traced curve was drawn to complete the trailing edge (Figure E.8 and Figure E.9).

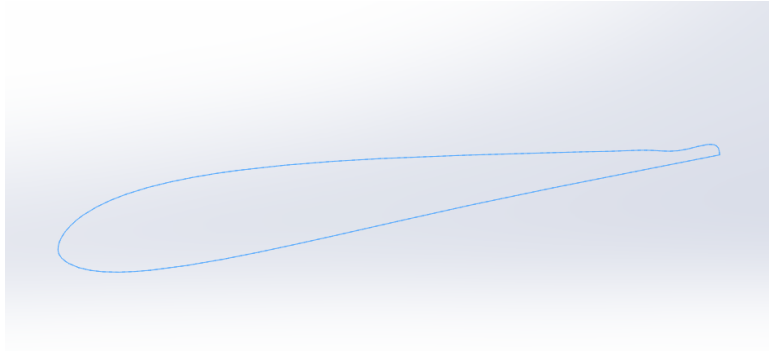


Figure E.6: Blade profile obtained when all points are connected automatically by the CAD software

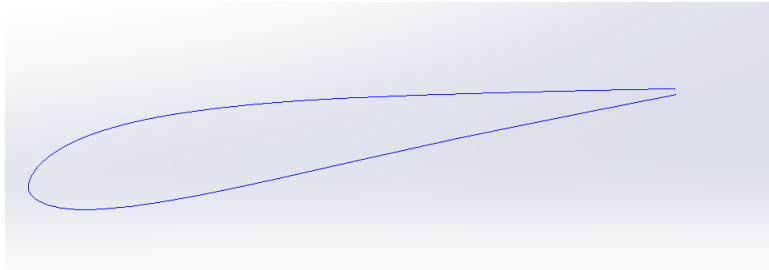


Figure E.7: Open-ended curve obtained before manual addition of trailing edge

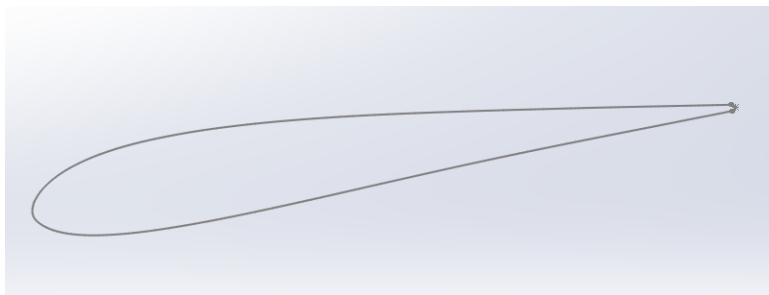


Figure E.8: Blade profile with manually added trailing edge

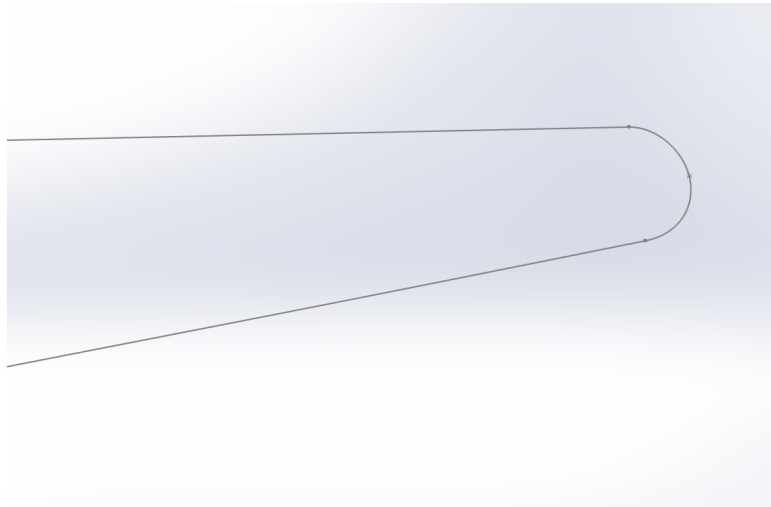


Figure E.9: Blade profile with manually added profile-zoom

Guide curves also need to be drawn as a preparation for the next step, which consists in tracing a lofted surface or body using all the aerodynamic profiles drawn.

The complete set of section coordinates can be found in Appendix F.4.

Appendix F

Blade geometry of the low Reynolds wind turbine based on the Drela AG04 profile

F.1 Original Drela AG04 profile coordinates

F.1. ORIGINAL DRELA AG04 PROFILE COORDINATES

Table F.1: Drela AG04 coordinates taken from Jackman (2005)

x	y
0.999999	0.00067
0.99487	0.001167
0.984963	0.002107
0.973288	0.003174
0.96091	0.004278
0.948332	0.005403
0.935708	0.006542
0.923068	0.007688
0.910423	0.008838
0.897782	0.009989
0.885148	0.011139
0.872522	0.012283
0.859901	0.01342
0.847283	0.014552
0.834669	0.015674
0.822056	0.016786
0.809443	0.017889
0.796831	0.01898
0.784217	0.020061
0.771601	0.021132
0.758985	0.022192
0.746366	0.023242
0.733743	0.024281
0.72112	0.025311
0.708496	0.026332
0.695872	0.027342
0.683249	0.028342
0.670629	0.02933
0.65801	0.030306
0.645393	0.031267
0.632779	0.032216
0.620167	0.033147
0.607557	0.034064
0.59495	0.034963

x	y
0.582346	0.035844
0.569745	0.036705
0.557147	0.037545
0.544551	0.038364
0.531959	0.039158
0.51937	0.039929
0.506783	0.040673
0.4942	0.041391
0.48162	0.042082
0.469042	0.042741
0.456467	0.04337
0.443895	0.043967
0.431325	0.044532
0.418758	0.045062
0.406195	0.045558
0.393636	0.046016
0.381082	0.046436
0.368533	0.046816
0.35599	0.047155
0.343456	0.047449
0.330929	0.047699
0.318413	0.047899
0.305908	0.048048
0.293416	0.048143
0.280938	0.04818
0.268477	0.048156
0.256036	0.048067
0.243615	0.047906
0.231219	0.047672
0.218852	0.047357
0.206516	0.046956
0.194219	0.04646
0.181965	0.045864
0.169762	0.045159
0.157618	0.044335
0.145544	0.043381

F.1. ORIGINAL DRELA AG04 PROFILE COORDINATES

x	y
0.133552	0.042286
0.121659	0.041034
0.109883	0.039614
0.098252	0.038005
0.086796	0.036191
0.075561	0.034151
0.064602	0.031864
0.054003	0.029317
0.043899	0.026506
0.034516	0.023466
0.026187	0.020297
0.01925	0.017178
0.013839	0.0143
0.009798	0.011763
0.006815	0.009556
0.004604	0.007625
0.002958	0.005908
0.001739	0.004355
0.000861	0.002932
0.000285	0.001613
0.000018	0.000382
0.000085	-0.000805
0.000554	-0.001985
0.001456	-0.003123
0.002756	-0.004215
0.004455	-0.005308
0.006633	-0.006445
0.009447	-0.007655
0.013152	-0.008964
0.018112	-0.010393
0.024689	-0.011906
0.032994	-0.013392
0.042729	-0.014711
0.053413	-0.015788
0.064674	-0.016627
0.076299	-0.017257

x	y
0.088178	-0.017709
0.100238	-0.018017
0.11243	-0.018202
0.124717	-0.018284
0.137072	-0.018277
0.149484	-0.018198
0.161943	-0.018058
0.174443	-0.017866
0.186982	-0.01763
0.199555	-0.017356
0.21216	-0.01705
0.224791	-0.016716
0.237445	-0.016358
0.250118	-0.015977
0.262807	-0.015581
0.275506	-0.015166
0.288211	-0.014738
0.300918	-0.014299
0.313621	-0.013852
0.326319	-0.013398
0.33901	-0.012941
0.351696	-0.012481
0.364379	-0.012021
0.377057	-0.011562
0.389731	-0.011106
0.402402	-0.010652
0.415069	-0.010206
0.427732	-0.009763
0.440393	-0.009328
0.453052	-0.008901
0.465714	-0.008484
0.478381	-0.008076
0.491052	-0.007677
0.503725	-0.00729
0.516399	-0.006917
0.529072	-0.006554

F.1. ORIGINAL DRELA AG04 PROFILE COORDINATES

x	y
0.541743	-0.006205
0.554416	-0.005866
0.567087	-0.00554
0.579758	-0.005227
0.592428	-0.00493
0.605099	-0.004643
0.617771	-0.004371
0.630444	-0.004115
0.643115	-0.00387
0.655786	-0.003641
0.668459	-0.003428
0.681132	-0.003228
0.693806	-0.003044
0.706482	-0.002875
0.71916	-0.00272
0.731838	-0.002579
0.744517	-0.002449
0.757198	-0.002333
0.769881	-0.002225
0.782566	-0.002127
0.795254	-0.002035
0.807944	-0.001951
0.820638	-0.001872
0.833336	-0.001792
0.84604	-0.001721
0.85875	-0.001652
0.871466	-0.001585
0.884186	-0.001519
0.896901	-0.001451
0.909612	-0.001377
0.922323	-0.001294
0.935033	-0.001202
0.947738	-0.001104
0.960407	-0.00101
0.972913	-0.000907
0.984778	-0.000805

x	y
0.994829	-0.000713
1.000001	-0.00067

F.2 Centreline of Drela AG04 airfoil

x	thickness	y of centreline	slope of centreline
0.00000	0.00000	0.000000	0.00000
0.01033	0.01980	0.001410	0.12837
0.03495	0.03701	0.004393	0.11535
0.04401	0.04113	0.005390	0.10575
0.05405	0.04493	0.006411	0.09438
0.06470	0.04831	0.007349	0.08288
0.07558	0.05120	0.008201	0.08674
0.07632	0.05138	0.008273	0.08342
0.08681	0.05370	0.009039	0.07853
0.08819	0.05399	0.009156	0.07536
0.09826	0.05585	0.009839	0.07086
0.10025	0.05619	0.009986	0.06775
0.10989	0.05767	0.010587	0.06294
0.11244	0.05803	0.010749	0.06035
0.12166	0.05920	0.011279	0.05690
0.12472	0.05956	0.011451	0.05478
0.13356	0.06048	0.011921	0.05210
0.13708	0.06081	0.012101	0.05004
0.14555	0.06153	0.012517	0.04767
0.14949	0.06183	0.012699	0.04582
0.15762	0.06238	0.013068	0.04374
0.16194	0.06263	0.013251	0.04201
0.16976	0.06304	0.013577	0.04012
0.17444	0.06325	0.013758	0.03851
0.18197	0.06354	0.014047	0.03677
0.18698	0.06370	0.014224	0.03528
0.19422	0.06389	0.014479	0.03369
0.19956	0.06400	0.014651	0.03229
0.20652	0.06411	0.014877	0.03075
0.21216	0.06416	0.015042	0.02939
0.21885	0.06420	0.015239	0.02798
0.22479	0.06420	0.015397	0.02674
0.23122	0.06418	0.015570	0.02541
0.23745	0.06413	0.015720	0.02427
0.24361	0.06406	0.015871	0.02308

F.2. CENTRELINE OF DRELA AG04 AIRFOIL

x	thickness	y of centreline	slope of centreline
0.25012	0.06395	0.016013	0.02194
0.25604	0.06384	0.016143	0.02067
0.26281	0.06368	0.016275	0.01965
0.26848	0.06354	0.016388	0.01859
0.27551	0.06333	0.016511	0.01760
0.28094	0.06315	0.016607	0.01652
0.28821	0.06289	0.016719	0.01558
0.29342	0.06269	0.016801	0.01453
0.30092	0.06238	0.016903	0.01360
0.30591	0.06217	0.016971	0.01258
0.31362	0.06180	0.017061	0.01172
0.31841	0.06158	0.017117	0.01074
0.32632	0.06117	0.017195	0.00986
0.33093	0.06093	0.017240	0.00882
0.33901	0.06048	0.017305	0.00799
0.34346	0.06023	0.017341	0.00707
0.35170	0.05974	0.017393	0.00627
0.35599	0.05948	0.017420	0.00525
0.36438	0.05895	0.017458	0.00446
0.36853	0.05869	0.017476	0.00348
0.37706	0.05812	0.017501	0.00273
0.38108	0.05785	0.017511	0.00163
0.38973	0.05725	0.017521	0.00091
0.39364	0.05698	0.017524	-0.00084
0.40240	0.05635	0.017522	-0.00041
0.40619	0.05608	0.017518	-0.00125
0.41507	0.05541	0.017498	-0.00235
0.41876	0.05514	0.017489	-0.00294
0.42773	0.05445	0.017456	-0.00392
0.43132	0.05417	0.017441	-0.00470
0.44039	0.05345	0.017392	-0.00562
0.44389	0.05318	0.017372	-0.00637
0.45305	0.05243	0.017308	-0.00726
0.45647	0.05216	0.017282	-0.00806
0.46571	0.05139	0.017202	-0.00890
0.46904	0.05112	0.017172	-0.00965

F.2. CENTRELINE OF DRELA AG04 AIRFOIL

x	thickness	y of centreline	slope of centreline
0.47838	0.05033	0.017077	-0.01046
0.48162	0.05005	0.017042	-0.01126
0.49105	0.04924	0.016931	-0.01213
0.49420	0.04897	0.016891	-0.01289
0.50372	0.04813	0.016764	-0.01371
0.50678	0.04787	0.016721	-0.01449
0.51640	0.04702	0.016578	-0.01521
0.51937	0.04675	0.016532	-0.01594
0.52907	0.04588	0.016373	-0.01673
0.53196	0.04563	0.016324	-0.01745
0.54174	0.04474	0.016150	-0.01811
0.54455	0.04449	0.016098	-0.01880
0.55442	0.04358	0.015909	-0.01953
0.55715	0.04333	0.015854	-0.02019
0.56709	0.04241	0.015651	-0.02086
0.56974	0.04217	0.015594	-0.02153
0.57976	0.04124	0.015376	-0.02225
0.58235	0.04100	0.015317	-0.02295
0.59243	0.04006	0.015083	-0.02353
0.59495	0.03982	0.015023	-0.02408
0.60510	0.03887	0.014776	-0.02473
0.60756	0.03864	0.014714	-0.02538
0.61777	0.03768	0.014452	-0.02601
0.62017	0.03746	0.014389	-0.02660
0.63044	0.03649	0.014113	-0.02712
0.63278	0.03627	0.014049	-0.02769
0.64311	0.03529	0.013761	-0.02830
0.64539	0.03508	0.013695	-0.02885
0.65579	0.03410	0.013394	-0.02942
0.65801	0.03389	0.013327	-0.03003
0.66846	0.03291	0.013011	-0.03056
0.67063	0.03271	0.012944	-0.03105
0.68113	0.03172	0.012616	-0.03159
0.68325	0.03152	0.012549	-0.03214
0.69381	0.03053	0.012208	-0.03265
0.69587	0.03034	0.012139	-0.03314

F.2. CENTRELINE OF DRELA AG04 AIRFOIL

x	thickness	y of centreline	slope of centreline
0.70648	0.02935	0.011786	-0.03362
0.70850	0.02917	0.011718	-0.03412
0.71916	0.02817	0.011352	-0.03459
0.72112	0.02799	0.011284	-0.03505
0.73184	0.02700	0.010907	-0.03544
0.73374	0.02682	0.010839	-0.03584
0.74452	0.02583	0.010451	-0.03630
0.74637	0.02566	0.010383	-0.03680
0.75720	0.02466	0.009983	-0.03719
0.75898	0.02449	0.009916	-0.03755
0.76988	0.02348	0.009505	-0.03795
0.77160	0.02333	0.009439	-0.03836
0.78257	0.02231	0.009017	-0.03870
0.78422	0.02216	0.008953	-0.03902
0.79525	0.02113	0.008521	-0.03937
0.79683	0.02099	0.008458	-0.03973
0.80794	0.01995	0.008015	-0.04005
0.80944	0.01981	0.007955	-0.04038
0.82064	0.01877	0.007501	-0.04059
0.82206	0.01863	0.007444	-0.04075
0.83334	0.01757	0.006983	-0.04109
0.83467	0.01744	0.006928	-0.04146
0.84604	0.01637	0.006455	-0.04171
0.84728	0.01625	0.006403	-0.04194
0.85875	0.01516	0.005920	-0.04213
0.85990	0.01505	0.005872	-0.04226
0.87147	0.01395	0.005383	-0.04239
0.87252	0.01385	0.005338	-0.04254
0.88419	0.01273	0.004841	-0.04262
0.88515	0.01264	0.004800	-0.04268
0.89690	0.01151	0.004297	-0.04264
0.89778	0.01142	0.004260	-0.04252
1.00000	0.00000	0.000000	-0.04252

F.3 Blade offsets for the MARIN stock wind turbine taken from Kimball et al. (2014)

Section number	Section name	r/R	c/R	θ (°)	xp/c	Trailing Edge thickness (mm)
1	Cylinder	0.046	0.07	42.71	0.5	
2	Blend 1	0.089	0.083	31.19	0.5	
3	Blend 2	0.132	0.0886	23.11	0.478	
4	Blend 3	0.187	0.092	16.39	0.449	
5	Blend 4	0.252	0.092	11.47	0.423	
6	Blend5	0.317	0.0885	8.5	0.375	
7	AG04 Mod	0.382	0.0841	6.52	0.375	2
8	AG04 Mod	0.447	0.0795	5.05	0.375	2
9	AG04 Mod	0.512	0.0747	3.88	0.375	2
10	AG04 Mod	0.577	0.0697	2.94	0.375	2
11	AG04 Mod	0.642	0.0647	2.22	0.375	2
12	AG04 Mod	0.707	0.0599	1.67	0.375	2
13	AG04 Mod	0.772	0.0552	1.24	0.375	2
14	AG04 Mod	0.837	0.0506	0.84	0.375	2
15	AG04 Mod	0.892	0.0462	0.5	0.375	2
16	AG04 Mod	0.935	0.0421	0.24	0.375	2
17	AG04 Mod	0.978	0.0277	0.06	0.375	2
18	AG04 Mod	0.9823	0.0249	0.056	0.375	2
19	AG04 Mod	0.9864	0.0219	0.048	0.375	2.04
20	AG04 Mod	0.9902	0.0187	0.04	0.375	1.98
21	AG04 Mod	0.9936	0.0154	0.032	0.375	1.82
22	AG04 Mod	0.9963	0.0118	0.024	0.375	1.55
23	AG04 Mod	0.9983	0.0082	0.016	0.375	1.18
24	AG04 Mod	0.9996	0.0045	0.008	0.375	0.71
25	AG04 Mod	1	0.0008	0	0.375	0.14

F.4 Aerodynamic profile coordinates

F.4.1 Section 1

x (mm)	y (mm)	z (mm)
32.40	29.91	57.96
30.46	31.89	57.96
28.40	33.74	57.96
26.23	35.45	57.96
23.95	37.03	57.96
21.58	38.46	57.96
19.12	39.74	57.96
16.58	40.86	57.96
13.99	41.82	57.96
11.33	42.62	57.96
8.63	43.25	57.96
5.90	43.70	57.96
3.15	43.99	57.96
0.38	44.10	57.96
-2.39	44.04	57.96
-5.15	43.80	57.96
-7.89	43.39	57.96
-10.60	42.81	57.96
-13.27	42.06	57.96
-15.88	41.14	57.96
-18.43	40.06	57.96
-20.91	38.83	57.96
-23.31	37.44	57.96
-25.62	35.90	57.96
-27.82	34.22	57.96
-29.91	32.40	57.96
-31.89	30.46	57.96
-33.74	28.40	57.96
-35.45	26.23	57.96
-37.03	23.95	57.96
-38.46	21.58	57.96
-39.74	19.12	57.96
-40.86	16.58	57.96
-41.82	13.99	57.96

x (mm)	y (mm)	z (mm)
-42.62	11.33	57.96
-43.25	8.63	57.96
-43.70	5.90	57.96
-43.99	3.15	57.96
-44.10	0.38	57.96
-44.04	-2.39	57.96
-43.80	-5.15	57.96
-43.39	-7.89	57.96
-42.81	-10.60	57.96
-42.06	-13.27	57.96
-41.14	-15.88	57.96
-40.06	-18.43	57.96
-38.83	-20.91	57.96
-37.44	-23.31	57.96
-35.90	-25.62	57.96
-34.22	-27.82	57.96
-32.40	-29.91	57.96
-30.46	-31.89	57.96
-28.40	-33.74	57.96
-26.23	-35.45	57.96
-23.95	-37.03	57.96
-21.58	-38.46	57.96
-19.12	-39.74	57.96
-16.58	-40.86	57.96
-13.99	-41.82	57.96
-11.33	-42.62	57.96
-8.63	-43.25	57.96
-5.90	-43.70	57.96
-3.15	-43.99	57.96
-0.38	-44.10	57.96
2.39	-44.04	57.96
5.15	-43.80	57.96
7.89	-43.39	57.96
10.60	-42.81	57.96
13.27	-42.06	57.96
15.88	-41.14	57.96

F.4. AERODYNAMIC PROFILE COORDINATES

x (mm)	y (mm)	z (mm)
18.43	-40.06	57.96
20.91	-38.83	57.96
23.31	-37.44	57.96
25.62	-35.90	57.96
27.82	-34.22	57.96
29.91	-32.40	57.96
31.89	-30.46	57.96
33.74	-28.40	57.96
35.45	-26.23	57.96
37.03	-23.95	57.96
38.46	-21.58	57.96
39.74	-19.12	57.96
40.86	-16.58	57.96
41.82	-13.99	57.96
42.62	-11.33	57.96
43.25	-8.63	57.96
43.70	-5.90	57.96
43.99	-3.15	57.96
44.10	-0.38	57.96
44.04	2.39	57.96
43.80	5.15	57.96
43.39	7.89	57.96
42.81	10.60	57.96
42.06	13.27	57.96
41.14	15.88	57.96
40.06	18.43	57.96
38.83	20.91	57.96
37.44	23.31	57.96
35.90	25.62	57.96
34.22	27.82	57.96
32.40	29.91	57.96

x (mm)	y (mm)	z (mm)
40.44	34.17	112.14
34.26	34.28	112.14
28.52	33.66	112.14
23.03	32.64	112.14
17.71	31.32	112.14
12.54	29.78	112.14
7.48	28.04	112.14
2.53	26.12	112.14
-2.32	24.02	112.14
-7.06	21.76	112.14
-11.69	19.31	112.14
-16.19	16.65	112.14
-20.57	13.79	112.14
-24.80	10.68	112.14
-28.86	7.28	112.14
-32.69	3.52	112.14
-36.24	-0.72	112.14
-39.36	-5.67	112.14
-40.67	-8.55	112.14
-41.70	-11.89	112.14
-42.25	-16.04	112.14
-42.11	-18.78	112.14
-41.87	-20.20	112.14
-41.67	-21.02	112.14
-41.32	-22.12	112.14
-40.96	-23.01	112.14
-39.40	-25.59	112.14
-38.82	-26.25	112.14
-38.08	-26.96	112.14
-37.47	-27.47	112.14
-36.41	-28.21	112.14
-34.18	-29.36	112.14
-30.49	-30.40	112.14
-27.26	-30.71	112.14
-24.26	-30.61	112.14
-18.68	-29.72	112.14

F.4.2 Section 2

x (mm)	y (mm)	z (mm)
48.99	30.15	112.14

F.4. AERODYNAMIC PROFILE COORDINATES

x (mm)	y (mm)	z (mm)
-13.47	-28.24	112.14
-8.49	-26.36	112.14
-3.68	-24.21	112.14
0.99	-21.82	112.14
5.54	-19.25	112.14
9.99	-16.51	112.14
14.36	-13.63	112.14
18.65	-10.61	112.14
22.85	-7.46	112.14
26.98	-4.18	112.14
31.02	-0.76	112.14
34.96	2.83	112.14
38.78	6.62	112.14
42.44	10.68	112.14
45.84	15.15	112.14
48.82	20.33	112.14
49.94	23.52	112.14
49.42	29.43	112.14

x (mm)	y (mm)	z (mm)
-21.08	3.89	166.32
-26.17	1.59	166.32
-31.09	-1.09	166.32
-35.77	-4.36	166.32
-37.95	-6.36	166.32
-39.97	-8.74	166.32
-41.68	-11.84	166.32
-42.31	-13.92	166.32
-42.45	-15.00	166.32
-42.50	-15.60	166.32
-42.45	-16.44	166.32
-42.35	-17.09	166.32
-41.65	-18.73	166.32
-41.29	-19.15	166.32
-40.77	-19.65	166.32
-40.33	-19.97	166.32
-39.51	-20.47	166.32
-37.70	-21.17	166.32
-34.48	-21.61	166.32
-31.52	-21.41	166.32
-28.71	-20.90	166.32
-23.32	-19.30	166.32
-18.13	-17.24	166.32
-13.06	-14.91	166.32
-8.06	-12.41	166.32
-3.10	-9.80	166.32
1.82	-7.10	166.32
6.72	-4.37	166.32
11.61	-1.60	166.32
16.50	1.16	166.32
21.39	3.92	166.32
26.29	6.66	166.32
31.21	9.35	166.32
36.14	12.01	166.32
41.09	14.65	166.32
46.04	17.27	166.32

F.4.3 Section 3

x (mm)	y (mm)	z (mm)
60.28	26.56	166.32
54.79	25.20	166.32
49.30	23.84	166.32
43.82	22.47	166.32
38.33	21.10	166.32
32.86	19.71	166.32
27.38	18.32	166.32
21.90	16.93	166.32
16.43	15.53	166.32
10.97	14.11	166.32
5.53	12.65	166.32
0.11	11.13	166.32
-5.27	9.51	166.32
-10.61	7.80	166.32
-15.89	5.94	166.32

F.4. AERODYNAMIC PROFILE COORDINATES

x (mm)	y (mm)	z (mm)
50.99	19.88	166.32
55.94	22.51	166.32
58.41	23.82	166.32
60.88	25.14	166.32

x (mm)	y (mm)	z (mm)
-40.673	-13.715	235.62
-40.287	-14	235.62
-39.558	-14.426	235.62
-37.86	-15.063	235.62
-34.71	-15.502	235.62
-31.714	-15.418	235.62
-28.8	-15.056	235.62
-23.112	-13.854	235.62
-17.532	-12.286	235.62
-12.017	-10.494	235.62
-6.5417	-8.5697	235.62
-1.0924	-6.5561	235.62
4.3405	-4.4869	235.62
9.7603	-2.3733	235.62
15.18	-0.25959	235.62
20.6	1.8541	235.62
26.026	3.9455	235.62
31.459	6.0147	235.62
36.902	8.0506	235.62
42.354	10.053	235.62
47.817	12.022	235.62
53.279	13.991	235.62
58.745	15.949	235.62
64.21	17.907	235.62
66.942	18.892	235.62
69.669	19.887	235.62

F.4.4 Section 4

x (mm)	y (mm)	z (mm)
69.342	21	235.62
63.55	20.154	235.62
57.76	19.297	235.62
51.971	18.44	235.62
46.185	17.571	235.62
40.405	16.681	235.62
34.625	15.791	235.62
28.849	14.889	235.62
23.076	13.977	235.62
17.313	13.031	235.62
11.559	12.051	235.62
5.8253	11.005	235.62
0.1144	9.8813	235.62
-5.5638	8.6462	235.62
-11.206	7.2887	235.62
-16.796	5.7533	235.62
-22.317	3.9844	235.62
-27.74	1.8818	235.62
-33.006	-0.75453	235.62
-35.541	-2.4063	235.62
-37.978	-4.3918	235.62
-40.235	-6.9889	235.62
-41.219	-8.7767	235.62
-41.553	-9.6965	235.62
-41.704	-10.212	235.62
-41.792	-10.939	235.62
-41.805	-11.511	235.62
-41.386	-12.934	235.62
-41.102	-13.285	235.62

F.4.5 Section 5

x (mm)	y (mm)	z (mm)
70.90	14.92	317.52
65.07	14.52	317.52
59.24	14.11	317.52
53.40	13.71	317.52
47.57	13.30	317.52
41.75	12.86	317.52

F.4. AERODYNAMIC PROFILE COORDINATES

x (mm)	y (mm)	z (mm)
35.92	12.42	317.52
30.10	11.97	317.52
24.28	11.50	317.52
18.47	11.01	317.52
12.66	10.47	317.52
6.87	9.87	317.52
1.09	9.19	317.52
-4.66	8.41	317.52
-10.39	7.51	317.52
-16.09	6.45	317.52
-21.74	5.15	317.52
-27.33	3.54	317.52
-32.82	1.42	317.52
-35.50	0.06	317.52
-38.11	-1.63	317.52
-40.61	-3.89	317.52
-41.77	-5.47	317.52
-42.19	-6.30	317.52
-42.39	-6.77	317.52
-42.55	-7.44	317.52
-42.62	-7.96	317.52
-42.36	-9.27	317.52
-42.11	-9.60	317.52
-41.73	-10.01	317.52
-41.38	-10.28	317.52
-40.71	-10.71	317.52
-39.09	-11.36	317.52
-36.02	-11.92	317.52
-33.05	-11.99	317.52
-30.13	-11.83	317.52
-24.37	-11.05	317.52
-18.69	-9.93	317.52
-13.04	-8.62	317.52
-7.41	-7.18	317.52
-1.81	-5.67	317.52
3.79	-4.12	317.52

x (mm)	y (mm)	z (mm)
9.38	-2.53	317.52
14.98	-0.94	317.52
20.57	0.65	317.52
26.17	2.21	317.52
31.77	3.75	317.52
37.38	5.25	317.52
42.99	6.72	317.52
48.61	8.17	317.52
54.24	9.60	317.52
59.86	11.02	317.52
65.48	12.46	317.52
68.30	13.17	317.52
71.11	13.90	317.52

F.4.6 Section 6

x (mm)	y (mm)	z (mm)
68.85	10.80	399.42
63.23	10.68	399.42
57.62	10.56	399.42
52.00	10.44	399.42
46.38	10.31	399.42
40.76	10.16	399.42
35.15	10.01	399.42
29.53	9.85	399.42
23.92	9.66	399.42
18.32	9.46	399.42
12.72	9.21	399.42
7.13	8.90	399.42
1.55	8.52	399.42
-4.02	8.05	399.42
-9.57	7.45	399.42
-15.10	6.71	399.42
-20.59	5.74	399.42
-26.04	4.49	399.42
-31.42	2.75	399.42
-34.06	1.60	399.42

F.4. AERODYNAMIC PROFILE COORDINATES

x (mm)	y (mm)	z (mm)
-36.67	0.15	399.42
-39.19	-1.85	399.42
-40.38	-3.27	399.42
-40.83	-4.03	399.42
-41.05	-4.44	399.42
-41.24	-5.06	399.42
-41.34	-5.55	399.42
-41.16	-6.77	399.42
-40.94	-7.09	399.42
-40.60	-7.48	399.42
-40.28	-7.74	399.42
-39.65	-8.16	399.42
-38.14	-8.83	399.42
-35.23	-9.47	399.42
-32.38	-9.66	399.42
-29.57	-9.62	399.42
-24.00	-9.13	399.42
-18.49	-8.33	399.42
-12.99	-7.37	399.42
-7.52	-6.28	399.42
-2.06	-5.11	399.42
3.40	-3.91	399.42
8.86	-2.68	399.42
14.31	-1.45	399.42
19.77	-0.23	399.42
25.22	0.98	399.42
30.68	2.16	399.42
36.15	3.31	399.42
41.62	4.42	399.42
47.10	5.51	399.42
52.57	6.58	399.42
58.05	7.65	399.42
63.53	8.73	399.42
66.27	9.26	399.42
69.00	9.81	399.42

F.4.7 Section 7

F.4. AERODYNAMIC PROFILE COORDINATES

x (mm)	y (mm)	z (mm)	x (mm)	y (mm)	z (mm)
65.87	6.52	481.32	32.63	1.02	481.32
55.14	4.64	481.32	32.41	0.98	481.32
55.05	4.62	481.32	31.31	0.80	481.32
53.81	4.42	481.32	31.08	0.76	481.32
53.71	4.41	481.32	29.99	0.57	481.32
52.48	4.21	481.32	29.76	0.53	481.32
52.37	4.20	481.32	28.67	0.35	481.32
51.16	4.00	481.32	28.44	0.31	481.32
51.04	3.98	481.32	27.36	0.12	481.32
49.83	3.79	481.32	27.11	0.08	481.32
49.70	3.77	481.32	26.04	-0.11	481.32
48.51	3.58	481.32	25.79	-0.15	481.32
48.37	3.56	481.32	24.72	-0.34	481.32
47.18	3.37	481.32	24.47	-0.38	481.32
47.03	3.35	481.32	23.41	-0.57	481.32
45.86	3.16	481.32	23.15	-0.61	481.32
45.70	3.14	481.32	22.09	-0.80	481.32
44.53	2.95	481.32	21.82	-0.85	481.32
44.37	2.93	481.32	20.78	-1.03	481.32
43.21	2.74	481.32	20.50	-1.08	481.32
43.04	2.72	481.32	19.47	-1.27	481.32
41.89	2.53	481.32	19.18	-1.32	481.32
41.71	2.50	481.32	18.16	-1.50	481.32
40.56	2.32	481.32	17.87	-1.55	481.32
40.38	2.29	481.32	16.85	-1.73	481.32
39.24	2.11	481.32	16.55	-1.79	481.32
39.05	2.08	481.32	15.54	-1.97	481.32
37.92	1.89	481.32	15.23	-2.03	481.32
37.72	1.86	481.32	14.23	-2.21	481.32
36.59	1.68	481.32	13.91	-2.26	481.32
36.39	1.64	481.32	12.92	-2.44	481.32
35.27	1.46	481.32	12.59	-2.50	481.32
35.06	1.42	481.32	11.61	-2.68	481.32
33.95	1.24	481.32	11.28	-2.74	481.32
33.74	1.20	481.32	10.31	-2.91	481.32
			9.96	-2.98	481.32

F.4. AERODYNAMIC PROFILE COORDINATES

x (mm)	y (mm)	z (mm)	x (mm)	y (mm)	z (mm)
9.00	-3.15	481.32	-14.35	-7.06	481.32
8.65	-3.21	481.32	-15.02	-7.15	481.32
7.70	-3.39	481.32	-15.63	-7.23	481.32
7.33	-3.45	481.32	-16.32	-7.32	481.32
6.39	-3.62	481.32	-16.91	-7.39	481.32
6.02	-3.69	481.32	-17.63	-7.48	481.32
5.09	-3.86	481.32	-18.18	-7.54	481.32
4.71	-3.92	481.32	-18.94	-7.62	481.32
3.79	-4.09	481.32	-19.46	-7.68	481.32
3.40	-4.16	481.32	-20.24	-7.76	481.32
2.48	-4.32	481.32	-20.72	-7.81	481.32
2.08	-4.39	481.32	-21.54	-7.89	481.32
1.18	-4.55	481.32	-21.98	-7.92	481.32
0.77	-4.62	481.32	-22.83	-7.99	481.32
-0.12	-4.78	481.32	-23.24	-8.02	481.32
-0.55	-4.85	481.32	-24.12	-8.08	481.32
-1.42	-5.01	481.32	-24.48	-8.10	481.32
-1.86	-5.08	481.32	-25.41	-8.15	481.32
-2.72	-5.23	481.32	-25.72	-8.16	481.32
-3.18	-5.31	481.32	-26.69	-8.19	481.32
-4.02	-5.45	481.32	-26.95	-8.20	481.32
-4.49	-5.53	481.32	-27.95	-8.21	481.32
-5.31	-5.67	481.32	-28.15	-8.21	481.32
-5.81	-5.75	481.32	-29.21	-8.19	481.32
-6.61	-5.88	481.32	-29.35	-8.19	481.32
-7.12	-5.97	481.32	-30.46	-8.14	481.32
-7.90	-6.09	481.32	-30.53	-8.13	481.32
-8.44	-6.18	481.32	-31.75	-8.04	481.32
-9.20	-6.30	481.32	-32.87	-7.90	481.32
-9.76	-6.38	481.32	-33.96	-7.71	481.32
-10.49	-6.50	481.32	-34.96	-7.48	481.32
-11.08	-6.59	481.32	-37.91	-6.29	481.32
-11.78	-6.69	481.32	-39.48	-4.51	481.32
-12.39	-6.78	481.32	-38.91	-2.19	481.32
-13.06	-6.88	481.32	-36.75	0.22	481.32
-13.70	-6.97	481.32	-35.87	0.88	481.32

F.4. AERODYNAMIC PROFILE COORDINATES

x (mm)	y (mm)	z (mm)	x (mm)	y (mm)	z (mm)
-34.86	1.53	481.32	-11.01	7.53	481.32
-33.77	2.12	481.32	-10.24	7.61	481.32
-32.72	2.65	481.32	-9.68	7.67	481.32
-32.63	2.69	481.32	-8.88	7.74	481.32
-31.55	3.16	481.32	-8.35	7.79	481.32
-31.40	3.22	481.32	-7.53	7.87	481.32
-30.36	3.62	481.32	-7.01	7.91	481.32
-30.14	3.70	481.32	-6.17	7.98	481.32
-29.13	4.05	481.32	-5.68	8.02	481.32
-28.86	4.14	481.32	-4.82	8.09	481.32
-27.89	4.44	481.32	-4.34	8.12	481.32
-27.57	4.54	481.32	-3.46	8.18	481.32
-26.64	4.80	481.32	-3.00	8.22	481.32
-26.27	4.90	481.32	-2.11	8.27	481.32
-25.38	5.14	481.32	-1.66	8.30	481.32
-24.96	5.24	481.32	-0.75	8.36	481.32
-24.11	5.44	481.32	-0.32	8.39	481.32
-23.65	5.55	481.32	0.60	8.44	481.32
-22.82	5.73	481.32	1.03	8.46	481.32
-22.32	5.83	481.32	1.95	8.51	481.32
-21.53	5.99	481.32	2.36	8.53	481.32
-21.00	6.10	481.32	3.31	8.57	481.32
-20.23	6.24	481.32	3.70	8.59	481.32
-19.66	6.34	481.32	4.66	8.63	481.32
-18.93	6.47	481.32	5.05	8.65	481.32
-18.33	6.56	481.32	6.02	8.69	481.32
-17.62	6.68	481.32	6.39	8.70	481.32
-16.98	6.77	481.32	7.37	8.74	481.32
-16.30	6.87	481.32	7.74	8.75	481.32
-15.64	6.97	481.32	8.72	8.78	481.32
-14.98	7.06	481.32	9.08	8.79	481.32
-14.29	7.15	481.32	10.08	8.82	481.32
-13.66	7.23	481.32	10.43	8.83	481.32
-12.94	7.31	481.32	11.44	8.86	481.32
-12.34	7.38	481.32	11.77	8.87	481.32
-11.59	7.47	481.32	12.79	8.89	481.32

F.4. AERODYNAMIC PROFILE COORDINATES

x (mm)	y (mm)	z (mm)
13.12	8.90	481.32
14.15	8.92	481.32
14.47	8.93	481.32
15.50	8.94	481.32
15.81	8.95	481.32
16.86	8.97	481.32
17.16	8.97	481.32
18.21	8.98	481.32
18.50	8.99	481.32
19.57	9.00	481.32
19.85	9.00	481.32
20.92	9.01	481.32
21.20	9.01	481.32
22.27	9.02	481.32
22.54	9.02	481.32
23.63	9.03	481.32
23.89	9.03	481.32
24.98	9.04	481.32
25.24	9.04	481.32
26.33	9.04	481.32
26.59	9.04	481.32
27.69	9.04	481.32
27.93	9.04	481.32
29.04	9.04	481.32
29.28	9.04	481.32
30.39	9.04	481.32
30.63	9.04	481.32
31.75	9.04	481.32
31.97	9.04	481.32
33.10	9.04	481.32
33.32	9.04	481.32
34.45	9.03	481.32
34.67	9.03	481.32
35.80	9.03	481.32
36.01	9.03	481.32
37.16	9.02	481.32

x (mm)	y (mm)	z (mm)
37.36	9.02	481.32
38.51	9.02	481.32
38.71	9.02	481.32
39.86	9.01	481.32
40.05	9.01	481.32
41.21	9.00	481.32
41.40	9.00	481.32
42.56	8.99	481.32
42.74	8.99	481.32
43.92	8.98	481.32
44.09	8.98	481.32
45.27	8.97	481.32
45.43	8.97	481.32
46.62	8.95	481.32
46.77	8.95	481.32
47.97	8.94	481.32
48.12	8.94	481.32
49.33	8.92	481.32
49.46	8.92	481.32
50.68	8.90	481.32
50.80	8.90	481.32
52.04	8.88	481.32
52.15	8.88	481.32
53.39	8.86	481.32
53.49	8.86	481.32
54.74	8.84	481.32
54.84	8.84	481.32
65.73	8.52	481.32

F.4.8 Section 8

x (mm)	y (mm)	z (mm)
62.41	4.51	563.22
52.22	2.99	563.22
52.13	2.98	563.22
50.96	2.83	563.22

F.4. AERODYNAMIC PROFILE COORDINATES

x (mm)	y (mm)	z (mm)	x (mm)	y (mm)	z (mm)
50.86	2.82	563.22	28.14	-0.25	563.22
49.70	2.66	563.22	27.11	-0.40	563.22
49.59	2.65	563.22	26.88	-0.43	563.22
48.44	2.50	563.22	25.86	-0.58	563.22
48.33	2.48	563.22	25.63	-0.62	563.22
47.18	2.33	563.22	24.61	-0.77	563.22
47.06	2.31	563.22	24.37	-0.80	563.22
45.93	2.17	563.22	23.36	-0.95	563.22
45.79	2.15	563.22	23.11	-0.99	563.22
44.67	2.00	563.22	22.11	-1.14	563.22
44.53	1.98	563.22	21.86	-1.17	563.22
43.41	1.83	563.22	20.86	-1.32	563.22
43.26	1.81	563.22	20.61	-1.36	563.22
42.16	1.67	563.22	19.61	-1.51	563.22
42.00	1.65	563.22	19.35	-1.55	563.22
40.90	1.50	563.22	18.37	-1.70	563.22
40.74	1.48	563.22	18.10	-1.74	563.22
39.65	1.33	563.22	17.12	-1.89	563.22
39.48	1.31	563.22	16.85	-1.93	563.22
38.39	1.17	563.22	15.88	-2.08	563.22
38.21	1.14	563.22	15.60	-2.12	563.22
37.13	1.00	563.22	14.64	-2.27	563.22
36.95	0.97	563.22	14.34	-2.31	563.22
35.88	0.83	563.22	13.39	-2.46	563.22
35.69	0.80	563.22	13.09	-2.50	563.22
34.62	0.66	563.22	12.15	-2.65	563.22
34.43	0.63	563.22	11.84	-2.69	563.22
33.37	0.49	563.22	10.91	-2.84	563.22
33.17	0.46	563.22	10.59	-2.89	563.22
32.12	0.31	563.22	9.67	-3.03	563.22
31.91	0.28	563.22	9.34	-3.08	563.22
30.86	0.14	563.22	8.43	-3.22	563.22
30.65	0.11	563.22	8.10	-3.27	563.22
29.61	-0.04	563.22	7.19	-3.41	563.22
29.40	-0.07	563.22	6.85	-3.46	563.22
28.36	-0.22	563.22	5.95	-3.60	563.22

F.4. AERODYNAMIC PROFILE COORDINATES

x (mm)	y (mm)	z (mm)	x (mm)	y (mm)	z (mm)
5.60	-3.65	563.22	-16.84	-6.65	563.22
4.72	-3.79	563.22	-17.37	-6.69	563.22
4.36	-3.84	563.22	-18.08	-6.76	563.22
3.48	-3.98	563.22	-18.57	-6.80	563.22
3.11	-4.03	563.22	-19.31	-6.85	563.22
2.24	-4.17	563.22	-19.77	-6.89	563.22
1.86	-4.22	563.22	-20.54	-6.94	563.22
1.01	-4.35	563.22	-20.96	-6.96	563.22
0.61	-4.41	563.22	-21.77	-7.01	563.22
-0.23	-4.53	563.22	-22.15	-7.03	563.22
-0.63	-4.59	563.22	-22.99	-7.06	563.22
-1.46	-4.72	563.22	-23.33	-7.07	563.22
-1.88	-4.78	563.22	-24.21	-7.09	563.22
-2.69	-4.90	563.22	-24.50	-7.10	563.22
-3.13	-4.96	563.22	-25.42	-7.10	563.22
-3.93	-5.07	563.22	-25.66	-7.10	563.22
-4.38	-5.14	563.22	-26.61	-7.09	563.22
-5.16	-5.25	563.22	-26.80	-7.08	563.22
-5.63	-5.31	563.22	-27.81	-7.04	563.22
-6.39	-5.42	563.22	-27.93	-7.03	563.22
-6.88	-5.48	563.22	-28.99	-6.95	563.22
-7.62	-5.58	563.22	-29.04	-6.95	563.22
-8.13	-5.65	563.22	-30.19	-6.84	563.22
-8.84	-5.74	563.22	-31.26	-6.67	563.22
-9.37	-5.81	563.22	-32.27	-6.47	563.22
-10.07	-5.90	563.22	-33.22	-6.23	563.22
-10.62	-5.97	563.22	-35.97	-5.02	563.22
-11.29	-6.05	563.22	-37.42	-3.31	563.22
-11.87	-6.12	563.22	-36.83	-1.13	563.22
-12.51	-6.19	563.22	-34.72	1.11	563.22
-13.12	-6.26	563.22	-33.88	1.71	563.22
-13.73	-6.33	563.22	-32.91	2.29	563.22
-14.36	-6.40	563.22	-31.86	2.83	563.22
-14.95	-6.46	563.22	-30.85	3.30	563.22
-15.60	-6.53	563.22	-30.77	3.34	563.22
-16.16	-6.58	563.22	-29.74	3.75	563.22

F.4. AERODYNAMIC PROFILE COORDINATES

x (mm)	y (mm)	z (mm)	x (mm)	y (mm)	z (mm)
-29.59	3.81	563.22	-6.92	7.63	563.22
-28.60	4.16	563.22	-6.44	7.66	563.22
-28.39	4.23	563.22	-5.64	7.71	563.22
-27.43	4.54	563.22	-5.17	7.74	563.22
-27.17	4.62	563.22	-4.36	7.78	563.22
-26.25	4.88	563.22	-3.91	7.80	563.22
-25.94	4.96	563.22	-3.08	7.84	563.22
-25.06	5.19	563.22	-2.64	7.86	563.22
-24.71	5.28	563.22	-1.79	7.89	563.22
-23.86	5.48	563.22	-1.37	7.91	563.22
-23.46	5.56	563.22	-0.51	7.94	563.22
-22.65	5.74	563.22	-0.10	7.95	563.22
-22.21	5.83	563.22	0.77	7.98	563.22
-21.43	5.98	563.22	1.17	7.99	563.22
-20.96	6.06	563.22	2.05	8.01	563.22
-20.20	6.20	563.22	2.44	8.02	563.22
-19.69	6.28	563.22	3.33	8.04	563.22
-18.97	6.40	563.22	3.71	8.05	563.22
-18.43	6.48	563.22	4.61	8.07	563.22
-17.73	6.58	563.22	4.98	8.07	563.22
-17.16	6.66	563.22	5.89	8.09	563.22
-16.49	6.75	563.22	6.25	8.09	563.22
-15.89	6.82	563.22	7.17	8.10	563.22
-15.24	6.90	563.22	7.52	8.11	563.22
-14.61	6.97	563.22	8.46	8.11	563.22
-13.99	7.04	563.22	8.79	8.11	563.22
-13.33	7.11	563.22	9.74	8.12	563.22
-12.74	7.17	563.22	10.07	8.12	563.22
-12.05	7.24	563.22	11.02	8.12	563.22
-11.48	7.29	563.22	11.34	8.12	563.22
-10.77	7.35	563.22	12.30	8.12	563.22
-10.22	7.40	563.22	12.61	8.12	563.22
-9.49	7.46	563.22	13.58	8.11	563.22
-8.96	7.50	563.22	13.88	8.11	563.22
-8.21	7.55	563.22	14.86	8.10	563.22
-7.70	7.58	563.22	15.16	8.10	563.22

F.4. AERODYNAMIC PROFILE COORDINATES

x (mm)	y (mm)	z (mm)
16.14	8.09	563.22
16.43	8.09	563.22
17.43	8.08	563.22
17.70	8.07	563.22
18.71	8.06	563.22
18.98	8.06	563.22
19.99	8.04	563.22
20.25	8.04	563.22
21.27	8.02	563.22
21.52	8.01	563.22
22.54	7.99	563.22
22.79	7.99	563.22
23.82	7.97	563.22
24.07	7.96	563.22
25.10	7.94	563.22
25.34	7.93	563.22
26.38	7.91	563.22
26.61	7.90	563.22
27.66	7.88	563.22
27.89	7.87	563.22
28.94	7.84	563.22
29.16	7.84	563.22
30.22	7.81	563.22
30.43	7.81	563.22
31.50	7.78	563.22
31.71	7.77	563.22
32.77	7.74	563.22
32.98	7.73	563.22
34.05	7.70	563.22
34.25	7.70	563.22
35.33	7.67	563.22
35.52	7.66	563.22
36.61	7.63	563.22
36.79	7.62	563.22
37.88	7.59	563.22
38.06	7.58	563.22

x (mm)	y (mm)	z (mm)
39.16	7.55	563.22
39.34	7.54	563.22
40.44	7.51	563.22
40.61	7.50	563.22
41.72	7.46	563.22
41.88	7.46	563.22
42.99	7.42	563.22
43.15	7.42	563.22
44.27	7.38	563.22
44.42	7.37	563.22
45.55	7.33	563.22
45.69	7.32	563.22
46.83	7.28	563.22
46.95	7.28	563.22
48.11	7.23	563.22
48.22	7.23	563.22
49.39	7.18	563.22
49.49	7.18	563.22
50.67	7.13	563.22
50.76	7.13	563.22
51.95	7.08	563.22
52.03	7.07	563.22
62.32	6.51	563.22

F.4.9 Section 9

x (mm)	y (mm)	z (mm)
58.72	2.98	645.12
49.12	1.76	645.12
49.03	1.75	645.12
47.93	1.63	645.12
47.84	1.62	645.12
46.74	1.49	645.12
46.64	1.48	645.12
45.56	1.36	645.12
45.45	1.35	645.12

F.4. AERODYNAMIC PROFILE COORDINATES

x (mm)	y (mm)	z (mm)	x (mm)	y (mm)	z (mm)
44.37	1.23	645.12	23.10	-1.23	645.12
44.26	1.22	645.12	22.88	-1.26	645.12
43.19	1.10	645.12	21.92	-1.38	645.12
43.06	1.09	645.12	21.70	-1.41	645.12
42.00	0.97	645.12	20.75	-1.53	645.12
41.87	0.96	645.12	20.51	-1.56	645.12
40.82	0.84	645.12	19.57	-1.68	645.12
40.68	0.83	645.12	19.33	-1.71	645.12
39.64	0.71	645.12	18.40	-1.83	645.12
39.49	0.69	645.12	18.15	-1.86	645.12
38.45	0.58	645.12	17.22	-1.98	645.12
38.30	0.56	645.12	16.97	-2.01	645.12
37.27	0.45	645.12	16.05	-2.13	645.12
37.11	0.43	645.12	15.79	-2.17	645.12
36.09	0.31	645.12	14.88	-2.29	645.12
35.92	0.30	645.12	14.61	-2.32	645.12
34.91	0.18	645.12	13.71	-2.44	645.12
34.73	0.16	645.12	13.43	-2.48	645.12
33.72	0.05	645.12	12.54	-2.60	645.12
33.55	0.03	645.12	12.25	-2.63	645.12
32.54	-0.09	645.12	11.37	-2.75	645.12
32.36	-0.11	645.12	11.08	-2.79	645.12
31.36	-0.23	645.12	10.20	-2.91	645.12
31.17	-0.25	645.12	9.90	-2.94	645.12
30.18	-0.37	645.12	9.03	-3.06	645.12
29.99	-0.39	645.12	8.72	-3.10	645.12
29.00	-0.51	645.12	7.86	-3.21	645.12
28.80	-0.53	645.12	7.54	-3.26	645.12
27.82	-0.65	645.12	6.69	-3.37	645.12
27.62	-0.67	645.12	6.37	-3.41	645.12
26.64	-0.79	645.12	5.53	-3.52	645.12
26.43	-0.82	645.12	5.19	-3.57	645.12
25.46	-0.94	645.12	4.36	-3.68	645.12
25.25	-0.96	645.12	4.02	-3.72	645.12
24.28	-1.08	645.12	3.20	-3.83	645.12
24.06	-1.11	645.12	2.85	-3.87	645.12

F.4. AERODYNAMIC PROFILE COORDINATES

x (mm)	y (mm)	z (mm)	x (mm)	y (mm)	z (mm)
2.02	-3.98	645.12	-18.70	-6.10	645.12
1.67	-4.03	645.12	-19.43	-6.13	645.12
0.86	-4.13	645.12	-19.83	-6.15	645.12
0.49	-4.18	645.12	-20.58	-6.17	645.12
-0.30	-4.28	645.12	-20.94	-6.18	645.12
-0.68	-4.33	645.12	-21.73	-6.20	645.12
-1.46	-4.42	645.12	-22.05	-6.20	645.12
-1.86	-4.47	645.12	-22.88	-6.21	645.12
-2.62	-4.57	645.12	-23.15	-6.20	645.12
-3.03	-4.62	645.12	-24.01	-6.19	645.12
-3.78	-4.71	645.12	-24.24	-6.19	645.12
-4.21	-4.76	645.12	-25.14	-6.15	645.12
-4.94	-4.85	645.12	-25.31	-6.14	645.12
-5.39	-4.90	645.12	-26.26	-6.08	645.12
-6.10	-4.98	645.12	-26.37	-6.07	645.12
-6.56	-5.04	645.12	-27.36	-5.98	645.12
-7.26	-5.12	645.12	-27.42	-5.97	645.12
-7.74	-5.17	645.12	-28.50	-5.85	645.12
-8.42	-5.24	645.12	-29.49	-5.67	645.12
-8.92	-5.30	645.12	-30.44	-5.46	645.12
-9.57	-5.37	645.12	-31.32	-5.21	645.12
-10.09	-5.42	645.12	-33.89	-4.03	645.12
-10.72	-5.48	645.12	-35.22	-2.39	645.12
-11.27	-5.54	645.12	-34.62	-0.35	645.12
-11.87	-5.59	645.12	-32.60	1.71	645.12
-12.44	-5.65	645.12	-31.79	2.25	645.12
-13.02	-5.70	645.12	-30.87	2.79	645.12
-13.61	-5.75	645.12	-29.88	3.27	645.12
-14.16	-5.80	645.12	-28.92	3.70	645.12
-14.78	-5.85	645.12	-28.84	3.73	645.12
-15.30	-5.89	645.12	-27.87	4.10	645.12
-15.95	-5.93	645.12	-27.73	4.15	645.12
-16.44	-5.97	645.12	-26.79	4.47	645.12
-17.11	-6.01	645.12	-26.59	4.53	645.12
-17.57	-6.04	645.12	-25.68	4.80	645.12
-18.27	-6.08	645.12	-25.44	4.87	645.12

F.4. AERODYNAMIC PROFILE COORDINATES

x (mm)	y (mm)	z (mm)	x (mm)	y (mm)	z (mm)
-24.57	5.10	645.12	-3.52	7.42	645.12
-24.28	5.17	645.12	-2.74	7.44	645.12
-23.45	5.37	645.12	-2.33	7.45	645.12
-23.11	5.44	645.12	-1.54	7.47	645.12
-22.31	5.61	645.12	-1.14	7.48	645.12
-21.93	5.69	645.12	-0.33	7.49	645.12
-21.17	5.83	645.12	0.06	7.50	645.12
-20.76	5.91	645.12	0.88	7.50	645.12
-20.02	6.04	645.12	1.25	7.51	645.12
-19.57	6.11	645.12	2.08	7.51	645.12
-18.86	6.22	645.12	2.44	7.52	645.12
-18.38	6.29	645.12	3.28	7.52	645.12
-17.70	6.38	645.12	3.63	7.52	645.12
-17.19	6.45	645.12	4.49	7.52	645.12
-16.53	6.53	645.12	4.83	7.52	645.12
-15.99	6.60	645.12	5.69	7.51	645.12
-15.36	6.67	645.12	6.03	7.51	645.12
-14.80	6.73	645.12	6.89	7.50	645.12
-14.18	6.79	645.12	7.22	7.50	645.12
-13.59	6.85	645.12	8.10	7.49	645.12
-13.01	6.90	645.12	8.42	7.48	645.12
-12.39	6.95	645.12	9.30	7.47	645.12
-11.83	7.00	645.12	9.61	7.46	645.12
-11.19	7.05	645.12	10.51	7.45	645.12
-10.65	7.09	645.12	10.81	7.44	645.12
-9.98	7.13	645.12	11.71	7.42	645.12
-9.46	7.16	645.12	12.00	7.41	645.12
-8.77	7.20	645.12	12.91	7.39	645.12
-8.28	7.23	645.12	13.20	7.39	645.12
-7.57	7.27	645.12	14.12	7.36	645.12
-7.09	7.29	645.12	14.39	7.35	645.12
-6.36	7.32	645.12	15.32	7.33	645.12
-5.90	7.34	645.12	15.59	7.32	645.12
-5.15	7.37	645.12	16.52	7.29	645.12
-4.71	7.39	645.12	16.78	7.28	645.12
-3.95	7.41	645.12	17.73	7.25	645.12

F.4. AERODYNAMIC PROFILE COORDINATES

x (mm)	y (mm)	z (mm)
17.98	7.24	645.12
18.93	7.20	645.12
19.18	7.20	645.12
20.13	7.16	645.12
20.37	7.15	645.12
21.33	7.11	645.12
21.57	7.10	645.12
22.53	7.06	645.12
22.76	7.05	645.12
23.73	7.01	645.12
23.96	7.00	645.12
24.93	6.96	645.12
25.15	6.95	645.12
26.13	6.91	645.12
26.35	6.90	645.12
27.34	6.85	645.12
27.54	6.85	645.12
28.54	6.80	645.12
28.74	6.79	645.12
29.74	6.74	645.12
29.93	6.73	645.12
30.94	6.69	645.12
31.13	6.68	645.12
32.14	6.63	645.12
32.32	6.62	645.12
33.33	6.57	645.12
33.52	6.56	645.12
34.53	6.51	645.12
34.71	6.50	645.12
35.73	6.45	645.12
35.90	6.44	645.12
36.93	6.39	645.12
37.10	6.38	645.12
38.13	6.32	645.12
38.29	6.32	645.12
39.33	6.26	645.12

x (mm)	y (mm)	z (mm)
39.48	6.25	645.12
40.53	6.20	645.12
40.67	6.19	645.12
41.73	6.13	645.12
41.86	6.12	645.12
42.93	6.06	645.12
43.06	6.05	645.12
44.13	5.99	645.12
44.25	5.99	645.12
45.33	5.92	645.12
45.44	5.92	645.12
46.53	5.85	645.12
46.63	5.85	645.12
47.73	5.78	645.12
47.82	5.77	645.12
48.93	5.71	645.12
49.02	5.70	645.12
58.67	4.98	645.12

F.4.10 Section 10

x (mm)	y (mm)	z (mm)
54.83	1.82	727.02
45.85	0.83	727.02
45.77	0.82	727.02
44.74	0.72	727.02
44.65	0.72	727.02
43.63	0.62	727.02
43.54	0.61	727.02
42.52	0.52	727.02
42.42	0.51	727.02
41.42	0.41	727.02
41.31	0.40	727.02
40.31	0.31	727.02
40.19	0.30	727.02
39.20	0.21	727.02
39.08	0.20	727.02

F.4. AERODYNAMIC PROFILE COORDINATES

x (mm)	y (mm)	z (mm)	x (mm)	y (mm)	z (mm)
38.10	0.11	727.02	18.24	-1.90	727.02
37.97	0.09	727.02	18.01	-1.93	727.02
36.99	0.00	727.02	17.14	-2.03	727.02
36.85	-0.01	727.02	16.91	-2.05	727.02
35.88	-0.10	727.02	16.04	-2.15	727.02
35.74	-0.12	727.02	15.80	-2.18	727.02
34.78	-0.21	727.02	14.94	-2.27	727.02
34.63	-0.22	727.02	14.70	-2.30	727.02
33.67	-0.31	727.02	13.85	-2.40	727.02
33.52	-0.33	727.02	13.60	-2.43	727.02
32.57	-0.42	727.02	12.75	-2.52	727.02
32.41	-0.43	727.02	12.50	-2.55	727.02
31.46	-0.52	727.02	11.66	-2.65	727.02
31.30	-0.54	727.02	11.39	-2.68	727.02
30.36	-0.63	727.02	10.56	-2.77	727.02
30.19	-0.65	727.02	10.29	-2.80	727.02
29.25	-0.74	727.02	9.47	-2.90	727.02
29.08	-0.76	727.02	9.19	-2.93	727.02
28.15	-0.85	727.02	8.38	-3.02	727.02
27.97	-0.87	727.02	8.09	-3.06	727.02
27.05	-0.96	727.02	7.29	-3.15	727.02
26.86	-0.98	727.02	6.99	-3.18	727.02
25.94	-1.08	727.02	6.19	-3.27	727.02
25.75	-1.10	727.02	5.89	-3.31	727.02
24.84	-1.19	727.02	5.10	-3.40	727.02
24.65	-1.21	727.02	4.79	-3.43	727.02
23.74	-1.31	727.02	4.01	-3.52	727.02
23.54	-1.33	727.02	3.69	-3.56	727.02
22.64	-1.42	727.02	2.92	-3.65	727.02
22.43	-1.45	727.02	2.60	-3.68	727.02
21.53	-1.54	727.02	1.83	-3.77	727.02
21.33	-1.56	727.02	1.50	-3.81	727.02
20.43	-1.66	727.02	0.74	-3.89	727.02
20.22	-1.69	727.02	0.40	-3.93	727.02
19.34	-1.78	727.02	-0.34	-4.01	727.02
19.12	-1.81	727.02	-0.70	-4.05	727.02

F.4. AERODYNAMIC PROFILE COORDINATES

x (mm)	y (mm)	z (mm)	x (mm)	y (mm)	z (mm)
-1.43	-4.13	727.02	-20.67	-5.46	727.02
-1.80	-4.17	727.02	-21.44	-5.45	727.02
-2.52	-4.24	727.02	-21.70	-5.44	727.02
-2.90	-4.28	727.02	-22.50	-5.42	727.02
-3.60	-4.36	727.02	-22.71	-5.41	727.02
-4.00	-4.40	727.02	-23.55	-5.36	727.02
-4.69	-4.47	727.02	-23.71	-5.35	727.02
-5.10	-4.51	727.02	-24.59	-5.28	727.02
-5.77	-4.58	727.02	-24.70	-5.27	727.02
-6.20	-4.62	727.02	-25.62	-5.17	727.02
-6.85	-4.68	727.02	-25.67	-5.16	727.02
-7.30	-4.72	727.02	-26.67	-5.02	727.02
-7.93	-4.78	727.02	-27.60	-4.84	727.02
-8.40	-4.82	727.02	-28.48	-4.63	727.02
-9.01	-4.88	727.02	-29.30	-4.39	727.02
-9.50	-4.92	727.02	-31.68	-3.24	727.02
-10.09	-4.97	727.02	-32.89	-1.69	727.02
-10.60	-5.01	727.02	-32.30	0.20	727.02
-11.16	-5.05	727.02	-30.39	2.09	727.02
-11.69	-5.09	727.02	-29.63	2.59	727.02
-12.23	-5.13	727.02	-28.76	3.07	727.02
-12.79	-5.17	727.02	-27.82	3.52	727.02
-13.30	-5.21	727.02	-26.93	3.90	727.02
-13.88	-5.24	727.02	-26.85	3.93	727.02
-14.37	-5.27	727.02	-25.94	4.26	727.02
-14.97	-5.30	727.02	-25.81	4.30	727.02
-15.43	-5.33	727.02	-24.93	4.58	727.02
-16.05	-5.36	727.02	-24.74	4.64	727.02
-16.49	-5.38	727.02	-23.89	4.88	727.02
-17.14	-5.40	727.02	-23.66	4.94	727.02
-17.54	-5.42	727.02	-22.84	5.14	727.02
-18.22	-5.44	727.02	-22.57	5.20	727.02
-18.59	-5.44	727.02	-21.79	5.37	727.02
-19.30	-5.46	727.02	-21.48	5.44	727.02
-19.63	-5.46	727.02	-20.73	5.59	727.02
-20.37	-5.46	727.02	-20.38	5.65	727.02

F.4. AERODYNAMIC PROFILE COORDINATES

x (mm)	y (mm)	z (mm)	x (mm)	y (mm)	z (mm)
-19.66	5.78	727.02	0.17	7.02	727.02
-19.27	5.84	727.02	0.93	7.01	727.02
-18.58	5.95	727.02	1.28	7.01	727.02
-18.17	6.01	727.02	2.05	7.00	727.02
-17.50	6.10	727.02	2.39	7.00	727.02
-17.05	6.16	727.02	3.18	6.99	727.02
-16.41	6.24	727.02	3.50	6.99	727.02
-15.94	6.29	727.02	4.30	6.97	727.02
-15.32	6.36	727.02	4.62	6.97	727.02
-14.82	6.41	727.02	5.42	6.95	727.02
-14.23	6.47	727.02	5.73	6.94	727.02
-13.70	6.52	727.02	6.54	6.92	727.02
-13.13	6.57	727.02	6.85	6.92	727.02
-12.58	6.61	727.02	7.67	6.89	727.02
-12.03	6.65	727.02	7.96	6.88	727.02
-11.45	6.69	727.02	8.79	6.86	727.02
-10.93	6.73	727.02	9.08	6.85	727.02
-10.33	6.76	727.02	9.91	6.82	727.02
-9.83	6.79	727.02	10.19	6.81	727.02
-9.20	6.82	727.02	11.04	6.78	727.02
-8.72	6.85	727.02	11.31	6.77	727.02
-8.08	6.87	727.02	12.16	6.73	727.02
-7.61	6.89	727.02	12.42	6.72	727.02
-6.95	6.92	727.02	13.28	6.69	727.02
-6.50	6.93	727.02	13.54	6.68	727.02
-5.82	6.95	727.02	14.40	6.64	727.02
-5.40	6.96	727.02	14.65	6.62	727.02
-4.70	6.98	727.02	15.53	6.58	727.02
-4.28	6.99	727.02	15.77	6.57	727.02
-3.57	7.00	727.02	16.65	6.53	727.02
-3.17	7.00	727.02	16.88	6.52	727.02
-2.44	7.01	727.02	17.77	6.47	727.02
-2.06	7.01	727.02	18.00	6.46	727.02
-1.32	7.02	727.02	18.89	6.41	727.02
-0.95	7.02	727.02	19.11	6.40	727.02
-0.19	7.02	727.02	20.01	6.35	727.02

F.4. AERODYNAMIC PROFILE COORDINATES

x (mm)	y (mm)	z (mm)
20.23	6.34	727.02
21.13	6.29	727.02
21.34	6.27	727.02
22.25	6.22	727.02
22.46	6.21	727.02
23.37	6.16	727.02
23.57	6.14	727.02
24.49	6.09	727.02
24.68	6.08	727.02
25.61	6.02	727.02
25.80	6.01	727.02
26.72	5.95	727.02
26.91	5.94	727.02
27.84	5.88	727.02
28.03	5.87	727.02
28.96	5.81	727.02
29.14	5.80	727.02
30.08	5.74	727.02
30.25	5.73	727.02
31.20	5.67	727.02
31.37	5.66	727.02
32.32	5.59	727.02
32.48	5.58	727.02
33.44	5.52	727.02
33.59	5.51	727.02
34.55	5.44	727.02
34.71	5.43	727.02
35.67	5.37	727.02
35.82	5.36	727.02
36.79	5.29	727.02
36.93	5.28	727.02
37.91	5.21	727.02
38.04	5.20	727.02
39.03	5.13	727.02
39.15	5.12	727.02
40.14	5.05	727.02

x (mm)	y (mm)	z (mm)
40.26	5.04	727.02
41.26	4.97	727.02
41.37	4.96	727.02
42.38	4.89	727.02
42.48	4.88	727.02
43.50	4.80	727.02
43.59	4.80	727.02
44.62	4.72	727.02
44.70	4.71	727.02
45.74	4.64	727.02
45.82	4.63	727.02
54.81	3.82	727.02

F.4.11 Section 11

x (mm)	y (mm)	z (mm)
50.91	0.97	808.92
42.57	0.17	808.92
42.49	0.16	808.92
41.53	0.09	808.92
41.46	0.08	808.92
40.50	0.00	808.92
40.42	0.00	808.92
39.48	-0.08	808.92
39.38	-0.08	808.92
38.45	-0.16	808.92
38.34	-0.17	808.92
37.42	-0.24	808.92
37.31	-0.25	808.92
36.39	-0.32	808.92
36.27	-0.33	808.92
35.36	-0.40	808.92
35.24	-0.41	808.92
34.33	-0.49	808.92
34.21	-0.50	808.92
33.31	-0.57	808.92
33.17	-0.58	808.92

F.4. AERODYNAMIC PROFILE COORDINATES

x (mm)	y (mm)	z (mm)	x (mm)	y (mm)	z (mm)
32.28	-0.65	808.92	13.84	-2.32	808.92
32.14	-0.66	808.92	13.62	-2.35	808.92
31.25	-0.74	808.92	12.83	-2.43	808.92
31.11	-0.75	808.92	12.59	-2.45	808.92
30.22	-0.82	808.92	11.81	-2.53	808.92
30.08	-0.83	808.92	11.57	-2.55	808.92
29.20	-0.90	808.92	10.79	-2.63	808.92
29.04	-0.92	808.92	10.54	-2.65	808.92
28.17	-0.99	808.92	9.77	-2.73	808.92
28.01	-1.00	808.92	9.52	-2.76	808.92
27.14	-1.08	808.92	8.76	-2.84	808.92
26.98	-1.09	808.92	8.50	-2.86	808.92
26.12	-1.17	808.92	7.74	-2.94	808.92
25.95	-1.18	808.92	7.47	-2.97	808.92
25.09	-1.26	808.92	6.73	-3.04	808.92
24.92	-1.27	808.92	6.45	-3.07	808.92
24.07	-1.35	808.92	5.71	-3.14	808.92
23.89	-1.36	808.92	5.43	-3.17	808.92
23.04	-1.44	808.92	4.70	-3.25	808.92
22.86	-1.46	808.92	4.41	-3.27	808.92
22.02	-1.54	808.92	3.69	-3.35	808.92
21.83	-1.55	808.92	3.39	-3.38	808.92
20.99	-1.63	808.92	2.67	-3.45	808.92
20.81	-1.65	808.92	2.37	-3.48	808.92
19.97	-1.73	808.92	1.65	-3.55	808.92
19.78	-1.75	808.92	1.35	-3.58	808.92
18.95	-1.82	808.92	0.65	-3.65	808.92
18.75	-1.84	808.92	0.32	-3.68	808.92
17.93	-1.92	808.92	-0.36	-3.75	808.92
17.72	-1.94	808.92	-0.70	-3.78	808.92
16.90	-2.02	808.92	-1.37	-3.84	808.92
16.70	-2.04	808.92	-1.72	-3.87	808.92
15.88	-2.12	808.92	-2.38	-3.93	808.92
15.67	-2.14	808.92	-2.74	-3.97	808.92
14.86	-2.22	808.92	-3.39	-4.03	808.92
14.64	-2.24	808.92	-3.76	-4.06	808.92

F.4. AERODYNAMIC PROFILE COORDINATES

x (mm)	y (mm)	z (mm)	x (mm)	y (mm)	z (mm)
-4.40	-4.12	808.92	-22.07	-4.70	808.92
-4.78	-4.15	808.92	-22.88	-4.62	808.92
-5.41	-4.20	808.92	-22.98	-4.61	808.92
-5.81	-4.24	808.92	-23.84	-4.50	808.92
-6.41	-4.29	808.92	-23.89	-4.49	808.92
-6.83	-4.32	808.92	-24.82	-4.35	808.92
-7.41	-4.37	808.92	-25.67	-4.18	808.92
-7.85	-4.40	808.92	-26.49	-3.97	808.92
-8.42	-4.44	808.92	-27.25	-3.73	808.92
-8.87	-4.47	808.92	-29.44	-2.64	808.92
-9.42	-4.51	808.92	-30.55	-1.18	808.92
-9.89	-4.54	808.92	-29.98	0.57	808.92
-10.42	-4.58	808.92	-28.18	2.30	808.92
-10.91	-4.61	808.92	-27.47	2.76	808.92
-11.41	-4.64	808.92	-26.66	3.19	808.92
-11.93	-4.67	808.92	-25.79	3.59	808.92
-12.41	-4.69	808.92	-24.95	3.94	808.92
-12.94	-4.72	808.92	-24.88	3.96	808.92
-13.40	-4.74	808.92	-24.03	4.26	808.92
-13.95	-4.76	808.92	-23.90	4.30	808.92
-14.38	-4.78	808.92	-23.08	4.55	808.92
-14.96	-4.80	808.92	-22.91	4.60	808.92
-15.37	-4.81	808.92	-22.12	4.81	808.92
-15.97	-4.83	808.92	-21.90	4.87	808.92
-16.34	-4.83	808.92	-21.15	5.04	808.92
-16.97	-4.84	808.92	-20.89	5.10	808.92
-17.32	-4.85	808.92	-20.17	5.25	808.92
-17.97	-4.85	808.92	-19.87	5.31	808.92
-18.29	-4.85	808.92	-19.18	5.44	808.92
-18.97	-4.84	808.92	-18.85	5.49	808.92
-19.25	-4.83	808.92	-18.18	5.60	808.92
-19.96	-4.82	808.92	-17.82	5.66	808.92
-20.20	-4.81	808.92	-17.18	5.75	808.92
-20.94	-4.77	808.92	-16.79	5.80	808.92
-21.14	-4.76	808.92	-16.17	5.88	808.92
-21.92	-4.71	808.92	-15.76	5.93	808.92

F.4. AERODYNAMIC PROFILE COORDINATES

x (mm)	y (mm)	z (mm)	x (mm)	y (mm)	z (mm)
-15.16	6.00	808.92	3.33	6.47	808.92
-14.72	6.04	808.92	4.07	6.45	808.92
-14.15	6.10	808.92	4.37	6.44	808.92
-13.68	6.14	808.92	5.11	6.42	808.92
-13.13	6.19	808.92	5.40	6.41	808.92
-12.64	6.23	808.92	6.15	6.38	808.92
-12.11	6.27	808.92	6.44	6.37	808.92
-11.60	6.30	808.92	7.20	6.34	808.92
-11.09	6.33	808.92	7.47	6.33	808.92
-10.56	6.36	808.92	8.24	6.30	808.92
-10.07	6.39	808.92	8.51	6.29	808.92
-9.51	6.42	808.92	9.28	6.25	808.92
-9.04	6.44	808.92	9.54	6.24	808.92
-8.46	6.46	808.92	10.32	6.20	808.92
-8.01	6.48	808.92	10.58	6.19	808.92
-7.42	6.49	808.92	11.36	6.15	808.92
-6.99	6.51	808.92	11.61	6.13	808.92
-6.37	6.52	808.92	12.41	6.09	808.92
-5.96	6.53	808.92	12.64	6.08	808.92
-5.32	6.54	808.92	13.45	6.03	808.92
-4.93	6.55	808.92	13.68	6.02	808.92
-4.28	6.55	808.92	14.49	5.97	808.92
-3.90	6.56	808.92	14.71	5.96	808.92
-3.23	6.56	808.92	15.53	5.91	808.92
-2.87	6.56	808.92	15.75	5.89	808.92
-2.19	6.56	808.92	16.57	5.84	808.92
-1.83	6.56	808.92	16.78	5.83	808.92
-1.14	6.55	808.92	17.61	5.77	808.92
-0.80	6.55	808.92	17.81	5.76	808.92
-0.10	6.54	808.92	18.64	5.70	808.92
0.23	6.54	808.92	18.85	5.69	808.92
0.94	6.53	808.92	19.68	5.63	808.92
1.27	6.52	808.92	19.88	5.62	808.92
1.99	6.51	808.92	20.72	5.56	808.92
2.30	6.50	808.92	20.92	5.55	808.92
3.03	6.48	808.92	21.76	5.49	808.92

F.4. AERODYNAMIC PROFILE COORDINATES

x (mm)	y (mm)	z (mm)
21.95	5.47	808.92
22.80	5.41	808.92
22.98	5.40	808.92
23.84	5.34	808.92
24.02	5.33	808.92
24.87	5.26	808.92
25.05	5.25	808.92
25.91	5.18	808.92
26.08	5.17	808.92
26.95	5.11	808.92
27.12	5.09	808.92
27.99	5.03	808.92
28.15	5.02	808.92
29.02	4.95	808.92
29.18	4.94	808.92
30.06	4.87	808.92
30.21	4.86	808.92
31.10	4.79	808.92
31.25	4.78	808.92
32.14	4.71	808.92
32.28	4.69	808.92
33.17	4.62	808.92
33.31	4.61	808.92
34.21	4.54	808.92
34.34	4.53	808.92
35.25	4.45	808.92
35.37	4.44	808.92
36.28	4.37	808.92
36.40	4.36	808.92
37.32	4.28	808.92
37.43	4.27	808.92
38.36	4.19	808.92
38.46	4.19	808.92
39.40	4.10	808.92
39.49	4.10	808.92
40.43	4.02	808.92

x (mm)	y (mm)	z (mm)
40.52	4.01	808.92
41.47	3.92	808.92
41.55	3.92	808.92
42.51	3.83	808.92
42.58	3.83	808.92
50.92	2.97	808.92

F.4.12 Section 12

x (mm)	y (mm)	z (mm)
47.14	0.37	890.82
39.41	-0.29	890.82
39.34	-0.29	890.82
38.45	-0.35	890.82
38.38	-0.36	890.82
37.50	-0.42	890.82
37.42	-0.43	890.82
36.54	-0.49	890.82
36.46	-0.49	890.82
35.59	-0.55	890.82
35.50	-0.56	890.82
34.64	-0.62	890.82
34.54	-0.62	890.82
33.69	-0.68	890.82
33.58	-0.69	890.82
32.73	-0.75	890.82
32.62	-0.76	890.82
31.78	-0.81	890.82
31.66	-0.82	890.82
30.83	-0.88	890.82
30.70	-0.89	890.82
29.88	-0.95	890.82
29.75	-0.96	890.82
28.93	-1.01	890.82
28.79	-1.02	890.82
27.97	-1.08	890.82
27.84	-1.09	890.82

F.4. AERODYNAMIC PROFILE COORDINATES

x (mm)	y (mm)	z (mm)	x (mm)	y (mm)	z (mm)
27.02	-1.15	890.82	9.97	-2.57	890.82
26.88	-1.16	890.82	9.74	-2.59	890.82
26.07	-1.22	890.82	9.02	-2.65	890.82
25.92	-1.23	890.82	8.79	-2.67	890.82
25.12	-1.29	890.82	8.08	-2.74	890.82
24.97	-1.30	890.82	7.84	-2.76	890.82
24.17	-1.36	890.82	7.14	-2.82	890.82
24.01	-1.38	890.82	6.89	-2.85	890.82
23.22	-1.44	890.82	6.20	-2.91	890.82
23.06	-1.45	890.82	5.95	-2.93	890.82
22.27	-1.51	890.82	5.26	-2.99	890.82
22.11	-1.53	890.82	5.00	-3.02	890.82
21.32	-1.59	890.82	4.32	-3.08	890.82
21.15	-1.60	890.82	4.05	-3.10	890.82
20.37	-1.67	890.82	3.38	-3.16	890.82
20.20	-1.68	890.82	3.11	-3.19	890.82
19.42	-1.74	890.82	2.44	-3.25	890.82
19.25	-1.76	890.82	2.16	-3.27	890.82
18.47	-1.82	890.82	1.50	-3.33	890.82
18.29	-1.84	890.82	1.21	-3.35	890.82
17.53	-1.90	890.82	0.57	-3.41	890.82
17.34	-1.92	890.82	0.27	-3.44	890.82
16.58	-1.98	890.82	-0.37	-3.49	890.82
16.39	-2.00	890.82	-0.68	-3.52	890.82
15.63	-2.07	890.82	-1.31	-3.57	890.82
15.44	-2.08	890.82	-1.62	-3.60	890.82
14.69	-2.15	890.82	-2.24	-3.65	890.82
14.49	-2.16	890.82	-2.57	-3.67	890.82
13.74	-2.23	890.82	-3.18	-3.72	890.82
13.54	-2.25	890.82	-3.52	-3.75	890.82
12.80	-2.31	890.82	-4.11	-3.79	890.82
12.59	-2.33	890.82	-4.46	-3.82	890.82
11.85	-2.40	890.82	-5.04	-3.87	890.82
11.64	-2.42	890.82	-5.41	-3.89	890.82
10.91	-2.48	890.82	-5.97	-3.93	890.82
10.69	-2.50	890.82	-6.36	-3.96	890.82

F.4. AERODYNAMIC PROFILE COORDINATES

x (mm)	y (mm)	z (mm)	x (mm)	y (mm)	z (mm)
-6.90	-4.00	890.82	-23.80	-3.64	890.82
-7.31	-4.02	890.82	-24.56	-3.44	890.82
-7.83	-4.06	890.82	-25.26	-3.22	890.82
-8.25	-4.08	890.82	-27.28	-2.18	890.82
-8.76	-4.11	890.82	-28.29	-0.82	890.82
-9.20	-4.14	890.82	-27.75	0.79	890.82
-9.68	-4.16	890.82	-26.07	2.38	890.82
-10.14	-4.19	890.82	-25.41	2.80	890.82
-10.61	-4.21	890.82	-24.65	3.20	890.82
-11.08	-4.23	890.82	-23.84	3.56	890.82
-11.52	-4.25	890.82	-23.06	3.87	890.82
-12.02	-4.27	890.82	-23.00	3.90	890.82
-12.44	-4.28	890.82	-22.21	4.16	890.82
-12.96	-4.30	890.82	-22.09	4.20	890.82
-13.36	-4.31	890.82	-21.33	4.43	890.82
-13.89	-4.32	890.82	-21.17	4.47	890.82
-14.27	-4.33	890.82	-20.43	4.66	890.82
-14.83	-4.34	890.82	-20.23	4.71	890.82
-15.17	-4.34	890.82	-19.53	4.87	890.82
-15.76	-4.35	890.82	-19.29	4.92	890.82
-16.07	-4.34	890.82	-18.62	5.05	890.82
-16.68	-4.34	890.82	-18.35	5.10	890.82
-16.97	-4.34	890.82	-17.71	5.22	890.82
-17.60	-4.32	890.82	-17.40	5.26	890.82
-17.86	-4.31	890.82	-16.78	5.36	890.82
-18.52	-4.29	890.82	-16.45	5.41	890.82
-18.74	-4.28	890.82	-15.85	5.49	890.82
-19.43	-4.24	890.82	-15.50	5.53	890.82
-19.61	-4.23	890.82	-14.92	5.60	890.82
-20.33	-4.17	890.82	-14.54	5.64	890.82
-20.47	-4.16	890.82	-13.99	5.70	890.82
-21.22	-4.08	890.82	-13.58	5.74	890.82
-21.32	-4.07	890.82	-13.05	5.79	890.82
-22.11	-3.96	890.82	-12.61	5.82	890.82
-22.15	-3.95	890.82	-12.10	5.86	890.82
-23.01	-3.82	890.82	-11.65	5.89	890.82

F.4. AERODYNAMIC PROFILE COORDINATES

x (mm)	y (mm)	z (mm)	x (mm)	y (mm)	z (mm)
-11.16	5.93	890.82	6.02	5.87	890.82
-10.68	5.95	890.82	6.72	5.84	890.82
-10.21	5.98	890.82	6.97	5.83	890.82
-9.72	6.00	890.82	7.68	5.79	890.82
-9.26	6.02	890.82	7.93	5.78	890.82
-8.75	6.04	890.82	8.65	5.74	890.82
-8.31	6.06	890.82	8.89	5.73	890.82
-7.78	6.08	890.82	9.61	5.68	890.82
-7.36	6.09	890.82	9.84	5.67	890.82
-6.81	6.10	890.82	10.57	5.63	890.82
-6.41	6.11	890.82	10.80	5.61	890.82
-5.84	6.12	890.82	11.54	5.57	890.82
-5.46	6.12	890.82	11.76	5.55	890.82
-4.87	6.13	890.82	12.50	5.50	890.82
-4.50	6.13	890.82	12.72	5.49	890.82
-3.90	6.13	890.82	13.46	5.44	890.82
-3.55	6.13	890.82	13.67	5.42	890.82
-2.94	6.13	890.82	14.43	5.37	890.82
-2.59	6.12	890.82	14.63	5.36	890.82
-1.97	6.12	890.82	15.39	5.30	890.82
-1.64	6.11	890.82	15.59	5.29	890.82
-1.00	6.10	890.82	16.35	5.23	890.82
-0.68	6.10	890.82	16.54	5.22	890.82
-0.04	6.09	890.82	17.31	5.16	890.82
0.27	6.08	890.82	17.50	5.15	890.82
0.93	6.06	890.82	18.27	5.09	890.82
1.23	6.06	890.82	18.46	5.07	890.82
1.90	6.04	890.82	19.23	5.01	890.82
2.19	6.03	890.82	19.41	5.00	890.82
2.86	6.00	890.82	20.19	4.93	890.82
3.14	5.99	890.82	20.37	4.92	890.82
3.83	5.97	890.82	21.15	4.86	890.82
4.10	5.96	890.82	21.32	4.84	890.82
4.79	5.93	890.82	22.12	4.78	890.82
5.06	5.92	890.82	22.28	4.77	890.82
5.75	5.89	890.82	23.08	4.70	890.82

F.4. AERODYNAMIC PROFILE COORDINATES

x (mm)	y (mm)	z (mm)
23.24	4.69	890.82
24.04	4.62	890.82
24.19	4.61	890.82
25.00	4.54	890.82
25.15	4.53	890.82
25.96	4.46	890.82
26.10	4.45	890.82
26.91	4.38	890.82
27.06	4.36	890.82
27.87	4.29	890.82
28.01	4.28	890.82
28.83	4.21	890.82
28.97	4.20	890.82
29.79	4.13	890.82
29.92	4.12	890.82
30.75	4.04	890.82
30.88	4.03	890.82
31.71	3.96	890.82
31.83	3.95	890.82
32.67	3.87	890.82
32.78	3.86	890.82
33.63	3.78	890.82
33.74	3.77	890.82
34.59	3.69	890.82
34.69	3.68	890.82
35.55	3.60	890.82
35.64	3.60	890.82
36.51	3.51	890.82
36.60	3.51	890.82
37.47	3.42	890.82
37.55	3.41	890.82
38.43	3.33	890.82
38.50	3.32	890.82
39.39	3.24	890.82
39.45	3.23	890.82
47.17	2.37	890.82

F.4.13 Section 13

x (mm)	y (mm)	z (mm)
43.44	-0.06	972.72
36.31	-0.61	972.72
36.25	-0.61	972.72
35.43	-0.66	972.72
35.36	-0.67	972.72
34.55	-0.72	972.72
34.48	-0.72	972.72
33.67	-0.77	972.72
33.59	-0.77	972.72
32.79	-0.82	972.72
32.71	-0.83	972.72
31.91	-0.87	972.72
31.82	-0.88	972.72
31.04	-0.93	972.72
30.94	-0.93	972.72
30.16	-0.98	972.72
30.05	-0.99	972.72
29.28	-1.03	972.72
29.17	-1.04	972.72
28.40	-1.09	972.72
28.29	-1.09	972.72
27.52	-1.14	972.72
27.41	-1.15	972.72
26.65	-1.19	972.72
26.52	-1.20	972.72
25.77	-1.25	972.72
25.64	-1.26	972.72
24.89	-1.31	972.72
24.76	-1.31	972.72
24.02	-1.36	972.72
23.88	-1.37	972.72
23.14	-1.42	972.72
23.00	-1.43	972.72

F.4. AERODYNAMIC PROFILE COORDINATES

x (mm)	y (mm)	z (mm)	x (mm)	y (mm)	z (mm)
22.26	-1.48	972.72	6.56	-2.69	972.72
22.12	-1.49	972.72	6.33	-2.71	972.72
21.39	-1.54	972.72	5.69	-2.76	972.72
21.24	-1.55	972.72	5.46	-2.78	972.72
20.51	-1.60	972.72	4.83	-2.83	972.72
20.36	-1.61	972.72	4.59	-2.85	972.72
19.63	-1.66	972.72	3.96	-2.90	972.72
19.48	-1.67	972.72	3.72	-2.92	972.72
18.76	-1.73	972.72	3.10	-2.97	972.72
18.60	-1.74	972.72	2.84	-2.99	972.72
17.89	-1.79	972.72	2.23	-3.04	972.72
17.72	-1.80	972.72	1.97	-3.06	972.72
17.01	-1.86	972.72	1.36	-3.11	972.72
16.85	-1.87	972.72	1.10	-3.13	972.72
16.14	-1.92	972.72	0.50	-3.18	972.72
15.97	-1.93	972.72	0.22	-3.20	972.72
15.26	-1.99	972.72	-0.36	-3.24	972.72
15.09	-2.00	972.72	-0.65	-3.26	972.72
14.39	-2.06	972.72	-1.23	-3.31	972.72
14.21	-2.07	972.72	-1.52	-3.33	972.72
13.52	-2.13	972.72	-2.09	-3.37	972.72
13.34	-2.14	972.72	-2.39	-3.39	972.72
12.65	-2.19	972.72	-2.95	-3.43	972.72
12.46	-2.21	972.72	-3.27	-3.46	972.72
11.78	-2.26	972.72	-3.81	-3.49	972.72
11.58	-2.28	972.72	-4.14	-3.52	972.72
10.91	-2.33	972.72	-4.67	-3.55	972.72
10.71	-2.35	972.72	-5.01	-3.57	972.72
10.04	-2.40	972.72	-5.53	-3.61	972.72
9.83	-2.42	972.72	-5.89	-3.63	972.72
9.17	-2.47	972.72	-6.39	-3.66	972.72
8.96	-2.49	972.72	-6.76	-3.68	972.72
8.30	-2.55	972.72	-7.24	-3.70	972.72
8.08	-2.56	972.72	-7.63	-3.73	972.72
7.43	-2.62	972.72	-8.10	-3.75	972.72
7.21	-2.64	972.72	-8.50	-3.77	972.72

F.4. AERODYNAMIC PROFILE COORDINATES

x (mm)	y (mm)	z (mm)	x (mm)	y (mm)	z (mm)
-8.95	-3.79	972.72	-24.01	2.38	972.72
-9.37	-3.81	972.72	-23.39	2.76	972.72
-9.80	-3.82	972.72	-22.70	3.12	972.72
-10.24	-3.84	972.72	-21.95	3.45	972.72
-10.65	-3.85	972.72	-21.23	3.73	972.72
-11.11	-3.87	972.72	-21.16	3.76	972.72
-11.49	-3.88	972.72	-20.44	4.00	972.72
-11.97	-3.89	972.72	-20.33	4.03	972.72
-12.34	-3.90	972.72	-19.63	4.23	972.72
-12.83	-3.90	972.72	-19.48	4.27	972.72
-13.18	-3.91	972.72	-18.80	4.44	972.72
-13.69	-3.91	972.72	-18.61	4.49	972.72
-14.01	-3.91	972.72	-17.97	4.63	972.72
-14.55	-3.91	972.72	-17.75	4.67	972.72
-14.84	-3.91	972.72	-17.13	4.79	972.72
-15.40	-3.90	972.72	-16.88	4.84	972.72
-15.67	-3.89	972.72	-16.28	4.94	972.72
-16.25	-3.87	972.72	-16.00	4.98	972.72
-16.49	-3.86	972.72	-15.43	5.07	972.72
-17.10	-3.84	972.72	-15.12	5.11	972.72
-17.30	-3.82	972.72	-14.57	5.18	972.72
-17.93	-3.78	972.72	-14.24	5.22	972.72
-18.10	-3.77	972.72	-13.71	5.28	972.72
-18.76	-3.71	972.72	-13.36	5.32	972.72
-18.89	-3.70	972.72	-12.85	5.37	972.72
-19.59	-3.62	972.72	-12.47	5.40	972.72
-19.67	-3.61	972.72	-11.98	5.44	972.72
-20.40	-3.50	972.72	-11.58	5.47	972.72
-20.44	-3.50	972.72	-11.11	5.50	972.72
-21.23	-3.36	972.72	-10.70	5.53	972.72
-21.96	-3.20	972.72	-10.24	5.56	972.72
-22.66	-3.00	972.72	-9.80	5.58	972.72
-23.30	-2.79	972.72	-9.37	5.60	972.72
-25.15	-1.82	972.72	-8.91	5.62	972.72
-26.08	-0.56	972.72	-8.50	5.64	972.72
-25.57	0.92	972.72	-8.02	5.65	972.72

F.4. AERODYNAMIC PROFILE COORDINATES

x (mm)	y (mm)	z (mm)	x (mm)	y (mm)	z (mm)
-7.62	5.66	972.72	8.23	5.25	972.72
-7.13	5.67	972.72	8.90	5.21	972.72
-6.74	5.68	972.72	9.11	5.20	972.72
-6.23	5.69	972.72	9.78	5.15	972.72
-5.87	5.70	972.72	9.99	5.14	972.72
-5.34	5.70	972.72	10.67	5.09	972.72
-4.99	5.70	972.72	10.87	5.08	972.72
-4.45	5.70	972.72	11.56	5.03	972.72
-4.11	5.70	972.72	11.76	5.01	972.72
-3.56	5.70	972.72	12.44	4.96	972.72
-3.23	5.70	972.72	12.64	4.95	972.72
-2.66	5.69	972.72	13.33	4.89	972.72
-2.35	5.69	972.72	13.52	4.88	972.72
-1.77	5.68	972.72	14.22	4.83	972.72
-1.47	5.67	972.72	14.40	4.81	972.72
-0.88	5.66	972.72	15.10	4.75	972.72
-0.59	5.65	972.72	15.28	4.74	972.72
0.01	5.64	972.72	15.99	4.68	972.72
0.29	5.63	972.72	16.16	4.67	972.72
0.90	5.61	972.72	16.87	4.61	972.72
1.18	5.60	972.72	17.04	4.59	972.72
1.79	5.58	972.72	17.76	4.53	972.72
2.06	5.57	972.72	17.92	4.52	972.72
2.68	5.55	972.72	18.64	4.46	972.72
2.94	5.54	972.72	18.80	4.44	972.72
3.57	5.51	972.72	19.53	4.38	972.72
3.82	5.50	972.72	19.68	4.37	972.72
4.45	5.47	972.72	20.41	4.30	972.72
4.70	5.45	972.72	20.57	4.29	972.72
5.34	5.42	972.72	21.30	4.23	972.72
5.58	5.41	972.72	21.45	4.21	972.72
6.23	5.37	972.72	22.18	4.15	972.72
6.47	5.36	972.72	22.33	4.13	972.72
7.12	5.32	972.72	23.07	4.07	972.72
7.35	5.31	972.72	23.21	4.05	972.72
8.01	5.27	972.72	23.95	3.99	972.72

F.4. AERODYNAMIC PROFILE COORDINATES

x (mm)	y (mm)	z (mm)
24.09	3.97	972.72
24.83	3.90	972.72
24.97	3.89	972.72
25.72	3.82	972.72
25.85	3.81	972.72
26.60	3.74	972.72
26.73	3.73	972.72
27.48	3.66	972.72
27.60	3.65	972.72
28.37	3.57	972.72
28.48	3.56	972.72
29.25	3.49	972.72
29.36	3.48	972.72
30.13	3.40	972.72
30.24	3.39	972.72
31.02	3.32	972.72
31.12	3.31	972.72
31.90	3.23	972.72
31.99	3.22	972.72
32.78	3.14	972.72
32.87	3.13	972.72
33.67	3.05	972.72
33.75	3.04	972.72
34.55	2.96	972.72
34.63	2.96	972.72
35.44	2.87	972.72
35.50	2.87	972.72
36.32	2.78	972.72
36.38	2.78	972.72
43.48	1.94	972.72

x (mm)	y (mm)	z (mm)
33.22	-0.87	1054.60
32.47	-0.91	1054.60
32.41	-0.91	1054.60
31.66	-0.95	1054.60
31.60	-0.95	1054.60
30.86	-0.99	1054.60
30.78	-1.00	1054.60
30.05	-1.03	1054.60
29.97	-1.04	1054.60
29.25	-1.07	1054.60
29.16	-1.08	1054.60
28.44	-1.12	1054.60
28.35	-1.12	1054.60
27.64	-1.16	1054.60
27.54	-1.16	1054.60
26.83	-1.20	1054.60
26.73	-1.21	1054.60
26.03	-1.24	1054.60
25.92	-1.25	1054.60
25.22	-1.29	1054.60
25.11	-1.29	1054.60
24.42	-1.33	1054.60
24.30	-1.34	1054.60
23.61	-1.37	1054.60
23.50	-1.38	1054.60
22.81	-1.42	1054.60
22.69	-1.42	1054.60
22.00	-1.46	1054.60
21.88	-1.47	1054.60
21.20	-1.51	1054.60
21.07	-1.52	1054.60
20.40	-1.56	1054.60
20.27	-1.56	1054.60
19.59	-1.60	1054.60
19.46	-1.61	1054.60
18.79	-1.65	1054.60

F.4.14 Section 14

x (mm)	y (mm)	z (mm)
39.82	-0.42	1054.60
33.28	-0.87	1054.60

F.4. AERODYNAMIC PROFILE COORDINATES

x (mm)	y (mm)	z (mm)	x (mm)	y (mm)	z (mm)
18.65	-1.66	1054.60	4.19	-2.68	1054.60
17.99	-1.70	1054.60	3.61	-2.72	1054.60
17.85	-1.71	1054.60	3.39	-2.74	1054.60
17.18	-1.76	1054.60	2.82	-2.78	1054.60
17.04	-1.77	1054.60	2.59	-2.79	1054.60
16.38	-1.81	1054.60	2.03	-2.84	1054.60
16.23	-1.82	1054.60	1.79	-2.85	1054.60
15.58	-1.86	1054.60	1.23	-2.89	1054.60
15.43	-1.87	1054.60	0.99	-2.91	1054.60
14.78	-1.92	1054.60	0.44	-2.95	1054.60
14.62	-1.93	1054.60	0.19	-2.96	1054.60
13.98	-1.97	1054.60	-0.35	-3.00	1054.60
13.82	-1.98	1054.60	-0.61	-3.02	1054.60
13.18	-2.03	1054.60	-1.15	-3.05	1054.60
13.01	-2.04	1054.60	-1.41	-3.07	1054.60
12.38	-2.08	1054.60	-1.94	-3.11	1054.60
12.21	-2.09	1054.60	-2.22	-3.12	1054.60
11.58	-2.14	1054.60	-2.73	-3.16	1054.60
11.41	-2.15	1054.60	-3.02	-3.17	1054.60
10.78	-2.20	1054.60	-3.52	-3.20	1054.60
10.60	-2.21	1054.60	-3.82	-3.22	1054.60
9.98	-2.25	1054.60	-4.30	-3.25	1054.60
9.80	-2.27	1054.60	-4.62	-3.27	1054.60
9.18	-2.31	1054.60	-5.09	-3.29	1054.60
9.00	-2.33	1054.60	-5.42	-3.31	1054.60
8.39	-2.37	1054.60	-5.88	-3.33	1054.60
8.19	-2.38	1054.60	-6.22	-3.35	1054.60
7.59	-2.43	1054.60	-6.66	-3.37	1054.60
7.39	-2.44	1054.60	-7.02	-3.39	1054.60
6.79	-2.49	1054.60	-7.45	-3.41	1054.60
6.59	-2.50	1054.60	-7.82	-3.42	1054.60
6.00	-2.55	1054.60	-8.23	-3.44	1054.60
5.79	-2.56	1054.60	-8.62	-3.45	1054.60
5.20	-2.60	1054.60	-9.01	-3.46	1054.60
4.99	-2.62	1054.60	-9.41	-3.47	1054.60
4.41	-2.66	1054.60	-9.78	-3.48	1054.60

F.4. AERODYNAMIC PROFILE COORDINATES

x (mm)	y (mm)	z (mm)	x (mm)	y (mm)	z (mm)
-10.21	-3.49	1054.60	-19.38	3.58	1054.60
-10.56	-3.50	1054.60	-18.71	3.80	1054.60
-11.00	-3.51	1054.60	-18.61	3.83	1054.60
-11.33	-3.51	1054.60	-17.96	4.01	1054.60
-11.79	-3.51	1054.60	-17.83	4.05	1054.60
-12.10	-3.51	1054.60	-17.20	4.20	1054.60
-12.58	-3.51	1054.60	-17.03	4.24	1054.60
-12.87	-3.51	1054.60	-16.44	4.37	1054.60
-13.36	-3.50	1054.60	-16.24	4.41	1054.60
-13.63	-3.50	1054.60	-15.67	4.52	1054.60
-14.14	-3.49	1054.60	-15.44	4.55	1054.60
-14.39	-3.48	1054.60	-14.89	4.64	1054.60
-14.92	-3.46	1054.60	-14.64	4.68	1054.60
-15.14	-3.45	1054.60	-14.11	4.76	1054.60
-15.69	-3.42	1054.60	-13.83	4.79	1054.60
-15.88	-3.40	1054.60	-13.33	4.86	1054.60
-16.46	-3.36	1054.60	-13.02	4.89	1054.60
-16.62	-3.35	1054.60	-12.54	4.94	1054.60
-17.22	-3.29	1054.60	-12.21	4.97	1054.60
-17.34	-3.28	1054.60	-11.74	5.02	1054.60
-17.98	-3.20	1054.60	-11.40	5.05	1054.60
-18.05	-3.19	1054.60	-10.95	5.08	1054.60
-18.72	-3.09	1054.60	-10.58	5.11	1054.60
-18.76	-3.08	1054.60	-10.15	5.13	1054.60
-19.48	-2.95	1054.60	-9.77	5.16	1054.60
-20.15	-2.79	1054.60	-9.35	5.18	1054.60
-20.79	-2.61	1054.60	-8.95	5.20	1054.60
-21.37	-2.41	1054.60	-8.55	5.21	1054.60
-23.07	-1.51	1054.60	-8.13	5.23	1054.60
-23.91	-0.35	1054.60	-7.75	5.24	1054.60
-23.43	1.01	1054.60	-7.32	5.25	1054.60
-21.99	2.34	1054.60	-6.95	5.26	1054.60
-21.43	2.68	1054.60	-6.50	5.27	1054.60
-20.78	3.01	1054.60	-6.15	5.28	1054.60
-20.09	3.31	1054.60	-5.68	5.28	1054.60
-19.43	3.57	1054.60	-5.34	5.28	1054.60

F.4. AERODYNAMIC PROFILE COORDINATES

x (mm)	y (mm)	z (mm)	x (mm)	y (mm)	z (mm)
-4.86	5.28	1054.60	9.81	4.64	1054.60
-4.54	5.29	1054.60	10.00	4.63	1054.60
-4.04	5.28	1054.60	10.63	4.58	1054.60
-3.73	5.28	1054.60	10.81	4.57	1054.60
-3.22	5.28	1054.60	11.44	4.51	1054.60
-2.92	5.27	1054.60	11.62	4.50	1054.60
-2.41	5.26	1054.60	12.25	4.45	1054.60
-2.12	5.26	1054.60	12.42	4.43	1054.60
-1.59	5.25	1054.60	13.06	4.38	1054.60
-1.31	5.24	1054.60	13.23	4.37	1054.60
-0.77	5.22	1054.60	13.88	4.31	1054.60
-0.50	5.22	1054.60	14.04	4.30	1054.60
0.04	5.20	1054.60	14.69	4.24	1054.60
0.31	5.19	1054.60	14.84	4.23	1054.60
0.86	5.17	1054.60	15.50	4.17	1054.60
1.12	5.16	1054.60	15.65	4.15	1054.60
1.67	5.14	1054.60	16.31	4.10	1054.60
1.92	5.13	1054.60	16.46	4.08	1054.60
2.49	5.10	1054.60	17.12	4.02	1054.60
2.73	5.09	1054.60	17.27	4.01	1054.60
3.30	5.06	1054.60	17.93	3.95	1054.60
3.54	5.05	1054.60	18.07	3.93	1054.60
4.12	5.02	1054.60	18.74	3.87	1054.60
4.34	5.01	1054.60	18.88	3.86	1054.60
4.93	4.97	1054.60	19.55	3.79	1054.60
5.15	4.96	1054.60	19.69	3.78	1054.60
5.75	4.92	1054.60	20.36	3.72	1054.60
5.96	4.91	1054.60	20.49	3.70	1054.60
6.56	4.87	1054.60	21.17	3.64	1054.60
6.77	4.86	1054.60	21.30	3.63	1054.60
7.37	4.82	1054.60	21.98	3.56	1054.60
7.58	4.80	1054.60	22.11	3.55	1054.60
8.19	4.76	1054.60	22.79	3.48	1054.60
8.38	4.75	1054.60	22.91	3.47	1054.60
9.00	4.70	1054.60	23.60	3.40	1054.60
9.19	4.69	1054.60	23.72	3.39	1054.60

F.4. AERODYNAMIC PROFILE COORDINATES

x (mm)	y (mm)	z (mm)
24.41	3.32	1054.60
24.52	3.31	1054.60
25.22	3.24	1054.60
25.33	3.23	1054.60
26.03	3.16	1054.60
26.13	3.15	1054.60
26.84	3.08	1054.60
26.94	3.07	1054.60
27.65	3.00	1054.60
27.74	2.99	1054.60
28.45	2.91	1054.60
28.55	2.90	1054.60
29.26	2.83	1054.60
29.35	2.82	1054.60
30.07	2.74	1054.60
30.15	2.73	1054.60
30.88	2.65	1054.60
30.96	2.65	1054.60
31.69	2.57	1054.60
31.76	2.56	1054.60
32.50	2.48	1054.60
32.56	2.47	1054.60
33.31	2.39	1054.60
33.37	2.39	1054.60
39.87	1.58	1054.60

x (mm)	y (mm)	z (mm)
28.17	-1.15	1123.90
28.10	-1.15	1123.90
27.43	-1.18	1123.90
27.36	-1.18	1123.90
26.69	-1.21	1123.90
26.62	-1.22	1123.90
25.96	-1.25	1123.90
25.88	-1.25	1123.90
25.22	-1.28	1123.90
25.14	-1.28	1123.90
24.49	-1.31	1123.90
24.40	-1.32	1123.90
23.75	-1.34	1123.90
23.66	-1.35	1123.90
23.02	-1.38	1123.90
22.92	-1.38	1123.90
22.28	-1.41	1123.90
22.18	-1.42	1123.90
21.55	-1.45	1123.90
21.44	-1.45	1123.90
20.82	-1.48	1123.90
20.70	-1.49	1123.90
20.08	-1.52	1123.90
19.97	-1.52	1123.90
19.35	-1.55	1123.90
19.23	-1.56	1123.90
18.61	-1.59	1123.90
18.49	-1.60	1123.90
17.88	-1.63	1123.90
17.76	-1.64	1123.90
17.14	-1.67	1123.90
17.02	-1.68	1123.90
16.41	-1.71	1123.90
16.28	-1.72	1123.90
15.68	-1.75	1123.90
15.55	-1.76	1123.90

F.4.15 Section 15

x (mm)	y (mm)	z (mm)
36.35	-0.68	1123.90
30.38	-1.05	1123.90
30.32	-1.05	1123.90
29.64	-1.08	1123.90
29.58	-1.08	1123.90
28.90	-1.11	1123.90
28.84	-1.12	1123.90

F.4. AERODYNAMIC PROFILE COORDINATES

x (mm)	y (mm)	z (mm)	x (mm)	y (mm)	z (mm)
14.95	-1.80	1123.90	1.83	-2.63	1123.90
14.81	-1.80	1123.90	1.62	-2.65	1123.90
14.21	-1.84	1123.90	1.11	-2.68	1123.90
14.08	-1.85	1123.90	0.88	-2.70	1123.90
13.48	-1.88	1123.90	0.38	-2.73	1123.90
13.34	-1.89	1123.90	0.15	-2.74	1123.90
12.75	-1.93	1123.90	-0.34	-2.77	1123.90
12.61	-1.94	1123.90	-0.58	-2.78	1123.90
12.02	-1.97	1123.90	-1.06	-2.81	1123.90
11.87	-1.98	1123.90	-1.31	-2.83	1123.90
11.29	-2.02	1123.90	-1.78	-2.86	1123.90
11.14	-2.03	1123.90	-2.04	-2.87	1123.90
10.56	-2.06	1123.90	-2.51	-2.90	1123.90
10.40	-2.07	1123.90	-2.77	-2.91	1123.90
9.83	-2.11	1123.90	-3.23	-2.93	1123.90
9.67	-2.12	1123.90	-3.50	-2.95	1123.90
9.10	-2.16	1123.90	-3.95	-2.97	1123.90
8.93	-2.17	1123.90	-4.23	-2.98	1123.90
8.37	-2.21	1123.90	-4.67	-3.01	1123.90
8.20	-2.22	1123.90	-4.96	-3.02	1123.90
7.64	-2.25	1123.90	-5.38	-3.04	1123.90
7.47	-2.26	1123.90	-5.70	-3.05	1123.90
6.92	-2.30	1123.90	-6.10	-3.07	1123.90
6.74	-2.31	1123.90	-6.43	-3.08	1123.90
6.19	-2.35	1123.90	-6.82	-3.09	1123.90
6.00	-2.36	1123.90	-7.16	-3.10	1123.90
5.46	-2.40	1123.90	-7.53	-3.11	1123.90
5.27	-2.41	1123.90	-7.88	-3.12	1123.90
4.74	-2.45	1123.90	-8.24	-3.13	1123.90
4.54	-2.46	1123.90	-8.61	-3.14	1123.90
4.01	-2.49	1123.90	-8.95	-3.15	1123.90
3.81	-2.51	1123.90	-9.34	-3.15	1123.90
3.28	-2.54	1123.90	-9.66	-3.16	1123.90
3.08	-2.55	1123.90	-10.06	-3.16	1123.90
2.56	-2.59	1123.90	-10.37	-3.16	1123.90
2.35	-2.60	1123.90	-10.78	-3.16	1123.90

F.4. AERODYNAMIC PROFILE COORDINATES

x (mm)	y (mm)	z (mm)	x (mm)	y (mm)	z (mm)
-11.07	-3.16	1123.90	-15.69	3.94	1123.90
-11.50	-3.15	1123.90	-15.53	3.97	1123.90
-11.77	-3.15	1123.90	-14.99	4.09	1123.90
-12.22	-3.14	1123.90	-14.80	4.12	1123.90
-12.46	-3.13	1123.90	-14.28	4.22	1123.90
-12.93	-3.12	1123.90	-14.07	4.25	1123.90
-13.15	-3.11	1123.90	-13.57	4.33	1123.90
-13.64	-3.09	1123.90	-13.34	4.37	1123.90
-13.84	-3.08	1123.90	-12.86	4.43	1123.90
-14.35	-3.05	1123.90	-12.60	4.47	1123.90
-14.52	-3.03	1123.90	-12.14	4.52	1123.90
-15.05	-2.99	1123.90	-11.86	4.55	1123.90
-15.19	-2.98	1123.90	-11.42	4.60	1123.90
-15.74	-2.92	1123.90	-11.12	4.62	1123.90
-15.85	-2.91	1123.90	-10.70	4.66	1123.90
-16.43	-2.83	1123.90	-10.38	4.69	1123.90
-16.50	-2.82	1123.90	-9.97	4.72	1123.90
-17.11	-2.72	1123.90	-9.64	4.74	1123.90
-17.14	-2.72	1123.90	-9.24	4.76	1123.90
-17.80	-2.59	1123.90	-8.89	4.78	1123.90
-18.41	-2.45	1123.90	-8.51	4.80	1123.90
-18.99	-2.28	1123.90	-8.15	4.81	1123.90
-19.53	-2.09	1123.90	-7.78	4.83	1123.90
-21.07	-1.26	1123.90	-7.40	4.84	1123.90
-21.83	-0.19	1123.90	-7.05	4.85	1123.90
-21.39	1.05	1123.90	-6.65	4.86	1123.90
-20.07	2.26	1123.90	-6.32	4.87	1123.90
-19.55	2.57	1123.90	-5.90	4.87	1123.90
-18.96	2.87	1123.90	-5.58	4.87	1123.90
-18.33	3.14	1123.90	-5.16	4.88	1123.90
-17.72	3.37	1123.90	-4.85	4.88	1123.90
-17.67	3.38	1123.90	-4.41	4.88	1123.90
-17.06	3.58	1123.90	-4.11	4.88	1123.90
-16.97	3.61	1123.90	-3.66	4.87	1123.90
-16.38	3.77	1123.90	-3.38	4.87	1123.90
-16.26	3.80	1123.90	-2.91	4.86	1123.90

F.4. AERODYNAMIC PROFILE COORDINATES

x (mm)	y (mm)	z (mm)	x (mm)	y (mm)	z (mm)
-2.64	4.86	1123.90	10.63	4.09	1123.90
-2.17	4.85	1123.90	11.21	4.04	1123.90
-1.91	4.84	1123.90	11.37	4.03	1123.90
-1.42	4.83	1123.90	11.95	3.98	1123.90
-1.17	4.82	1123.90	12.10	3.97	1123.90
-0.68	4.81	1123.90	12.69	3.91	1123.90
-0.43	4.80	1123.90	12.84	3.90	1123.90
0.07	4.78	1123.90	13.43	3.84	1123.90
0.31	4.77	1123.90	13.58	3.83	1123.90
0.81	4.75	1123.90	14.17	3.78	1123.90
1.05	4.74	1123.90	14.31	3.76	1123.90
1.56	4.72	1123.90	14.91	3.71	1123.90
1.78	4.71	1123.90	15.05	3.69	1123.90
2.30	4.68	1123.90	15.65	3.63	1123.90
2.52	4.67	1123.90	15.79	3.62	1123.90
3.04	4.64	1123.90	16.39	3.56	1123.90
3.26	4.63	1123.90	16.52	3.55	1123.90
3.79	4.60	1123.90	17.13	3.49	1123.90
3.99	4.59	1123.90	17.26	3.48	1123.90
4.53	4.55	1123.90	17.87	3.42	1123.90
4.73	4.54	1123.90	18.00	3.40	1123.90
5.27	4.50	1123.90	18.61	3.34	1123.90
5.47	4.49	1123.90	18.73	3.33	1123.90
6.02	4.45	1123.90	19.35	3.27	1123.90
6.21	4.44	1123.90	19.47	3.26	1123.90
6.76	4.40	1123.90	20.09	3.19	1123.90
6.94	4.39	1123.90	20.20	3.18	1123.90
7.50	4.35	1123.90	20.83	3.12	1123.90
7.68	4.33	1123.90	20.94	3.11	1123.90
8.24	4.29	1123.90	21.57	3.04	1123.90
8.42	4.28	1123.90	21.68	3.03	1123.90
8.99	4.23	1123.90	22.31	2.97	1123.90
9.16	4.22	1123.90	22.41	2.96	1123.90
9.73	4.17	1123.90	23.04	2.89	1123.90
9.89	4.16	1123.90	23.14	2.88	1123.90
10.47	4.11	1123.90	23.78	2.81	1123.90

F.4. AERODYNAMIC PROFILE COORDINATES

x (mm)	y (mm)	z (mm)
23.88	2.80	1123.90
24.52	2.73	1123.90
24.61	2.72	1123.90
25.26	2.66	1123.90
25.35	2.65	1123.90
26.00	2.58	1123.90
26.08	2.57	1123.90
26.74	2.49	1123.90
26.81	2.49	1123.90
27.48	2.41	1123.90
27.55	2.41	1123.90
28.21	2.33	1123.90
28.28	2.32	1123.90
28.95	2.25	1123.90
29.02	2.24	1123.90
29.69	2.16	1123.90
29.75	2.16	1123.90
30.43	2.08	1123.90
30.48	2.08	1123.90
36.42	1.32	1123.90

x (mm)	y (mm)	z (mm)
24.25	-1.29	1178.10
23.65	-1.32	1178.10
23.57	-1.32	1178.10
22.98	-1.34	1178.10
22.90	-1.34	1178.10
22.31	-1.37	1178.10
22.22	-1.37	1178.10
21.64	-1.39	1178.10
21.55	-1.40	1178.10
20.97	-1.42	1178.10
20.88	-1.42	1178.10
20.30	-1.45	1178.10
20.20	-1.45	1178.10
19.63	-1.47	1178.10
19.53	-1.48	1178.10
18.96	-1.50	1178.10
18.86	-1.51	1178.10
18.29	-1.53	1178.10
18.19	-1.53	1178.10
17.62	-1.56	1178.10
17.51	-1.56	1178.10
16.95	-1.59	1178.10
16.84	-1.59	1178.10
16.28	-1.62	1178.10
16.17	-1.63	1178.10
15.61	-1.65	1178.10
15.50	-1.66	1178.10
14.95	-1.69	1178.10
14.83	-1.69	1178.10
14.28	-1.72	1178.10
14.16	-1.73	1178.10
13.61	-1.75	1178.10
13.49	-1.76	1178.10
12.94	-1.79	1178.10
12.82	-1.80	1178.10
12.28	-1.82	1178.10

F.4.16 Section 16

x (mm)	y (mm)	z (mm)
33.12	-0.86	1178.10
27.67	-1.16	1178.10
27.63	-1.16	1178.10
27.00	-1.19	1178.10
26.95	-1.19	1178.10
26.33	-1.21	1178.10
26.27	-1.21	1178.10
25.66	-1.24	1178.10
25.60	-1.24	1178.10
24.99	-1.26	1178.10
24.92	-1.27	1178.10
24.32	-1.29	1178.10

F.4. AERODYNAMIC PROFILE COORDINATES

x (mm)	y (mm)	z (mm)	x (mm)	y (mm)	z (mm)
12.15	-1.83	1178.10	0.13	-2.53	1178.10
11.61	-1.86	1178.10	-0.32	-2.56	1178.10
11.48	-1.87	1178.10	-0.54	-2.57	1178.10
10.94	-1.90	1178.10	-0.98	-2.59	1178.10
10.81	-1.91	1178.10	-1.20	-2.60	1178.10
10.28	-1.94	1178.10	-1.64	-2.63	1178.10
10.14	-1.94	1178.10	-1.87	-2.64	1178.10
9.61	-1.97	1178.10	-2.30	-2.66	1178.10
9.47	-1.98	1178.10	-2.54	-2.67	1178.10
8.95	-2.01	1178.10	-2.95	-2.69	1178.10
8.80	-2.02	1178.10	-3.20	-2.70	1178.10
8.28	-2.05	1178.10	-3.61	-2.72	1178.10
8.13	-2.06	1178.10	-3.87	-2.73	1178.10
7.62	-2.09	1178.10	-4.26	-2.75	1178.10
7.46	-2.10	1178.10	-4.54	-2.76	1178.10
6.96	-2.13	1178.10	-4.92	-2.77	1178.10
6.80	-2.14	1178.10	-5.20	-2.78	1178.10
6.29	-2.17	1178.10	-5.57	-2.79	1178.10
6.13	-2.18	1178.10	-5.87	-2.80	1178.10
5.63	-2.21	1178.10	-6.22	-2.81	1178.10
5.46	-2.22	1178.10	-6.53	-2.82	1178.10
4.97	-2.25	1178.10	-6.87	-2.83	1178.10
4.79	-2.26	1178.10	-7.20	-2.83	1178.10
4.31	-2.29	1178.10	-7.52	-2.84	1178.10
4.13	-2.30	1178.10	-7.86	-2.85	1178.10
3.64	-2.33	1178.10	-8.17	-2.85	1178.10
3.46	-2.34	1178.10	-8.52	-2.85	1178.10
2.98	-2.37	1178.10	-8.81	-2.85	1178.10
2.79	-2.38	1178.10	-9.18	-2.85	1178.10
2.32	-2.41	1178.10	-9.46	-2.85	1178.10
2.13	-2.42	1178.10	-9.84	-2.85	1178.10
1.66	-2.44	1178.10	-10.10	-2.85	1178.10
1.46	-2.46	1178.10	-10.49	-2.84	1178.10
1.00	-2.48	1178.10	-10.73	-2.84	1178.10
0.79	-2.49	1178.10	-11.14	-2.83	1178.10
0.34	-2.52	1178.10	-11.37	-2.82	1178.10

F.4. AERODYNAMIC PROFILE COORDINATES

x (mm)	y (mm)	z (mm)	x (mm)	y (mm)	z (mm)
-11.79	-2.80	1178.10	-12.81	3.95	1178.10
-12.00	-2.79	1178.10	-12.35	4.02	1178.10
-12.44	-2.77	1178.10	-12.14	4.05	1178.10
-12.62	-2.76	1178.10	-11.70	4.11	1178.10
-13.09	-2.73	1178.10	-11.47	4.14	1178.10
-13.24	-2.71	1178.10	-11.05	4.19	1178.10
-13.73	-2.67	1178.10	-10.79	4.21	1178.10
-13.85	-2.66	1178.10	-10.39	4.25	1178.10
-14.36	-2.60	1178.10	-10.12	4.28	1178.10
-14.45	-2.59	1178.10	-9.73	4.31	1178.10
-14.98	-2.52	1178.10	-9.44	4.33	1178.10
-15.05	-2.51	1178.10	-9.07	4.36	1178.10
-15.60	-2.42	1178.10	-8.76	4.38	1178.10
-15.63	-2.41	1178.10	-8.40	4.40	1178.10
-16.23	-2.30	1178.10	-8.08	4.41	1178.10
-16.79	-2.16	1178.10	-7.74	4.43	1178.10
-17.32	-2.00	1178.10	-7.40	4.44	1178.10
-17.80	-1.83	1178.10	-7.07	4.45	1178.10
-19.21	-1.06	1178.10	-6.72	4.46	1178.10
-19.89	-0.08	1178.10	-6.40	4.47	1178.10
-19.48	1.05	1178.10	-6.04	4.48	1178.10
-18.28	2.14	1178.10	-5.74	4.48	1178.10
-17.80	2.42	1178.10	-5.36	4.49	1178.10
-17.27	2.69	1178.10	-5.07	4.49	1178.10
-16.69	2.94	1178.10	-4.68	4.49	1178.10
-16.14	3.15	1178.10	-4.40	4.49	1178.10
-16.09	3.16	1178.10	-4.00	4.49	1178.10
-15.53	3.34	1178.10	-3.73	4.49	1178.10
-15.45	3.36	1178.10	-3.32	4.48	1178.10
-14.91	3.51	1178.10	-3.06	4.48	1178.10
-14.80	3.54	1178.10	-2.64	4.47	1178.10
-14.28	3.66	1178.10	-2.39	4.47	1178.10
-14.14	3.70	1178.10	-1.96	4.46	1178.10
-13.64	3.80	1178.10	-1.72	4.45	1178.10
-13.47	3.83	1178.10	-1.28	4.44	1178.10
-13.00	3.92	1178.10	-1.05	4.43	1178.10

F.4. AERODYNAMIC PROFILE COORDINATES

x (mm)	y (mm)	z (mm)	x (mm)	y (mm)	z (mm)
-0.60	4.41	1178.10	11.58	3.57	1178.10
-0.37	4.41	1178.10	11.72	3.55	1178.10
0.08	4.39	1178.10	12.26	3.50	1178.10
0.30	4.38	1178.10	12.39	3.49	1178.10
0.76	4.36	1178.10	12.93	3.44	1178.10
0.97	4.35	1178.10	13.06	3.42	1178.10
1.44	4.33	1178.10	13.61	3.37	1178.10
1.64	4.32	1178.10	13.73	3.36	1178.10
2.12	4.29	1178.10	14.28	3.30	1178.10
2.31	4.28	1178.10	14.40	3.29	1178.10
2.79	4.25	1178.10	14.95	3.24	1178.10
2.99	4.24	1178.10	15.07	3.23	1178.10
3.47	4.21	1178.10	15.63	3.17	1178.10
3.66	4.20	1178.10	15.74	3.16	1178.10
4.15	4.17	1178.10	16.30	3.10	1178.10
4.33	4.16	1178.10	16.41	3.09	1178.10
4.82	4.12	1178.10	16.97	3.03	1178.10
5.00	4.11	1178.10	17.09	3.02	1178.10
5.50	4.08	1178.10	17.65	2.96	1178.10
5.67	4.06	1178.10	17.76	2.95	1178.10
6.18	4.03	1178.10	18.32	2.89	1178.10
6.35	4.01	1178.10	18.43	2.88	1178.10
6.85	3.97	1178.10	18.99	2.82	1178.10
7.02	3.96	1178.10	19.10	2.81	1178.10
7.53	3.92	1178.10	19.67	2.75	1178.10
7.69	3.91	1178.10	19.77	2.74	1178.10
8.21	3.87	1178.10	20.34	2.68	1178.10
8.36	3.85	1178.10	20.44	2.67	1178.10
8.88	3.81	1178.10	21.01	2.61	1178.10
9.03	3.80	1178.10	21.10	2.60	1178.10
9.56	3.75	1178.10	21.69	2.53	1178.10
9.70	3.74	1178.10	21.77	2.52	1178.10
10.23	3.69	1178.10	22.36	2.46	1178.10
10.38	3.68	1178.10	22.44	2.45	1178.10
10.91	3.63	1178.10	23.03	2.39	1178.10
11.05	3.62	1178.10	23.11	2.38	1178.10

F.4. AERODYNAMIC PROFILE COORDINATES

x (mm)	y (mm)	z (mm)
23.70	2.31	1178.10
23.78	2.30	1178.10
24.38	2.24	1178.10
24.45	2.23	1178.10
25.05	2.16	1178.10
25.12	2.15	1178.10
25.72	2.08	1178.10
25.78	2.08	1178.10
26.40	2.01	1178.10
26.45	2.00	1178.10
27.07	1.93	1178.10
27.12	1.92	1178.10
27.74	1.85	1178.10
27.79	1.84	1178.10
33.19	1.14	1178.10

x (mm)	y (mm)	z (mm)
14.61	-1.22	1232.30
14.22	-1.23	1232.30
14.17	-1.23	1232.30
13.78	-1.24	1232.30
13.72	-1.24	1232.30
13.34	-1.25	1232.30
13.28	-1.25	1232.30
12.90	-1.26	1232.30
12.84	-1.27	1232.30
12.46	-1.28	1232.30
12.40	-1.28	1232.30
12.02	-1.29	1232.30
11.95	-1.29	1232.30
11.58	-1.30	1232.30
11.51	-1.31	1232.30
11.14	-1.32	1232.30
11.07	-1.32	1232.30
10.70	-1.33	1232.30
10.63	-1.34	1232.30
10.26	-1.35	1232.30
10.19	-1.35	1232.30
9.82	-1.36	1232.30
9.75	-1.37	1232.30
9.38	-1.38	1232.30
9.31	-1.38	1232.30
8.95	-1.40	1232.30
8.87	-1.40	1232.30
8.51	-1.42	1232.30
8.42	-1.42	1232.30
8.07	-1.43	1232.30
7.98	-1.44	1232.30
7.63	-1.45	1232.30
7.54	-1.46	1232.30
7.19	-1.47	1232.30
7.10	-1.47	1232.30
6.75	-1.49	1232.30

F.4.17 Section 17

x (mm)	y (mm)	z (mm)
21.77	-0.98	1232.30
18.19	-1.13	1232.30
18.16	-1.13	1232.30
17.75	-1.14	1232.30
17.72	-1.14	1232.30
17.31	-1.15	1232.30
17.27	-1.15	1232.30
16.87	-1.16	1232.30
16.83	-1.16	1232.30
16.43	-1.17	1232.30
16.38	-1.17	1232.30
15.99	-1.18	1232.30
15.94	-1.18	1232.30
15.54	-1.20	1232.30
15.50	-1.20	1232.30
15.10	-1.21	1232.30
15.05	-1.21	1232.30
14.66	-1.22	1232.30

F.4. AERODYNAMIC PROFILE COORDINATES

x (mm)	y (mm)	z (mm)	x (mm)	y (mm)	z (mm)
6.66	-1.49	1232.30	-1.23	-1.85	1232.30
6.32	-1.51	1232.30	-1.51	-1.86	1232.30
6.22	-1.51	1232.30	-1.67	-1.86	1232.30
5.88	-1.53	1232.30	-1.95	-1.87	1232.30
5.78	-1.53	1232.30	-2.11	-1.88	1232.30
5.44	-1.55	1232.30	-2.38	-1.89	1232.30
5.34	-1.55	1232.30	-2.55	-1.89	1232.30
5.01	-1.57	1232.30	-2.81	-1.90	1232.30
4.90	-1.57	1232.30	-2.99	-1.90	1232.30
4.57	-1.59	1232.30	-3.24	-1.91	1232.30
4.46	-1.59	1232.30	-3.43	-1.91	1232.30
4.13	-1.61	1232.30	-3.67	-1.92	1232.30
4.03	-1.61	1232.30	-3.86	-1.92	1232.30
3.70	-1.63	1232.30	-4.10	-1.92	1232.30
3.59	-1.63	1232.30	-4.30	-1.93	1232.30
3.26	-1.65	1232.30	-4.53	-1.93	1232.30
3.15	-1.66	1232.30	-4.74	-1.93	1232.30
2.83	-1.67	1232.30	-4.95	-1.93	1232.30
2.71	-1.68	1232.30	-5.17	-1.93	1232.30
2.39	-1.69	1232.30	-5.38	-1.93	1232.30
2.27	-1.70	1232.30	-5.61	-1.93	1232.30
1.96	-1.71	1232.30	-5.80	-1.93	1232.30
1.83	-1.72	1232.30	-6.04	-1.93	1232.30
1.52	-1.73	1232.30	-6.23	-1.92	1232.30
1.39	-1.74	1232.30	-6.48	-1.92	1232.30
1.09	-1.75	1232.30	-6.65	-1.91	1232.30
0.96	-1.76	1232.30	-6.91	-1.91	1232.30
0.65	-1.77	1232.30	-7.07	-1.90	1232.30
0.52	-1.78	1232.30	-7.34	-1.89	1232.30
0.22	-1.79	1232.30	-7.48	-1.88	1232.30
0.08	-1.79	1232.30	-7.76	-1.87	1232.30
-0.22	-1.81	1232.30	-7.90	-1.86	1232.30
-0.36	-1.81	1232.30	-8.19	-1.84	1232.30
-0.65	-1.82	1232.30	-8.31	-1.83	1232.30
-0.80	-1.83	1232.30	-8.61	-1.81	1232.30
-1.08	-1.84	1232.30	-8.72	-1.80	1232.30

F.4. AERODYNAMIC PROFILE COORDINATES

x (mm)	y (mm)	z (mm)	x (mm)	y (mm)	z (mm)
-9.03	-1.77	1232.30	-7.09	2.85	1232.30
-9.12	-1.76	1232.30	-6.83	2.88	1232.30
-9.45	-1.72	1232.30	-6.65	2.90	1232.30
-9.51	-1.71	1232.30	-6.39	2.92	1232.30
-9.86	-1.66	1232.30	-6.21	2.94	1232.30
-9.90	-1.65	1232.30	-5.96	2.96	1232.30
-10.27	-1.59	1232.30	-5.76	2.97	1232.30
-10.29	-1.58	1232.30	-5.52	2.98	1232.30
-10.68	-1.50	1232.30	-5.31	3.00	1232.30
-11.05	-1.40	1232.30	-5.08	3.01	1232.30
-11.40	-1.30	1232.30	-4.86	3.02	1232.30
-11.72	-1.18	1232.30	-4.65	3.03	1232.30
-12.64	-0.66	1232.30	-4.42	3.04	1232.30
-13.09	-0.01	1232.30	-4.21	3.04	1232.30
-12.82	0.73	1232.30	-3.97	3.05	1232.30
-12.02	1.46	1232.30	-3.77	3.05	1232.30
-11.71	1.65	1232.30	-3.52	3.06	1232.30
-11.36	1.83	1232.30	-3.33	3.06	1232.30
-10.98	1.99	1232.30	-3.07	3.06	1232.30
-10.61	2.13	1232.30	-2.89	3.06	1232.30
-10.58	2.14	1232.30	-2.62	3.07	1232.30
-10.21	2.26	1232.30	-2.45	3.07	1232.30
-10.16	2.28	1232.30	-2.17	3.06	1232.30
-9.81	2.38	1232.30	-2.00	3.06	1232.30
-9.73	2.40	1232.30	-1.73	3.06	1232.30
-9.39	2.48	1232.30	-1.56	3.06	1232.30
-9.30	2.50	1232.30	-1.28	3.05	1232.30
-8.97	2.57	1232.30	-1.12	3.05	1232.30
-8.86	2.59	1232.30	-0.83	3.04	1232.30
-8.55	2.65	1232.30	-0.68	3.04	1232.30
-8.42	2.67	1232.30	-0.38	3.03	1232.30
-8.12	2.72	1232.30	-0.24	3.03	1232.30
-7.98	2.74	1232.30	0.06	3.02	1232.30
-7.69	2.78	1232.30	0.21	3.01	1232.30
-7.54	2.80	1232.30	0.51	3.00	1232.30
-7.26	2.83	1232.30	0.65	2.99	1232.30

F.4. AERODYNAMIC PROFILE COORDINATES

x (mm)	y (mm)	z (mm)	x (mm)	y (mm)	z (mm)
0.95	2.98	1232.30	8.96	2.41	1232.30
1.09	2.98	1232.30	9.05	2.40	1232.30
1.40	2.96	1232.30	9.41	2.36	1232.30
1.53	2.96	1232.30	9.49	2.36	1232.30
1.85	2.94	1232.30	9.85	2.32	1232.30
1.97	2.93	1232.30	9.93	2.32	1232.30
2.29	2.92	1232.30	10.30	2.28	1232.30
2.42	2.91	1232.30	10.37	2.27	1232.30
2.74	2.89	1232.30	10.74	2.24	1232.30
2.86	2.88	1232.30	10.81	2.23	1232.30
3.18	2.86	1232.30	11.18	2.20	1232.30
3.30	2.86	1232.30	11.26	2.19	1232.30
3.63	2.83	1232.30	11.63	2.15	1232.30
3.74	2.83	1232.30	11.70	2.15	1232.30
4.07	2.80	1232.30	12.07	2.11	1232.30
4.19	2.80	1232.30	12.14	2.10	1232.30
4.52	2.77	1232.30	12.51	2.07	1232.30
4.63	2.77	1232.30	12.58	2.06	1232.30
4.97	2.74	1232.30	12.95	2.02	1232.30
5.07	2.73	1232.30	13.02	2.02	1232.30
5.41	2.71	1232.30	13.40	1.98	1232.30
5.51	2.70	1232.30	13.46	1.97	1232.30
5.85	2.67	1232.30	13.84	1.93	1232.30
5.95	2.66	1232.30	13.90	1.93	1232.30
6.30	2.64	1232.30	14.28	1.89	1232.30
6.40	2.63	1232.30	14.34	1.88	1232.30
6.74	2.60	1232.30	14.73	1.84	1232.30
6.84	2.59	1232.30	14.78	1.84	1232.30
7.19	2.56	1232.30	15.17	1.80	1232.30
7.28	2.56	1232.30	15.22	1.79	1232.30
7.63	2.52	1232.30	15.61	1.75	1232.30
7.72	2.52	1232.30	15.66	1.75	1232.30
8.08	2.49	1232.30	16.05	1.71	1232.30
8.16	2.48	1232.30	16.10	1.70	1232.30
8.52	2.45	1232.30	16.50	1.66	1232.30
8.61	2.44	1232.30	16.54	1.65	1232.30

F.4. AERODYNAMIC PROFILE COORDINATES

x (mm)	y (mm)	z (mm)
16.94	1.61	1232.30
16.98	1.61	1232.30
17.38	1.56	1232.30
17.42	1.56	1232.30
17.83	1.52	1232.30
17.86	1.51	1232.30
18.27	1.47	1232.30
18.30	1.46	1232.30
21.86	1.02	1232.30

x (mm)	y (mm)	z (mm)
11.95	-1.21	1237.70
11.61	-1.21	1237.70
11.55	-1.22	1237.70
11.22	-1.22	1237.70
11.16	-1.23	1237.70
10.82	-1.23	1237.70
10.76	-1.24	1237.70
10.42	-1.25	1237.70
10.36	-1.25	1237.70
10.03	-1.26	1237.70
9.96	-1.26	1237.70
9.63	-1.27	1237.70
9.57	-1.27	1237.70
9.24	-1.28	1237.70
9.17	-1.28	1237.70
8.84	-1.29	1237.70
8.77	-1.30	1237.70
8.45	-1.31	1237.70
8.38	-1.31	1237.70
8.05	-1.32	1237.70
7.98	-1.33	1237.70
7.66	-1.34	1237.70
7.58	-1.34	1237.70
7.26	-1.35	1237.70
7.19	-1.35	1237.70
6.87	-1.37	1237.70
6.79	-1.37	1237.70
6.47	-1.38	1237.70
6.39	-1.39	1237.70
6.08	-1.40	1237.70
6.00	-1.40	1237.70
5.69	-1.41	1237.70
5.60	-1.42	1237.70
5.29	-1.43	1237.70
5.20	-1.43	1237.70
4.90	-1.45	1237.70

F.4.18 Section 18

x (mm)	y (mm)	z (mm)
19.59	-0.98	1237.70
16.37	-1.11	1237.70
16.34	-1.11	1237.70
15.97	-1.11	1237.70
15.94	-1.12	1237.70
15.58	-1.12	1237.70
15.54	-1.12	1237.70
15.18	-1.13	1237.70
15.14	-1.13	1237.70
14.78	-1.14	1237.70
14.74	-1.14	1237.70
14.39	-1.15	1237.70
14.34	-1.15	1237.70
13.99	-1.16	1237.70
13.94	-1.16	1237.70
13.59	-1.17	1237.70
13.55	-1.17	1237.70
13.20	-1.18	1237.70
13.15	-1.18	1237.70
12.80	-1.19	1237.70
12.75	-1.19	1237.70
12.40	-1.19	1237.70
12.35	-1.20	1237.70
12.01	-1.20	1237.70

F.4. AERODYNAMIC PROFILE COORDINATES

x (mm)	y (mm)	z (mm)	x (mm)	y (mm)	z (mm)
4.81	-1.45	1237.70	-2.30	-1.73	1237.70
4.51	-1.46	1237.70	-2.53	-1.74	1237.70
4.41	-1.47	1237.70	-2.69	-1.74	1237.70
4.11	-1.48	1237.70	-2.92	-1.75	1237.70
4.02	-1.49	1237.70	-3.08	-1.75	1237.70
3.72	-1.50	1237.70	-3.30	-1.75	1237.70
3.62	-1.50	1237.70	-3.48	-1.76	1237.70
3.33	-1.52	1237.70	-3.69	-1.76	1237.70
3.23	-1.52	1237.70	-3.87	-1.76	1237.70
2.94	-1.53	1237.70	-4.07	-1.76	1237.70
2.83	-1.54	1237.70	-4.27	-1.76	1237.70
2.54	-1.55	1237.70	-4.46	-1.76	1237.70
2.44	-1.55	1237.70	-4.66	-1.76	1237.70
2.15	-1.57	1237.70	-4.84	-1.76	1237.70
2.04	-1.57	1237.70	-5.05	-1.76	1237.70
1.76	-1.58	1237.70	-5.22	-1.76	1237.70
1.65	-1.59	1237.70	-5.44	-1.75	1237.70
1.37	-1.60	1237.70	-5.60	-1.75	1237.70
1.26	-1.61	1237.70	-5.83	-1.75	1237.70
0.98	-1.62	1237.70	-5.98	-1.74	1237.70
0.86	-1.62	1237.70	-6.22	-1.73	1237.70
0.59	-1.63	1237.70	-6.36	-1.73	1237.70
0.47	-1.64	1237.70	-6.60	-1.72	1237.70
0.20	-1.65	1237.70	-6.74	-1.71	1237.70
0.07	-1.65	1237.70	-6.99	-1.70	1237.70
-0.19	-1.66	1237.70	-7.11	-1.69	1237.70
-0.32	-1.67	1237.70	-7.37	-1.67	1237.70
-0.58	-1.68	1237.70	-7.48	-1.66	1237.70
-0.72	-1.68	1237.70	-7.75	-1.64	1237.70
-0.97	-1.69	1237.70	-7.84	-1.63	1237.70
-1.11	-1.70	1237.70	-8.13	-1.60	1237.70
-1.36	-1.70	1237.70	-8.21	-1.59	1237.70
-1.51	-1.71	1237.70	-8.50	-1.56	1237.70
-1.75	-1.72	1237.70	-8.56	-1.55	1237.70
-1.90	-1.72	1237.70	-8.88	-1.50	1237.70
-2.14	-1.73	1237.70	-8.91	-1.49	1237.70

F.4. AERODYNAMIC PROFILE COORDINATES

x (mm)	y (mm)	z (mm)	x (mm)	y (mm)	z (mm)
-9.24	-1.43	1237.70	-5.18	2.69	1237.70
-9.26	-1.43	1237.70	-4.97	2.71	1237.70
-9.62	-1.36	1237.70	-4.78	2.72	1237.70
-9.94	-1.27	1237.70	-4.58	2.73	1237.70
-10.26	-1.17	1237.70	-4.38	2.74	1237.70
-10.55	-1.06	1237.70	-4.18	2.75	1237.70
-11.38	-0.59	1237.70	-3.98	2.76	1237.70
-11.78	-0.01	1237.70	-3.79	2.76	1237.70
-11.54	0.66	1237.70	-3.57	2.77	1237.70
-10.82	1.32	1237.70	-3.39	2.78	1237.70
-10.54	1.49	1237.70	-3.17	2.78	1237.70
-10.22	1.65	1237.70	-3.00	2.78	1237.70
-9.88	1.80	1237.70	-2.76	2.79	1237.70
-9.55	1.93	1237.70	-2.60	2.79	1237.70
-9.53	1.94	1237.70	-2.36	2.79	1237.70
-9.19	2.04	1237.70	-2.20	2.79	1237.70
-9.15	2.06	1237.70	-1.96	2.79	1237.70
-8.83	2.15	1237.70	-1.80	2.79	1237.70
-8.76	2.17	1237.70	-1.55	2.79	1237.70
-8.45	2.24	1237.70	-1.41	2.79	1237.70
-8.37	2.26	1237.70	-1.15	2.78	1237.70
-8.07	2.32	1237.70	-1.01	2.78	1237.70
-7.97	2.34	1237.70	-0.75	2.77	1237.70
-7.69	2.40	1237.70	-0.61	2.77	1237.70
-7.58	2.42	1237.70	-0.35	2.76	1237.70
-7.31	2.46	1237.70	-0.21	2.76	1237.70
-7.18	2.48	1237.70	0.06	2.75	1237.70
-6.92	2.52	1237.70	0.18	2.75	1237.70
-6.79	2.54	1237.70	0.46	2.74	1237.70
-6.54	2.57	1237.70	0.58	2.73	1237.70
-6.39	2.59	1237.70	0.86	2.72	1237.70
-6.15	2.61	1237.70	0.98	2.72	1237.70
-5.99	2.63	1237.70	1.26	2.71	1237.70
-5.76	2.65	1237.70	1.38	2.70	1237.70
-5.59	2.66	1237.70	1.66	2.69	1237.70
-5.36	2.68	1237.70	1.78	2.68	1237.70

F.4. AERODYNAMIC PROFILE COORDINATES

x (mm)	y (mm)	z (mm)	x (mm)	y (mm)	z (mm)
2.06	2.67	1237.70	9.27	2.12	1237.70
2.18	2.66	1237.70	9.34	2.11	1237.70
2.46	2.65	1237.70	9.67	2.08	1237.70
2.57	2.64	1237.70	9.74	2.08	1237.70
2.87	2.62	1237.70	10.07	2.05	1237.70
2.97	2.62	1237.70	10.13	2.04	1237.70
3.27	2.60	1237.70	10.47	2.01	1237.70
3.37	2.59	1237.70	10.53	2.00	1237.70
3.67	2.57	1237.70	10.87	1.97	1237.70
3.77	2.57	1237.70	10.93	1.96	1237.70
4.07	2.55	1237.70	11.27	1.93	1237.70
4.17	2.54	1237.70	11.33	1.93	1237.70
4.47	2.52	1237.70	11.66	1.89	1237.70
4.56	2.51	1237.70	11.72	1.89	1237.70
4.87	2.49	1237.70	12.06	1.86	1237.70
4.96	2.48	1237.70	12.12	1.85	1237.70
5.27	2.46	1237.70	12.46	1.82	1237.70
5.36	2.45	1237.70	12.52	1.81	1237.70
5.67	2.43	1237.70	12.86	1.78	1237.70
5.76	2.42	1237.70	12.91	1.77	1237.70
6.07	2.40	1237.70	13.26	1.74	1237.70
6.16	2.39	1237.70	13.31	1.73	1237.70
6.47	2.36	1237.70	13.66	1.70	1237.70
6.55	2.36	1237.70	13.71	1.69	1237.70
6.87	2.33	1237.70	14.06	1.66	1237.70
6.95	2.32	1237.70	14.10	1.65	1237.70
7.27	2.30	1237.70	14.46	1.62	1237.70
7.35	2.29	1237.70	14.50	1.61	1237.70
7.67	2.26	1237.70	14.85	1.58	1237.70
7.75	2.26	1237.70	14.89	1.57	1237.70
8.07	2.23	1237.70	15.25	1.53	1237.70
8.15	2.22	1237.70	15.29	1.53	1237.70
8.47	2.19	1237.70	15.65	1.49	1237.70
8.54	2.19	1237.70	15.69	1.49	1237.70
8.87	2.16	1237.70	16.05	1.45	1237.70
8.94	2.15	1237.70	16.08	1.45	1237.70

F.4. AERODYNAMIC PROFILE COORDINATES

x (mm)	y (mm)	z (mm)
16.45	1.41	1237.70
16.48	1.41	1237.70
19.68	1.02	1237.70

x (mm)	y (mm)	z (mm)
9.464	-1.0935	1242.9
9.1693	-1.1017	1242.9
9.1142	-1.1032	1242.9
8.8211	-1.1117	1242.9
8.7646	-1.1133	1242.9
8.473	-1.1221	1242.9
8.4152	-1.1239	1242.9
8.1251	-1.1331	1242.9
8.0658	-1.135	1242.9
7.7772	-1.1444	1242.9
7.7166	-1.1465	1242.9
7.4297	-1.1562	1242.9
7.3675	-1.1584	1242.9
7.0823	-1.1685	1242.9
7.0185	-1.1708	1242.9
6.7348	-1.181	1242.9
6.6695	-1.1834	1242.9
6.3877	-1.194	1242.9
6.3207	-1.1965	1242.9
6.0409	-1.2073	1242.9
5.972	-1.2099	1242.9
5.6939	-1.2208	1242.9
5.6234	-1.2235	1242.9
5.3475	-1.2346	1242.9
5.2751	-1.2375	1242.9
5.0011	-1.2487	1242.9
4.9267	-1.2517	1242.9
4.655	-1.263	1242.9
4.5785	-1.2662	1242.9
4.3089	-1.2775	1242.9
4.2303	-1.2807	1242.9
3.9633	-1.2921	1242.9
3.8824	-1.2955	1242.9
3.6177	-1.3068	1242.9
3.5345	-1.3103	1242.9
3.2725	-1.3217	1242.9

F.4.19 Section 19

x (mm)	y (mm)	z (mm)
17.237	-0.87109	1242.9
14.402	-0.98068	1242.9
14.378	-0.98123	1242.9
14.052	-0.98846	1242.9
14.026	-0.98905	1242.9
13.702	-0.99608	1242.9
13.673	-0.99672	1242.9
13.353	-1.0037	1242.9
13.321	-1.0043	1242.9
13.004	-1.0112	1242.9
12.969	-1.012	1242.9
12.655	-1.0188	1242.9
12.618	-1.0196	1242.9
12.306	-1.0265	1242.9
12.267	-1.0274	1242.9
11.957	-1.0342	1242.9
11.916	-1.0351	1242.9
11.609	-1.0418	1242.9
11.565	-1.0428	1242.9
11.26	-1.0496	1242.9
11.215	-1.0507	1242.9
10.911	-1.0576	1242.9
10.864	-1.0587	1242.9
10.563	-1.0658	1242.9
10.514	-1.067	1242.9
10.214	-1.0742	1242.9
10.164	-1.0754	1242.9
9.8661	-1.083	1242.9
9.8139	-1.0843	1242.9
9.5176	-1.0921	1242.9

F.4. AERODYNAMIC PROFILE COORDINATES

x (mm)	y (mm)	z (mm)	x (mm)	y (mm)	z (mm)
3.1868	-1.3253	1242.9	-3.0604	-1.5454	1242.9
2.9275	-1.3367	1242.9	-3.2455	-1.5476	1242.9
2.8394	-1.3405	1242.9	-3.4066	-1.549	1242.9
2.5826	-1.3516	1242.9	-3.5841	-1.5502	1242.9
2.492	-1.3555	1242.9	-3.7524	-1.5509	1242.9
2.2379	-1.3665	1242.9	-3.9223	-1.5512	1242.9
2.1449	-1.3705	1242.9	-4.0975	-1.5508	1242.9
1.8934	-1.3814	1242.9	-4.2593	-1.55	1242.9
1.798	-1.3854	1242.9	-4.4417	-1.5485	1242.9
1.5491	-1.3961	1242.9	-4.5952	-1.5467	1242.9
1.4512	-1.4002	1242.9	-4.7849	-1.5437	1242.9
1.205	-1.4107	1242.9	-4.9299	-1.5409	1242.9
1.1042	-1.4149	1242.9	-5.1273	-1.5362	1242.9
0.86098	-1.425	1242.9	-5.2634	-1.5324	1242.9
0.75776	-1.4291	1242.9	-5.4685	-1.5256	1242.9
0.51465	-1.439	1242.9	-5.5953	-1.5208	1242.9
0.4101	-1.4432	1242.9	-5.8085	-1.5116	1242.9
0.17246	-1.4526	1242.9	-5.9253	-1.5057	1242.9
0.063367	-1.4568	1242.9	-6.1473	-1.4935	1242.9
-0.17073	-1.4658	1242.9	-6.2533	-1.4868	1242.9
-0.28361	-1.4699	1242.9	-6.4845	-1.471	1242.9
-0.51388	-1.4784	1242.9	-6.5788	-1.4636	1242.9
-0.63053	-1.4825	1242.9	-6.82	-1.4432	1242.9
-0.85665	-1.4904	1242.9	-6.9015	-1.4353	1242.9
-0.9777	-1.4944	1242.9	-7.153	-1.4093	1242.9
-1.1993	-1.5017	1242.9	-7.2198	-1.4014	1242.9
-1.3247	-1.5056	1242.9	-7.4816	-1.3684	1242.9
-1.5414	-1.5121	1242.9	-7.5321	-1.361	1242.9
-1.6719	-1.5159	1242.9	-7.8078	-1.3194	1242.9
-1.8833	-1.5217	1242.9	-7.8417	-1.3132	1242.9
-2.0192	-1.5251	1242.9	-8.1304	-1.2607	1242.9
-2.2246	-1.5301	1242.9	-8.1463	-1.2567	1242.9
-2.3664	-1.5332	1242.9	-8.4603	-1.1917	1242.9
-2.5655	-1.5373	1242.9	-8.7485	-1.1142	1242.9
-2.7135	-1.54	1242.9	-9.0236	-1.0277	1242.9
-2.9058	-1.5432	1242.9	-9.2769	-0.93326	1242.9

F.4. AERODYNAMIC PROFILE COORDINATES

x (mm)	y (mm)	z (mm)	x (mm)	y (mm)	z (mm)
-10.008	-0.52124	1242.9	-3.4972	2.4284	1242.9
-10.364	-0.0086828	1242.9	-3.3312	2.4344	1242.9
-10.15	0.58231	1242.9	-3.142	2.4399	1242.9
-9.5202	1.1603	1242.9	-2.9832	2.4442	1242.9
-9.2728	1.3104	1242.9	-2.787	2.4481	1242.9
-8.993	1.4538	1242.9	-2.6347	2.451	1242.9
-8.6926	1.5836	1242.9	-2.4318	2.4534	1242.9
-8.4049	1.6961	1242.9	-2.2859	2.455	1242.9
-8.3802	1.7042	1242.9	-2.0766	2.456	1242.9
-8.0888	1.7995	1242.9	-1.9367	2.4565	1242.9
-8.0464	1.8122	1242.9	-1.7217	2.4561	1242.9
-7.7654	1.8921	1242.9	-1.5873	2.4557	1242.9
-7.7063	1.9077	1242.9	-1.367	2.4538	1242.9
-7.4351	1.9743	1242.9	-1.2376	2.4526	1242.9
-7.3611	1.9913	1242.9	-1.0125	2.4493	1242.9
-7.1026	2.047	1242.9	-0.8878	2.4475	1242.9
-7.0151	2.0646	1242.9	-0.65844	2.4428	1242.9
-6.768	2.1114	1242.9	-0.53774	2.4404	1242.9
-6.6677	2.1289	1242.9	-0.30429	2.4344	1242.9
-6.4306	2.1681	1242.9	-0.18755	2.4315	1242.9
-6.3189	2.1851	1242.9	0.049526	2.4242	1242.9
-6.0913	2.218	1242.9	0.16292	2.4208	1242.9
-5.9691	2.2342	1242.9	0.40337	2.4124	1242.9
-5.7502	2.2618	1242.9	0.51467	2.4086	1242.9
-5.6182	2.2769	1242.9	0.75612	2.3989	1242.9
-5.4075	2.2999	1242.9	0.86256	2.3948	1242.9
-5.2663	2.3138	1242.9	1.1099	2.384	1242.9
-5.0637	2.3329	1242.9	1.213	2.3795	1242.9
-4.9138	2.3455	1242.9	1.4628	2.3676	1242.9
-4.7187	2.3612	1242.9	1.5636	2.3628	1242.9
-4.5602	2.3724	1242.9	1.8159	2.3498	1242.9
-4.3727	2.3852	1242.9	1.9141	2.3448	1242.9
-4.2063	2.395	1242.9	2.1687	2.3308	1242.9
-4.0262	2.4052	1242.9	2.2645	2.3256	1242.9
-3.8519	2.4135	1242.9	2.5216	2.3106	1242.9
-3.6791	2.4215	1242.9	2.6149	2.3052	1242.9

F.4. AERODYNAMIC PROFILE COORDINATES

x (mm)	y (mm)	z (mm)	x (mm)	y (mm)	z (mm)
2.8743	2.2892	1242.9	9.2084	1.7701	1242.9
2.9653	2.2836	1242.9	9.2647	1.7648	1242.9
3.2274	2.2666	1242.9	9.5595	1.737	1242.9
3.3157	2.2609	1242.9	9.6142	1.7319	1242.9
3.5802	2.243	1242.9	9.9104	1.7037	1242.9
3.6661	2.2372	1242.9	9.9635	1.6987	1242.9
3.9329	2.2184	1242.9	10.261	1.6702	1242.9
4.0162	2.2126	1242.9	10.313	1.6653	1242.9
4.2855	2.1929	1242.9	10.612	1.6365	1242.9
4.3665	2.1871	1242.9	10.662	1.6317	1242.9
4.6378	2.1666	1242.9	10.963	1.6024	1242.9
4.7165	2.1607	1242.9	11.011	1.5977	1242.9
4.9901	2.1394	1242.9	11.314	1.568	1242.9
5.0666	2.1335	1242.9	11.36	1.5635	1242.9
5.3421	2.1115	1242.9	11.665	1.5332	1242.9
5.4166	2.1056	1242.9	11.708	1.5289	1242.9
5.6942	2.0829	1242.9	12.015	1.4982	1242.9
5.7668	2.077	1242.9	12.057	1.494	1242.9
6.046	2.0537	1242.9	12.366	1.4627	1242.9
6.1165	2.0478	1242.9	12.405	1.4587	1242.9
6.3977	2.0239	1242.9	12.717	1.4268	1242.9
6.4665	2.0181	1242.9	12.754	1.423	1242.9
6.7494	1.9935	1242.9	13.068	1.3906	1242.9
6.8165	1.9877	1242.9	13.102	1.387	1242.9
7.1009	1.9628	1242.9	13.419	1.354	1242.9
7.1662	1.957	1242.9	13.45	1.3507	1242.9
7.4523	1.9314	1242.9	13.769	1.3172	1242.9
7.516	1.9258	1242.9	13.799	1.3142	1242.9
7.8037	1.8998	1242.9	14.12	1.2802	1242.9
7.8659	1.8942	1242.9	14.147	1.2774	1242.9
8.155	1.8678	1242.9	14.471	1.2429	1242.9
8.2156	1.8623	1242.9	14.495	1.2404	1242.9
8.5062	1.8355	1242.9	17.311	0.90003	1242.9
8.5654	1.8301	1242.9			
8.8573	1.8029	1242.9			
8.9151	1.7975	1242.9			

F.4.20 Section 20

F.4. AERODYNAMIC PROFILE COORDINATES

x (mm)	y (mm)	z (mm)	x (mm)	y (mm)	z (mm)
14.72	-0.75	1247.70	7.24	-0.96	1247.70
12.30	-0.84	1247.70	7.19	-0.96	1247.70
12.28	-0.84	1247.70	6.94	-0.97	1247.70
12.00	-0.85	1247.70	6.89	-0.97	1247.70
11.98	-0.85	1247.70	6.64	-0.98	1247.70
11.70	-0.86	1247.70	6.59	-0.98	1247.70
11.68	-0.86	1247.70	6.34	-0.99	1247.70
11.40	-0.86	1247.70	6.29	-0.99	1247.70
11.38	-0.86	1247.70	6.05	-1.00	1247.70
11.11	-0.87	1247.70	5.99	-1.00	1247.70
11.08	-0.87	1247.70	5.75	-1.01	1247.70
10.81	-0.88	1247.70	5.70	-1.01	1247.70
10.78	-0.88	1247.70	5.46	-1.02	1247.70
10.51	-0.88	1247.70	5.40	-1.03	1247.70
10.48	-0.88	1247.70	5.16	-1.04	1247.70
10.21	-0.89	1247.70	5.10	-1.04	1247.70
10.18	-0.89	1247.70	4.86	-1.05	1247.70
9.91	-0.90	1247.70	4.80	-1.05	1247.70
9.88	-0.90	1247.70	4.57	-1.06	1247.70
9.62	-0.90	1247.70	4.50	-1.06	1247.70
9.58	-0.90	1247.70	4.27	-1.07	1247.70
9.32	-0.91	1247.70	4.21	-1.07	1247.70
9.28	-0.91	1247.70	3.98	-1.08	1247.70
9.02	-0.92	1247.70	3.91	-1.09	1247.70
8.98	-0.92	1247.70	3.68	-1.09	1247.70
8.72	-0.92	1247.70	3.61	-1.10	1247.70
8.68	-0.92	1247.70	3.38	-1.11	1247.70
8.43	-0.93	1247.70	3.32	-1.11	1247.70
8.38	-0.93	1247.70	3.09	-1.12	1247.70
8.13	-0.94	1247.70	3.02	-1.12	1247.70
8.08	-0.94	1247.70	2.79	-1.13	1247.70
7.83	-0.95	1247.70	2.72	-1.14	1247.70
7.78	-0.95	1247.70	2.50	-1.14	1247.70
7.53	-0.95	1247.70	2.42	-1.15	1247.70
7.48	-0.96	1247.70	2.21	-1.16	1247.70
			2.13	-1.16	1247.70

F.4. AERODYNAMIC PROFILE COORDINATES

x (mm)	y (mm)	z (mm)	x (mm)	y (mm)	z (mm)
1.91	-1.17	1247.70	-3.35	-1.33	1247.70
1.83	-1.17	1247.70	-3.50	-1.33	1247.70
1.62	-1.18	1247.70	-3.64	-1.32	1247.70
1.54	-1.19	1247.70	-3.79	-1.32	1247.70
1.32	-1.19	1247.70	-3.92	-1.32	1247.70
1.24	-1.20	1247.70	-4.09	-1.32	1247.70
1.03	-1.21	1247.70	-4.21	-1.32	1247.70
0.94	-1.21	1247.70	-4.38	-1.31	1247.70
0.74	-1.22	1247.70	-4.50	-1.31	1247.70
0.65	-1.22	1247.70	-4.67	-1.30	1247.70
0.44	-1.23	1247.70	-4.78	-1.30	1247.70
0.35	-1.23	1247.70	-4.96	-1.29	1247.70
0.15	-1.24	1247.70	-5.06	-1.29	1247.70
0.05	-1.25	1247.70	-5.25	-1.28	1247.70
-0.15	-1.25	1247.70	-5.34	-1.27	1247.70
-0.24	-1.26	1247.70	-5.54	-1.26	1247.70
-0.44	-1.26	1247.70	-5.62	-1.25	1247.70
-0.54	-1.27	1247.70	-5.82	-1.23	1247.70
-0.73	-1.27	1247.70	-5.89	-1.23	1247.70
-0.84	-1.28	1247.70	-6.11	-1.20	1247.70
-1.02	-1.28	1247.70	-6.17	-1.20	1247.70
-1.13	-1.29	1247.70	-6.39	-1.17	1247.70
-1.32	-1.29	1247.70	-6.43	-1.16	1247.70
-1.43	-1.30	1247.70	-6.67	-1.13	1247.70
-1.61	-1.30	1247.70	-6.70	-1.12	1247.70
-1.72	-1.30	1247.70	-6.94	-1.08	1247.70
-1.90	-1.31	1247.70	-6.96	-1.07	1247.70
-2.02	-1.31	1247.70	-7.23	-1.02	1247.70
-2.19	-1.31	1247.70	-7.47	-0.95	1247.70
-2.32	-1.32	1247.70	-7.71	-0.88	1247.70
-2.48	-1.32	1247.70	-7.92	-0.80	1247.70
-2.61	-1.32	1247.70	-8.55	-0.44	1247.70
-2.77	-1.32	1247.70	-8.85	-0.01	1247.70
-2.91	-1.32	1247.70	-8.67	0.50	1247.70
-3.06	-1.32	1247.70	-8.13	0.99	1247.70
-3.20	-1.33	1247.70	-7.92	1.12	1247.70

F.4. AERODYNAMIC PROFILE COORDINATES

x (mm)	y (mm)	z (mm)	x (mm)	y (mm)	z (mm)
-7.68	1.24	1247.70	-2.25	2.10	1247.70
-7.42	1.35	1247.70	-2.08	2.10	1247.70
-7.18	1.45	1247.70	-1.95	2.10	1247.70
-7.16	1.46	1247.70	-1.77	2.10	1247.70
-6.91	1.54	1247.70	-1.65	2.10	1247.70
-6.87	1.55	1247.70	-1.47	2.10	1247.70
-6.63	1.62	1247.70	-1.36	2.10	1247.70
-6.58	1.63	1247.70	-1.17	2.10	1247.70
-6.35	1.69	1247.70	-1.06	2.10	1247.70
-6.29	1.70	1247.70	-0.86	2.09	1247.70
-6.07	1.75	1247.70	-0.76	2.09	1247.70
-5.99	1.76	1247.70	-0.56	2.09	1247.70
-5.78	1.80	1247.70	-0.46	2.09	1247.70
-5.69	1.82	1247.70	-0.26	2.08	1247.70
-5.49	1.85	1247.70	-0.16	2.08	1247.70
-5.40	1.87	1247.70	0.04	2.07	1247.70
-5.20	1.90	1247.70	0.14	2.07	1247.70
-5.10	1.91	1247.70	0.34	2.06	1247.70
-4.91	1.93	1247.70	0.44	2.06	1247.70
-4.80	1.95	1247.70	0.65	2.05	1247.70
-4.62	1.97	1247.70	0.74	2.05	1247.70
-4.50	1.98	1247.70	0.95	2.04	1247.70
-4.32	1.99	1247.70	1.04	2.03	1247.70
-4.20	2.00	1247.70	1.25	2.02	1247.70
-4.03	2.02	1247.70	1.34	2.02	1247.70
-3.89	2.03	1247.70	1.55	2.01	1247.70
-3.73	2.04	1247.70	1.63	2.00	1247.70
-3.59	2.05	1247.70	1.85	1.99	1247.70
-3.44	2.06	1247.70	1.93	1.99	1247.70
-3.29	2.06	1247.70	2.15	1.98	1247.70
-3.14	2.07	1247.70	2.23	1.97	1247.70
-2.99	2.08	1247.70	2.46	1.96	1247.70
-2.84	2.08	1247.70	2.53	1.95	1247.70
-2.68	2.09	1247.70	2.76	1.94	1247.70
-2.55	2.09	1247.70	2.83	1.93	1247.70
-2.38	2.09	1247.70	3.06	1.92	1247.70

F.4. AERODYNAMIC PROFILE COORDINATES

x (mm)	y (mm)	z (mm)
3.13	1.91	1247.70
3.36	1.90	1247.70
3.43	1.89	1247.70
3.66	1.88	1247.70
3.73	1.87	1247.70
3.96	1.85	1247.70
4.03	1.85	1247.70
4.26	1.83	1247.70
4.33	1.82	1247.70
4.56	1.81	1247.70
4.63	1.80	1247.70
4.86	1.78	1247.70
4.93	1.78	1247.70
5.16	1.76	1247.70
5.22	1.75	1247.70
5.46	1.73	1247.70
5.52	1.73	1247.70
5.76	1.71	1247.70
5.82	1.70	1247.70
6.06	1.68	1247.70
6.12	1.67	1247.70
6.36	1.65	1247.70
6.42	1.65	1247.70
6.66	1.63	1247.70
6.72	1.62	1247.70
6.96	1.60	1247.70
7.02	1.59	1247.70
7.26	1.57	1247.70
7.32	1.57	1247.70
7.56	1.54	1247.70
7.61	1.54	1247.70
7.86	1.51	1247.70
7.91	1.51	1247.70
8.16	1.49	1247.70
8.21	1.48	1247.70
8.46	1.46	1247.70

x (mm)	y (mm)	z (mm)
8.51	1.45	1247.70
8.76	1.43	1247.70
8.81	1.43	1247.70
9.06	1.40	1247.70
9.11	1.40	1247.70
9.36	1.37	1247.70
9.40	1.37	1247.70
9.66	1.34	1247.70
9.70	1.34	1247.70
9.96	1.31	1247.70
10.00	1.31	1247.70
10.26	1.28	1247.70
10.30	1.28	1247.70
10.56	1.25	1247.70
10.60	1.25	1247.70
10.86	1.22	1247.70
10.89	1.22	1247.70
11.16	1.19	1247.70
11.19	1.19	1247.70
11.46	1.16	1247.70
11.49	1.16	1247.70
11.76	1.13	1247.70
11.79	1.13	1247.70
12.06	1.10	1247.70
12.08	1.09	1247.70
12.36	1.06	1247.70
12.38	1.06	1247.70
14.78	0.77	1247.70

F.4.21 Section 21

x (mm)	y (mm)	z (mm)
12.07	-0.62	1251.90
10.08	-0.70	1251.90
10.07	-0.70	1251.90
9.84	-0.70	1251.90

F.4. AERODYNAMIC PROFILE COORDINATES

x (mm)	y (mm)	z (mm)	x (mm)	y (mm)	z (mm)
9.82	-0.70	1251.90	5.40	-0.81	1251.90
9.59	-0.71	1251.90	5.20	-0.82	1251.90
9.57	-0.71	1251.90	5.16	-0.82	1251.90
9.35	-0.71	1251.90	4.96	-0.83	1251.90
9.33	-0.71	1251.90	4.91	-0.83	1251.90
9.10	-0.72	1251.90	4.72	-0.83	1251.90
9.08	-0.72	1251.90	4.67	-0.84	1251.90
8.86	-0.72	1251.90	4.47	-0.84	1251.90
8.83	-0.72	1251.90	4.43	-0.84	1251.90
8.62	-0.73	1251.90	4.23	-0.85	1251.90
8.59	-0.73	1251.90	4.18	-0.85	1251.90
8.37	-0.73	1251.90	3.99	-0.86	1251.90
8.34	-0.73	1251.90	3.94	-0.86	1251.90
8.13	-0.74	1251.90	3.74	-0.87	1251.90
8.10	-0.74	1251.90	3.69	-0.87	1251.90
7.88	-0.74	1251.90	3.50	-0.88	1251.90
7.85	-0.75	1251.90	3.45	-0.88	1251.90
7.64	-0.75	1251.90	3.26	-0.89	1251.90
7.61	-0.75	1251.90	3.21	-0.89	1251.90
7.40	-0.76	1251.90	3.02	-0.90	1251.90
7.36	-0.76	1251.90	2.96	-0.90	1251.90
7.15	-0.76	1251.90	2.77	-0.91	1251.90
7.12	-0.76	1251.90	2.72	-0.91	1251.90
6.91	-0.77	1251.90	2.53	-0.92	1251.90
6.87	-0.77	1251.90	2.47	-0.92	1251.90
6.66	-0.77	1251.90	2.29	-0.93	1251.90
6.63	-0.77	1251.90	2.23	-0.93	1251.90
6.42	-0.78	1251.90	2.05	-0.94	1251.90
6.38	-0.78	1251.90	1.99	-0.94	1251.90
6.18	-0.79	1251.90	1.81	-0.95	1251.90
6.14	-0.79	1251.90	1.74	-0.95	1251.90
5.93	-0.79	1251.90	1.57	-0.96	1251.90
5.89	-0.79	1251.90	1.50	-0.96	1251.90
5.69	-0.80	1251.90	1.33	-0.97	1251.90
5.65	-0.80	1251.90	1.26	-0.97	1251.90
5.44	-0.81	1251.90	1.08	-0.98	1251.90

F.4. AERODYNAMIC PROFILE COORDINATES

x (mm)	y (mm)	z (mm)	x (mm)	y (mm)	z (mm)
1.02	-0.98	1251.90	-3.35	-1.08	1251.90
0.84	-0.99	1251.90	-3.45	-1.08	1251.90
0.77	-0.99	1251.90	-3.59	-1.08	1251.90
0.60	-1.00	1251.90	-3.69	-1.07	1251.90
0.53	-1.00	1251.90	-3.83	-1.07	1251.90
0.36	-1.01	1251.90	-3.92	-1.07	1251.90
0.29	-1.01	1251.90	-4.07	-1.06	1251.90
0.12	-1.02	1251.90	-4.15	-1.05	1251.90
0.04	-1.02	1251.90	-4.30	-1.05	1251.90
-0.12	-1.03	1251.90	-4.38	-1.04	1251.90
-0.20	-1.03	1251.90	-4.54	-1.03	1251.90
-0.36	-1.04	1251.90	-4.61	-1.02	1251.90
-0.44	-1.04	1251.90	-4.78	-1.01	1251.90
-0.60	-1.05	1251.90	-4.83	-1.00	1251.90
-0.68	-1.05	1251.90	-5.01	-0.99	1251.90
-0.84	-1.05	1251.90	-5.06	-0.98	1251.90
-0.93	-1.06	1251.90	-5.24	-0.96	1251.90
-1.08	-1.06	1251.90	-5.27	-0.95	1251.90
-1.17	-1.06	1251.90	-5.47	-0.92	1251.90
-1.32	-1.07	1251.90	-5.49	-0.92	1251.90
-1.41	-1.07	1251.90	-5.69	-0.88	1251.90
-1.56	-1.07	1251.90	-5.70	-0.88	1251.90
-1.66	-1.08	1251.90	-5.92	-0.83	1251.90
-1.80	-1.08	1251.90	-6.13	-0.78	1251.90
-1.90	-1.08	1251.90	-6.32	-0.72	1251.90
-2.03	-1.08	1251.90	-6.50	-0.65	1251.90
-2.14	-1.08	1251.90	-7.01	-0.36	1251.90
-2.27	-1.09	1251.90	-7.26	0.00	1251.90
-2.39	-1.09	1251.90	-7.11	0.41	1251.90
-2.51	-1.09	1251.90	-6.67	0.81	1251.90
-2.63	-1.09	1251.90	-6.49	0.92	1251.90
-2.75	-1.09	1251.90	-6.30	1.02	1251.90
-2.87	-1.09	1251.90	-6.09	1.11	1251.90
-2.98	-1.09	1251.90	-5.88	1.19	1251.90
-3.11	-1.09	1251.90	-5.87	1.20	1251.90
-3.22	-1.08	1251.90	-5.66	1.26	1251.90

F.4. AERODYNAMIC PROFILE COORDINATES

x (mm)	y (mm)	z (mm)	x (mm)	y (mm)	z (mm)
-5.63	1.27	1251.90	-1.21	1.72	1251.90
-5.44	1.33	1251.90	-1.11	1.72	1251.90
-5.40	1.34	1251.90	-0.96	1.72	1251.90
-5.21	1.38	1251.90	-0.87	1.72	1251.90
-5.15	1.40	1251.90	-0.71	1.72	1251.90
-4.97	1.44	1251.90	-0.62	1.72	1251.90
-4.91	1.45	1251.90	-0.46	1.71	1251.90
-4.74	1.48	1251.90	-0.38	1.71	1251.90
-4.67	1.49	1251.90	-0.21	1.71	1251.90
-4.50	1.52	1251.90	-0.13	1.71	1251.90
-4.42	1.53	1251.90	0.04	1.70	1251.90
-4.26	1.56	1251.90	0.11	1.70	1251.90
-4.18	1.57	1251.90	0.28	1.69	1251.90
-4.03	1.59	1251.90	0.36	1.69	1251.90
-3.93	1.60	1251.90	0.53	1.68	1251.90
-3.79	1.61	1251.90	0.60	1.68	1251.90
-3.69	1.62	1251.90	0.78	1.67	1251.90
-3.55	1.64	1251.90	0.85	1.67	1251.90
-3.44	1.65	1251.90	1.02	1.66	1251.90
-3.30	1.66	1251.90	1.10	1.66	1251.90
-3.19	1.66	1251.90	1.27	1.65	1251.90
-3.06	1.67	1251.90	1.34	1.65	1251.90
-2.94	1.68	1251.90	1.52	1.64	1251.90
-2.82	1.69	1251.90	1.59	1.63	1251.90
-2.70	1.69	1251.90	1.77	1.62	1251.90
-2.58	1.70	1251.90	1.83	1.62	1251.90
-2.45	1.70	1251.90	2.01	1.61	1251.90
-2.33	1.71	1251.90	2.08	1.60	1251.90
-2.20	1.71	1251.90	2.26	1.59	1251.90
-2.09	1.71	1251.90	2.32	1.59	1251.90
-1.95	1.72	1251.90	2.51	1.57	1251.90
-1.84	1.72	1251.90	2.57	1.57	1251.90
-1.70	1.72	1251.90	2.75	1.56	1251.90
-1.60	1.72	1251.90	2.81	1.55	1251.90
-1.45	1.72	1251.90	3.00	1.54	1251.90
-1.36	1.72	1251.90	3.06	1.54	1251.90

F.4. AERODYNAMIC PROFILE COORDINATES

x (mm)	y (mm)	z (mm)
3.25	1.52	1251.90
3.30	1.52	1251.90
3.49	1.50	1251.90
3.55	1.50	1251.90
3.74	1.48	1251.90
3.79	1.48	1251.90
3.99	1.46	1251.90
4.04	1.46	1251.90
4.23	1.44	1251.90
4.28	1.44	1251.90
4.48	1.42	1251.90
4.53	1.42	1251.90
4.73	1.40	1251.90
4.77	1.40	1251.90
4.97	1.38	1251.90
5.02	1.37	1251.90
5.22	1.36	1251.90
5.26	1.35	1251.90
5.46	1.33	1251.90
5.51	1.33	1251.90
5.71	1.31	1251.90
5.75	1.31	1251.90
5.96	1.29	1251.90
6.00	1.29	1251.90
6.20	1.27	1251.90
6.24	1.26	1251.90
6.45	1.24	1251.90
6.49	1.24	1251.90
6.69	1.22	1251.90
6.73	1.22	1251.90
6.94	1.20	1251.90
6.98	1.19	1251.90
7.19	1.17	1251.90
7.22	1.17	1251.90
7.43	1.15	1251.90
7.47	1.15	1251.90

x (mm)	y (mm)	z (mm)
7.68	1.13	1251.90
7.71	1.12	1251.90
7.92	1.10	1251.90
7.95	1.10	1251.90
8.17	1.08	1251.90
8.20	1.08	1251.90
8.41	1.05	1251.90
8.44	1.05	1251.90
8.66	1.03	1251.90
8.69	1.03	1251.90
8.90	1.00	1251.90
8.93	1.00	1251.90
9.15	0.98	1251.90
9.17	0.98	1251.90
9.40	0.95	1251.90
9.42	0.95	1251.90
9.64	0.93	1251.90
9.66	0.93	1251.90
9.89	0.90	1251.90
9.91	0.90	1251.90
10.13	0.88	1251.90
10.15	0.87	1251.90
12.12	0.64	1251.90

F.4.22 Section 22

x (mm)	y (mm)	z (mm)
9.31	-0.48	1255.30
7.78	-0.54	1255.30
7.76	-0.54	1255.30
7.59	-0.55	1255.30
7.57	-0.55	1255.30
7.40	-0.55	1255.30
7.38	-0.55	1255.30
7.21	-0.55	1255.30
7.19	-0.55	1255.30

F.4. AERODYNAMIC PROFILE COORDINATES

x (mm)	y (mm)	z (mm)	x (mm)	y (mm)	z (mm)
7.02	-0.56	1255.30	3.64	-0.65	1255.30
7.00	-0.56	1255.30	3.60	-0.65	1255.30
6.83	-0.56	1255.30	3.45	-0.65	1255.30
6.81	-0.56	1255.30	3.41	-0.65	1255.30
6.64	-0.57	1255.30	3.26	-0.66	1255.30
6.62	-0.57	1255.30	3.22	-0.66	1255.30
6.46	-0.57	1255.30	3.07	-0.67	1255.30
6.43	-0.57	1255.30	3.04	-0.67	1255.30
6.27	-0.57	1255.30	2.89	-0.67	1255.30
6.24	-0.57	1255.30	2.85	-0.68	1255.30
6.08	-0.58	1255.30	2.70	-0.68	1255.30
6.05	-0.58	1255.30	2.66	-0.68	1255.30
5.89	-0.58	1255.30	2.51	-0.69	1255.30
5.87	-0.58	1255.30	2.47	-0.69	1255.30
5.70	-0.59	1255.30	2.33	-0.70	1255.30
5.68	-0.59	1255.30	2.28	-0.70	1255.30
5.51	-0.59	1255.30	2.14	-0.70	1255.30
5.49	-0.59	1255.30	2.10	-0.71	1255.30
5.33	-0.59	1255.30	1.95	-0.71	1255.30
5.30	-0.60	1255.30	1.91	-0.71	1255.30
5.14	-0.60	1255.30	1.77	-0.72	1255.30
5.11	-0.60	1255.30	1.72	-0.72	1255.30
4.95	-0.60	1255.30	1.58	-0.73	1255.30
4.92	-0.61	1255.30	1.53	-0.73	1255.30
4.76	-0.61	1255.30	1.39	-0.74	1255.30
4.73	-0.61	1255.30	1.35	-0.74	1255.30
4.57	-0.62	1255.30	1.21	-0.74	1255.30
4.54	-0.62	1255.30	1.16	-0.75	1255.30
4.39	-0.62	1255.30	1.02	-0.75	1255.30
4.35	-0.62	1255.30	0.97	-0.75	1255.30
4.20	-0.63	1255.30	0.84	-0.76	1255.30
4.17	-0.63	1255.30	0.78	-0.76	1255.30
4.01	-0.63	1255.30	0.65	-0.77	1255.30
3.98	-0.63	1255.30	0.60	-0.77	1255.30
3.82	-0.64	1255.30	0.46	-0.77	1255.30
3.79	-0.64	1255.30	0.41	-0.78	1255.30

F.4. AERODYNAMIC PROFILE COORDINATES

x (mm)	y (mm)	z (mm)	x (mm)	y (mm)	z (mm)
0.28	-0.78	1255.30	-3.02	-0.82	1255.30
0.22	-0.78	1255.30	-3.14	-0.82	1255.30
0.09	-0.79	1255.30	-3.20	-0.81	1255.30
0.03	-0.79	1255.30	-3.32	-0.81	1255.30
-0.09	-0.80	1255.30	-3.38	-0.80	1255.30
-0.15	-0.80	1255.30	-3.50	-0.79	1255.30
-0.28	-0.80	1255.30	-3.55	-0.79	1255.30
-0.34	-0.80	1255.30	-3.68	-0.78	1255.30
-0.46	-0.81	1255.30	-3.73	-0.77	1255.30
-0.53	-0.81	1255.30	-3.86	-0.76	1255.30
-0.65	-0.81	1255.30	-3.90	-0.76	1255.30
-0.72	-0.82	1255.30	-4.04	-0.74	1255.30
-0.83	-0.82	1255.30	-4.07	-0.73	1255.30
-0.90	-0.82	1255.30	-4.22	-0.71	1255.30
-1.02	-0.82	1255.30	-4.23	-0.71	1255.30
-1.09	-0.83	1255.30	-4.39	-0.68	1255.30
-1.20	-0.83	1255.30	-4.40	-0.68	1255.30
-1.28	-0.83	1255.30	-4.57	-0.64	1255.30
-1.39	-0.83	1255.30	-4.72	-0.60	1255.30
-1.47	-0.83	1255.30	-4.87	-0.55	1255.30
-1.57	-0.84	1255.30	-5.01	-0.50	1255.30
-1.65	-0.84	1255.30	-5.40	-0.28	1255.30
-1.75	-0.84	1255.30	-5.60	0.00	1255.30
-1.84	-0.84	1255.30	-5.48	0.32	1255.30
-1.94	-0.84	1255.30	-5.14	0.63	1255.30
-2.03	-0.84	1255.30	-5.01	0.71	1255.30
-2.12	-0.84	1255.30	-4.86	0.79	1255.30
-2.21	-0.84	1255.30	-4.69	0.86	1255.30
-2.30	-0.84	1255.30	-4.54	0.92	1255.30
-2.40	-0.84	1255.30	-4.52	0.92	1255.30
-2.48	-0.84	1255.30	-4.37	0.97	1255.30
-2.58	-0.83	1255.30	-4.34	0.98	1255.30
-2.66	-0.83	1255.30	-4.19	1.02	1255.30
-2.77	-0.83	1255.30	-4.16	1.03	1255.30
-2.84	-0.83	1255.30	-4.01	1.07	1255.30
-2.95	-0.82	1255.30	-3.97	1.08	1255.30

F.4. AERODYNAMIC PROFILE COORDINATES

x (mm)	y (mm)	z (mm)	x (mm)	y (mm)	z (mm)
-3.83	1.11	1255.30	-0.48	1.33	1255.30
-3.79	1.12	1255.30	-0.35	1.32	1255.30
-3.65	1.14	1255.30	-0.29	1.32	1255.30
-3.60	1.15	1255.30	-0.16	1.32	1255.30
-3.47	1.17	1255.30	-0.10	1.32	1255.30
-3.41	1.18	1255.30	0.03	1.31	1255.30
-3.29	1.20	1255.30	0.09	1.31	1255.30
-3.22	1.21	1255.30	0.22	1.31	1255.30
-3.10	1.22	1255.30	0.28	1.30	1255.30
-3.03	1.23	1255.30	0.41	1.30	1255.30
-2.92	1.24	1255.30	0.47	1.30	1255.30
-2.84	1.25	1255.30	0.60	1.29	1255.30
-2.73	1.26	1255.30	0.66	1.29	1255.30
-2.65	1.27	1255.30	0.79	1.28	1255.30
-2.55	1.28	1255.30	0.84	1.28	1255.30
-2.46	1.28	1255.30	0.98	1.27	1255.30
-2.36	1.29	1255.30	1.03	1.27	1255.30
-2.27	1.30	1255.30	1.17	1.26	1255.30
-2.17	1.30	1255.30	1.22	1.26	1255.30
-2.08	1.31	1255.30	1.36	1.25	1255.30
-1.99	1.31	1255.30	1.41	1.25	1255.30
-1.89	1.31	1255.30	1.55	1.24	1255.30
-1.80	1.32	1255.30	1.60	1.24	1255.30
-1.70	1.32	1255.30	1.74	1.23	1255.30
-1.61	1.32	1255.30	1.79	1.23	1255.30
-1.50	1.33	1255.30	1.93	1.22	1255.30
-1.42	1.33	1255.30	1.98	1.21	1255.30
-1.31	1.33	1255.30	2.12	1.20	1255.30
-1.23	1.33	1255.30	2.17	1.20	1255.30
-1.12	1.33	1255.30	2.31	1.19	1255.30
-1.05	1.33	1255.30	2.36	1.19	1255.30
-0.93	1.33	1255.30	2.50	1.17	1255.30
-0.86	1.33	1255.30	2.55	1.17	1255.30
-0.74	1.33	1255.30	2.69	1.16	1255.30
-0.67	1.33	1255.30	2.74	1.16	1255.30
-0.55	1.33	1255.30	2.88	1.14	1255.30

F.4. AERODYNAMIC PROFILE COORDINATES

x (mm)	y (mm)	z (mm)
2.93	1.14	1255.30
3.08	1.13	1255.30
3.11	1.13	1255.30
3.26	1.11	1255.30
3.30	1.11	1255.30
3.45	1.10	1255.30
3.49	1.09	1255.30
3.64	1.08	1255.30
3.68	1.08	1255.30
3.83	1.06	1255.30
3.87	1.06	1255.30
4.02	1.05	1255.30
4.06	1.04	1255.30
4.21	1.03	1255.30
4.25	1.03	1255.30
4.40	1.01	1255.30
4.44	1.01	1255.30
4.59	1.00	1255.30
4.63	0.99	1255.30
4.78	0.98	1255.30
4.81	0.98	1255.30
4.97	0.96	1255.30
5.00	0.96	1255.30
5.16	0.94	1255.30
5.19	0.94	1255.30
5.35	0.93	1255.30
5.38	0.92	1255.30
5.54	0.91	1255.30
5.57	0.90	1255.30
5.73	0.89	1255.30
5.76	0.89	1255.30
5.92	0.87	1255.30
5.95	0.87	1255.30
6.11	0.85	1255.30
6.13	0.85	1255.30
6.30	0.83	1255.30

x (mm)	y (mm)	z (mm)
6.32	0.83	1255.30
6.49	0.81	1255.30
6.51	0.81	1255.30
6.68	0.80	1255.30
6.70	0.79	1255.30
6.87	0.78	1255.30
6.89	0.77	1255.30
7.06	0.76	1255.30
7.07	0.75	1255.30
7.25	0.74	1255.30
7.26	0.74	1255.30
7.44	0.72	1255.30
7.45	0.72	1255.30
7.62	0.70	1255.30
7.64	0.70	1255.30
7.81	0.68	1255.30
7.83	0.68	1255.30
9.35	0.49	1255.30

F.4.23 Section 23

x (mm)	y (mm)	z (mm)
6.46	-0.34	1257.90
5.40	-0.38	1257.90
5.39	-0.38	1257.90
5.27	-0.38	1257.90
5.26	-0.38	1257.90
5.14	-0.38	1257.90
5.12	-0.39	1257.90
5.00	-0.39	1257.90
4.99	-0.39	1257.90
4.87	-0.39	1257.90
4.86	-0.39	1257.90
4.74	-0.39	1257.90
4.73	-0.39	1257.90
4.61	-0.40	1257.90
4.60	-0.40	1257.90

F.4. AERODYNAMIC PROFILE COORDINATES

x (mm)	y (mm)	z (mm)	x (mm)	y (mm)	z (mm)
4.48	-0.40	1257.90	2.13	-0.46	1257.90
4.47	-0.40	1257.90	2.11	-0.47	1257.90
4.35	-0.40	1257.90	2.00	-0.47	1257.90
4.33	-0.40	1257.90	1.98	-0.47	1257.90
4.22	-0.40	1257.90	1.87	-0.47	1257.90
4.20	-0.40	1257.90	1.85	-0.48	1257.90
4.09	-0.41	1257.90	1.74	-0.48	1257.90
4.07	-0.41	1257.90	1.72	-0.48	1257.90
3.96	-0.41	1257.90	1.61	-0.48	1257.90
3.94	-0.41	1257.90	1.59	-0.49	1257.90
3.83	-0.41	1257.90	1.49	-0.49	1257.90
3.81	-0.41	1257.90	1.45	-0.49	1257.90
3.70	-0.42	1257.90	1.36	-0.50	1257.90
3.68	-0.42	1257.90	1.32	-0.50	1257.90
3.57	-0.42	1257.90	1.23	-0.50	1257.90
3.55	-0.42	1257.90	1.19	-0.50	1257.90
3.44	-0.42	1257.90	1.10	-0.51	1257.90
3.42	-0.42	1257.90	1.06	-0.51	1257.90
3.31	-0.43	1257.90	0.97	-0.51	1257.90
3.28	-0.43	1257.90	0.93	-0.51	1257.90
3.18	-0.43	1257.90	0.84	-0.52	1257.90
3.15	-0.43	1257.90	0.80	-0.52	1257.90
3.05	-0.43	1257.90	0.71	-0.52	1257.90
3.02	-0.43	1257.90	0.67	-0.52	1257.90
2.91	-0.44	1257.90	0.58	-0.53	1257.90
2.89	-0.44	1257.90	0.54	-0.53	1257.90
2.78	-0.44	1257.90	0.45	-0.53	1257.90
2.76	-0.44	1257.90	0.41	-0.53	1257.90
2.65	-0.45	1257.90	0.32	-0.54	1257.90
2.63	-0.45	1257.90	0.28	-0.54	1257.90
2.52	-0.45	1257.90	0.19	-0.54	1257.90
2.50	-0.45	1257.90	0.15	-0.54	1257.90
2.39	-0.45	1257.90	0.06	-0.55	1257.90
2.37	-0.46	1257.90	0.02	-0.55	1257.90
2.26	-0.46	1257.90	-0.06	-0.55	1257.90
2.24	-0.46	1257.90	-0.11	-0.55	1257.90

F.4. AERODYNAMIC PROFILE COORDINATES

x (mm)	y (mm)	z (mm)	x (mm)	y (mm)	z (mm)
-0.19	-0.56	1257.90	-2.47	-0.55	1257.90
-0.24	-0.56	1257.90	-2.56	-0.54	1257.90
-0.32	-0.56	1257.90	-2.59	-0.54	1257.90
-0.37	-0.56	1257.90	-2.68	-0.53	1257.90
-0.45	-0.57	1257.90	-2.71	-0.52	1257.90
-0.50	-0.57	1257.90	-2.80	-0.51	1257.90
-0.58	-0.57	1257.90	-2.82	-0.51	1257.90
-0.63	-0.57	1257.90	-2.93	-0.49	1257.90
-0.71	-0.57	1257.90	-2.94	-0.49	1257.90
-0.76	-0.57	1257.90	-3.05	-0.47	1257.90
-0.83	-0.58	1257.90	-3.05	-0.47	1257.90
-0.89	-0.58	1257.90	-3.17	-0.45	1257.90
-0.96	-0.58	1257.90	-3.28	-0.42	1257.90
-1.02	-0.58	1257.90	-3.38	-0.38	1257.90
-1.09	-0.58	1257.90	-3.48	-0.35	1257.90
-1.15	-0.58	1257.90	-3.75	-0.19	1257.90
-1.22	-0.58	1257.90	-3.88	0.00	1257.90
-1.28	-0.58	1257.90	-3.80	0.22	1257.90
-1.34	-0.58	1257.90	-3.57	0.44	1257.90
-1.41	-0.58	1257.90	-3.48	0.49	1257.90
-1.47	-0.58	1257.90	-3.37	0.55	1257.90
-1.54	-0.58	1257.90	-3.26	0.60	1257.90
-1.60	-0.58	1257.90	-3.15	0.64	1257.90
-1.67	-0.58	1257.90	-3.14	0.64	1257.90
-1.72	-0.58	1257.90	-3.03	0.68	1257.90
-1.79	-0.58	1257.90	-3.02	0.68	1257.90
-1.85	-0.58	1257.90	-2.91	0.71	1257.90
-1.92	-0.58	1257.90	-2.89	0.72	1257.90
-1.97	-0.58	1257.90	-2.79	0.74	1257.90
-2.05	-0.57	1257.90	-2.76	0.75	1257.90
-2.10	-0.57	1257.90	-2.66	0.77	1257.90
-2.18	-0.57	1257.90	-2.63	0.78	1257.90
-2.22	-0.56	1257.90	-2.54	0.79	1257.90
-2.30	-0.56	1257.90	-2.50	0.80	1257.90
-2.34	-0.56	1257.90	-2.41	0.82	1257.90
-2.43	-0.55	1257.90	-2.37	0.82	1257.90

F.4. AERODYNAMIC PROFILE COORDINATES

x (mm)	y (mm)	z (mm)	x (mm)	y (mm)	z (mm)
-2.28	0.83	1257.90	0.06	0.91	1257.90
-2.24	0.84	1257.90	0.15	0.91	1257.90
-2.15	0.85	1257.90	0.19	0.91	1257.90
-2.11	0.86	1257.90	0.28	0.90	1257.90
-2.03	0.86	1257.90	0.32	0.90	1257.90
-1.97	0.87	1257.90	0.42	0.90	1257.90
-1.90	0.88	1257.90	0.46	0.90	1257.90
-1.84	0.88	1257.90	0.55	0.89	1257.90
-1.77	0.89	1257.90	0.59	0.89	1257.90
-1.71	0.89	1257.90	0.68	0.88	1257.90
-1.64	0.90	1257.90	0.72	0.88	1257.90
-1.58	0.90	1257.90	0.81	0.88	1257.90
-1.51	0.90	1257.90	0.85	0.88	1257.90
-1.44	0.91	1257.90	0.95	0.87	1257.90
-1.38	0.91	1257.90	0.98	0.87	1257.90
-1.31	0.91	1257.90	1.08	0.86	1257.90
-1.25	0.92	1257.90	1.11	0.86	1257.90
-1.18	0.92	1257.90	1.21	0.85	1257.90
-1.12	0.92	1257.90	1.24	0.85	1257.90
-1.04	0.92	1257.90	1.34	0.84	1257.90
-0.99	0.92	1257.90	1.37	0.84	1257.90
-0.91	0.92	1257.90	1.47	0.84	1257.90
-0.86	0.92	1257.90	1.51	0.83	1257.90
-0.78	0.92	1257.90	1.61	0.83	1257.90
-0.73	0.92	1257.90	1.64	0.82	1257.90
-0.64	0.92	1257.90	1.74	0.82	1257.90
-0.59	0.92	1257.90	1.77	0.81	1257.90
-0.51	0.92	1257.90	1.87	0.81	1257.90
-0.46	0.92	1257.90	1.90	0.80	1257.90
-0.38	0.92	1257.90	2.00	0.80	1257.90
-0.33	0.92	1257.90	2.03	0.79	1257.90
-0.25	0.92	1257.90	2.13	0.79	1257.90
-0.20	0.92	1257.90	2.16	0.78	1257.90
-0.11	0.92	1257.90	2.27	0.77	1257.90
-0.07	0.92	1257.90	2.29	0.77	1257.90
0.02	0.91	1257.90	2.40	0.76	1257.90

F.4. AERODYNAMIC PROFILE COORDINATES

x (mm)	y (mm)	z (mm)
2.42	0.76	1257.90
2.53	0.75	1257.90
2.56	0.75	1257.90
2.66	0.74	1257.90
2.69	0.74	1257.90
2.79	0.73	1257.90
2.82	0.73	1257.90
2.93	0.72	1257.90
2.95	0.71	1257.90
3.06	0.70	1257.90
3.08	0.70	1257.90
3.19	0.69	1257.90
3.21	0.69	1257.90
3.32	0.68	1257.90
3.34	0.68	1257.90
3.45	0.67	1257.90
3.47	0.67	1257.90
3.58	0.66	1257.90
3.60	0.65	1257.90
3.72	0.64	1257.90
3.74	0.64	1257.90
3.85	0.63	1257.90
3.87	0.63	1257.90
3.98	0.62	1257.90
4.00	0.62	1257.90
4.11	0.61	1257.90
4.13	0.60	1257.90
4.24	0.59	1257.90
4.26	0.59	1257.90
4.37	0.58	1257.90
4.39	0.58	1257.90
4.50	0.57	1257.90
4.52	0.57	1257.90
4.64	0.55	1257.90
4.65	0.55	1257.90
4.77	0.54	1257.90

x (mm)	y (mm)	z (mm)
4.78	0.54	1257.90
4.90	0.53	1257.90
4.91	0.53	1257.90
5.03	0.51	1257.90
5.04	0.51	1257.90
5.16	0.50	1257.90
5.17	0.50	1257.90
5.29	0.49	1257.90
5.30	0.48	1257.90
5.42	0.47	1257.90
5.43	0.47	1257.90
6.49	0.34	1257.90

F.4.24 Section 24

x (mm)	y (mm)	z (mm)
3.56	-0.19	1259.50
2.97	-0.21	1259.50
2.97	-0.21	1259.50
2.90	-0.21	1259.50
2.90	-0.21	1259.50
2.83	-0.21	1259.50
2.82	-0.21	1259.50
2.76	-0.21	1259.50
2.75	-0.22	1259.50
2.68	-0.22	1259.50
2.68	-0.22	1259.50
2.61	-0.22	1259.50
2.60	-0.22	1259.50
2.54	-0.22	1259.50
2.53	-0.22	1259.50
2.47	-0.22	1259.50
2.46	-0.22	1259.50
2.40	-0.22	1259.50
2.39	-0.22	1259.50
2.32	-0.22	1259.50
2.32	-0.22	1259.50

F.4. AERODYNAMIC PROFILE COORDINATES

x (mm)	y (mm)	z (mm)	x (mm)	y (mm)	z (mm)
2.25	-0.23	1259.50	0.96	-0.27	1259.50
2.24	-0.23	1259.50	0.95	-0.27	1259.50
2.18	-0.23	1259.50	0.89	-0.27	1259.50
2.17	-0.23	1259.50	0.87	-0.27	1259.50
2.11	-0.23	1259.50	0.82	-0.27	1259.50
2.10	-0.23	1259.50	0.80	-0.27	1259.50
2.04	-0.23	1259.50	0.75	-0.27	1259.50
2.03	-0.23	1259.50	0.73	-0.27	1259.50
1.96	-0.23	1259.50	0.68	-0.28	1259.50
1.95	-0.23	1259.50	0.66	-0.28	1259.50
1.89	-0.23	1259.50	0.60	-0.28	1259.50
1.88	-0.23	1259.50	0.59	-0.28	1259.50
1.82	-0.24	1259.50	0.53	-0.28	1259.50
1.81	-0.24	1259.50	0.51	-0.28	1259.50
1.75	-0.24	1259.50	0.46	-0.29	1259.50
1.74	-0.24	1259.50	0.44	-0.29	1259.50
1.68	-0.24	1259.50	0.39	-0.29	1259.50
1.67	-0.24	1259.50	0.37	-0.29	1259.50
1.61	-0.24	1259.50	0.32	-0.29	1259.50
1.59	-0.24	1259.50	0.30	-0.29	1259.50
1.53	-0.24	1259.50	0.25	-0.29	1259.50
1.52	-0.24	1259.50	0.23	-0.30	1259.50
1.46	-0.25	1259.50	0.18	-0.30	1259.50
1.45	-0.25	1259.50	0.16	-0.30	1259.50
1.39	-0.25	1259.50	0.11	-0.30	1259.50
1.38	-0.25	1259.50	0.08	-0.30	1259.50
1.32	-0.25	1259.50	0.04	-0.30	1259.50
1.30	-0.25	1259.50	0.01	-0.30	1259.50
1.25	-0.25	1259.50	-0.04	-0.31	1259.50
1.23	-0.25	1259.50	-0.06	-0.31	1259.50
1.18	-0.26	1259.50	-0.11	-0.31	1259.50
1.16	-0.26	1259.50	-0.13	-0.31	1259.50
1.10	-0.26	1259.50	-0.18	-0.31	1259.50
1.09	-0.26	1259.50	-0.20	-0.31	1259.50
1.03	-0.26	1259.50	-0.25	-0.31	1259.50
1.02	-0.26	1259.50	-0.27	-0.31	1259.50

F.4. AERODYNAMIC PROFILE COORDINATES

x (mm)	y (mm)	z (mm)	x (mm)	y (mm)	z (mm)
-0.32	-0.31	1259.50	-1.56	-0.28	1259.50
-0.35	-0.31	1259.50	-1.61	-0.27	1259.50
-0.39	-0.32	1259.50	-1.62	-0.27	1259.50
-0.42	-0.32	1259.50	-1.68	-0.26	1259.50
-0.46	-0.32	1259.50	-1.68	-0.26	1259.50
-0.49	-0.32	1259.50	-1.75	-0.25	1259.50
-0.53	-0.32	1259.50	-1.81	-0.23	1259.50
-0.56	-0.32	1259.50	-1.86	-0.21	1259.50
-0.60	-0.32	1259.50	-1.92	-0.19	1259.50
-0.63	-0.32	1259.50	-2.07	-0.11	1259.50
-0.67	-0.32	1259.50	-2.14	0.00	1259.50
-0.70	-0.32	1259.50	-2.10	0.12	1259.50
-0.74	-0.32	1259.50	-1.97	0.24	1259.50
-0.77	-0.32	1259.50	-1.91	0.27	1259.50
-0.81	-0.32	1259.50	-1.86	0.30	1259.50
-0.85	-0.32	1259.50	-1.79	0.33	1259.50
-0.88	-0.32	1259.50	-1.74	0.35	1259.50
-0.92	-0.32	1259.50	-1.73	0.35	1259.50
-0.95	-0.32	1259.50	-1.67	0.37	1259.50
-0.99	-0.32	1259.50	-1.66	0.38	1259.50
-1.02	-0.32	1259.50	-1.60	0.39	1259.50
-1.06	-0.32	1259.50	-1.59	0.40	1259.50
-1.09	-0.32	1259.50	-1.53	0.41	1259.50
-1.13	-0.32	1259.50	-1.52	0.41	1259.50
-1.16	-0.31	1259.50	-1.47	0.42	1259.50
-1.20	-0.31	1259.50	-1.45	0.43	1259.50
-1.22	-0.31	1259.50	-1.40	0.44	1259.50
-1.27	-0.31	1259.50	-1.38	0.44	1259.50
-1.29	-0.31	1259.50	-1.33	0.45	1259.50
-1.34	-0.30	1259.50	-1.30	0.45	1259.50
-1.36	-0.30	1259.50	-1.26	0.46	1259.50
-1.41	-0.30	1259.50	-1.23	0.46	1259.50
-1.43	-0.30	1259.50	-1.19	0.47	1259.50
-1.48	-0.29	1259.50	-1.16	0.47	1259.50
-1.49	-0.29	1259.50	-1.12	0.48	1259.50
-1.54	-0.28	1259.50	-1.09	0.48	1259.50

F.4. AERODYNAMIC PROFILE COORDINATES

x (mm)	y (mm)	z (mm)	x (mm)	y (mm)	z (mm)
-1.05	0.48	1259.50	0.25	0.49	1259.50
-1.01	0.49	1259.50	0.30	0.49	1259.50
-0.97	0.49	1259.50	0.32	0.49	1259.50
-0.94	0.49	1259.50	0.38	0.49	1259.50
-0.90	0.49	1259.50	0.40	0.49	1259.50
-0.87	0.50	1259.50	0.45	0.48	1259.50
-0.83	0.50	1259.50	0.47	0.48	1259.50
-0.79	0.50	1259.50	0.52	0.48	1259.50
-0.76	0.50	1259.50	0.54	0.48	1259.50
-0.72	0.50	1259.50	0.59	0.48	1259.50
-0.69	0.50	1259.50	0.61	0.47	1259.50
-0.65	0.51	1259.50	0.67	0.47	1259.50
-0.62	0.51	1259.50	0.68	0.47	1259.50
-0.58	0.51	1259.50	0.74	0.47	1259.50
-0.54	0.51	1259.50	0.76	0.46	1259.50
-0.50	0.51	1259.50	0.81	0.46	1259.50
-0.47	0.51	1259.50	0.83	0.46	1259.50
-0.43	0.51	1259.50	0.89	0.46	1259.50
-0.40	0.51	1259.50	0.90	0.45	1259.50
-0.36	0.51	1259.50	0.96	0.45	1259.50
-0.33	0.51	1259.50	0.97	0.45	1259.50
-0.28	0.51	1259.50	1.03	0.44	1259.50
-0.26	0.51	1259.50	1.05	0.44	1259.50
-0.21	0.51	1259.50	1.10	0.44	1259.50
-0.18	0.51	1259.50	1.12	0.44	1259.50
-0.14	0.51	1259.50	1.18	0.43	1259.50
-0.11	0.51	1259.50	1.19	0.43	1259.50
-0.06	0.51	1259.50	1.25	0.43	1259.50
-0.04	0.50	1259.50	1.26	0.43	1259.50
0.01	0.50	1259.50	1.32	0.42	1259.50
0.03	0.50	1259.50	1.34	0.42	1259.50
0.08	0.50	1259.50	1.39	0.41	1259.50
0.11	0.50	1259.50	1.41	0.41	1259.50
0.16	0.50	1259.50	1.47	0.41	1259.50
0.18	0.50	1259.50	1.48	0.41	1259.50
0.23	0.49	1259.50	1.54	0.40	1259.50

F.4. AERODYNAMIC PROFILE COORDINATES

x (mm)	y (mm)	z (mm)
1.55	0.40	1259.50
1.61	0.40	1259.50
1.62	0.39	1259.50
1.68	0.39	1259.50
1.70	0.39	1259.50
1.76	0.38	1259.50
1.77	0.38	1259.50
1.83	0.38	1259.50
1.84	0.37	1259.50
1.90	0.37	1259.50
1.91	0.37	1259.50
1.97	0.36	1259.50
1.99	0.36	1259.50
2.05	0.36	1259.50
2.06	0.35	1259.50
2.12	0.35	1259.50
2.13	0.35	1259.50
2.19	0.34	1259.50
2.20	0.34	1259.50
2.26	0.33	1259.50
2.27	0.33	1259.50
2.34	0.33	1259.50
2.35	0.33	1259.50
2.41	0.32	1259.50
2.42	0.32	1259.50
2.48	0.31	1259.50
2.49	0.31	1259.50
2.55	0.31	1259.50
2.56	0.30	1259.50
2.63	0.30	1259.50
2.63	0.30	1259.50
2.70	0.29	1259.50
2.71	0.29	1259.50
2.77	0.28	1259.50
2.78	0.28	1259.50
2.84	0.28	1259.50

x (mm)	y (mm)	z (mm)
2.85	0.28	1259.50
2.92	0.27	1259.50
2.92	0.27	1259.50
2.99	0.26	1259.50
2.99	0.26	1259.50
3.57	0.19	1259.50

F.4.25 Section 25

x (mm)	y (mm)	z (mm)
0.63	-0.03	1260.00
0.53	-0.04	1260.00
0.52	-0.04	1260.00
0.51	-0.04	1260.00
0.51	-0.04	1260.00
0.50	-0.04	1260.00
0.50	-0.04	1260.00
0.49	-0.04	1260.00
0.49	-0.04	1260.00
0.47	-0.04	1260.00
0.47	-0.04	1260.00
0.46	-0.04	1260.00
0.46	-0.04	1260.00
0.45	-0.04	1260.00
0.45	-0.04	1260.00
0.44	-0.04	1260.00
0.43	-0.04	1260.00
0.42	-0.04	1260.00
0.42	-0.04	1260.00
0.41	-0.04	1260.00
0.41	-0.04	1260.00
0.40	-0.04	1260.00
0.40	-0.04	1260.00
0.39	-0.04	1260.00
0.38	-0.04	1260.00
0.37	-0.04	1260.00

F.4. AERODYNAMIC PROFILE COORDINATES

x (mm)	y (mm)	z (mm)	x (mm)	y (mm)	z (mm)
0.37	-0.04	1260.00	0.14	-0.05	1260.00
0.36	-0.04	1260.00	0.13	-0.05	1260.00
0.36	-0.04	1260.00	0.13	-0.05	1260.00
0.35	-0.04	1260.00	0.12	-0.05	1260.00
0.35	-0.04	1260.00	0.12	-0.05	1260.00
0.33	-0.04	1260.00	0.11	-0.05	1260.00
0.33	-0.04	1260.00	0.10	-0.05	1260.00
0.32	-0.04	1260.00	0.09	-0.05	1260.00
0.32	-0.04	1260.00	0.09	-0.05	1260.00
0.31	-0.04	1260.00	0.08	-0.05	1260.00
0.31	-0.04	1260.00	0.08	-0.05	1260.00
0.30	-0.04	1260.00	0.07	-0.05	1260.00
0.29	-0.04	1260.00	0.07	-0.05	1260.00
0.28	-0.04	1260.00	0.06	-0.05	1260.00
0.28	-0.04	1260.00	0.05	-0.05	1260.00
0.27	-0.04	1260.00	0.04	-0.05	1260.00
0.27	-0.04	1260.00	0.04	-0.05	1260.00
0.26	-0.04	1260.00	0.03	-0.05	1260.00
0.26	-0.04	1260.00	0.03	-0.05	1260.00
0.25	-0.04	1260.00	0.02	-0.05	1260.00
0.24	-0.04	1260.00	0.01	-0.05	1260.00
0.23	-0.04	1260.00	0.01	-0.05	1260.00
0.23	-0.04	1260.00	0.00	-0.05	1260.00
0.22	-0.05	1260.00	-0.01	-0.05	1260.00
0.22	-0.05	1260.00	-0.01	-0.05	1260.00
0.21	-0.05	1260.00	-0.02	-0.05	1260.00
0.21	-0.05	1260.00	-0.02	-0.05	1260.00
0.19	-0.05	1260.00	-0.03	-0.05	1260.00
0.19	-0.05	1260.00	-0.04	-0.05	1260.00
0.18	-0.05	1260.00	-0.04	-0.06	1260.00
0.18	-0.05	1260.00	-0.05	-0.06	1260.00
0.17	-0.05	1260.00	-0.06	-0.06	1260.00
0.17	-0.05	1260.00	-0.06	-0.06	1260.00
0.16	-0.05	1260.00	-0.07	-0.06	1260.00
0.15	-0.05	1260.00	-0.07	-0.06	1260.00
0.14	-0.05	1260.00	-0.08	-0.06	1260.00

F.4. AERODYNAMIC PROFILE COORDINATES

x (mm)	y (mm)	z (mm)	x (mm)	y (mm)	z (mm)
-0.09	-0.06	1260.00	-0.31	-0.04	1260.00
-0.09	-0.06	1260.00	-0.32	-0.04	1260.00
-0.10	-0.06	1260.00	-0.33	-0.04	1260.00
-0.11	-0.06	1260.00	-0.34	-0.03	1260.00
-0.11	-0.06	1260.00	-0.37	-0.02	1260.00
-0.12	-0.06	1260.00	-0.38	0.00	1260.00
-0.12	-0.06	1260.00	-0.37	0.02	1260.00
-0.13	-0.06	1260.00	-0.35	0.04	1260.00
-0.14	-0.06	1260.00	-0.34	0.05	1260.00
-0.14	-0.06	1260.00	-0.33	0.05	1260.00
-0.15	-0.06	1260.00	-0.32	0.06	1260.00
-0.16	-0.06	1260.00	-0.31	0.06	1260.00
-0.16	-0.06	1260.00	-0.31	0.06	1260.00
-0.17	-0.06	1260.00	-0.29	0.07	1260.00
-0.17	-0.06	1260.00	-0.29	0.07	1260.00
-0.18	-0.06	1260.00	-0.28	0.07	1260.00
-0.19	-0.06	1260.00	-0.28	0.07	1260.00
-0.19	-0.06	1260.00	-0.27	0.07	1260.00
-0.20	-0.06	1260.00	-0.27	0.07	1260.00
-0.20	-0.06	1260.00	-0.26	0.08	1260.00
-0.21	-0.06	1260.00	-0.26	0.08	1260.00
-0.22	-0.05	1260.00	-0.25	0.08	1260.00
-0.22	-0.05	1260.00	-0.24	0.08	1260.00
-0.23	-0.05	1260.00	-0.23	0.08	1260.00
-0.24	-0.05	1260.00	-0.23	0.08	1260.00
-0.24	-0.05	1260.00	-0.22	0.08	1260.00
-0.25	-0.05	1260.00	-0.22	0.08	1260.00
-0.25	-0.05	1260.00	-0.21	0.08	1260.00
-0.26	-0.05	1260.00	-0.20	0.08	1260.00
-0.26	-0.05	1260.00	-0.20	0.08	1260.00
-0.27	-0.05	1260.00	-0.19	0.08	1260.00
-0.27	-0.05	1260.00	-0.18	0.09	1260.00
-0.28	-0.05	1260.00	-0.18	0.09	1260.00
-0.29	-0.05	1260.00	-0.17	0.09	1260.00
-0.30	-0.05	1260.00	-0.17	0.09	1260.00
-0.30	-0.05	1260.00	-0.16	0.09	1260.00

F.4. AERODYNAMIC PROFILE COORDINATES

x (mm)	y (mm)	z (mm)
-0.15	0.09	1260.00
-0.15	0.09	1260.00
-0.14	0.09	1260.00
-0.13	0.09	1260.00
-0.13	0.09	1260.00
-0.12	0.09	1260.00
-0.11	0.09	1260.00
-0.11	0.09	1260.00
-0.10	0.09	1260.00
-0.10	0.09	1260.00
-0.09	0.09	1260.00
-0.08	0.09	1260.00
-0.08	0.09	1260.00
-0.07	0.09	1260.00
-0.06	0.09	1260.00
-0.06	0.09	1260.00
-0.05	0.09	1260.00
-0.05	0.09	1260.00
-0.04	0.09	1260.00
-0.03	0.09	1260.00
-0.02	0.09	1260.00
-0.02	0.09	1260.00
-0.01	0.09	1260.00
-0.01	0.09	1260.00
0.00	0.09	1260.00
0.01	0.09	1260.00
0.01	0.09	1260.00
0.02	0.09	1260.00
0.03	0.09	1260.00
0.03	0.09	1260.00
0.04	0.09	1260.00
0.04	0.09	1260.00
0.05	0.09	1260.00
0.06	0.09	1260.00
0.07	0.09	1260.00
0.07	0.09	1260.00

x (mm)	y (mm)	z (mm)
0.08	0.09	1260.00
0.08	0.09	1260.00
0.09	0.08	1260.00
0.10	0.08	1260.00
0.10	0.08	1260.00
0.11	0.08	1260.00
0.12	0.08	1260.00
0.12	0.08	1260.00
0.13	0.08	1260.00
0.13	0.08	1260.00
0.14	0.08	1260.00
0.15	0.08	1260.00
0.16	0.08	1260.00
0.16	0.08	1260.00
0.17	0.08	1260.00
0.17	0.08	1260.00
0.18	0.08	1260.00
0.18	0.08	1260.00
0.19	0.08	1260.00
0.20	0.08	1260.00
0.21	0.08	1260.00
0.21	0.08	1260.00
0.22	0.08	1260.00
0.22	0.08	1260.00
0.23	0.07	1260.00
0.24	0.07	1260.00
0.25	0.07	1260.00
0.25	0.07	1260.00
0.26	0.07	1260.00
0.26	0.07	1260.00
0.27	0.07	1260.00
0.27	0.07	1260.00
0.28	0.07	1260.00
0.29	0.07	1260.00
0.30	0.07	1260.00
0.30	0.07	1260.00

F.4. AERODYNAMIC PROFILE COORDINATES

x (mm)	y (mm)	z (mm)
0.31	0.07	1260.00
0.31	0.07	1260.00
0.32	0.07	1260.00
0.33	0.07	1260.00
0.34	0.07	1260.00
0.34	0.07	1260.00
0.35	0.06	1260.00
0.35	0.06	1260.00
0.36	0.06	1260.00
0.36	0.06	1260.00
0.37	0.06	1260.00
0.38	0.06	1260.00
0.39	0.06	1260.00
0.39	0.06	1260.00
0.40	0.06	1260.00
0.40	0.06	1260.00
0.41	0.06	1260.00
0.41	0.06	1260.00
0.43	0.06	1260.00
0.43	0.06	1260.00
0.44	0.06	1260.00
0.44	0.06	1260.00
0.45	0.05	1260.00
0.45	0.05	1260.00
0.46	0.05	1260.00
0.47	0.05	1260.00
0.48	0.05	1260.00
0.48	0.05	1260.00
0.49	0.05	1260.00
0.49	0.05	1260.00
0.50	0.05	1260.00
0.50	0.05	1260.00
0.52	0.05	1260.00
0.52	0.05	1260.00
0.53	0.05	1260.00
0.53	0.05	1260.00

x (mm)	y (mm)	z (mm)
0.63	0.03	1260.00

Appendix G

Additional information for the experiments with the model wind turbine

G.1 Iterative procedure for applying the BEM Method

The calculation steps are taken from Hansen (2000) and presented in a summarized way.

1. Initialize a and a' to 0.

a is the axial induction factor and a' is the tangential induction factor.

2. Compute the flow angle φ , which is the angle between the rotor plane and the relative wind speed using Equation G.1.

$$\varphi = \arctan\left(\frac{(1-a)V_0}{(1+a')\omega r}\right) \quad (\text{G.1})$$

where V_0 is the incoming wind, ω is the angular velocity of the rotor and r is the distance from the rotor centre.

3. Compute the local angle of attack using Equation G.2.

$$\alpha = \varphi - \text{pitch} - \theta \quad (\text{G.2})$$

where θ is the local twist.

4. Compute Prandtl's tip and hub loss factor using Equations G.3 through G.7.

$$f_{tip} = \frac{B_n (R-r)}{2 r \sin \varphi} \quad (\text{G.3})$$

where B_n is the number of blades, R is the radius of the wind turbine and R_{hub} is the radius of the hub.

$$f_{hub} = \frac{B_n (r-R_{hub})}{2 R_{hub} \sin \varphi} \quad (\text{G.4})$$

$$F_{tip} = \frac{2}{\pi} \arccos(e^{-f_{tip}}) \quad (\text{G.5})$$

$$F_{hub} = \frac{2}{\pi} \arccos(e^{-f_{hub}}) \quad (\text{G.6})$$

$$F = F_{tip} \times F_{hub} \quad (\text{G.7})$$

5. Get $C_L(\alpha)$ and $C_D(\alpha)$ from a table. C_L is the lift coefficient and C_D is the drag coefficient of the aerodynamic profile of the blade.

G.1. ITERATIVE PROCEDURE FOR APPLYING THE BEM METHOD

6. Calculate C_n and C_t using Equations G.8 and G.9. C_n is the normal load coefficient and C_t is the tangential load coefficient.

$$C_n = C_L \cos \varphi + C_D \sin \varphi \quad (\text{G.8})$$

$$C_t = C_L \sin \varphi - C_D \cos \varphi \quad (\text{G.9})$$

7. Calculate σ , the solidity, that is, the fraction of annular area in the control volume covered by the blades using Equation G.10.

$$\sigma(r) = \frac{c(r)B_n}{2\pi r} \quad (\text{G.10})$$

where $c(r)$ is the local chord.

8. Calculate new a and a' using Equation G.11 and Equation G.12.

$$a = \frac{1}{4F \sin^2 \varphi / (\sigma C_n) + 1} \quad (\text{G.11})$$

$$a' = \frac{1}{4F \sin \varphi \cos \varphi / (\sigma C_t) - 1} \quad (\text{G.12})$$

9. Apply Glauert correction if $a > a_c$, where $a_c \approx 0.2$.

Using Equation G.26, a new value is calculated for a , when $a > a_c$ (Equation G.13):

$$a = \frac{1}{2} [2 + K(1 - 2a_c) - \sqrt{(K(1 - 2a_c) + 2)^2 + 4(Ka_c^2 - 1)}] \quad (\text{G.13})$$

where $K = \frac{4F \sin^2 \varphi}{\sigma C_n}$

10. Calculate $\varepsilon_a = |a_{new} - a|$ and $\varepsilon_{a'} = |a'_{new} - a'|$

11. Test $\varepsilon_a < 0.001$ and $\varepsilon_{a'} < 0.001$

12. Recalculate from step 2 for sections where it is needed

13. Once $\varepsilon_a < 0.001$ and $\varepsilon_{a'} < 0.001$ for all blade sections, calculate the relative wind speed (Equation G.14):

$$V_{rel} = \sqrt{(V_0(1 - a))^2 + (\omega r(1 + a'))^2} \quad (\text{G.14})$$

Then, calculate local tangential and normal forces (Equation G.15 and Equation G.16) per unit length:

$$F_n = \frac{1}{2} \rho V_{rel}^2 \times C_n \times c \quad (\text{G.15})$$

$$F_t = \frac{1}{2} \rho V_{rel}^2 \times C_t \times c \quad (\text{G.16})$$

Thanks to the above, calculate local component of Thrust and Torque (Equations G.17 and G.18):

$$dT = BF_n dr \quad (\text{G.17})$$

$$dM = rBF_i dr \quad (G.18)$$

To calculate the total torque, Equation G.19 needs to be used:

$$M_{TOT} = B \sum_1^{N-1} M_{i,i+1} \quad (G.19)$$

with

$$M_{i,i+1} = \frac{1}{3}A_i(r_{i+1}^3 - r_i^3) + \frac{1}{2}B_i(r_{i+1}^2 - r_i^2) \quad (G.20)$$

where

$$A_i = \frac{F_{T,i+1} - F_{T,i}}{r_{i+1} - r_i} \quad (G.21)$$

$$B_i = \frac{F_{T,i}r_{i+1} - F_{T,i+1}r_i}{r_{i+1} - r_i} \quad (G.22)$$

G.2 Various suggestions for Glauert correction found in literature

Glauert correction

- Found in Ozkan (2013):

$$a = \frac{0.5(18\sigma C_n + 36F^2 \sin^2 \varphi - 40F \sin^2 \varphi \pm 6(18F \sin^2 \varphi \sigma C_n + 36F^4 \sin^4 \varphi - 48F^3 \sin^4 \varphi)^{0.5})}{9\sigma C_n - 50F \sin^2 \varphi + 36F^2 \sin^2 \varphi} \quad (G.23)$$

for $a \geq 0.4$

- Found in Liao et al. (2019)

For $C_T \geq 0.96F$

$$a' = \frac{1 - k_1 + \sqrt{k_1^2 - 4k_2(k_0 - C_T)}}{2k_2} \quad (G.24)$$

with $k_2 = \frac{1}{0.18} - 4F$

$k_1 = -(\frac{0.8}{0.18} - 4F)$

$k_0 = \frac{0.16}{0.18}$

- Hansen and Sommers (2002) proposes two different formulas for C_T (Equation G.25 and Equation G.26)

$$C_T = \begin{cases} 4a(1-a)F & a \leq \frac{1}{3} \\ 4a(1 - \frac{1}{4}(5-3a)a)F & a > \frac{1}{3} \end{cases} \quad (G.25)$$

$$C_T = \begin{cases} 4a(1-a)F & a \leq a_c \\ 4(a_c^2 + (1-2a_c)a)F & a > a_c \end{cases} \quad (G.26)$$

with $a_c \approx 0.2$

G.2. VARIOUS SUGGESTIONS FOR GLAUERT CORRECTION FOUND IN LITERATURE

Using Equation G.26, a new value is calculated for a , when $a > a_c$ (Equation G.27):

$$a = \frac{1}{2} [2 + K(1 - 2a_c) - \sqrt{(K(1 - 2a_c) + 2)^2 + 4(Ka_c^2 - 1)}] \quad (\text{G.27})$$

where $K = \frac{4F \sin^2 \varphi}{\sigma C_N}$

G.3 Lift and Drag coefficients used in the BEM method

angle of attack (°)	Lift coefficient
-180.33	0.037
-178.60	0.136
-177.21	0.218
-175.48	0.305
-174.09	0.348
-167.52	0.436
-158.17	0.432
-150.03	0.465
-138.95	0.482
-129.91	0.459
-122.15	0.409
-115.52	0.347
-109.55	0.277
-104.56	0.214
-99.44	0.139
-94.31	0.062
-88.22	-0.030
-81.99	-0.122
-77.48	-0.190
-71.74	-0.262
-65.36	-0.337
-57.98	-0.406
-50.40	-0.444
-41.59	-0.462
-31.84	-0.444
-23.81	-0.411
-16.37	-0.413
-9.27	-0.425
-4.42	-0.302
-3.38	-0.192
-1.65	-0.079
-0.61	0.188
-0.26	0.311
-0.26	0.243

angle of attack (°)	Lift coefficient
1.12	0.447
1.81	0.521
5.62	0.632
5.05	0.696
5.97	0.805
13.93	0.604
25.98	0.632
33.44	0.671
48.04	0.665
54.10	0.623
60.10	0.557
65.67	0.476
70.03	0.409
73.84	0.335
77.99	0.255
81.46	0.182
84.75	0.110
88.15	0.038
91.15	-0.017
96.69	-0.101
102.09	-0.177
107.77	-0.252
115.05	-0.337
120.24	-0.388
132.01	-0.450
140.09	-0.462
170.45	-0.397
173.22	-0.323
175.30	-0.240
176.68	-0.166
178.07	-0.094
179.45	-0.025

Table G.1: Lift coefficient of modified Drela AG04 profile (taken from Kimball et al. (2014))

G.3. LIFT AND DRAG COEFFICIENTS USED IN THE BEM METHOD

angle of attack (°)	Drag coefficient
-175.90	0.063
-166.94	0.121
-160.82	0.190
-156.43	0.260
-152.28	0.327
-148.47	0.396
-145.01	0.464
-141.54	0.536
-138.08	0.609
-134.62	0.682
-131.16	0.753
-127.69	0.826
-124.23	0.896
-120.42	0.966
-115.92	1.041
-111.19	1.111
-104.26	1.187
-97.22	1.230
-88.02	1.242
-80.60	1.210
-73.10	1.143
-68.13	1.076
-63.63	1.005
-59.82	0.939
-56.36	0.871
-52.90	0.800
-49.44	0.728
-45.97	0.656
-42.51	0.584
-39.05	0.511
-35.58	0.440
-32.12	0.373
-28.31	0.307
-24.16	0.239
-18.96	0.170

angle of attack (°)	Drag coefficient
-12.18	0.100
-4.57	0.047
3.11	0.053
19.40	0.192
23.63	0.258
27.44	0.321
31.59	0.399
35.06	0.464
38.69	0.535
41.98	0.606
45.10	0.671
48.91	0.751
52.72	0.829
56.53	0.906
61.03	0.983
65.18	1.049
69.88	1.120
76.91	1.194
85.34	1.238
93.51	1.238
101.97	1.194
108.12	1.132
113.31	1.059
117.82	0.987
121.62	0.918
125.09	0.850
128.55	0.777
132.01	0.705
135.48	0.633
138.94	0.561
142.40	0.489
145.86	0.419
149.67	0.348
153.83	0.278
158.10	0.209
164.17	0.132

G.3. LIFT AND DRAG COEFFICIENTS USED IN THE BEM METHOD

angle of attack (°)	Drag coefficient
170.40	0.082
178.41	0.052

Table G.2: Drag coefficient of modified Drela AG04 profile (taken from Kimball et al. (2014))

G.4 Design and manufacture of the blades

G.4.1 CFD calculation of aerodynamic loads

In order to have access not only to global loads on the turbine blade, but also to localised loads, a CFD simulation in Ansys was done on the model wind turbine blade for rated conditions (highest thrust). The results of this CFD simulation could then be directly imported into the FEA analysis, which was done in Ansys.

For this CFD simulation, a cylindrical domain was used. The cylinder was 10 m high and the diameter was 10 m. A single blade was placed inside, not the rest of the rotor, not the hub or the tower. The centre of the rotor was at the centre of the cylinder and the blade was placed in the corresponding position with the correct pitch for rated conditions (see Figure G.1).

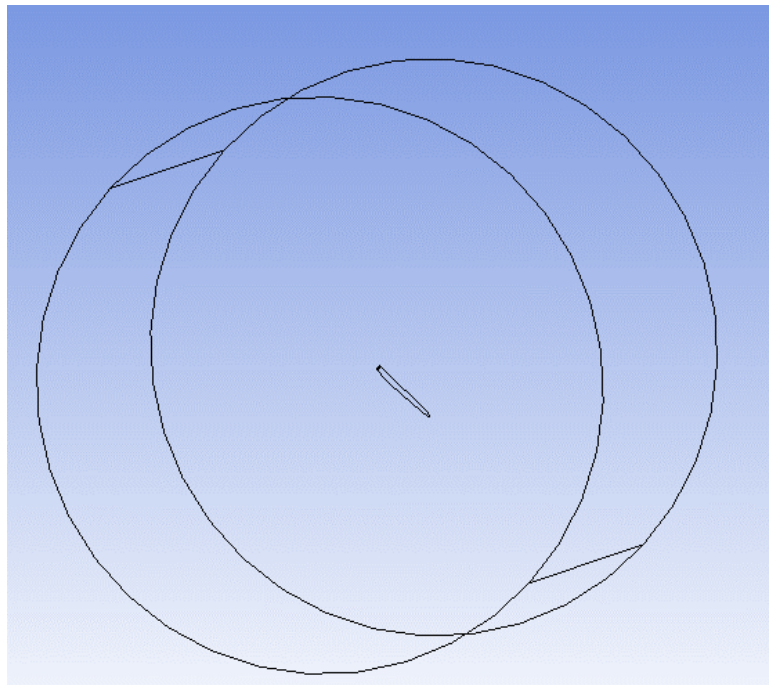


Figure G.1: CFD domain for aerodynamic loads on the model wind turbine blade

One side of the cylinder was the inlet, the opposite side was the outlet. The sides of the cylinder were considered to be walls. The blade itself was considered to be a moving wall, rotating at rated rotor speed for the model, that is 85.6 rpm. The turbulence model chosen for this simulation was k-epsilon. At the inlet, air is coming in at a speed of 1.61 m/s (scaled down rated wind speed).

G.4. DESIGN AND MANUFACTURE OF THE BLADES

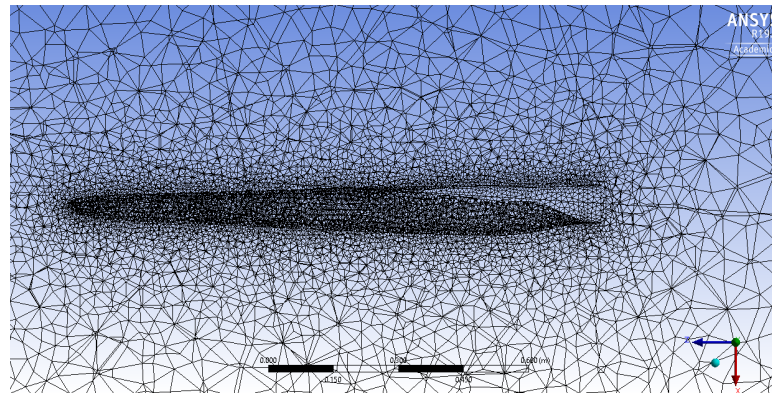


Figure G.2: Mesh around blade

Figure G.2 shows the mesh around the blade. The elements closest to the blade were 4 mm wide. The elements furthest away from the blade were at a maximum size of 1.7 m. The total number of elements was 190,903. No layers were used. This simulation gave the following pressure distribution on the blade (Figure G.3 and Figure G.4).

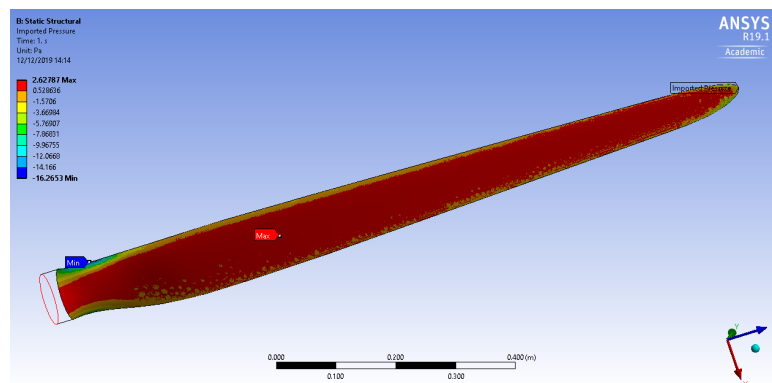


Figure G.3: Pressure distribution on pressure side of the blade

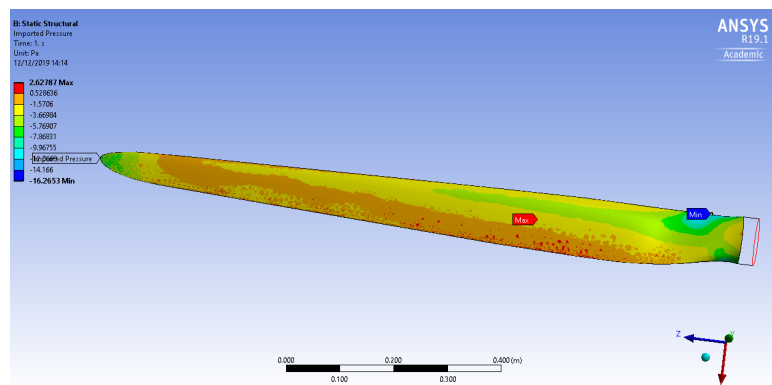


Figure G.4: Pressure distribution on suction side of the blade

The maximum pressure was 2.63 Pa and situated at about one third of the blade length

from the root of the blade. The minimum pressure (suction) was close to the root and was -16.27 Pa.

G.4.2 Finite Element (FE) Analysis of the wind turbine blade

The FE Analysis was done to determine the minimum material thickness and properties necessary for the blade to withstand the various forces it is exposed to (aerodynamic loads, gravity, centrifugal forces). Various simplifications of those forces were done. The first calculation corresponded to a simple load test (so not corresponding to conditions where the turbine is spinning). A load was applied to the tip of the blade to create a flapwise bending moment. There are two reasons to look at the flapwise bending moment only. The first one is that the deflection is expected to be greatest in this direction. The second one is that the main effect of aerodynamic loads is flapwise bending. This reasoning was taken from Martin et al. (2012). This thesis also cites a source for flapwise bending moment in extreme conditions. In Jonkman (2007), a simulation for the NREL 5 MW reference wind turbine on the floating ITI Energy barge was done which resulted in a flapwise bending moment of 34,000 kNm at full scale. At scale 1:50, in Froude scaling, this results in a bending moment of 5.44 Nm. Given the length of the blade, this equates to applying a load of 4.42 N at the tip of the blade.

The mesh of the blade in this simulation was made up of 276198 elements with an average size of 1 mm. The material used in the simulation was a material contained in the Ansys library of materials. It was called Epoxy Carbon Woven (230 GPa) PrePreg. Its properties can be seen in Appendix G.4.3. The ply is formed of two layers of this material, assumed to have a thickness of 0.253 mm. The layers were stacked with the angles 0 degree and 90 degree. The 0 degree angle corresponds to a direction parallel to the blade root section, perpendicular to the span of the blade, whereas the 90 degree angle goes in the direction of the span of the blade.

Applying the 4.42 N at the tip of the blade resulted in a deflection of the blade of 19 mm (see Figure G.5). At full size, this would correspond to 900 mm. This is a very reasonable deflection. For the full size wind turbine, the tip deflection was calculated to be up to 13.9 m in a fully coupled simulation of the NREL 5 MW wind turbine on the ITI Energy barge under sea state conditions (Jonkman (2007)).

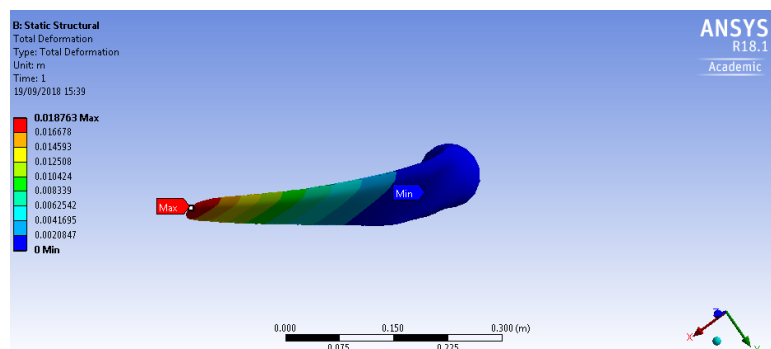


Figure G.5: Blade deflection when applying a tip load (4.42 N) which gives an extreme flapwise bending moment (5.44 Nm) obtained in extreme sea conditions

G.4. DESIGN AND MANUFACTURE OF THE BLADES

The maximum stress was determined to be about 51.6 MPa (see Figure G.6). It is situated rather close to the root of the blade. This is 10 times smaller than the stress limit of the material.

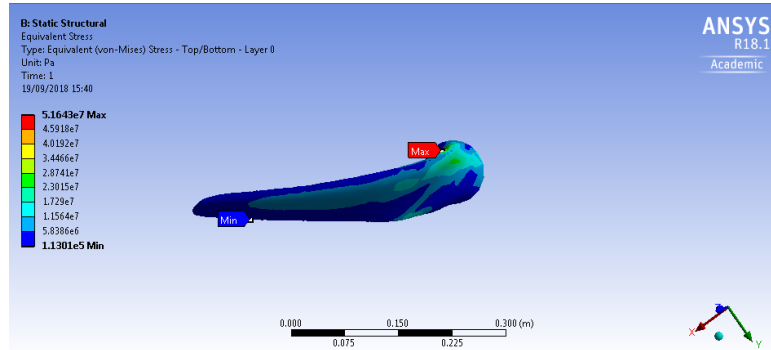


Figure G.6: Stress distribution on blade when applying load at tip of the blade (4.42 N) giving a bending moment near the root of 5.44 Nm, which correspond to extreme load obtained in simulation of extreme sea conditions.

Using the results of the CFD calculations done in Ansys, FEA calculations were done to observe the behaviour of the blade in conditions at rated wind speed. The same mesh and stack up as for the previous calculation was used. However, the material used was slightly different, though with similar properties (see Appendix G.4.3). A material that was going to be used was identified, so its properties were used to create a new material in Ansys. The material is called XPReg XC110. This resulted in a deflection of 0.46 mm (see Figure G.7)

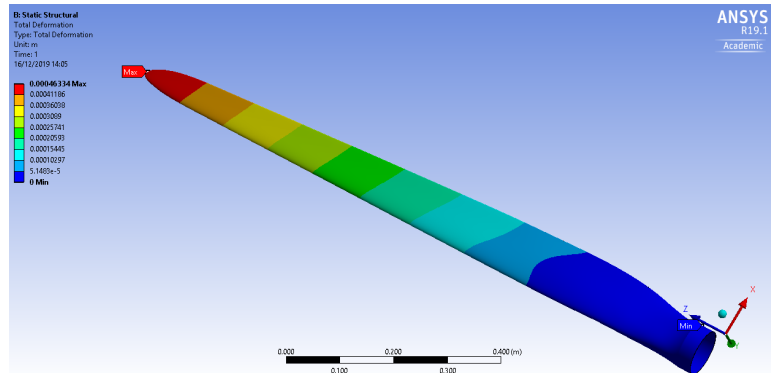


Figure G.7: Deflection of blade at rated wind speed conditions (determined through CFD calculation in Ansys)

The maximum stress determined was 1.9 MPa, which was well below the stress limit of the material. It was situated near the root of the blade (see Figure G.8).

G.4. DESIGN AND MANUFACTURE OF THE BLADES

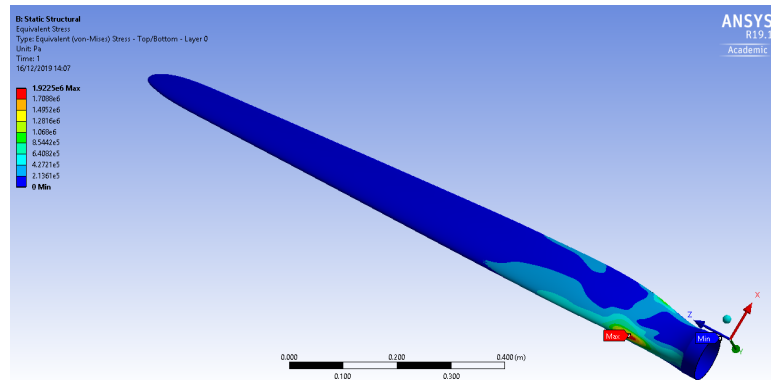


Figure G.8: Maximum stress under rated wind speed conditions determined through CFD in Ansys

G.4.3 Properties of material used in FEA calculation

Properties of Outline Row 7: XPReg XC110				
	A	B	C	D E
1	Property	Value	Unit	
2	Density	1448	kg m ⁻³	
3	Orthotropic Secant Coefficient of Thermal Expansion			
8	Orthotropic Elasticity			
9	Young's Modulus X direction	5.51E+10	Pa	
10	Young's Modulus Y direction	5.51E+10	Pa	
11	Young's Modulus Z direction	7.5E+09	Pa	
12	Poisson's Ratio XY	0.04		
13	Poisson's Ratio YZ	0.3		
14	Poisson's Ratio XZ	0.3		
15	Shear Modulus XY	1.75E+10	Pa	
16	Shear Modulus YZ	2.7E+09	Pa	
17	Shear Modulus XZ	2.7E+09	Pa	
18	Orthotropic Stress Limits			
19	Tensile X direction	5.21E+08	Pa	
20	Tensile Y direction	5.21E+08	Pa	
21	Tensile Z direction	5E+07	Pa	
22	Compressive X direction	-4.83E+08	Pa	
23	Compressive Y direction	-4.83E+08	Pa	
24	Compressive Z direction	-1.5E+08	Pa	
25	Shear XY	1.2E+08	Pa	
26	Shear YZ	6.47E+07	Pa	
27	Shear XZ	6.47E+07	Pa	
28	Orthotropic Strain Limits			
29	Tensile X direction	0.0092		
30	Tensile Y direction	0.0092		
31	Tensile Z direction	0.0078		
32	Compressive X direction	-0.0084		
33	Compressive Y direction	-0.0084		
34	Compressive Z direction	-0.011		
35	Shear XY	0.02		
36	Shear YZ	0.015		
37	Shear XZ	0.015		

Figure G.9: Properties of Epoxy Carbon Woven (230 GPa) PrePreg

G.5. LIST OF MEASUREMENTS DONE WITH THE MODEL WIND TURBINE

Property	Test Standard	Units	Result
Compressive strength	BS EN ISO 14126 : 1999	MPa	483
Tensile strength	BS EN ISO 527-4 : 1997	MPa	521
Tensile modulus	BS EN ISO 527-4 : 1997	GPa	55.1
Flexural strength	BS EN ISO 14125 : 1998	MPa	777
Flexural modulus	BS EN ISO 14125 : 1998	GPa	46.7
Interlaminar shear strength	BS EN 2563 : 1997	MPa	64.7
Tg Onset (DMA)	ASTM 1-0003 Issue 3	°C	121
Tg Peak (DMA)	ASTM 1-0003 Issue 3	°C	135

Figure G.10: Properties of XPRegXC110

G.5 List of measurements done with the model wind turbine

Table G.3 shows all the combinations of wind speed and rotor speed done with the model wind turbine when set at blade pitch=0°.

Table G.3: Overview of measurements done with the model wind turbine set at blade pitch=0°

Wind speed (m/s)	Rotor speeds (rpm)
0	50, 59, 73, 81, 87, 90, 94, 97, 101, 104
3	50, 51, 53, 56, 59, 60
7	42, 44, 46, 48, 50, 52, 53, 56, 59, 60, 61, 64, 67, 69
9	71, 73, 74, 76
10	81, 82, 84, 87, 88, 90, 93
11.4	87, 88, 90, 93, 94, 96
12	84, 87, 89, 90, 93, 94, 96
12.5	87, 94
13	42, 44, 46, 48, 50, 52, 53, 56, 59, 60, 62, 67, 70, 72, 79, 82, 84, 87, 90, 93, 96, 97
13.5	87
14	87

For the wind turbine set at blade pitch = -30°, no wind was blown on the wind turbine. Thrust was measured for the following rotor speeds:

9.99, 20.03, 30.08, 40.04, 50.15, 60.11, 63.81 and 67.71 rpm.

Nomenclature

α	opening angle of conic diffuser
α_c	parameter used to describe amount of shear in power law profile of sheared wind of atmospheric boundary layer
β	porosity of honeycomb
Δp	static pressure drop
Δr	width of the blade section
Δs	first layer thickness
Δ_h	surface roughness in honeycomb cells
ε	turbulent dissipation=rate of dissipation of the turbulence kinetic energy per unit mass
$\frac{D}{Dt}$	material derivative
Γ	diffusion coefficient
κ	von Karman's constant
λ	scale
μ	dynamic viscosity
ν	kinematic viscosity
ω	specific dissipation rate=rate of dissipation of energy per unit volume and time
ω_r	rotor rotational speed
\bar{U}_i	Mean velocity in tensor notation
$\bar{U}, \bar{V}, \bar{W}$	average wind speeds in the above 3 directions
$\vec{\Omega}$	rotational velocity vector of platform around pitch and yaw axes
$\vec{\omega}$	rotational velocity vector of the rotor around its axis
\vec{a}_i	acceleration vector at connection to the platform tower top
\vec{e}_2	normalized vector in pulling wire's direction
\vec{F}_p	Force applied at the scaled model tower top
ρ	density of fluid

NOMENCLATURE

ρ_{air}	density of air
σ	solidity=fraction of annular area in the control volume covered by the blades
τ_w	surface shear stress
θ	local twist of blade
\vec{n}	vector normal to surface element dA
\vec{u}	velocity vector
A	unsigned absolute difference
a	axial induction factor
a'	tangential induction factor
A_C	Charnock's constant
A_m	area of the model
A_p	area of the prototype
B	centre of buoyancy
B_n	number of blades
C	additive constant in the law of the wall
c	chord
C_D	drag coefficient
C_L	lift coefficient
C_n	normal load coefficient
C_P	power coefficient
C_T	thrust coefficient
C_t	tangential load coefficient
C_w	Wave celerity
C_μ	constant of $k - \epsilon$ model ~ 0.09
CV	control volume
d	wire diameter
D_h	hydraulic diameter, $D_h = \frac{4 \times \text{cross-sectional area}}{\text{perimeter}}$
dA	surface element

NOMENCLATURE

dV	surface element
E	relative difference
Fr	Froude number
G	global centre of gravity of the platform and the wind turbine
g	acceleration of gravity
GB	distance between G and B
GM_T	distance between G and M_T
h	fixed height above ground
H_s	significant wave height
h_1	distance between the first guide vanes and the outer wall
h_2	distance between the central axis of the diffuser and the first guide vane
I	moment of inertia of spinning rotor
I_p	rotational inertia of pulley wheel around axis going through the centre of the pulley wheel
I_{uu}, I_{vv}, I_{ww}	turbulence intensity
J	second moment of area of the intersecting surface of the floating platform with the mean water surface
K	pressure drop coefficient
k	turbulence kinetic energy
L	length dimension
l	turbulence length scale
l_c	characteristic length
l_i	Integral scale of initial turbulence
L_m	length of the model
l_m	length characteristic of the model
L_p	length of the prototype
l_p	length characteristic of the prototype
L_h	Length of honeycomb cell
M	mass dimension

NOMENCLATURE

m	mass of suspended weight
m_p	mass of pulley wheel
M_T	metacentre of the floating platform
N	number of blade sections
n	number of the blade section
N_m	Number of measuring points
N_{new}	new number of sections
N_{old}	previous number of sections
P	instantaneous pressure
q	dynamic pressure of main flow through manipulator
R	radius of wind turbine
r	radius/distance of blade section from the rotor centre
R_A	ratio between areas of the prototype and areas of the model
r_n	radius for blade section number n
R_{hub}	radius of the hub
R_p	radius of pulley wheel
R_{Vol}	ratio between volumes of the prototype and volumes of the model
Re	Reynolds number
Re_m	Reynolds number characterizing the model
Re_p	Reynolds number characterizing the prototype
Re_{Δ_h}	Reynolds number inside the honeycomb, using the roughness as length scale
S_ϕ	source term in the transport equation of property ϕ
S_u	Constant component of the linear form of S_ϕ
T	time dimension
t	time
T_M	scaled wind turbine thrust
T_p	peak period
t_{new}	newly calculated thickness
t_{old}	original thickness

NOMENCLATURE

TE	new target thickness of the trailing edge
Tr	thrust
TRF	turbulence reduction factor
TSR	tip speed ratio
U	average initial velocity
U	instantaneous wind speed perpendicular to the main flow direction
u', v', w'	turbulent components in the above 3 directions
u'_i	fluctuating velocity in tensor notation
u^+	dimensionless, sublayer-scaled, velocity
U_i	instantaneous velocity in tensor notation
U_∞	free stream velocity
u_τ	friction velocity
V	instantaneous wind speed in the main horizontal direction
V_0	upstream wind speed
V_c	characteristic speed
V_m	wind speed characteristic for the model (m/s)
V_p	wind speed characteristic of the prototype
V_s	wind speed across the screen
V_{10min}	time averaged value of wind speed for a period of 10 minutes
V_∞	free stream velocity
v_{airM}	model air velocity
V_{cal}	calculated wind speed
V_{meas}	measured wind speed
V_{rel}	relative wind speed
Vel	wind speed, $Vel = \sqrt{U^2 + V^2 + W^2}$
Vol	volume of buoyancy
Vol_m	volume of the model
Vol_p	volume of the prototype
W	instantaneous wind speed in the vertical direction

X, Y, Z 3D blade section coordinates
 x_i position vector in tensor notation
 x_n, y_n normalised airfoil coordinates
 x_p airfoil pitch axis location, close to or coinciding with the centre of pressure/lift
 x_{LE} distance from the leading edge
 y^+ dimensionless, sublayer-scaled, distance
 z_0 roughness length
 ASME American Society of Mechanical Engineers
 BEM Blade Element Momentum
 CFD Computational Fluid Dynamics
 DOF Degrees of Freedom
 DTU Technical University of Denmark
 FE Finite Element
 FEA Finite Element Analysis
 LCOE levelized cost of electricity
 MPD Multi-Propeller Device
 MSWT MARIN stock wind turbine
 NREL National Renewable Energy Laboratory
 PISO Pressure-Implicit with Splitting of Operators
 RANS Reynolds-averaged Navier-Stokes
 SDG Sustainable Development Goal
 SIMPLE semi-implicit method for pressure-linked equations
 SPAR Single Point Anchor Reservoir
 SST Shear Stress Transport
 TRL Technology Readiness Level
 WACC weighted average cost of capital

List of references

- Anderson, J. D. (1995), *Computational Fluid Dynamics: The Basics with Applications*, McGraw-Hill.
- Aubrun, S., Loyer, S., Espana, G., Hayden, P. and Hancock, P. (2011), Experimental study on the wind turbine wake meandering with the help of a non-rotating simplified model and of a rotating model, *in* 'AIAA'.
- Aubrun, S., Loyer, S., Hancock, P. E. and Hayden, P. (2013), 'Wind turbine wake properties: Comparison between a non-rotating simplified wind turbine model and a rotating model', *Journal of Wind Engineering and Industrial Aerodynamics* **120**, 1–8.
URL: <http://dx.doi.org/10.1016/j.jweia.2013.06.007>
- Azcona, J., Bredmose, H., Campagnolo, F. and Pereira, R. (2017), D4 . 22 : Methods for performing scale- tests for method and model validation of floating wind turbines, Technical report.
- Bachynski, E., Chabaud, V. and Thys, M. (2016), 'Real-time hybrid testing of a braceless semi-submersible wind turbine', Presentation by SINTEF Ocean (formerly MARINTEK) and NTNU.
URL: https://www.sintef.no/globalassets/project/eera-deepwind2016/presentations/g1_bachynski.pdf
- Bachynski, E. E., Chabaud, V. and Sauder, T. (2015), Real-time hybrid model testing of floating wind turbines: sensitivity to limited actuation, *in* '12th Deep Sea Offshore Wind R&D Conference'.
- Barlow, J. B., Rae, W. H. and Pope, A. (1999), *Low-Speed Wind Tunnel Testing*, 3rd edn, Wiley, New York.
- Borg, M., Shires, A. and Collu, M. (2014), 'Offshore floating vertical axis wind turbines, dynamics modelling state of the art. part i: Aerodynamics', *Renewable and Sustainable Energy Reviews* .
- Brown, S. A. (2017), Numerical modelling of turbulence and sediment concentrations under breaking waves using OpenFOAM, PhD thesis, School of Marine Science and Engineering, University of Plymouth.
- Bulat, M. P. and Bulat, P. V. (2013), 'Comparison of turbulence models in the calculation of supersonic separated flows', *World Applied Sciences Journal* **27**(10), 1263–1266.
- Bureau Veritas (2019), Classification and certification of floating offshore wind turbines, Technical report.
- CFD-Online (2010), 'Rng k-epsilon model'. Last accessed on 2020/01/15.
URL: https://www.cfd-online.com/Wiki/RNG_k-epsilon_model

- Cobra (n.d.), 'Kincardine offshore floating wind farm scotland'. Accessed 2020/02/07.
URL: <http://www.grupocobra.com/en/proyecto/kincardine-offshore-floating-wind-farm/>
- Courbois, A. (2013), Étude expérimentale du comportement dynamique d'une éolienne offshore flottante soumise à l'action conjuguée de la houle et du vent, Phd thesis, École centrale de Nantes.
- De Ridder, E.-J., Otto, W., Zondervan, G.-J., Huijs, F. and Vaz, G. (2014), 'Development of a scaled-down floating wind turbine for offshore basin testing', *Proceedings of the ASME 2014 33rd International Conference on Ocean, Offshore and Arctic Engineering*.
- DiSchino, J. C., Broughton, P., Davies, R. and Carlisle, O. (2016), The Articulated Wind Column (AWC) as a cost-effective solution for mid to deep water environments, in 'Official Conference Proceedings 2nd International Conference on Offshore Renewable Energy (CORE 2016)'.
- DNV (2010), DNV-RP-C205 Environmental conditions and environmental loads, Technical report, DNV.
- DNV (2014), DNV-OS-J101 Design of Offshore Wind Turbine Structures, Technical report, DNV.
- DNV-GL (2018), DNVGL-SE-0422 Certification of floating wind turbines, Technical report.
- Dryden, H. L. and Schubauer, G. B. (1947), 'The Use of Damping Screens for the Reduction of Wind-Tunnel Turbulence', *Journal of the Aeronautical Sciences* **14**(4), 221–228.
- Eckert, W., Mort, K. W. and Jope, J. (1976), Aerodynamic Design Guidelines and computer program for estimation of subsonic wind tunnel performance, Technical report.
- Equinor (2020), 'Hywind tampen: the world's first renewable power for offshore oil and gas'. last accessed on 2020/10/03.
URL: <https://www.equinor.com/en/what-we-do/hywind-tampen.html>
- EWEA-WindEurope (2013), Deep water - The next step for offshore wind energy, Technical report.
URL: http://www.ewea.org/fileadmin/files/library/publications/reports/Deep_Water.pdf
- Fanchon, J.-L. (2008), *Guide de Mécanique*, Nathan, Paris, France.
- Fans & Blowers Ltd. (2016), JG - 400sBSZ100 Backward Inclined Fan. Unpublished Internal Document.
- Farrugia, R., Sant, T. and Micallef, D. (2014), 'Investigating the aerodynamic performance of a model offshore floating wind turbine', *Renewable Energy* **70**, 24–30.
URL: <https://doi.org/10.1016/j.renene.2013.12.043>

- Foster, M. (2016), 'Floating platform keels over in japan - updated', *windpower-monthly.com/*. accessed on 12/10/2020.
URL: <https://www.windpowermonthly.com/article/1394760/floating-platform-keels-japan-updated>
- Fox, R. W. and Kline, S. J. (1962), 'Flow regimes in curved subsonic diffusers', *Journal of Basic Engineering* **84**, 303–312.
- Frye, J., Horvath, N., Ndegwa, A. and Olinger, D. (2011), Design of scale-model floating wind turbine: Spar Buoy, Technical report, Worcester Polytechnic Institute.
- Fukushima Offshore Wind Consortium (2015), 'World's Largest Floating Offshore Wind Turbine "Fukushima Shimpuu" Arrived at the Testing Area'. Accessed on 03/10/2020.
URL: http://www.fukushima-forward.jp/project01/english/news_release/news150730.html
- Fukushima Offshore Wind Consortium (n.d.a), 'Fukushima Floating Offshore Wind Farm Demonstration Project (Fukushima FORWARD) - Construction of Phase I -'.
URL: <http://www.fukushima-forward.jp/pdf/pamphlet4en.pdf>
- Fukushima Offshore Wind Consortium (n.d.b), 'Fukushima Hamakaze and Fukushima Shinpu, Fukushima Floating Offshore Wind Farm Demonstration Project (Fukushima FORWARD), - Construction of Phase II -'.
URL: <http://www.fukushima-forward.jp/english/pdf/pamphlet5.pdf>
- Gao, Z. (2013), Deliverable D4.5 Functionality testing & Survival testing, Technical report, MARINA.
- Gomez, P., Sanchez, G. D., Llana, A., Gonzalez, G., Berque, J. and Aguirre, G. (2015), D1.1 Oceanographic and meteorological conditions for the design, Technical report, LIFES50+ Qualification of innovative floating substructures for 10MW wind turbines and water depths greater than 50m.
- Hall, M., Moreno, J. and Thiagarajan, K. (2014), Performance specifications for real-time hybrid testing of 1:50 - scale floating wind turbine models.
- Hansen, K. S. and Sommers, A. (2002), Program for measuring wind, wave and current at Horns Rev, Technical report, Tech-wise.
- Hansen, M. O. L. (2000), *Aerodynamics of Wind Turbines - Rotors, Loads and Structure*, James & James (Science Publishers) Ltd.
- Harvey, A. (2017), 'World's First Floating Wind Farm Powers Up off Scottish Coast'. Accessed on 2017-12-01.
URL: <http://www.powermag.com/worlds-first-floating-wind-farm-powers-up-off-scottish-coast>
- Idelchik, I. E. (1966), *Handbook of hydraulic resistance*, Vol. 8, Israel Program for Scientific Translations Ltd.
- IDEOL (2017), 'History of Ideol'. Accessed on 2017-12-14.
URL: <http://ideol-offshore.com/en/history>

- IEA Wind (2020), Definition of the IEA Wind15-Megawatt Offshore Reference Wind Turbine, Technical report.
- Imperial College London (n.d.), 'Low speed wind tunnels at imperial college'. consulted on 23/12/2021.
URL: <https://www.imperial.ac.uk/aeronautics/about/low-speed-wind-tunnels-at-imperial-college/>
- International Energy Agency (2019), Offshore Wind Outlook 2019, Technical report.
- International Energy Agency (2020a), 'Stated policies scenario'. accessed on 22/10/2020.
URL: <https://www.iea.org/reports/world-energy-model/stated-policies-scenario>
- International Energy Agency (2020b), 'Sustainable development scenario'. accessed on 22/10/2020.
URL: <https://www.iea.org/reports/world-energy-model/sustainable-development-scenario>
- Ishihara, T., Phuc, P. V., Sukegawa, H., Shimada, K. and Ohyama, T. (2007), A study on the dynamic response of a semi-submersible floating offshore wind turbine system Part 1: A water tank test, *in* 'Proceedings of the 12th ICWE', pp. 2511–2518.
- Ishihara, T., Yamaguchi, A. and Taki, S. (2014), The challenge to the world's first floating wind farm, *in* 'Grand Renewable Energy 2014'. Poster.
URL: <http://www.fukushima-forward.jp/reference/pdf/study014.pdf>
- Ishii, T. (2018), 'Poor windmill output hurts fukushima region recovery', Asahi Shimbun. accessed on 12/10/2020.
URL: <http://www.windaction.org/posts/48552-poor-windmill-output-hurts-fukushima-region-recovery.X4SMLMFKiUk>
- Jackman, T. (2005), 'Mark Drela's AG and HT Airfoils', Charles River Radio Controllers. Last accessed on 2020/01/15.
URL: <http://www.charlesriverrc.org/articles/drela-airfoilshop/markdrela-ag-ht-airfoils.htm>
- Jakubowski, M. (2009), 'The first floating wind turbines', Presentation in Brindisi, Italy, 23rd of May 2009. Accessed on 07/10/2020.
URL: <https://slideplayer.com/slide/3285597/>
- Jasak, H. (1996), Error Analysis and Estimation for the Finite Volume Method with Applications to Fluid Flows, PhD thesis, University of London.
- Jonkman, J., Butterfield, S., Musial, W. and Scott, G. (2009), 'Definition of a 5mw reference wind turbine for offshore system development', *National Renewable Energy Laboratory (NREL)*.
- Jonkman, J. M. (2007), Dynamics modeling and loads analysis of an offshore floating wind turbine, Technical report, NREL.

- Josset, C. (2018), 'Energies marines, la nouvelle vague', L'Express. Accessed on 17/10/2020.
URL: https://www.lexpress.fr/actualite/sciences/energies-marines-la-nouvelle-vague_1997079.html
- Kimball, R., Goupee, A. J., Fowler, M. J., De Ridder, E.-J., Wageningen, M. and Helder, N. J. (2014), 'Wind/Wave Basin Verification of a Performance-Matched Scale- Model Wind Turbine on a Floating Offshore Wind Turbine Platform', pp. 1–10.
- King, E. B. (2020), 'Ideol pilot doubles power yield and is 'ready for deployment'', Wind Power monthly. Accessed on 04/10/2020.
URL: <https://www.windpowermonthly.com/article/1671567/ideol-pilot-doubles-power-yield-ready-deployment>
- Kulkarni, V., Sahoo, N. and Chavan, S. D. (2011), 'Journal of Wind Engineering Simulation of honeycomb – screen combinations for turbulence management in a subsonic wind tunnel', *Jnl. of Wind Engineering and Industrial Aerodynamics* **99**(1), 37–45.
URL: <http://dx.doi.org/10.1016/j.jweia.2010.10.006>
- Kurnia, J. C., Sasmito, A. P. and Mujumdar (2014), 'Cfd simulation of methane dispersion and innovative methane management in underground mining faces', *Applied Mathematical Modelling* .
- Lai, Y. G., So, R. M. C. and Hwang, B. C. (1989), 'Calculation of planar and conical diffuser flows', *AIAA Journal* **27**(5), 542–548.
URL: <https://doi.org/10.2514/3.10144>
- Larsen, S. E., Matha, D. and Sætran, L. (2012), 'D2 . 4 : Collation of off - shore wind - wave dynamics'.
- Liao, C., Shi, K. and Zhao, X. (2019), 'Predicting the extreme loads in power production of large wind turbines using an improved pso algorithm', *Applied Sciences* **9**, 521.
- Lignarolo, L. E. M., Ragni, D., Ferreira, C. J. and van Bussel, G. J. W. (2016), 'Experimental comparison of a wind-turbine and of an actuator-disc near wake', *Journal of Renewable and Sustainable Energy* .
- Lumley, J. L. and McMahon, J. F. (1967), 'Reducing water tunnel turbulence by means of a honeycomb', *Journal of basic engineering* pp. 764–770.
- MacMahon, E., Stock, A., Jamieson, P. and Leithead, B. (2015), Yaw control for 20 mw offshore multi-rotor system.
- Maric, T., Hopken, J. and Kyle, M. (2014), *The OpenFOAM Technology Primer*, source-flux.
- Martin, H. R. (2011), Development of a scale model wind turbine for testing of offshore floating wind turbine systems, Master's thesis, University of Maine.
- Martin, H. R., Kimball, R. W., Viselli, A. M. and Goupee, A. J. (2012), Methodology for Wind/Wave Basin Testing of Floating Offshore Wind Turbines, in 'ASME 2012 31 st

- International Conference on Ocean, Offshore and Arctic Engineering OMAE 2012', Vol. 136, ASME, Rio de Janeiro, Brazil, July 1-6, pp. 445–454.
- Matha, D., Sandner, F., Molins, C., Campos, A. and Cheng, P. W. (2015), 'Efficient preliminary floating offshore wind turbine design and testing methodologies and application to a concrete spar design', *Philosophical Transactions of the Royal Society A Mathematical, Physical and Engineering Sciences* .
- Mehta, R. D. and Bradshaw, P. (1979), 'Design Rules for Small Low Speed Wind Tunnels', *The Aeronautical Journal of the Royal Aeronautical Society* (November 1979), 443–449.
- Menter, F. R. (1993), Zonal two equation k-omega turbulence models for aerodynamic flows, in '24th Fluid Dynamics Conference'.
- Meyer, K. E., Nielsen, L. and Nielsen, N. (2004), Flow structures in large-angle conical diffusers measured by piv, in 'Proceedings of 12th International Symposium on Application of Laser Techniques to Fluid Mechanics'.
- Ministère de la transition écologique (2018), 'Énergies marines renouvelables'. accessed on 17/10/2020.
URL: <https://www.ecologie.gouv.fr/energies-marines-renouvelables-0>
- Molga, P. (2021), 'BW prend le contrôle d'Ideol pour créer un leader de l'éolien offshore', LesEchos.
URL: <https://www.lesechos.fr/pme-regions/innovateurs/bw-prend-le-contrôle-d-ideol-pour-creer-un-leader-de-leolien-offshore-1303879>
- Naqvi, S. K. (2012), Scale model experiments on floating offshore wind turbines, Master's thesis, Worcester Polytechnic Institute.
- NREL (2019), 'Nrel 5-mw reference turbine'. Last accessed on 2020/01/15.
URL: <https://wind.nrel.gov/forum/wind/viewtopic.php?t=363>
- NS Energy (n.d.), 'Kincardine floating offshore wind farm, scotland'. accessed 2020/02/07.
URL: <https://www.nsenergybusiness.com/projects/kincardine-floating-offshore-wind-farm-scotland/>
- OffshoreWIND.biz (2017), 'Stiesdal TetraSpar Floating Offshore Wind Foundation Put to the Test'. Accessed on 2017-12-01.
URL: [offshorewind.biz/2017/06/15/stiesdal-tetraspar-floating-offshore-wind-foundation-put-to-the-test/](https://www.offshorewind.biz/2017/06/15/stiesdal-tetraspar-floating-offshore-wind-foundation-put-to-the-test/)
- offshorewind.biz (2020a), 'Construction starts on world's largest floating offshore wind farm'. Last consulted 03/10/2020.
URL: <https://www.offshorewind.biz/2020/10/01/construction-starts-on-worlds-largest-floating-offshore-wind-farm/>
- offshoreWIND.biz (2020b), 'Windfloat atlantic fully up and running'. Last consulted 03/10/2020.

- URL:** <https://www.offshorewind.biz/2020/07/27/windfloat-atlantic-fully-up-and-running/>
- Ohana, J., Le Boulluec, M., Peron, E., Klinghammer, C., Tancray, A. and Mansuy, E. (2014), Open jet blower type wind generator with variable wind speed capability for physical model testing of offshore structures, *in* 'Coastlab14 -5th International Conference on Application of Physical Modelling to Port and Coastal Protection', Varna, Bulgaria, 29 September - 2 October.
- Ohana, J., Le Boulluec, M., Peron, E., Klinghammer, C., Tancray, A. and Mansuy, E. (2014a), 'Générateur de vent pour le modélisation physique de structures offshore', Poster for Journées de l'Hydrodynamique, Val de Reuil.
URL: <https://archimer.ifremer.fr/doc/00233/34390/>
- OLDSAILOR, m. (2007), 'Blue h technologies launches world's first floating wind turbine'. consulted on 23 September 2020.
URL: <http://www.marinebuzz.com/2007/12/08/blue-h-technologies-launches-worlds-first-floating-wind-turbine/>
- OpenFOAM (2012).
URL: https://www.openfoam.com/documentation/guides/latest/api/classFoam_1_1RASModels_1_1kOmega.html
- OpenFOAM (2015a), 'airfoil2d'. last accessed on 2020/01/25.
URL: <https://github.com/OpenFOAM/OpenFOAM-2.4.x/tree/master/tutorials/incompressible/simpleFoam/airFoil2D>
- OpenFOAM (2015b), 'Openfoam differencing schemes'. last accessed on 2020/02/06.
URL: <https://cfd.direct/openfoam/user-guide/v4-fvSchemes/#x19-1370004.4>
- OpenFOAM (2016).
URL: <https://github.com/OpenFOAM/OpenFOAM-4.x/blob/master/src/TurbulenceModels/turbulenceModels/RAS/kOmega/kOmega.H>
- Otter, A., Murphy, J. and Desmond, C. J. (2020), 'Emulating aerodynamic forces and moments for hybrid testing of floating wind turbine models', *Journal of Physics: Conference Series* **1618**, 032022.
URL: <https://doi.org/10.1088%2F1742-6596%2F1618%2F3%2F032022>
- Ozkan, A. (2013), Aerodynamic Design of Turbine Blades Using Full Dynamic Analysis of a Wind Turbine, *in* 'Proceedings of the Conference on Wind Energy Science and Technology'.
- Pegalajar-Jurado, A., Hansen, A. M., Laugesen, R., Mikkelsen, R. F., Borg, M., Kim, T., Heilskov, N. F. and Bredmose, H. (2016), 'Experimental and numerical study of a 10MW TLP wind turbine in waves and wind', *Journal of Physics: Conference Series* **753**, 092007.
- Philippe, M. (2012), Couplages aéro-hydrodynamiques pour l'étude de la tenue à la mer des éoliennes offshore flottantes, PhD thesis, Ecole Centrale de Nantes.

- PowerTechnology (n.d.), 'Fukushima floating offshore wind farm'. Accessed on 06/10/2020.
URL: <https://www.power-technology.com/projects/fukushima-floating-offshore-wind-farm/>
- Prandtl, L. (1933), Attaining a steady air stream in wind tunnels, Technical report.
- Principle Power (2011), 'Principle Power Facebook page'. Post from 4th Dec. 2011.
URL: <https://www.facebook.com/photo/?fbid=10150499764971142>
- Principle Power News (2020), 'WindFloat Atlantic project starts supplying clean energy in Portugal'. Accessed on 2020-02-07.
URL: <https://www.edpr.com/en/news/2020/01/02/windfloat-atlantic-project-starts-supplying-clean-energy-portugal>
- Prync-Skotniczny, K. (2006), 'Numerical analysis of the impact of conical diffuser geometry change on velocity distribution in its outlet cross-section', *Mechanics / AGH University of Science and Technology* **25**(2).
URL: <https://journals.bg.agh.edu.pl/MECHANICS/2006-02/mech03.pdf>
- Radtke, K. (2018), 'Setback for japanese offshore wind efforts', windfair.net. accessed on 06/10/2020.
URL: <https://w3.windfair.net/wind-energy/news/29116-wind-turbine-floater-japan-coast-capacity-factor-yield-turbine-lower>
- renewableUK (2020), 'Wind energy statistics'. accessed on 22/10/2020.
URL: <https://www.renewableuk.com/page/UKWEDhome>
- Roddier, D., Cermelli, C., Aubault, A. and Weinstein, A. (2010), 'WindFloat: A floating foundation for offshore wind turbines', *Journal of Renewable and Sustainable Energy* **2**, 1–34.
URL: <https://doi.org/10.1063/1.3435339>
- Runstadler, P. W. and Dolan, F. X. (1975), *Diffuser Data Book*, Creare Incorporate. Can be obtained upon request at info@creare.com.
- Sajben, M., Chen, C. and Kroutil, J. (1977), 'A new passive boundary-layer control device', *Journal of Aircraft* **14**(7), 654–660.
- Sandner, F., Amann, F., Matha, D., Azcona, J., Munduate, X., Bottaso, C. L., Campagnolo, F., Bredmose, H., Manjock, A., Pereira, R. and Robertson, A. (2014), 'Model Building and Scaled Testing of 5 MW and 10 MW Semi-Submersible Floating Wind Turbines', Presentation for EERA Deepwind'2015, Trondheim.
URL: https://www.sintef.no/globalassets/project/eera-deepwind-2015/presentations/e/e2_sandner_univ-stuttgart.pdf
- Sarmiento, J., Iturrioz, A., Ayllon, V., Guanche, R. and Losada, I. J. (2019), 'Experimental modelling of a multi-use floating platform for wave and wind energy harvesting', *Ocean Engineering*.

- Sauder, T., Chabaud, V., Thys, M., Bachynski, E. E. and Saether, L. O. (2016a), Real-Time Hybrid Model Testing of a Braceless Semi-Submersible Wind Turbine: Part I — The Hybrid Approach, *in* 'ASME 2016 35th International Conference on Ocean, Offshore and Arctic Engineering'.
- Sauder, T., Chabaud, V., Thys, M., Bachynski, E. E. and Saether, L. O. (2016b), Real-time hybrid model testing of a braceless semi-submersible wind turbine. Part II: Experimental results, *in* 'ASME 2016 35th International Conference on Ocean, Offshore and Arctic Engineering'.
- Sawaji, O. (2016), 'The World's Largest Floating Wind Farm', Public Relations Office Government of Japan. Accessed on 04/10/2020.
URL: https://www.gov-online.go.jp/eng/publicity/book/hlj/html/201609/201609_03_en.html
- Scheimann, J. (1981), Comparison of Experimental and Theoretical Turbulence Reduction Characteristics for Screens, Honeycomb, and Honeycomb-Screen Combinations, Technical report, NASA.
- SeekPNG (n.d.), 'Wind Turbine Line Art - Wind Turbine Line Drawing'.
URL: https://www.seekpng.com/ipng/u2q8q8i1o0i1o0u2_wind-turbine-line-art-wind-turbine-line-drawing/
- Shaheed, R. and Mohammadian, A. (2019), 'A comparison of standard $k-\epsilon$ and realizable $k-\epsilon$ turbulence models in curved and confluent channels', *Environmental Fluid Mechanics* .
- Sheerin, P., Sforza, P. M. and Smorto, M. (1981), 'Three-dimensional wakes of simulated wind turbines', *American Institute of Aeronautics and Astronautics* **19**, 1101–1107.
- Shukri, E. (2018), 'Analytical velocity study in a conical diffuser with screw tape inserts', *MATEC Web of Conferences* **153**, 06003.
- Skopljak, N. (2020), '7 MW Fukushima Turbine Starts Final Voyage', offshoreWIND.biz. Last consulted 04/10/2020.
URL: <https://www.offshorewind.biz/2020/06/24/7-mw-fukushima-turbine-starts-final-voyage/>
- Spalart, P. and Allmaras, S. R. (1994), 'A one-equation turbulence model for aerodynamic flows', *La Recherche Aéronautique* .
- Sparrow, E. M., Abraham, J. P. and Minkowycz, W. J. (2009), 'Flow separation in a diverging conical duct: Effect of reynolds number and divergence angle', *International Journal of Heat and Mass Transfer* .
- Steffen, L. (2019), 'The world's biggest wind turbine starts generating enough electricity to power 30,000 homes'.
URL: <https://www.intelligentliving.co/worlds-biggest-wind-turbine/>
- Stiesdal, H. (2016), 'Stiesdal TetraSpar Industrialized Floating Foundation'.

- Tomasicchio, G. R., Felice, D., Musci, E., Fonseca, N., Mavrakos, S. A., Kirkegaard, J., Katsaounis, G. M., Penchev, V., Schuttrumpf, H., Wolbring, J. and Armenio, E. (2014), Physical model experiments on floating off-shore wind turbines, in 'Hydralab IV Joint User meeting, Lisbon'.
- Tran, T.-T. and Kim, D.-H. (2015), 'The platform pitching motion of floating offshore wind turbine: A preliminary unsteady aerodynamics analysis', *Journal of Wind Engineering and Industrial Aerodynamics*.
- Twele, J. and Gasch, R. (2007), *Windkraftanlagen: Grundlagen, Entwurf, Planung und Betrieb*, 5th edn, Teubner, Wiesbaden, Germany.
- UIUC Applied Aerodynamics Group - Department of Aerospace Engineering (n.d.), 'UIUC Airfoil Coordinates Database'.
URL: https://m-selig.ae.illinois.edu/ads/coord_database.html
- Vadlamani, U. (2010), Field measurement and verification of residential duct leakage methods and cfd analysis of hvac mixing box, Master's thesis, University of Nevada, Las Vegas.
- Veldhuis, L., Jansen, D., El Haddar, J. and Correale, G. (2012), Novel passive and active flow control for high lift, in 'Proc. 28th International Congress of the Aeronautical Sciences, Brisbane, Australia'.
- Verne, J. (1870), *20,000 leagues under the sea*.
- Versteeg, H. K. and Malalasekera (2007), *An Introduction to Computational Fluid Dynamics: The Finite Volume Method*, 2nd edn, Pearson Prentice Hall.
- Wan, L., Gao, Z. and Moan, T. (2014a), Model Test of the STC Concept in Survival Modes, in 'International conference on Ocean, Offshore and Arctic Engineering', ASME.
- Wan, L., Gao, Z. and Moan, T. (2014b), Survival modes tests of a combined wind and wave concept – spar torus combination (stc), Technical report, MARINET.
- Wang, C. M., Utsunomiya, T., Wee, S. C. and Choo, Y. S. (2010), 'Research on floating wind turbines: a literature survey', *The IES Journal Part A: Civil & Structural Engineering* **3**(4), 267–277.
URL: <http://www.tandfonline.com/doi/abs/10.1080/19373260.2010.517395>
- White, F. M. (2008), *Fluid mechanics*, McGraw Hill, Berlin.
- White, F. M. (2016), *Fluid mechanics - Eighth Edition in SI Units*, McGraw-Hill Education.
- Wilcox, D. C. (1998), *Turbulence modeling for CFD*, DCW Industries, La Canada, CA.
- Wilcox, D. C. (2006), *Turbulence Modeling for CFD*, DCW Industries.
- Wiser, R., Jenni, K., Seel, J., Baker, E., Hand, M., Lantz, E. and Smith, A. (2016), 'Expert elicitation survey on future wind energy costs', *nature energy* (16135).

- Wright, C., Desmond, C. and Lynch, K. (2015a), Report on physical modelling methods for floating wind turbines, Technical report, Marinet, UCC-HMRC.
- Wright, C., O'Sullivan, K., Murphy, J. and Pakrashi, V. (2015), Experimental Comparison of Dynamic Responses of a Tension Moored Floating Wind Turbine Platform with and without Spring Dampers, *in* '11th International Conference on Damage Assessment of Structures (DAMAS 2015)'.
- Yakhot, V., Orszag, S., Thangam, S., Gatski, T. and Speziale, C. (1992), 'Development of turbulence models for shear flows by a double expansion technique.', *Physics of Fluids A Fluid Dynamics* **4**.
- Yang, J., Zhang, Y., Chen, H. and Fu, S. (2020), 'Flow separation control in a conical diffuser with a Karman-vortex generator', *Aerospace Science and Technology* **106**, 106076.
URL: <https://www.sciencedirect.com/science/article/pii/S1270963820307586>
- Zhu, S., Srebric, J., Rudnick, S. N., Vincent, R. L. and Nardell, E. A. (2014), 'Numerical modeling of indoor environment with a ceiling fan and an upper-room ultraviolet germicidal irradiation system', *Build Environ.* .